

Quasi-Optical Design and Analysis of a Bolometric Interferometer for Cosmic Microwave Background Radiation Experiments



**Maynooth
University**

National University
of Ireland Maynooth

**Maynooth University
Department of Experimental Physics**

Stephen Scully BSc (Eng) HDip (App Phy)

A thesis submitted for the degree of
Doctor of Philosophy

February 2016

Department Head
Prof. J. Anthony Murphy

Supervisor
Dr. Cr  idhe O'Sullivan

TABLE OF CONTENTS

1	INTRODUCTION	1
1.1	COSMOLOGY AND THE CMB.....	1
1.1.1	<i>Historical</i>	1
1.1.2	<i>The Big Bang Theory</i>	3
1.1.3	<i>Inflation</i>	7
1.1.4	<i>Angular power spectrum of the CMB</i>	7
1.2	MEASURING THE CMB	8
1.2.1	<i>Temperature</i>	9
1.2.2	<i>Polarisation</i>	13
1.2.3	<i>Constraining cosmological models</i>	19
1.2.4	<i>Measurements</i>	21
1.3	INTERFEROMETRY	23
1.3.1	<i>Interferometry basics</i>	23
1.3.2	<i>Interferometry operation</i>	23
1.4	SUMMARY.....	33
1.5	THESIS OUTLINE.....	34
2	OPTICAL AND ELECTROMAGNETIC MODELLING	36
2.1	FEED HORN ANALYSIS TECHNIQUES.....	38
2.1.1	<i>TE and TM modes</i>	38
2.1.2	<i>Mode matching techniques</i>	44
2.1.3	<i>Singular value decomposition</i>	51
2.1.4	<i>Dispersion curves</i>	54
2.1.5	<i>Hybrid modes</i>	56
2.2	FREE-SPACE ANALYSIS TECHNIQUES	59
2.2.1	<i>Geometrical optics (GO) and geometric theory of diffraction (GTD)</i>	60
2.2.2	<i>Physical optics (PO) and theory of diffraction (PTD)</i>	62
2.2.3	<i>Gaussian beam modes (GBM)</i>	65
2.3	SYSTEM ANALYSIS TOOLS	83
2.3.1	<i>Overview</i>	84
2.3.2	<i>Model system components</i>	85
2.3.3	<i>Propagating the aperture field</i>	88
2.3.4	<i>Sampling density</i>	89
2.3.5	<i>Extracting data from the simulations</i>	90
2.3.6	<i>Automation of simulations</i>	92
2.3.7	<i>Comparing MODAL and GRASP</i>	93

2.4	CONCLUSION	95
3	QUBIC	97
3.1	PATHFINDERS.....	97
3.1.1	<i>MBI</i>	97
3.1.2	<i>BRAIN</i>	103
3.2	QUBIC DESIGN	105
3.2.1	<i>Overview</i>	105
3.2.2	<i>QUBIC v1.0</i>	107
3.2.3	<i>QUBIC design v2.0</i>	121
3.3	QUBIC v2.0 DETAILS OF MIRROR DESIGN.....	125
3.3.1	<i>Definition of global reference frame</i>	125
3.3.2	<i>Definition of primary mirror</i>	127
3.3.3	<i>Definition of secondary mirror</i>	130
3.3.4	<i>Definition of input feed horn array</i>	132
3.4	PRELIMINARY QUBIC MODELLING	134
3.4.1	<i>Gaussian beam mode analysis</i>	134
3.4.2	<i>PO analysis</i>	137
3.5	CONCLUSION	142
4	QUBIC ANALYSIS AND OPTIMISATION	144
4.1	SPILLOVER AND BEAM TRUNCATION.....	144
4.1.1	<i>Visualisation of 400 beams</i>	144
4.1.2	<i>Beam truncation by the primary mirror</i>	147
4.1.3	<i>Beam truncation by the secondary mirror</i>	149
4.1.4	<i>Beam truncation at the detector plane</i>	151
4.1.5	<i>Bolometer detector array</i>	154
4.2	MIRROR TOLERANCE ANALYSIS	157
4.3	POLARISER AND SIDE DETECTOR	160
4.3.1	<i>Orientation of polariser and side detector</i>	160
4.3.2	<i>Separation of polariser and side detector</i>	168
4.3.3	<i>Determination of polariser dimensions</i>	177
4.3.4	<i>Polariser optical surface imperfections</i>	183
4.4	COLDSTOP	196
4.5	MANUFACTURING LIMITATIONS.....	201
4.5.1	<i>Source relocation</i>	201
4.5.2	<i>Truncation (420 mm limit)</i>	208
4.6	CONCLUSION	219

5	QUBIC PERFORMANCE	220
5.1	BASELINE SEPARATION	220
5.2	THE WINDOW FUNCTION	225
5.3	THE POINT SPREAD FUNCTION (PSF).....	226
5.3.1	<i>Calculation of the real PSF</i>	226
5.3.2	<i>Input and detector array orientation</i>	228
5.4	SUMMARY AND CONCLUSIONS.....	230
6	DUAL-BAND COMBINER OPTIMISATION	231
6.1	12.9° ELEMENT OPTIMISATION.....	231
6.1.1	<i>Primary mirror</i>	231
6.1.2	<i>Secondary mirror</i>	233
6.1.3	<i>Polariser and side detector</i>	234
6.1.4	<i>Polariser thickness</i>	237
6.1.5	<i>Large side detector blockage</i>	240
6.1.6	<i>Coldstop</i>	242
6.1.7	<i>Bolometer array</i>	244
6.1.8	<i>Stray light</i>	246
6.2	APERTURE FEED HORN ARRAY POSITION OPTIMISATION	247
6.3	NEW FEED HORN DESIGN	257
6.4	DUAL BAND OPERATION (220 GHz ANALYSIS)	264
6.4.1	<i>The PSF of the dual-band combiner</i>	275
6.5	EFFECT OF COMBINER ELEMENTS ON SENSITIVITY.....	281
6.6	CONCLUSION	283
7	CONCLUSIONS	285
	FUTURE WORK	288
	PUBLICATIONS.....	288
8	BIBLIOGRAPHY.....	290

Acknowledgements

I would like to start by expressing my sincere gratitude to my supervisor, Dr. Cr  idhe O’Sullivan, who over the last 4 years has provided continuous support imparting vital knowledge and showing amazing patience in the proofing of this thesis. A better supervisor, I cannot imagine. In addition I would also like to thank Dr. Marcin Gradziel for the countless hours of development work on MODAL and the maintenance of the cluster without which the enormous task of simulating QUBIC would not have been possible. I would also like to thank the head of the department, Professor Anthony Murphy, whose quasi-optical mathematical knowledge came in extremely useful on several occasions. I would like to give a big thank you to the remainder of the department whom all, on various occasions, aided my research journey in the completion of this PhD. For financial support throughout this project I would like to thank the graduate studies offices who awarded me a full scholarship for the duration of this PhD. Special thanks goes out to my fellow roommates, Dr. Daniel Wilson, Mr. Donnacha Gayer and Mr. Fiacra Cahill for the in-depth stimulating discussions on topics far, wide and reaching. Generally, thanks to all the staff and post-graduates of the Experimental Physics Department, without exception you all added to a great experience here at Maynooth University. Last but not least,

A special dedication

A journey that started with a novel concept of returning to college after 15 years led to one of the most amazing experiences in my life. I would like to dedicate this thesis to my wife, Ciara, for all her love and support, who supported me emotionally (and financially), was there at every turn. I mean every turn of every proof read page in this thesis.

Thank you all for making my time here one to remember.

Abstract

From humble beginnings in 2008, a group met to propose the idea of observing the Cosmic Microwave Background (CMB) in order to determine its polarisation properties, i.e. E- and B-modes. B-modes, a smoking gun for inflation theory, are a long sought after observation for cosmologists. From this the QUBIC collaboration was born. Here we explore the scientific justification for such a mission and the aims of the QUBIC telescope in furthering this knowledge with emphasis on the author's contribution to this end. B-modes are far fainter than any other signal that cosmology has attempted detection of before making them a challenge and requiring a new type of telescope with exceptional sensitivity and control of systematics. The author was heavily involved in the design and analysis of the optical combiner here at the Department of Experimental Physics in Maynooth University.

This thesis describes the analysis techniques used for the characterisation of the operation of the QUBIC instrument. These techniques: TE/TM mode matching, Gaussian beam mode analysis and physical optics were used in determination of the behaviour of the instrument in 2 bands, 150 GHz and 220 GHz with 25% bandwidth in each case. The analysis was done mainly using 2 software packages, SCATTER and MODAL, both of which are in-house developments and as such offer customisation of their capabilities. QUBIC required detailed analysis which led to design modifications and allowed for confident design of new elements for inclusion in the optical-combiner.

I present an optical design for QUBIC, a bolometric interferometer for cosmology which, at the time printing, is under construction awaiting shipping to Dome-C Antarctica to commence observation.

1 Introduction

The Cosmic Microwave Background (CMB) is the remnant radiation of the Big Bang, first detected at radio frequencies and exhibiting today a blackbody spectrum peaking in the THz band. It holds within it details of the primordial structure of the universe. Current missions have given us unprecedented levels of detail on the CMB but until now we have been limited to the temperature maps and some measurements of E-mode polarisation.

It is the next step that this thesis concerns itself with: the design of an instrument to measure B-mode polarisation in the CMB, namely the QUBIC (Q and U Bolometric Interferometer for Cosmology) instrument. It is this B-Mode polarisation that holds the key to breaking the degeneracy in the determination of the cosmological parameters from the inhomogeneities in the temperature maps. Its detection would also be the first direct measurement of inflation and place constraints on its energy scale.

In this chapter I give a brief introduction to the CMB, describing its polarisation properties in particular. I then discuss interferometry techniques as they are used to make astronomical measurements, concentrating on a Fizeau implementation as used in the QUBIC instrument.

1.1 Cosmology and the CMB

1.1.1 Historical

Modern-day precision cosmology builds on work started in 1931 when the first radio-astronomical measurements taken showed radio waves coming from the Milky Way Galaxy (Jansky, 1933). Jansky found and categorised various signals, one of which he termed “star noise”. This star noise was a faint steady hiss of unknown origin, strongest in the direction of the Galactic centre. It repeated every 23 hours and 56 minutes, the sidereal period, showing it came from outside our solar system. The birth of radio astronomy and the pairing of its measurements with optical counterparts over the next few decades paved the way for measurements across all

frequency bands. By 1948, the theory of relativity and measurements by Hubble, confirming the theories of Friedmann in 1922, showed the universe could not remain static and that it was expanding. There were 2 main competing theories, the “Steady State” and “Big Bang” theories, which could account for this expansion. The main concepts of each are described below

The Steady State theory: Matter is continuously created to fill the void left by an expanding universe and therefore on the whole does not change overtime (*the perfect cosmological principle*); this leads to an always existing never ending universe (Jeans, 1928). The rate of mass creation required to achieve this is quite low at roughly 1 atom per m^3 per billion years and about 5 times as much dark matter (Hoyle, 1948). The major failing of this theory was its lack of accountability for heavier atoms. Nucleosynthesis alone could not account for the observable abundances.

The Big Bang theory: Lemaitre, in the late 1920s, proposed what he termed the *primeval atom* (Lemaître, 1927) where the expanding universe is getting less dense and cooler as time advances. The theory of the primeval atom was called “The Big Bang” by Fred Hoyle in an attempt to ridicule it but ironically ended up giving it its famous name with all cosmologies now that theorise an expanding universe referred to as *Big Bang Cosmologies*. Stemming from this theory of expansion and cooling, running time in reverse would yield a denser and hotter universe where heavier elements, up to ^4He , could be created by means of nuclear reactions (Gamow, et al., 1948) thus explaining the large abundances of the lighter elements. First envisaged in 1948, the remnant radiation from this early phase was predicted to be observable, with an estimated present day value of 5 K (Alpher & Herman, 1948).

Both theories had their strengths. For example, the Big Bang theory explained matter abundances, especially that of ^4He , and the distribution of galaxies of different ages. The Steady State theory explained matter/energy density and constancy of physical laws and age of the universe. Observations of the 1950s were

unable to categorically state which was correct. In the 1960s, using a radio telescope, a faint background radiation with a temperature of 3.5 ± 1.0 K (Penzias & Wilson, 1965) that was not coming from any specific astronomical object was accidentally detected. It was determined to be the CMB, (Dicke, et al., 1965) illustrated in *Figure 1.1* below, for the discovery of which Penzias & Wilson were awarded the Nobel Prize in 1978.

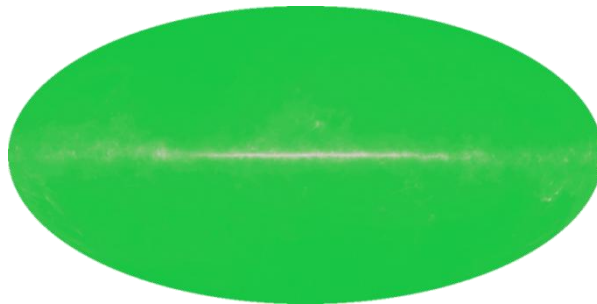


Figure 1.1: This is a simulated image showing a view of the sky as would have been seen by the microwave receiver of Penzias and Wilson (1965), if it could have surveyed the whole sky. The average value of 3.5 K in green with the galactic foregrounds shown in white (NASA / WMAP Science Team, 2010).

The Steady State theory could not account for this background radiation but the Big Bang explained it naturally as the remnant radiation from that hot dense phase almost 14 billion years earlier. It was this observation that solidified the Big Bang theory as the leading theory and helped sway theorists from the Steady State theory.

1.1.2 The Big Bang Theory

The Primordial Universe: According to the Big Bang theory, the universe started from a hot dense phase, expanded and cooled. For the first 380,000 years, see *Figure 1.2*, the early universe remained at a temperature > 4000 K (4000 K only ionises $\sim 10\%$ of the baryonic-matter but this is sufficient, through collisions, to maintain thermal equilibrium). The universe contained a primordial soup of essentially plasma, ions and electrons strongly coupled to the photon field (the photon-baryon fluid). The large scattering cross-section of the free electrons resulted in the photons being continually scattered, making this early universe opaque and keeping it in a state of thermal equilibrium and therefore exhibiting a

blackbody spectrum. This spectrum was confirmed experimentally, to within 1% of peak intensity, to have a temperature of 2.735 ± 0.06 K over a wavelength range of 10 to 0.5 mm (Mather, et al., 1990) using NASA's COBE satellite (Smoot, et al., 1992).

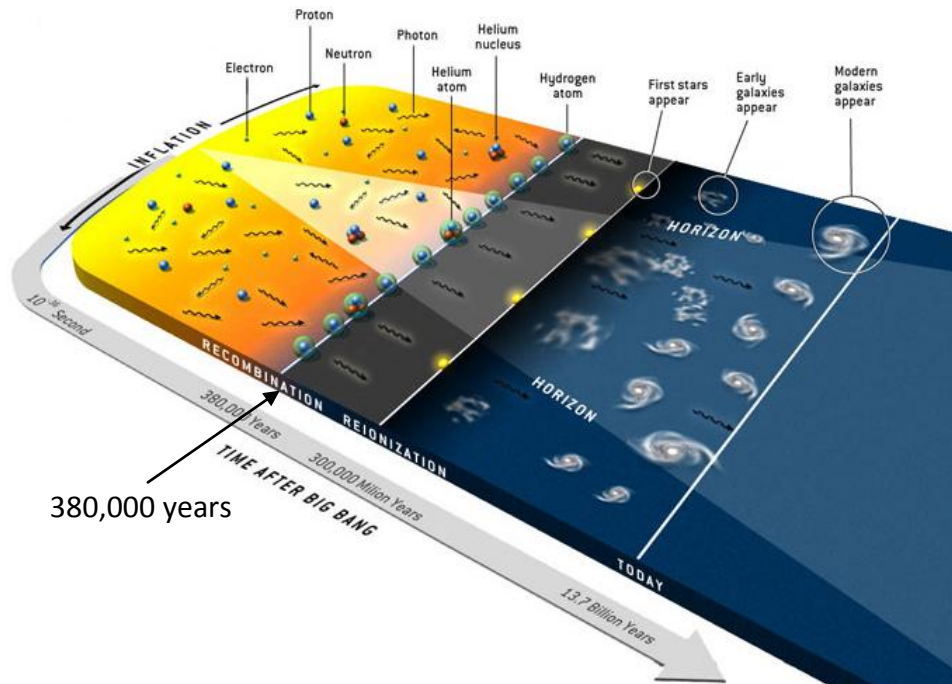


Figure 1.2: Expansion of the Universe and particle horizon (Credit: Bryan Christie Design)

Recombination: After the initial $\sim 380,000$ year period the temperature dropped, below 4000 K, allowing the electrons and protons to combine to form the first atoms, a process known as recombination (Peebles, 1968). As photons do not interact strongly with neutral atoms, the photons decoupled from the matter and the mean free path of the photons became comparable to the size of the observable universe. Matter now free of the pressure of radiation began to coalesce under gravity in the denser regions where the first galaxies and stars began to form.

The Last Scattering Surface: The background radiation, composed of the photons from the initial hot dense phase, now with a mean free path comparable to the size of the universe, were free to travel subject only to the effects of cosmological redshift. This radiation, expanding with the universe, fills all of space. The photons today appear to originate from a spherical surface, see [Figure 1.3](#), with a radius equal

to their travel distance since last scattering $\sim 380,000$ years after the Big Bang. This spherical surface, known as the last scattering surface (LSS), contains within it an imprint of the structure of the universe at this time.

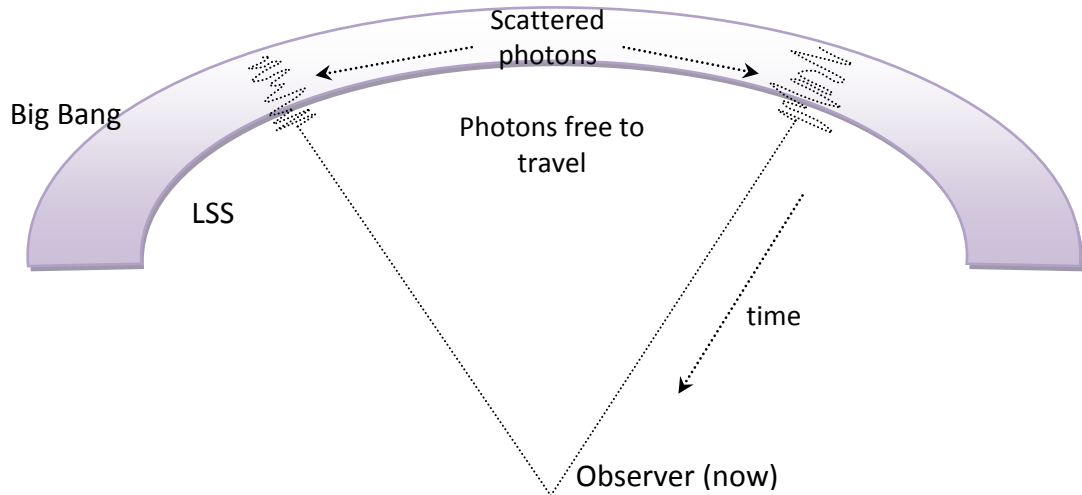


Figure 1.3: LSS as it appears to us today, a spherical surface with radius equal to that of the travel distance of the photons since they were last scattered 380,000 years after the Big Bang.

Today: Observations show the temperature variations in the LSS (COBE showing $\frac{\Delta T}{T} \approx 10^{-5}$ (Smoot, et al., 1992)) are of a size and magnitude that would be expected for a universe with our large scale structure (Zhan, et al., 2014). The most recent measurements give a Hubble constant $H_0 = 67.80 \pm 0.77$ km/s/Mpc and an age of the universe of 13.798 ± 0.037 billion years (PLANCK-Collaboration, 2013a).

These early successes of the Big Bang theory were immense but there were several issues that it couldn't account for (see Ostlie and Carroll (Ostlie & Carroll, 2007) for a review).

Problems: A finite universe, expanding from a hot dense state, implies a limit to the distance which photons and matter can have travelled. Regions subtending more than $\sim 1^\circ$ on the LSS today are at the limit of causal connection and yet are still observed to be essentially in thermal equilibrium. How could regions that cannot have exchanged photons have the same temperature to within $\frac{\Delta T}{T} \approx 10^{-5}$? (This is known as the horizon problem).

A universe expanding from a dense state should eventually collapse or expand forever depending on the energy/density component of the universe. There is a critical density above which the universe's fate is sealed in an eventual collapse or below which it will expand forever, see *Figure 1.4*. The total energy density of the universe has several constituents: Ω_b , the fractional density of baryonic matter, Ω_m , the fractional density of both baryonic and dark matter and Ω_Λ , the fractional density of dark energy. The total energy density is therefore $\Omega_o = \Omega_m + \Omega_\Lambda$. Cosmological models that include contributions from dark energy and cold dark matter are known as Λ CDM models. Density is often measured as a fraction of the critical density, ρ_c , i.e. $\Omega_m = \frac{\rho_m}{\rho_c}$ etc.. Ω_o is currently known to have a value very close to unity. In fact, latest measurements show the constituents of Ω_o are: $\Omega_\Lambda \approx 0.683$, $\Omega_m \approx 0.317$ and $\Omega_b \approx 0.049$ (Hinshaw, et al., 2013; PLANCK-Collaboration, 2013c; ESA, 2015). In the past it must have been even closer to 1 ($\Omega_o - 1$ is an increasing function of time). This essentially infers a value of $\Omega_o = 1$ for the initial density of the universe making it exactly flat, remarkable if purely coincidence (this is known as the flatness problem).

Another issue lies in Grand Unified Theories (GUT's) which predict relic particles e.g. magnetic monopoles. Theories not predicting them are not compatible with hot Big Bang theories. The Big Bang theory cannot account for the lack of magnetic monopoles which as of today have still eluded detection.

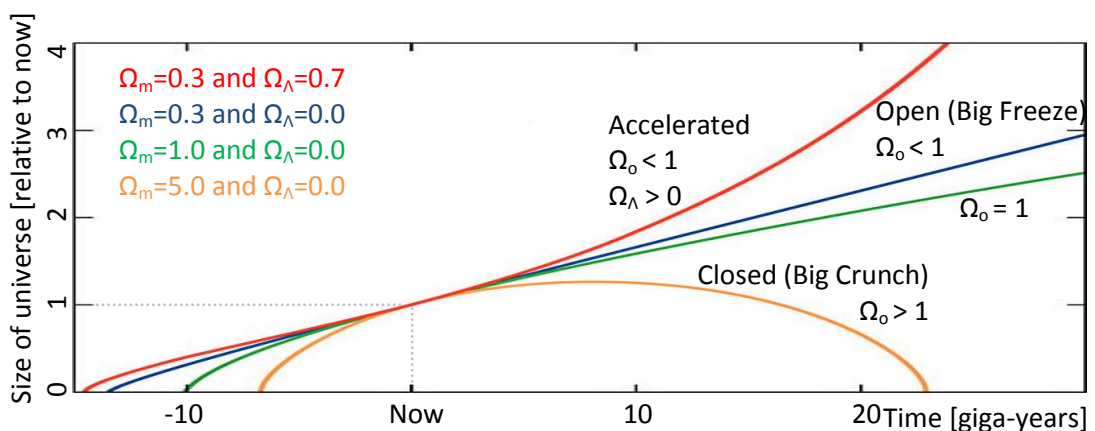


Figure 1.4: The universe extent as a function of time, showing an open and closed universe corresponding to the 'Big Freeze' and 'Big Crunch'. The parameters: Ω_o (mass energy), Ω_Λ (dark energy) and Ω_c (critical density), determine which path the universe will follow. (NASA/WMAP Science Team, 2010)

Something created inhomogeneities in the universe allowing large scale structure to form, equalised the temperature of the observable universe, caused the universe to expand faster than light, left it extremely flat and eradicated magnetic monopoles or at least made them very scarce. The Big Bang theory alone could not account for these issues.

1.1.3 Inflation

In an attempt to explain these issues, and others, the theory of Inflation (Guth, 1981) was added to the Big Bang theory. Inflation states that the early universe was dominated by vacuum energy and shortly after the Big Bang it underwent an exponential expansion, of the order of a factor of e^{100} . This meant that initially causally connected regions of the universe became separated by distances greater than the Big Bang causal horizon. The inflationary expansion also caused the local universe to appear flat driving the density towards the critical density, regardless of its initial curvature. The expansion also dilutes the relic particles in space giving some explanation as to why they are as yet undiscovered. Quantum fluctuations in the ylem¹ resulting from Heisenberg's uncertainty principle were magnified to cosmic scales during Inflation. These primordial quantum inhomogeneities growing due to gravity give rise to the large scale structure in the universe today (Guth & Pi, 1982).

1.1.4 Angular power spectrum of the CMB

Initially proposed to answer questions resulting from the Big Bang theory, the addition of Inflation theory as a starting point for the Big Bang gave us a source for the inhomogeneities in the universe. The gravitational instabilities, created in the inflationary epoch, caused a contraction of surrounding material but the tight coupling of the photon-baryon fluid resulted in this in-fall being resisted by photonic pressure. This set up oscillating sequences of compressions and

¹ A Middle English term, ylem, a transliteration of Aristotle's concept of "(fundamental) matter"; it is an historical reference to the hot and dense plasma of the early cosmos. First known to have been used in modern English in by George Gamow (Gamow, et al., 1948).

rarefactions which would repeat until equilibrium was reached or one of the forces was removed. At recombination the baryons and photons decoupled and the matter was released from the force of the radiation. Now, free of the pressure of radiation, the oscillations ceased and the under-dense and over-dense regions became permanent structures with their compressed and rarefied states imprinted onto the LSS (White & Cohn, 2002).

The fluctuations, created on all scales, can be decomposed mathematically into plane wave modes. As they are part of the same fluid, we can take the sound speed as the same for all modes; the period of oscillation is directly related to the modes' wavelength. The largest structures were on a scale where only the initial compression took place; in this case half the wavelength of this mode is equal to the sound horizon (Hu & White, 2004). This results in a peak in the spatial angular power spectrum of temperature fluctuations, see *Figure 1.5* and *Figure 1.6*. There also exist higher order modes where there was time to rarefy and re-compress, and so on. All waves got 'locked' in but it was those at their extreme when this occurred that had the largest scale-variance and so are seen as the peaks in the LSS angular power spectrum. It is therefore the odd numbered peaks that relate to compression and the even numbers that relate to rarefaction. The LSS causal limit is $\sim 1^\circ$ ($l \approx 180$) so scales much larger than this contain information on the initial conditions of the universe and those smaller contain information on the acoustic oscillations and large scale structure of the universe. There is a wealth of other information that can be extracted from CMB and the interested reader should see Hu and White (Hu & White, 2004) for a good overview.

1.2 Measuring the CMB

Measuring the CMB angular power spectrum will allow us to extract details on the sources of inhomogeneities and evolution of the early universe and constrain current Λ CDM models. If inflationary theory is correct the CMB will also contain details on the quantum fluctuations that expanded during this epoch. There are 2

properties of the CMB which we can measure to achieve these goals: temperature and polarisation.

1.2.1 Temperature

In 1992 the COBE mission (Smoot, et al., 1992) detailed the largest scales on the power spectrum with a 7° resolution and found fluctuations at the 10^{-5} K level. Follow-on missions, a list of which can be found in (Tegmark, 1996), using ground and balloon based experiments began filling in the power spectrum making measurements on smaller angular scales and detailing the first acoustic peak. This was a major step forward from the earlier 1965 measurements as definite structure was now visible, as shown in *Figure 1.5*.

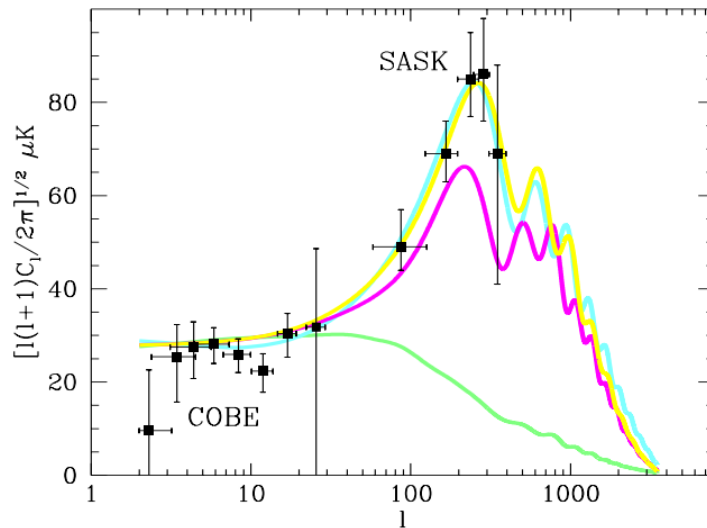


Figure 1.5: 1992 - COBE power spectrum of the CMB (Tegmark, 1996). The observations (at that time) are plotted with 1σ error bars for a selection of experiments. The vertical error bars include both pixel noise and cosmic variance, and the horizontal bars show the width of the window functions used. The COBE data is the power spectrum observed by COBE averaged over 8 multipole bands, and the rest are from the Saskatoon experiment (Netterfield, et al., 1996). The data points from COBE and Saskatoon are compared with the predictions from four variants of the standard CDM model from Sugiyama (1995), all with $n = 1$ and $\Omega_b = 0.05$. From top to bottom at $\ell = 200$, they are a flat model ($\Omega_\Lambda = 0.7$), a model with $h = 0.3$, the standard $h = 0.5$ model and a model with a reionization optical depth $\tau \sim 2$.

The BOOMERanG (Melchiorri, et al., 2000), MAXIMA (Hanany, et al., 2000) and DASI (Leitch, et al., 2002) experiments provided evidence for the second peak but we had to wait for the next large space based mission, WMAP (Spergel, et al., 2007), before it was fully resolved. With the data from WMAP the second acoustic peak was

defined and some tentative measurements were made of the third as shown in *Figure 1.6*.

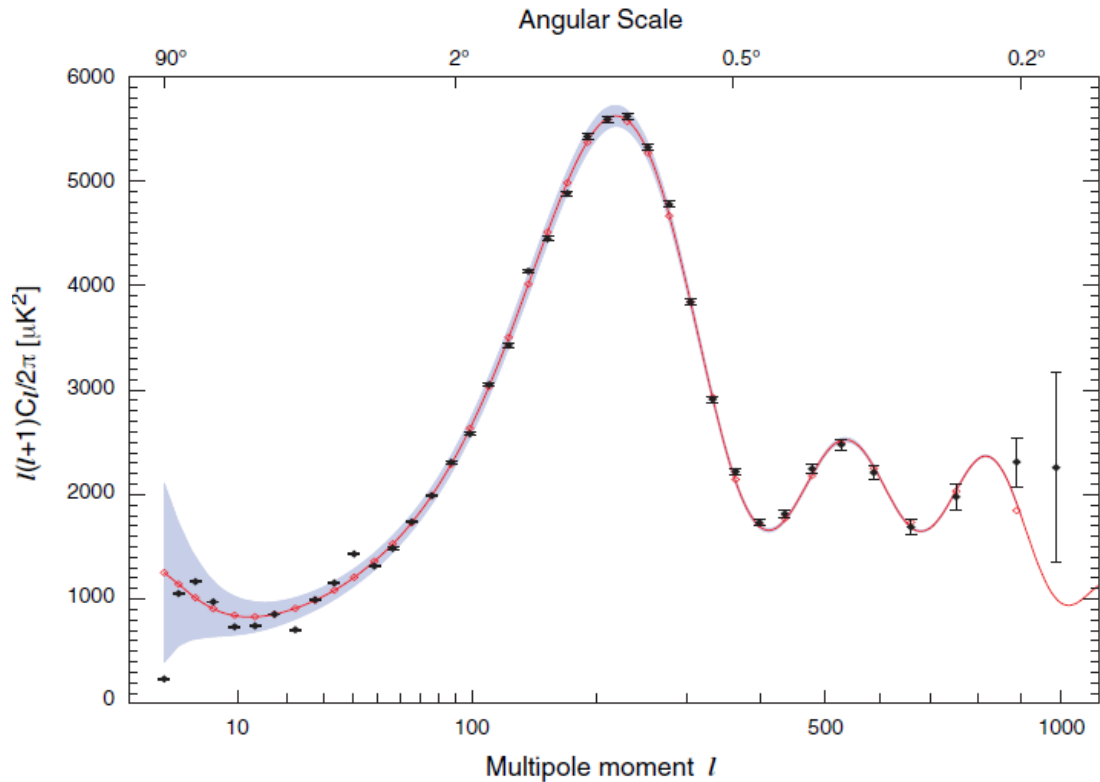


Figure 1.6: 2003 - WMAP power spectrum of the CMB (Hinshaw, et al., 2007). The binned three-year angular power spectrum (in black) is shown from $l = 2 - 1000$, where it provides a cosmic variance limited measurement of the first acoustic peak, a robust measurement of the second peak, and clear evidence for rise to the third peak. The points are plotted with noise errors only. Note that these errors decrease linearly with continued observing time. The red curve is the best-fit Λ CDM model, fit to WMAP data only (Spergel, et al., 2007), and the band is the binned 1σ cosmic variance error. The red diamonds show the model points when binned in the same way as the data

Over the last several years experiments have been aimed at refining our knowledge of the temperature power spectrum and extending it out to higher multipole moments. A list of some of these missions is given in *Table 1-1*.

Table 1-1: List of recent CMB polarisation missions

Name	Year	l	Frequency (GHz)	Detectors	Type
Archeops (Benoit, et al., 2004)	1999-2002	10 - 700	143,217,353,545	Bolometer	Balloon
BICEP1 (Keating, et al., 2003)	2006-2008	21 - 335	100, 150, 220	Bolometer	Ground
BOOMERanG (MacTavish, et al., 2006)	1997-2003	25 - 1025	90-420	Bolometer	Balloon
CAPMAP (Barkats, et al., 2005)	2002-2008	500 - 1500	90 and 40	MMIC/ HEMT	Ground
QUaD (Brown, et al., 2009)	2005-2010	~200-2000	100, 150	Bolometer	Ground
POLARBEAR (Arnold, et al., 2010)	2012-date	50 - 2000	150	Bolometer	Ground
QUIET (Bischoff, et al., 2011)	2008-2010	60 - 3500	40, 90	HEMT	Ground
WMAP (Spergel, et al., 2007)	2001-2010	2 - 1200	23,33,41,61,94	HEMT	Satellite
Planck (PLANCK-Collaboration)	2009-2013	2 - 2500	30 -- 857	Radio, Bol	Satellite
BICEP2 (Ade, et al., 2014)	2009-2012	21 - 335	150	Bolometer	Ground
KECKArray (Sheehy, et al., 2010)	2010-date	21 - 335	95, 150, 220	Bolometer	Ground
ACTPol (Niemack, et al., 2010)	2013-date	225 - 8725	90, 146	Bolometer	Ground
SPTpol (Austermann, et al., 2012)	2012-date	501 - 5000	95, 150	Bolometer	Ground
QUIJOTE (Génova-Santos, et al.)	2012-date	10 - 300	11,13,17,19,30,40	Pol/OMT	Ground
AMiBA (Park & Park, 2002)	2007-date	4300	90	-	Ground
COMPASS (Abbon, et al., 2007)	2003-date	200 - 600	26-36	HEMT	Ground
PIQUE (Barkats, et al., 2005)	2002	69 - 362	90	Bolometer	Ground
POLAR (Keating, et al., 2001)	2000	2 - 30	26-46	HEMT	Ground
SK (Wollack, et al., 1994)	1993-1995	52 - 401	26-46	HEMT	Ground
BEAST (Figueiredo, et al., 2005)	2000-date	10 - 1000	100 and 150	HEMT	Balloon Ground
KUPID (Gundersen, 2003)	2003-date	100 - 600	43435	HEMT	Ground
ABS (Simon, et al., 2014)	2011-date	25 - 200	145	Bolometer	Ground
SPIDER (Crill, et al., 2008)	-	10 - 300	90, 150, 280	Bolometer	Balloon
ARCADE (Kogut, et al., 2006)	2001-2006	-	3, 5, 7, 10, 30, 90	HEMT	Balloon

Today cosmology is data-rich and high precision. The standard model has been well constrained by missions like COBE (Smoot, et al., 1992), WMAP (Spergel, et al., 2008), QUIET (Bischoff, et al., 2011) and in 2012 the PLANCK (PLANCK-Collaboration, 2013a) satellite gave the best images of the CMB to date, see [Figure 1.7](#). PLANCK marks the end of the major temperature missions with the main acoustic peaks and multipoles out to $l \approx 2500$ detailed to a high precision.

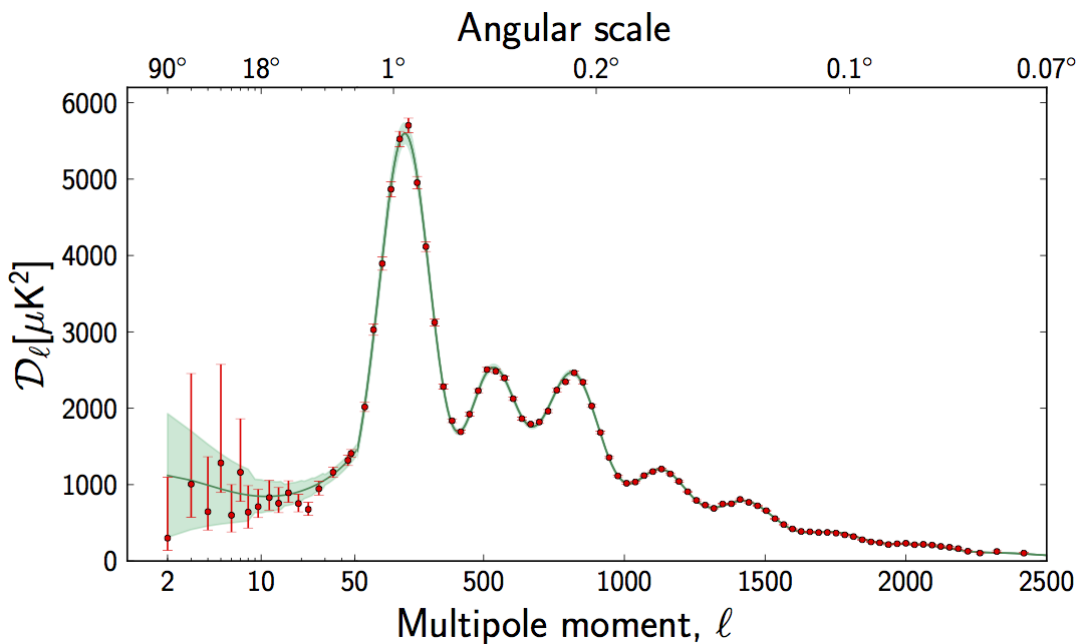


Figure 1.7: 2012 - Temperature angular power spectrum of the primary CMB from Planck, showing a precise measurement of seven acoustic peaks that are well-fitted by a six-parameter Λ CDM model (the model plotted is the one labelled [Planck+WP+highL] in Planck Collaboration XVI 2014). The shaded area around the best-fit curve represents cosmic variance. The error bars on individual points also include cosmic variance. The horizontal axis is logarithmic up to $l = 50$, and linear beyond. The vertical scale is $D_\ell = \ell(\ell + 1)C_\ell$.

Temperature measurements tell us about the large scale structure of the universe, showing energy variations at the time of the LSS. However, temperature alone cannot distinguish between the various sources of these perturbations: density fluctuations, gravity waves or vortices. It is predicted that polarisation measurements of the CMB (Rees, 1968) will show distinct patterns which can be used to make this determination, see for example (Tucker, et al., 2008), and remove degeneracy in determination of the cosmological constants. Therefore the next logical step is the measurement of the polarisation which will aid in placing further constraints on cosmological models of the universe.

1.2.2 Polarisation

In order to quantify the level of polarisation we decompose it into constituent components. Here we will outline potential sources of anisotropies in the primordial universe that lead to a net polarisation and two decomposition choices, Stokes Q and U parameters and the observer-independent E- and B-modes. Finally we will look at some of the information that can be extracted from these measurements.

Quadrupole anisotropies and Thompson scattering

Linear polarisation in the CMB requires the existence of quadrupole temperature anisotropies. There is no known process in the CMB that yields circularly polarised radiation and monopole, dipole or higher order multipoles will not yield a net polarisation. For a quadrupole, $l = 2$, we have 3 possible orthogonal orientations, $m = 0, \pm 1, \pm 2$, shown graphically in *Figure 1.8*.

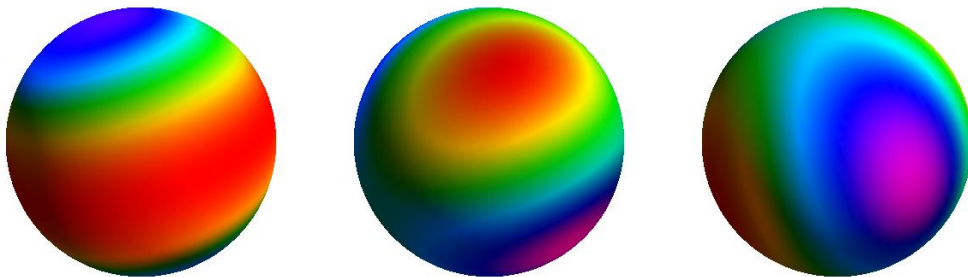


Figure 1.8: A quadrupole represented in 3 possible orientations, for $m = 0$ (Scalar: Compression), ± 1 (Vector: Vortices) and ± 2 (Tensor: Gravitational).

Thompson scattering, (the low energy limit of Compton scattering) from non-relativistic particles (in this case free electrons), will cause an acceleration of the particle proportional to the electric field of the incident waves as shown in *Figure 1.9*.

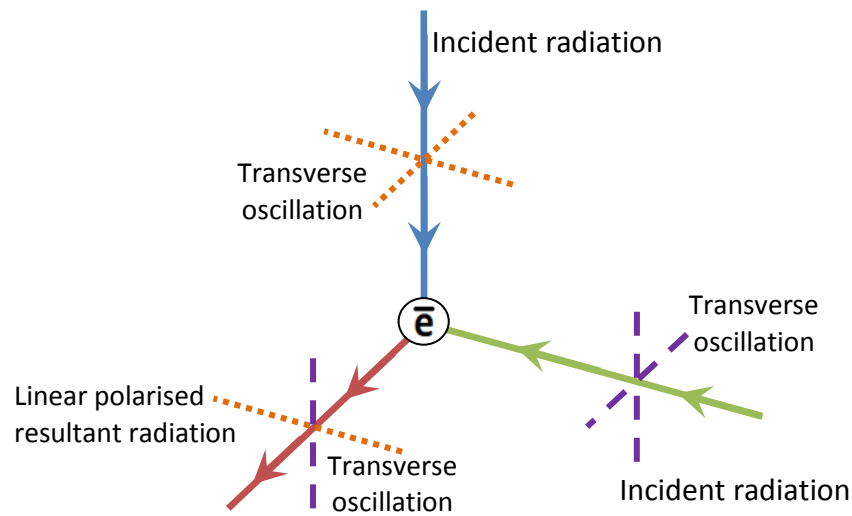


Figure 1.9: Thomson scattering at a quadrupole. Incident radiation is shown in blue and green with the transverse oscillating plane of each indicated by the dashed lines. The scattered photon, indicated in red, has the transverse oscillation shown. The oscillation caused by each incident photon is illustrated by means of the colours of the dashed lines,

Radiation with a quadrupole temperature anisotropy incident on a free electron will result in a scattered photon that is polarised in the direction of the lower energy incident photon. The detection of quadrupole temperature anisotropies in the CMB therefore leads to the expectation that it will be partially polarised at some level. There are two sources of quadrupole temperature variation expected in the CMB, scalar and tensor perturbations, which will be explained in the following sections. The third type, vector perturbations, are expected to be negligible (Delabrouille, et al., 2003).

Scalar (density, $m = 0$) sources

For a gravitational (scalar) instability, where there is an oscillation due to the opposing forces of pressure and gravity, a velocity gradient is set up. Taking a single Fourier component of this perturbation, particles are accelerated faster towards the over-density the closer they are to it. From the point of view of a test particle some distance from the centre of the over density, the plasma appears to be moving away from it radially whereas tangentially it appears to be getting closer. Due to a Doppler shift, this sets up a flux quadrupole. As the photons and baryons are tightly coupled, the quadrupole holds true for the temperature also, as shown in *Figure 1.10*.

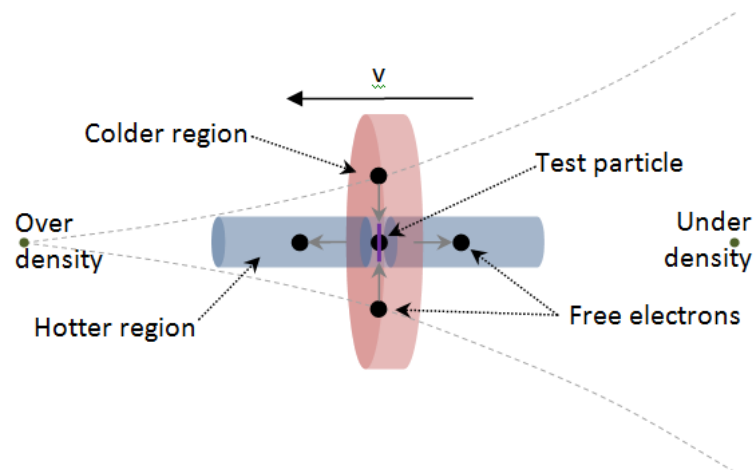


Figure 1.10: A single plane-wave Fourier component of a density quadrupole (White & Wu, 1999b) and resultant polarization as a result of a velocity gradient (Kaplan, et al., 2003). The fluid (dashed lines) is shown as being accelerated towards the over density. The relative fluid velocities (relative to the test particle) are indicated by the gray arrows, with v showing the movement of the fluid.

The resultant polarization direction is shown by the purple line on top of the test particle. Polarisation in the opposite direction occurs for a particle decelerated away from the cold spot.

For a free electron within the region, the test particle as shown in *Figure 1.10*, incident photons from the hotter region combined with those along the plane of the colder region will excite the electron and photons will be emitted along the plane of the colder region. As the temperature distribution in this plane is radially symmetric, there is no preferred direction of emission within this plane. In this case the higher energy photons will cause the radiated photons to be polarised (tangentially with respect to the over density) in the plane of the cold region. Conversely a hot region in the centre will tend to radiate vertically polarised radiation.

Tensor (gravitational, $m \pm 2$) sources

For an instability caused by a passing gravitational wave (tensor), a second source of quadrupole anisotropy occurs. Consider a set of test particles, in a circular pattern, as shown in *Figure 1.11* on the left. Taking a single Fourier component of a passing gravitational wave (taking its direction as towards the reader out of the page) the space is stretched and compressed and the particle pattern is distorted, as shown in *Figure 1.11* on the right, as the wave passes. This stretching and compression is transverse and no alteration of space occurs in the direction of wave propagation.



Figure 1.11: Ring of test particles (White & Wu, 1999b), on the left the particles are in their undistorted state and on the right the particles pattern is shown in a perturbed state.

This expansion and compression of space causes the wavelengths of the photons in the region to correspondingly get compressed and expanded and hence quadrupole anisotropies are created as illustrated in Figure 1.12, which are not radially symmetric.

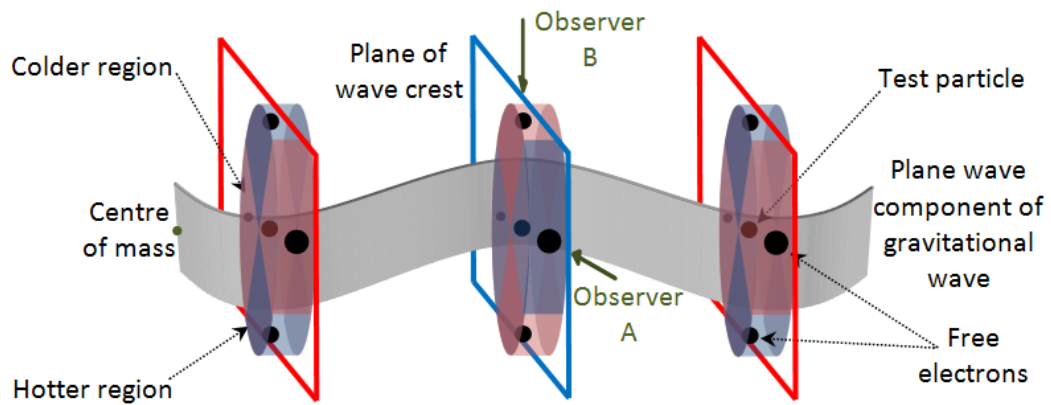


Figure 1.12: A single plane-wave Fourier component of a gravitational quadrupole. The blue and red rectangles represent the plane-wave's crest and trough respectively. The blue pie-regions correspond to the higher energy (hotter) regions and pink pie-regions the lower energy (cooler) regions. The direction of the particles displacement in this case is perpendicular to the direction of propagation of the plane wave.

Looking into the plane of the crest, from Observer A's location, we expect that emitted radiation, out of the plane in our direction, would be polarised in the plane of the incident colder (red) radiation, termed horizontal. Now orient the observer to position B, and the emitted photons would appear vertically polarised. As an observer traverses from A to B the observed polarisation changes orientation yielding a pattern as shown in Figure 1.13 (in purple) that starts at one orientation and revolves over 90° to the other and back again repeating for the full revolution.

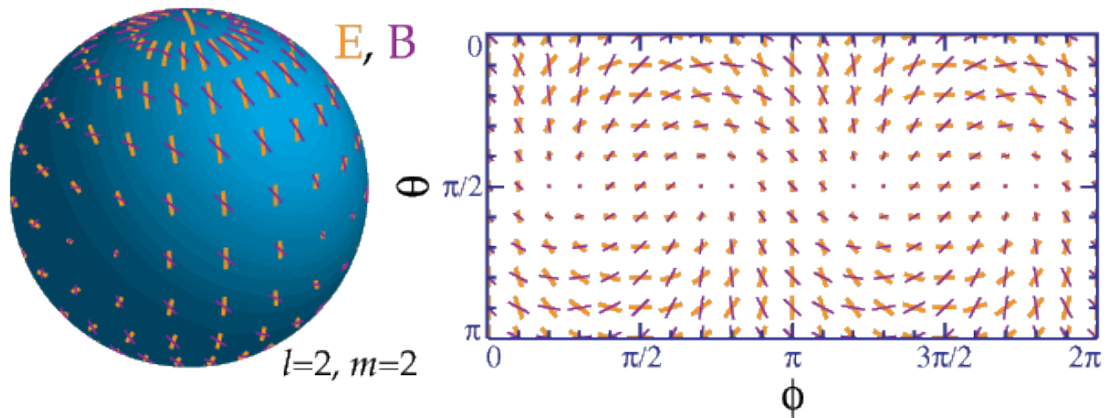


Figure 1.13: Gravitational polarisation pattern (White & Wu, 1999b)

Stokes parameters (I, Q, U and V)

A polarisation state can be fully described using Stokes' method which uses the 4 parameters (Stokes, 1852), shown in Table 1-2 below.

Table 1-2: Stokes parameters. Taking a reference frame in some arbitrary orientation, E_x and E_y represent the complex electric field components along the x and y axis.

Parameter	In terms of electric field	Description
I	$ E_x ^2 + E_y ^2$	Intensity
Q	$ E_x ^2 - E_y ^2$	Degree of vertical/horizontal polarization
U	$2\text{Re}[E_x E_y^*]$	Degree of diagonal polarization
V	$2\text{Im}[E_x E_y^*]$	Degree of circular polarization

Photon polarisation is transverse; Figure 1.14 shows a graphical representation of a polarised beam quantified by these parameters, as it would appear for a beam travelling into the page.

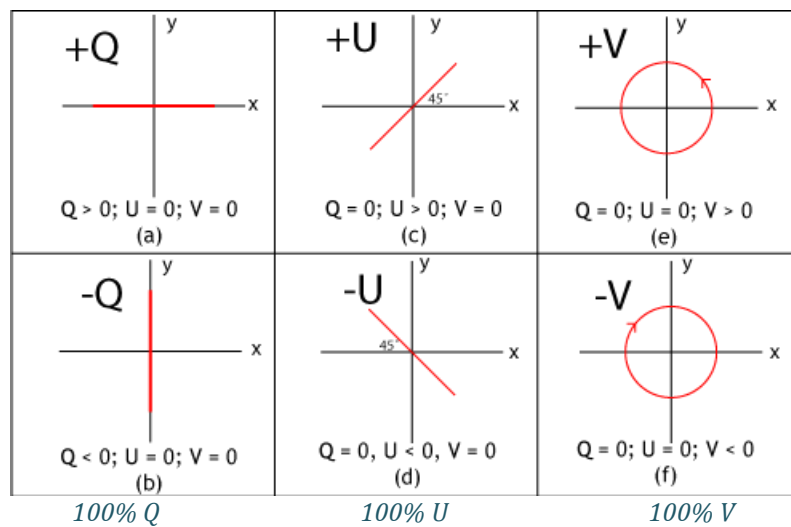


Figure 1.14: Stokes Parameters (Stokes, 1852)

The problem with this approach is that the values of Q and U are coordinate dependent with a 45° change in observer reference frame swapping the Q and U coefficients. An alternative observer independent method is that of decomposition into E- and B-modes (gradient and curl terms, respectively).

E- and B-Modes

The scalar and tensor cases outlined above are single Fourier components of the perturbations; the observed patterns are the superposition of all possible components. Correlating these patterns with temperature maps, taking the hot and cold spots as the centres of the perturbations, we expect a certain pattern about these points. If the polarisation pattern is purely radial or tangential with respect to the centre of the perturbation, as in the case of the radially symmetric scalars, we call this an E-mode, as shown in *Figure 1.15*, where the tangential lines represent the horizontally radiated photons and the radial lines those of the vertically polarised photons.



Figure 1.15: Polarisation pattern – vertical (left) and horizontal (right)

For tensor modes a degree of deviation from a pure E-mode is expected, due to it being radially asymmetric. Quantifying the degree to which the polarisation deviates from a purely radial or tangential component is termed finding the B-mode component. A pure B-mode results in patterns as shown in *Figure 1.16*.

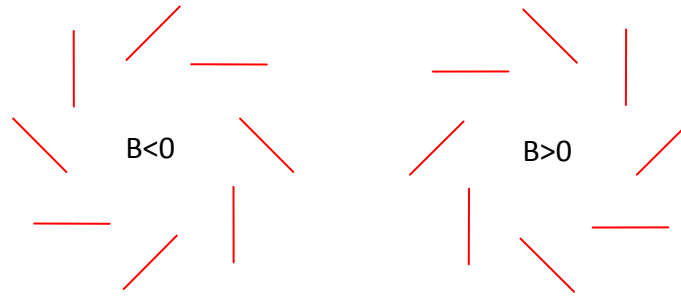


Figure 1.16: Polarisation pattern – B-modes

The result is that scalars yield E-modes and tensors yield almost equal quantities of E- and B-modes. When correlated with the temperature maps, the patterns are identifiable due to the parity of the modes ($E = -1^l$ and $B = -1^{l+1}$), where in the case of B-modes the handedness flips as you cross the perturbation. For more information and an excellent overview of this topic the interested reader can see (Hu & White, 1997; White & Wu, 1999b; Kaplan, et al., 2003; Hu & White, 2004).

The contribution level from vortices is expected to be small compared to those of scalars and tensors, as any such vortices would be dampened by cosmic expansion (Kaplan, et al., 2003). With only scalars and tensors to consider it is the value of r (the tensor to scalar ratio) which the new generation of telescopes hopes to constrain.

1.2.3 Constraining cosmological models

If a sky CMB signal is decomposed into spherical harmonics with coefficients a_{lm} , then because of isotropy, $\langle a_{lm} \cdot a_{l'm'}^* \rangle = \delta_{ll'} \cdot \delta_{mm'} \cdot C_l$. The tensor-to-scalar ratio, r , is defined as,

$$r = \frac{C_l^T}{C_l^S} \text{ (for } l = 2) \quad (1.1)$$

'r' the tensor to scalar ratio.

where:

r is the tensor to scalar ratio

C_l^T is the power coefficient for the tensor component

C_l^S is the power coefficient for the scalar component

l is the multipole moment

Finding r will improve constraints on Λ CDM models, give the first direct measurement of Inflation's gravitational instability paradigm and place an upper bound on the energy of Inflation (Liddle & Lyth, 2000) given by,

$$r = 0.1 \left(\frac{E_{\text{Inflation}}}{2 \times 10^{16} \text{ GeV}} \right)^4 \quad (1.2)$$

'r' and the energy of inflation

where:

r is the tensor to scalar ratio

E_{Inflation} is the energy of inflation

The gravitational instability paradigm for seeding the universe's inhomogeneities requires that the CMB will be polarised at some level (Hu & White, 1997) and B-mode signature patterns, which must exist if Inflation holds true, are its 'smoking-gun'. Polarisation patterns will allow the separation of scalar and tensor sources (B-modes are caused by tensor modes only) in the temperature maps and as polarisation is only caused by scattering it is also a direct probe into events at the LSS. It will also confirm angular power spectrum acoustic wave interpretations, which are a general prediction of Inflation (e.g. see Kaplan, Liddle and Lyth (Kaplan, et al., 2003; Liddle & Lyth, 2000) for a summary).

Polarisation, arising from the scattering of photons at quadrupole anisotropies in the CMB, only occurred during the period where the CMB was optically thin enough to allow the polarised photons to traverse the universe unimpeded and there were still free electrons left to scatter off. As such the anisotropies from polarisation are lower than those of temperature (a value of r is assumed here). The expected relative levels are shown in [Figure 1.17](#) where it can be seen that there is an anti-correlation between T and E polarisation resulting from the inherent out-of-phase relationship between density and velocity peaks, with no such correlation expected between T and B (Carlstrom, et al., 2003). Detection of B-modes on large angular scales ($> 2^\circ$, non-causally connected regions) will be direct evidence of gravitational sources in the early universe as gravitational lensing of E-modes can contribute to B-modes on smaller scales.

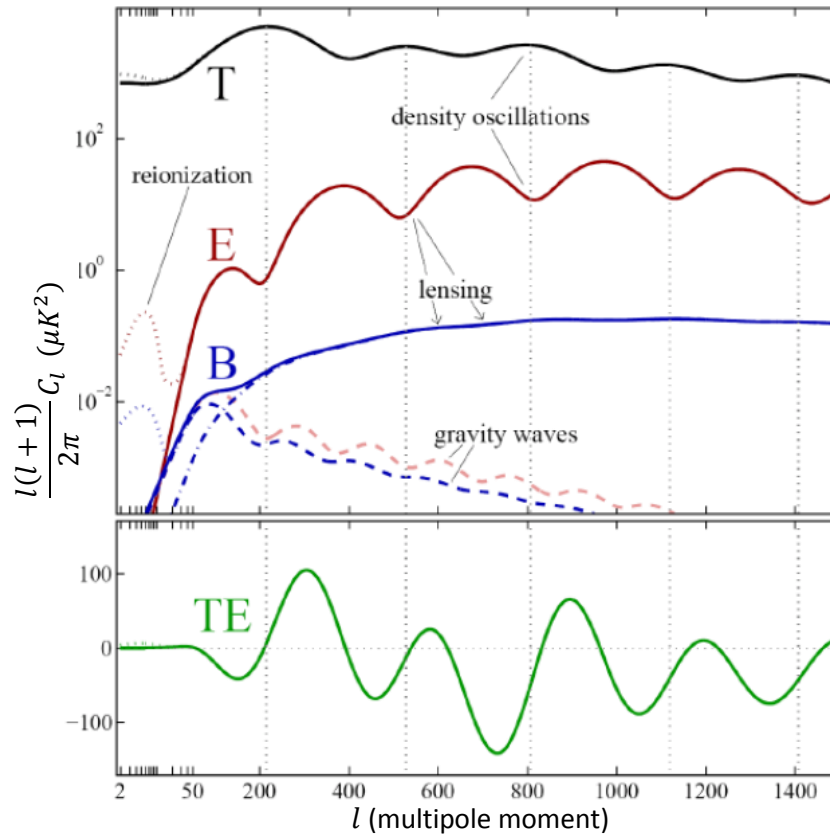


Figure 1.17: (Carlstrom, et al., 2003). Predicted power spectra for the “standard” model. Top to bottom: (T) Temperature, (E) E-mode polarisation, (B) B-mode polarisation, and (TE) Temperature-E-mode cross correlation spectra. The modification of each spectrum resulting from reionization of the magnitude observed by WMAP is shown by the dotted lines. Gravitational waves at a level allowed by current data introduce contributions to the E-mode and B-mode spectra shown by the dashed lines. The dot-dash line shows the contribution to the B-mode signal resulting from lensed E-modes. (Spectra calculated using CMBFAST, Seljak & Zaldarriaga 1996)

1.2.4 Measurements

DASI (Degree Angular Scale Interferometer), a heterodyne interferometer, made one of the first CMB polarisation measurements, using a 13-element array in the 26-36 GHz band over 3 years of operation (Leitch, et al., 2002). As well as the detection of E-Modes (Kovac, et al., 2002; Brown, et al., 2009) upper limits could be placed on B-mode components. SPTpol detected gravitationally-lensed B-modes in 2013 (Hanson, et al., 2013). WMAP put an upper limit on $r \leq 0.2$ while PLANCK tentatively refines this value at $r_{0.002} \leq 0.11$ (PLANCK-Collaboration, 2013b; Lau, et al., 2014), (see Figure 1.18 for PLANCK’s EE-spectrum from their 2013 data release). Different inflationary scenarios predict varying levels for B-modes, their actual value is unknown, and they are expected to be at least another order of magnitude lower than E-modes.

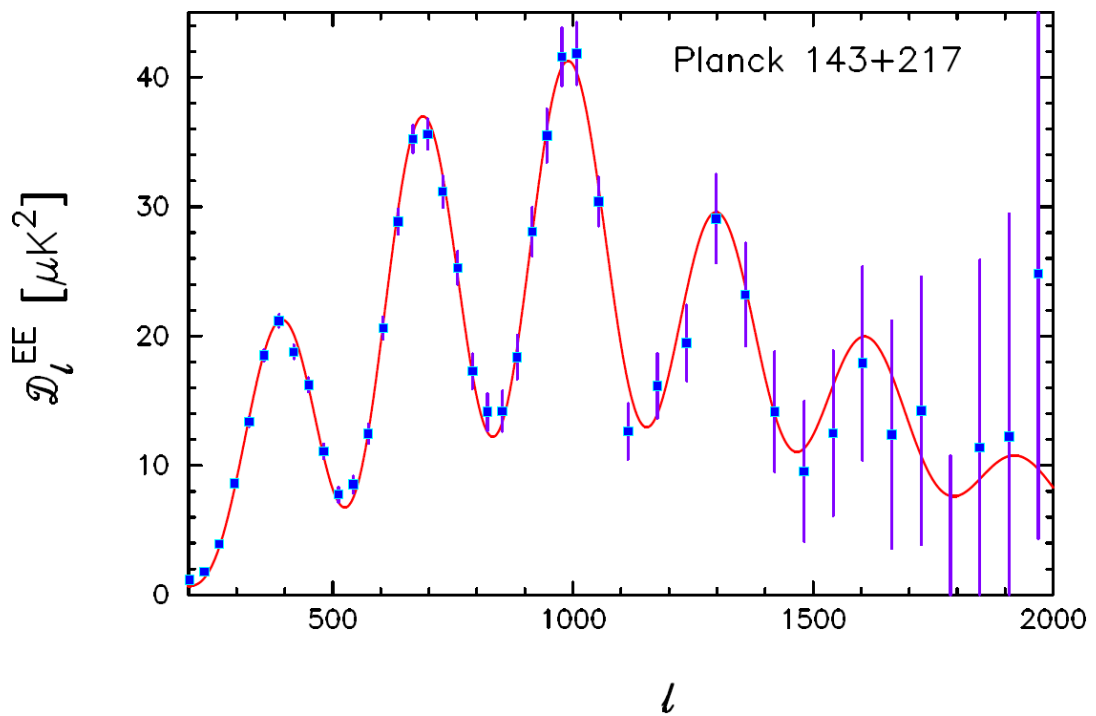


Figure 1.18: *EE* spectra (PLANCK-Collaboration, 2013c). The solid lines show the theoretical *TE* and *EE* spectra expected in the best-fit Planck+WP+highL Λ CDM model (i.e. the model used to compute the theory *TT* spectrum plotted in Figure 1.7). These theoretical spectra are determined entirely from the *TT* analysis and make no use of the Planck polarization data. As with the *TT* spectra, the Λ CDM model provides an extremely good match to the polarization spectra.

At the time of writing there has been no confirmed detection of primordial B-modes. In 2014 primordial B-modes were purportedly detected in the CMB for the first time by BICEP2 (Ade, et al., 2014) but the latest PLANCK results show that the detection is consistent with foreground cosmic dust. Telescope projects have been developed specifically for the detection of primordial B-modes, such as BRAIN (Masi, et al., 2005) and MBI (Tucker, et al., 2003), and the next generation of telescope missions will be focused on detecting and detailing primordial B-modes.

There are technological hurdles to overcome. The polarisation fluctuations are several orders of magnitude lower than that of the temperature fluctuations and polarised foregrounds must be removed. To make these measurements unprecedented levels of control over systematic errors and extremely high sensitivity will be required. QUBIC, which will be detailed in Chapter 3, will achieve this level of control with a combination of bolometric imagery for the sensitivity and interferometry for the systematic error control.

1.3 Interferometry

Interferometry combines EM fields in a way that their interference pattern can be used to determine properties about the sources of the EM fields under observation. The QUBIC instrument uses a homodyne, common path, wavefront splitting bolometric interferometer configured to additively combine the signals at the image plane, i.e. a Fizeau interferometer. In this section interferometry is discussed with an overview of the design as used by QUBIC. QUBIC itself is discussed in greater detail in Chapter 3. In this section the principle of interferometry for observations of a point source followed by extended sources is given. The definition of visibility and the theorem of van-Cittert Zernike, central concepts for interferometry, will be discussed. Finally we will briefly describe imaging and Fizeau interferometry.

1.3.1 Interferometry basics

In terms of sensitivity, a bigger telescope is always better, but there is a practical limit to the size to which a telescope can be built. If atmospheric effects are small or can be corrected for, size is the limiting factor in determining the resolving power which can be achieved by a single telescope and hence the information that can be obtained. For sub-arcsec resolution a single telescope is impractical, for example at 150 GHz ($\lambda = 2$ mm) arc-sec resolution requires a ~ 500 km diameter telescope ($D \approx \frac{\lambda}{\theta}$, where D is the aperture diameter, λ is the wavelength and θ the resolution). In this case diffraction is the primary limitation on resolving power and the requirement for better angular resolution, in order to determine finer and finer detail, is the driving force behind the need for ever larger telescopes. Interferometry offers an alternative to these super-massive monolithic structures.

1.3.2 Interferometry operation

With an interferometer, the wave nature of light is exploited to obtain details on an observed source with multiple small telescopes equivalent to those that would have been obtained using a single massive telescope. Using interferometry, the resolution that can be obtained is equivalent to that of a telescope with a diameter equal to the largest distance between the individual apertures in the interferometer

array. This separation distance between 2 telescope apertures is known as a baseline, s .

Consider 2 such telescope apertures separated by a distance, s , with a monochromatic point source in the farfield directly overhead, essentially the source of a coherent plane-wave. For telescopes observing this source at the zenith, the waves arrive in phase, as shown in *Figure 1.19*.

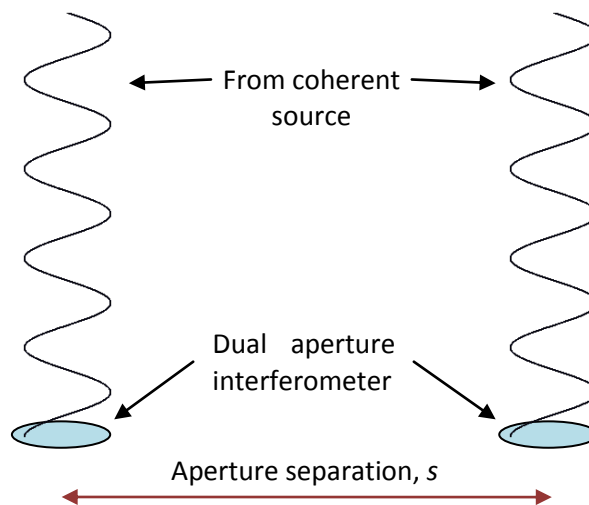


Figure 1.19: Phase difference of a plane parallel wave. The on-axis source arrives at the detectors as a plane parallel wave, the waves at each detector are in phase (coherent source).

For a source that is off-axis, at some angle θ , the plane wave travels a different path length to each telescope, the path length difference being given by, $L_{PD} = s \sin \theta$, as shown in *Figure 1.20*.

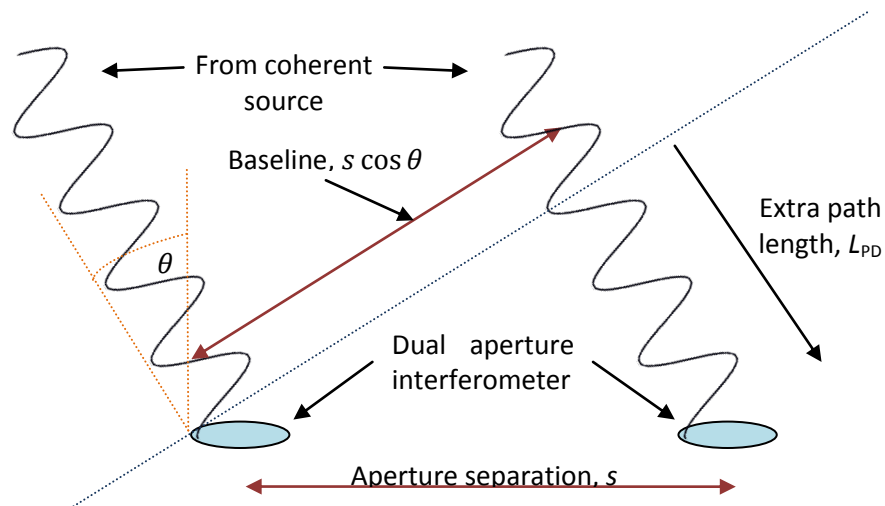


Figure 1.20: Phase difference of a plane parallel wave. The off-axis source arrives at the detectors as a plane parallel wave, the wave at each detector is out of phase by an amount proportional to the angle of the source with respect to the normal of the aperture plane.

The phase difference, φ , for a source at an angle θ from the zenith is therefore given by Equation (1.3).

$$\varphi = 2\pi s_{\lambda} \sin(\theta) \quad (1.3)$$

Signal phase difference

where:

θ is the source angle (in radians)

s_{λ} is the separation distance in wavelengths (s/λ)

φ is the phase angle between the two signals (in radians)

A Michelson interferometer, for example, brings the beams together at the pupil plane. The observed total intensity is then given by,

$$\begin{aligned}
 I &= (E_1 + E_2)(E_1^* + E_2^*) = E_1E_1^* + E_2E_2^* + E_1E_2^* + E_2E_1^* \\
 &= \underbrace{I_1 + I_2}_{\text{Average power}} + \underbrace{E_1E_2^* + E_2E_1^*}_{\substack{\text{Mutual coherence} \\ \text{or visibility}}} \quad (1.4)
 \end{aligned}$$

where

$$E_n = e^{i2\pi\left(\frac{r_n}{\lambda} - vt\right)} \quad (1.5)$$

Observed intensity interference pattern of 2 beams added together coherently

where:

I , I_1 and I_2 are the electric fields total intensity and source intensity at apertures 1 and 2

E_1 and E_2 are the electric field amplitude of the source at apertures 1 and 2

n is an index (in this case 1 or 2)

A is the amplitude

r_n is the distance from the source to aperture number n

The relative phase difference between the signals at each aperture varies as a function of angle. Where the signals are in phase they will add constructively and conversely they will add destructively where out of phase creating an oscillating pattern of maxima and minima as the source moves across the sky. The separation of these maxima and minima is known as the *fringe-spacing*, as shown in [Figure 1.21](#). The average power signal offset, resulting from the $I_1 + I_2$ term, can be isolated and removed through an appropriately applied modulation.

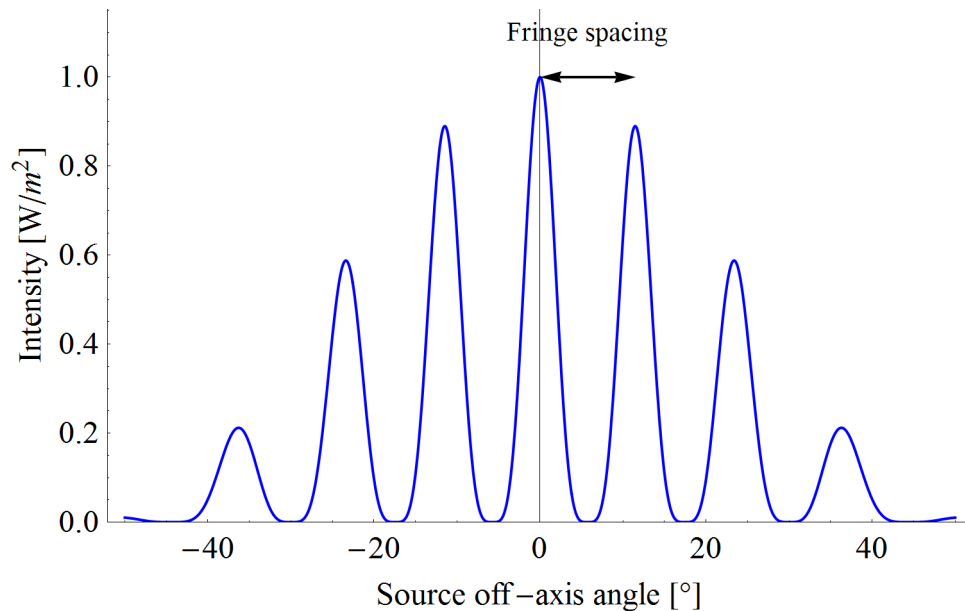


Figure 1.21: Idealised fringe pattern, assuming a telescope separation distance of 5λ and an aperture Gaussian response with FWHM of 50° (non-tracking telescopes). The relative path lengths preceding the aperture inducing a phase shift at one feed horn with respect to the other.

The fringe spacing is related to the separation distance, s_λ , where the distance, s , is measured in units of wavelengths. The larger the separation the more fringes are observed, as shown in *Figure 1.22*, with the total number of fringes over an horizon $= 2s_\lambda$.

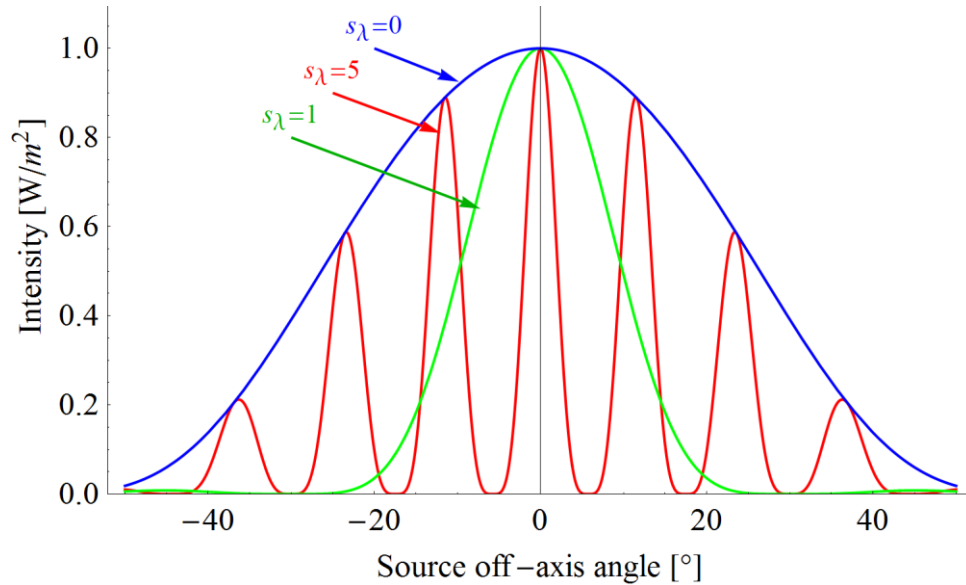


Figure 1.22: Interferometer pattern for $s_\lambda = 0, 1$ and 5 .

Specific baseline separations are therefore related to particular angular extents on the sky and, as with Fourier analysis, are a sampling of features in the source of that angular extent. The single antenna case ($s_\lambda = 0$) gives us the average value of the source and as s_λ increases the fringe spacing decreases giving access to finer and finer detail. Larger s_λ values give more information regarding the fine structure and conversely small s_λ values give more information about the coarse structure. In all cases the values obtained are weighted by the reception pattern of the antenna, a Gaussian in the case of *Figure 1.21* to *Figure 1.23*.

Now consider a source that is not a point but has some angular extent, for example, if the source is of angular extent equal to that of the fringe spacing then at all times there will be equal contributions from the constructive and destructive components. The fringe vanishes with the difference between the maxima and minima $\rightarrow 0$. In this situation we say that the source is *resolved*. Therefore there is a

correlation between the fringe maxima and minima and the angular extent of the source. The fringe maxima and minima are related to the *visibility*, defined as,

$$V = \frac{I_{\max} - I_{\min}}{I_{\max} + I_{\min}} \quad (1.6)$$

Visibility

where

I_{\max} and I_{\min} are the maximum and minimum intensity values for the fringe

For $V = 1$ we have a point source and for $V = 0$ an extended source with angular extent equivalent to that of the fringe spacing that ‘just’ resolves it. For the intermediate case we get $0 < V < 1$ and a fringe pattern like that in *Figure 1.23*.

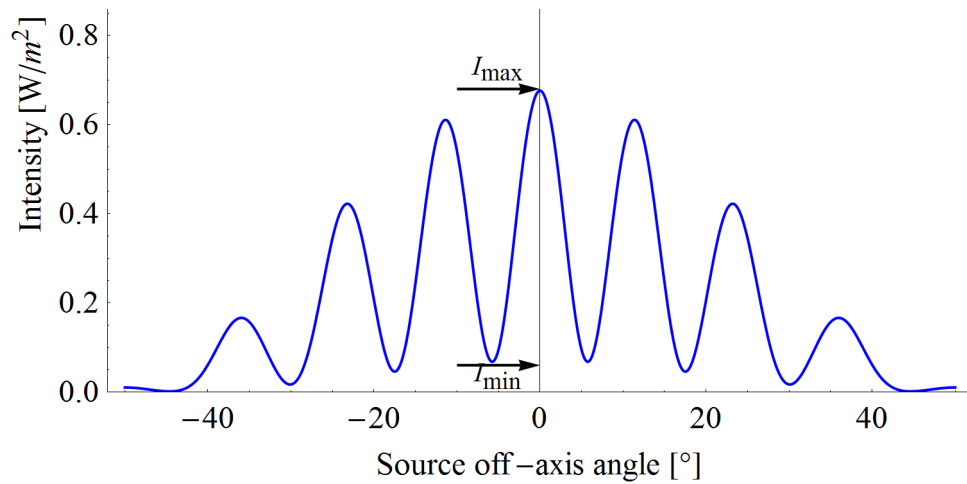


Figure 1.23: Interferometer pattern for fringe spacing < source angular extent, showing the visibility variation extremes, I_{\max} and I_{\min} . This simple example is shows 2 point sources, separated by 4° sampled with an aperture baseline of separation, $s_\lambda = 5$.

As the complexity increases, e.g. observing the sky which contains many sources, the interference fringes become more complex with the observed pattern being a superposition of all contributing sources, making deciphering them increasingly difficult. In the 1930’s a relationship was discovered showing that the visibility (as a function of baseline) is the Fourier transform of the intensity distribution of the sky (Cittert, 1934). To derive this relationship, for a total source surface area, σ , we take the contribution from each possible source element, $\delta\sigma$, with complex amplitude, A , and propagate it a distance, r_1 , to telescope aperture 1 and distance, r_2 , to telescope aperture 2. The field from each source element arriving at aperture 1 is

given an index, k , and aperture 2, l , as illustrated in *Figure 1.24* (see Martinache (Martinache, MOOC 2015) for an overview).

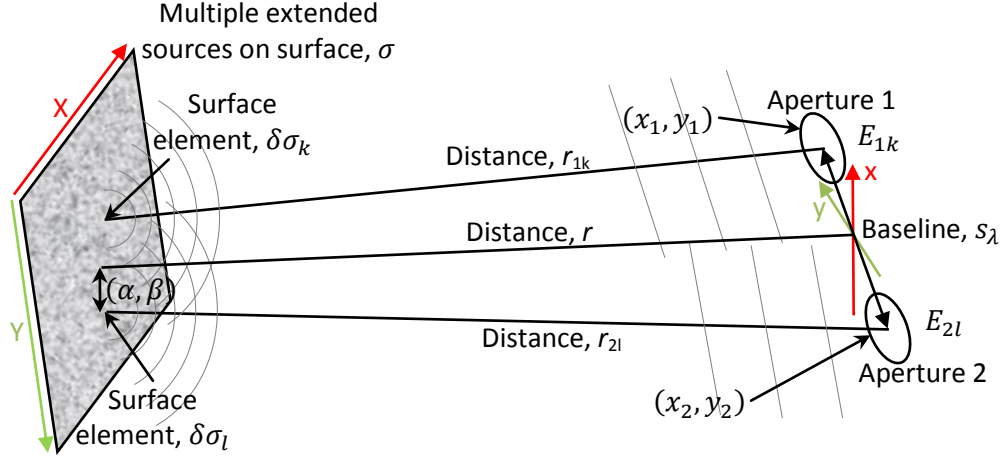


Figure 1.24: Multiple extended sources propagated from the farfield onto 2 telescope apertures.

The apertures are in the xy -plane centred at x_1, y_1 and x_2, y_2 . r is the distance from the centre of the source distribution to the centre of the baseline (assumed large so that $r \approx r_1 \approx r_2 \gg x_1, x_2, y_1, y_2$). The source is in the XY -plane. Points in this plane are referred to by their direction cosines, $\alpha = \frac{x}{r}$ and $\beta = \frac{y}{r}$. The mutual coherence function determined by the 2 telescope apertures from *Equation (1.4)* can be written as,

$$\langle E_1 E_2^* \rangle = \langle \sum E_{1k}(t) \sum E_{2l}^*(t) \rangle \quad (1.7)$$

where

$$E_{1k}(t) = \frac{A_k}{r_{1k}} e^{i2\pi(\frac{r_{1k}}{\lambda} - vt)} \delta\sigma_k \text{ and } E_{2l}^*(t) = \frac{A_l^*}{r_{2l}} e^{-i2\pi(\frac{r_{2l}}{\lambda} - vt)} \delta\sigma_l \quad (1.8)$$

As the sources are incoherent, for all cases where $k \neq l$ the product $\langle E_{1k}(t) \times E_{2l}(t) \rangle = 0$, therefore we can write,

$$\langle E_1 E_2^* \rangle = \langle \sum E_{1k}(t) E_{2k}^*(t) \rangle \quad (1.9)$$

Considering a single point source for a moment and assuming the source is stable over the observation period, the field power can be written in terms of intensity, I and total distance, r (as $r_1 \approx r_2$ since $r_1, r_2 \gg s_\lambda$).

$$E_{1k}E_{2k}^* = \frac{A_k A_k^*}{r_{1k} r_{2k}} e^{\frac{i2\pi}{\lambda}(r_{1k} - r_{2k})} \delta\sigma_k^2 \approx \frac{I_k}{r^2} e^{\frac{i2\pi}{\lambda}(r_{1k} - r_{2k})} \delta\sigma_k \quad (1.10)$$

Replacing the discrete point source representations with continuous functions over the source XY -plane (which we reference by its direction cosines) the discrete sum can be replaced by the continuous integral for the surface element, $\delta\sigma$,

$$\langle E_1 E_2^* \rangle = \int I(\alpha, \beta) e^{i\frac{2\pi}{\lambda}(r_1 - r_2)} \delta\sigma \quad (1.11)$$

Using the relationships for $r_1 = \sqrt{(X - x_1)^2 + (Y - y_1)^2 + r^2}$ and $r_2 = \sqrt{(X - x_2)^2 + (Y - y_2)^2 + r^2}$ and taking a Taylor expansion with $r \gg x_1, y_1, x_2, y_2$ (array sources are far away) we obtain $r_1 - r_2 = \frac{X}{r}(x_2 - x_1) + \frac{Y}{r}(y_2 - y_1)$. Defining $u = \frac{x_2 - x_1}{\lambda}$ and $v = \frac{y_2 - y_1}{\lambda}$ we can restate in terms of direction cosines to obtain,

$$\langle E_1 E_2^* \rangle = \iint I(\alpha, \beta) e^{i2\pi(\alpha u - \beta v)} \delta\alpha \delta\beta \quad (1.12)$$

Therefore the mutual coherence of two apertures, simultaneously measuring field(s), with baseline separation determined by u and v , is equal to the Fourier transform of the intensity distribution $I(\alpha, \beta)$ describing the source. This is the van-Cittert Zernike theorem (Cittert, 1934),

$$V(u, v) = \mathcal{F}(I(\alpha, \beta)) \quad (1.13)$$

van-Cittert Zernike theorem

where:

V is the fringe visibility as a function of spatial coordinates, u and v

I is the intensity distribution of the source as a function of angle, α and β

\mathcal{F} is the Fourier transform operator

In 1936, Fizeau developed this concept and led the way for the beginning of astronomical interferometry.

Each baseline gives a Fourier component of the sky and therefore measurements need to be made at each possible separation and orientation in order to recover all information on the sky. Extending the previous 1D cases, in *Figure 1.21* to *Figure 1.23*, to a 2D plane, the visibility measured by 1 baseline gives 2 points on the uv -plane, positioned symmetrically about the centre a distance s_λ from it and oriented in the same direction as the baseline, as illustrated in *Figure 1.25*.

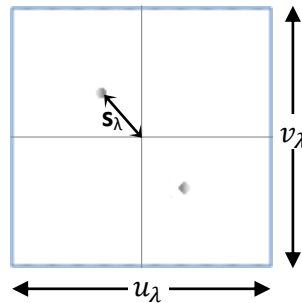


Figure 1.25: The 2 uv -plane points sampled by 1 baseline.

In order to generate an image we need to obtain as many components as possible. For a real interferometer it is impossible to obtain all components but a subset gives good approximations yielding a synthetic image of the sky. An example is shown for 2 point sources, in *Figure 1.26*, for a 6 element aperture array giving 15 baselines and *Figure 1.27* for a 36 element aperture array giving 630 baselines, the latter resulting in a very good reconstruction (the synthesised beam of the telescope is the Fourier transform of the points sampled in the uv -plane).

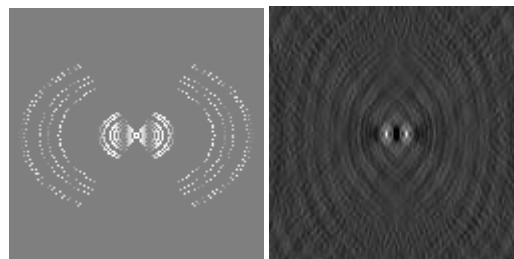


Figure 1.26: Aperture Synthesis Interference Pattern and Sky Brightness Image – 6 element array. Images generated using the online tool ‘Virtual Radio Interferometer’ (McKay, et al., 2006)

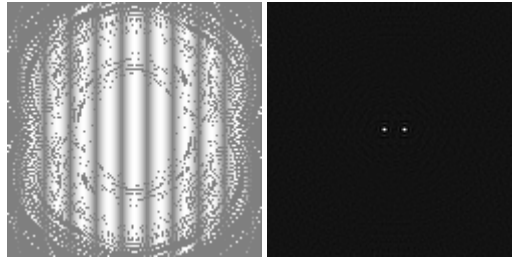


Figure 1.27 Aperture Synthesis Interference Pattern and Sky Brightness Image – 36 element array. Images generated using the online tool ‘Virtual Radio Interferometer’ (McKay, et al., 2006)

In the case of a Fizeau homothetic² interferometer, as used in the QUBIC instrument, the beams are brought together at the image plane by means of an optical-combiner and the resultant image is a summation of the fields from each aperture. We therefore produce a spatial fringe pattern on the image plane (rather than the temporal one detailed previously where intensity maxima and minima are recorded as the source moves across the sky). In the case of an image plane interferometer it is the geometric phase shift that gives rise to the fringes, as shown in Figure 1.28.

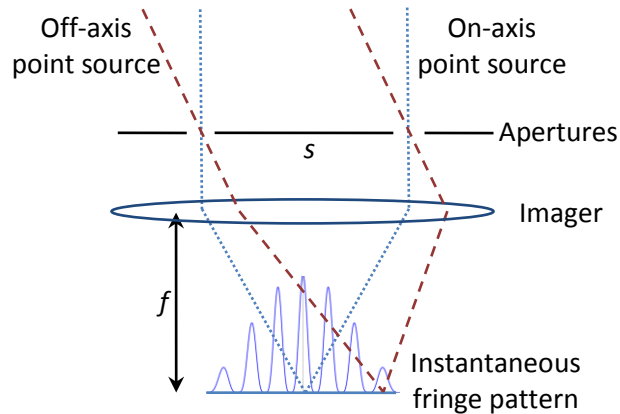


Figure 1.28: Shown here is an equivalent lens based combiner highlighting the induced geometric phase shift.

The fringes can be analysed in exactly the same way as before to give the amplitude (from fringe maxima and minima) and phase (fringe offset) of the visibility function. This is Fourier transformed to give the intensity distribution on the sky.

² A homothetic transform is a linear spacial transform such that angle is preserved while the magnification varies with propagation distance.

Homothetic interferometers such as QUBIC offer another possibility to be used as a synthetic imager. In this case the fringe patterns from all baselines are superimposed at the image plane and their sum detected by an array of bolometers. In the limit of a very large number of apertures the sum of all the fringe patterns is just the image of the sky. More generally we get the image of the sky with a point spread function (PSF) that is determined by the Fourier transform of the aperture array pattern. QUBIC has an enormous 400-element aperture array providing $\frac{N(N-1)}{2} = 79800$ baselines (including equivalent baselines³) which should yield exquisite detail on the sky. In order to be competitive, in terms of sensitivity, with imaging experiments it was decided to operate QUBIC in this mode. The advantage that QUBIC offers over an imager is that interferometry can be used to provide a method of calibrating the contributions from each aperture baseline pair within the array. Calibration is achieved by making use of equivalent baselines; equivalent baselines should produce the same fringe patterns so therefore any variations between these patterns can be used to calibrate the gain, phase and polarisation mismatches, thus minimising systematic errors in the measurement of Stokes visibilities. The novel method for QUBIC is described by Charlassier (Charlassier, et al., 2010b). QUBIC's use of the synthetic image will be discussed in Chapter 3 when looking into the operation of the instrument and the generation of synthetic images from simulated skies will be discussed in Chapter 6.

1.4 Summary

In this chapter we discussed the early cosmological theories which attempted to ascertain the nature and history of the universe along with an outline of their successes and failings. We then furthered the discussion on the Big Bang theory which came to the forefront after the detection of the CMB. The CMB was first detected back in 1965 by Penzias and Wilson and it is the basis of all modern precision cosmology. Due to some observations that could not be accounted for by

³ Equivalent baselines are those whose baseline antenna pairs have the same spatial separation and orientation as each other (Charlassier, et al., 2009).

the Big Bang theory alone, the theory of Inflation was developed. Some predictions of inflation were described and from here we looked at measurements of the CMB that have already been made, namely temperature maps and the associated power spectrum, these have been measured in exquisite detail. We looked at the next logical step, that of making polarisation measurements and the quantifying its constituent B- and E-modes. The B-mode component of polarisation in the CMB is often called the ‘smoking-gun’ for the theory of Inflation. If successfully measured it will be the first direct measurement of Inflation and will provide an estimate of its energy scale. As such it is a highly sought after detection.

Finally in this chapter we looked at the use of interferometry which uses multiple baselines at various orientations to measure details that the individual elements alone could not achieve. Interferometry allows for exceptional control over systematics and so combined with the high sensitivity of bolometric detectors, it is hoped that QUBIC will provide unprecedented levels of systematic control with a sensitivity level much greater than that of a standard interferometer. In the following chapters I outline the design, simulation, implementation and testing of the QUBIC interferometer instrument.

1.5 Thesis outline

This thesis is concerned with the design and modelling of the quasi-optical combiner for the QUBIC telescope which will attempt measurement of the elusive B-mode polarisation signature in the CMB or at least constrain the tensor to scalar ratio, r , to ≤ 0.01 . It will use the novel technique of bolometric synthetic-imaging interferometry. In this first chapter I have given a brief introduction to the CMB B-modes and the use of interferometry in astronomy.

Chapter 2 introduces the analytical methods and tools used throughout this thesis for the modelling of the QUBIC instrument. We begin with a look at mode matching techniques used in the determination of the characteristics of the QUBIC feed horns. We then briefly look at ray tracing, a technique in which diffraction effects are neglected. Although useful in initial design, more precise methods for the THz

region of the EM spectrum are required. We then look at physical optics which provides excellent insight into the behaviour of the instrument with a full vector analysis but is computationally time consuming. The final method we discuss is that of Gaussian beam mode analysis which assumes a scalar paraxial field but includes diffraction effects. The chapter finishes with a description of the software packages, GRASP and MODAL, used for the instrument simulations in this thesis.

Chapter 3 first gives a brief history of the QUBIC instrument starting with its predecessors, MBI and BRAIN. From the results of MBI and BRAIN a collaboration was put together in 2008 to form the current mission, QUBIC. The operation of the instrument is detailed: its scientific goals and how it will achieve them.

Chapter 4 looks in detail at the QUBIC v2.0 instrument and the design process by which new components, the polariser and coldstop, were included. Its performance and operation at 150 GHz is analysed.

Chapter 5 investigates the performance of the optical combiner as a synthetic imager. The fringe patterns, the window function and the instrument point spread function (PSF) will be discussed and compared to the ideal case.

Chapter 6 discusses the change to a dual-band operation. These largely involve a redesign of the input feed horns and the addition of a dichroic.

Chapter 7 looks at the overall conclusions from the analysis carried out in this thesis. The final design of the optical combiner and its main performance parameters are highlighted and future possible work on the analysis of the instrument is discussed.

2 Optical and electromagnetic modelling

This thesis is particularly concerned with the QUBIC instrument which will be described in detail in Chapter 3. Briefly, the QUBIC beam combiner, shown in *Figure 2.1*, consists of an off-axis Gregorian imager operating at 150 GHz. An array of back-to-back corrugated feed horns captures radiation from the sky and re-emits it through the combiner which superimposes the output from each feed horn at the detector plane. In order to model the instrument the beams produced by the feed horns must be calculated, propagated in free-space through the optical combiner, and their distribution on the detector plane calculated.

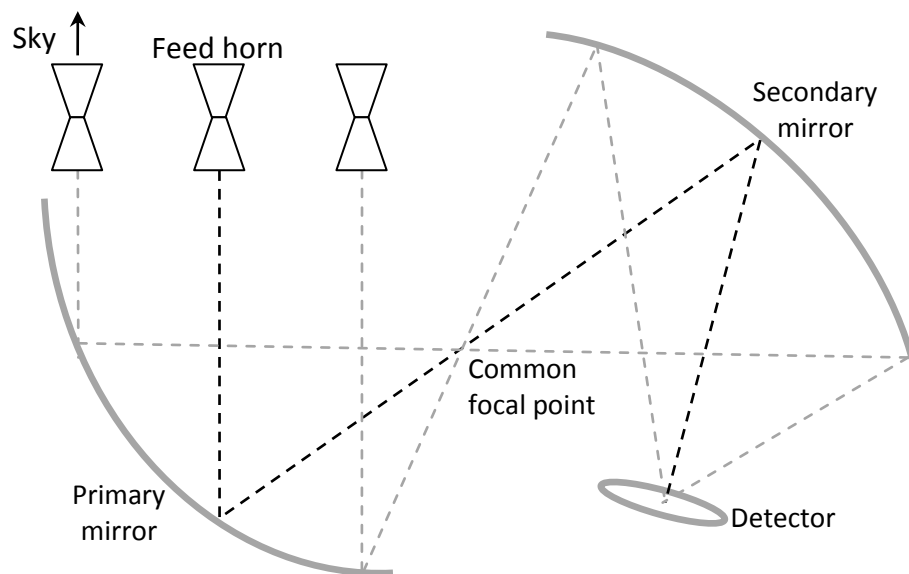


Figure 2.1: Schematic of the QUBIC optical beam combiner

In this chapter we look at several methods for beam analysis, each having its advantages and disadvantages depending on the application and analysis needed. Unfortunately using a precise theory, i.e. that of full-wave electromagnetism, is impractical for the simulation of many optical designs as it is computationally expensive and is usually excessive for many design considerations. We therefore use approximate theories, the particular one selected depending on the system under consideration and the accuracy being sought.

In the frequency range that we are concerned with, GHz – THz, waveguides and horn antennas are a good way to couple a free space beam to a source or detector.

We will concentrate on conical corrugated feed horns as used in the QUBIC instrument and I will describe mode-matching techniques that are used to calculate the output beam pattern in terms of TE (transverse electric) and TM (transverse magnetic) modes. Conical corrugated feed horns can transmit both orthogonal mode sets and are therefore well suited to bolometric polarimeters such as QUBIC. We will then look at the utilisation of SVD (single value decomposition) as a computational technique to write these TE and TM modes in terms of hybrid modes (HE and EH). QUBIC feed horn output fields can be efficiently described by a small number of propagating hybrid modes.

There are several appropriate methods that can be used to determine the evolution of this beam from the aperture of the QUBIC feed horns through the elements of the optical combiner. We will look at 3 of these:

- Geometric optics (GO) also known as ray tracing, which is valid in the geometric limit where the wavelength is negligible compared with component sizes but ignores wave effects such as diffraction.
- Gaussian beam modes (GBM) and ABCD matrices are an intermediate scalar method, see (Murphy & Egan, 1993), valid in cases where the aperture is still large compared to the wavelength. It takes diffraction but not cross-polarisation into account and is limited to the accuracy of the paraxial equation. It is possible to account for a vector field in the limiting case where there is no additional cross-polarisation induced by the optical system by modelling both polarisations independently.
- Physical optics (PO), a more computationally expensive vector method, is very precise in cases where the elements are flat-and-large compared to the wavelength. In the case of QUBIC there is also some cross-polarisation and so, to assess this, PO is required.

Finally we will briefly look at two software packages:

- GRASP (TICRA, 2005) developed by TICRA which uses PO and GO
- MODAL (White, 2006; Gradziel, et al., 2008) developed at Maynooth University which uses PO and GBM.

These simulation packages and their respective analysis methods are used in tandem in order to ascertain the optical properties of the QUBIC instrument in the THz band. The implementation and details of the QUBIC instrument will then be looked at in Chapter 3.

2.1 Feed Horn Analysis Techniques

The techniques explored here relate primarily to those used in the calculation of the aperture field of a circular corrugated feed horn. The method employed is a modal analysis which characterises the propagation of radiation in a metallic waveguide in terms of modes that are determined by the boundary conditions imposed by the walls of a feed horn. The feed horn is modelled as a series of cylindrical sections of varying radii and a mode matching technique is used to calculate the propagation from one section to the next.

2.1.1 TE and TM modes

In many systems a field can be broken down into simpler components. One decomposition suited to metallic waveguides is in terms of the orthogonal sets of TE and TM modes. These are so named due to having no electric and magnetic components, respectively, in the direction of propagation. Generally the transverse plane is taken as being the xy -plane and by extension the direction of propagation is along the z -axis. By applying the boundary conditions of the waveguide, we can derive expressions for the modes (that involve integers known as mode numbers) with the number of each mode type that can propagate depending upon the excitation frequency and radius of the waveguide section in question. The cut-off wave number, below which the mode will not propagate, is related to the wave number by,

$$k_c^2 = k^2 - \beta^2 \quad (2.1)$$

Mode cut off wave number

where:

k_c is the cut-off wave number of a mode

β is the waveguide wave number

k is the waveguide wave number of the material filling the waveguide

Note: k is interchangeable with frequency using $k = 2\pi\nu_0\sqrt{\mu\epsilon}$,

ν_0 is the free space frequency

ϵ is the dielectric constant

μ is the medium permeability

Fields travelling in the z direction vary as $e^{-i\beta z}$. For a β that is purely real there is no attenuation, when β is imaginary there is an exponential decay of the field and it is called evanescent. In order to derive expressions for the propagating modes we start with the Helmholtz equation $(\nabla^2 + k^2)\Psi = 0$ (Clarricoats & Olver, 1984) and writing it in terms of transverse and longitudinal components for both the Laplacian and the wave number we get,

$$(\nabla_{xy}^2 + \nabla_z^2)\Psi = -(k_c^2 + \beta^2)\Psi \quad (2.2)$$

Helmholtz wave equation split for transverse (xy) and longitudinal (z) components

where:

Ψ is any monochromatic electromagnetic field component, E or H

∇_{xy}^2 is the Laplacian transverse component

∇_z^2 is the Laplacian longitudinal component

k_c is the cut-off wave number

β is the waveguide wave number

which we can split into two parts one each for the longitudinal and transverse components:

$$\nabla_z^2\Psi = -\beta^2\Psi \quad (2.3)$$

$$\nabla_{xy}^2\Psi = -k_c^2\Psi \quad (2.4)$$

Helmholtz wave equation with longitudinal and transverse components equated separately

Using Maxwell's equations and *Equation (2.4)*, it can be shown (Ramo, et al., 1994) that by applying the boundary conditions to the electromagnetic wave equation we can obtain a description of a field in a transverse plane,

$$E_r = -\frac{j}{k_c^2} \left(\beta \frac{\delta E_z}{\delta r} + \frac{\omega \mu}{r} \frac{\delta H_z}{\delta \phi} \right) \quad (2.5)$$

$$E_\phi = \frac{j}{k_c^2} \left(\frac{\beta}{r} \frac{\delta E_z}{\delta \phi} + \omega \mu \frac{\delta H_z}{\delta r} \right) \quad (2.6)$$

$$H_r = \frac{j}{k_c^2} \left(\frac{\omega \mu}{r} \frac{\delta E_z}{\delta \phi} - \beta \frac{\delta H_z}{\delta r} \right) \quad (2.7)$$

$$H_\phi = -\frac{j}{k_c^2} \left(\omega \mu \frac{\delta E_z}{\delta r} + \frac{\beta}{r} \frac{\delta H_z}{\delta \phi} \right) \quad (2.8)$$

Expressions for E and H field components derived from Maxwell's equations in cylindrical coordinates (Ramo, et al., 1994)

Expanding the transverse component of the Laplacian for E_z in cylindrical coordinates gives,

$$\nabla_{xy}^2 E_z = \frac{1}{r} \frac{\delta}{\delta r} \left(r \frac{\delta E_z}{\delta r} \right) + \frac{1}{r^2} \frac{\delta^2 E_z}{\delta \phi^2} = -k_c^2 E_z \quad (2.9)$$

Expansion of the Laplacian

From Olver (Olver, et al., 1994), using separation of variables, a solution pair to the above equation is:

$$E_{nl,z} = A_{nl} J_n(k_c r) \begin{pmatrix} \cos n\phi \\ \sin n\phi \end{pmatrix} e^{j(\omega t - \beta z)} \quad (2.10)$$

$$E_{nl,r} = -\frac{j\beta}{k_c^2 r} A_{nl} J_n'(k_c r) \begin{pmatrix} \cos n\phi \\ \sin n\phi \end{pmatrix} e^{j(\omega t - \beta z)} \quad (2.11)$$

$$E_{nl,\phi} = -\frac{j\beta n}{k_c^2 r} A_{nl} J_n(k_c r) \begin{pmatrix} -\sin n\phi \\ \cos n\phi \end{pmatrix} e^{j(\omega t - \beta z)} \quad (2.12)$$

$$H_{nl,r} = -\frac{E_{nl,\phi}}{Z_{nl}} \quad (2.13)$$

$$H_{nl,\phi} = \frac{E_{nl,r}}{Z_{nl}} \quad (2.14)$$

$$H_{nl,z} = 0 \quad (2.15)$$

Solution to Maxwell's equations with boundary conditions appropriate for conical waveguides

where:

n is the azimuthal mode number and l is the radial mode number

J_n is a Bessel function of the first kind of order n

J'_n is the derivative of the Bessel function

A_{nl} is a constant

Z_{nl} is the impedance of the waveguide = β/ωε

In this case $H_{nl,z} = 0$ so these are TM modes. Taking the electric field along the surface of a perfect conductor as zero, it follows $E_{z|r=a} = E_{\phi|r=a} = 0$, where a is the radius of the waveguide. Therefore using *Equation (2.10)* at $r = a$ we must have $J_n(k_c a) = 0$. It follows that $k_c a$ must be a root of the Bessel function.

$$k_c a = \frac{2\pi}{\lambda_c} a = P_{nl} \quad (2.16)$$

Root of the Bessel function of order n

where:

P_{nl} is the lth root of the Bessel function of order n

The cut-off wave number is now simply $k_c = \frac{P_{nl}}{a}$ and substituting this into the relationship for impedance $Z_{nl} = \frac{\beta}{\omega\epsilon}$ and using $k = \omega\sqrt{\mu\epsilon}$ and the identity defined in *Equation (2.1)* we get

$$Z_{nl} = Z_0 \sqrt{1 - \left(\frac{P_{nl}}{\omega\sqrt{\mu\epsilon}a} \right)^2} \quad (2.17)$$

TM Waveguide impedance

where:

Z_{nl} is the waveguide impedance seen by a mode of azimuthal order n and radial order l

Z₀ is the characteristic impedance of the waveguide medium, given by $Z_0 = \sqrt{\mu/\epsilon}$

The fields can be normalised such that *Equation (2.18)* holds true

$$\int_0^{2\pi} \int_0^a (|e_{nl,r}|^2 + |e_{nl,\phi}|^2) r dr d\phi = 1 \quad (2.18)$$

Normalisation

where:

$$e_{nl,r} \text{ is the field from Equation (2.11) without the propagation term } e^{j(\omega t - \beta z)}$$

$$E_{nl,r} = e_{nl,r} e^{j(\omega t - \beta z)}$$

$$e_{nl,\phi} \text{ is the field from Equation (2.12) without the propagation term } e^{j(\omega t - \beta z)}$$

$$E_{nl,\phi} = e_{nl,\phi} e^{j(\omega t - \beta z)}$$

Solving the integral in Equation (2.18) and converting to Cartesian coordinates yields the following set of equations which will be utilised for feed horn analysis throughout this thesis:

$$e_{nl,x} = \frac{1}{2} C_{nl} \left(J_{n-1} \left(P_{nl} \frac{r}{a} \right) \begin{pmatrix} \cos(n-1)\phi \\ -\sin(n-1)\phi \end{pmatrix} + J_{n+1} \left(P_{nl} \frac{r}{a} \right) \begin{pmatrix} -\cos(n+1)\phi \\ \sin(n+1)\phi \end{pmatrix} \right) \quad (2.19)$$

$$e_{nl,y} = \frac{1}{2} C_{nl} \left(J_{n-1} \left(P_{nl} \frac{r}{a} \right) \begin{pmatrix} -\sin(n-1)\phi \\ -\cos(n-1)\phi \end{pmatrix} + J_{n+1} \left(P_{nl} \frac{r}{a} \right) \begin{pmatrix} -\sin(n+1)\phi \\ -\cos(n+1)\phi \end{pmatrix} \right) \quad (2.20)$$

$$h_{nl,x} = \frac{1}{2} \frac{C_{nl}}{Z_{nl}} \left(J_{n-1} \left(P_{nl} \frac{r}{a} \right) \begin{pmatrix} \sin(n-1)\phi \\ \cos(n-1)\phi \end{pmatrix} + J_{n+1} \left(P_{nl} \frac{r}{a} \right) \begin{pmatrix} \sin(n+1)\phi \\ \cos(n+1)\phi \end{pmatrix} \right) \quad (2.21)$$

$$h_{nl,y} = \frac{1}{2} \frac{C_{nl}}{Z_{nl}} \left(J_{n-1} \left(P_{nl} \frac{r}{a} \right) \begin{pmatrix} \cos(n-1)\phi \\ -\sin(n-1)\phi \end{pmatrix} + J_{n+1} \left(P_{nl} \frac{r}{a} \right) \begin{pmatrix} -\cos(n+1)\phi \\ \sin(n+1)\phi \end{pmatrix} \right) \quad (2.22)$$

TM equation set

where:

$$C_{nl} \text{ is the normalisation factor} = \sqrt{\frac{2 - \frac{1}{|n+1|}}{\pi a^2 J_{n+1}^2(P_{nl})}}$$

For TE modes we set $E_{nl,z} = 0$ and there is an equivalent set of equations to those of the TM mode Equations (2.10) to (2.14) which can be shown to be (Olver, et al., 1994),

$$E_{nl,r} = -\frac{j\omega\mu n}{k_c^2 r} B_{nl} J_n(k_c r) \begin{pmatrix} \cos n\phi \\ -\sin n\phi \end{pmatrix} e^{j(\omega t - \beta z)} \quad (2.23)$$

$$E_{nl,\phi} = -\frac{j\omega\mu}{k_c} B_{nl} J'_n(k_c r) \begin{pmatrix} \sin n\phi \\ \cos n\phi \end{pmatrix} e^{j(\omega t - \beta z)} \quad (2.24)$$

$$E_{nl,z} = 0 \quad (2.25)$$

$$H_{nl,z} = B_{nl} J_n(k_c r) \begin{pmatrix} \sin n\phi \\ \cos n\phi \end{pmatrix} e^{j(\omega t - \beta z)} \quad (2.26)$$

$$H_{nl,r} = \frac{E_{nl,\phi}}{Z_{nl}} \quad (2.27)$$

$$H_{nl,\phi} = -\frac{E_{nl,r}}{Z_{nl}} \quad (2.28)$$

Solution pair to the Laplacian expansion of Maxwell's equations

where:

J_n is a Bessel function of the first kind of order n

J'_n is the derivative of the Bessel function

B_{nl} is a constant

Z_{nl} is the impedance of the waveguide = $\beta/\omega\epsilon$

and similarly to the TM modes *Equation (2.17)* there is an expression for the TE waveguide impedance,

$$Z_{nl} = \frac{Z_o}{\sqrt{1 - \left(\frac{Q_{nl}}{\omega\sqrt{\mu\epsilon}a}\right)^2}} \quad (2.29)$$

TE Waveguide impedance

where:

Q_{nl} is the l^{th} root of the derivative of the n^{th} order Bessel function

Again normalising and converting to Cartesian coordinates we obtain

$$e_{nl,x} = \frac{1}{2} D_{nl} \left(J_{n-1} \left(Q_{nl} \frac{r}{a} \right) \begin{pmatrix} \cos(n-1)\phi \\ -\sin(n-1)\phi \end{pmatrix} + J_{n+1} \left(Q_{nl} \frac{r}{a} \right) \begin{pmatrix} \cos(n+1)\phi \\ -\sin(n+1)\phi \end{pmatrix} \right) \quad (2.30)$$

$$e_{nl,y} = \frac{1}{2} D_{nl} \left(J_{n-1} \left(Q_{nl} \frac{r}{a} \right) \begin{pmatrix} -\sin(n-1)\phi \\ -\cos(n-1)\phi \end{pmatrix} + J_{n+1} \left(Q_{nl} \frac{r}{a} \right) \begin{pmatrix} \sin(n+1)\phi \\ \cos(n+1)\phi \end{pmatrix} \right) \quad (2.31)$$

$$h_{nl,x} = \frac{1}{2} \frac{D_{nl}}{Z_{nl}} \left(J_{n-1} \left(Q_{nl} \frac{r}{a} \right) \begin{pmatrix} \sin(n-1)\phi \\ \cos(n-1)\phi \end{pmatrix} + J_{n+1} \left(Q_{nl} \frac{r}{a} \right) \begin{pmatrix} -\sin(n+1)\phi \\ -\cos(n+1)\phi \end{pmatrix} \right) \quad (2.32)$$

$$h_{nl,y} = \frac{1}{2} \frac{D_{nl}}{Z_{nl}} \left(J_{n-1} \left(Q_{nl} \frac{r}{a} \right) \begin{pmatrix} \cos(n-1)\phi \\ -\sin(n-1)\phi \end{pmatrix} + J_{n+1} \left(Q_{nl} \frac{r}{a} \right) \begin{pmatrix} \cos(n+1)\phi \\ -\sin(n+1)\phi \end{pmatrix} \right) \quad (2.33)$$

TE equation set

where:

$$D_{nl} \text{ is the normalisation factor} = \sqrt{\frac{2 - \frac{1}{|n+1|}}{\pi a^2 J_n^2(Q_{nl}) \left(1 - \frac{n}{Q_{nl}}\right)^2}}$$

The upper and lower case terms in the brackets show the azimuthal dependence of the two orthogonal mode sets.

Modes become excited in a horn in an order determined by the roots of the Bessel function (or its derivative) with which they are associated. Below the cut-on wave number, as defined in *Equation (2.16)*, the modes become evanescent. Taking note of the operating frequency and dimensions of a waveguide one can readily determine the modes that can be supported. Modes with the same roots are degenerate but contain different azimuthal profiles due to their differing dependencies on the $\sin(n\phi)$ and $\cos(n\phi)$ functions.

To calculate the field at the aperture of the feed horn, the mode amplitudes need to be calculated. The approach taken here is that of a mode matching technique (Wexler, 1967) which is utilised in Maynooth University's SCATTER software package (Colgan, 2001; Gleeson, 2004).

2.1.2 Mode matching techniques

SCATTER utilises a mode matching technique, first developed by Wexler (Wexler, 1967) and implemented by Colgan and Gleeson (Colgan, 2001; Gleeson, 2004) here at Maynooth University. The scattering matrix and mode matching techniques described are optimised for a conical corrugated feed horn with variable mode content at each junction, an example of which is shown in *Figure 2.2* below.

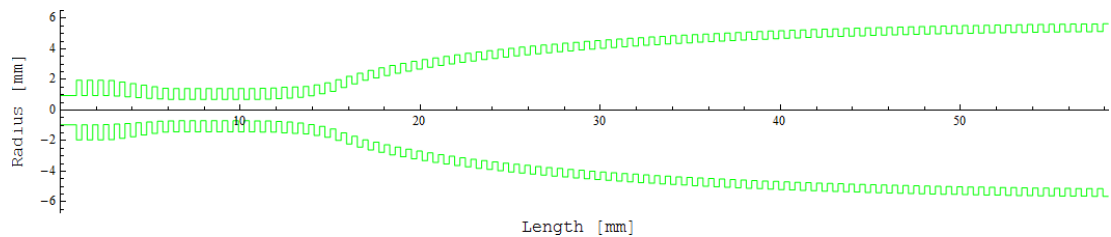


Figure 2.2: Profile of the 14° QUBIC feed horn design, a scaled version of the 100 GHz CLOVER (Taylor, et al., 2004) feed horn re-designed to operate at a central frequency of 150 GHz. This initial feed horn design was later modified to emit a 12.9° beam and will be used in a back-to-back format

The analysis of a typical corrugated conical feed horn starts with dividing it into sections at the points where the radius varies. The corrugated cylindrical waveguides are now treated as a cascaded group of cylindrical waveguides. Theoretically there are an infinite number of modes to consider but as we have seen in §2.1.1 there is a cut-off frequency (high pass) which depends on the mode

number and radius of the section. It follows that the geometry of a waveguide section can be used to determine an upper limit on the number of propagating modes. The actual number of modes required to accurately describe the system is found by trial and error as there are evanescent modes which will traverse small sections with non-negligible power and must be considered. As scattering only occurs between modes with the same azimuthal order each order can be considered independently. Even though there are a variable number of modes supported by each section the number considered is standardised to the maximum number in SCATTER to allow for efficient processing.

Using the approach detailed by Olver (Olver, et al., 1994) each junction of the corrugated horn is considered as a two-port system. At the junction between two sections of differing radii, as shown in *Figure 2.3*, the coupling between each mode on the input side and each mode on the output side is calculated. These ‘scattering’ relationships are stored in matrix form called a scattering matrix, $[S]$.

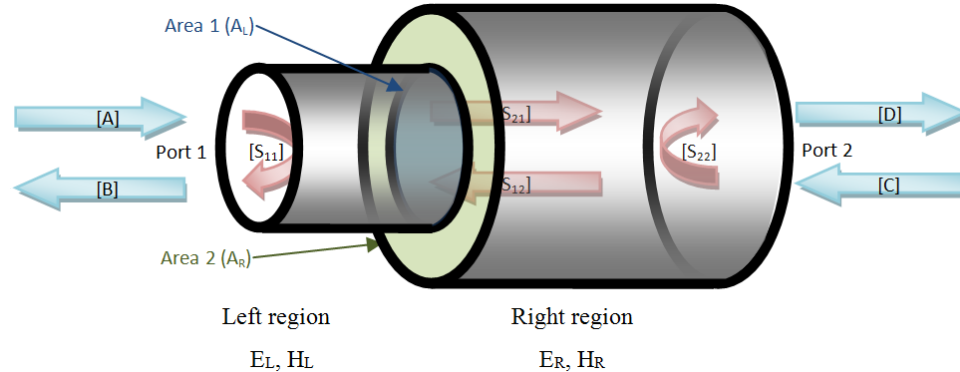


Figure 2.3: Sub-section of a feed horn geometry showing the relevant transmissions and reflections and the change in radius from one section to the next. It should be noted that the same applies in the case of a step-down in radius as does in the step-up case illustrated above. The column matrix, $[A]$ represents the transmission coefficients from the ‘fed’ side of the horn, $[B]$ contains the reflection coefficients. On the aperture side, $[C]$ represents the forward coefficients and $[D]$ the reflected coefficients. The scattering matrix, $[S]$, contains 4 sub matrices containing the coupling coefficients between the TE and TM modes for this junction in the feed horn.

The $[S]$ matrix consists of 4 sub-matrices describing power that goes from port 1 to 2 (S_{21}), 2 to 1 (S_{12}), 1 back to 1 (S_{11}) and 2 back to 2 (S_{22}). This gives us the transmission and reflection coefficients from the perspective of both the input and output ports. Under the assumption that the number of considered modes on both

sides of the junction are kept the same, $[S]$ is a $4m \times 4m$ matrix with each of the 4 component matrices being $2m \times 2m$, where m TE and m TM modes are considered. The vectors $[A]$ and $[D]$ represent the forward propagating field (i.e. the amplitude of each component mode) and $[B]$ and $[C]$ the reverse propagating field. The relationship between the excitation and emission coefficients is shown in *Equations (2.34) to (2.37)*.

$$[S] = \begin{bmatrix} [S_{11}] & [S_{12}] \\ [S_{21}] & [S_{22}] \end{bmatrix} \quad (2.34)$$

$$\begin{bmatrix} [B] \\ [D] \end{bmatrix} = \begin{bmatrix} [S_{11}] & [S_{12}] \\ [S_{21}] & [S_{22}] \end{bmatrix} \begin{bmatrix} [A] \\ [C] \end{bmatrix} \quad (2.35)$$

or

$$[B] = \underbrace{[S_{11}][A]}_{\text{reflection}} + \underbrace{[S_{12}][C]}_{\text{transmission}} \quad (2.36)$$

$$[D] = \underbrace{[S_{21}][A]}_{\text{transmission}} + \underbrace{[S_{22}][C]}_{\text{reflection}} \quad (2.37)$$

Scattering matrix format

where:

- S₁₁ is the reflection at port 1 from port 1*
- S₁₂ is the transmission from port 2 to port 1*
- S₂₁ is the transmission from port 1 to port 2*
- S₂₂ is the reflection at port 2 from port 2*
- A is the power entering at port 1*
- B is the power exiting at port 1*
- C is the power entering at port 2*
- D is the power exiting at port 2*

In cases where the assumption can be made that there is no reflection at an aperture, the column matrix $[C]$ becomes $[0]$ and the above equations simplify to

$$[B] = \underbrace{[S_{11}]}_{\text{reflection}}[A] \quad (2.38)$$

$$[D] = \underbrace{[S_{21}]}_{\text{transmission}}[A] \quad (2.39)$$

Simplified scattering matrix under the assumption of no reflection at aperture (exit port) where:

- S₁₁ is the reflection at port 1 from port 1*
- S₂₁ is the transmission from port 1 to port 2*
- A is the power entering at port 1*
- B is the power exiting at port 1*
- D is the power exiting at port 2*

A common design is that of a single moded system where a TE₁₁ mode is the only excitation considered. In this case we use a column excitation matrix, $[A]$, like that in *Equation (2.40)*. In feed horns with more than one coherent mode propagating, the vector $[A]$ has non-zero entries at positions relating to each mode that propagates. A value $A_i = 1 \forall i$ means that equal power is carried by each mode. The $[A]$ vector contains an entry for each coherent mode considered and a unique vector is required for each azimuthal order and mutually incoherent mode set.

$$[A] = \begin{bmatrix} A_{TE_{11}} \\ A_{TE_{12}} \\ A_{TE_{13}} \\ \dots \\ A_{TE_{1m}} \\ A_{TM_{11}} \\ A_{TM_{12}} \\ A_{TM_{13}} \\ \dots \\ A_{TM_{1m}} \end{bmatrix} = \begin{bmatrix} 1 \\ 0 \\ 0 \\ \dots \\ 0 \\ 0 \\ 0 \\ 0 \\ \dots \\ 0 \end{bmatrix} \quad (2.40)$$

Simplified scattering matrix for assumption of no reflection at aperture where:

- A is the power entering at port 1*
- The azimuthal order in this case is 1*
- m is the number of the highest mode considered*

Within the uniform waveguide section (where no scattering occurs) the propagation matrices are given by Olver (Olver, et al., 1994) diagonal matrices of the form,

$$\begin{aligned} [S_{11}] &= [S_{22}] = [0] \\ [S_{12}] &= [S_{21}] = [e^{-j\beta_i L}] \end{aligned} \quad (2.41)$$

Propagation matrices (Olver, et al., 1994)

where:

L is the length of the waveguide section

i is the diagonal element index (mode number)

β is the waveguide wave number for the i^{th} mode (TE or TM)

real for propagating modes, imaginary for evanescent modes

Only those modes (including evanescent modes) that satisfy Maxwell's equations, taking account of the boundary conditions, are considered. The different cross-sectional area on the left and right side of the junction, shown in *Figure 2.3*, dictates that a different finite set of propagating modes is supported on either side of the junction. As detailed in Olver (Olver, et al., 1994) the respective electric and magnetic fields are,

$$E_L = \sum_{i=1}^N (A_i e^{-j\beta_i z} + B_i e^{j\beta_i z}) e_{i_L} \quad (2.42)$$

$$H_L = \sum_{i=1}^N (A_i e^{-j\beta_i z} - B_i e^{j\beta_i z}) h_{i_L} \quad (2.43)$$

$$E_R = \sum_{i=1}^N (D_i e^{-j\beta_i z} + C_i e^{j\beta_i z}) e_{i_R} \quad (2.44)$$

$$H_R = \sum_{i=1}^N (D_i e^{-j\beta_i z} - C_i e^{j\beta_i z}) h_{i_R} \quad (2.45)$$

Electric and magnetic fields at the left and right side of a conical junction

where:

R and L refer to the right and left hand side of the junction

A, B, C & D are the transmission and reflection coefficients (as calculated previously)

i is the mode index and N the total number of modes

$\pm\beta$ is the waveguide number for the i^{th} mode (TE or TM)

real for propagating modes, imaginary for evanescent modes

+ denotes propagation in a negative z direction, - denote positive z propagation

e_{i_L} is the electric field for the i^{th} mode on the LHS

e_{i_R} is the electric field for the i^{th} mode on the RHS

h_{i_L} is the magnetic field for the i^{th} mode on the LHS

h_{i_R} is the magnetic field for the i^{th} mode on the RHS

As the left and right hand side of the equations are continuous and z is taken as 0 at the junction, conserving complex power at the junction gives:

$$\sum_{i=1}^N (A_i + B_i) e_{i_L} = \sum_{i=1}^N (D_i + C_i) e_{i_R} \quad (2.46)$$

$$\sum_{i=1}^N (A_i - B_i) h_{i_L} = \sum_{i=1}^N (D_i - C_i) h_{i_R} \quad (2.47)$$

Equated left side and right side power for the electric and magnetic fields at a conical junction

In considering the region of cross-sectional area not common to both sections ($A_L - A_R$) in *Figure 2.3*, the field can be considered to be zero because of the conducting wall at the junction. From this it can be shown in matrix form (Ramo, et al., 1994) that,

$$[P][[A] + [B]] = [Q][[D] + [C]] \quad (2.48)$$

$$[P^{T*}][[D] - [C]] = [R^*][[A] - [B]] \quad (2.49)$$

Conservation of complex power (Ramo, et al., 1994)

where:

[A] and [B] are N-column modal coefficient matrices for the left side of the junction

[C] and [D] are N-column modal coefficient matrices for the right side of the junction

[P] is an NxN power coupling integral matrix with $P_{nm} = \int_{A_L} e_{nL} \times h_{mR} dA$

[Q] is an NxN right hand side self coupling matrix with $Q_{mm} = \int_{A_R} e_{mR} \times h_{mR} dA$

[R] is an NxN left hand side self coupling matrix with $R_{mm} = \int_{A_L} e_{mL} \times h_{mL} dA$

Finally re-arranging we obtain, as detailed in Olver (Olver, et al., 1994),

$$[S_{11}] = [[R]^* + [P]^{T*}[Q]^{-1}[P]]^{-1} [[R]^* - [P]^{T*}[Q]^{-1}[P]] \quad (2.50)$$

$$[S_{12}] = 2[[R]^* + [P]^{T*}[Q]^{-1}[P]]^{-1} [P]^{T*} \quad (2.51)$$

$$[S_{21}] = 2[[Q] + [P][R]^{*-1}[P]^{T*}]^{-1} [P] \quad (2.52)$$

$$[S_{22}] = [[Q] + [P][R]^{*-1}[P]^{T*}]^{-1} [[Q] - [P][R]^{*-1}[P]^{T*}] \quad (2.53)$$

Scattering matrices

Solving these equations numerically would be computationally intensive and so SCATTER uses analytical expressions for the overlap integrals in $[P]$, $[Q]$ and $[R]$ see (Colgan, 2001; Gleeson, 2004) for implementation.

With a scattering matrix for each waveguide section, the matrix for the overall description is simply calculated by cascading the individual matrices. For the junction in *Figure 2.3* for example, the left hand side scattering matrix $[S^L]$ is cascaded with the scattering matrix for the right hand side $[S^R]$ as in *Equations (2.54) to (2.57)*. The resultant scattering matrix $[S]$ is then used as $[S^L]$ for the next junction. These steps are repeated for each section in the feed horn yielding a matrix describing the output for the feed horn as a whole.

$$[S_{11}] = [S_{12}^L][[I] - [S_{11}^R][S_{22}^L]]^{-1} [S_{11}^R][S_{21}^L] + [S_{11}^L] \quad (2.54)$$

$$[S_{12}] = [S_{12}^L][[I] - [S_{11}^R][S_{22}^L]]^{-1} [S_{12}^R] \quad (2.55)$$

$$[S_{21}] = [S_{21}^R][[I] - [S_{22}^L][S_{11}^R]]^{-1} [S_{21}^L] \quad (2.56)$$

$$[S_{22}] = [S_{21}^R][[I] - [S_{22}^L][S_{11}^R]]^{-1} [S_{22}^L][S_{12}^R] + [S_{22}^R] \quad (2.57)$$

Cascaded scattering matrices

where:

$[\]^{-1}$ is the inverse of the matrix

$[I]$ is the identity matrix

R and L refer to the left- and right-hand side of the junction

We now have, in the overall scatter matrices, a description of the transmission and reflection properties of the full feed horn. These matrices can then be used to give the beam patterns for the horn geometry analysed in both the near and far fields.

2.1.3 Singular value decomposition

Near their design frequency, feed horns normally have significant contributions from relatively few eigenmodes, and so considering the contribution from a large number of TE/TM modes to create the overall aperture field is quite inefficient.

At the aperture, multiple groups of modes are independently coherent. Each set of modes that are mutually coherent can be considered together and propagated as a single entity, known as a hybrid mode. Most feed horns are designed to be single-moded, meaning they possess only one hybrid mode but multi-moded (sometimes called over-moded) feed horns are also popular. Single-moded feed horns excited at a frequency far higher than their design frequency can become multi-moded. In order to model a field propagating through free space, each hybrid mode must be analysed and propagated independently and summed at the destination (in quadrature for incoherent sources/detectors). Even so the use of hybrid modes drastically reduces the number of modes that must be propagated.

A method known as singular value decomposition (SVD) can be utilised to find these coherent sets. SVD is a way of writing an $m \times n$ matrix as a product of 3 matrices, $[S_{21}] = [U][W][V^{T*}]$, the first matrix, $[U]$, is of size $m \times m$ and the last, $[V]$, is $n \times n$ in size, with the central one, $[W]$, being $m \times n$ in size but with only the diagonal elements being non-zero. Both $[U]$ and $[V]$ matrices are unitary and the values in the diagonal matrix $[W]$ are positive real numbers which by convention are arranged in descending order, as shown in [Equation \(2.58\)](#). SVD explicitly constructs orthonormal basis in the input $[U]$ and output $[V]$ spaces. Since $[S][V] = [W][U]$ the scatter matrix transforms the input modes described by the columns of $[V]$ into the output modes described by $[W][U]$. One only needs to consider columns in the $[U]$ matrix that correspond to non-zero diagonal elements in the $[W]$ matrix. Due to

the diagonal nature of the $[W]$ matrix the modes are independent and can be considered separately, these are the hybrid modes.

$$[S] = [U] \begin{bmatrix} w_1 & 0 & 0 & 0 \\ 0 & w_2 & 0 & 0 \\ 0 & 0 & w_3 & 0 \\ 0 & 0 & 0 & \dots \end{bmatrix} [V]^{T*} \quad (2.58)$$

Singular value decomposition – matrix representation

Note: This approach is not an approximation of the full scatter matrix method; it will yield the exact same result as the full method, once all non-zero columns are included.

The number of TE/TM waveguide modes required to reproduce the aperture field is much higher than the number of hybrid modes. For example, to accurately model the aperture field of QUBIC’s back-to-back conical corrugated feed horn, as shown in *Figure 2.2*, requires ~ 20 TE and ~ 20 TM modes for one azimuthal order. This gives a total of 40 modes at the aperture to propagate. When SVD is performed on the $[S_{21}]$ matrix it has only one entry in the $[W]$ matrix with any significant power. The feed horn is therefore single moded with only one hybrid mode present at the aperture. The $[U]$ matrix can be used to construct the hybrid mode from appropriate combinations of the TE and TM modes. This single mode exists over the desired frequency range and analysis showed that the feed horn only became multi-moded for frequencies beyond ~ 180 GHz (its original design frequency is 150 GHz with 25% bandwidth). This can be seen in *Figure 2.4* where the output from the feed horn deviates from its single-mode nature with increasing frequency. At the design frequency one only needs to consider the single hybrid mode allowing the efficient modelling of the QUBIC system.

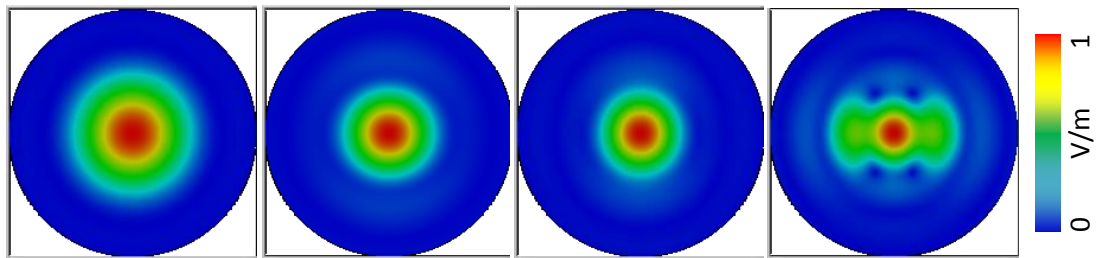


Figure 2.4: Scaled version of the 14° CLOVER (Taylor, et al., 2004) output field amplitude 100 mm from horn. All beams are normalised to their individual maximum peaks for comparison. The frequencies of operation are 150, 195.5, 220 and 247 GHz.

An analysis of the feed horn was carried out, in 1 GHz steps, over the range of operation (including the extended operation described in §6.3) from 130 GHz to 250 GHz. The transmitted power (calculated from S_{21}) as a function of frequency is shown in *Figure 2.5*. For the initial operating range (150 GHz \pm 12.5%) the output was stable but beyond 180 GHz the output became erratic.

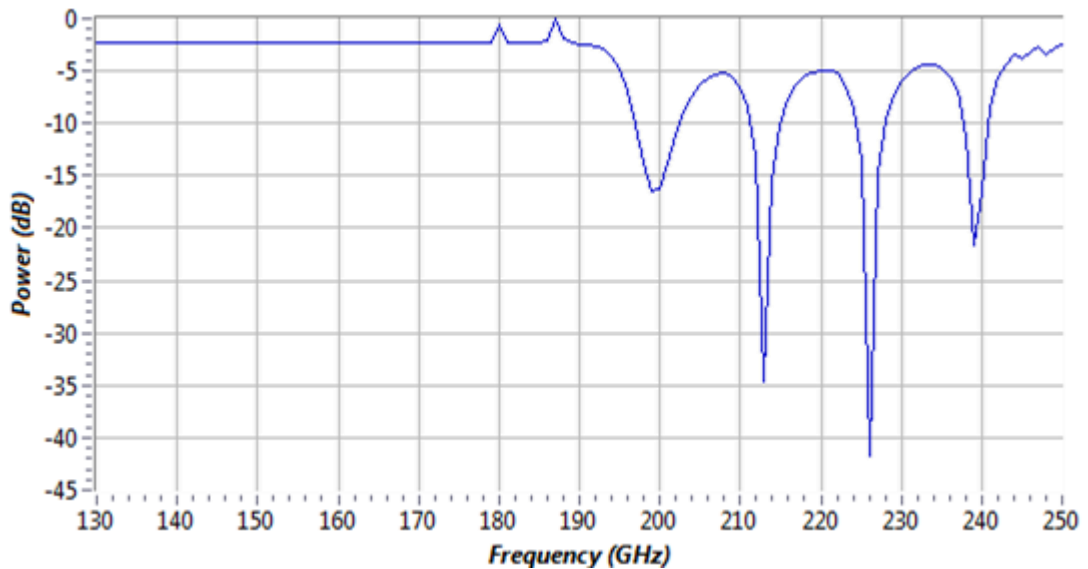


Figure 2.5: Frequency response of the 14° feed horn for an on-axis plane wave excitation.

Table 2-1 shows a sample of the output from SCATTER, using 80 modes (40 TE and 40 TM) for each frequency, where only one entry per azimuthal order, n , was found with significant power ($\geq 0.1\%$). Azimuthal orders 0 to 5 were tested but orders 0 to 2 were the only ones with any significant power.

Table 2-1: 14° feed horn mode power as a function of excitation frequency (generated from Mathematica SCATTER based on SVD 'w' matrix elements)

GHz	Az0	Az1	Az2	Power
130	-	70.3%	-	70.3%
140	-	66.2%	-	66.2%
150	-	67.8%	-	67.8%
160	-	66.2%	-	66.2%
170	-	67.6%	-	67.6%
180	21.0%	59.2%	-	69.7%
190	38.5%	66.0%	-	85.3%
200	0.2%	36.1%	0.1%	36.3%
210	-	14.7%	-	14.7%
220	-	43.2%	23.5%	66.7%
230	0.2%	27.2%	20.4%	47.6%
240	0.3%	1.2%	0.5%	1.9%
250	-	62.1%	10.7%	72.8%

The cut-on of hybrid-modes and the response from the feed horn becoming unstable can clearly be seen at higher frequencies. The instability in part led to the requirement for a new feed horn design which will be analysed in greater detail in §6.3.

2.1.4 Dispersion curves

The QUBIC feed horn was designed to be single moded at 150 GHz and the SVD analysis showed that at higher frequencies additional modes cut-on. It would be advantageous to be able to do a quick check to see if a feed horn is expected to be single moded in the region of operation. As previously seen the low frequency cut-off for modes occurs when $k = k_c$ resulting in $\bar{\beta} = 0$ where $\beta = \sqrt{k^2 - k_c^2}$ and $\bar{\beta} = \frac{\beta}{k}$. Unlike modes from other geometries, the hybrid modes of corrugated feed horns, also have a high cut-off frequency given by $\bar{\beta} \rightarrow \infty$. Applying this to the wave equations and solving we arrive at (Clarricoats & Olver, 1984),

$$F_n(k_c r_i) - \frac{(n\bar{\beta})^2}{F_n(k_c r_i)} = \left(\frac{k_c}{k}\right)^2 S_n(kr_i, kr_o) \quad (2.59)$$

where:

S_n is the cylindrical function of order n (Clarricoats & Olver, 1984)

k is the free space wave number = $\sqrt{k_c^2 + \beta^2}$

k_c is the transverse wave number

β is the waveguide wave number

r_i is the inner radius of the corrugated horn

r_o is the outer radius of the corrugated horn

J_n is a Bessel function of the first kind of order n

Y_n is a Bessel function of the second kind of order n

J'_n is the derivative of a Bessel function of the first kind of order n

Y'_n is the derivative of a Bessel function of the second kind of order n

and

$$F_n(x) = x \frac{J'_n(x)}{J_n(x)} \quad (2.60)$$

$$S_n(x, y) = \frac{x(Y_n(y)J'_n(x) - J_n(y)Y'_n(x))}{J_n(x)Y_n(y) - Y_n(x)J_n(y)} \quad (2.61)$$

Equation (2.59) gives a set of dispersion curves and therefore cut-on and -off frequencies, for a specified corrugated waveguide (the narrowest part of the feed horn geometry is used as it acts as the mode filter). This is very useful when estimating the number of modes present in a feed horn at a given or range of frequencies. The waveguide section is described by inner, r_i , and outer, r_o , radii as shown in Figure 2.6. The inner and outer radii in the case of the 14° QUBIC feed horn are, $r_i = 0.694$ mm and $r_o = 1.416$ mm.

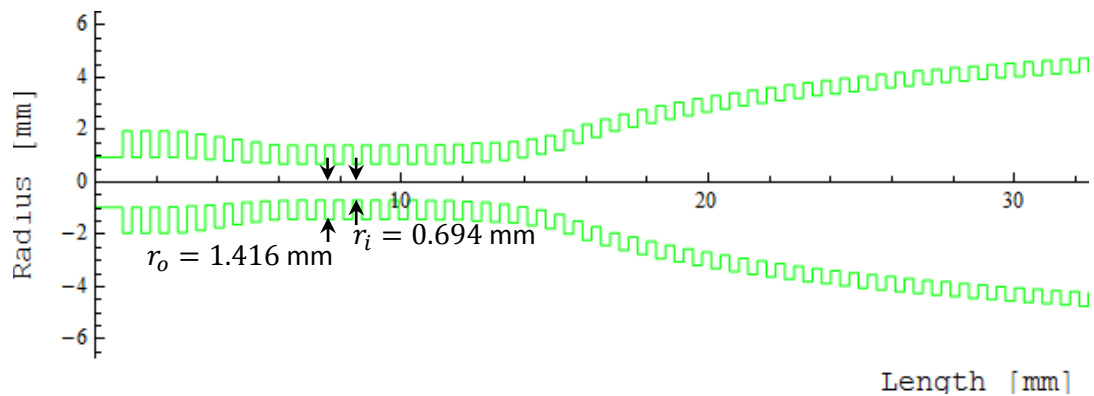


Figure 2.6: Profile of the 14° QUBIC feed horn design showing the section around the narrowest part of the feed horn highlighting the inner, r_i , and outer, r_o , radii for that section.

In Figure 2.7 I show an example of the calculations for the QUBIC feed horn where it can be clearly seen that there is only 1 intersection with the $kr_i = 2.18$ ($\cong 150$ GHz, the design frequency) line and therefore the feed horn is expected to be single-moded (HE_{11}) at the design frequency.

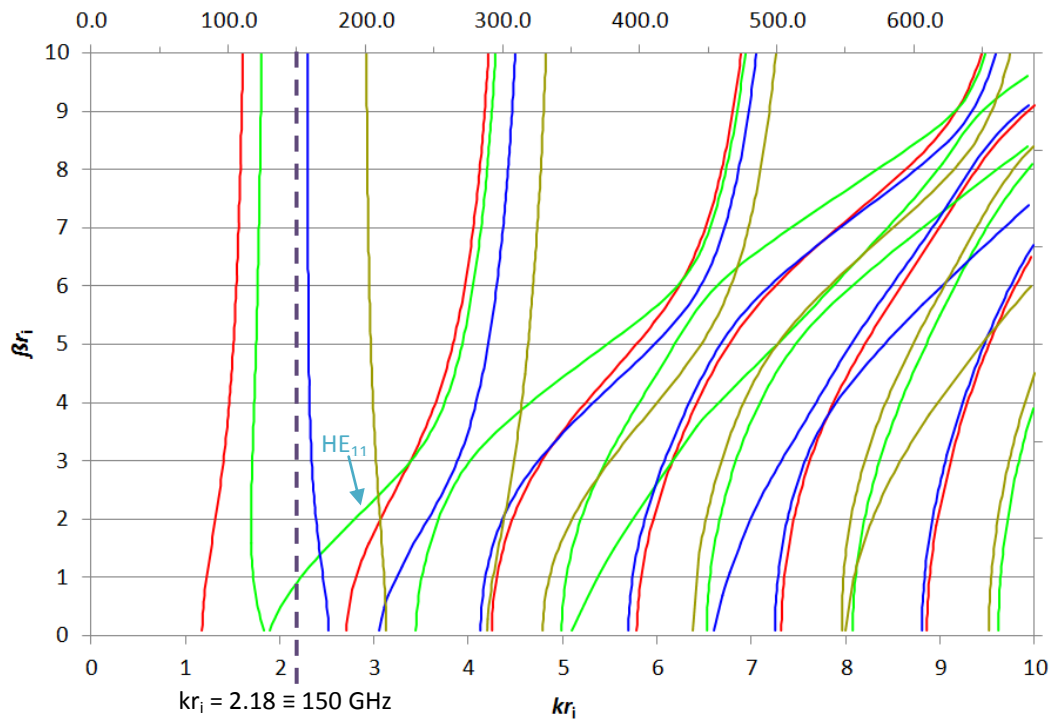


Figure 2.7: Dispersion curves for QUBIC 150 GHz 14° feed horn design. The dispersion curves are shown for azimuthal orders 0 to 3 (Red, Green, Blue and Tan respectively) with the cut-on and cut-off points. The dashed vertical line is for $\nu = 150$ GHz which using the relationship $kr_1 = \frac{2\pi r_1 \nu}{c\nu}$, occurs at $kr_1 = 2.18$. There is one intersection at this frequency indicating the feed horn is single moded.

2.1.5 Hybrid modes

The HE_{11} hybrid mode consists of a coherent pair of waveguide TE/TM modes. A corrugated horn with $\frac{1}{4}\lambda$ deep corrugations at the aperture, as is the case with the QUBIC horns, emits a ‘balanced’ HE_{11} mode with the TE_{11} and TM_{11} modes in the ratio 85:15. Assuming a constraint of a circular aperture, the formulae for the TE_{nl} and TM_{nl} modes and their x and y components are given by *Equations (2.62)-(2.67)* (Balanis, 1989), this is equivalent to *Equations (2.19)-(2.20)* and *(2.30)-(2.31)* but including normalisation constants.

$$TE_{nl_{norm}}(R) = \frac{1}{2RJ_n(P'_{nl})} \sqrt{\frac{2 - \left| \frac{1}{n+1} \right|}{\pi \left(1 - \left(\frac{n}{P'_{nl}} \right)^2 \right)}} \quad (2.62)$$

$$TM_{nl_{norm}}(R) = \frac{1}{2RJ_{n+1}(P_{nl})} \sqrt{\frac{2 - \left| \frac{1}{n+1} \right|}{\pi}} \quad (2.63)$$

$$\begin{aligned} TE_{x_{nl}}(r, \phi) = & TE_{nl_{norm}}(R) \left(J_{n-1} \left(p'_{nl} \frac{r}{R} \right) \cos((n-1)\phi) \right. \\ & \left. + J_{n+1} \left(p'_{nl} \frac{r}{R} \right) \cos((n+1)\phi) \right) \end{aligned} \quad (2.64)$$

$$\begin{aligned} TE_{y_{nl}}(r, \phi) = & TE_{nl_{norm}}(R) \left(-J_{n-1} \left(p'_{nl} \frac{r}{R} \right) \sin((n-1)\phi) \right. \\ & \left. + J_{n+1} \left(p'_{nl} \frac{r}{R} \right) \sin((n+1)\phi) \right) \end{aligned} \quad (2.65)$$

$$\begin{aligned} TM_{x_{nl}}(r, \phi) = & TM_{nl_{norm}}(R) \left(J_{n-1} \left(P_{nl} \frac{r}{R} \right) \cos((n-1)\phi) \right. \\ & \left. - J_{n+1} \left(P_{nl} \frac{r}{R} \right) \cos((n+1)\phi) \right) \end{aligned} \quad (2.66)$$

$$\begin{aligned} TM_{y_{nl}}(r, \phi) = & TM_{nl_{norm}}(R) \left(-J_{n-1} \left(P_{nl} \frac{r}{R} \right) \sin((n-1)\phi) \right. \\ & \left. - J_{n+1} \left(P_{nl} \frac{r}{R} \right) \sin((n+1)\phi) \right) \end{aligned} \quad (2.67)$$

Formulae for the calculation of a TE_{nl} and TM_{nl} field

where:

n and l are the azimuthal and radial order of the mode

J is a Bessel function of the first kind and J' is its derivative

P is the root of the Bessel function of the first kind and P' is that of the Bessel's derivative

r is the radial distance $r = \sqrt{x^2 + y^2}$

ϕ is the azimuthal direction $\phi = \tan^{-1}(x, y)$

R is the radius of the waveguide section (in this case the edge of the field)

TE_x is the transverse electric field x-polarisation component at a point x,y

TE_y is the transverse electric field y-polarisation component at a point x,y

TM_x is the transverse magnetic field x-polarisation component at a point x,y

TM_y is the transverse magnetic field y-polarisation component at a point x,y

The amplitude of the x and y components were used to generate the mode plots in *Figure 2.8* (left and centre). The TE_{11} and TM_{11} modes were then added to produce the hybrid mode *Figure 2.8* (right).

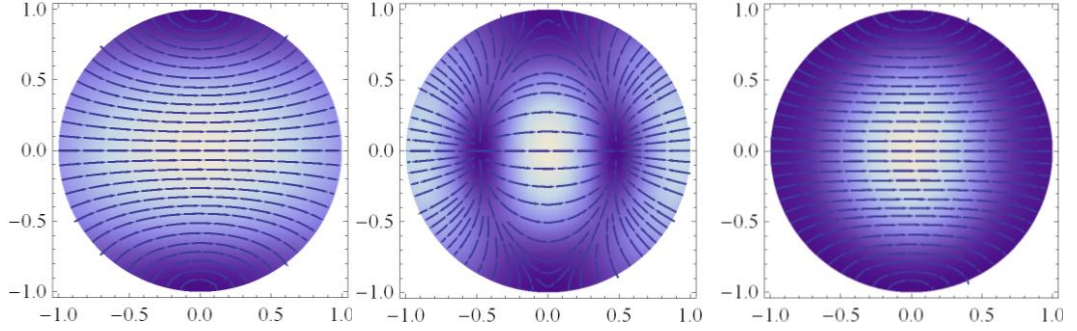


Figure 2.8: Left – TE_{11} , Centre – TM_{11} and Right – HE_{11} ($0.85TE + 0.15TM$). In each case the magnitude is indicated by the brightening of the plot and the polarisation by the lines/arrows superimposed. The guide radius, R , was set = 1.

It can be clearly seen that coherent waveguide modes, in this ratio, produce linearly polarised outputs ideal for a polarisation instrument such as QUBIC. The cross-polar component as a function of the TE/TM amplitude ratio, R_{em} , was calculated using *Equation (2.68)* and plotted in *Figure 2.9*.

$$\frac{\sum_{r,\phi} \left(\sqrt{R_{em}^2} TE_{y11}(r, \phi) + \sqrt{1 - R_{em}^2} TM_{y11}(r, \phi) \right)^2}{\sum_{r,\phi} \left(\left(\sqrt{R_{em}^2} TE_{x11}(r, \phi) + \sqrt{1 - R_{em}^2} TM_{x11}(r, \phi) \right)^2 + \left(\sqrt{R_{em}^2} TE_{y11}(r, \phi) + \sqrt{1 - R_{em}^2} TM_{y11}(r, \phi) \right)^2 \right)} \quad (2.68)$$

Cross-polar content of a field for varying relative contributions of TE_{11} and TM_{11}
where:

R_{em} is the ratio of the TE to TM modes under test

The plot shows that the ideal ratio for minimising cross-polarisation does indeed lie at about 0.85/0.15 TE/TM and the cross-polarisation is close to zero in this case. It also shows that there is a reasonable range of R_{em} , about $\pm 5\%$, allowed where the cross-polar content is low. It also indicates that a pure TE_{11} mode (right hand side of graph) contains $\sim 5\%$ cross-polarisation and $TM_{11} \sim 25\%$.

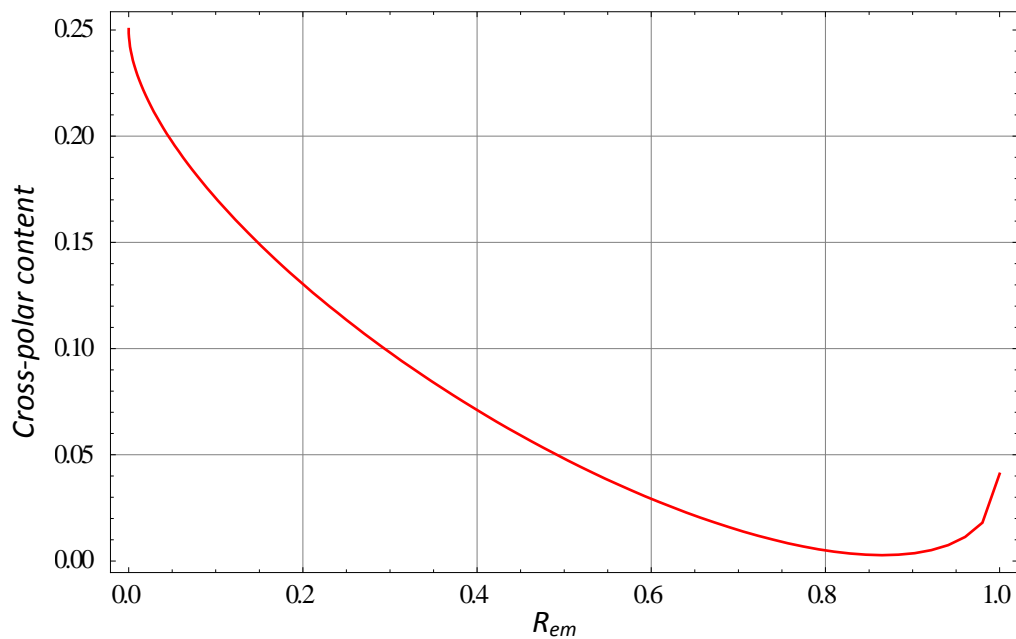


Figure 2.9: The cross-polar content of the HE_{11} hybrid mode as a function of the ratio of TE_{11} to TM_{11} mode content, R_{em} .

2.2 Free-space analysis techniques

In designing and modelling optical and quasi-optical systems there are several techniques available, each having its own advantages and disadvantages. At short wavelengths, at optical and higher frequencies, the geometric limit is assumed (where $\lambda \rightarrow 0$) and geometric optics (GO) is the preferred method. In this case minor diffraction effects can be ignored and rays give the direction of the energy flow in the instrument. At the other extreme, i.e. for long wavelengths, such as those in the radio band, the preferred approach uses full-electromagnetic (EM) modelling. Although computationally intensive, it is a precise theory and the relatively large wavelength (not too much smaller than the component sizes) makes it feasible. Physical optics (PO) uses this approach along with the assumption that the radius of curvature of the scattering surface is very many wavelengths. This is not valid at an edge and so methods such as the physical theory of diffraction (PTD) have been devised to deduce edge currents. For the sub-mm THz region the GO approximation is not ideal. PO is still possible but with extensive processing power required. Another approach, Gaussian beam modes (GBM) a scalar method, obtains relatively good accuracy and is computationally efficient enough to allow for quick

calculations. The majority of antenna based instruments have beam patterns that are Gaussian in nature lending them to analysis with a small Gaussian mode set or even a single Gaussian. The number of modes needed to accurately represent the field is related to the complexity and shape of the field.

In this section we will look at the various approximate theories and 2 software packages, GRASP and MODAL, which employ these methods. For GRASP there are 2 methods used, PO/PTD and GO/GTD (geometric theory of diffraction). MODAL also uses PO but adds the additional method of GBM. Although, as we will show, GO is not well suited to THz optics it will be discussed briefly as it is used in visualisation of chief rays.

2.2.1 Geometrical optics (GO) and geometric theory of diffraction (GTD)

GO is based on the Snell-Descartes Law relating the paths of direct and nominal rays traversing from points S to F, satisfying the condition that the path length is a minimum (Fermat's principle), as shown in *Figure 2.10*. GO traces rays from the source and propagates them through the system under analysis, taking into account reflected and direct rays. GO does not take into account the finite wavelength of the EM radiation nor edge diffraction effects.

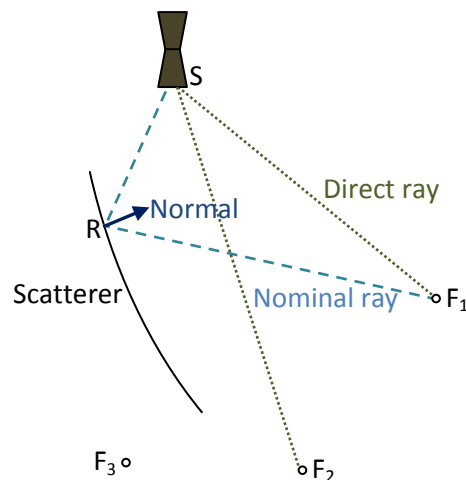


Figure 2.10: Ray optics illustrated using a source with 2 ray types under consideration, those of reflection from the main body of the scatterer and direct rays. There are 3 points in the system to consider, source point S , reflection point R and field points F_1 , F_2 and F_3 .

For example, in the GRASP package, the first step in the GO calculation is determining those rays that can contribute significant power. Ignoring rays that do not impact a scatterer, when one wishes to calculate the scatterer's reflected field, aids in creating an optimised computation. The second step is the tracing of rays through the system and determining their scattering points, this is the most difficult part. In the calculation of ray propagation and scattering, the order of the rays to be considered is set by the user. For example a ray from the source is of order 0, after a single reflection it is order 1, increasing in order for each scatterer interaction. As the considered order increases, the calculations become increasingly complex as every possible path of rays must be considered and their interactions computed. For any given position of a point in the field the number of rays contributing significant power will vary and typically it is only the main lobe and spillover regions that contain a large number of rays and the inclusion of high order rays may not yield any significant increase in accuracy. This order limit places a cap on the calculations that need to be considered. The third and final step is to reconstruct the field at the output plane. For rays at the edge of the scatterer where rays are diffracted rather than reflected an alternative approach is needed, GTD (not discussed here). A basic system is shown in [Figure 2.11](#) for a direct ray (in green), a reflected ray (in blue) and an edge diffracted ray (in red).

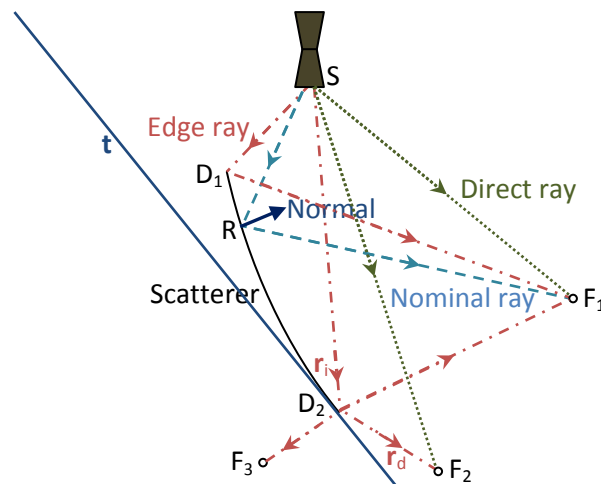


Figure 2.11: Ray optics illustrated using a source with 3 ray types under consideration, those of reflection from the main body of the scatterer, reflection from the edge of the scatterer and direct rays. There are 3 points in the system to consider, source point S , reflection point R and field points F_1 , F_2 and F_3 .

The total field at an observation point F_1 is written in terms of GO and GTD components $\mathbf{E}_r(F_1) = \mathbf{E}_{GO}(F_1) + \mathbf{E}_{GTD}(F_1)$. For rays intersecting an edge the intersection point and local tangent plane are determined. If $\mathbf{t} \cdot (\mathbf{r}_i - \mathbf{r}_d) = 0$ holds true then the intersection point is a valid diffraction point, where \mathbf{t} is a tangent vector at the point of intersection and \mathbf{r}_i and \mathbf{r}_d are the incident and diffracted ray vectors (TICRA, 2005). Once the diffraction points are located (the number of diffraction points depends on the geometrical structure) and ray tracing has been performed, the diffracted field is calculated using GTD as described in Kouyoumjian & Pathak (Kouyoumjian & Pathak, 1974) and propagated using GO. Although GO/GTD can be quick for calculating the field in an optical system, in quasi-optics where the diffraction effects cannot be ignored, an alternative method is desired.

2.2.2 Physical optics (PO) and theory of diffraction (PTD)

PO calculates the scattered field resulting from an incident electromagnetic field inducing currents on the surface of a scatterer. The PO approximation offers a very precise vector analysis of propagating radiation. There are two approximations used in PO

1. The surface of the scatterer is assumed to be a perfect conductor

2. The surface of the scatterer is assumed to be locally flat with an infinite tangential plane to the surface at the intersection point, with the normal taken in the same hemi-sphere as the incident radiation.

With these assumptions the currents on any part of the surface of the scatterer due to the incident field can be considered the same as those of an infinite plane, tangent to the surface at that point. In this case the electric (**E**) and magnetic (**H**) fields can be found from the induced electric (**J**) and magnetic (**M**) currents giving rise to electric (**F**) and magnetic (**A**) vector potentials (Collin & Zucker, 1969)

$$\mathbf{F} = \frac{\mu}{4\pi} \iint_S \mathbf{J}(\mathbf{r}) \frac{e^{-ikR}}{R} ds \quad \text{and} \quad \mathbf{A} = \frac{\epsilon_0}{4\pi} \iint_S \mathbf{M}(\mathbf{r}) \frac{e^{-ikR}}{R} ds \quad (2.69)$$

Electric and magnetic vector potential

where:

F and **A** are the electric and magnetic vector potentials

J and **M** are the electric and magnetic currents

ϵ_0 is the permeability of free space

μ is the permittivity of the surface

S is the surface of the scatterer

R is the radial propagation distance

k is the wave number related to wavelength, λ , by $k = 2\pi/\lambda$

Using Maxwell's relationships for,

- electric and magnetic fields, $\nabla \times \mathbf{E} = -i\omega\mu\mathbf{H}$
- magnetic field and electric potential vector, $\mathbf{H}_F = \frac{1}{\mu} \nabla \times \mathbf{F}$
- electric field and magnetic potential vector, $\mathbf{E}_A = -\frac{1}{\epsilon_0} \nabla \times \mathbf{A}$

we can derive the equivalent electric $\mathbf{E}_F = -i\omega\mathbf{F} - i\frac{1}{\omega^2\mu\epsilon_0} \nabla(\nabla \cdot \mathbf{F})$ and magnetic

$\mathbf{H}_A = -i\omega\mathbf{A} - i\frac{1}{\omega^2\mu\epsilon_0} \nabla(\nabla \cdot \mathbf{A})$ field. Combining to give the total fields,

$$\mathbf{E} = \underbrace{-i\omega\mathbf{F} - i\frac{1}{\omega^2\mu\epsilon_0}\nabla(\nabla\cdot\mathbf{F})}_{\mathbf{E}_F} - \underbrace{\frac{1}{\epsilon_0}\nabla\times\mathbf{A}}_{\mathbf{E}_A} \quad (2.70)$$

$$\mathbf{H} = \underbrace{\frac{1}{\mu}\nabla\times\mathbf{F}}_{\mathbf{H}_F} - \underbrace{i\omega\mathbf{A} - i\frac{1}{\omega\mu\epsilon_0}\nabla(\nabla\cdot\mathbf{A})}_{\mathbf{H}_A} \quad (2.71)$$

Electric and magnetic fields

where:

\mathbf{F} and \mathbf{A} are the electric and magnetic vector potentials

\mathbf{E} and \mathbf{H} are the electric and magnetic fields

\mathbf{E}_A and \mathbf{E}_F are the electric fields resultant from magnetic and electric potential vectors

\mathbf{H}_A and \mathbf{H}_F are the magnetic fields resultant from magnetic and electric potential vectors

ω is the angular frequency related to frequency, ν , by $\omega = 2\pi\nu$

Substituting Equation (2.69) into Equations (2.70) and (2.71) to give the field equations,

$$\mathbf{E} = \underbrace{\frac{Z}{4\pi} \iint_S \left(\begin{array}{l} \mathbf{J} \left(-i\frac{1}{kR} - \frac{1}{k^2R^2} + i\frac{1}{k^3R^3} \right) + \\ (\mathbf{J} \cdot \hat{\mathbf{R}}) \hat{\mathbf{R}} \left(i\frac{1}{kR} + \frac{3}{k^2R^2} - i\frac{3}{k^3R^3} \right) \end{array} \right) e^{-jkR} k^2 ds}_{\mathbf{E}_F} - \underbrace{\frac{1}{4\pi} \iint_S \mathbf{M} \times \hat{\mathbf{R}} \frac{1}{k^2R^2} (1 + jkR) e^{-jkR} k^2 ds}_{\mathbf{E}_A} \quad (2.72)$$

$$\mathbf{H} = -\underbrace{\frac{1}{4\pi} \iint_S \mathbf{J} \times \hat{\mathbf{R}} \frac{1}{k^2R^2} (1 + jkR) e^{-jkR} k^2 ds}_{\mathbf{H}_F} + \underbrace{\frac{1}{4\pi Z} \iint_S \left(\begin{array}{l} \mathbf{M} \left(-i\frac{1}{kR} - \frac{1}{k^2R^2} + i\frac{1}{k^3R^3} \right) + \\ (\mathbf{M} \cdot \hat{\mathbf{R}}) \hat{\mathbf{R}} \left(i\frac{1}{kR} + \frac{3}{k^2R^2} - i\frac{3}{k^3R^3} \right) \end{array} \right) e^{-jkR} k^2 ds}_{\mathbf{H}_A} \quad (2.73)$$

Electric and magnetic fields

where:

\mathbf{E} and \mathbf{H} are the electric and magnetic fields

\mathbf{E}_A and \mathbf{E}_F are the electric fields resultant from magnetic and electric potential vectors

\mathbf{H}_A and \mathbf{H}_F are the magnetic fields resultant from magnetic and electric potential vectors

$\hat{\mathbf{R}}$ is the unit vector in the direction of propagation

ω is the angular frequency related to frequency, ν , by $\omega = 2\pi\nu$

Z is the free-space impedance given by $Z = \sqrt{\mu/\epsilon}$

The total radiated field is now the sum of the incident and scattered fields, $\mathbf{E}_T = \mathbf{E}_I + \mathbf{E}_S$ (TICRA, 2005). For PO to give accurate results the surface must be sampled sufficiently well so as to produce a valid representation of the induced currents but an over sampled surface will make the computation time consuming. A balance must be selected based on the geometry and convergence requirements of the system. This will be explored in greater detail when dealing with the auto-convergence features in GRASP in §2.3.4. The PO calculations assume an infinite planar field when generating surface currents, inaccurate results may be obtained near the edges of scatterers or for systems that have scatterers in close proximity (in terms of wavelength). In this case for points near or at the edges of the scatterer, the physical theory of diffraction (PTD) is used. PTD evaluates the surface as an infinite half-plane (Johansen, 1996) in order to obtain the equivalent edge currents. The total resultant field over the surface of the scatterer including this correction for edge currents is then given by,

$$\mathbf{E}_S = \mathbf{E}_{PO} + \mathbf{E}_{PTD} \quad (2.74)$$

Total scatterer field given by PO and PTD calculations

PO/PTD is computationally expensive and so a middle ground between that and GO/GTD is also very useful. The characteristics of corrugated feed horn outputs closely match those of Gaussian beams as seen in §2.3.4. This opens the door for Gaussian beam mode (GBM) analysis which takes into account the diffraction properties of THz optics.

2.2.3 Gaussian beam modes (GBM)

In the propagation of a wave at THz frequencies, with component sizes of the order of the wavelengths under study, diffraction effects dominate. The accuracy of GO, which assumes that the wavelength is negligible compared to the component sizes, is poor in this range but as we have seen to analyse a system using full electromagnetic wave theory and the PO approximation is computationally expensive (Siegman, 1986). In this case GBM, a simple solution to the paraxial wave

equation, is an ideal solution for the scalar analysis of a beam varying slowly in the transverse direction compared to the direction of propagation, as it takes diffraction effects into account.

The GBM approach involves some simplifying assumptions (Lesurf, 1990),

1. A paraxial approximation: that is, the beam is essentially collimated but some diffraction is occurring (the divergence of the beam is within $\sim 10^\circ$ of the propagation axis).
2. The radiation can be represented as a scalar field. If the polarisation is to be preserved the beam must be represented as two scalar fields and propagated separately (Goldsmith, 1998).
3. The transverse variation of the beam compared to the wavelength is small.

The geometric conventions used in the following derivation are illustrated graphically in *Figure 2.12*.

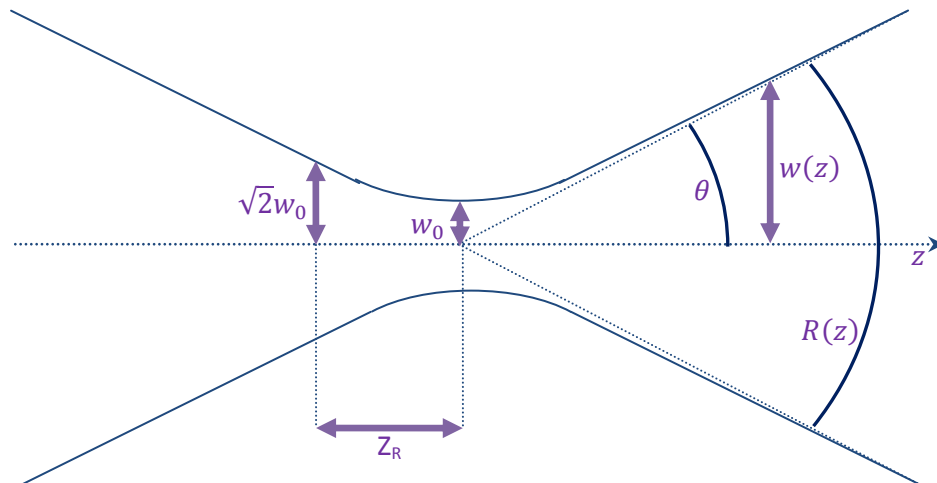


Figure 2.12: Gaussian beam propagation. Z_R is the confocal distance (near/far field transition). θ is the divergence angle and $w(z)$ the width of the beam at a distance z from the waist w_0 .

The source is assumed to be finite in spatial extent, coherent and monochromatic. For a single component, Ψ , of a field (electric \mathbf{E} , or magnetic \mathbf{H}) propagating through free space the Helmholtz equation is satisfied and we get, (Goldsmith, 1998)

$$(\nabla^2 + k^2)\Psi = 0 \quad (2.75)$$

or in Cartesian coordinates,

$$\frac{\partial^2 \Psi}{\partial x^2} + \frac{\partial^2 \Psi}{\partial y^2} + \frac{\partial^2 \Psi}{\partial z^2} + k^2 \Psi = 0 \quad (2.76)$$

Helmholtz wave equation

where:

Ψ is any monochromatic electromagnetic field component of \mathbf{E} or \mathbf{H}

∇^2 is the Laplacian

k is the wave number related to wavelength, λ , by $k = 2\pi/\lambda$

The component of the field may be written as,

$$\Psi(x, y, z) = u(x, y, z)e^{-jkz} \quad (2.77)$$

General solution to the Helmholtz wave equation

where:

$u(x, y, z)$ is a complex scalar function describing the non-plane wave part of the beam

By convention it is taken that the direction of propagation is parallel to the z-axis with the profile of the beam given by $u(x, y, z)$ and the phase by the exponential term in Equation (2.77) above. Substituting Equation (2.77) into (2.76) we obtain,

$$\frac{\partial^2 u}{\partial x^2} + \frac{\partial^2 u}{\partial y^2} + \frac{\partial^2 u}{\partial z^2} - 2jk \frac{\partial u}{\partial z} = 0 \quad (2.78)$$

Reduced wave equation

As the variation with z is assumed small compared to the wavelength it follows that

$\frac{\partial^2 u}{\partial z^2} \ll \frac{\partial u}{\partial z}$ and the second derivative of z can be neglected giving the paraxial wave equation,

$$\frac{\partial^2 u}{\partial x^2} + \frac{\partial^2 u}{\partial y^2} - 2jk \frac{\partial u}{\partial z} = 0 \quad (2.79)$$

Paraxial wave equation (Cartesian form)

$$\frac{\partial^2 u}{\partial r^2} + \frac{1}{r} \frac{\partial u}{\partial r} + \frac{1}{r^2} \frac{\partial^2 u}{\partial \theta^2} - 2jk \frac{\partial u}{\partial z} = 0 \quad (2.80)$$

Paraxial wave equation (cylindrical polar form)

The simplest solution (zero order mode) is a Gaussian which maintains its amplitude profile as it propagates scaling in width slowly with z . The solutions to the paraxial wave equation are the basis of the mode sets used in GBM analysis. In Cartesian coordinates the solutions take the form of Hermite Gaussians and in cylindrical polar coordinates Laguerre Gaussians. There is no absolute cut-off for the paraxial approximation but generally beams that have the majority of power within 30° off- z -axis can be catered for (Goldsmith, 1998). If the beam is radially symmetric then

$$\frac{\partial^2 u}{\partial \theta^2} = 0 \text{ and hence we get,}$$

$$\frac{\partial^2 u}{\partial r^2} + \frac{1}{r} \frac{\partial u}{\partial r} - 2jk \frac{\partial u}{\partial z} = 0 \quad (2.81)$$

Radially symmetric paraxial wave equation

The precise form of the solutions to the paraxial wave equation depends on the coordinate system chosen and the symmetry conditions (Lesurf, 1990), e.g. cylindrically symmetric. To find an analytical solution to the paraxial wave equation we can try a solution of the form given in [Equation \(2.82\)](#) with derivatives given in [Equation \(2.83a, b and c\)](#).

$$u(r, z) = A(z) e^{-jk \frac{r^2}{2q(z)}} \quad (2.82)$$

$$\frac{\partial u}{\partial r} = \frac{\partial}{\partial r} \left(A e^{-jk \frac{r^2}{2q}} \right) = -jk \frac{r}{q} A e^{-jk \frac{r^2}{2q}} \quad (2.83a)$$

$$\frac{\partial^2 u}{\partial r^2} = \frac{\partial}{\partial r} \left(-jk \frac{r}{q} A e^{-jk \frac{r^2}{2q}} \right) = \left(-jk \frac{1}{q} A - k^2 \frac{r^2}{q^2} A \right) e^{-jk \frac{r^2}{2q}} \quad (2.83b)$$

$$\frac{\partial u}{\partial z} = \frac{\partial}{\partial z} \left(A e^{-jk \frac{r^2}{2q}} \right) = \left(\frac{\partial A}{\partial z} + jkA \frac{r^2}{2} \frac{\partial q}{\partial z} \right) e^{-jk \frac{r^2}{2q}} \quad (2.83c)$$

Equations (2.83a, b and c) are then substituted into Equation (2.81) giving

$$\begin{aligned} & \left(-jk \frac{1}{q} A - k^2 \frac{r^2}{q^2} A \right) e^{-jk \frac{r^2}{2q}} - \frac{1}{r} jk \frac{r}{q} A e^{-jk \frac{r^2}{2q}} \\ & \quad - 2jk \left(\frac{\partial A}{\partial z} + jkA \frac{r^2}{2q} \frac{\partial q}{\partial z} \right) e^{-jk \frac{r^2}{2q}} = 0 \\ & -2jk \left(\frac{A}{q} + \frac{\partial A}{\partial z} \right) + k^2 r^2 \frac{A}{q^2} \left(\frac{\partial q}{\partial z} - 1 \right) = 0 \end{aligned} \quad (2.84)$$

Trial analytical solution to the paraxial equation

where:

$A(z)$ and $q(z)$ are some functions of distance z yet to be defined

As the solution must be valid for all z and r , for both the real and imaginary parts it follows, $\frac{\partial q}{\partial z} = 1$ and $\frac{\partial A}{\partial z} = -\frac{A}{q}$. For $\frac{\partial q}{\partial z} = 1$ a possible solution is $q(z) = q(z_0) + (z - z_0)$ (Goldsmith, 1998) which can be rewritten as $q(z) = q(0) + z$ by taking the origin along z as z_0 . From Equation (2.82) $\frac{1}{q}$ (the complex beam parameter) can be split into its real and imaginary parts, $\frac{1}{q} = \left(\frac{1}{q} \right)_r - j \left(\frac{1}{q} \right)_i$ giving,

$$u(r, z) = A(z) e^{-j \frac{kr^2}{2} \left(\frac{1}{q(z) \right)_r} e^{-\frac{kr^2}{2} \left(\frac{1}{q(z) \right)_i} \quad (2.85)$$

The imaginary term is a phase variation where $\left(\frac{1}{q(z)}\right)_r = \frac{1}{R(z)}$ and R is the phase radius of curvature. The real term has the form of a Gaussian distribution $(e^{-\left(\frac{r}{w}\right)^2})$ and we can set $\left(\frac{1}{q(z)}\right)_i = \frac{2}{kw^2(z)}$ giving,

$$\frac{1}{q(z)} = \frac{1}{R(z)} - j \frac{2}{kw^2(z)} \quad (2.86)$$

At $z = 0$ we see $\frac{1}{q(0)} = \frac{1}{R(0)} - j \frac{2}{kw_0^2} = -j \frac{2}{kw_0^2} \Rightarrow q_0 = j \frac{kw_0^2}{2}$ where $w_0 = w(0)$, the beam waist, allowing us to state $q(z) = z + j \frac{kw_0^2}{2}$. Using Equation (2.86) we can define (Goldsmith, 1998),

$$R(z) = \text{Re} \left(\frac{1}{z + j \frac{kw_0^2}{2}} \right)^{-1} = z + \frac{1}{z} \left(\frac{\pi}{\lambda} w_0^2 \right)^2 \quad (2.87)$$

Radius of curvature

$$w^2(z) = \text{Im} \left(\frac{\frac{k}{2}}{z + j \frac{kw_0^2}{2}} \right)^{-1} = w_0^2 \left(1 + \left(\frac{\lambda}{\pi} \frac{z}{w_0^2} \right)^2 \right) \quad (2.88)$$

Beam width

From $\frac{\partial q}{\partial z} = 1$ it follows that $\partial z = \partial q$ and therefore $\frac{\partial A}{\partial z} = -\frac{A}{q}$ can be rewritten as

$$\frac{\partial A}{A} = -\frac{\partial q}{q} . \text{ Integrating to obtain } \frac{A(z)}{A(0)} = \frac{q(0)}{q(z)} = \frac{1 + \frac{j\lambda z}{\pi w_0^2}}{1 + \left(\frac{\lambda z}{\pi w_0^2}\right)^2} = \frac{w_0}{w} e^{j\phi_0} \text{ with } \phi_0 =$$

$\tan^{-1} \left(\frac{\lambda z}{\pi w_0^2} \right)$. From this a complete solution to the paraxial equation is given by

$$u(r, z) = \frac{w_0}{w(z)} e^{-\frac{r^2}{w(z)^2} - j \frac{\pi r^2}{\lambda R(z)} + j \phi_0} \quad (2.89)$$

$$E(r, z) = \frac{w_0}{w(z)} e^{-\frac{r^2}{w(z)^2} - j \frac{\pi r^2}{\lambda R(z)} - j k z + j \phi_0} \quad (2.90)$$

Complete solution to the paraxial equation

Higher order Gaussian Beam Modes

The solution given thus far is for the fundamental Gaussian only (the simplest solution) but higher order solutions can also be found. These entail the use of an additional parameter in the trial solution, $S(r)e^{jm\psi} = \left(\frac{\sqrt{2}r}{\omega^2}\right)^m L_{pm}\left(\frac{2r^2}{\omega^2}\right) e^{jm\psi}$, such that the profile of the higher orders can be defined. L_{pm} is a Laguerre polynomial of radial order p and azimuthal order m . The identities defined in *Equations (2.89) and (2.90)* can be extended and solved to include the additional parameter yielding,

$$u(r, \psi, z) = \frac{1}{\alpha(z)} e^{-j \frac{k r^2}{2q}} S(r) e^{jm\psi} \quad (2.91)$$

$$E(r, \psi, z) = \left(\frac{2p!}{\pi(p+m)!}\right) \frac{1}{w} \left(\frac{\sqrt{2}r}{w^2}\right)^m L_{pm}\left(\frac{2r^2}{w^2}\right) e^{-\frac{r^2}{w^2} - j \frac{\pi r^2}{\lambda R} - j k z + j(2p+m+1)\phi_0} e^{jm\psi} \quad (2.92)$$

Complete solution to the paraxial equation for higher orders

It should be noted here that the phase shift is mode dependent, given by the $e^{j\phi} = e^{j(2p+m+1)\phi_0}$ term. The QUBIC feed horn is designed to operate single moded with an ultra-Gaussian beam and as such these solutions are not detailed any further here, the interested reader can find more in-depth solutions in Goldsmith (Goldsmith, 1998).

Gaussian beam modes form a complete orthonormal set and can be used to represent any beam. An arbitrary field, \mathbf{E} , can be represented as a summation of

Gaussian beams of various orders, propagating through free space individually maintaining their amplitude profiles as shown in *Equation (2.93)*.

$$E = \sum_0^n A_n \Psi_n \quad (2.93)$$

Field determination from the summation of the weighted Gaussian components
where:

Ψ_n *Complex independently propagating free-space modes of order n*
 A_n *Mode coefficient, power relationship between modes*

The mode coefficients, A_n , can be found using overlap integrals as shown in *Equation (2.94)*.

$$A_n = \int E \Psi_n^* dA \quad (2.94)$$

Determination of the Gaussian coefficients

where:

Ψ_n *Complex independently propagating free-space modes of order n*
 A_n *Mode coefficient, power relationship between modes*
 E *Electric field*
 dA *Infinitesimal area*

The above solutions are useful for circularly symmetric beam geometries. For asymmetric fields other solutions exist in the form of Hermite-Gaussians, also a complete orthonormal set. Although any field can be represented using Laguerre-Gaussians the number of modes required can be reduced by choosing a set appropriate to the field under analysis, minimising the processing involved. Propagation of the field then is a case of propagating each significantly contributing mode and summing at the destination plane. Propagating each individual mode is straightforward as they maintain their amplitude profile. Only $w(z)$, $R(z)$ and $\phi(z)$ change, as described next. When considering the simulation of antenna instruments in the THz band, we find that a large proportion have a high degree of Gaussicity. This readily lends them to this method requiring relatively few modes to represent

the beam. For QUBIC's ultra-Gaussian 150 GHz beam horn design, with Gaussicity $> 99.9\%$, the use of a Gaussian source, with appropriate waist, is an extremely useful simplification. This, when considered in terms of QUBIC's 400 sources, is a significant time saver in analysing the outputs from the system.

ABCD matrices

The previous calculations provide the user with valuable tools for the analysis of a propagating beam. Allowing the beam to propagate from a source of finite size will result in a diverging beam but, using mirrors and lenses, the beam can be focused and channelled through a system. In this case, a simple method to allow for the calculation of the GBM parameters, namely w , R and ϕ , is that of ABCD matrices.

The complex parameter, q from *Equation (2.86)*, is analogous to radius of curvature in GO and allows the use of ABCD matrices in the modelling of the propagation of a Gaussian beam. In the case of GO the position and slope of a ray leaving the system as shown in *Figure 2.14* and described by $\begin{bmatrix} A & B \\ C & D \end{bmatrix}$ is given by (see for example Goldsmith (Goldsmith, 1998)),

$$x_{out} = A \cdot x_{in} + B \cdot \theta_{in} \quad (2.95)$$

$$\theta_{out} = C \cdot x_{in} + D \cdot \theta_{in}$$

or

$$\begin{bmatrix} x_{out} \\ \theta_{out} \end{bmatrix} = \begin{bmatrix} A & B \\ C & D \end{bmatrix} \begin{bmatrix} x_{in} \\ \theta_{in} \end{bmatrix} \quad (2.96)$$

ABCD matrix for geometric optics

where

x_{in} and θ_{in} are the input position and slope

x_{out} and θ_{out} are the output position and slope

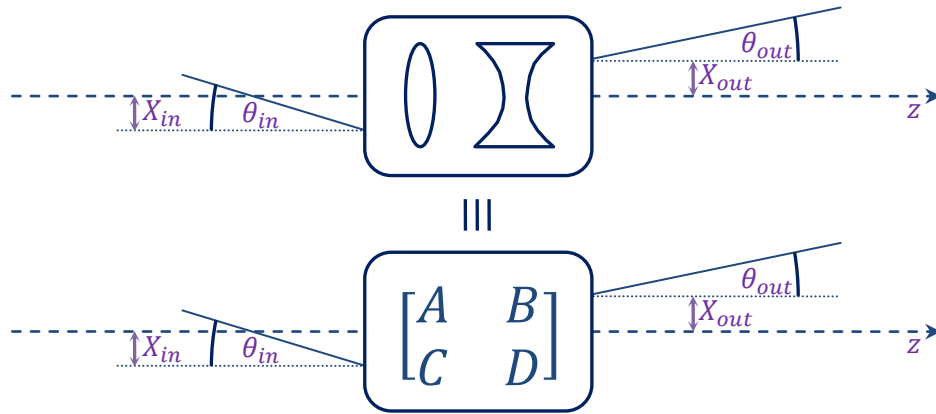


Figure 2.13: ABCD input and output parameters indicating the equivalency to that of a cascaded (quasi) optical system.

For a ray propagated a distance x with a divergence angle θ , the radius of curvature is given by $R = \frac{x}{\theta}$ and this can be used to generate a relationship between ABCD matrices and R ,

$$R_{out} = \frac{A R_{in} + B}{C R_{in} + D} = \frac{A + \frac{B}{R_{in}}}{C + \frac{D}{R_{in}}} \quad (2.97)$$

Output phase radius of curvature in terms of an ABCD matrix

and by extension for GBMs

$$q_{out} = \frac{A q_{in} + B}{C q_{in} + D} = \frac{A + \frac{B}{q_{in}}}{C + \frac{D}{q_{in}}} \quad (2.98)$$

Output complex phase radius of curvature in terms of an ABCD matrix

So the ABCD matrix formalism commonly used in ray optics (GO) can also be used in determining the evolution of q (and hence $w(z)$, $R(z)$ and $\phi(z)$), in GBM optics. We then have

$$\begin{aligned} \frac{1}{R_{out}} &= \operatorname{Re}\left(\frac{1}{q_{out}}\right) = \operatorname{Re}\left(\frac{C + \frac{D}{q_{in}}}{A + \frac{B}{q_{in}}}\right) \\ &= \operatorname{Re}\left(\frac{C + \frac{D}{R_{in}} - j\left(\frac{D\lambda}{\pi w_{in}^2(z)}\right)}{A + \frac{B}{R_{in}} - j\left(\frac{B\lambda}{\pi w_{in}^2(z)}\right)}\right) \end{aligned} \quad (2.99)$$

Output phase radius of curvature from the complex beam parameter in terms of ABCD matrix elements and input phase radius of curvature and beam radius.

$$\begin{aligned} w_{out} &= \sqrt{\frac{\lambda/\pi}{\operatorname{Im}\left(-\frac{1}{q_{out}}\right)}} = \sqrt{\frac{\lambda/\pi}{\operatorname{Im}\left(-\frac{C q_{in} + D}{A q_{in} + B}\right)}} \\ &= \sqrt{\frac{-\lambda/\pi}{\operatorname{Im}\left(\frac{C + \frac{D}{R_{in}} - j\left(\frac{D\lambda}{\pi w_{in}^2(z)}\right)}{A + \frac{B}{R_{in}} - j\left(\frac{B\lambda}{\pi w_{in}^2(z)}\right)}\right)}} \end{aligned} \quad (2.100)$$

Output beam radius from the complex beam parameter in terms of ABCD matrix elements and input phase radius of curvature and beam radius.

$$\phi_{out} = \phi_{in} - \operatorname{Arg}\left(A + \frac{B}{q_{in}}\right) \quad (2.101)$$

Output phase slippage from the complex beam parameter in terms of ABCD matrix elements and input phase.

where:

In and Out subscripts refer to the excitation and emission parameters

q_{out} is the complex beam parameter

R_{out} is the beam phase radius of curvature, obtained from the real part of the q_{out} .

w_{out} is the beam width, obtained from the imaginary part of the q_{out} .

Finally to determine the values of the matrix elements A, B, C and D we need to look at the type of element on a case by case basis. We will take one such case, that of propagation through free space, where we can state, $\theta_{out} = \theta_{in}$, and,

$$x_{out} = x_{in} + (z_{out} - z_{in})\theta_{in}$$

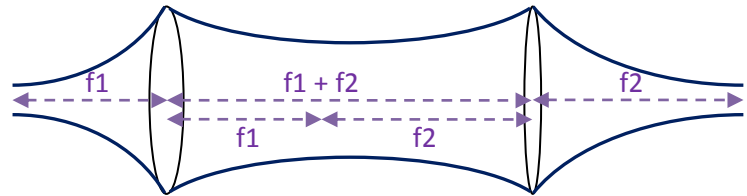
giving, in matrix form,

$$\begin{bmatrix} x_{out} \\ \theta_{out} \end{bmatrix} = \begin{bmatrix} 1 & z_{out} - z_{in} \\ 0 & 1 \end{bmatrix} \begin{bmatrix} x_{in} \\ \theta_{in} \end{bmatrix}$$

where B is now simply $B = z_{out} - z_{in}$, the propagation distance, $C = 0$ and $A = D = 1$. There are many more relationships and for the interested reader they are detailed in (Goldsmith, 1998; Siegman, 1986). A brief list of the most common is given in *Table 2-2* below.

Table 2-2: Some commonly used ABCD matrices

ABCD Matrix	Description
$\begin{bmatrix} 1 & L \\ 0 & 1 \end{bmatrix}$	Propagation through free space, a distance L
$\begin{bmatrix} 1 & 0 \\ -\frac{1}{f} & 1 \end{bmatrix}$	Propagation through a thin lens, of focal length f
$\begin{bmatrix} 1 & 0 \\ -\frac{2}{R} & 1 \end{bmatrix}$	Reflection from a curved mirror with radius of curvature R
$\begin{bmatrix} -\frac{f_2}{f_1} & 0 \\ 0 & -\frac{f_1}{f_2} \end{bmatrix}$	Gaussian beam telescope (from the first elements focal point to the second elements focal point)



The application of ABCD matrices in quasi-optical systems has advantages in the modular design of instruments and by its very nature is applicable to a broad frequency range. The output from any system is simply the cascaded multiplication of the pre-pended matrices for each section, yielding a total system matrix. For example, a system involving free-space propagation before and after each of two focusing elements (of d_{in} and d_{out} respectively), with focal lengths f_1 and f_2 , with coincident focal points we get,

$$\begin{bmatrix} 1 & d_{out} \\ 0 & 1 \end{bmatrix} \cdot \begin{bmatrix} 1 & 0 \\ -\frac{1}{f_2} & 1 \end{bmatrix} \cdot \begin{bmatrix} 1 & f_2 + f_1 \\ 0 & 1 \end{bmatrix} \cdot \begin{bmatrix} 1 & 0 \\ -\frac{1}{f_1} & 1 \end{bmatrix} \cdot \begin{bmatrix} 1 & d_{in} \\ 0 & 1 \end{bmatrix} \quad (2.102)$$

ABCD matrix for dual scatterer system

A practical example is that of the QUBIC beam combiner, with mirror separation and focal lengths shown in [Figure 2.14](#) below for the chief ray of a feed horn placed at the centre of the source array. The distance from the aperture of the feed horn to the surface of the primary mirror is 400 mm. By calculating the intersection and local normal on the surface the reflected ray path was calculated and its propagation the distance to the common focal point was determined to be 0.231 m. This is the primary mirror focal length (for this ray). Propagating the ray through the common focal point towards the secondary mirror, the intersection point and local normal on the secondary mirror were determined and the propagation distance was found to be 0.348 m. The reflected ray from the secondary mirror was then propagated towards detector plane which was found to be a distance of 0.451 m away. The equivalent focal length of the secondary mirror for this ray was calculated from $\frac{1}{f} = \frac{1}{d_i} + \frac{1}{d_o} = \frac{1}{0.348} + \frac{1}{0.451} = \frac{1}{0.196}$ where d_i is the incident distance of the ray and d_o is the output propagation distance and the focal length was determined to be 0.196 m.

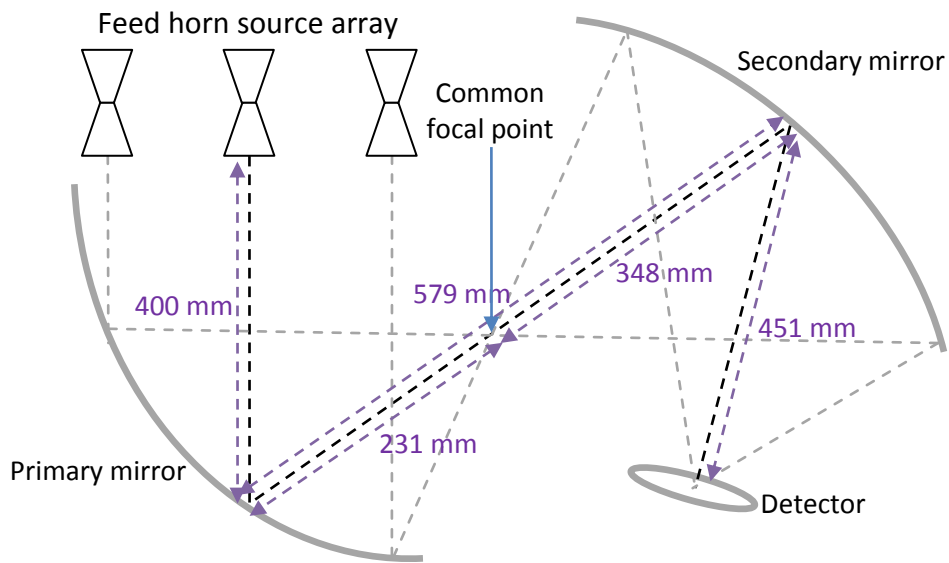


Figure 2.14: QUBIC schematic showing the path of the systems chief ray

The equivalent set of focal lengths and propagation distances are tabulated in Table 2-3 and an equivalent on-axis system, based on lenses, that can be modelled using ABCD matrices is shown in Figure 2.15.

Table 2-3: QUBIC system parameters

Parameter	Value	Unit
Distance from source to primary	0.400	m
Primary focal length	0.231	m
Distance from primary to secondary	0.579	m
Secondary focal length	0.196	m
Distance form secondary to image	0.451	m

The ABCD matrices for the equivalent lens system are shown in Equation (2.103). The matrices were used to create a 3-part piecewise function. M_1 is used for propagation up to the first element, M_2 for reflection from the primary mirror (through the primary lens in this case) until intersection with the secondary mirror, and finally M_3 for the free-space propagation upon reflection from the secondary mirror.

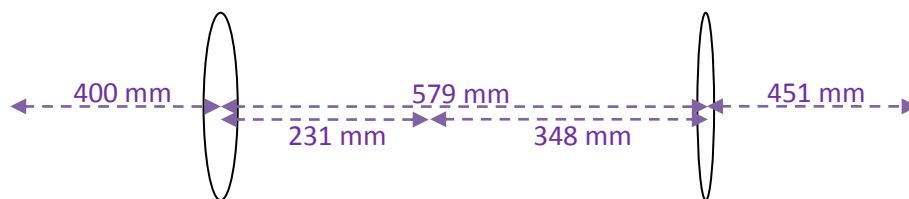


Figure 2.15: QUBIC equivalent lens system schematic showing the path of the chief ray

$$M_1(x) = \begin{bmatrix} 1 & x \\ 0 & 1 \end{bmatrix}$$

with $0 \leq x < 0.400$ m

$$M_2(x) = \begin{bmatrix} 1 & x \\ 0 & 1 \end{bmatrix} \begin{bmatrix} 1 & 0 \\ -0.231 & 1 \end{bmatrix} \begin{bmatrix} 1 & 0.4 \\ 0 & 1 \end{bmatrix} \\ = \begin{bmatrix} 2.732 - 4.329x & 0.693 - 0.732x \\ -4.329 & -0.732 \end{bmatrix}$$

with $0 \leq x < 0.579$ m

$$M_3(x) = \begin{bmatrix} 1 & x \\ 0 & 1 \end{bmatrix} \begin{bmatrix} 1 & 0 \\ -1 & 1 \end{bmatrix} \begin{bmatrix} 1 & 0.579 \\ 0 & 1 \end{bmatrix} \begin{bmatrix} 1 & 0 \\ -1 & 1 \end{bmatrix} \begin{bmatrix} 1 & 0.4 \\ 0 & 1 \end{bmatrix} \\ = \begin{bmatrix} -4.793 + 3.357x & 0.575 - 0.611x \\ 3.357 & -0.611 \end{bmatrix}$$

with $0 \leq x \leq 0.451$ m (2.103)

Piecewise ABCD matrices for the equivalent QUBIC lens system

where:

- x is the propagation point at which the beams properties are to be determined*
- M₁ is the matrix used in calculations up to the location of the first scatterer*
- M₂ is the matrix used in calculations from the first scatterer up until the second scatterer.*
- M₃ is the matrix used in the calculations from the second scatterer onwards.*

Using the piecewise matrices defined in Equation (2.103) the width and phase radius of curvature of the beam can be calculated. The starting waist radius for the input QUBIC beam Gaussian was 3.074 mm, giving a beam with a 14° divergence angle at 150 GHz (obtained from Equation (3.19) which will be discussed in §3.2). The initial phase radius of curvature was $R(0) = \infty$. From this the input complex beam parameter was calculated,

$$q_{in} = \frac{1}{\frac{1}{r} - \frac{i\lambda}{\pi w^2}} = 0. + i0.01484$$

and the output complex beam parameter was determined to be

$$q_{out}(x) = \frac{(q_{in} A_{M_n}(x) + B_{M_n}(x))}{(q_{in} C_{M_n}(x) + D_{M_n}(x))}$$

where $A_{M_n}(x)$ is the A element (and similarly B, C and D) from the ABCD matrix structure of the active piecewise matrix where $n = 1, 2, 3$ as used in *Equation (2.103)*. From this the phase radius of curvature, beam width and phase slippage were determined from,

$$R(x) = \frac{1}{\operatorname{Re}\left(\frac{1}{q_{out}(x)}\right)}, w(x) = \sqrt{\frac{-\lambda}{\pi \operatorname{Im}\left(\frac{1}{q_{out}(x)}\right)}} \text{ and } \phi_{out} = \phi_{in} - \operatorname{Arg}\left(A + \frac{B}{q_{in}}\right)$$

The phase radius of curvature and beam radius as a function of propagation distance were calculated and are shown in *Figure 2.16* to *Figure 2.20*. The properties calculated here give insight into the behaviour of the QUBIC optical combiner. The width of the beam specified in these equations relates to the radius of the beam at which the intensity of the beam has dropped to $\frac{1}{e^2}$. The power contained in the beam out to this radius ($r = w$) is given by,

$$P(r, w) = 1 - e^{-2\frac{r^2}{w^2}} \quad (2.104)$$

Fraction of power captured for a Gaussian beam

where:

P is the fraction of power
w is the width of the Gaussian beam
r is the radius of the detector plane

$P(r = w) = 1 - e^{-2\frac{r^2}{w^2}} = 1 - \frac{1}{e^2} \approx 86.4\%$. The beam is considered essentially fully captured at twice this radius, $P(r = 2w) = 1 - \frac{1}{e^8} \approx 99.9\%$. It can be seen from this that the expected beam size at the detector plane is $w = 62$ mm. This quick analysis allowed us to determine the approximate sizes of components needed to capture a given fraction of power in the beam.

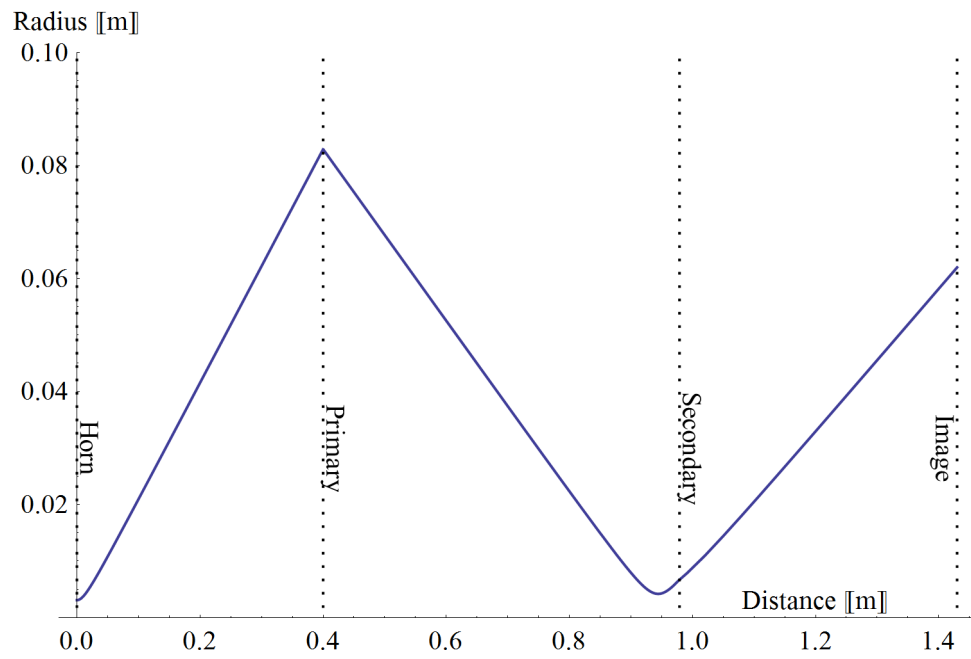


Figure 2.16: Width of a beam as it propagates through a QUBIC equivalent lens system.

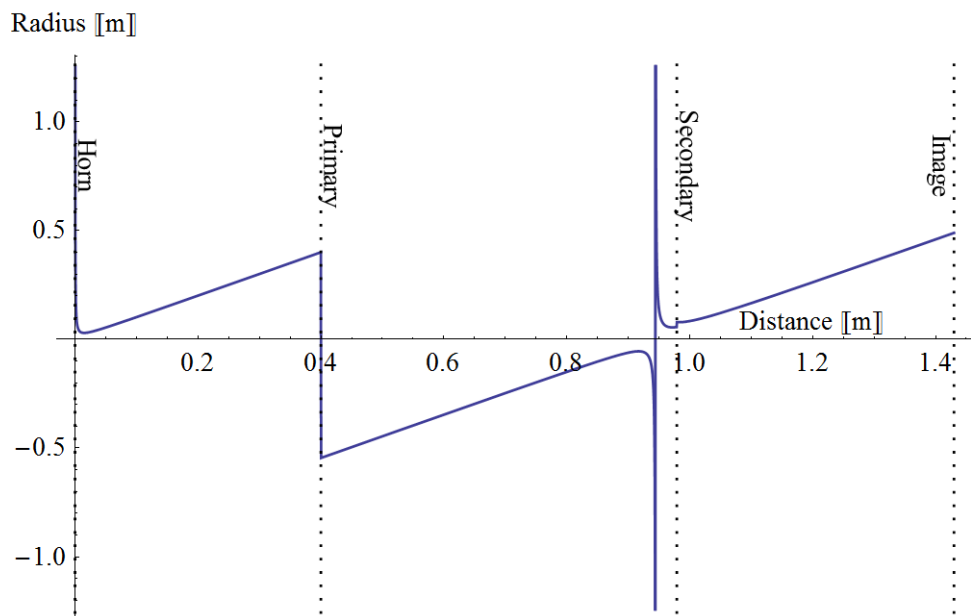


Figure 2.17: Beam radius of curvature as it propagates through a QUBIC equivalent lens system.

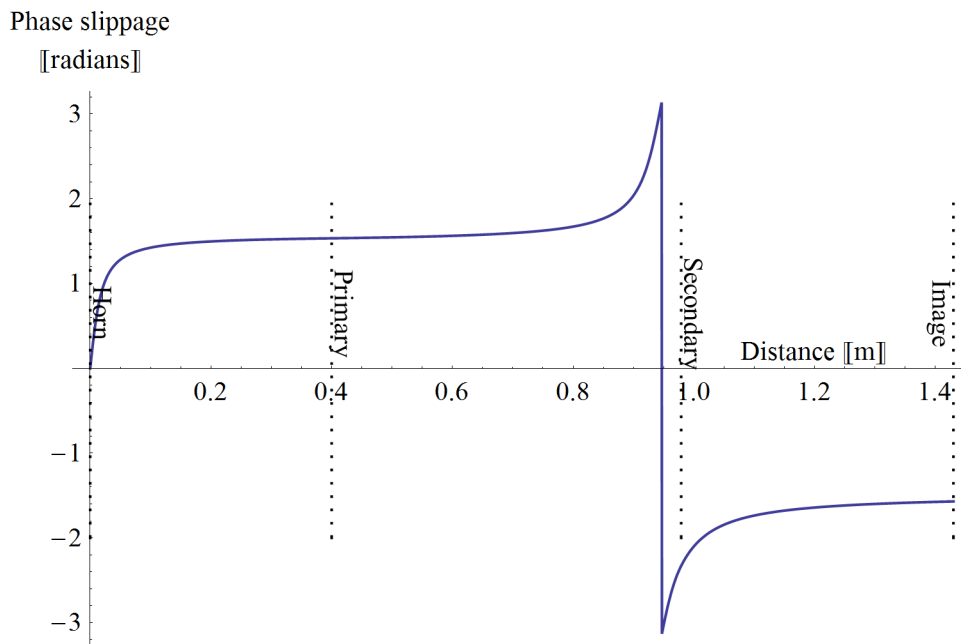


Figure 2.18: Beam phase slippage as it propagates through a QUBIC equivalent lens system.

The actual feed horns to be used in the QUBIC combiner are scaled versions of the ultra-Gaussian feed horns designed for the CLOVER CMB experiment (Taylor, et al., 2004). As a check of the usefulness of the Gaussian approximation above the actual aperture field (calculated using SCATTER) and the best-fit Gaussian field were both propagated through the combiner model of Figure 2.14. Using PO Figure 2.19 and Figure 2.20 show that a single Gaussian is an excellent approximation to the real feed horn beam.

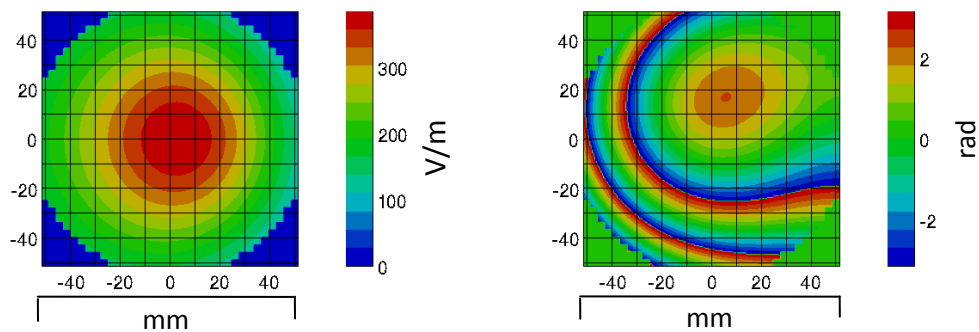


Figure 2.19: Detector plane field for a Gaussian source propagated through QUBIC using PO, amplitude (left) and phase (right).

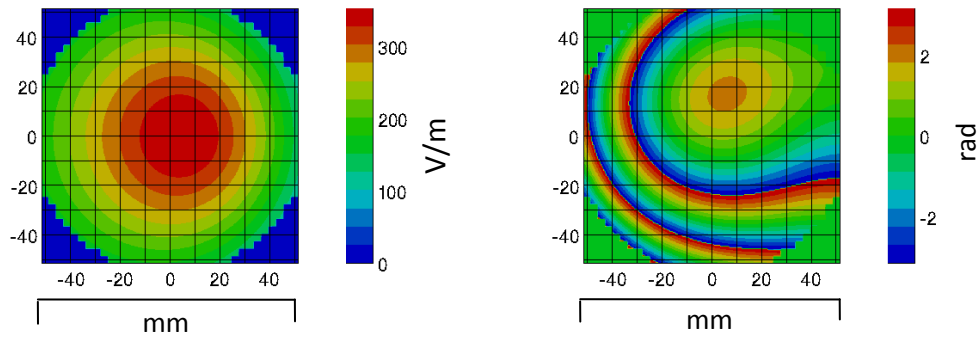


Figure 2.20: Detector plane field for the CLOVER (Taylor, et al., 2004) feed horn propagated through QUBIC using PO, amplitude (left) and phase (right).

The width at the detector plane was calculated to be 67 mm in both cases.

2.3 System Analysis Tools

There are several specialist software packages for the modelling of systems in this part of the EM spectrum, e.g. GRASP (by TICRA) and MODAL (by Maynooth University). The descriptions for both are given here in parallel as there is quite a degree of overlap. Where they do differ it will be highlighted in the relevant sections.

GRASP (General Reflector Antenna Software Package) by TICRA, is the industry standard software package. It was used for the initial design of QUBIC as well as legacy projects such as PLANCK (ESA, 2014), Herschel (Pilbratt, 2003) and ALMA (Wootten, 2003).

MODAL (Maynooth Optical Design and Analysis Laboratory) by Maynooth University (MU), initially developed by David White (White, 2006) with follow on work by Marcin Gradziel (Gradziel, et al., 2008), was the primary package used in this thesis for the modelling of QUBIC. MODAL offers some advantages when dealing with quasi-optics, namely its native GBM analysis as well as its in-house development. This makes it highly configurable with new modules and features being added as requirements dictate.

Both are capable of handling the QUBIC optics as they allow the design, visualisation and analysis of reflector and lens based systems. Analysis can primarily

be performed through 3 different methods, GO/GTD and PTD in GRASP, GBM in MODAL and PO in both suites. A general overview of the software packages is presented here with the specific implementation of QUBIC in these packages dealt with in Chapter 3.

2.3.1 Overview

Both suites are available in Windows and Linux versions. For GRASP the latter is used in a command line interface without any visualisation. In both cases the Linux versions offer the advantage of being able to harness the power of MU's 106-core cluster, without which the analysis of the QUBIC system would be impossible.

The primary use of the suites is for the calculation of the electromagnetic radiation characteristics in multi-feed and multi-reflector designs. The use of PO for the calculation of fields normally yields accurate results but has its limitations. Where there are multiple reflections and blockages in the system it can become hard and/or time consuming to model correctly. PO calculates the current on a scatterer due to some excitation. Then the currents on this scatterer are used for the sources in the next leg of the simulation and so on. In GRASP, GO takes account of reflections and blockages more readily but for the THz region, where diffraction effects are important, it fails to achieve an accurate model of the system's behaviour. In MODAL, GBM takes account of the diffraction but only considers scalar beams and yields inaccurate results for systems with significant cross-polar content.

Both suites use a hierarchical approach with the top level being the project file (.mdl for MODAL and .tor for GRASP). This file contains all information pertaining to the configuration and specific hierarchical dependencies and relationships of each object including all information necessary for the visualisation of the model. GRASP also uses one more top level file, .tci, where the commands for the generation of the currents and fields for use in the analysis of the optical system are stored. MODAL stores these commands as part of the .mdl file.

The Windows GUI, in both systems, allows access to the configuration tools and visualisation in 3D. They use a vectored graphics approach and the image can be rotated, zoomed and panned in real time. A typical example of this visualisation is shown in *Figure 2.21*.

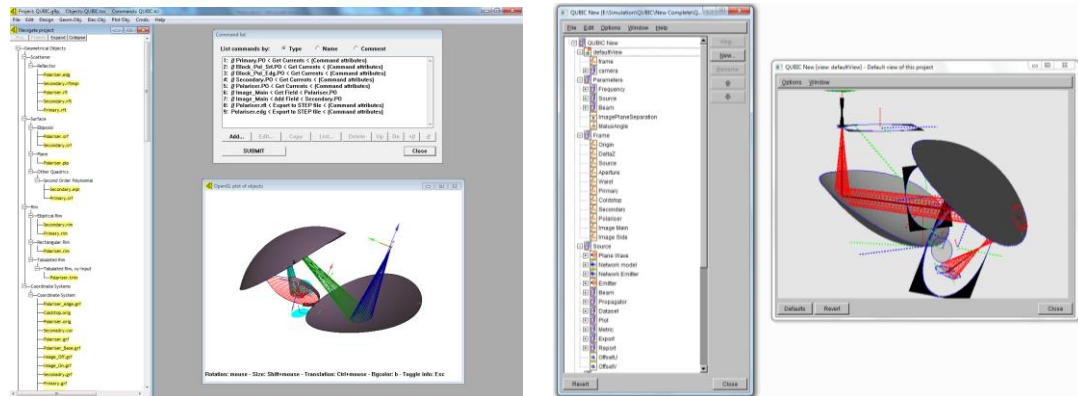


Figure 2.21: Left is the GRASP visualisation example showing the GUI displaying the configuration view on the left (stored in the tor file), the command list on the top (stored in the tci file) and the 3D vector image of the model at the bottom. Right is the MODAL visualisation showing the equivalent hierarchy on the left and visualisation on the right. The commands are embedded in the tree view hierarchy in the case of MODAL.

2.3.2 Model system components

The physical elements of the optical system consist of scatterers (mirrors, lenses), sources and detectors. Each of these requires a frame, which is defined as a fixed location in space specifying the local position and orientation of the anchor point for the element(s) associated with it. Each frame can be absolute (i.e. defined with respect to a global coordinate frame) or relative to another user defined frame. An example configuration from each suite is shown in *Figure 2.22*.

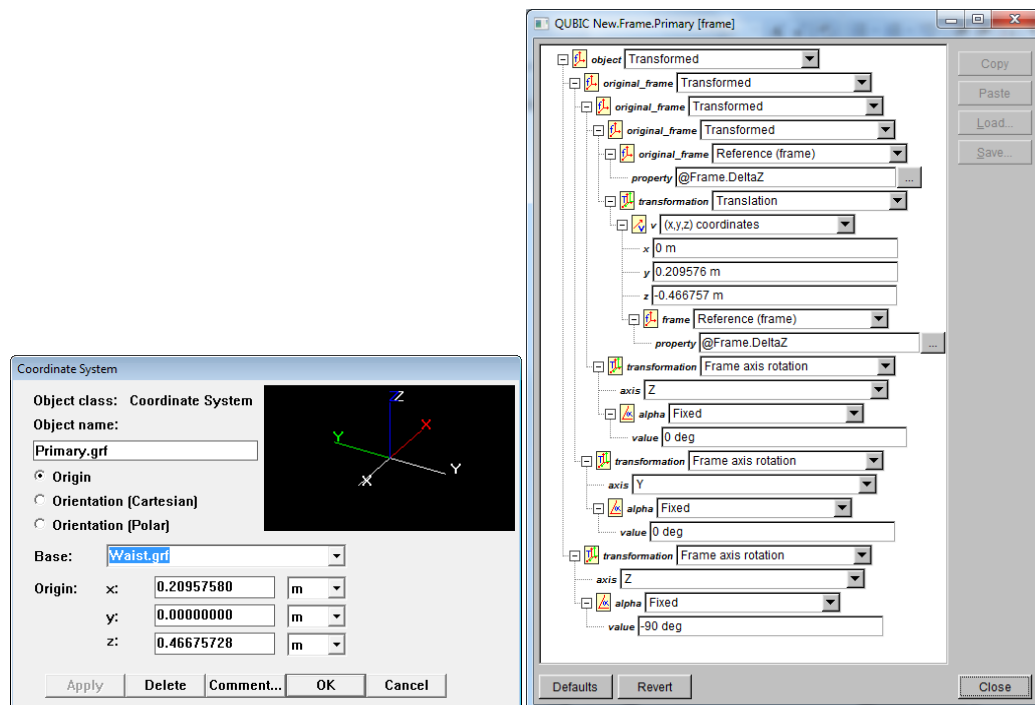


Figure 2.22: Left is the GRASP frame definition and right the equivalent configuration in MODAL.

With the position and orientation of an element defined, their surface and rim can be configured. In both suites a list of predefined items, for example parabolic or quadratic mirrors with circular or rectangular rims, can be configured. In the case of GRASP additional files, .sfc and .rim, for the storage of custom definitions of surfaces and rims respectively allow for extensive flexibility in design. There is a limitation here in that the rim is specified in polar coordinates in rotational order from a single fixed point and as such this does not allow for highly complex rim designs. For MODAL, tabulated surfaces are not possible but the system allows the user to combine fundamental shapes in any combination (union, difference, etc.) to achieve any level of complexity in order to arrive at the desired shape.

In both suites the most common smooth walled feed horn designs are predefined; the geometries can be entered directly and the aperture field calculated and used as the excitation. The user only need specify the width, height, profile (circular or rectangular) and flare lengths. Alternately the user can specify one of a list of common beam shapes, for example a Gaussian source which is very useful as many corrugated feed horns have beam patterns that are close to Gaussian. Example configurations for a Gaussian beam and a feed horn are shown in [Figure 2.23](#).

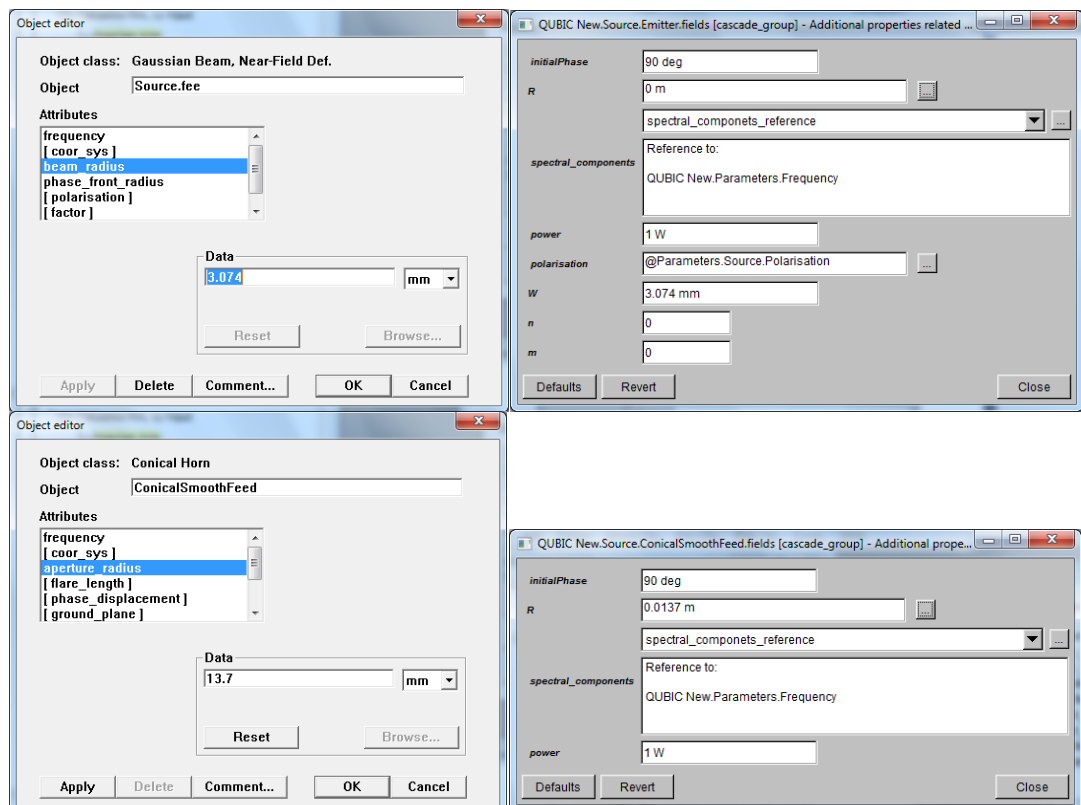


Figure 2.23: Top Left is the GRASP Gaussian definition and bottom left is the GRASP smooth walled conical feed horn definition. The right hand side shows the equivalent configurations in MODAL.

For GRASP, corrugated or uncommon feed horn designs must have the aperture field pre-calculated, tabulated and stored in a .grd file (TICRA, 2011). The tabulated field can then be used as a source in the simulation. MU's SCATTER package can generate the outputs in the required .grd format with all 6 columns for the complex values of x , y and z components (the z components are set to zero as SCATTER only provides a field description in the xy -plane).

One must be careful with multi-moded systems as the correct normalisation of power levels must be carried out and each mode has to be treated separately and combined at the destination. MODAL excels here with the ability to read in the geometry of a corrugated feed horn (stored in what we call a .i file) directly and by specifying an excitation for the feed horn, calculate the scatter matrix and corresponding aperture field. The major advantage here is that MODAL takes care of the multi-moded propagation without any further user interaction.

2.3.3 Propagating the aperture field

To propagate the field from the source through the system the software suite must be told the order in which to process the defined elements.

In GRASP a set of commands are created where, taking a dual reflector example, command 1 takes the selected source as excitation for the calculation of currents on the primary scatterer. Then command 2 takes the result of command 1 as the excitation and calculates the currents on the secondary scatterer. Finally command 3 calculates the output field at the detector plane using the results of command 2 as the excitation. The command type determines the method used, GO or PO, in the propagation calculations, an example of a typical command set is shown below. The auto-convergence will be detailed in the §2.3.4.

```
#
COMMAND OBJECT Primary.PO get_currents ( source : sequence(ref(Source.fee)), &
auto_convergence_of_po : on, convergence_on_scatterer : &
sequence(ref(Secondary.rft)), field_accuracy : -60.0) Primary.po
#
COMMAND OBJECT Secondary.PO get_currents ( source : sequence(ref(Primary.PO)), &
auto_convergence_of_po : on, convergence_on_scatterer : &
sequence(ref(Polariser.rft)), convergence_on_output_grid : &
sequence(ref(Image)), field_accuracy : -60.0) Secondary.po
#
COMMAND OBJECT Image get_field ( source : ref(Secondary.PO)) Image.cmd
#
QUIT
```

In MODAL, using the same example, a propagator is created for each element, the source, primary, secondary and detector plane. They are daisy-chained so that each has the previous one as its source. A dataset is linked to the propagator from which information can be extracted. The dataset's columns are the output. Typically a dataset contains the amplitude and phase of a particular polarisation component of a field at a grid of points in the xy -plane. The propagator type determines which propagation method, GBM or PO, is used.

In either suite multiple sources can be used which are added or subtracted to give the total resultant field.

2.3.4 Sampling density

As we have seen in §2.2.2, with PO the accuracy of the field is determined mainly by the sampling. In PO the sampling density is key and at each stage in the calculation of the field and/or currents in the system there is a requirement to sample at a sufficient density to yield a representative field. GRASP excels here in that it allows the user to specify the sampling, if required, but also offers a marvellous feature that auto-calculates the sampling density for each element. This is achieved using an iterative process increasing the sampling points for each iteration. This is repeated until successive iterations result in field calculations that differ by less than a preconfigured amount. This variation value is set by the user in dB and is given by, $20 \log(\text{calculated field variation}) < \text{accuracy_param}$ (dB) with a default value of -80 dB. In order for GRASP to be able to calculate this correctly the user must specify the convergence criteria for the scatterers. The convergence criteria tell GRASP where the beam accuracy is required. For example, in a dual reflector as shown in *Figure 2.14* for field calculations on the primary mirror, convergence is specified for the secondary mirror and focal-plane. GRASP calculates the number of sample points required on the primary mirror in order to achieve the accuracy as specified above (*accuracy_param*) at the convergence surfaces, in this case the secondary mirror and detector plane. In general all elements that the source in each calculation illuminates, either directly or through subsequent scattering should be specified as convergence elements. This convergence calculation can be time consuming. A careful user can pre-define the sampling required, bypassing the convergence routine, but too low a value and incorrect results will be obtained, too high and the processing time can become unacceptably long. In MODAL this value must be entered manually in all cases. An estimate for the PO sampling layout shown in *Figure 2.24*, can be made from *Equations (2.105) and (2.106)* (TICRA, 2005) but precise determination can only be made from a convergence test.

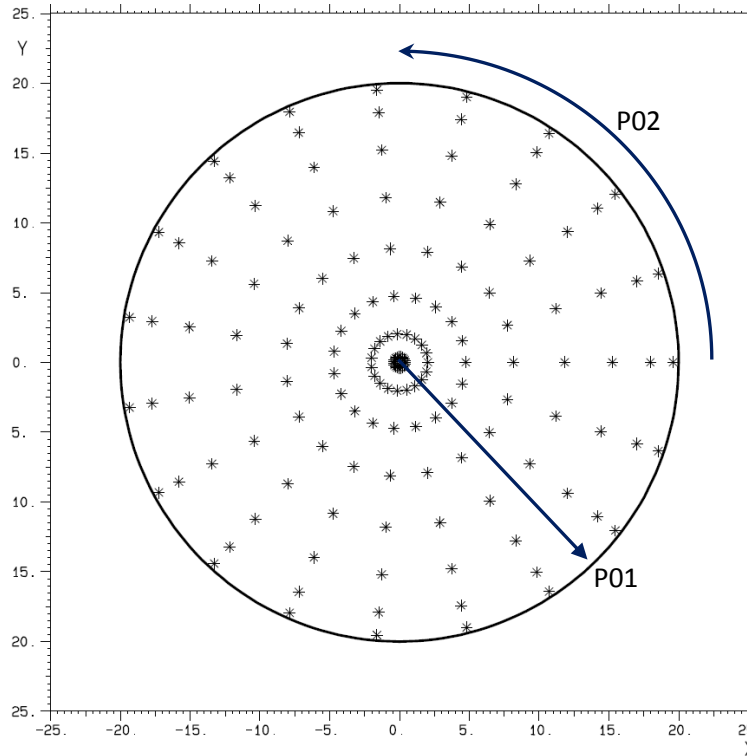


Figure 2.24: Example of the PO sampling distribution for a polar grid in GRASP (TICRA, 2011)

$$P_{O1} = 1.09 \pi \frac{D}{\lambda} \sin(\theta_0) + 10 \quad (2.105)$$

P_{O1} number of sample points along radial direction required

$$P_{O2} = \frac{P_{O1}}{2.4} \quad (2.106)$$

P_{O2} number of sample points along azimuthal direction required

where:

D is the diameter of the surface

λ is the wavelength

θ_0 is the maximum beam angle to a point on the surface

This calculation for P_{O2} can also be used to determine the number of PTD points required along the edge of the surface at the rim. As MODAL cannot auto-calculate the required sample density, a value must be selected that yields a representative field in an acceptable time frame. The above formulae can be used to give an estimate for the initial sampling values to use.

2.3.5 Extracting data from the simulations

The final step is to export data from the fields in GRASP or datasets in MODAL. For GRASP this is simply done by using the plot or export command with the relevant

field selected. Exporting of the fields can be done to either .grd (grid field storage) and/or .cut (cut through field) files. These data files also contain header information pertaining to the measurements taken, the size of the region, frequency, sampling etc.. In MODAL the user can link an export function and/or a plot to the dataset. The export function will export the entire dataset contents, with no options here to allow further filtering of the file content. The plot will display, depending on type selected, a graph(s) or cut(s) representative of the data columns selected. MODAL offers a range of metrics (e.g. coupling, power) that can also be extracted and subsequently exported or plotted.

Beams and rays, which are separate objects, are not required for the calculation of the field, but do add a convenient way to visualise propagation through the system. In GRASP one can display the rays from the source to a set propagation distance. GRASP will reflect the rays at each intersection with a scatterer automatically and the rays are configurable for spread and density, but this spread is not representative of the field and the user must manually set the angle out to which to display. In MODAL the beam “envelope” (size out to xw , where x is a user defined parameter) can be displayed to represent a field. The beam radius is calculated using the GBM analysis described earlier. An example of various visualisations is shown in [Figure 2.25](#) for 2 sources at either side of the QUBIC input array. The beams emitted from the sources are reflected from the primary mirror out towards the secondary mirror. The first 2 cases are for MODAL with GBM analysis showing the calculated field out to $r = 0.1w$ and $1w$ and the final case is for GRASP showing the beam out to an angle of 7° (manually configured) from the chief ray propagation axis.

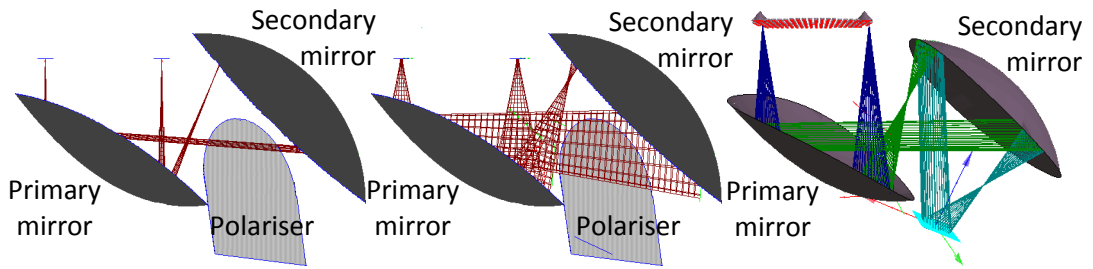


Figure 2.25: QUBIC beams from MODAL at 0.1w (left), 1w (centre) and GRASP out to 7° (right).

2.3.6 Automation of simulations

There are several ways to automate large operations where, for example, the output of a system is needed as the source position is varied, as would be the case in tolerance analysis. In GRASP, using a text editor, objects can be manually created at the desired locations with subsets of commands to process them, and then the entire set run in one go. This is a useful tool but can be prone to error and great care must be taken. In MODAL there are 2 main options. Firstly a sweep where you can select up to 2 parameters, for example the x and y location of a source, giving them a start and end value with a number of steps. These can be assigned as the positions of an element and the system will then automatically iterate through all possible combinations, calculate the output and record the result. This is then stored in a special sweep dataset and can be utilised like any other dataset. This approach is limited to 2 parameters and only existing metrics can be calculated. A more advanced method using batch operations utilises command line instructions which allows the user full control of the system and setup. The commands are placed in a Linux bash script which allows the use of loops, counters, variables etc. The command line instructions given to MODAL allow access to almost every configured item in the model. This allows interim manipulation, renaming or moving of files, before carrying out the next iteration in the calculation set. There are no practical limits on the number of parameters that can be set or the number of exports or plots that can be generated. An example of a typical script is given in Appendix 1.a. This script calls MODAL with all the necessary parameters set from the command line, including filenames so that when output files are generated the files created are named and stored as desired. The bash script loops over each

source to be tested and the complete set can be re-run for each corresponding parameter variation required. To automate the process of generating these complex bash-scripts, a vb-script in Excel was utilised, where the user selects the source(s) from the GUI, as illustrated in *Figure 2.26*, and the scatterers from the vb-script. Once selected, the bash-script is generated creating all the relevant output files. The vb-script is shown in Appendix 1.b.

Batch Scripting Generator

22 22	21 22	20 22	19 22	18 22	17 22	16 22	15 22	14 22	13 22	12 22	11 22	10 22	09 22	08 22	07 22	06 22	05 22	04 22	03 22	02 22	01 22	-0.147	22
22 21	21 21	20 21	19 21	18 21	17 21	16 21	15 21	14 21	13 21	12 21	11 21	10 21	09 21	08 21	07 21	06 21	05 21	04 21	03 21	02 21	01 21	-0.133	21
22 20	21 20	20 20	19 20	18 20	17 20	16 20	15 20	14 20	13 20	12 20	11 20	10 20	09 20	08 20	07 20	06 20	05 20	04 20	03 20	02 20	01 20	-0.119	20
22 19	21 19	20 19	19 19	18 19	17 19	16 19	15 19	14 19	13 19	12 19	11 19	10 19	09 19	08 19	07 19	06 19	05 19	04 19	03 19	02 19	01 19	-0.105	19
22 18	21 18	20 18	19 18	18 18	17 18	16 18	15 18	14 18	13 18	12 18	11 18	10 18	09 18	08 18	07 18	06 18	05 18	04 18	03 18	02 18	01 18	-0.091	18
22 17	21 17	20 17	19 17	18 17	17 17	16 17	15 17	14 17	13 17	12 17	11 17	10 17	09 17	08 17	07 17	06 17	05 17	04 17	03 17	02 17	01 17	-0.077	17
22 16	21 16	20 16	19 16	18 16	17 16	16 16	15 16	14 16	13 16	12 16	11 16	10 16	09 16	08 16	07 16	06 16	05 16	04 16	03 16	02 16	01 16	-0.063	16
22 15	21 15	20 15	19 15	18 15	17 15	16 15	15 15	14 15	13 15	12 15	11 15	10 15	09 15	08 15	07 15	06 15	05 15	04 15	03 15	02 15	01 15	-0.049	15
22 14	21 14	20 14	19 14	18 14	17 14	16 14	15 14	14 14	13 14	12 14	11 14	10 14	09 14	08 14	07 14	06 14	05 14	04 14	03 14	02 14	01 14	-0.035	14
22 13	21 13	20 13	19 13	18 13	17 13	16 13	15 13	14 13	13 13	12 13	11 13	10 13	09 13	08 13	07 13	06 13	05 13	04 13	03 13	02 13	01 13	-0.021	13
22 12	21 12	20 12	19 12	18 12	17 12	16 12	15 12	14 12	13 12	12 12	11 12	10 12	09 12	08 12	07 12	06 12	05 12	04 12	03 12	02 12	01 12	-0.007	12
22 11	21 11	20 11	19 11	18 11	17 11	16 11	15 11	14 11	13 11	12 11	11 11	10 11	09 11	08 11	07 11	06 11	05 11	04 11	03 11	02 11	01 11	0.007	11
22 10	21 10	20 10	19 10	18 10	17 10	16 10	15 10	14 10	13 10	12 10	11 10	10 10	09 10	08 10	07 10	06 10	05 10	04 10	03 10	02 10	01 10	0.021	10
22 09	21 09	20 09	19 09	18 09	17 09	16 09	15 09	14 09	13 09	12 09	11 09	10 09	09 09	08 09	07 09	06 09	05 09	04 09	03 09	02 09	01 09	0.035	9
22 08	21 08	20 08	19 08	18 08	17 08	16 08	15 08	14 08	13 08	12 08	11 08	10 08	09 08	08 08	07 08	06 08	05 08	04 08	03 08	02 08	01 08	0.049	8
22 07	21 07	20 07	19 07	18 07	17 07	16 07	15 07	14 07	13 07	12 07	11 07	10 07	09 07	08 07	07 07	06 07	05 07	04 07	03 07	02 07	01 07	0.063	7
22 06	21 06	20 06	19 06	18 06	17 06	16 06	15 06	14 06	13 06	12 06	11 06	10 06	09 06	08 06	07 06	06 06	05 06	04 06	03 06	02 06	01 06	0.077	6
22 05	21 05	20 05	19 05	18 05	17 05	16 05	15 05	14 05	13 05	12 05	11 05	10 05	09 05	08 05	07 05	06 05	05 05	04 05	03 05	02 05	01 05	0.091	5
22 04	21 04	20 04	19 04	18 04	17 04	16 04	15 04	14 04	13 04	12 04	11 04	10 04	09 04	08 04	07 04	06 04	05 04	04 04	03 04	02 04	01 04	0.105	4
22 03	21 03	20 03	19 03	18 03	17 03	16 03	15 03	14 03	13 03	12 03	11 03	10 03	09 03	08 03	07 03	06 03	05 03	04 03	03 03	02 03	01 03	0.119	3
22 02	21 02	20 02	19 02	18 02	17 02	16 02	15 02	14 02	13 02	12 02	11 02	10 02	09 02	08 02	07 02	06 02	05 02	04 02	03 02	02 02	01 02	0.133	2
22 01	21 01	20 01	19 01	18 01	17 01	16 01	15 01	14 01	13 01	12 01	11 01	10 01	09 01	08 01	07 01	06 01	05 01	04 01	03 01	02 01	01 01	0.147	1
0.147	0.133	0.119	0.105	0.091	0.077	0.063	0.049	0.035	0.021	0.007	-0.007	-0.021	-0.035	-0.049	-0.063	-0.077	-0.091	-0.105	-0.119	-0.133	-0.147		
22	21	20	19	18	17	16	15	14	13	12	11	10	9	8	7	6	5	4	3	2	1		

Figure 2.26: MODAL Linux bash script generator source selection screen

2.3.7 Comparing MODAL and GRASP

Finally in this section we look at a simple setup to compare the outputs of both MODAL and GRASP. Source definitions are different in MODAL and GRASP, for example MODAL specifies the source peak amplitude as 1 V/m and GRASP normalises the total power to 4π W and there is a 90° start phase difference. For this test, MODAL’s default configuration was changed to match GRASP, which is being used as the benchmark software. With the sources matched, the outputs of

both systems were compared in a simple optical setup where a plane mirror is introduced at 45° . The 2 systems are set up identically as illustrated in *Figure 2.27*.

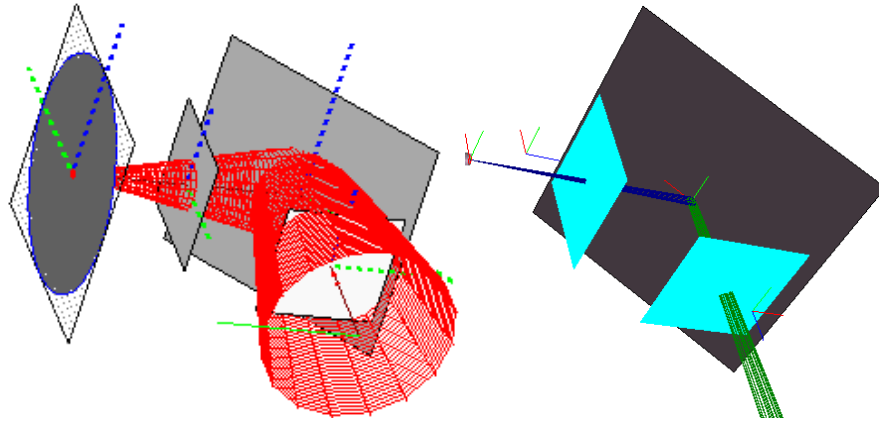


Figure 2.27: Plane mirror system implemented in MODAL (left) and GRASP (right)

Figure 2.28 shows the magnitude of the field after 100 mm propagation from the waist of the Gaussian sources configured in each system. There is excellent agreement between the 2 packages and so the beams were calculated after reflection from the plane mirror.

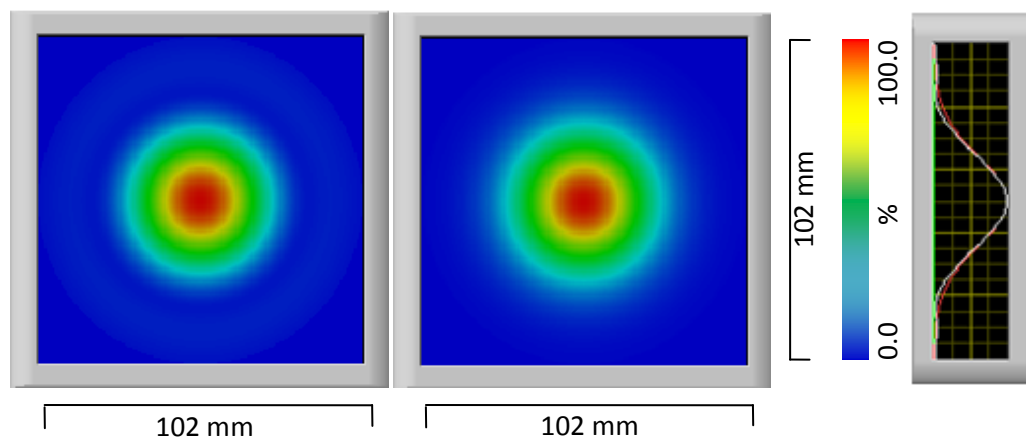


Figure 2.28: Magnitude of the field after a propagation of 100 mm from the waist: MODAL (left), GRASP (centre) and on the right cuts for MODAL (white) and GRASP (red).

Figure 2.29 and *Figure 2.30* show the magnitude and phase of both systems where again there is excellent agreement. Subsequent testing will be outlined in Chapters 3 and 4 when considering the implementation of QUBIC for simulation, analysis and optimisation.

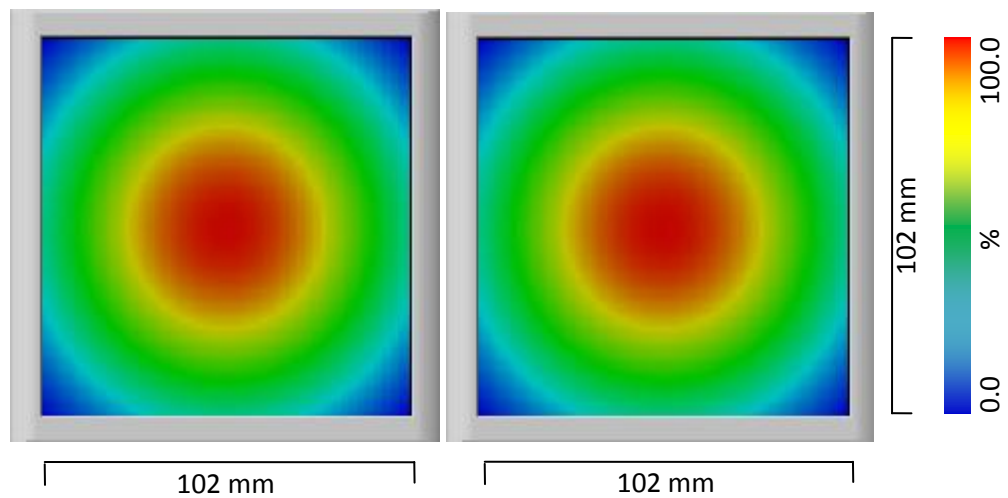


Figure 2.29: Magnitude of the field after a propagation of 100 mm from a plane mirror: MODAL (left) & GRASP (right).

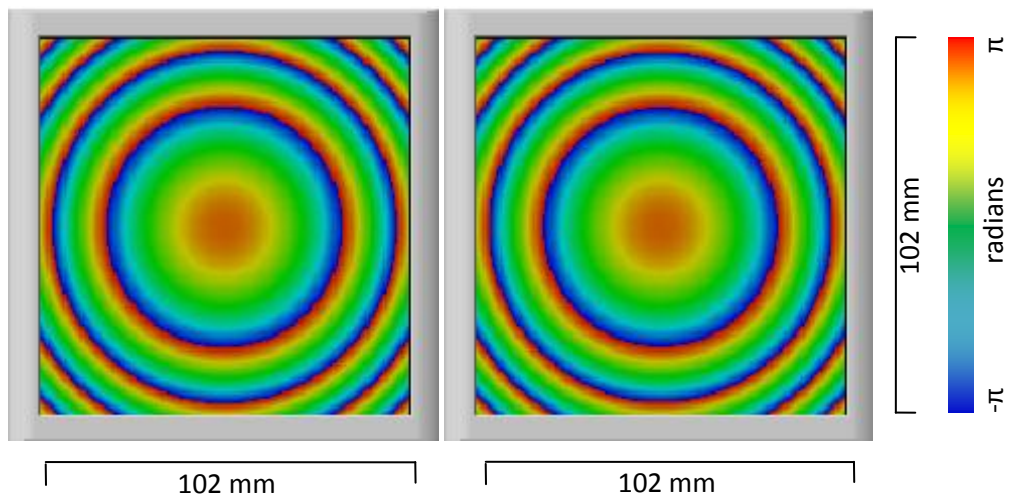


Figure 2.30: Phase of the field after a propagation of 100 mm from a plane mirror: MODAL (left) & GRASP (right).

2.4 Conclusion

In this chapter the theoretical techniques and simulation tools used to model the behaviour of the QUBIC combiner and its predecessor MBI were discussed.

We first discussed a mode matching technique used to model conical corrugated feed horn antennas including a brief look at one implementation of this method used in the MU code SCATTER. This was then extended to include SVD allowing hybrid mode analysis of the feed horn outputs. This proved particularly useful for the revised QUBIC v2.0, explored in Chapter 6, using a second frequency where the feed horn operation was multi-moded.

We described the GRASP and MODAL software packages and discussed the various modelling methods employed by each. These are (1) geometric optics (GO) and the geometric theory of diffraction (GTD), (2) physical optics (PO) and the physical theory of diffraction (PTD) and (3) Gaussian beam mode (GBM) analysis and the application of ABCD matrices. GO/GTD was useful for the initial design stages for approximating component positions and orientations but its lack of ability to account for diffraction effects, which are prominent at these wavelengths, required that other methods were employed. PO is the most accurate of the methods looked at but also is the most time consuming due to the computations involved. This is especially concerning for a project like QUBIC with 400 individual sources to be considered. Finally an intermediate method was investigated, GBM analysis, which accounts for diffraction effects and is more efficient than PO. It represents the beam as a complex scalar field and as such cannot account for cross-polarisation effects. The field is constructed from the summation of independently propagating Gaussian modes. GBM works well for beams that obey the paraxial approximation and where the scattering elements do not markedly truncate the beams. Examples from the QUBIC beam combiner were used throughout.

We then briefly looked at the propagation of a Gaussian source in GRASP and MODAL, for a basic optical system and compared the 2 simulations. Both packages have their strengths and weaknesses, MODAL, as an in-house developed package, is flexible and was customised for the modelling requirements of QUBIC. GRASP is an industry standard and was used as a benchmark for MODAL. Good agreement was found between both models, where all testing to date indicates that PO has been implemented correctly in MODAL.

In the next chapter the operation and the goals of the QUBIC combiner will be detailed after starting with a brief description of the predecessors that paved the way for its design.

3 QUBIC

The QUBIC (Q and U Bolometric Interferometer for Cosmology) polarimeter aims to measure the CMB B-mode component and therefore the tensor to scalar ratio, r (Kaplan & collaboration, 2009). The goal of the QUBIC project is to create an instrument that is as sensitive as an imager and has the systematic error control inherent in interferometers. The latest iteration of the QUBIC design observes the sky using an array of ultra-Gaussian feed horns whose outputs are superimposed by an optical combiner yielding a synthetic image of the sky on a detector plane consisting of a bare array of bolometers. The synthetic image will be decomposed to extract polarisation properties of the CMB. This novel technique will improve upon existing measurements of the CMB shedding light on the structure of the early universe. QUBIC is the work of a collaboration of several institutions from France, Italy, UK, USA and Ireland which formed from the precursory missions: BRAIN (Background RAdiation INterferometer (Masi, et al., 2005)) and MBI (Millimetre-wave Bolometric Interferometer (Tucker, et al., 2003)). In this chapter we will briefly look at the outline QUBIC design, starting with the predecessors MBI and BRAIN.

3.1 Pathfinders

3.1.1 MBI

MBI (Tucker, et al., 2003) was a US (NASA, University of Richmond, University of California, North-western University, Brown University and University of Wisconsin) and European (Maynooth University, Ireland, Cardiff University, Wales) collaboration. It set out to check the feasibility of using Fizeau interferometry for the control of systematics in conjunction with cryogenically cooled bolometers for increased sensitivity over the traditional heterodyne approach. It was specifically designed to observe in the far-infrared in an atmospheric window at 90 GHz, as shown in *Figure 3.1*.

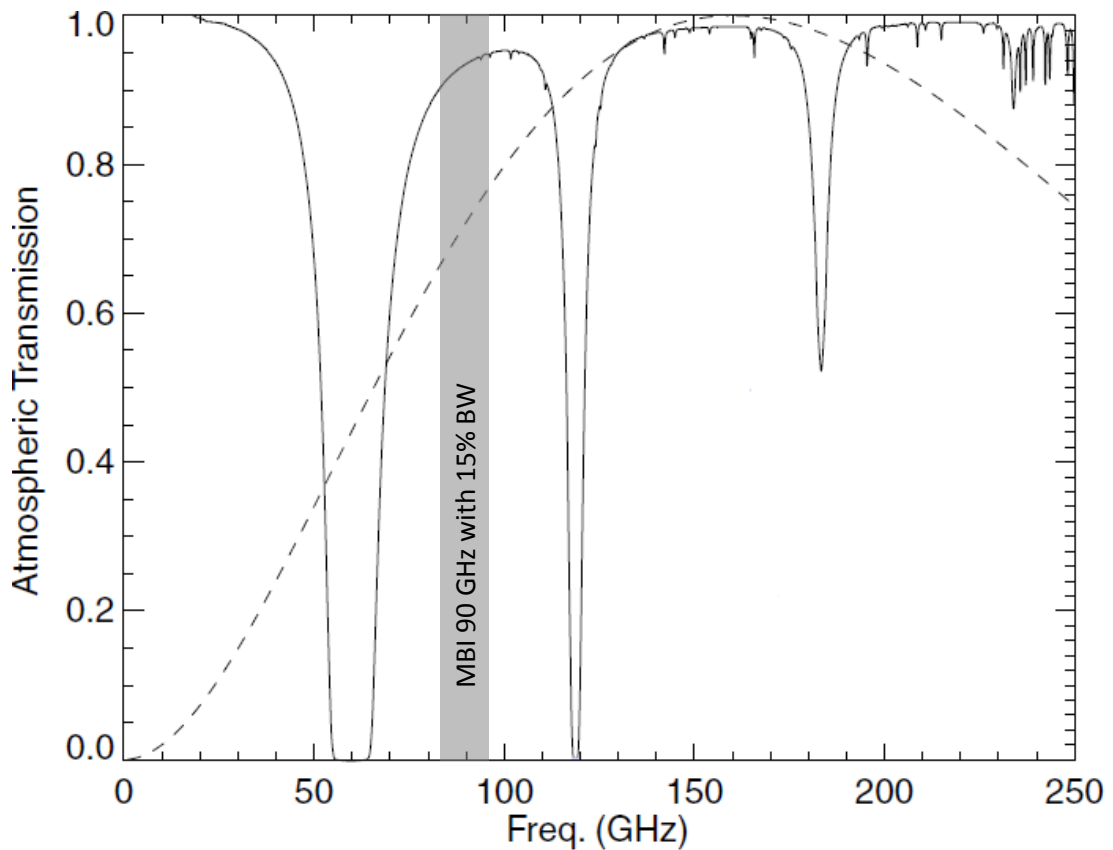


Figure 3.1: Atmospheric transmission as a function of frequency at Antarctica. Image taken from (Hinderks, et al., 2009) the CMB spectrum is shown by the dotted line. The operating bandwidth of the MBI experiment is also shown.

MBI used an on-axis Cassegrain design as shown in [Figure 3.2](#). The on-axis design is inefficient, only propagating $\sim 30\%$ of feed horn power to the detector plane, but it was chosen because of several restrictions: it had to fit inside a pre-existing cryostat and the arrangement, size and position of the detector and the back-to-back feed horn arrays were also fixed. It was adequate for the goal at hand and offered the advantage of minimised system induced aberrations. MBI consisted of 4 back-to-back feed horns, 2 of each orthogonal polarisation making up the multi-baseline adding interferometer, and 19 bolometers at the detector plane. The optical arrangement is briefly modelled here as a useful starting point for QUBIC simulations.

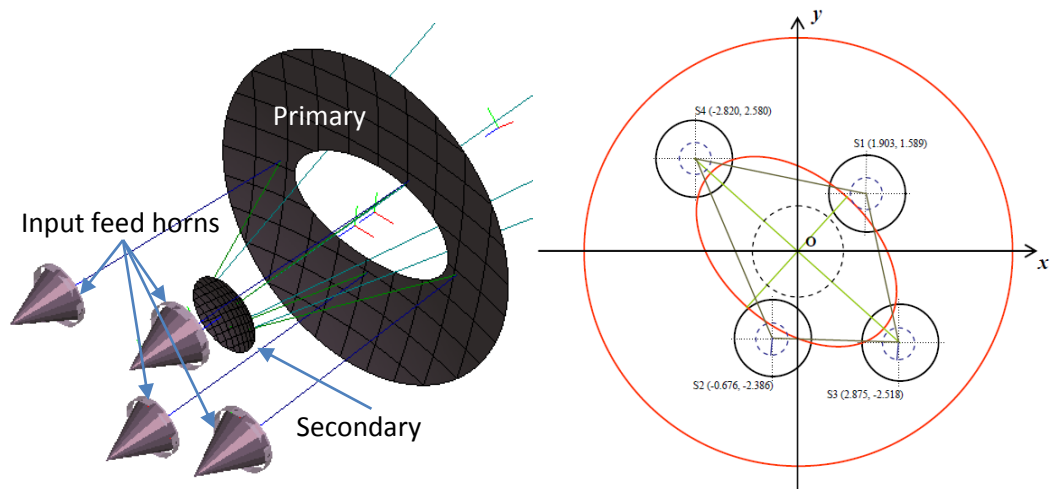


Figure 3.2: MBI-4 Schematic: Left from GRASP and right from Curran (Curran, 2010) showing the four inward-facing horn antennas and their coordinate offset from the centre (in inches). The primary mirror, a paraboloid with elliptical aperture, is also shown on the left along with the secondary mirror, a hyperboloid. The view is from the detector plane looking out towards the sky.

MBI used conical corrugated feed horns with an aperture radius of 25 mm yielding, (Goldsmith, 1998), an aperture (best-fit Gaussian) beam width

$w_a = 0.6435 \times 25 = 16.1$ mm, waist radius of $w_0 = \frac{w_a}{\sqrt{1 + \left(\frac{\pi w_a^2}{\lambda R}\right)^2}} = 7.67$ mm located

$\Delta z = \frac{R}{1 + \left(\frac{\lambda R}{\pi w_a^2}\right)^2} = 102.34$ mm behind the aperture as shown in Figure 3.3.

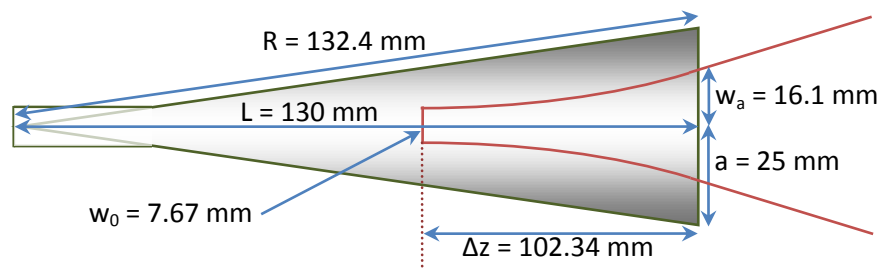


Figure 3.3: Schematic (not to scale) diagram of the MBI corrugated feed horn antenna (corrugations are omitted for clarity). Designed to operate single moded at a frequency $\nu = 90$ GHz with a 15% bandwidth.

As an initial check an ABCD/GBM analysis was carried out. An equivalent lens system was configured as shown in Figure 3.4 with system parameters as detailed in Table 3-1 and a Gaussian beam ($w = 16.1$ mm, $\Delta z = 102.34$ mm) was propagated through the system.

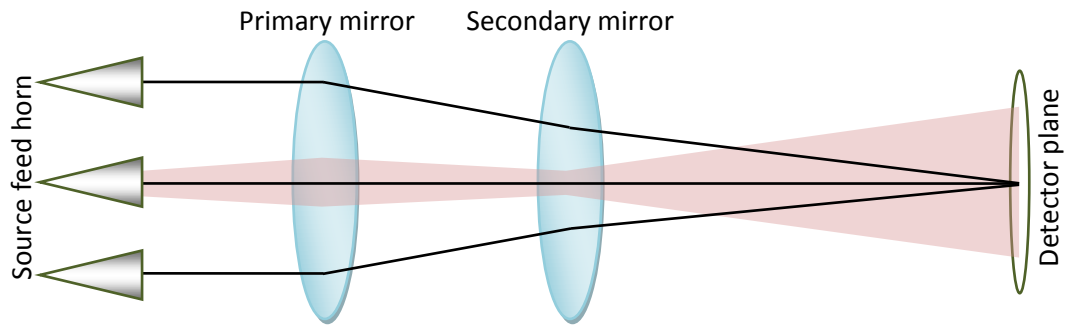


Figure 3.4: MBI equivalent lens system.

Table 3-1: MBI equivalent lens system parameters (for ABCD model)

Parameter	Value	Unit
Distance from aperture plane to primary mirror	250	mm
Primary mirror focus length	228.57	mm
Distance from primary to secondary mirror	200	mm
Secondary focus length (negative for hyperbolic mirror)	-30.93	mm
Distance from secondary to detector plane	375	mm

Using this approach it was possible to calculate the phase radius of curvature and beam width for a central beam propagating through this configuration as shown in

Figure 3.5 and Figure 3.6.

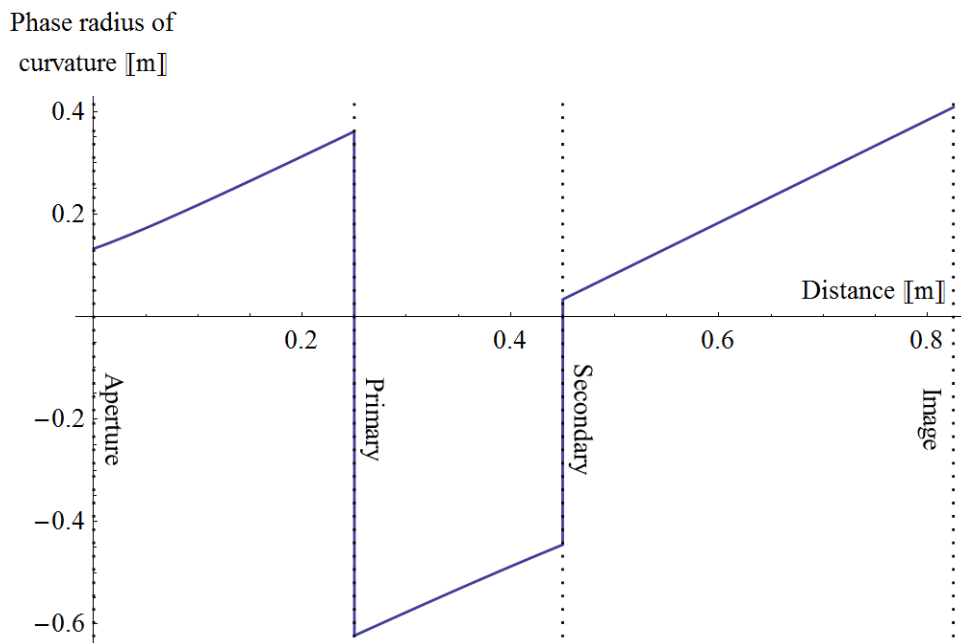


Figure 3.5: Beam phase radius of curvature as a function of propagation distance. Radius of curvature at waist = ∞ , aperture = 132.4 mm, primary = 361.1 mm, secondary = -445.4 mm and image plane = 408.2 mm

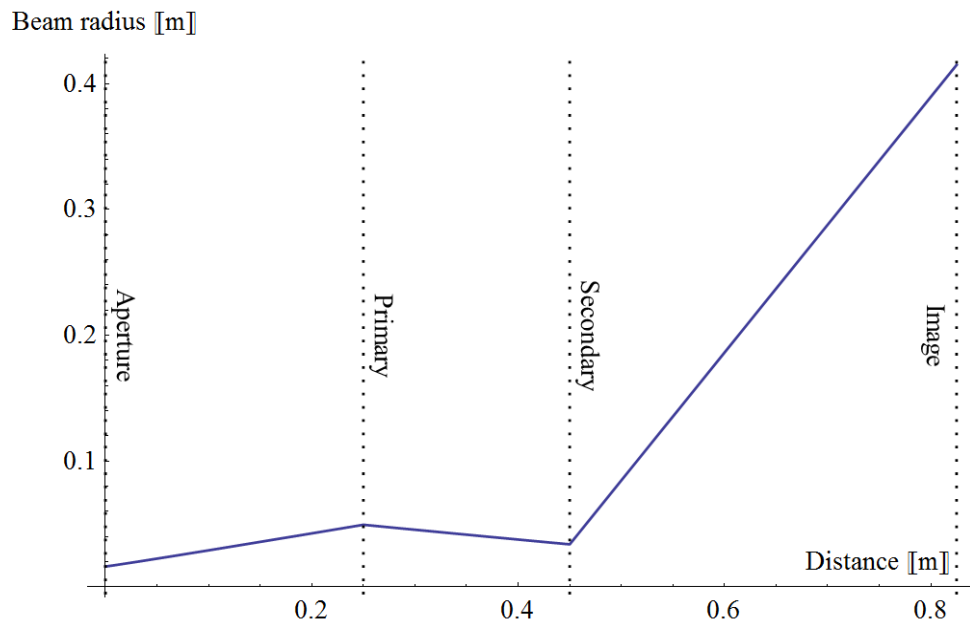


Figure 3.6: Beam radius as a function of propagation distance. Beam radius at waist = 7.7 mm, 16.1 mm, primary = 49.3 mm, secondary = 33.8 mm and image plane = 414.9 mm

A further analysis was carried out in both GRASP *Figure 3.2* and MODAL *Figure 3.7*, these simulations could be used to compare with preliminary measurements. The on-axis design had problems in that there was spillover (leakage) present due to an available path directly from the sky horns through to the detector plane, these effects were modelled using MODAL. The outputs from the system with and without this leakage being included in the detector plane image can be seen in *Figure 3.8* and *Figure 3.9*.

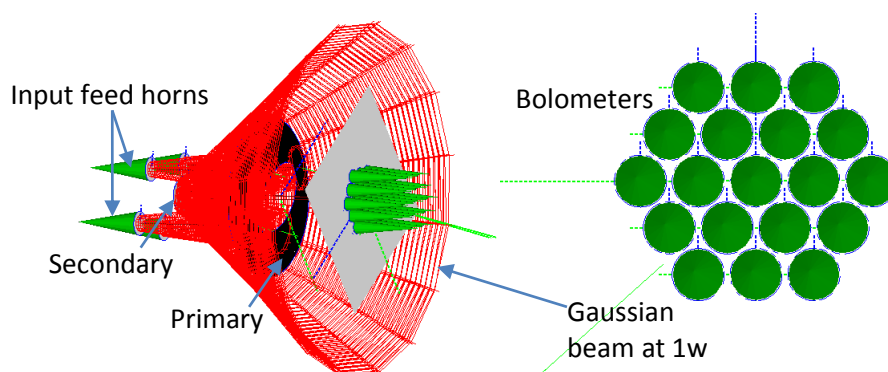


Figure 3.7: Images from MODAL: (left) overview of MBI system showing the source beams projected and reflected off of the mirrors, out to 1w and (right) layout of detector bolometers on the detector plane.

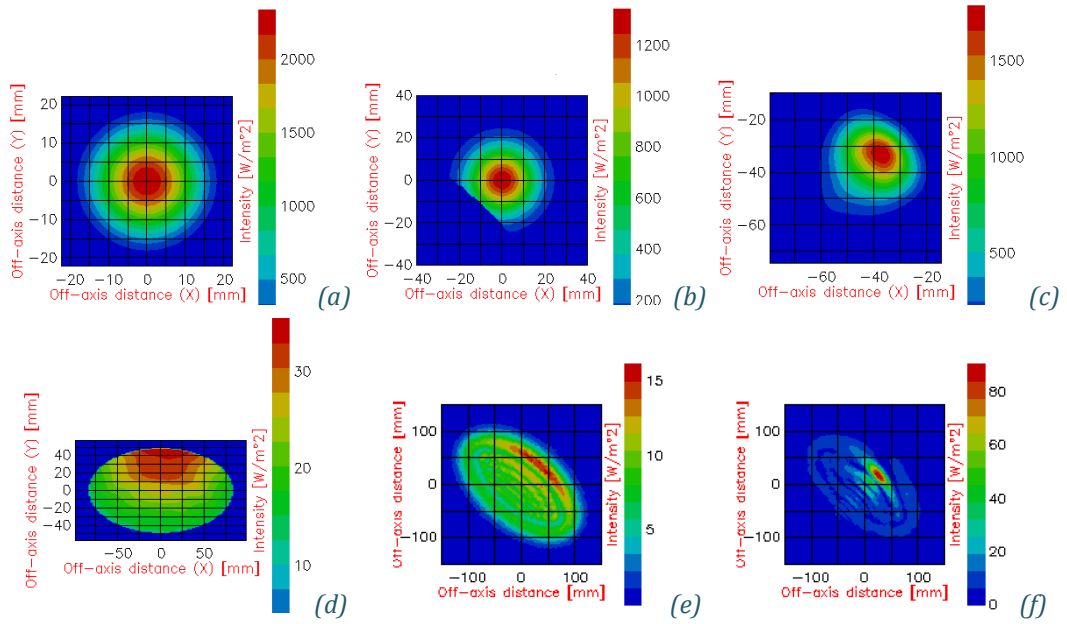


Figure 3.8: Source 1 amplitude at (a) source, (b) primary, (c) secondary, (d) primary centre hole, (e) detector plane, for an idealised situation where no leakage from the feed horns or truncation by the secondary is taken into account and (f) detector plane taking leakage and truncation into account.

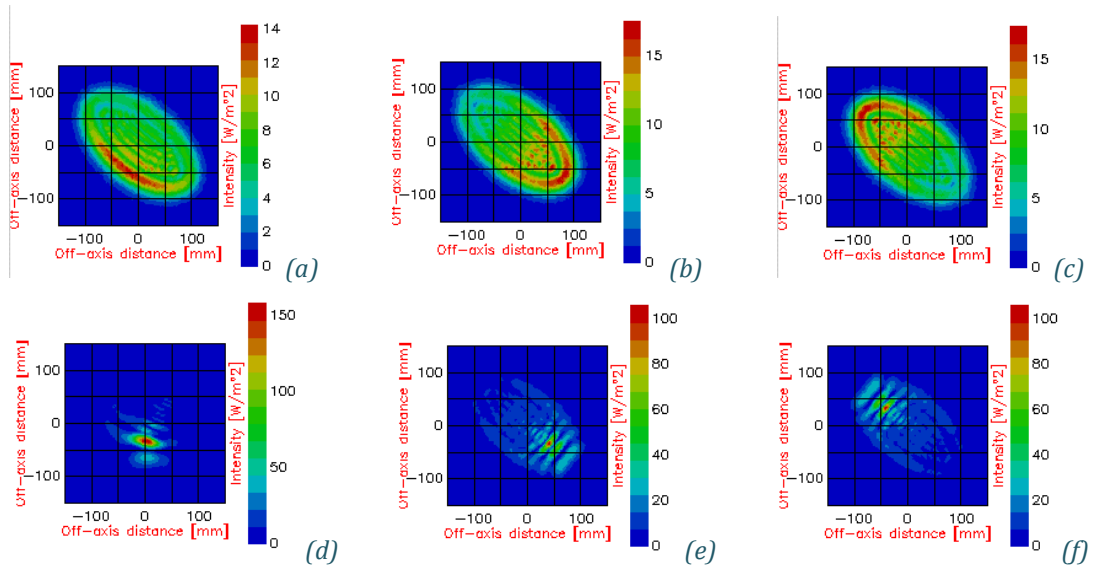


Figure 3.9: Detector plane outputs with no leakage for (a) source 2, (b) source 3 and (c) source 4 and with leakage for (d) source 2, (e) source 3 and (f) source 4.

It can be clearly seen by comparison of *Figure 3.9 (a), (b) and (c)* with *(d), (e) and (f)*, that the output at the detector plane is heavily affected by the inclusion of the blockages and leaks. From calculations carried out on these simulations it was found that approximately 30% of the power from each source reached the detector plane. As an example the power from source 1 (*Figure 3.2*) at each component is listed in *Table 3-2*. These are in line with the analysis of (Curran, 2010).

Table 3-2: Power transmission report

Description	Power level
Source emission	100.00%
Secondary (transmission past secondary)	99.98%
Primary reflection	89.86%
Secondary reflection	87.46%
Primary (transmission through centre hole)	27.91%
Detector plane	27.53%

The MBI (Tucker, et al., 2003; Timbie, et al., 2006) prototype detected fringes (Curran, 2010, p. 243) from a Gunn-oscillator in 2009 (Ghribi, et al., 2010), as shown in *Figure 3.10*. Successfully proving the concept of bolometric interferometry for millimetre wave measurements and in conjunction with BRAIN, discussed in the next section, lead the way for the QUBIC mission.

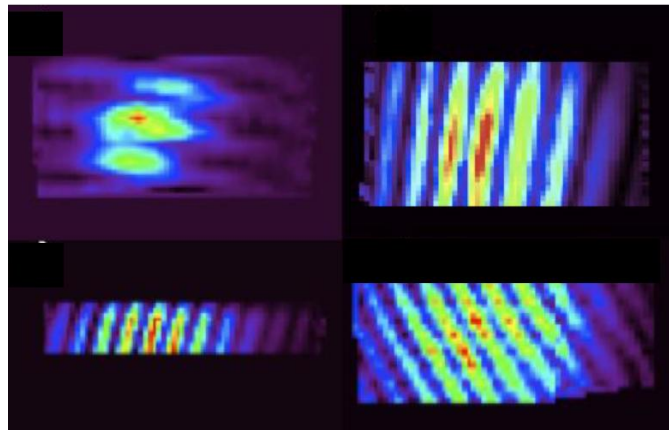


Figure 3.10: Fringes observed with the MBI-4 instrument in early 2009 (Curran, 2010, p. 243). Baseline 1-2 (top-left), 1-3 (top-right), 2-3 (bottom-left) and 2-4 (bottom-right).

3.1.2 BRAIN

BRAIN (Polenta, et al., 2007) is a group effort from the University of Rome, the University of Milano Bicocca, ISTARs and Agenzia Spaziale, Italy, the College de France and CESR, France and University of Cardiff, UK. BRAIN's main goal was to check the feasibility of detecting B-modes in the CMB from ground based observations in the future. The all year-round extremely dry and stable atmosphere made Concordia Station Dome-C, Antarctica, shown in *Figure 3.11*, a good choice for the tests. These conditions would minimise the effects of the atmosphere.

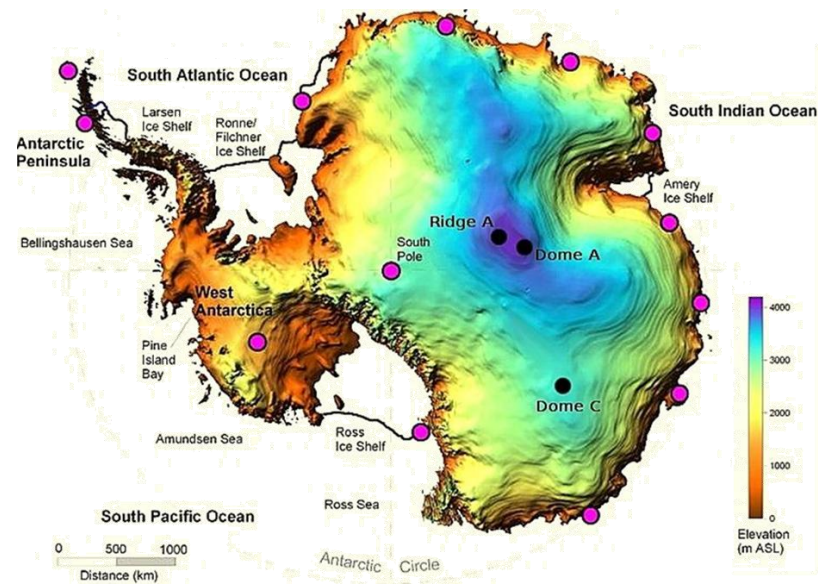


Figure 3.11: Concordia Station, Dome-C Antarctica (Spencer, 2013)

The project attempted to detect, from ground based observations, the polarised microwave emission from the atmosphere and Galaxy during an Antarctic winter, in order to confirm the suitability of Antarctica for this type of observation. This was achieved using a 0.3 K cryogenic bolometric detector and the design concept shown in Figure 3.12.

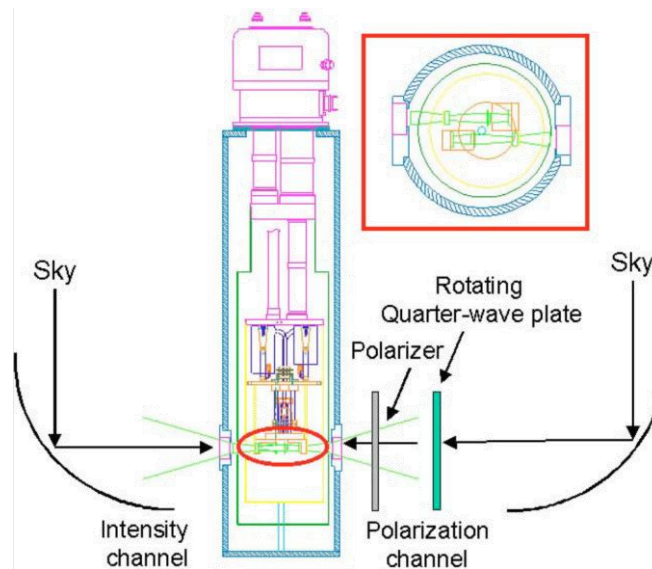


Figure 3.12: BRAIN pathfinder schematic – block diagram of 1 baseline of the BRAIN interferometer (Masi, et al., 2005)

In 2008 it was decided to consolidate the MBI and BRAIN missions and move directly to the next iteration, QUBIC.

3.2 QUBIC design

Leading on from the experiences of both the BRAIN and MBI projects the respective collaborations teamed up to build a state of the art telescope: QUBIC (Q & U Bolometric interferometer for Cosmology). At the time of writing the collaboration consists of a number of institutions, including from France (*APC; Paris Diderot; CSNSM; OIRAP; IAS; CNRS; NEEL Institute; CESR – Universite Paul Sabatier*), Italy (*Sapienza Universita di Roma; Bicocca, Universita Degli Studi di Milano; Universita di Senarum; ASDC ASI; INAF*), the U.K. (*Manchester University*), Ireland (*Maynooth University*) and the U.S.A. (*Brown University*). Pioneering missions like DASI (Leitch, et al., 2002) and CBI (Padin, et al., 2001) have already observed E-mode polarisation in the CMB but the detection of the elusive B-modes requires a more sensitive detector than has been previously developed. QUBIC will have the express goal of detecting B-mode polarisation in the CMB or at least placing a refined upper limit on the tensor to scalar ratio, r .

3.2.1 Overview

The QUBIC mission proposes to combine the advantages of the sensitivity offered by imaging with the systematic error control and calibration afforded by interferometry, in this case additive interferometry. The primary driving force for the QUBIC collaboration is to create an instrument capable of detecting B-mode polarisation in the CMB constraining the tensor-to-scalar ratio, r , to 0.01 with a 90% confidence level with first year data. To achieve this, the general concept of QUBIC will utilise 6 modules (2 at each frequency of 90, 150 and 220 GHz based on available atmospheric windows as shown in [Figure 3.13](#)) consisting of an input feed horn array, an optical combiner and a detector array all contained within a cryostat, as shown in [Figure 3.14](#). The feed horn array gives a large number of baselines and the optical combiner will be used to sum individual baseline contributions. The QUBIC instrument will discriminate between orthogonally polarised components of

the incoming CMB signal and use incoherent detectors to observe fringe patterns for the measurement of Stokes visibilities. With Stokes parameters recovered the TT, TE, EE and BB power spectra can then be reconstructed using standard techniques (Zaldarriaga, 2001; Hamilton, et al., 2008).

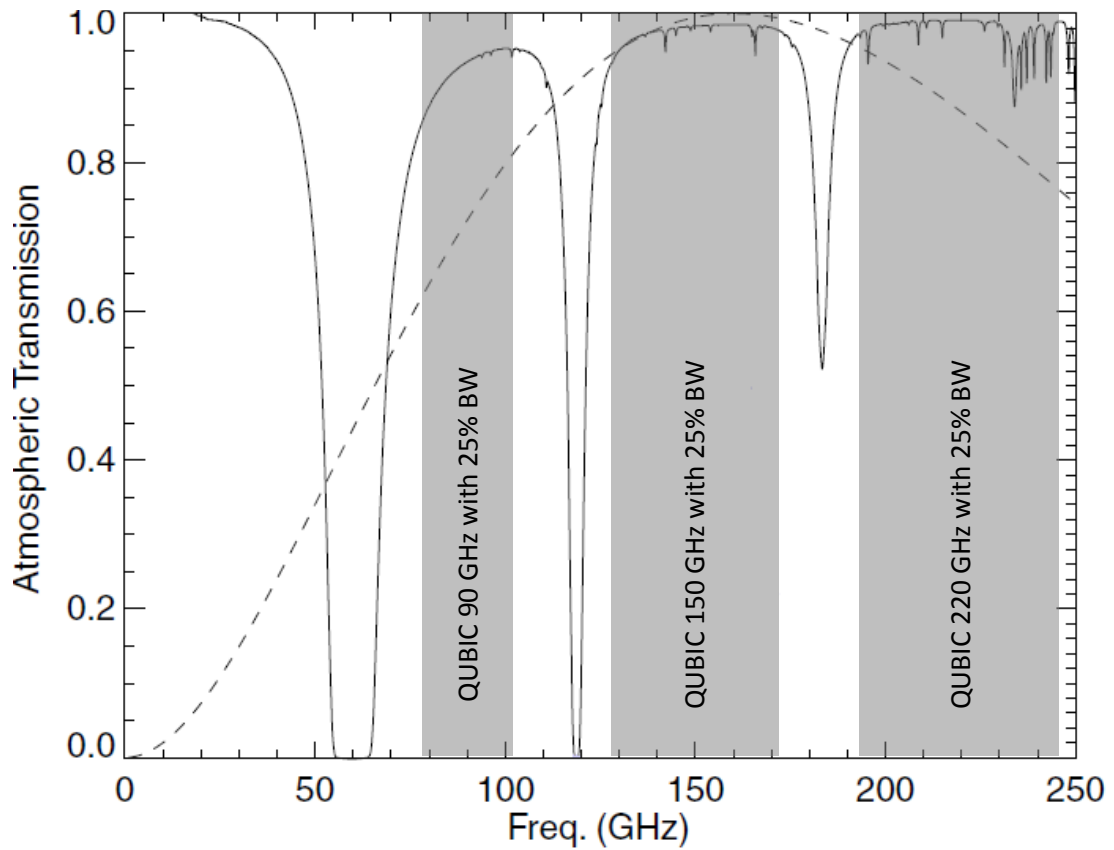


Figure 3.13: Atmospheric transmission as a function of frequency at Antarctica. Image taken from (Hinderks, et al., 2009) the CMB spectrum is shown with the dotted line. Superimposed are the frequency bands proposed for the QUBIC experiment.

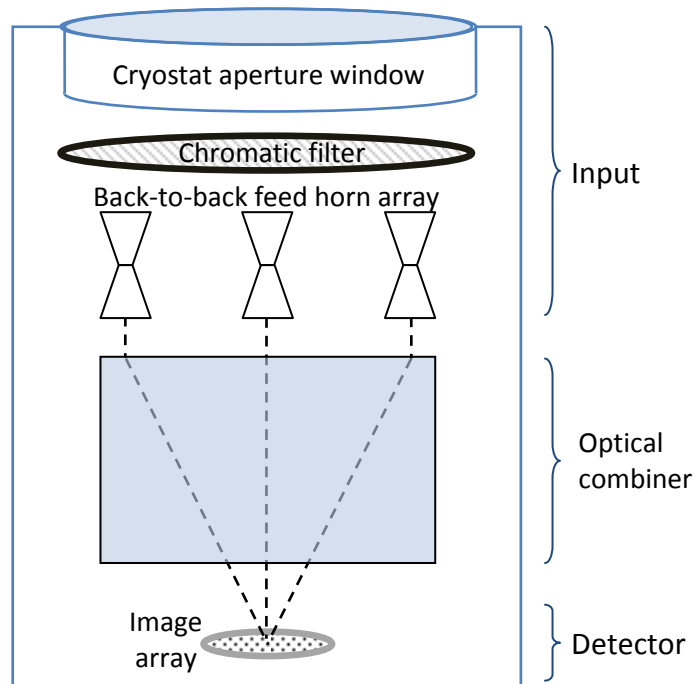


Figure 3.14: QUBIC basic structure

It is hoped that the broadband nature of incoherent detectors (bolometers) will improve upon the more traditional heterodyne approach in previous missions like DASI (Leitch, et al., 2002). In the next section we will briefly look at some of the decisions that were made and rejected for each of the three main sections, input, detectors and combiner, and ultimately the problems that led to a redesign, QUBIC v2.0.

3.2.2 QUBIC v1.0

Input: There are two main parameters that drive the design of QUBIC for the detection of B-modes: the sky beam size and the number of beams, and these are directly related to the tensor-to-scalar ratio, r , which is observed. There is a physical upper limit on the number of horns possible related simply to the cryostat aperture window size that can be manufactured. A typical cryostat window made of zotefoam of diameter 300 mm needs to be ~100 mm thick, thickness increasing rapidly as twice the diameter. A low-pass chromatic filter is located after the window to restrict the frequency band entering the combiner. These are poor heat conductors (Hamilton, et al., 2009) and therefore to avoid an undesirable

temperature gradient an additional 60 mm clearance to the feed horn array is required. To minimise truncation of the array's edge feed horns, this thickness and separation has to be taken into account, implying a reduced usable diameter for the feed horn array which can be calculated from *Equation (3.1)*.

$$D_{window} = D_{array} + 2H \tan\left(\frac{3}{2} \text{FWHM}\right) \quad (3.1)$$

Aperture window and feed horn array diameters to ensure no truncation (Hamilton, et al., 2009)

where:

D_{window} is the diameter of the input aperture array window

D_{array} is the diameter of the input aperture feed horn array

H is the separation distance from the top of the feed horn array to the aperture window

FWHM is the full width half maximum angle of the feed horn beam profile (intensity)

It was estimated by APC (Université Paris Diderot) that an input aperture window diameter of 400 mm with 3 modules each of 144 feed horns and a FWHM $\geq 12^\circ$ operating for one year would achieve the desired level of $r \leq 0.01$, as shown, in red, in *Figure 3.15*. This excludes effects from bandwidth smearing which it was hoped could be compensated for with appropriate data processing.

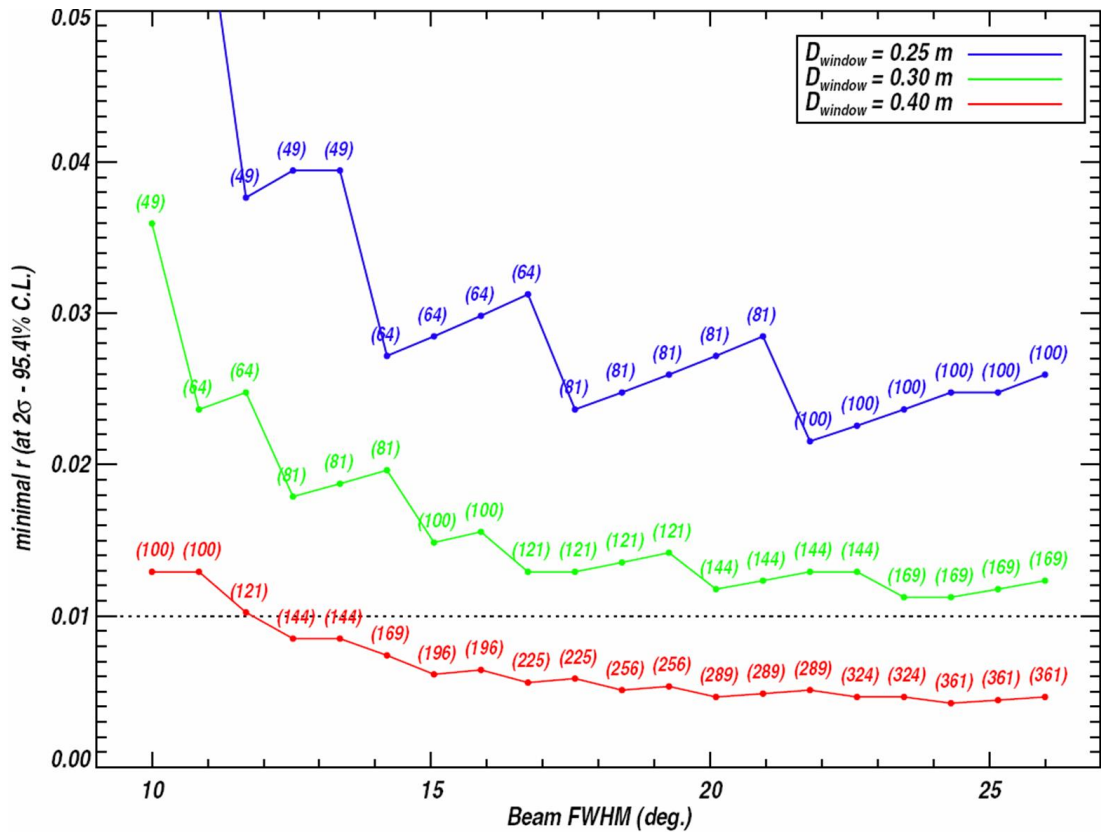


Figure 3.15: The tensor-to-scalar ratio, r , detectable as a function of primary beam FWHM (Bennett, 2014; Hamilton, et al., 2008). There are three plots for aperture windows of size 200 (blue), 300 (green) and 400 mm (red). The number of feed horns in each case that can fit within the aperture window are shown in brackets. This assumes the building of three modules and that the effect of bandwidth smearing can be completely compensated for.

Feed horn selection for QUBIC was based on the requirement that the beam cross-polar and side-lobe content are low and well understood and it was hoped to purchase the cancelled CLOVER mission feed horns (Taylor, et al., 2004). The conical corrugated feed horns designed for the CLOVER mission operating at 97 GHz had a 14° FWHM ultra-Gaussian beam profile with 25% BW and were seen as an ideal choice for inclusion in QUBIC. As a result initial analysis of the feasibility of additive bolometric interferometry was carried out in the band 90 – 100 GHz.

The region where the primordial B-modes are most likely to be observed is for multipoles in the range $25 \leq l \leq 200$ (Hamilton, et al., 2008). The observed multipole, assuming a flat-sky approximation, is given by $l = 2\pi s_\lambda$ (White, et al., 1999a; Bunn & White, 2007) where s_λ is the baseline separation in wavelengths.

Using these limits for the required observable multipoles, the equivalent required baseline range was calculated to be approximately $5 \leq s_\lambda \leq 32$.

In a meeting in Paris in July 2009 several decisions regarding the initial design of the QUBIC telescope were made. The aperture array for each module would consist of 144 back-to-back ultra-Gaussian 14° FWHM feed horns (suggested re-use of CLOVER design) with $\sim 25\%$ bandwidth. There would be 2 sets of 3 modules operating at 90, 150, and 220 GHz. The selected frequencies were based on the CMB intensity compared with foregrounds and the atmospheric windows available at Dome-C Antarctica, as previously shown in *Figure 3.13*. The feed horns were to be arranged in a square grid capable of observing multipoles in the range $30 \leq l \leq 200$. The skyward facing 144 feed horns would couple through co-located ortho-mode transducers (OMT's) and multiplexed strip-line phase delays to 288 re-emitting feed horns. The re-emitting feed horns would each contain one of the two orthogonal components of the incident radiation from the sky. The OMTs provide the means for the discrimination between the orthogonal polarisation components and phase shifters (phase-sensitive detection) would be used to aid in the recovery of Stokes visibilities.

It was proposed that individual sequencing of phase shifts would be imposed on the signal from each feed horn and then visibilities from each baseline would be determined using phase sensitive detection. Charlassier (Charlassier, et al., 2009) showed that the reconstruction of the visibilities involves solving a set of equations with the number of unknowns given by $N_u = 3 + 8 \times N_b$, where N_b is the number of baselines. The phase shifting sequence becomes problematic as there are $N_h = 144$ feed horns in the input array yielding $\frac{N_h(N_h-1)}{2} = 10296$ baselines. To solve this set of equations one needs at least the same number of data samples and the manipulation of such large matrices rapidly becomes unmanageable. The exploitation of equivalent baselines, those with the same spatial separation and orientation, introduced by Charlassier (Charlassier, et al., 2009), was proposed. In this technique equivalent baselines are treated as a single unit during phase shifting

sequences. The number of equivalent baselines was calculated as $2 \times (N_h - \sqrt{N_h}) = 264$, vastly reducing the computational complexity for the recovery of the visibilities. When the contributions from each equivalent baseline are summed coherently the noise on a bolometer, taking into account the noise equivalent temperature and beam size, can be calculated from *Equation (3.2)*, as shown by Hamilton (Hamilton, et al., 2008). *Equation (3.2)* has been used to calculate the number of equivalent baselines required to bring the noise level down sufficiently to enable detection of B-modes (see *Figure 3.15* for an example, where it can be seen that a FWHM of about 12° or more with 144 feed horns is sufficient to reduce the noise to a level where detection can be achieved).

$$N_{ij} = \delta_{ij} \frac{4(NE T^2)\Omega^2 N_h}{N_t} \frac{1}{N_{eq}^2} \quad (3.2)$$

Bolometer noise level

where:

i and j are bolometer array indices

N_{ij} is the noise on bolometers, indexed within the array by i and j

N_{eq} is the number of equivalent baselines

N_h is the number of feed horns

N_t is the number of time samples

Ω is the beam size

NET is the noise equivalent temperature of the bolometers (assumed = 200 μK/Hz^{1/2})

Detector: QUBIC was to utilise the broadband high sensitivity nature of bolometers (compared with more traditional narrowband lower sensitivity heterodyne detectors) in order to measure the spectral power density of visibility patterns. Bolometers have been used on previous telescopic missions, e.g. HFI on PLANCK (Holmes, et al., 2008), and can be made polarisation sensitive through the addition of a polarising grid, see for example (Yun, et al., 2004). Detection is made by means of incident radiation causing a heating effect. This heating alters the resistance of an appropriately biased bolometer, as shown in *Figure 3.16*, and is proportional to the power of the incident radiation. For QUBIC, bolometers require a short thermal time constant $\tau_t = C/G$ as they need to be able to process signals faster than the effects from the instrument or weather can significantly impact them (where *C* is the thermal capacitance and *G* is the thermal conductance, see *Figure 3.16*).

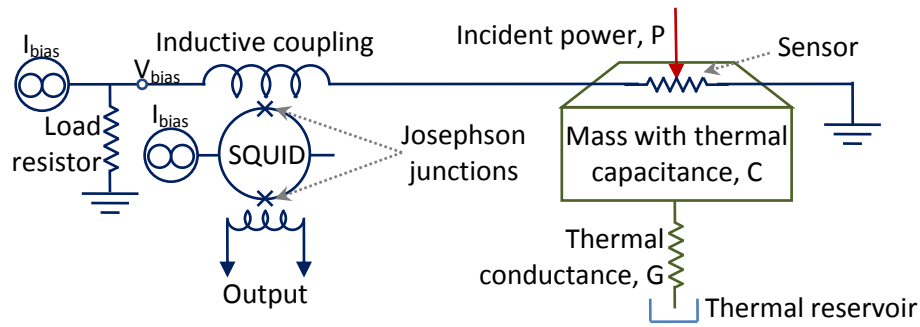


Figure 3.16: Bolometer schematic with inductive interface to a SQUID (super conducting quantum interference devices).

If the required integration time is too long for the detection of a signal the time averaging losses result in a washing out of the interference patterns which are being sought. The time constant for bolometers is short (of the order of 10 ms) and therefore they are ideal at minimising this effect. The extent and density of the detector array, and hence the number of bolometers that must be multiplexed, is dependent on the field of view and the telescope focal length (discussed next). The NbSi transition edge sensor (TES) bolometers proposed for QUBIC can be multiplexed together with an upper limit of 2500 possible in a single array.

In the case of QUBIC, a telecentric system with the objective at infinity, it is not sensible to talk in terms of the telescope magnification but rather in terms of plate scale, that is the mm/° relationship for the detector plane and the sky respectively. In this case the required observable angular extent on the sky is related to the required detector extent. Using the paraxial and small angle approximations, the image scale as a function of detector plane size relationship is given by Equation (3.3), the parameters are explained in Figure 3.17.

$$r = \theta f \quad (3.3)$$

Image scale relationship of sky angular extent and detector plane translational offset where:

- r is the radial offset of the detector plane
- f is the focal (effective) length of the telescope system
- Note: r and f can be any units, once they are the same
- θ is the angular offset on the sky, in radians

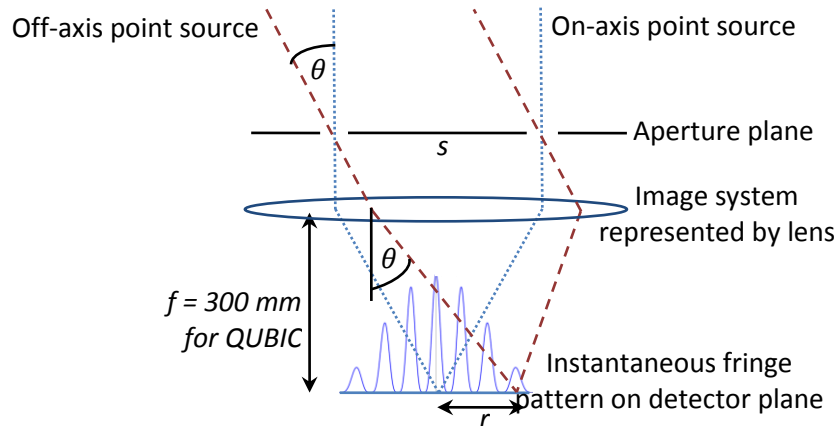


Figure 3.17: Shown here is an equivalent lens based combiner highlighting the induced geometric phase shift. Position of the peak of the first fringe on the detector plane occurs at some angular offset, θ , when the path difference is equal to the wavelength, λ , for a given baseline separation, s . Plate scale $r = \theta f$ gives the position on the detector plane for radiation incident at angle θ .

It follows that in order to detect a certain fringe spacing we have a related detector plane extent so, to calculate this, we take the shortest baseline (largest fringe size) and calculate the fringe separation at the detector plane giving us the spatial extent of the bolometer array required for the detection (at least one complete fringe must be measured).

We must also be sure to sample the fringes sufficiently (Nyquist sampling requires at least 2 detectors per fringe) and for this we take the longest baseline (smallest fringe size) and calculate the fringe separation at the detector plane to give us the density of bolometers required for the detection.

The first off-axis fringe occurs when the path length difference for radiation arriving at the detector plane from 2 points in the aperture (separated by a distance, s) is one wavelength, λ . From *Figure 3.17* this path difference is given by $s \sin \theta \approx s\theta$ for small θ , so for the first fringe we have $s\theta = \lambda$ or $\theta = \frac{1}{s_\lambda}$ (where $s_\lambda = \frac{s}{\lambda}$) and from *Equation (3.3)* this is focused to a position $r = \theta f = \frac{f}{s_\lambda}$. *Table 3-3* shows the requirements for various beam combiner focal lengths and the positions of the first fringe. The detector plane extent, shown in *Table 3-3*, was selected to capture

~95% of the incident power from CLOVERs 14° feed horn and the number of bolometers are shown for this capture level (Bennett, 2014, p. 47).

Table 3-3: Position of first fringe on the detector plane for various focal lengths and the number of bolometers required, assuming a square grid, in order to detect 95% of the incident power. Bolometers of 3×3 mm and 5×5 mm were considered and calculations are based on CLOVERs 14° feed horns.

f (mm)	Fringe location (mm) $S_{\lambda_{\max}} = 32$	Fringe location (mm) $S_{\lambda_{\min}} = 5$	Detector plane size (mm)	# of Bolometers (3 mm)	# of Bolometers (5 mm)
100	3.1	20	50	289	100
200	6.3	40	100	1156	400
300	9.4	60	150	2500	900
400	12.6	80	200	4356	1600

The bolometers are required to be, at most, half the size of the fringe spacing on the detector plane for the longest baseline, based on Nyquist sampling of at least two samples per fringe. Bolometers under consideration for the QUBIC telescope can be fabricated in sizes from 3 mm × 3 mm to 5 mm × 5 mm (Prêle, et al., 2009) therefore 100 mm focal length systems were immediately ruled out as the bolometers are too large. Focal lengths much larger than 300 mm were also ruled out because of the number of bolometers required.

At the meeting in July 2009 it was also decided that detection would be done using a bare array of the order of 900 TES bolometers amplified by SQUIDs (superconducting quantum interference devices) with a 100% fill factor capable of capturing 95% of the incident power with an NEP (noise equivalent power) $\approx 10^{-18}$ W/Hz^{1/2} and $\tau \approx 10$ ms. These would be cryogenically cooled in two stages: a primary stage consisting of a 4 K pulse tube cooler and a secondary stage 100 mK dilution unit for the detector plane. The total volume for the cryostat was to be $< 1 \text{ m}^3$ so it would fit in available laboratory space and the transport plane to Antarctica. The selection of the 900 element detector array led to the selection of the 5 mm bolometers and an effective focal length of 300 mm for the design.

Optical combiner: It is not possible to manufacture an optical combiner that will not introduce aberrations to some degree. On-axis systems minimise aberrations however if an on-axis system were to be chosen it would have to use lenses to avoid

the shadowing effects of mirrors (as illustrated by the MBI example earlier). QUBICs large 400-mm aperture window requires a large lens, not without precedence as QUaD (Ade, et al., 2008) and BICEP (Keating, et al., 2003) missions had large lenses although not as large as what would be required by QUBIC. At the proposed operational frequencies there are dominant diffraction effects which need to be considered which cannot be modelled using a ray tracing technique. The aforementioned missions also highlighted an unpredictable, suspected birefringent, behaviour of the polycarbonate and silicon lenses, which is difficult to model, hence a lens design was deemed unsuitable. Reflectors offer an alternative as they are well understood and can be modelled extremely accurately taking into account polarisation and diffraction effects, which are difficult to model for lenses. The baseline separations required for QUBIC are much smaller than those in MBI making an on-axis reflector design impossible as the shadowing from the secondary mirror would exclude central baselines. For this reason an off-axis reflector design was selected.

In practice imagers in general and off-axis imagers in particular introduce aberrations. These phase aberrations are known as third order Seidel aberrations: spherical, coma, astigmatism, curvature of field and distortion, some examples are shown in [Figure 3.18](#). The configuration of the combiner must be designed so as to ensure the aberrations are minimised and do not adversely affect the goals of the project. So far we have looked at aperture size and focal length but there are several other parameters that can be chosen in order to minimise aberrations.

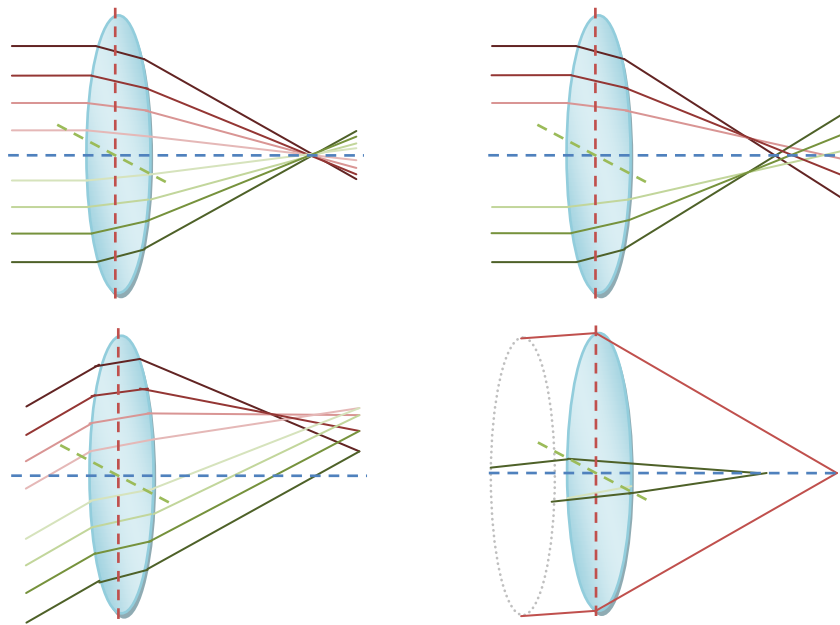


Figure 3.18: Top left is the ideal case where all parallel rays are focused to a single point. Top right, spherical aberrations, where parallel rays converge at different points along the optical axis and the distance to the point of convergence is proportional to the distance from the optical axis of the incident parallel rays. Bottom left, coma, where off-axis parallel rays converge at different points along the detector plane, the distance from the optical axis inversely proportional to the distance from the optical axis of the incident parallel rays. Bottom right, astigmatism, where the focal length along one axis is at a different distance than that of the orthogonal axis. Note: In all cases the colouring of the lines is for ease of visualisation only and not indicative of frequency or any other properties of the incident rays.

Two conditions, the Rusch and Mizuguchi-Dragone conditions, if met will allow the minimisation of spherical aberration, astigmatism, spillover and cross polarization. The parameters (ϕ, α, β) used in *Equations (3.4)* and *(3.5)* are graphically illustrated in *Figure 3.19*.

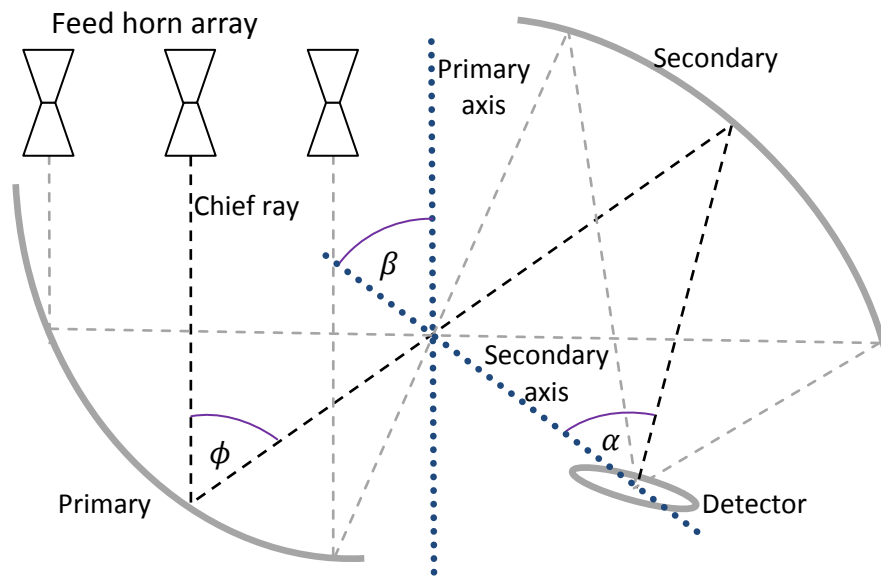


Figure 3.19: Mizuguchi-Dragone and Rusch condition parameters. ϕ is the angle of throw of the primary mirror. α is the angle between the chief ray and the secondary axis. β is the angle between the primary and secondary axis. The layout here is that of an off-axis Gregorian but these parameters are applicable to other off-axis designs.

It has been shown that any dual reflector system consisting of offset confocal conic sections has an equivalent paraboloid (Rusch, et al., 1990). The Rusch condition optimises the dual reflector system such that the line of sight of the off-axis equivalent paraboloid will be aligned with the centre of the sub-reflector, minimising spillover. The condition is given by,

$$\tan\left(\frac{\beta}{2}\right) = \frac{(e-1)^2}{(e+1)^2} \tan\left(\frac{\beta-\phi}{2}\right) \quad (3.4)$$

Rusch condition

where:

e is the eccentricity of the secondary mirror

β is the reflector axis tilt

ϕ is the primary mirror angle of throw

Altering the angle between the symmetry axes allows selection of an equivalent paraboloid that is rotationally symmetric (the equivalent paraboloid offset angle is zero) which will induce minimal spherical aberration, astigmatism and geometrical cross polarization. Such a design is referred to as conforming to the Mizuguchi-Dragone condition (Dragone, 1978; Mizuguchi, et al., 1978), given by,

$$\tan\left(\frac{\alpha}{2}\right) = \frac{e+1}{e-1} \tan\left(\frac{\beta}{2}\right) \quad (3.5)$$

Mizuguchi-Dragone condition

where:

e is the eccentricity of the secondary mirror
 α is the chief ray angle to secondary axis
 β is the reflector axis tilt

Systems that obey the Rusch and Mizuguchi-Dragone conditions are referred to as compensated dual reflectors. The parameters for QUBIC are shown in *Figure 3.20*, the eccentricity is given by $e = \frac{D_f}{D_v} = \frac{287.81}{799.99889} = 0.359763$, where D_f is the focal point separation and D_v is the vertex separation for the secondary mirror.

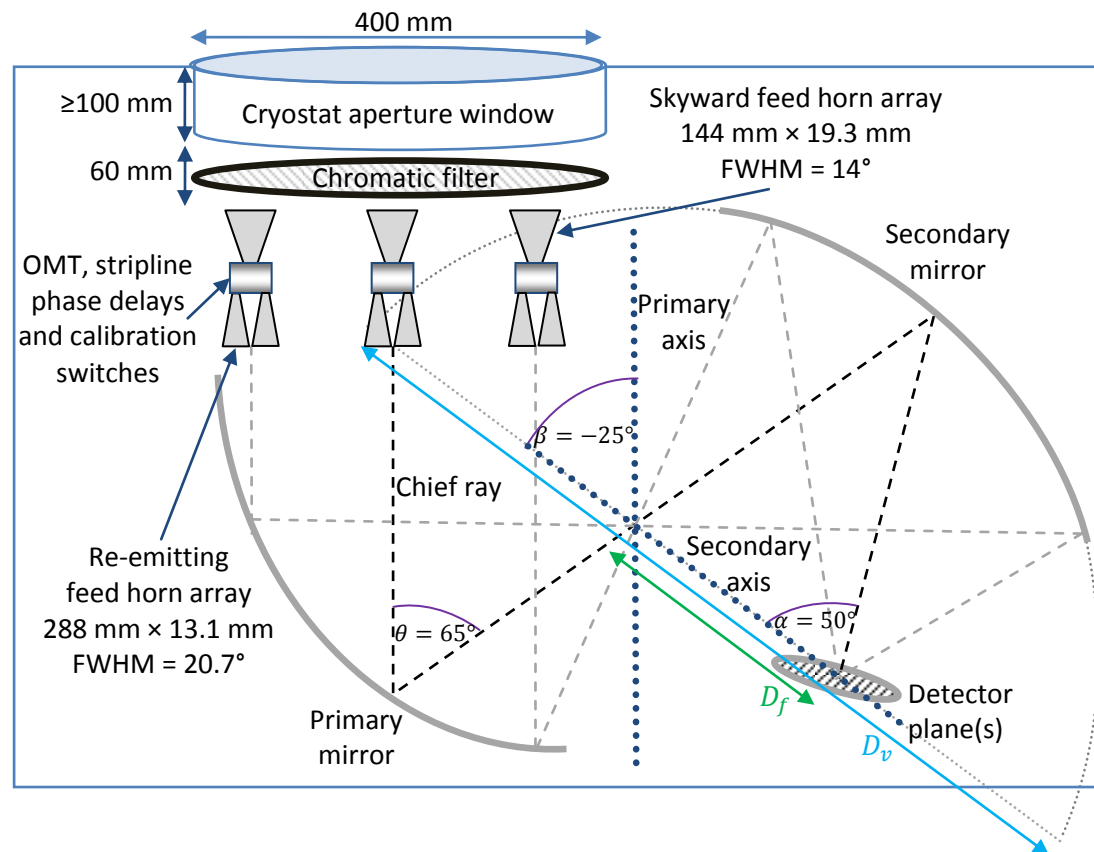


Figure 3.20: QUBIC v1.0. It is designed to operate with 6 modules, 2 at each of 90, 150 and 220 GHz. The feed horns will be operated single-moded with a 25% bandwidth.

In addition to phase aberrations mentioned above, which will modify the beam wavefront, there can be amplitude aberrations which distort the beam profile. For example a simple beam with a Hermite-Gaussian profile, defined by *Equation (3.7)*, diverges as it propagates, spreading out over the surface of the mirror. Ideally the

reflected beam has a Gaussian profile but different parts of the beam reflect off different parts of the mirror surface and so each part of the reflected beam experiences a different effective focal length, introducing an asymmetry. This causes power to be scattered into higher order modes causing the beam profile to be modified. The fraction of power scattered into higher modes is given in *Equation (3.6)* (Murphy, 1987).

$$E_r = E_0 + \underbrace{\frac{w \tan(\theta_i)}{2 \sqrt{2} f}}_{\text{Fraction of power scattered to higher orders}} \frac{\sqrt{3}E_3 + E_1}{2} \quad (3.6)$$

$$E_n = \sqrt{\frac{2}{\pi}} \sqrt{\frac{1}{2^n n!}} H_n \left(\sqrt{2} \frac{x}{w} \right) e^{-\left(\frac{x^2}{w^2}\right)} \quad (3.7)$$

Scattering of Gaussian modes to higher orders for beam reflected off a curved mirror where:

H_n is the Hermite mode of order n

E_n is the electric field component of a mode of order n

x is the radial distance from the centre of the beam

w is the beam radius at the surface of the mirror

θ_i is the incident angle

f is the effective focal length of the mirror

E₀ is the amplitude of the reflected field component, order 0 (Gaussian)

E₁ is the amplitude of the reflected field component, order 1

E₃ is the amplitude of the reflected field component, order 3

E_r is the amplitude of the reflected field

An example of this effect is shown in *Figure 3.21* where it can be seen that the peak intensity no longer aligns with the propagation axis. For QUBIC this aberration is also applicable to the different feed horns, reflecting off of various parts of the mirror surface.

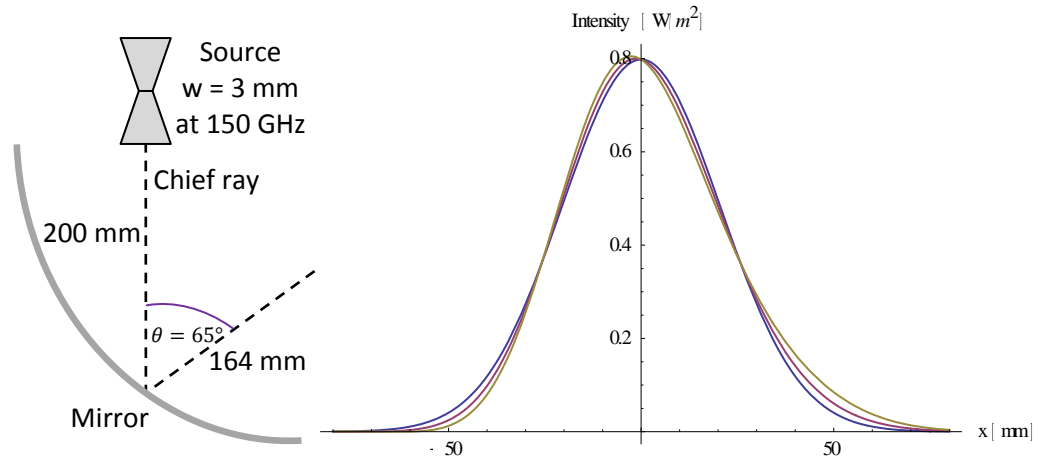


Figure 3.21: Left is shown the setup for a single source emitting a Gaussian beam with a waist radius of 3 mm at 150 GHz. The beam is propagated 200 mm to the reflector surface that has a focal length of 164 mm. It intersects the reflector surface at an incident angle of 32.5° with respect to the normal as seen by the chief ray. The beam is then propagated to the detector plane. Right is the 1D case for the source where the blue plot is the incident field and the purple the reflected field. The tan plot shows, for comparison, the effect of using the same setup but a reflector with an effective focal length of 82 mm.

Applying this to a dual mirror system, like QUBIC, taking into account the reflection off of the secondary mirror, the calculation of scattered power into the higher orders can be calculated from Equation (3.8). The ‘ \pm ’ indicates that the secondary mirror can add-to or compensate-for the scattering depending on its orientation with respect to the primary mirror. Therefore with correct configuration of the primary and secondary mirrors this aberration can be minimised (Murphy & Withington, 1996).

$$E_r = E_0 + \left(\underbrace{\frac{w_s \tan(\theta_{is})}{2\sqrt{2}f_s}}_{\text{Power fraction scattered to higher orders}} \pm \underbrace{\frac{w_p \tan(\theta_{ip})}{2\sqrt{2}f_p}}_{\text{Power fraction scattered to higher orders}} e^{-j\Delta_{12}} \right) \frac{\sqrt{3}E_3 + E_1}{2} \quad (3.8)$$

Scattering of Gaussian modes to higher orders for a beam reflected from 2 curved mirrors. The symbols used are the same as those of Equation (3.7) with the additional subscripts ‘p’ and ‘s’ referring to the primary and secondary mirrors. The additional Δ_{12} term relates to the change in the Gaussian beam phase slippage as it travels between the primary and secondary mirrors.

Bennett (Bennett, 2014) investigated a range of compensated dual reflector combiner designs for QUBIC. In the selection of the combiner there were several

front runners, the two main ones being the compensated Gregorian (CG) and general crossed Cassegrain (GCC). The relative performance of these designs for CMB astronomy applications has been described by Tran (Tran, et al., 2008). Crossed Cassegrain designs in particular have been shown to have a large diffraction-limited field-of-view. Following on from initial estimates, as discussed in §3.2.2, further testing at APC in 2009 found that the requirement for just 144 feed horns was too optimistic (original calculations had not considered effects such as bandwidth smearing). The combiner was not alone in its difficulties as, for example, the individual phase shifting of 100+ input channels was too cumbersome and non-linearities over the bandwidth too great. They concluded that in order to achieve the sensitivity comparable to that of an imager and meet the minimum requirements to measure a tensor-to-scalar ratio, $r = 0.01$, the input aperture array must be increased to a minimum of 20×20 feed horns. In order to fit the increased array into the effective window size the frequency was increased to 150 GHz. A 20×20 array of such feed horns requires an aperture size of $300 \text{ mm} \times 300 \text{ mm}$. The required increase in aperture array size ruled out all but one combiner design and the compensated off-axis Gregorian was duly selected. It was the only design which could physically meet all the requirements for the QUBIC project and is shown in *Figure 3.20*. A combiner with 300 mm focal length, the longest possible that will fit in a cryostat with internal dimensions of $0.9 \text{ m} \times 0.9 \text{ m} \times 0.6 \text{ m}$, was chosen and this in turn led to the selection of the 3 mm bolometers. In the summer of 2010, considering the engineering difficulties faced by various groups, the requirements of QUBIC were re-examined and the design was revised to what was termed version 2.0.

3.2.3 QUBIC design v2.0

After several revision meetings a new design was devised in spring of 2010 (Charlassier, et al., 2010b). There was a change in the philosophy, QUBIC was no longer to measure visibilities directly but now would take a synthetic image of the sky (sum all baseline fringe patterns). The proposed new design is shown in *Figure 3.22* and here the revised operation of the QUBIC instrument is explored.

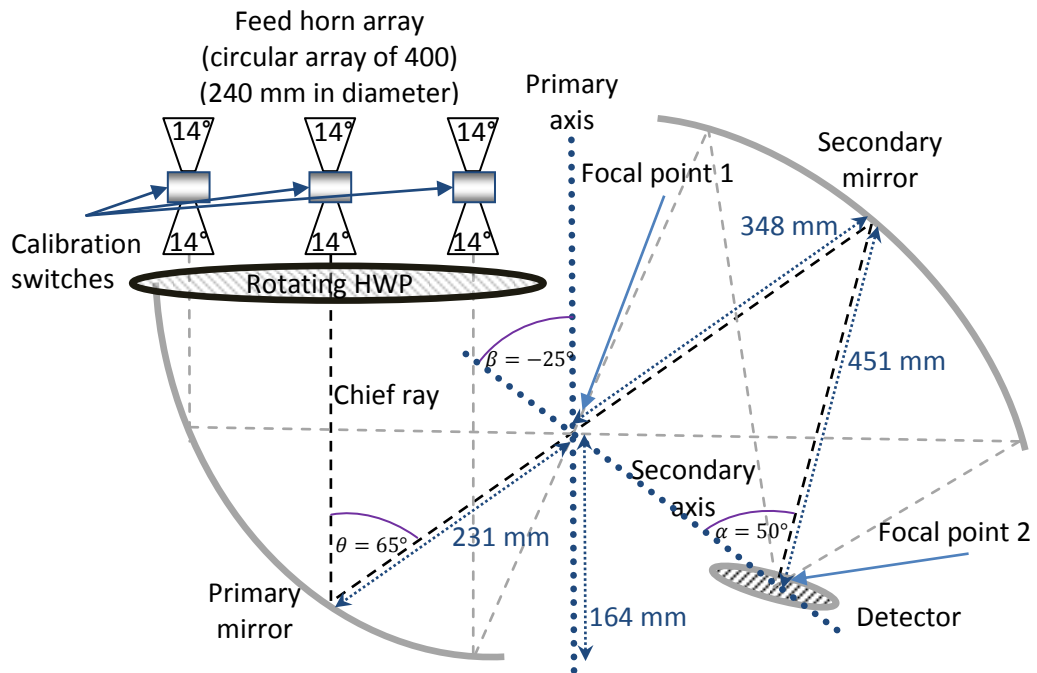


Figure 3.22: QUBIC v2.0

The synthetic image is the sum of all feed horn outputs and this image of the sky will offer the advantage of measuring all baselines simultaneously. A polarising grid prior to the bolometer array, the details of which will be discussed in §4.3, provides the means to discriminate between the orthogonal polarisation components of the sky signal. A rotating half wave plate (RHWP), now placed after the feed horns (Battistelli, et al., 2010), is used to modulate the sky signal. The combination of the RHWP and the polariser replaces the need for phase delays and OMTs to modulate and separate the incoming signal and consequently removes the requirement for a dual array of secondary horns. The RHWP also offers a way to separate combiner induced aberrations as the modulation will not be present on artefacts introduced after the RHWP in the instrument. At the time of writing the exact details of these components are not finalised. The RHWP rotates the polarisation by twice the angle between the optical axis of the half-wave plate and the incident field's polarisation. Combining with the spin-2 nature of polarisation the modulation of the incident field induces an oscillation at a rate of 4 times the rotation frequency of the plate. The power measured by a bolometer at position, **b**, within the detector plane array is given by *Equations (3.9) and (3.10)*.

$$R_x(\mathbf{b}, t) = S_I(\mathbf{b}) + \cos(4\omega t) S_Q(\mathbf{b}) + \sin(4\omega t) S_U(\mathbf{b}) \quad (3.9)$$

$$R_y(\mathbf{b}, t) = S_I(\mathbf{b}) - \cos(4\omega t) S_Q(\mathbf{b}) - \sin(4\omega t) S_U(\mathbf{b}) \quad (3.10)$$

Field component oscillation due to RWHP (Charlassier, et al., 2010b)

where:

R_x is the power in the x direction

R_y is the power in the y direction

***b** is the position of a bolometer within the detector plane array*

ω is the angular rotation frequency of the half-wave plate

t is time

I, Q and U are Stokes parameters and S_I, S_Q and S_U are the corresponding detector plane images

QUBIC measures a synthetic image (of the sky). The synthetic image (<100% aperture fill factor) is a combination of Stokes parameters (*I*, *Q* and *U*) convolved with the instrument synthesised beam. From *Equations (3.9) and (3.10)* we see that the *x* and *y* components are modulated in different ways. Their differing modulation allows for the recovery of Stokes parameters (Charlassier, et al., 2010b). QUBIC v2.0 will use a novel approach to obtain the power spectrum without the need for obtaining Stokes parameters first. The synthetic image can be written as $S_x(\mathbf{b}, \mathbf{n}_0) = \int X(\mathbf{n}) \underbrace{B(\mathbf{n} - \mathbf{n}_0)^2 |A_s(\mathbf{b} - \mathbf{n} - \mathbf{n}_0)|^2}_{\text{Synthesised beam}} d\mathbf{n}$, where $X = \{I, Q, U\}$ is a

Stoke's component of the sky signal, *B* is the feed horn beam, *A_s* is the array point spread function (PSF), **n** is the direction of incident signal with **n**₀ the pointing direction of the telescope, and **b** is the bolometer location on the detector plane. Expanding the sky signal in terms of spherical harmonics $X(\mathbf{n}) = \sum a_{lm} Y_{lm}^*(\mathbf{n})$ and grouping the feed horn beam and array PSF, $\beta(\mathbf{b}, \mathbf{n}, \mathbf{n}_0) = B(\mathbf{b} - \mathbf{n}_0)^2 |A_s(\mathbf{b} - \mathbf{n} - \mathbf{n}_0)|^2$ we obtain $S_x(\mathbf{b}, \mathbf{n}_0) = \int \sum a_{lm} Y_{lm}^*(\mathbf{n}) \beta(\mathbf{b}, \mathbf{n}, \mathbf{n}_0) d\mathbf{n}$. Grouping *Y_{lm}* and β we obtain the response of the combiner for each harmonic $S_x(\mathbf{b}, \mathbf{n}_0) = \sum a_{lm} \beta_{lm}(\mathbf{b}, \mathbf{n}_0)$. Taking the covariance of *S* we obtain the so-called window function

$$\langle S_X(\mathbf{b}, \mathbf{n}_0) \cdot S_X'^*(\mathbf{b}', \mathbf{n}_0') \rangle = \sum_{lm} \sum_{l'm'} \langle a_{lm} a_{l'm'}^* \beta_{lm}(\mathbf{b}, \mathbf{n}_0) \beta_{l'm'}^*(\mathbf{b}', \mathbf{n}_0') \rangle = \sum_l C_l W_l(\mathbf{b}, \mathbf{n}_0, \mathbf{b}', \mathbf{n}_0')$$

where $\langle a_{lm} a_{l'm'}^* \rangle = C_l$ (as the CMB is isotropic) giving us the relationship $W_l(\mathbf{b}, \mathbf{n}_0, \mathbf{b}', \mathbf{n}_0') = \sum_m \beta_{lm}(\mathbf{b}, \mathbf{n}_0) \beta_{l'm'}^*(\mathbf{b}', \mathbf{n}_0')$. Essentially the synthesised beam is the optical system's PSF and is directly related to the baselines

of the combiner and the window function gives the instrument's weighted response in the uv -plane, which for 400 feed horns is shown in *Figure 3.23*.

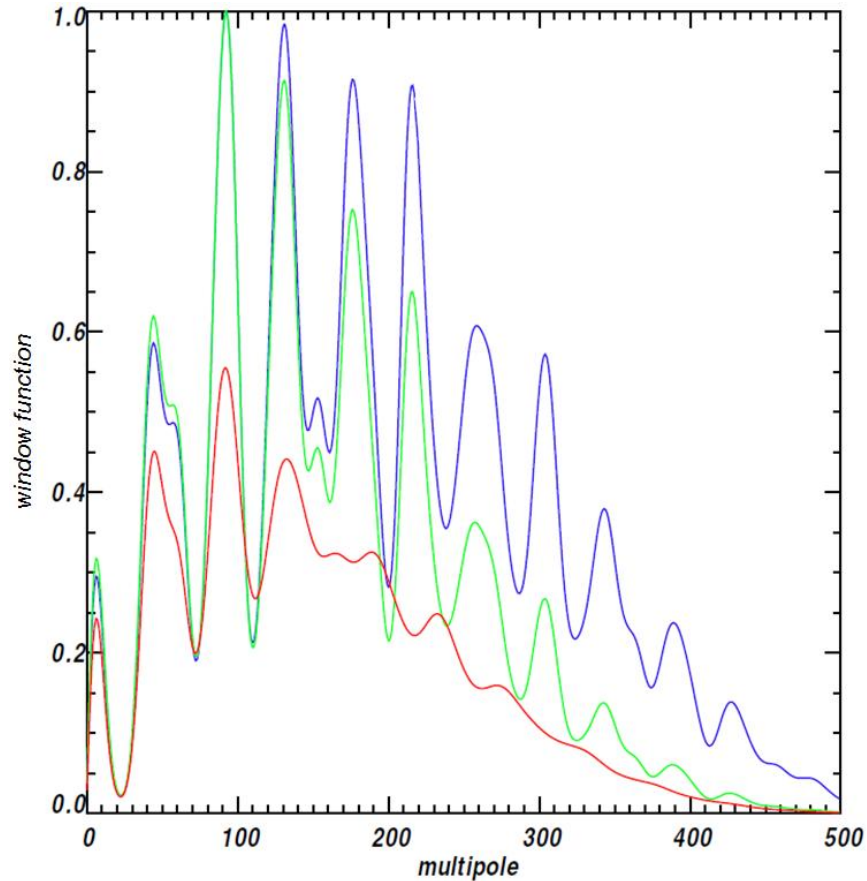


Figure 3.23: Window-function of an instrument with 400 primary feed horns. In blue the window function is shown for a monochromatic instrument with point detectors, green for a monochromatic instrument with 3 mm diameter detectors and red for an instrument with 25% bandwidth and 3 mm detectors. (Bigot-Sazy, 2013)

The window function in QUBIC will be discussed further in Chapter 5. Subsequent collaboration meetings lead to further revisions streamlining the QUBIC design. The addition of a polariser, tilted with respect to the detector plane, allows for the addition of a second detector plane, each detector plane receiving one polarisation component. The exact position, size and orientation of the polariser will need to be investigated and will be further analysed in Chapter 4.

The polarization patterns in the CMB are now simply the combination of the images from the detector planes as the power measured by each bolometer is a combination of Stokes I , Q and U parameters. Conversion to E- and B- modes and

subsequent reconstruction of the TT, TE, EE, BB power spectra can be done using standard techniques as described by Zaldarriaga and Hamilton (Zaldarriaga, 2001; Hamilton, et al., 2008).

3.3 QUBIC v2.0 details of mirror design

3.3.1 Definition of global reference frame

A global reference frame (GRF) was defined to aid the integration of contributions from each member of the consortium into the overall instrument. The global reference frame origin was selected as the centre of the source array aperture plane with the z-origin at the downward emitting aperture of the 150 GHz feed horns as shown in *Figure 3.24*. The position of the primary mirror is defined with respect to the waist of the 150 GHz beam from the feed horn. The vertex of the primary mirror is placed at a distance of 0.46676 m from the waist plane. The waist itself is located within the feed horn, a distance Δz back from the aperture plane (the exact distance is dependent on the final design of the feed horn). The GRF is defined with respect to the feed horn aperture plane and the quantity Δz which separates the aperture and the waist will need to be calculated in order to exactly position the combiner with respect to the GRF. The GRF z-axis is positive towards the sky as shown in *Figure 3.24* and for consistency all elements within the instrument will be defined with respect to the GRF.

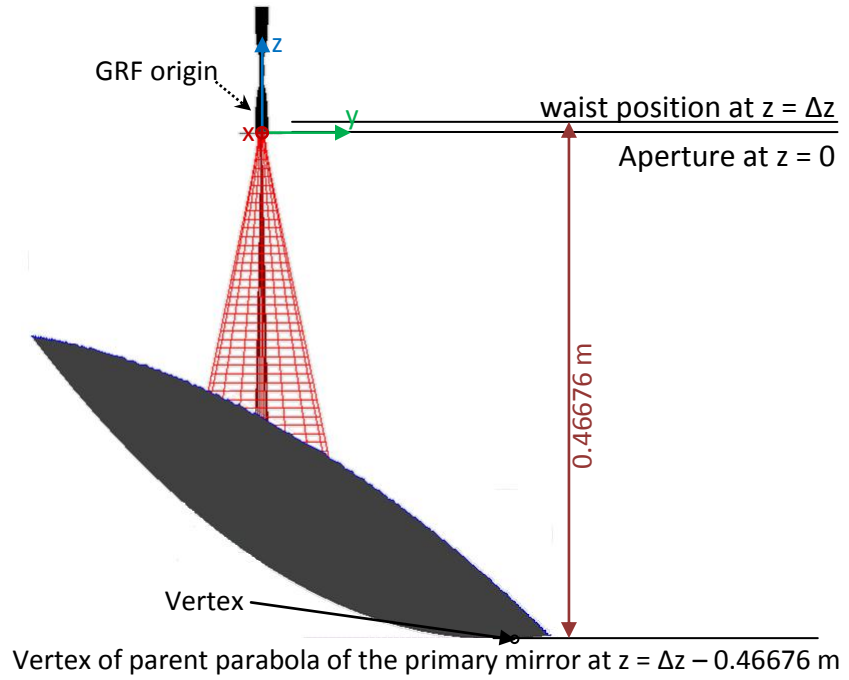


Figure 3.24: Primary mirror shown with vertex coordinates with respect to the GRF.

All element surfaces are expressed as quadratic equations (with all units in meters). As well as the GRF each element has a local reference frame with translations with respect to the GRF and rotations about the translated origin but axis orientations taken as those of the GRF. Each element may then also have additional translations and rotations with respect to the local reference frame (LRF). All rotations are expressed in terms of Euler $ZY'Z''$ rotations taken about the z -axis, then the new y -axis (y') then the new z -axis (z''). Euler rotation equations are defined as:

$$\begin{pmatrix} \cos(\theta_y) & 0 & \sin(\theta_y) & 0 \\ 0 & 1 & 0 & 0 \\ -\sin(\theta_y) & 0 & \cos(\theta_y) & 0 \\ 0 & 0 & 0 & 1 \end{pmatrix} \begin{pmatrix} \cos(\theta_z) & -\sin(\theta_z) & 0 & 0 \\ \sin(\theta_z) & \cos(\theta_z) & 0 & 0 \\ 0 & 0 & 1 & 0 \\ 0 & 0 & 0 & 1 \end{pmatrix} \quad (3.11)$$

Euler rotation about Y axis

Euler rotation about Z axis

$$\begin{pmatrix} \cos(\theta_y)\cos(\theta_z)\cos(\theta_{z'}) - \sin(\theta_z)\sin(\theta_{z'}) & -\cos(\theta_y)\cos(\theta_{z'})\sin(\theta_z) - \cos(\theta_z)\sin(\theta_{z'}) & \cos(\theta_z)\sin(\theta_y) & 0 \\ \cos(\theta_{z'})\sin(\theta_z) + \cos(\theta_y)\cos(\theta_z)\sin(\theta_{z'}) & \cos(\theta_z)\cos(\theta_{z'}) - \cos(\theta_y)\sin(\theta_z)\sin(\theta_{z'}) & \sin(\theta_y)\sin(\theta_{z'}) & 0 \\ -\cos(\theta_z)\sin(\theta_y) & \sin(\theta_y)\sin(\theta_z) & \cos(\theta_y) & 0 \\ 0 & 0 & 0 & 1 \end{pmatrix} \quad (3.12)$$

Euler $ZY'Z''$ rotation

The inverse of this operation, to allow for extraction of rotation angles, θ_z , θ_y and $\theta_{z'}$, from a given Euler matrix, and can be calculated from Equation (3.13).

$$\theta_z = \tan^{-1}[-M_{13}, M_{23}] = \tan^{-1}\left(\frac{\sin(\theta_y) \sin(\theta_z)}{\cos(\theta_z) \sin(\theta_y)}\right)$$

$$\theta_y = \cos^{-1}[M_{33}] = \cos^{-1}(\cos(\theta_y)) \quad (3.13)$$

$$\theta_{z'} = \tan^{-1}[M_{31}, M_{32}] = \tan^{-1}\left(\frac{\sin(\theta_y) \sin(\theta_{z'})}{\cos(\theta_{z'}) \sin(\theta_y)}\right)$$

Inverse Euler ZY'Z'' rotation

where

*M_{cr} refers to a matrix element of the EULER ZY'Z'' rotation matrix defined above
r is the row and c the column index*

3.3.2 Definition of primary mirror

The initial design of the primary mirror was a section of a parabola of focal length 164.484 mm as shown in *Figure 3.25* and *Table 3.4*. The rim, parallel to the directrix, was offset from the vertex along the y-axis by 0.190 m. The resultant parabolic surface has an equivalent focal length of 0.231 m as shown in *Figure 3.25*.

Table 3.4: Original system setup. All translations are given with respect to the global axis origin as defined in Figure 3.24. Rotations are centred about the local reference frame origin with the GRF for orientation of the axis. Bounding volume dimensions are given with respect to the local reference frame.

Parameters	Definition of local reference frame with respect to GRF						Definition of bounding rim with respect to LRF		
	Translation (m)			Rotation (°)			Bounding volume dimension (m)		
	X	Y	Z	X	Y	Z	X	Y	Z
Centre of input array	0	0	0	0	0	0	-	-	-
Primary mirror vertex	0.190	0	-0.46676	0	0	0	0.480	0.600	∞

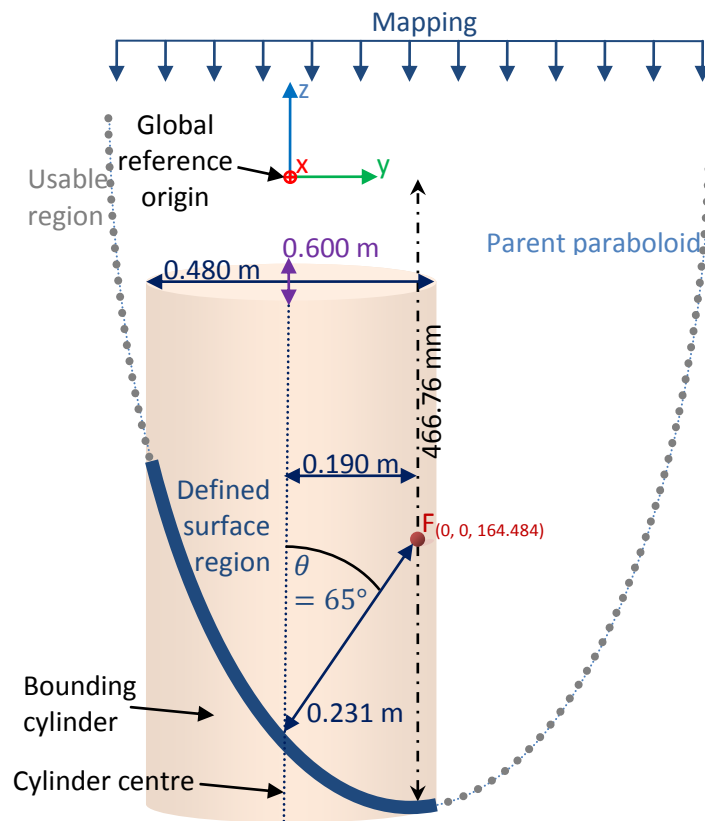


Figure 3.25: QUBIC primary mirror paraboloid. The usable section is that which is seen from $+\infty$ towards the origin along the z-axis, in this case the usable and complete parent paraboloid are one and the same. The surface is a section of the useable region, determined by the extent of the rim definition.

Using ZEMAX, optimisation of this primary surface was carried out (Bennett, 2014). Here, Zemax was used to improve the initial performance of the system (reduce aberrations) by modifying the surface. The optimization proceeds by altering surface parameters until a system that produces the lowest obtainable RMS spot size at the detector plane has been found. This resulted in a quadratic surface given by Equation (3.14) with parameters as per Table 3-5 (the surface is very close to parabolic). The implementation of the quadratic equations is not the same in MODAL and GRASP and care should be taken in the sign usage in the parameters when switching between GRASP with Equation (3.15) and MODAL with Equation (3.14).

Table 3-5: QUBIC instrument primary mirror quadratic parameters, all parameters in both MODAL and GRASP are with respect to the LRF.

Parameter	MODAL (m)	GRASP (m)
A_1	-2.77×10^{-3}	-2.77×10^{-3}
A_2	-2.77×10^{-3}	-2.77×10^{-3}
A_3	-7.15×10^{-5}	7.15×10^{-5}
A_4	0	0
A_5	0	0
A_6	0	0
A_7	0	0
A_8	0	0
A_9	1.84×10^{-3}	1.84×10^{-3}
c	-1.00×10^{-6}	-1.00×10^{-6}

$$A_1x^2 + A_2y^2 + A_3z^2 + A_4xy + A_5xz + A_6yz + A_7x + A_8y + A_9z + c = 0 \quad (3.14)$$

MODAL Equation Reference: MODAL Source Code

$$A_1x^2 + A_2y^2 + A_4xy + A_7x + A_8y + c = A_3z^2 + A_5xz + A_6yz + A_9z \quad (3.15)$$

GRASP Equation Reference: GRASP Technical Manual → Antenna System Definition → Mirrors → Reflectors → Reflector Surfaces → Surface expressed as a 2nd order polynomial

The axis colours (used in the respective visualisations) and directions for MODAL and GRASP are shown in *Figure 3.26*. A surface in GRASP is defined using the largest root and in MODAL the smallest root, yielding a rotation in this case of 180° about the x-axis. This is applicable only to surface definitions and not the axis orientations.



Figure 3.26: MODAL vs. GRASP axis visualisation colour scheme.

3.3.3 Definition of secondary mirror

The secondary mirror is defined as a rotated elliptical mirror as in *Figure 3.27*, with a focal point separation of 287.81 mm and vertex separation of 799.99889 mm. These values can be directly used by GRASP. MODAL requires the definition in terms of spacial coordinates for the 2 foci and a point on the surface. In this case, for convenience and in keeping with the method defined in GRASP's reference manual (TICRA, 2011, p. 112), the primary/secondary mirror common focal point F_1 was selected as being the LRF origin and F_2 to be on the local positive z-axis, prior to the 67.35° rotation, as shown in *Figure 3.27*. The location of the vertex is then at $x = y = 0$ and $z = -\frac{\text{Vertex-Focal separation}}{2} = -\frac{0.79999-0.28781}{2} = -0.25609$ m. The secondary mirror reference frame is a 205° rotation about the y-axis with respect to the global reference frame. The rotation is taken as positive in moving the z-axis about the y-axis towards the negative x-axis. The total 205° rotation is made up of 2 parts. Part 1 is a 67.35° rotation which is the angle between the ellipsoid surface axis and the axis of the bounding volume. From here the usable part of the surface is defined by the bounding volume projected along the unrotated z-axis from +z-infinity towards the origin onto the 67.35° rotated ellipsoid as shown in *Figure 3.27*. Part 2 takes the combined surface and bounding volume as a whole and rotates it a further 137.65° . Part 1 of the rotation of the ellipsoid surface definition is shown in isolation in *Figure 3.27* and the total rotation combination in *Figure 3.28*. Both rotations are about F_1 . As presented in §2.2.3 the equivalent focal length of the secondary mirror is given by $\frac{1}{f} = \frac{1}{d_i} + \frac{1}{d_o} = \frac{1}{0.348} + \frac{1}{0.451} = \frac{1}{0.196}$. The effective focal length of the instrument is to be 0.300 m. As described the primary mirror is close to a paraboloid with circular projected aperture with a focal length of 0.164 m and for the chief ray, an angle of throw of 65° with an effective focal length of 0.231 m. The secondary, an ellipsoid, has a vertex separation of $D_v = 0.79999889$ m and a focal separation of $D_f = 0.28781$ m giving an eccentricity of $e = \frac{D_f}{D_v} = \frac{0.28781}{0.79999889} = 0.359763$. The magnification factor can be calculated using *Equation (3.16)* with parameters as defined in *Table 2-3* and the effective focal length of the telescope obtained using *Equation (3.17)*,

$$m = \frac{d_i}{d_o} = \frac{451}{348} = 1.30 \tag{3.16}$$

Secondary mirror magnification factor

where:

d_o is the chief ray object incident distance from focal point 1 to the secondary mirror
 d_i is the chief ray image distance from the secondary mirror to focal point 2

$$f_{effective} = f_p \times m = 0.231 \times 1.30 = 0.299 \text{ m} \tag{3.17}$$

Dual reflector system equivalent focal length

where:

f_p is the effective focal length of the primary mirror

In quadratic form the equation for the secondary mirror is given in Equation (3.18) and all values are in meters with respect to the secondary's local reference frame.

$$x^2 + 1.1239y^2 + 1.1023z^2 + 0.1034xz + 0.25987x - 0.1085z = 0.1363 \tag{3.18}$$

MODAL Equation for the secondary mirror in quadratic form

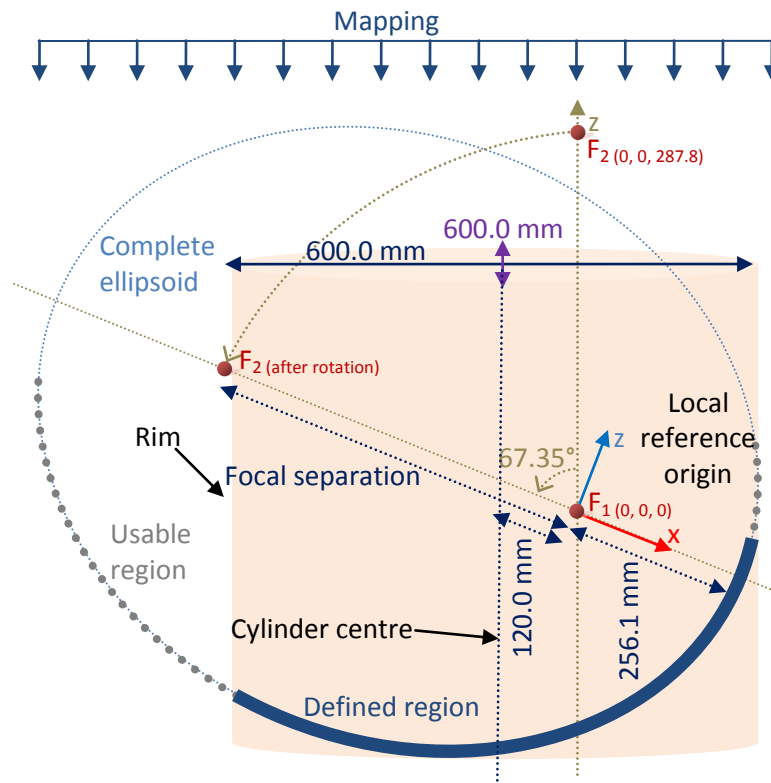


Figure 3.27: QUBIC ellipsoid, 67.35° rotation of surface in relation to rim. Usable section is that which is seen from +infinity towards the origin along the original z-axis. The surface is a section of the useable region, determined by the extent of the rim definition.

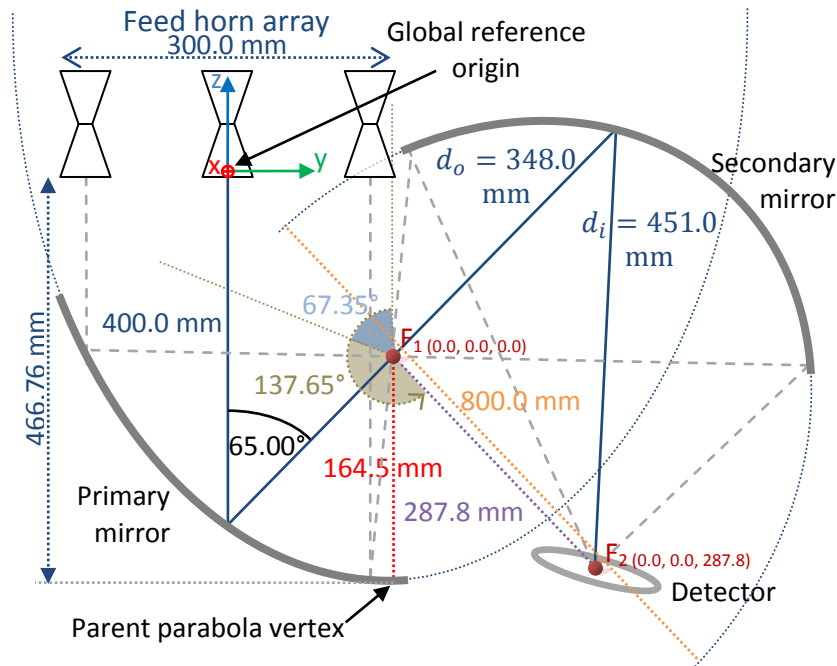


Figure 3.28: QUBIC (not to scale) schematic showing the parameters of the main components of the optical combiner.

3.3.4 Definition of input feed horn array

The feed horn array was reshaped, primarily due to cryostat aperture window manufacturing requirements but still incorporating 400 back-to-back feed horns. The input feed horns are now in a circular array of 22 horns in diameter. The internal diameter of each horn is 12.3 mm and their centre-to-centre spacing is 13.7 mm. The observed multipoles were recalculated from the baseline range of $6.85 \leq s_\lambda \leq 32$ giving $43 \leq l \leq 200$. Feed horns are referred to by their index where $xNNyMM$ is a horn with offset in the x direction (offsets are calculated with respect to the centre of the array) given by index NN and in the y direction by MM . The array position indices are tabulated against the mm offset positions in [Table 3-6](#). The total diameter is given by $\frac{12.3}{2} + (13.7 \times 21) + \frac{12.3}{2} = 300$ mm as shown in [Figure 3.29](#).

Table 3-6: QUBIC feed array offset positions with respect to GRF versus index (an index for the x- and y- direction is specified for each horn)

Offset (mm)	Index	Offset (mm)	Index
143.85	21	-143.85	00
130.15	20	-130.15	01
116.45	19	-116.45	02
102.75	18	-102.75	03
89.05	17	-89.05	04
75.35	16	-75.35	05
61.65	15	-61.65	06
47.95	14	-47.95	07
34.25	13	-34.25	08
20.55	12	-20.55	09
6.85	11	-6.85	10

The feed horns emit a 14° FWHM beam (equivalent to a 3.074 mm waist Gaussian, see Table 3-8) at an operating frequency of 150 GHz with a 25% bandwidth.

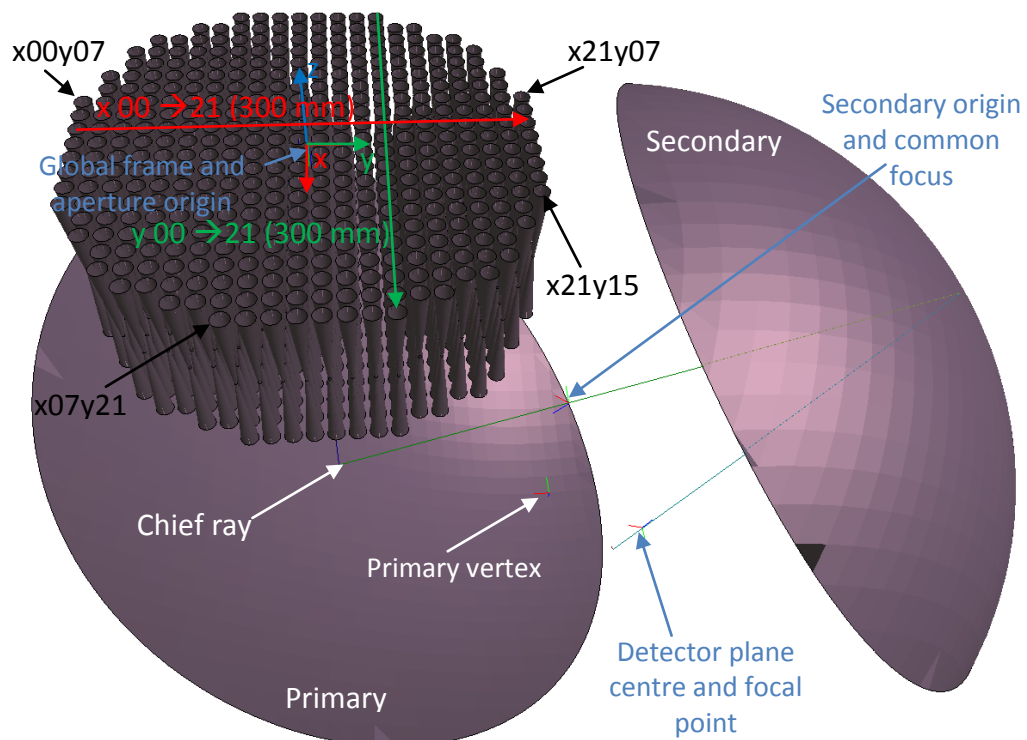


Figure 3.29: QUBIC feed horn array. Array shows the indexing values used for reference in this chapter, with 4 examples highlighted in red. All 400 back-to-back feed horns are shown here with the chief ray for a single feed horn in the centre propagating through the QUBIC instrument.

3.4 Preliminary QUBIC modelling

3.4.1 Gaussian beam mode analysis

At this stage the QUBIC design calls for the use of 14° FWHM back-to-back feed horns but this has varied from $\sim 12^\circ$ to $\sim 15^\circ$ since its inception. The divergence of the beams used determines the detector plane size required for a given percentage of power to be captured. As other feed horns may be considered in the future the impact of a changing the beam waist radius is important. Such a GBM analysis of the QUBIC system was carried out in §2.2.3. This is extended here to find a suitable size for the detector plane. The equivalent on-axis lens system was configured, as shown in *Figure 3.30*, with parameters as detailed in *Table 3-7*. Here we consider a simplified on-axis system with the emission from a centrally positioned feed horn (approximated by a Gaussian beam).

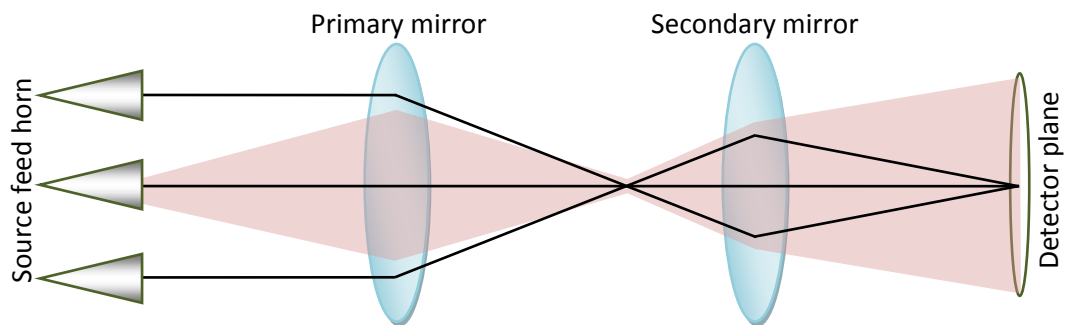


Figure 3.30: QUBIC equivalent lens system.

Table 3-7: QUBIC system parameters (Table 2-3 reproduced here for convenience)

Parameter	Value	Unit
Distance from source to primary mirror	0.400	m
Primary mirror focal length	0.231	m
Distance from primary mirror to secondary mirror	0.579	m
Secondary mirror focal length	0.196	m
Distance from secondary mirror to image plane	0.451	m

The piecewise ABCD function previously defined in *Equation (2.103)* and *Equations (2.98) to (2.100)* was used to calculate the beam's phase radius of curvature and beam radius at each point of the optical system. The waist radius of the beam at the feed horn was varied to produce a beam divergence that ranged from 10° to 15° in

1° steps and calculated using Equation (3.19). The waist radius values used are tabulated in Table 3-8.

$$w_0 = \sqrt{2 \ln(2)} \frac{\lambda}{\pi \theta} \tag{3.19}$$

waist (w_0) as a function of farfield divergence angle (θ) for a Gaussian beam

where:

λ is the wavelength

w_0 is the waist of the Gaussian beam

θ is the farfield divergence angle of the beam (FWHM of intensity)

Table 3-8: Calculation of beam waist versus divergence angle

Waist radius (mm)	Farfield divergence (°)
2.870	15
3.074	14
3.311	13
3.587	12
3.912	11
4.304	10

Using the values for w_0 from Table 3-8 the phase radius of curvature and beam radius as a function of propagation distance were plotted as the beam traverses the instrument as shown in Figure 3.31 and Figure 3.32 below.

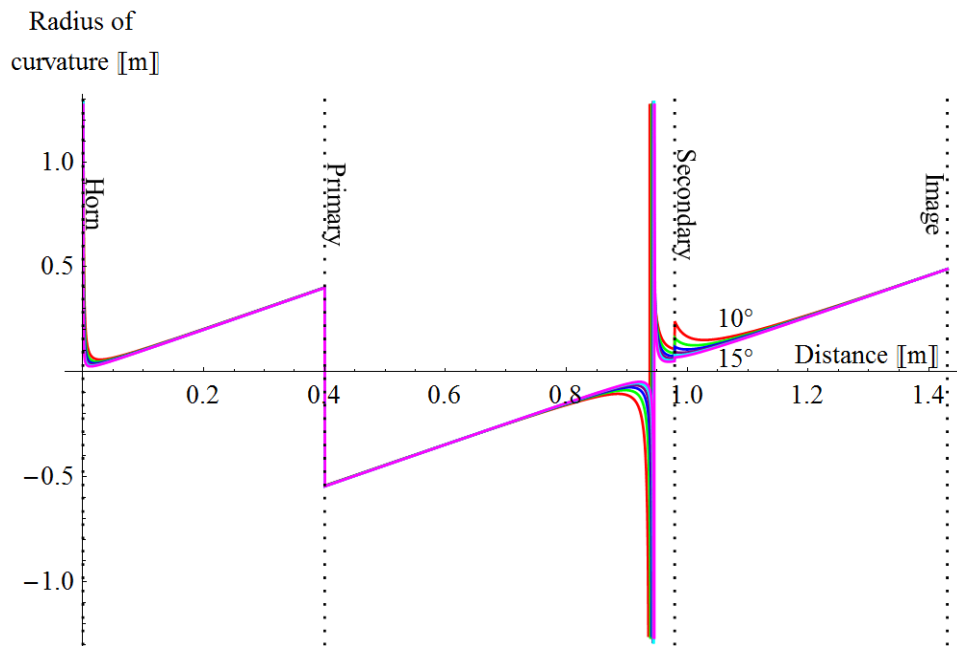


Figure 3.31: QUBIC phase radius of curvature as the beam propagates through QUBIC, for beams with starting waists that are equivalent to FWHM in the range from 10° to 15°.

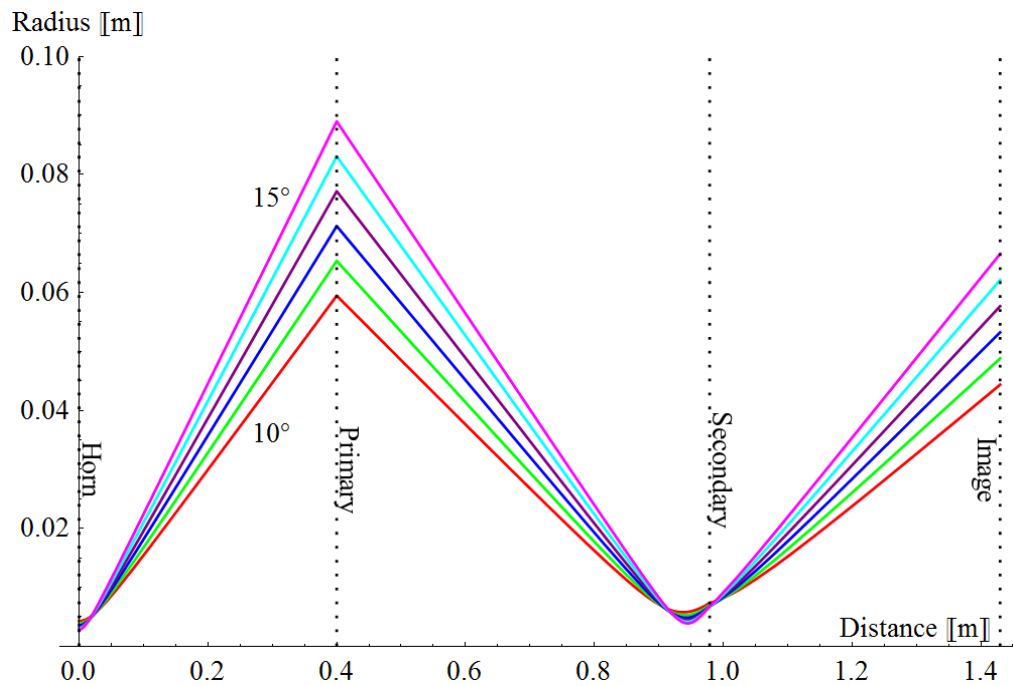


Figure 3.32: QUBIC beam width as the beam propagates through QUBIC, for beams with starting waists that are equivalent to FWHM in the range from 10° to 15°.

From *Figure 3.32* the expected size of the beam at the detector plane varies significantly with the starting waist size. The expected power captured by a circular detector plane of radius, r , can be calculated from *Equation (2.104)* and is tabulated in *Table 3-9*. Assuming a circular detector plane detection grid and taking 2 example sizes: a radius of 51 mm and 60 mm, we tabulate the expected power captured by the detector plane as shown in *Table 3-9*.

Table 3-9: Calculation of beam source waist versus detector plane size and captured power.

For field with FWHM (°)	Source waist radius (mm)	Beam radius at detector plane (mm)	51 mm power captured (%)	60 mm power captured (%)
15	2.870	66.4	69.2	80.5
14	3.074	62.0	74.2 ⁴	84.7
13	3.311	57.5	79.2	88.6
12	3.587	53.1	84.1	92.2
11	3.912	48.7	88.8	95.1
10	4.304	44.2	92.9	97.5

⁴ 74.2% power will be captured by an idealised Gaussian beam of radius 62 mm on a detector of radius 51 mm in an idealised combiner. For simplicity 0.8w (or 72%) is quoted instead of 0.8225w throughout the thesis as an approximation of expected upper limit on power captured.

3.4.2 PO analysis

To extend the findings in the ABCD analysis of the system we need to account for aberrations and to this end the combiner was simulated in both GRASP and MODAL using PO. The schematic in *Figure 3.33* (GRASP) shows the system with and without the chief ray from each feed horn. In addition MODAL, *Figure 3.34*, is able to display the extent of the divergent beams, shown here out to $1w$, giving visual insight into any spillover in the design.

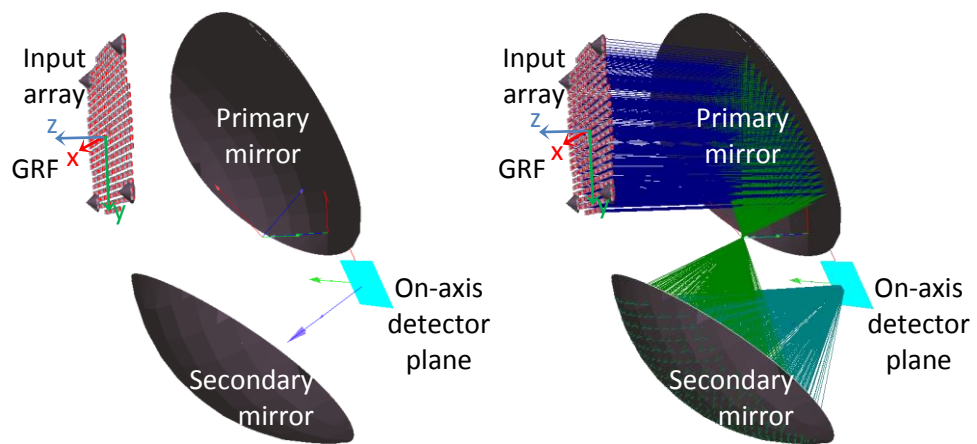


Figure 3.33: QUBIC Schematic (GRASP without rays left and with rays right). This is a GO illustration showing only the chief ray for each of the 400 feed horns.

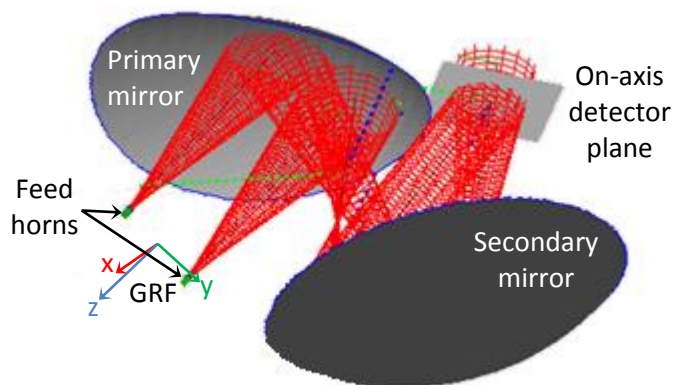


Figure 3.34: QUBIC schematic (MODAL) showing the beams from 2 feed horns.

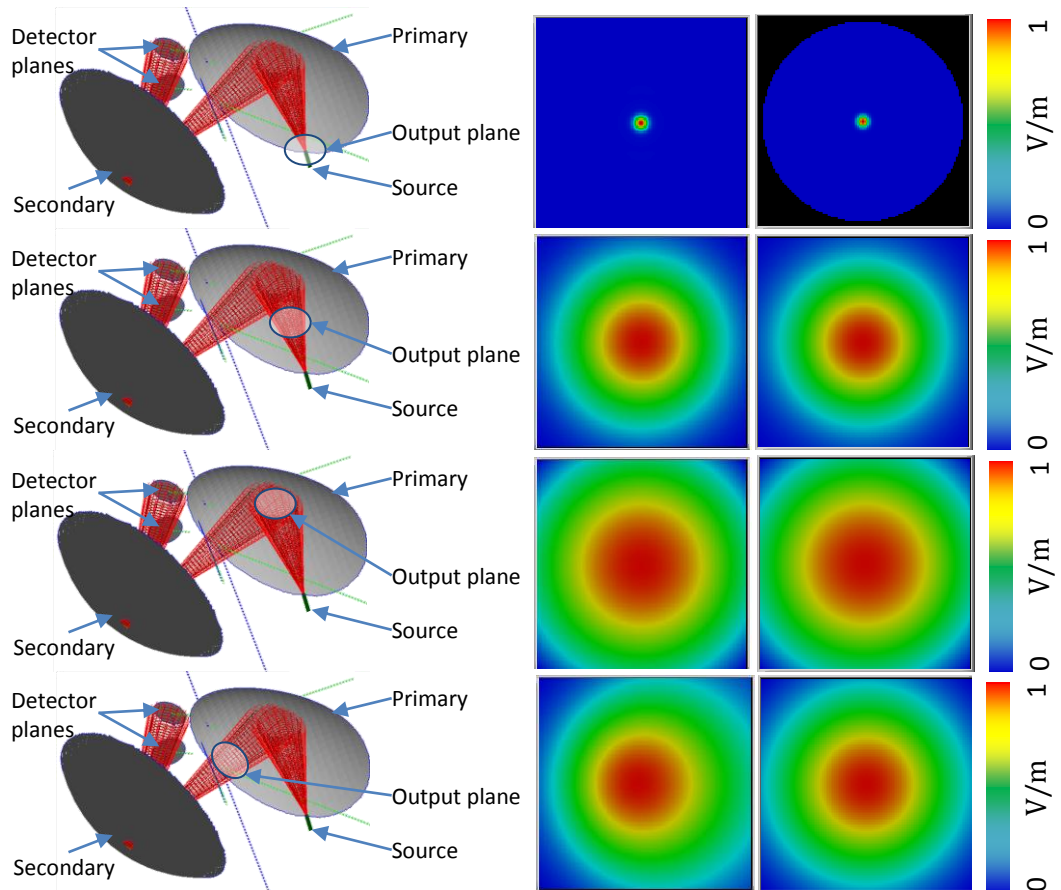
The 14° (3.074 mm waist) feed horn beam was modelled using PO for the varying propagation distances and the radius recorded, see *Table 3-10*. The beam's radius

was determined by calculating the radius at which the intensity dropped to $\frac{1}{e^2}$ of its peak value. The radius was taken as the average of the value recorded along orthogonal axes. *Table 3-10* compares these to the values given by the ABCD analysis.

Table 3-10: Calculation of beam radius versus propagation distance using ABCD matrices and PO.

Propagation distance (mm)	ABCD radius (mm)	PO radius (mm)
0	3	3
200	42	44
400	83	87
600	53	53
700	37	32
800	22	14
970	6	11
1100	20	15
1200	33	32
1430	64	59

The selected outputs are shown for propagation from the source to the detector plane in *Figure 3.35* giving an overview of the beam's evolution.



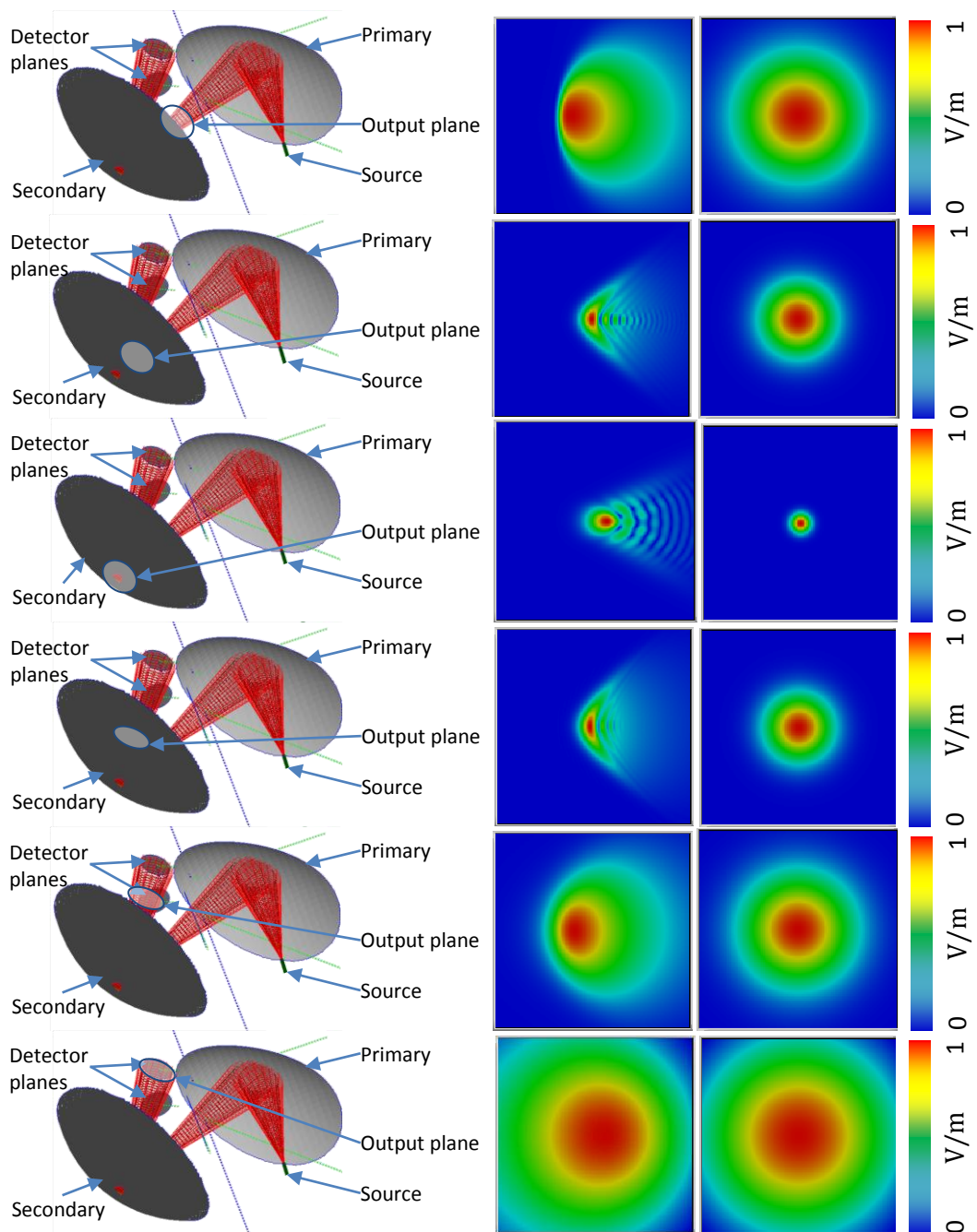


Figure 3.35: Evolution of a Gaussian beam propagating through the QUBIC system from the input aperture array to the detector plane. In all cases the detector plane is 120×120 mm² and beam amplitudes are individually normalised to utilise the full colour scale at each location. From left to right, first is the mirror system showing the central feed horn with a disc indicating the position under consideration. Second is the PO output of the field as calculated in MODAL and finally a Gaussian at the same scale with a radius as predicted by the ABCD analysis for comparison

In this analysis we can see the beam loose and regain its Gaussian shape. Some power in the incident Gaussian beams on the primary mirror is scattered into higher order modes upon reflection due to the curvature of the mirror and the angle of throw, as previously shown in *Figure 3.21*. The beam gradually becomes increasingly

distorted exhibiting coma as it propagates to the secondary mirror. The secondary mirror compensates for the first angle of throw by cancelling out the effects of the first reflection through a second throw upon its reflection. As the beam propagates from the secondary it returns towards its original Gaussian profile as can be seen in *Figure 3.35*.

Even with the large non-Gaussian nature of the beam in parts of the system, as shown in *Figure 3.35*, it can be seen that the ABCD method gives a very good approximation to the overall beam footprint (although it can clearly be seen that a full PO analysis is required for detailed information at some intermediary planes). Here we extend this analysis to calculate the Gaussian beam radius for peripheral feed horns in the array, with locations as highlighted in *Figure 3.36*.

The beam sizes at the mirrors and approximate mirror sizes required can then be calculated. We do not need to consider the top most position as the combiner design is symmetric about the global y -axis as shown in *Figure 3.36*.

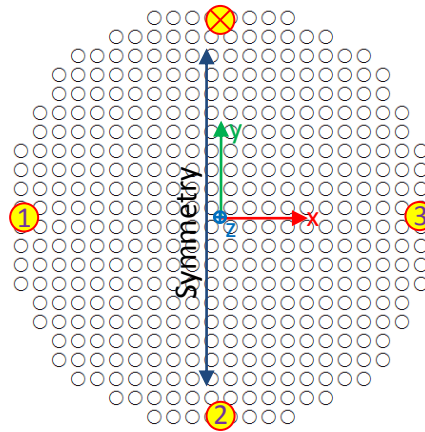


Figure 3.36: Feed horn positions used for the ABCD analysis.

For the analysis of the peripheral sources, system parameters for each beam were calculated. The schematic in *Figure 3.37* shows the paths through the system and *Table 3-11* the calculated parameters.

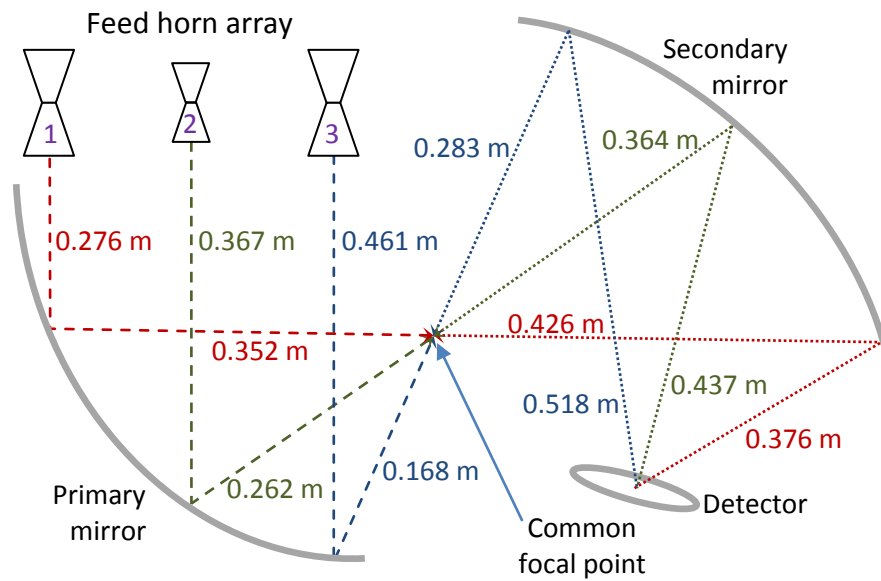


Figure 3.37: QUBIC schematic showing the path of the chief ray from peripheral feed horns.

Table 3-11: QUBIC system parameters

Parameter	Feed horn 1	Feed horn 2	Feed horn 3	Unit
Distance from source to primary	0.276	0.367	0.461	m
Primary equivalent focal length	0.352	0.262	0.168	m
Distance from primary to secondary	0.778	0.626	0.451	m
Secondary equivalent focal length	0.200	0.199	0.183	m
Distance from secondary to image	0.376	0.437	0.518	m
Secondary magnification	0.883	1.201	1.830	
Equivalent focal length	0.311	0.315	0.308	m
Detector plane image size	64.5	65.6	63.7	mm
Detector plane power capture (% of source)	71.4	70.1	72.4	%

Using the parameters in *Table 3-11* the ABCD matrices can be populated and the radius calculated for the propagating beams, in this case we assume a 14° beam from the feed horn and the results of these calculations can be seen in *Figure 3.38*.

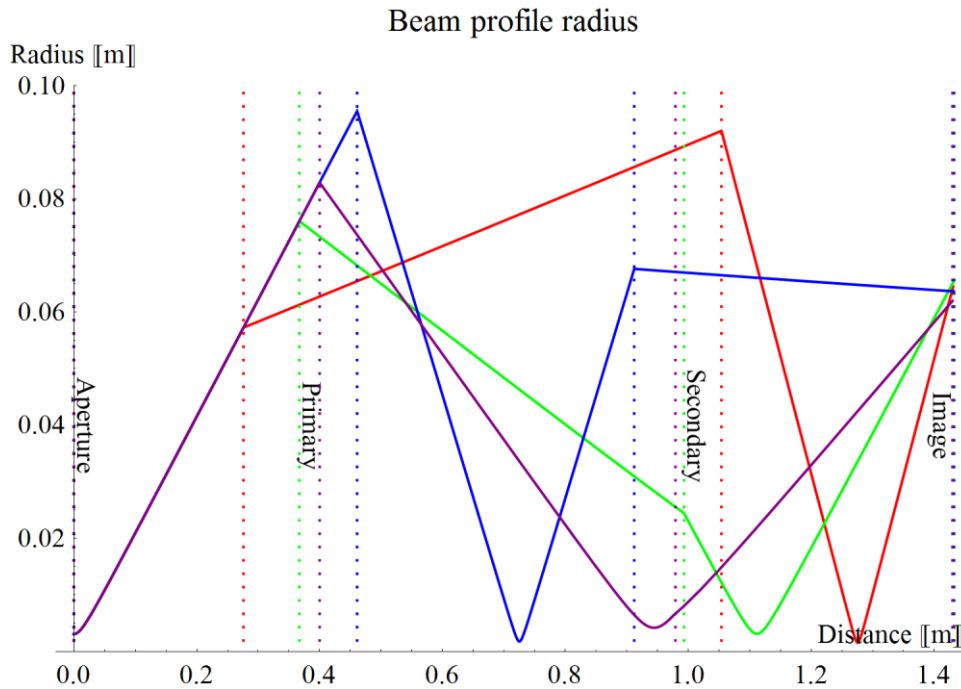


Figure 3.38: Beam width as a function of propagation distance for feed horn 1 (red), 2 (green), 3 (blue) and for comparison a central feed horn, x11y11 (purple) calculated using ABCD matrices.

The width varies from feed horn to feed horn but due to the compensating nature of the dual reflector, the detector plane beams size's only vary from 6.37 mm to 6.56 mm, as shown in *Table 3-11*, a total variation of $\pm 1.5\%$ in the width of the beam at the detector plane (it should be noted that these are the extremes). The size of the detector image is proportional to the effective focal length for its source.

3.5 Conclusion

In this chapter we have presented QUBIC v1.0 based on the novel concept of bolometric interferometry and showed how Stokes visibilities could be recovered from the Fizeau combiner image. Unfortunately the technical criteria of this design were too restrictive and the project was given a design overhaul in 2009. The outcome was QUBIC v2.0 which recovers the CMB polarisation properties from a synthetic image. The synthetic image is a convolution of the sky image and feed horn/combiner array PSF's. The new design will use a feed horn array, 22 in diameter, operating at 150 GHz covering multipoles in the range $43 \leq l \leq 200$. A summary of its geometry was shown. The revamped design QUBIC v2.0 can now achieve the primary goal of detection to a level of $r_{0.002} = 0.01$. A detailed design

of the combiner primary and secondary mirrors, and detector plane was presented. It was shown that GO and GBM analysis can be used to determine the initial design of the combiner but the time-intensive PO is required for the details, especially at the intermediary surfaces. This requirement for multiple techniques only serves to highlight the difficulties involved in designing long-wavelength systems. In Chapter 4 we will present the design of additional elements required for the discrimination of the polarisation properties in the CMB and the refinement and analysis of the combiners' surfaces.

4 QUBIC analysis and optimisation

As detailed in Chapter 3, the QUBIC combiner consists of 2 mirrors, a primary parabolic and a secondary elliptical, configured as an off-axis Gregorian. They are illuminated by a 300-mm diameter circular array of 14° feed horns operating at $150 \text{ GHz} \pm 12.5\%$. The entire setup is contained within a cryostat with forebaffles and a ground shield as shown in *Figure 4.1*. In this chapter I analyse the performance of this combiner in detail taking into account effects such as beam truncation and mechanical/manufacturing tolerances. I also design the remaining components of the combiner: the coldstop and the polariser.

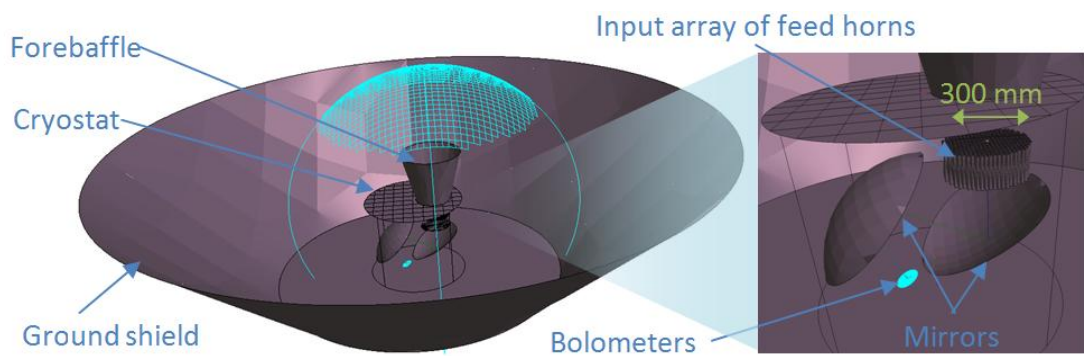


Figure 4.1: QUBIC simulation setup

4.1 Spillover and beam truncation

4.1.1 Visualisation of 400 beams

In order to ascertain the overall size of the beams propagating through the combiner, and the extent to which spillover could be an issue, a method was devised to combine all 400 feed horns to give an envelope or footprint of the beams. There are several approaches which can be taken. Consider two beams, shown in *Figure 4.2*, incident on a plane where we want to show the beam footprint out to the $1w$ level (where power falls to $1/e^2$ of its maximum intensity value). In this example, both have the same total power but beam 2 is more focussed.

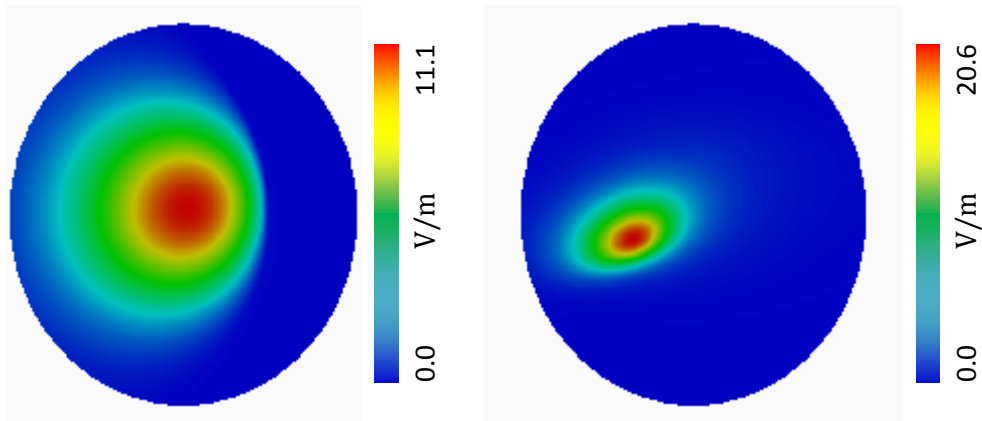


Figure 4.2: 2 Beams incident on a plane, beam 1 (left) and beam 2 (right)

The first approach squares each field separately and the total power for each beam is obtained. The footprint is considered the area which has a $(P_1 + P_2) > \frac{(P_1 + P_2)_{\max}}{e^2}$, where for each pixel in beam 1 and 2, P_1 and P_2 are the power in the respective pixels. $(P_1 + P_2)_{\max}$ is where this combination is at a maximum. This yields the result in Figure 4.3 where the main footprint contribution is from beam 2.

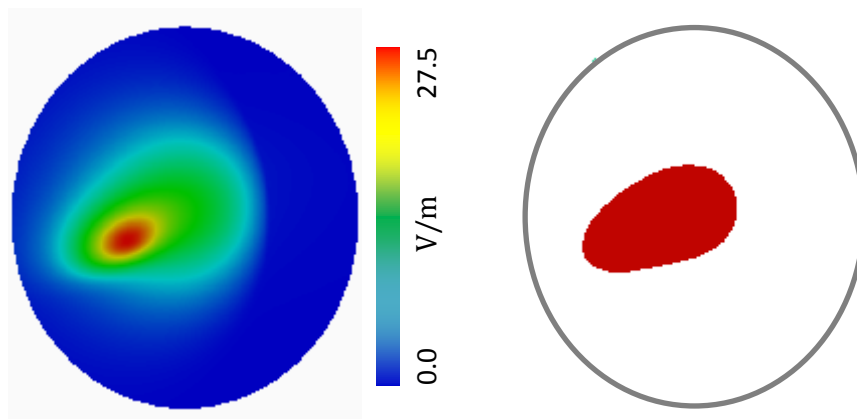


Figure 4.3: Additive beam contours (left) and beam footprint (right)

Using this approach a highly focused beam will wash out the contributions from other beams giving a false indication as to where truncation is occurring (some beams could be severely truncated, some not at all). An alternative is to determine the footprint of each beam separately and then merge the footprints. This total footprint then includes any part where $P_1 > \frac{P_{1\max}}{e^2}$ or $P_2 > \frac{P_{2\max}}{e^2}$, as shown in Figure 4.4.

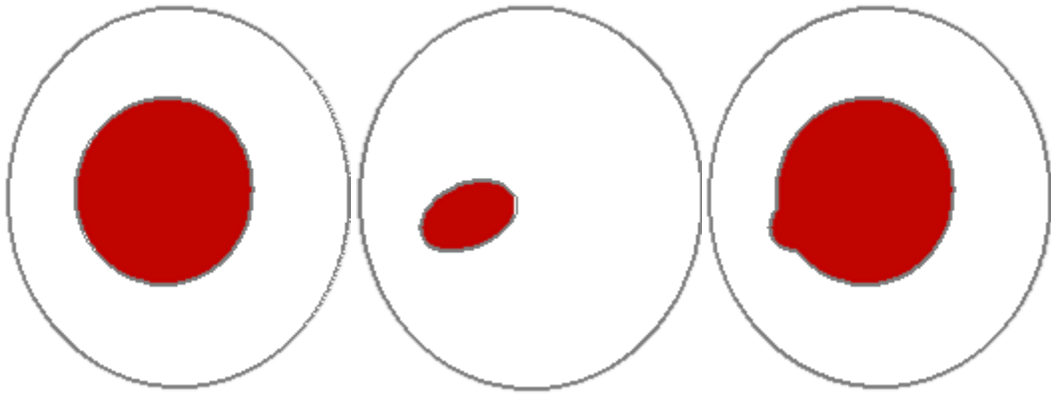


Figure 4.4: Beam 1 footprint (left), beam 2 footprint (centre) and the combined beam footprint (right)

This method was selected as it is the most restrictive (gives the largest footprint). We are therefore asking not what size the optics has to be to capture $n\%$ of the total power but what size it has to be to capture at least $n\%$ of the total power from each beam (more than $n\%$ will be captured for most beams). For this example we considered $1w$ (P/e^2) so $n = 86\%$, see Table 4.1. Figure 4.5 shows the primary mirror footprint using this method. There are several colour divisions in the image. From Table 3-9 the expected capture at the detector plane is $\sim 0.8w$ (assuming a 51 mm radius detector plane) which is $\sim 72\%$ of the power. Using Equation (2.104) the expected power levels for a given radius of capture can be calculated and are also tabulated in Table 4.1.

Table 4.1: The % of total power contained within a given off-axis distance (r/w) for a Gaussian beam of radius w .

Distance from centre (r/w)	Power at r (W)	Power at r (dB)	Total power within r (%)
0.8	$P = P_0 e^{-2(0.8^2)} = P_0 e^{-1.28}$	-5.6	$P = 1 - e^{-2(0.8^2)} = 72$
1.0	$P = P_0 e^{-2(1^2)} = P_0 e^{-2}$	-8.7	$P = 1 - e^{-2(1^2)} = 86$
2.0	$P = P_0 e^{-2(2^2)} = P_0 e^{-8}$	-34.7	$P = 1 - e^{-2(2^2)} = 99$
3.0	$P = P_0 e^{-2(3^2)} = P_0 e^{-18}$	-78.2	$P = 1 - e^{-2(3^2)} = 100$

Figure 4.5 shows a footprint diagram with several levels, this is for the primary mirror which will be detailed §4.1.2. The first section is shown in red and corresponds approximately to the power that will be captured at the detector plane ($r = 51$ mm equivalent to $r = 0.8w$). The yellow region shows the extent required to capture out to $r = 1w$ for all beams and green out to $r = 2w$ (which is essentially all power

captured). The remaining power (<0.1%) is shown in cyan. The zero power regions and regions beyond the rim of the mirror are shown in blue.

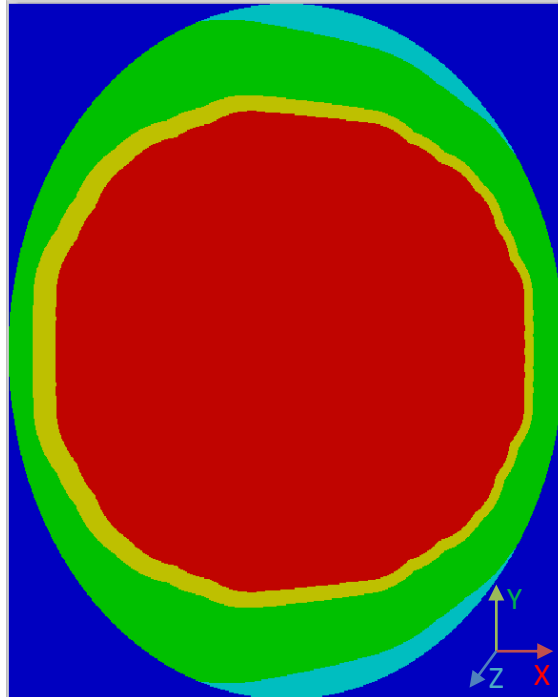


Figure 4.5: Primary mirror beam footprint for all 400 sources.

Image Key

0.8W ($1/e^{1.28} = -5.6\text{dB}$) $\approx 72\%$ of incident power [51 mm radius detector plane]

1.0W ($1/e^2 = -8.7\text{dB}$) $\approx 84\%$ of Incident Power)

2.0W ($1/e^8 = -34.7\text{dB}$) $\approx 99\%$ of Incident Power)

3.0W ($1/e^{18} = -78.2\text{dB}$) $\approx 100\%$ of Incident Power)

It is desirable to minimise the size of the mirrors (to fit inside the limited space within the cryostat and to reduce the overall mass to be cooled) to aid in the cryostat operation. *Figure 4.5* shows that all power that could potentially be captured by the detector plane is intercepted by the primary mirror. Truncation is sufficiently low ($r \approx 2w$) that diffraction effects on the final image will also be small. As described next, it was decided that the losses were sufficiently low not to need to extend the primary mirror beyond that used in the initial GBM analysis.

4.1.2 Beam truncation by the primary mirror

The beam from each feed horn was propagated onto the primary mirror (480 mm \times 600 mm) and the percentage of feed horn power incident on it was calculated. CLOVER feed horns scaled to operate at 150 GHz (14° farfield

divergence) were used as inputs for these simulations. *Figure 4.6* shows each result placed in a 2D array according to the feed horn position in the aperture array. The power captured from the feed horns varies from 98.7% - 100%, and averages 99.9% (high, as expected from *Figure 4.5*).

In *Figure 4.6* we can see that the feed horns nearest to the secondary are losing up to 1.3% (e.g. x21y07) of their power due to spillover at the primary mirror. *Figure 4.7* shows the individual beam patterns on the surface of the primary mirror where the beams in the column x21 show an incident position close to the left hand edge of the mirror which is leading to the loss of up to 1.3% of power in these cases. This part of the mirror is the side closest to the secondary and although extending it could decrease the spillover this proved impractical when other combiner components were later added (see §4.3 and §4.4).

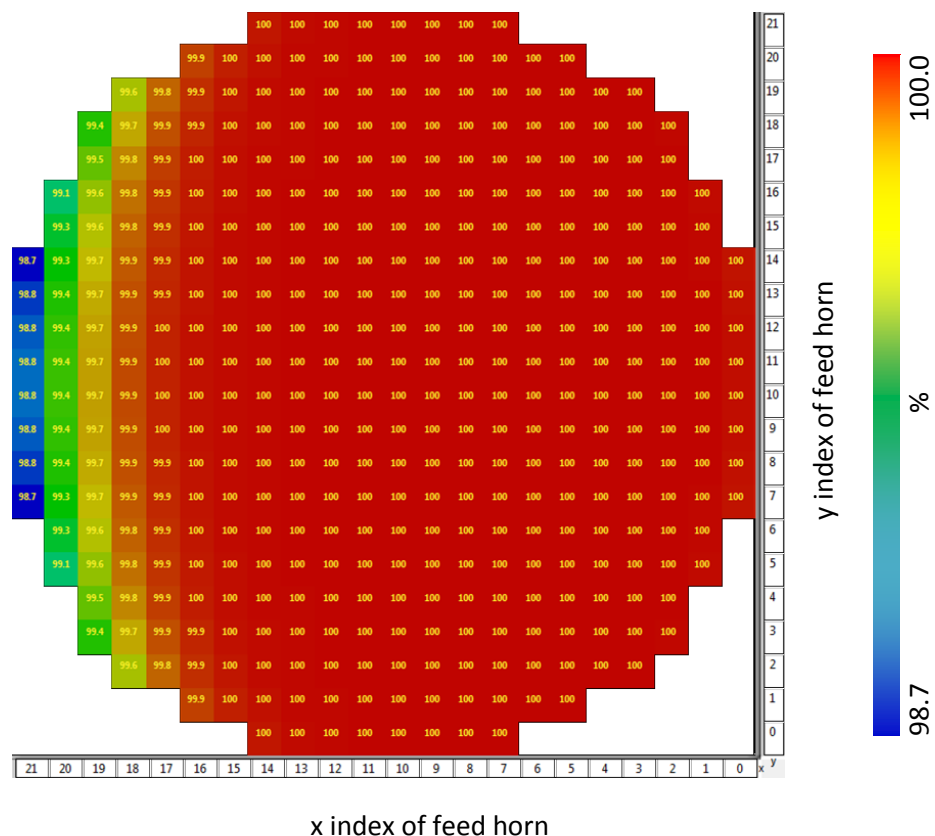


Figure 4.6: Primary mirror power overview (average power collected is $\approx 99.9\%$). The feed horn corresponding to each power value is indicated by its x and y value.

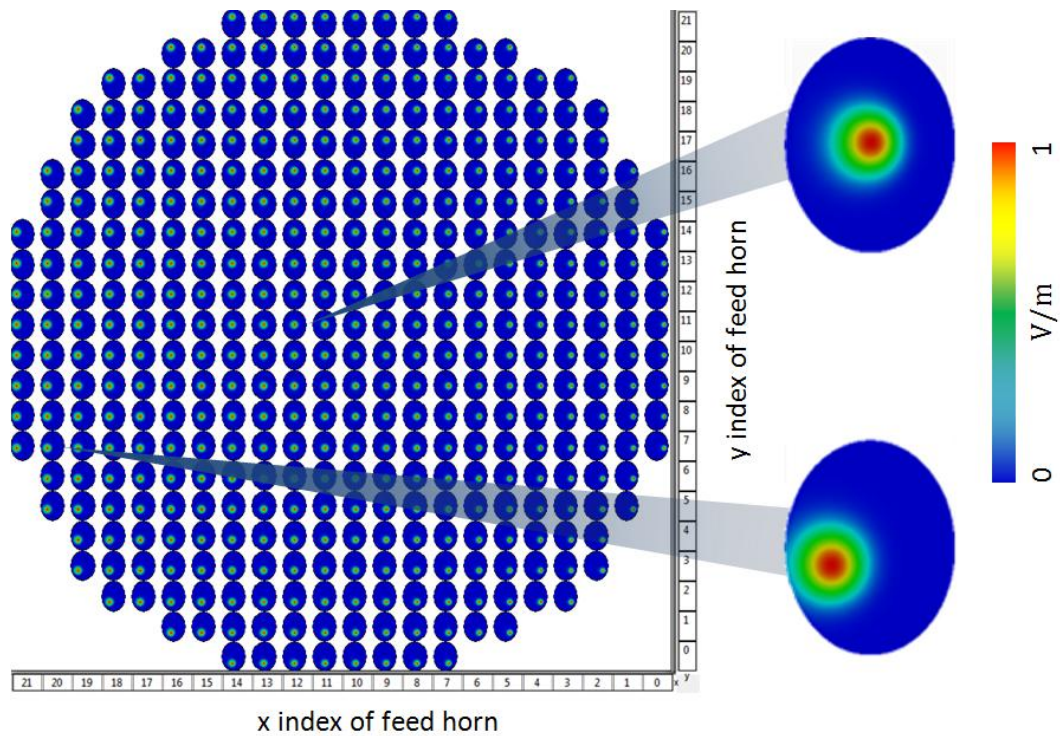


Figure 4.7: Primary mirror beam intensity overview (average power collected is $\approx 99.9\%$). The feed horn corresponding to each power value is indicated by its x and y value. On the right is shown two expanded views of the beam from sources x20y07 and x12y11.

4.1.3 Beam truncation by the secondary mirror

Figure 4.8 shows the analysis of truncation for the same sources propagated from the primary and onto the secondary mirror (600 mm \times 600 mm). From Figure 4.9 we can see that the sources nearest the left hand side of array (e.g. x21y07) are losing up to 1.4% of their power. This value is the total power lost up to this point. To determine the power lost as a result of the secondary alone we need to exclude any prior losses in each beam. Figure 4.9 shows the power lost from each beam due to the secondary alone and that the power lost is 0.1% in the worst case (e.g. x21y07).

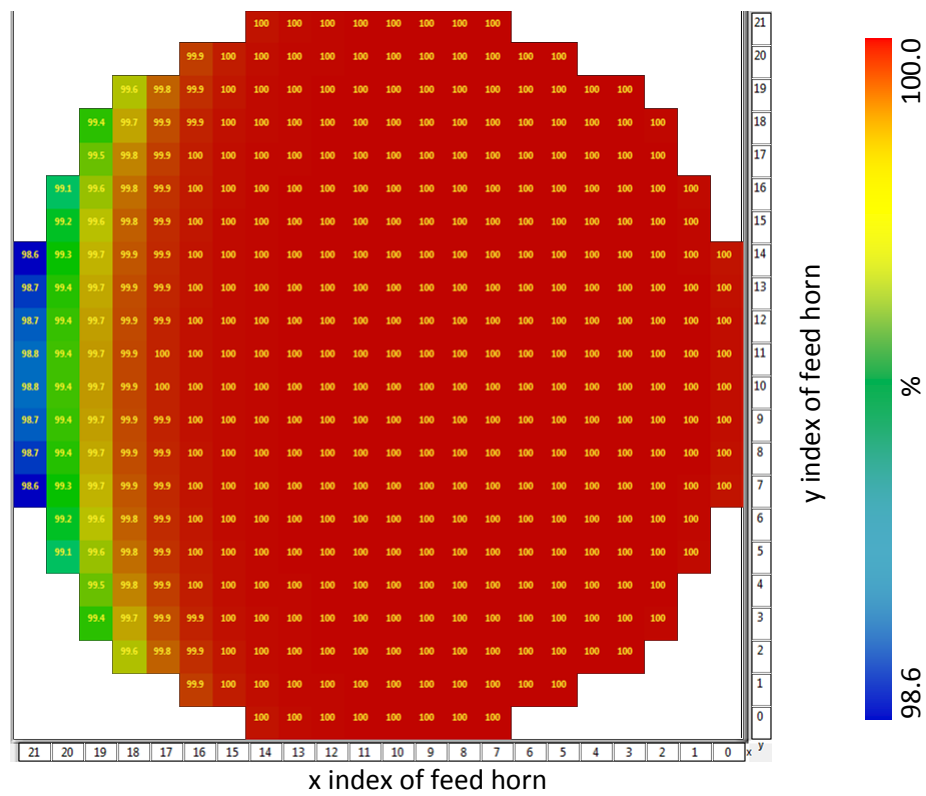


Figure 4.8: Secondary mirror power capture overview (average power collected is $\approx 99.9\%$). The feed horn corresponding to each power value is indicated by its x and y value.

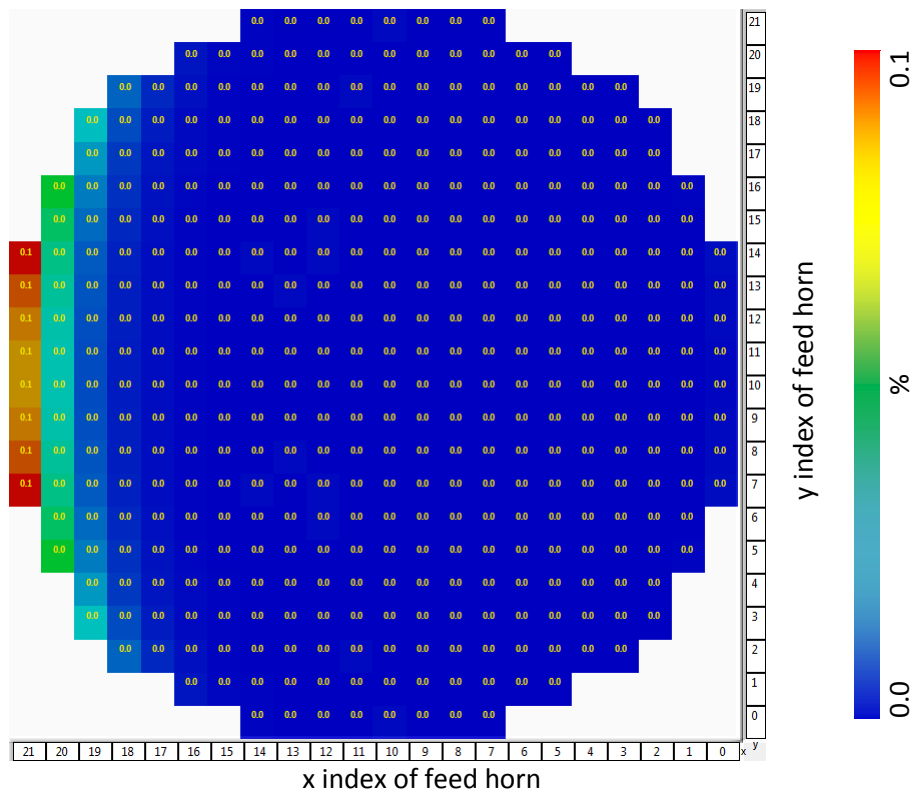


Figure 4.9: Secondary mirror power loss overview. The feed horn corresponding to each power value is indicated by its x and y value.

The combined footprint for all 400 beams on the secondary mirror is shown in *Figure 4.10* where it can be seen that each beam is intercepted by the secondary out to more than $r = 2w$. As with the primary mirror, the secondary mirror could be extended, in this case towards the primary mirror, but since other components (e.g. the polariser mentioned in Chapter 3) will be required any further extension of the primary and secondary mirrors was not considered necessary at this stage.

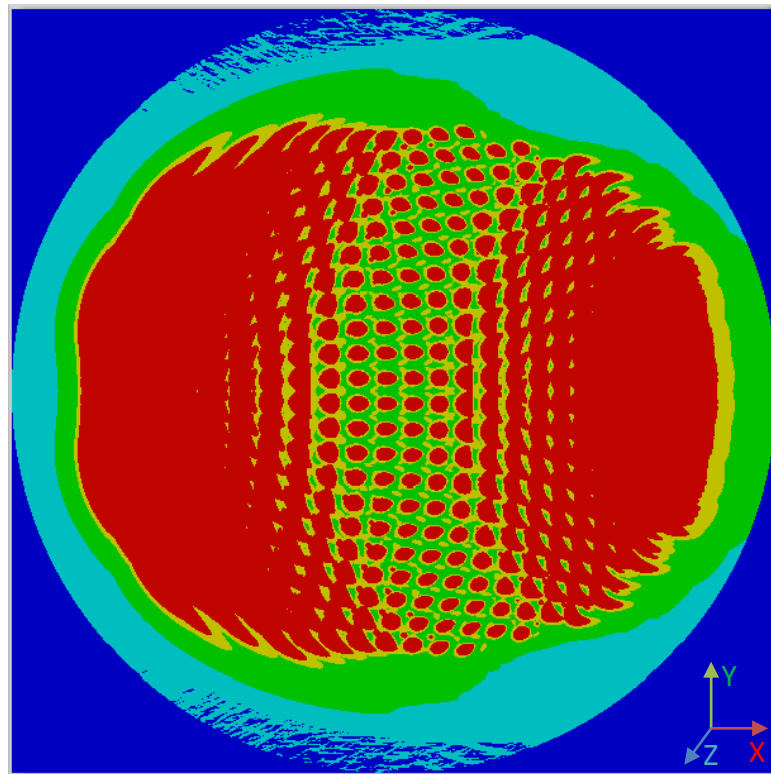


Figure 4.10: Secondary mirror beam footprint for all 400 sources. Colour is the same as in Figure 4.5 image key.

4.1.4 Beam truncation at the detector plane

The detector plane is first approximated as a circle of radius 51 mm (*APC, private communication*). The power, from all sources, reaching the detector plane was calculated as before and in *Figure 4.11* we can see that the feed horns nearest to the primary (e.g. x21y07) are losing the most power with losses up to 40%. Taking into account the power lost on previous elements and determining the net losses at the detector plane, the power lost from each beam at the detector plane was calculated and is shown in *Figure 4.12*. The power lost at the 51 mm radius detector plane ranges from 38.6% to 28.8% with an average of 33.3%. The 28.8% loss for central

sources is in good agreement with the expected power loss of ~26% for a beam of radius 62 mm being captured by a detector plane of radius 51 mm, calculated using Equation (2.104) $\left(P_{loss} = e^{-2\frac{(0.051)^2}{(0.062)^2}} = 25.8\%\right)$. The beams have varying degrees of non-Gaussianity, off-centre peaks and off-axis incident angles, which can all contribute to additional power losses, accounting for the 2.8% difference.

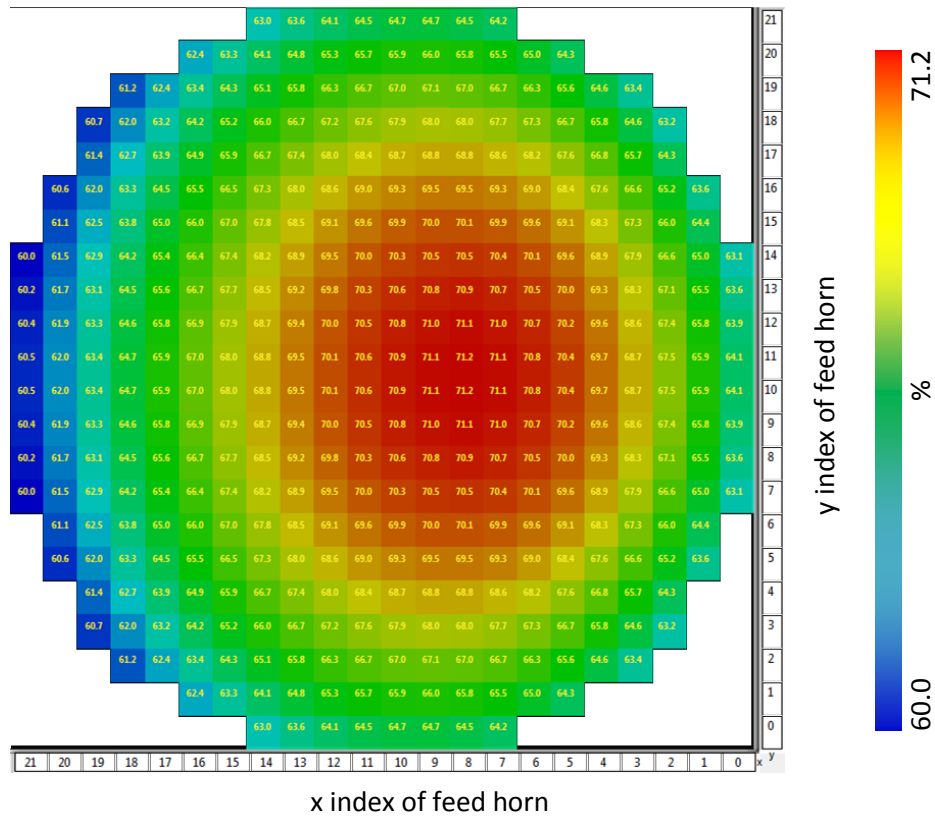


Figure 4.11: Detector plane (circular with 51 mm radius) power capture overview (average power captured is 66.7%). The feed horn corresponding to each power value is indicated by its x and y value.

The difference in power captured from a central feed horn (e.g. x10y10) and an edge one (e.g. x03y03) is about 6%. We have seen from Figure 4.8 that a difference in truncation by the 2 mirrors can only account for about a 1.4% difference. There is also a contribution due to a difference in beam size on the detector plane. In the case of an edge source (x03y03) the detector plane beam radius is ~72 mm × 66 mm. Taking 69 mm as the average beam radius and 51 mm for the detector plane size and using Equation (2.104) the power hitting the surface of the detector plane for the beam is 66.5%. The corresponding power levels based on PO

calculations for this feed horn are 64.6% which is within 2% of the predicted value. The remaining difference can be attributed to the elliptical shape of the beam and aberrations due to the off-axis incident angle.

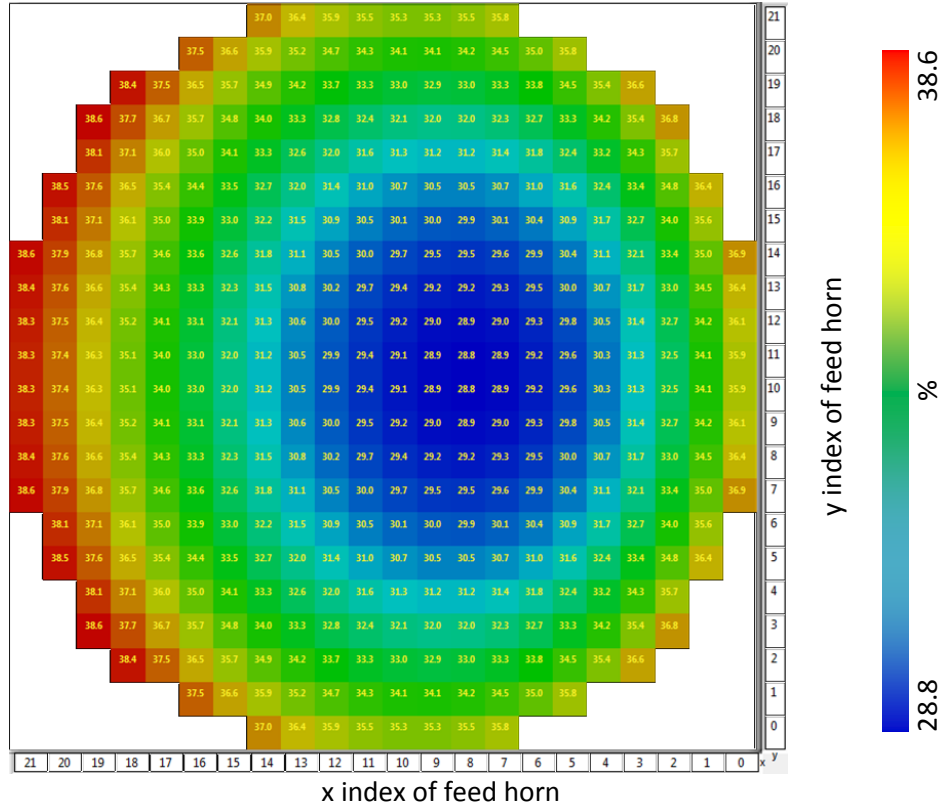


Figure 4.12: Detector plane (circular with 51 mm radius) power loss overview. The feed horn corresponding to each power value is indicated by its x and y value.

This spread of power captured from different sources could be reduced by increasing the size of the detector plane (in practice this is limited by the number of bolometers that can be made). In Figure 4.14 the power captured as a function of detector plane was plotted for a subset of sources as highlighted in green in Figure 4.13.

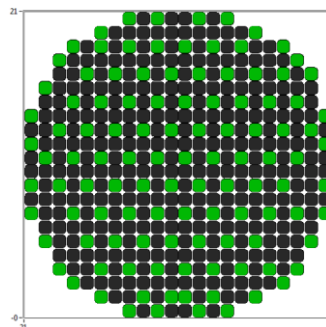


Figure 4.13: 111 sources (shown in green) from the total array of 400 sources used in the generation of the variation of the output power captured on the detector plane.

Figure 4.14 shows the power collected by the detector plane as a function of size for each of the sources. For an $r = 51$ mm detector extent the power levels range from 59.1 - 71.2% and for an $r = 60$ mm detector plane from 71.3 - 80.2%.

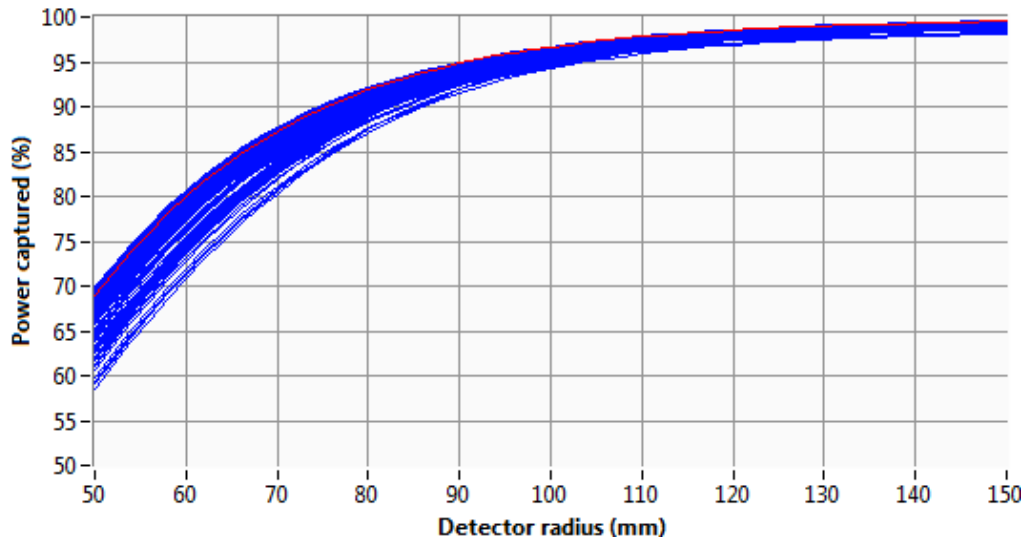


Figure 4.14: Power captured versus varying detector plane extent, for 111 Gaussian sources (in the aperture array) with a waist of 3.074 mm operating at a frequency of 150 GHz (far-field FWHM of 14°). A central source (x11y13) is shown in red.

From the ABCD analysis a 51 mm detector plane has an ideal 74% power capture (equivalent to ~ 0.8 w) based on a 62 mm beam width. For the central feed horn, x11y11, this is in good agreement with a level of 71.2% calculated using PO.

4.1.5 Bolometer detector array

The footprint of the bolometer array previously defined as a disc of radius 51 mm was finalised in 2015. The array will have $2.8 \text{ mm} \times 2.8 \text{ mm}$ bolometers with a centre-to-centre separation of 3 mm (the gap between bolometers is therefore 0.2 mm) arranged in a circular array. Manufacturing restrictions and fitting in readout circuitry required dividing the bolometer array into 4 quadrants with 2 mm gaps between quadrants along in the x- and y-axis as shown in Figure 4.15. Displayed here is one quadrant of the bolometer array; all the other quadrants are identical.

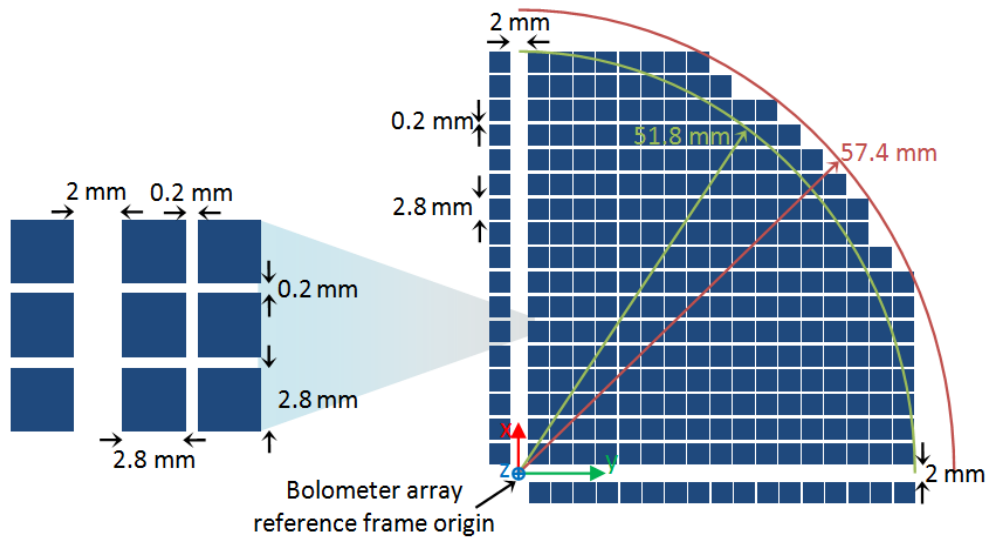


Figure 4.15 Bolometer array schematic showing the upper right quadrant with a 2 mm gap between quadrants to allow for circuitry. The bolometers measure $2.8 \times 2.8 \text{ mm}^2$ with a 0.2 mm gap between each giving a centre-to-centre spacing of 3.0 mm. The green circle centered on the array centre is of radius 51.8 mm indicating the footprint for the detector array where all power is captured and the red 57.4 mm circle is indicating footprint that encompasses all bolometers, although some power is lost at this radius.

In considering the impact of the latest design, 3 versions of the bolometer array were modelled in MODAL as shown in Figure 4.16.

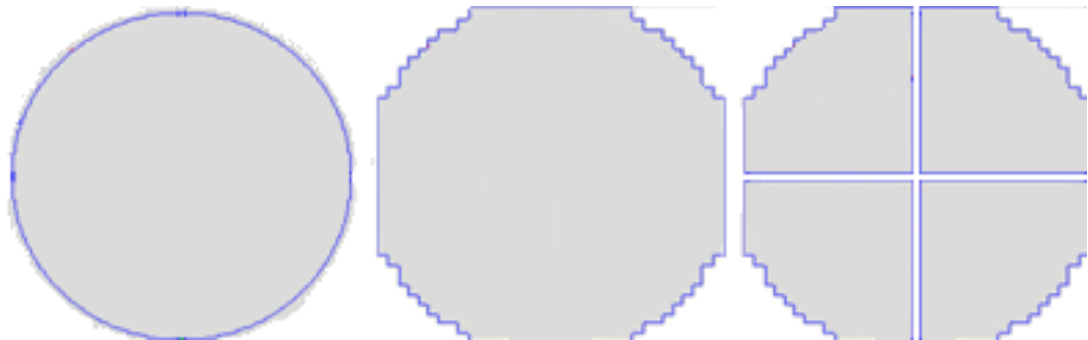


Figure 4.16 Bolometer array designs modelled in MODAL. On the left is shown a circular detector plane 102 mm in diameter as originally modelled. In the centre is a bolometer array of diameter 103.6 mm (from $2 \times 51.8 \text{ mm}$ as highlighted in green in Figure 4.15) in diameter without gaps and right a bolometer array of 103.6 mm diameter including main central gap of 2 mm.

Feed horn x10y10 (a central feed horn within the array) was selected as an example source and a Gaussian beam with a 3.074 mm waist radius (14° far-field FWHM beam) at 150 GHz was used. In lieu of a detailed model to calculate bolometer coupling, see for example Reese (Reese, 2006), the power captured was calculated by adding all the power that fell on the bolometer array (regardless of polarisation, incident angle etc.). The detected power levels were calculated for the three

versions of the simulated bolometer array from *Figure 4.16*. The results are shown in *Figure 4.17*.

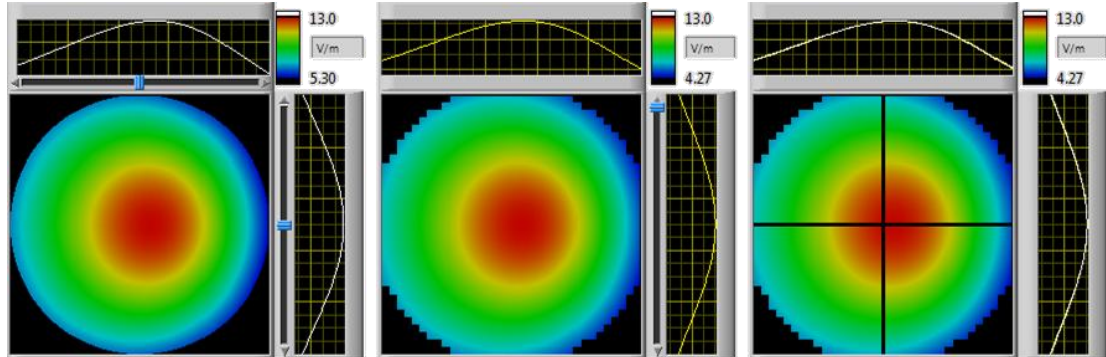


Figure 4.17: Detector plane on-axis power levels, ignoring polariser & coldstop, for Source x10y10 (as defined in §3.3.4) with a 3.074 mm waist radius at 150 GHz. Left 51 mm radius circular detector plane, centre bolometer array footprint and right bolometer array footprint and main central gap as outlined at the start of this section.

The 51 mm radius circular detector plane captured 71.0% of the source power. The second bolometer array (without gaps) increased this to 75.0% and finally taking the two main (2 mm) gaps into account the power captured dropped to 70.0%. It was then decided to include the effects of the 0.2 mm gaps between the bolometers (effectively reducing the collecting area of each bolometer by $\left(\frac{2.8}{3.0}\right)^2$), and the power was found to have dropped to 58.7%, a loss of 11.3%. The test was repeated for other sources and tabulated in *Table 4.2*. There was ~5% power drop caused by the main gap regions in the bolometer array. This is almost cancelled by the slightly larger array size compared to the original 51 mm circular test plane that was used. This gives a net loss of ~1%. Although, including losses for all the gaps between bolometers gives a ~10% drop in power in this simple model, this is not expected to be the case in the actual system as the small 0.2 mm gaps are $\ll \lambda$.

Table 4.2: Bolometer array detector power capture tests

Test source	Test type	3.074 mm waist (14° beam)
x10y10	Circular (r= 51 mm)	71.0%
	Bolometer Footprint	75.0%
	Bolometers + Main Gaps	70.0%
	Bolometers + All Gaps	58.7%
x05y05	Bolometers + All Gaps	57.1%
x17y17	Bolometers + All Gaps	53.7%

4.2 Mirror tolerance analysis

In the construction of the combiner there will be imperfections in the alignment and position of mirrors when mounted. In order to ascertain manufacturing tolerance limits, the effects of translations and rotations in element positions were calculated. At the time of writing the location of the mounting points have yet to be confirmed and these are required for accurately determining the rotation tolerances. For these tests the geometric centre of each mirror was selected as a pivot point with the orientation of the axes for all tolerance tests given by the axis direction of the GRF. The pivot points and global coordinate system are shown in

Figure 4.18.

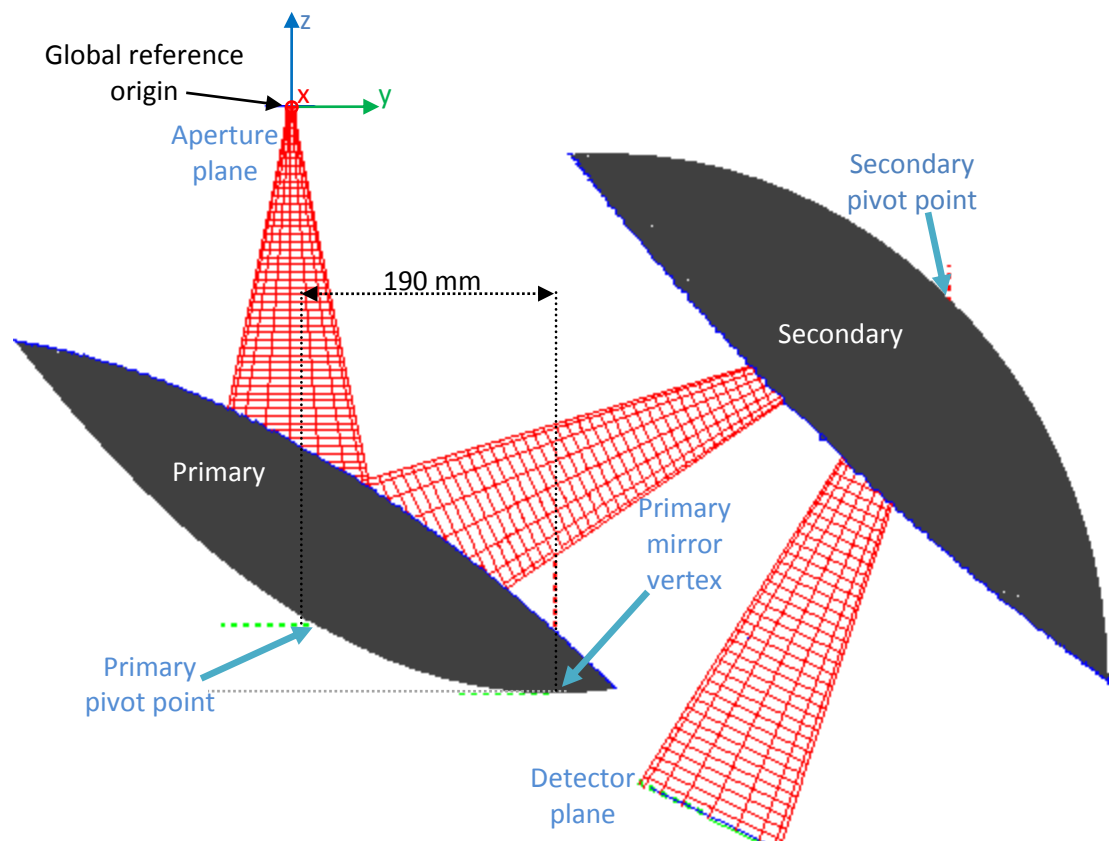


Figure 4.18: QUBIC tolerance test pivot point definitions. All rotations are anti-clockwise when viewed from $+\infty$ towards the origin.

A Gaussian source with waist radius = 3.074 mm (equivalent to a 14° beam) emitted at 150 GHz was again used for testing and the source locations selected are highlighted in green in Figure 4.19.

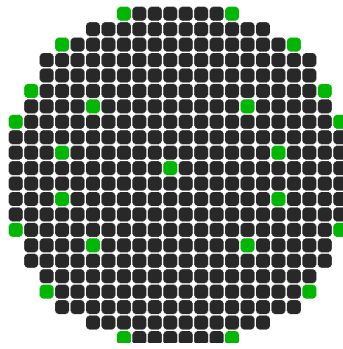


Figure 4.19: Horn Selection for Tolerance Tests

In order to determine the impact of tolerance variations a measure of the power at the detector plane and the footprint on the surface of the secondary mirror were calculated as figures of merit. In the latter case the edge sources were used to determine the footprint. Rotations of the primary cause a shift in the angle of throw of the reflected beam at the secondary. We first look at the variation in footprint of the secondary beam and the variation in the power collected at the detector plane when the primary is rotated $\pm 1^\circ$ about each axis. In *Figure 4.20* and *Figure 4.21* we see the unperturbed footprint of the edge feed horns followed by the footprint after the primary has been rotated about the x , y and z axis.

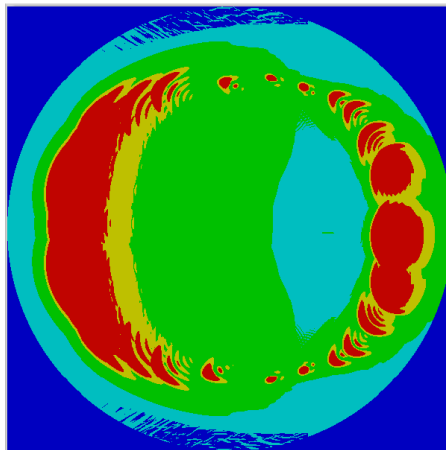


Figure 4.20: Secondary Mirror Beam Footprint (Edge Sources - Normalised and W). Colour is the same as in *Figure 4.5* image key.

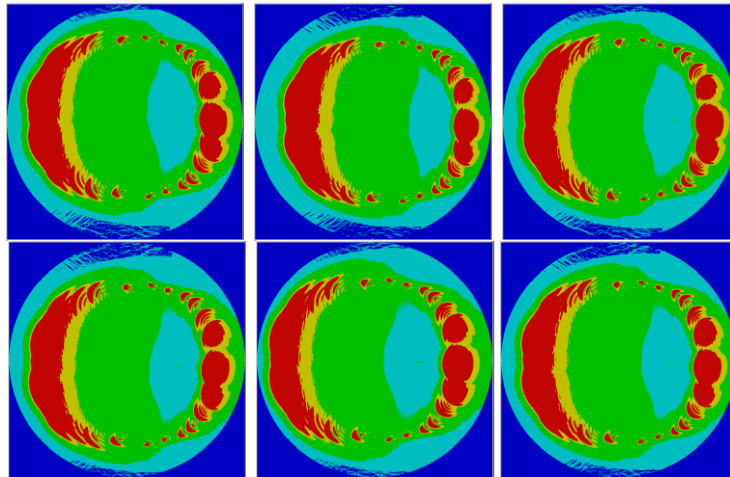


Figure 4.21: The top row of plots show the effect of rotations by $+1^\circ$, the bottom row for -1° . Left to right are shown the footprint on the secondary mirror as a result of the primary mirror x, y and z rotations. The colour scheme is the same as in Figure 4.5 image key.

An overview of the variation in power level intercepted at the detector plane is shown in Table 4.3 and the full result set is available in Appendix 2. The loss of power in these cases is due to shifts in the point of intersection of the centre of the beams on the detector plane, causing the edges of the beams to be truncated.

Table 4.3: Summary of 1 mm and 1° tolerance testing showing the nominal power variation on the detector plane for several feed horn locations as a percentage of feed horn power.

	x03y03 (%)	x07y14 (%)	x11y11 (%)	x18y18 (%)
Primary translation	± 0.10	± 0.15	± 0.20	± 0.30
Primary rotation	± 1.00	± 1.60	± 2.70	± 2.95
Secondary translation	± 0.15	± 0.10	± 0.30	± 0.25
Secondary rotation	± 0.85	± 0.50	± 0.65	± 0.25

Rotation of the primary mirror has the largest impact on the detected output with respect to the variation in the detected power levels. This was expected as the beams have more distance to travel the earlier the perturbation is introduced leading to a larger variation from the nominal beam path. Anthony Donohoe of MU carried out similar tests using the ZEMAX-RT package. The vertex of the primary and the centre of the secondary were selected as the pivot points and found the order of importance as shown in Table 4.4.

Table 4.4: Zemax tolerance test results for 1 mm and 1° tolerance testing showing the root-mean-square spot size variation on the detector plane for rays over the entire surface.

Mirror and operation	Change (%)	
	Min	Max
Primary rotation	1.4	5.3
Secondary rotation	0.7	1.5
Primary translation	0.7	0.7
Secondary translation	0.5	0.5

Even with the differing selection in pivot points, there is broad agreement between the two simulations. The rotations are more problematic than the translations and the primary rotation is the biggest problem. The PO calculations are an average of the variations in power levels for single sources whereas Zemax uses a GO approach and an average of the impact for rays over the entire surface. The total variation for this preliminary tolerance analysis, with a worst case of ~3% (from Table 4.3), was deemed acceptable (*Report issued by the author to QUBIC group in conjunction with performance analysis by Bigot-Sazy, private communication*).

4.3 Polariser and side detector

4.3.1 Orientation of polariser and side detector

QUBIC will require the inclusion of a polariser and second detector plane for the separation and determination of the co- and cross-polarisation components. The compact combiner design necessitates detailed analysis in order to minimise blockages and maximise beam capture but a complete PO analysis for all possible polariser locations, orientations and sources is impractical. Therefore visual inspection with GBM was used to reduce the potential candidates. In this section the separation and angle of the detector planes is investigated and consequently the optimum position, size and angle of the polariser determined. The polariser must be placed at an angle that exactly splits the angle between the two detector planes. The origin of the polariser's local reference frame is located at the intersection of the normals of the main and side detector planes and the side detector plane and the polariser position are specified with respect to the position of main detector plane.

The polariser was initially placed facing back towards the primary, as shown in *Figure 4.22*. Here the side detector plane potentially blocks the path of the incident radiation at point A. In order to capture the reflected beams from the secondary, the polariser extent at point B almost intersects the secondary with the potential for some power to leak around the polariser at point B. The possible polariser locations in this configuration were investigated more closely to see if a solution could be found with acceptable levels of blockage at A and B. One important parameter to adjust is the separation distance of the detector planes. The closer the detector planes are together the smaller the polariser needs to be and the less intrusive it is on the paths of the beams within the combiner between the primary and secondary mirrors. The trade-off is that the side detector plane moves closer to the centre of the combiner hence increasing its shadow on the beams propagating from the secondary towards the main detector. Physically the separation distance of the two planes must be at least 88.4 mm (*private communication, QUBIC group, 2012*) in x and y as shown in *Figure 4.23*, as this is the minimum possible physical distance to accommodate the detector array's associated electronics. An upper limit of 110 mm is imposed as if this is exceeded a polariser capable of capturing the secondary mirror's reflected beams becomes too cumbersome. Depending on the orientation it either intersects the secondary mirror or cannot capture all incident beams, or both. This will be looked at in greater detail when the orientation is finalised. The assembly concept for the QUBIC combiner is shown in *Figure 4.24*.

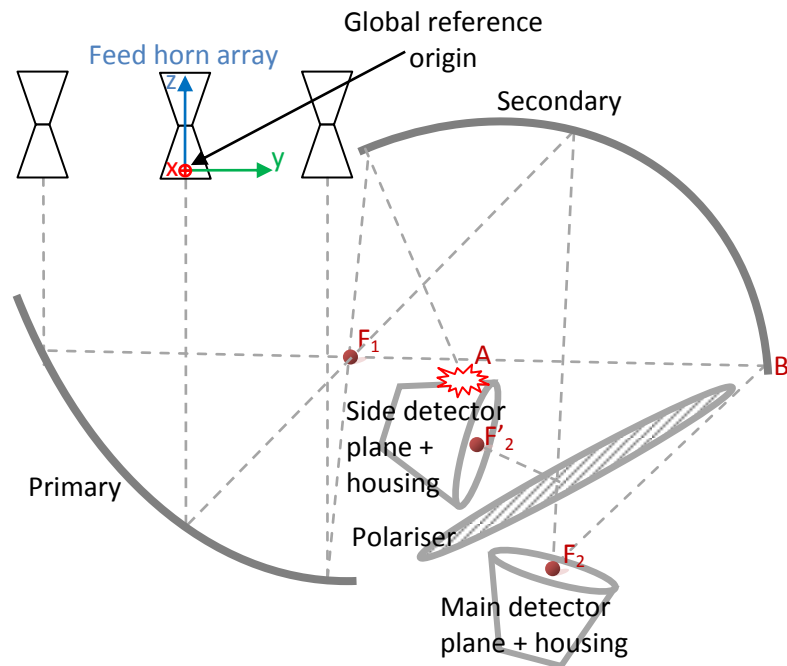


Figure 4.22: QUBIC (not to scale) schematic showing the position of the polariser facing the primary mirror. The side detector plane is placed between the primary and secondary. The side detector plane and the associated electronics obstruct the path of the incoming radiation.

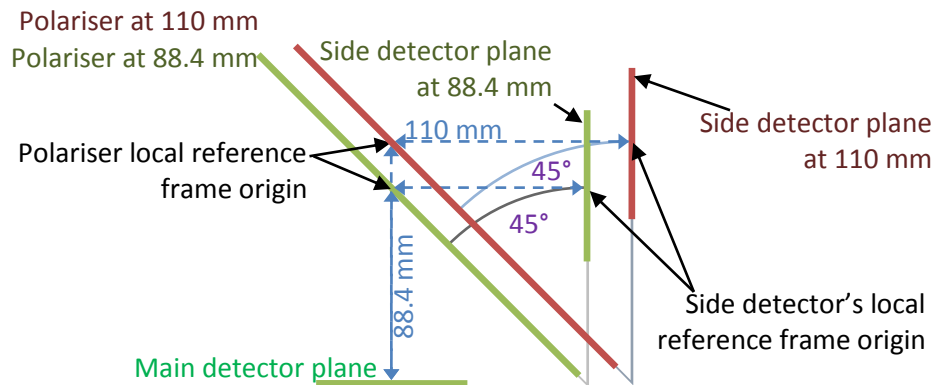


Figure 4.23: Polariser and detector plane setup. The main detector plane is a fixed point in the design, located at the second focal point of the secondary mirror. All other elements in this figure are relative to its position. The polariser local reference frame origin is located 88.4-110 mm along normal from the main detector plane then rotated 45° about the main detector planes x-axis. The side detector plane is offset 88.4-110 mm along the normal and translated the same along the main detectors plane, then rotated 90° about the main detectors x-axis.

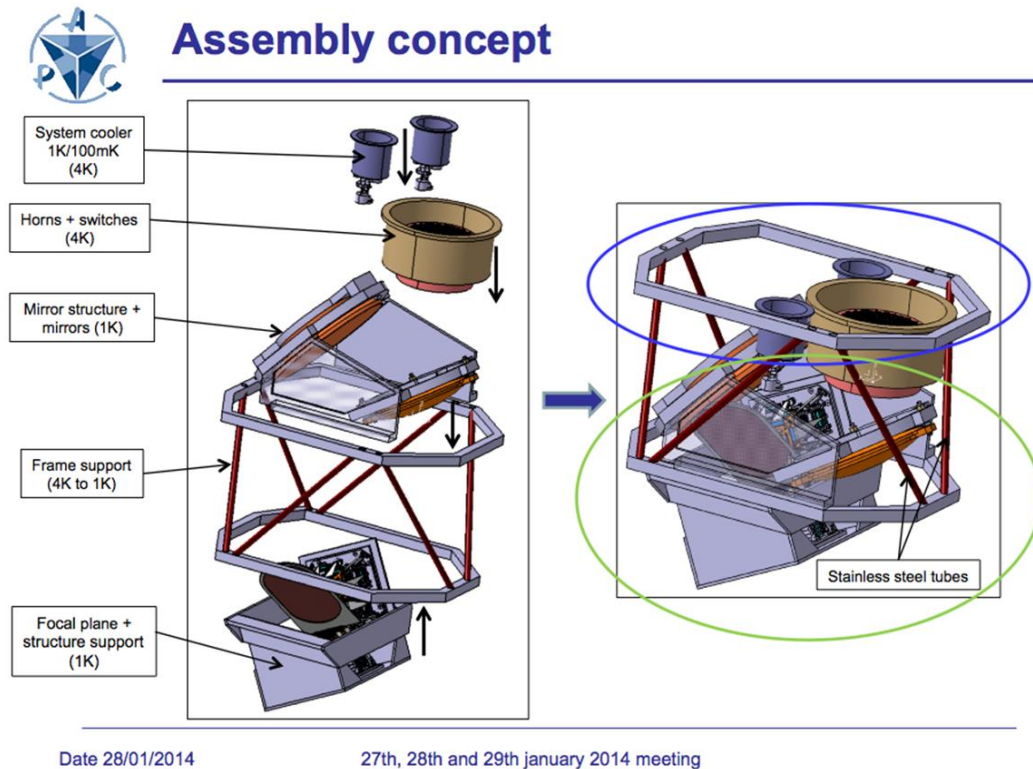


Figure 4.24: QUBIC assembly concept (private communication, APC 2014).

Using GBM visualisation in MODAL (Figure 4.25) for a detector plane separation ranging from 88.4 mm (blue) to 110 mm (black) we can see that the position of the side detector is very close to the primary mirror. The two detector planes are shown at 90° to one another with the polariser equidistant from both detectors and bisecting the angle at 45° to each. Taking into account the electronics that will be required behind the detector plane there is not enough room to position the components in this orientation. Increasing the angle between the detector planes, causing the polariser to rotate in the direction of the purple arrow in Figure 4.25 will result in increasing spillover at the polariser. Decreasing the angle between the detector planes will result in the detector plane moving into the path of the incident rays. It can be concluded that this layout is unfeasible due to the blockages, spillover and the second detector plane impeding upon rays at the primary mirror.

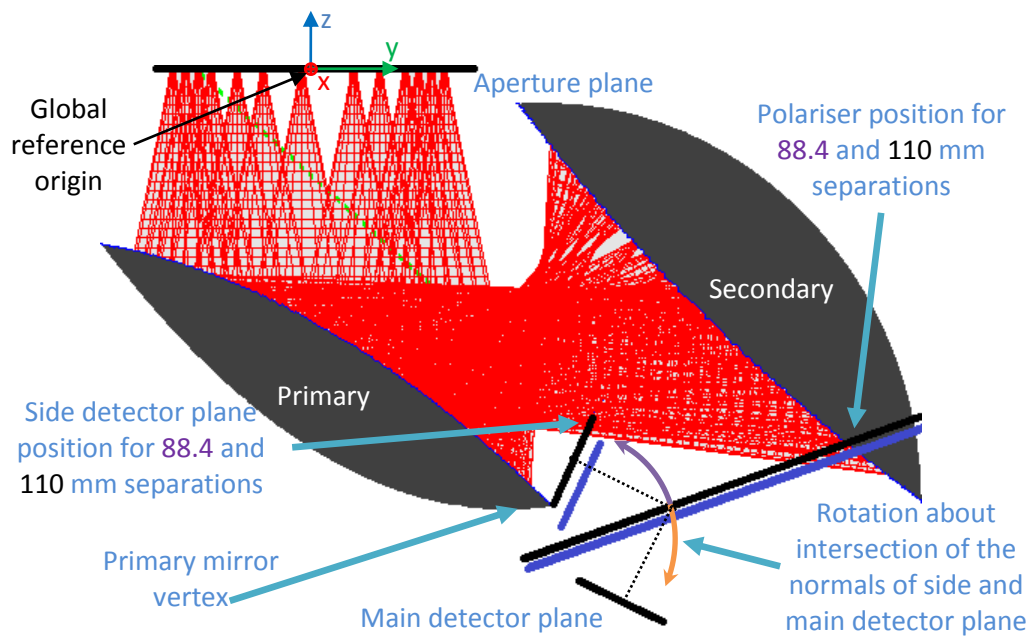


Figure 4.25: QUBIC GBM simulation in MODAL showing the position of the polariser (90 mm separation in lilac and 110 mm separation in black) facing the primary mirror. The side detector plane is placed between the primary and secondary. The side detector plane and the associated electronics obstruct the path of the incoming radiation. The secondary to detector plane rays have been omitted for clarity.

By reversing the orientation as shown in *Figure 4.26* the problem with the second detector plane causing an obstruction is reduced but a polariser large enough to capture the beam from the secondary mirror now impinges the path of the beam from the primary to the secondary as highlighted by points A and B.

From *Figure 4.27* we can see that the issues are primarily related to the polariser which is impeding the beams propagating from the primary to the secondary. From *Figure 4.28*, which illustrates the reflections from the secondary mirror, we see that the polariser is insufficient in extent to ensure capture of all the sources. Rotating the polariser from the 45° position shown will result in the detector plane moving even further into the path of the incident rays (orange arc) or the detector plane impeding the secondary beams (purple arc). The blockages inherent in this orientation already require that the polariser is reduced even further and so we can conclude that the polariser in this orientation is also unfeasible.

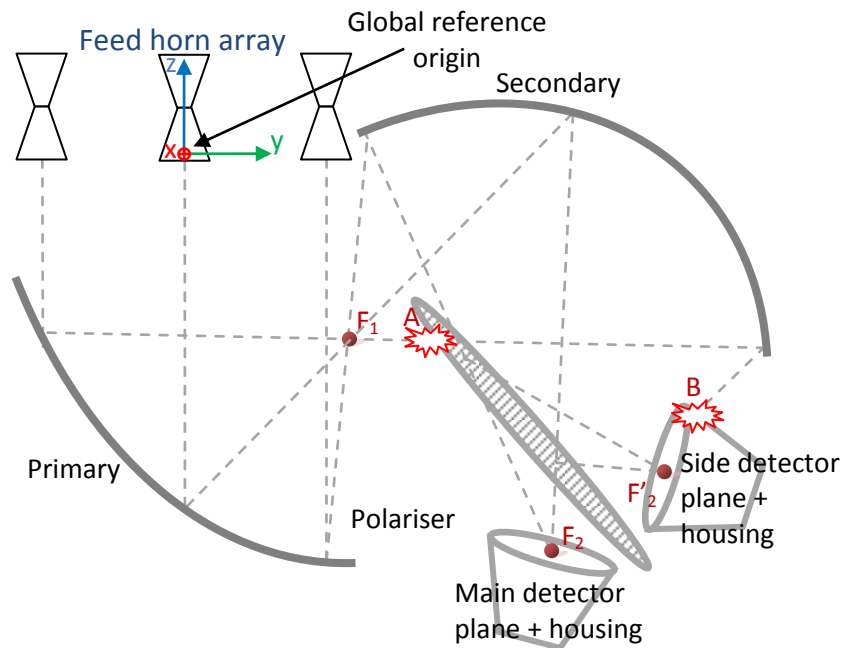


Figure 4.26: QUBIC (not to scale) schematic showing the position of the polariser facing away from the primary mirror. The side detector plane is now to the outside of the combiner. Here the blockages are minimised but the range of possible detector plane separations is hampered by the extent of the secondary at this part of the combiner.

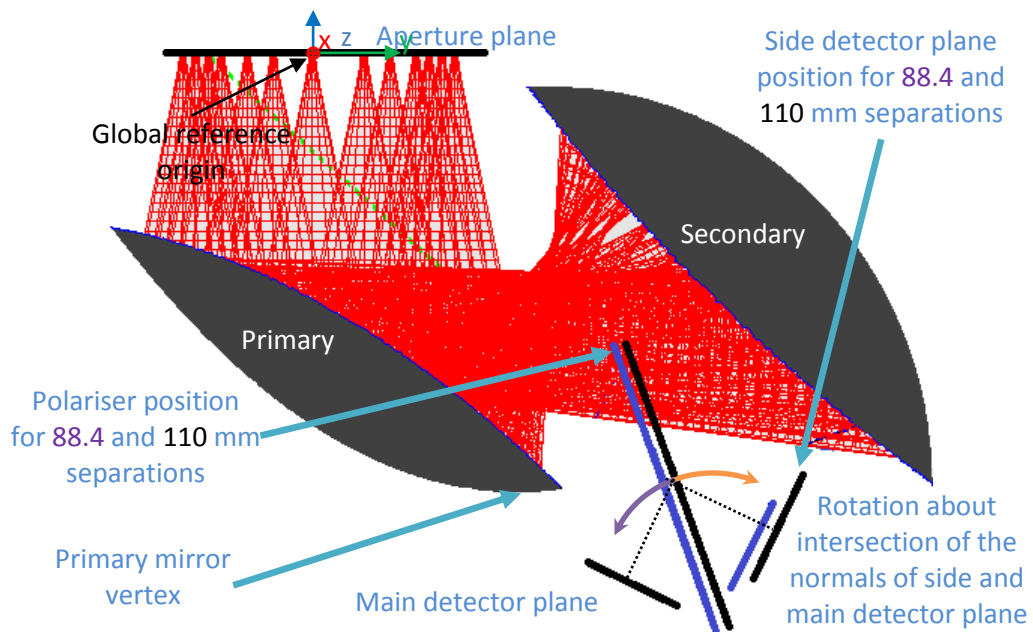


Figure 4.27: QUBIC GBM simulation in MODAL showing the position of the polariser facing away from the primary mirror. The side detector plane is now to the outside of the combiner. Here the blockages are minimised but the range of possible detector plane separations is hampered by the extent of the secondary at this part of the combiner. The secondary-to-detector-plane rays have been omitted for clarity.

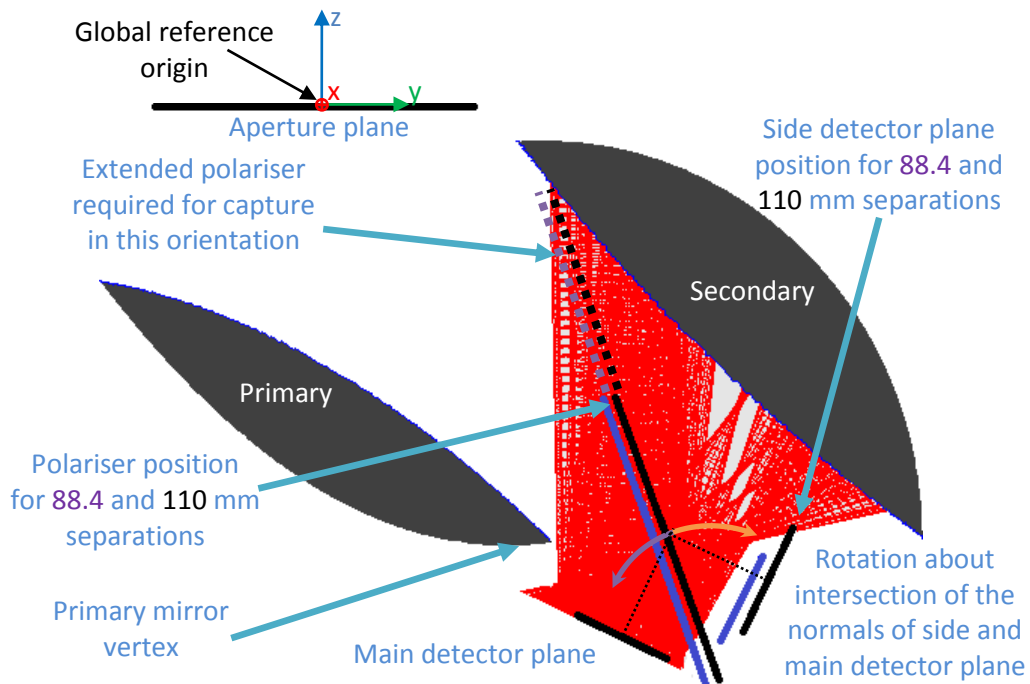


Figure 4.28: QUBIC GBM simulation in MODAL showing the position of the polariser facing away from the primary mirror with rays from secondary mirror shown. An extended polariser is required for the capture of rays off of the secondary mirror. Rays from the input array and primary mirror have been omitted for clarity.

Next, the polariser and second detector were positioned to the side orientated out of the way of the beam paths. Due to the orientation of the polariser it is not immediately obvious if there are blockages in the system from the schematic in

Figure 4.29.

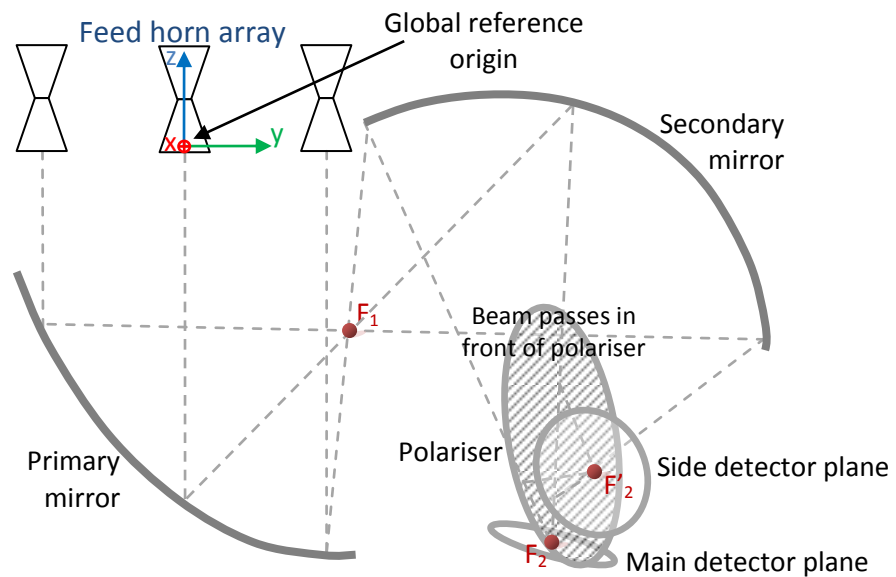


Figure 4.29: QUBIC (not to scale) schematic showing the position of the polariser facing side-on to the primary mirror. The side detector plane is now to the opposite side of the combiner. Here the blockages are minimised and the range of possible detector plane separations no longer hampered by the extent of the secondary at this part of the combiner.

From the simulation in *Figure 4.30* and *Figure 4.31*, using just a visual inspection we can see that blockages in the system are vastly reduced over that of the previous orientations. For the 110 mm separation, the polariser size seems to cater for capturing all beams and minimises leakage around the polariser. Rotating the polariser from 45° leads to leakage around the polariser (orange arc in *Figure 4.28*) or the side detector plane obstructing the path of the beams from the primary en route to the secondary (purple arc in *Figure 4.28*) mirror. The 45° orientation offers the best chance of enabling the inclusion of a polariser into the design of the QUBIC combiner.

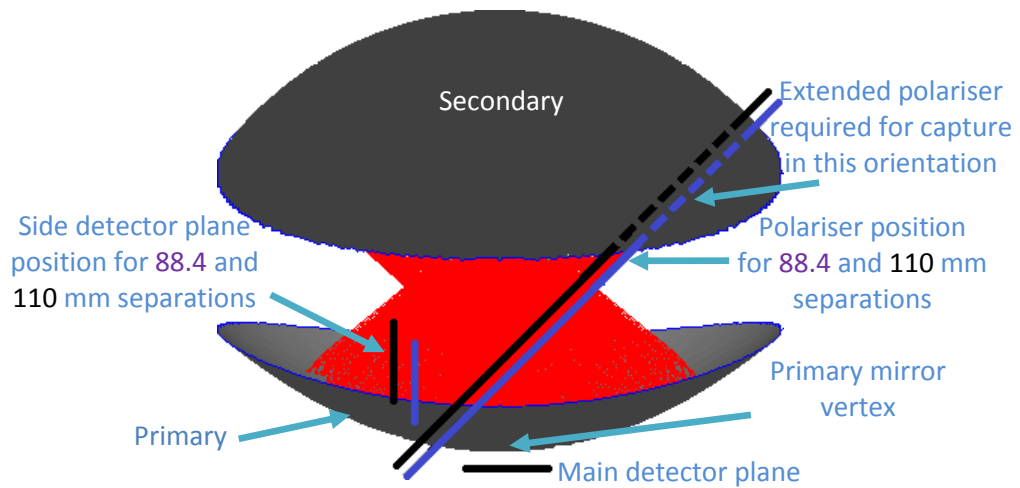


Figure 4.30: QUBIC schematic showing the position of the polariser (90 mm separation in blue and 110 mm separation in black) facing side on to the primary mirror. The side detector plane is placed on the opposite side of the combiner to the polariser. The source-to-primary and secondary-to-detector-plane rays have been omitted for clarity.

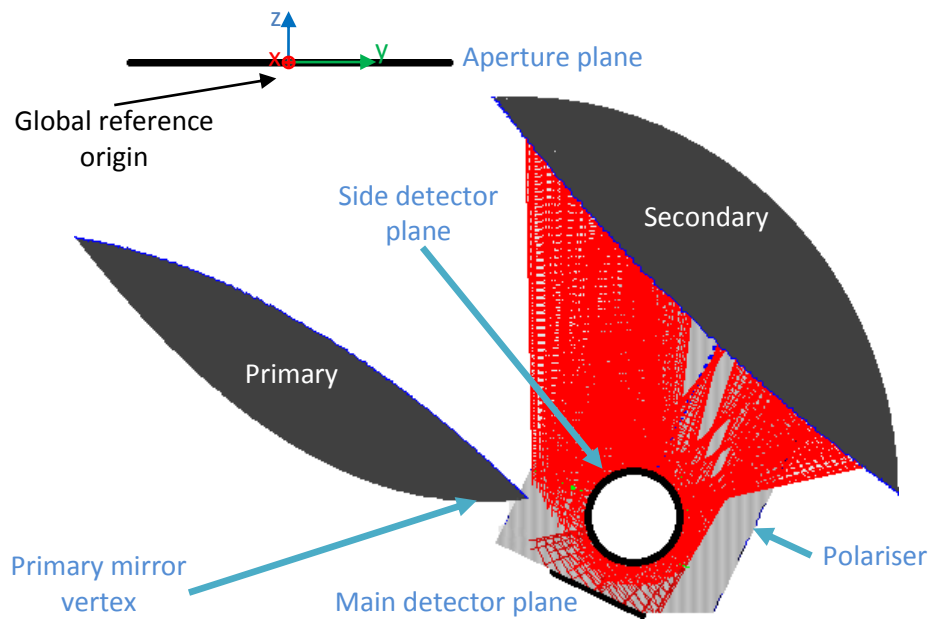


Figure 4.31: QUBIC schematic showing the position of the polariser at 90 mm separation. Shown here are the secondary to detector plane rays only which are convergent upon the polariser. This orientation offers the best chance at locating a polariser within the confines of the combiner.

4.3.2 Separation of polariser and side detector

The required size of the polariser and the detector plane separation distance are inherently linked. A larger separation of the detector planes requires a polariser positioned further from them; this requires a larger polariser to capture all power in the beams. *Figure 4.32* shows the combination of the beams from the edge sources out to $1w$. The side detector plane blockage indicates that beams in part pass behind the side detector plane.

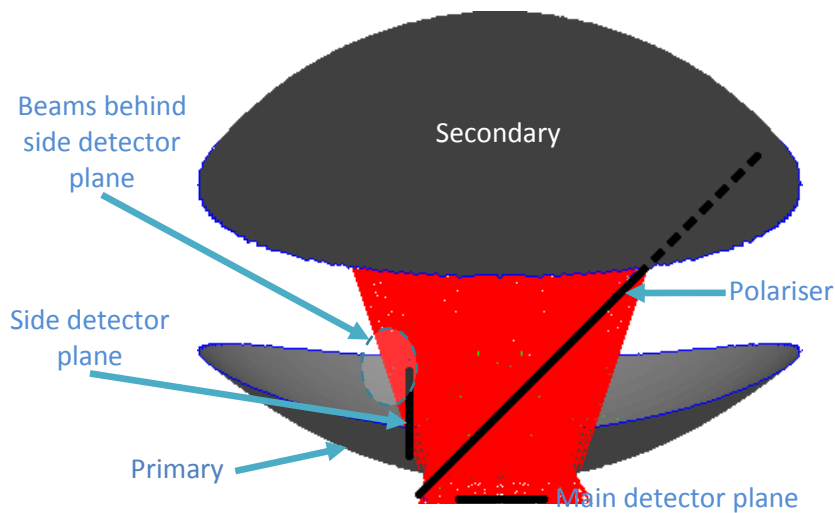


Figure 4.32: Blockages in the combiner resulting from the position of the side detector plane at a separation distance of 88.4 mm. Beams shown are edge sources out to 1W reflecting off the secondary mirror towards the polariser. The beams from the input array and primary mirror are omitted for clarity.

For beams reflecting off of the right hand side of the primary mirror in *Figure 4.32* and propagating up towards the left hand side of the secondary mirror there is a potential blockage possible. The extent of this blockage will depend on the final position, size and orientation of polariser and this will need to be catered for in a trade-off between the separation distances of the detector planes and the size of the polariser. This will be looked at in §4.3.3.

This visual inspection was repeated for each feed horn and a list was generated for those affected by this blockage. A total of 109 were affected at the 1.5w level and 69 at the 1w level. It should be noted only a small portion of these beams were blocked. The results are tabulated in *Table 4.5* and the affected feed horns shown in *Figure 4.33*.

Table 4.5: For a detector plane separation of 88.4 mm the sources affected depend on the criteria chosen (e.g.: 1.5w or 1.0w). X and Y are the feed horn indices.

X	Y (1.5w)	Y (1.0w)	Y (0.8w)
0-6	-	-	-
7	19-21	19-21	21
8	18-21	19-21	20-21
9	17-21	18-21	20-21
10	16-21	18-21	19-21
11	15-21	17-21	19-21
12	14-21	17-21	18-21
13	13-21	16-21	18-21
14	13-21	16-21	17-21
15	12-20	15-20	17-20
16	11-20	15-20	17-20
17	11-19	14-19	16-19
18	11-19	14-19	16-19
19	10-18	14-18	16-18
20	10-16	14-16	16
21	10-14	14	-

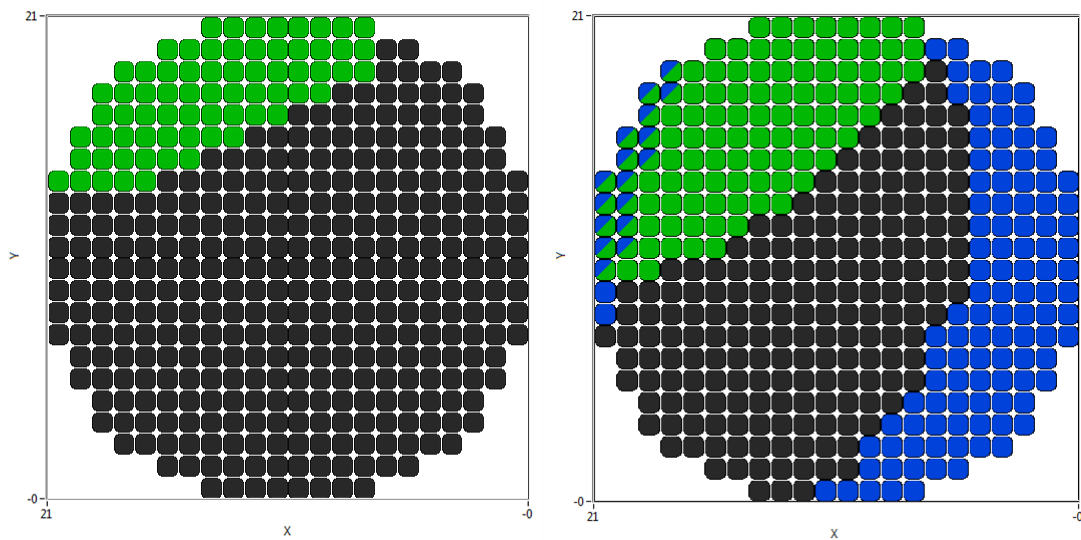


Figure 4.33: The result of a GBM visual inspection of feed horns at the 1w (left) and 1.5w (right) level in the MODAL simulation. If an intersection with the side detector plane occurred, to a beam propagating from the secondary mirror to the main detector plane, it is highlighted in green. If an intersection with the polariser occurred for a beam propagating from the primary to the secondary mirror, it is highlighted in blue. An 88.4 mm detector plane separation and a 2w polariser capture were used.

At the time of writing the exact side detector plane housing was not defined and so it was assumed that power to the rear of the side detector plane would be blocked. To quantify this blockage, a rectangular plane was placed above the side detector plane, as shown in Figure 4.34 in red. Power incident upon this plane is deemed

blocked by the side detector. The specific size, orientation and position was selected based on a simplification from early CAD models as a reasonable attempt to determine power to the back of the side detector and does not indicate any real device dimensions. The dimensions of the rectangular plane are $0.150\text{ m} \times 0.102\text{ m}$ and it sits directly above the side detector plane sloping upwards at an angle of 15° with respect to the normal of the side detector plane.

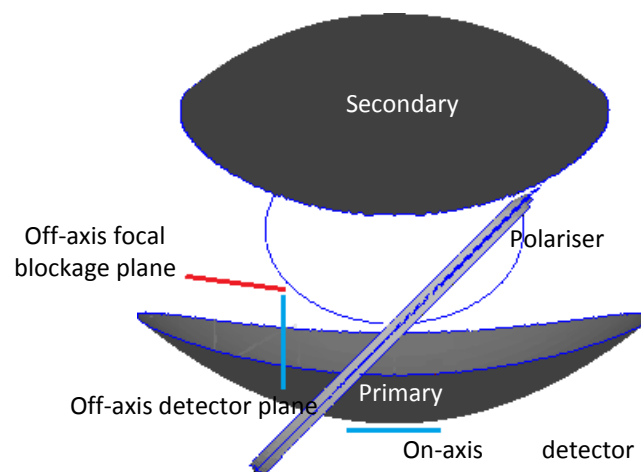


Figure 4.34: Side detector plane blockage shown in red as a plane that captures all power to the back of the side detector plane.

To help determine the extent of the blockage for beams en route to the detector plane a series of planes were created as shown in *Figure 4.35* and the beam footprints calculated on each. The system was setup as before with the source plane at a distance of 466.76 mm from primary mirror. The footprint output planes are numbered from 1 (closest to the detector plane) to 12 (closest to the secondary mirror). The dimensions of the output planes are 550 mm \times 600 mm (projection size of secondary mirror onto detector plane reference frame). The distances from the detector plane to the footprint planes are 40, 50, 60, 70, 80, 90, 100, 110, 120, 130, 140 and 200 mm respectively.

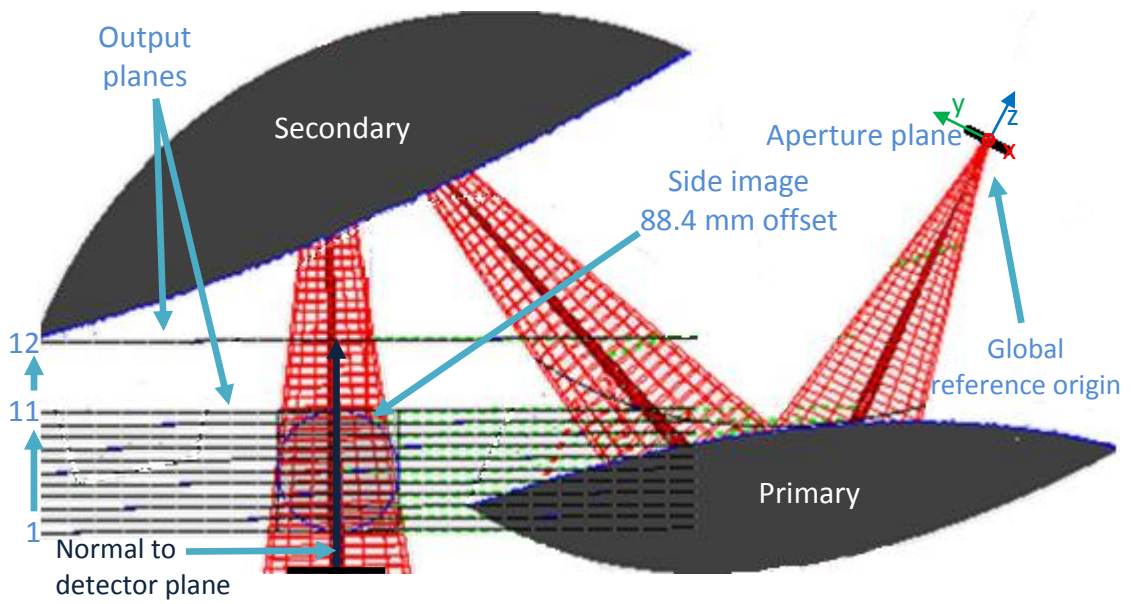


Figure 4.35: QUBIC system setup for calculation of the blockage caused by the side detector plane and associated mountings.

Figure 4.36 shows the footprints on the planes as defined in *Figure 4.35* with the side detector plane blockage superimposed for an 88.4 mm detector plane separation in purple and 110 mm detector plane separation in black.

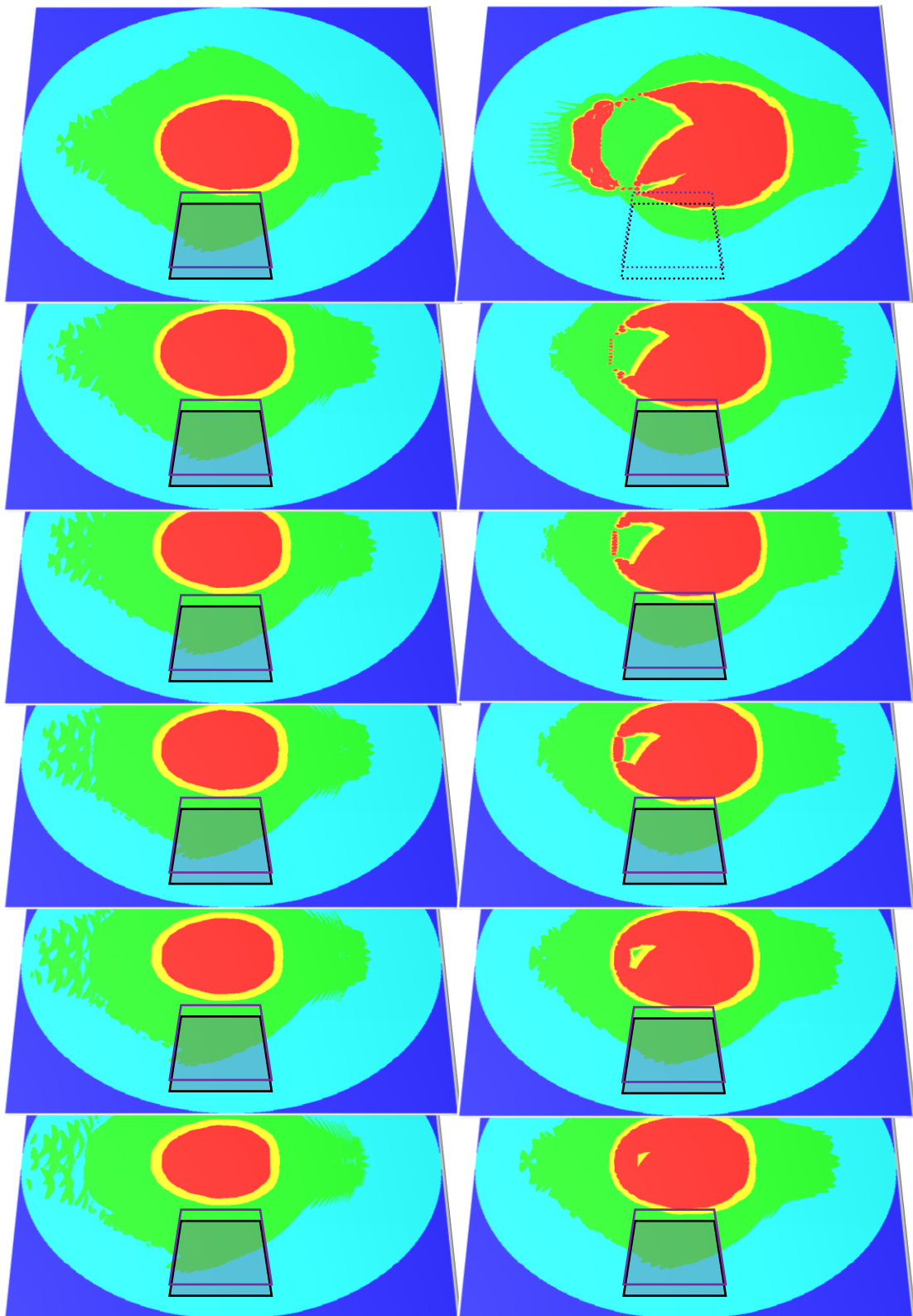


Figure 4.36: Left hand side, from bottom to top, are the footprints at 40, 50, 60, 70, 80 and 90 mm offset along the normal from the detector plane as shown in Figure 4.35. Right hand side, from bottom to top, are the footprints at 100, 110, 120, 130, 140 and 200 mm offset along the normal from the detector plane. The sources used are the edge sources and those most likely to be blocked to some degree. The black box indicates the approximate position of the side detector plane at 88.4 mm and magenta at 110 mm separation.

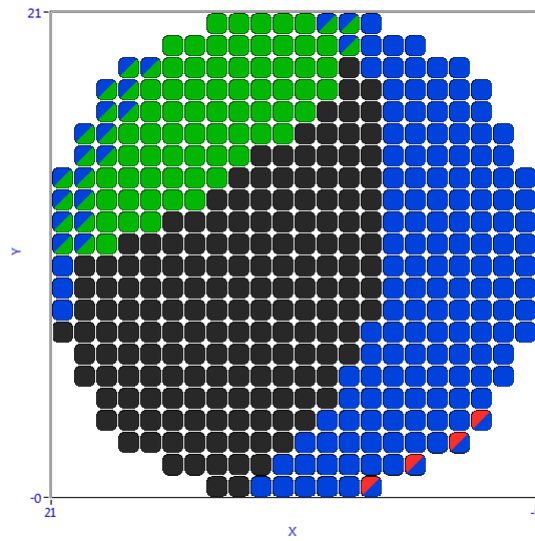


Figure 4.39: The result of a GBM visual inspection of feed horns intersected by the side detector plane at the $1.5w$ (99% of the beam) level in MODAL simulation. The detector planes were separated by 100 mm and the polariser was sized to capture beams out to $r = 2w$. If an intersection with the side detector plane occurred, while a beam traversed from the secondary to the main detector plane, it is highlighted in green. If an intersection with the polariser occurred, for a beam in transit from the primary to the secondary, it is highlighted in blue. Highlighted in red are beams that cannot be fully captured by the polariser. Split colouring indicates both aberrations apply to that source.

Figure 4.40 shows an overview for 110 mm separation. The polariser is sufficiently sized to capture the entire beam where possible (out to $r = 2w$ of the beams). The visual inspection of the blockages is calculated out to $1.5w$ as at $2w$ tiny, but non-zero, percentages of a majority of beams were found to intersect the polariser. In order to better determine the level of impact of the blockage, the beams were investigated out to $\sim 99\%$ of total power ($r = 1.5w$) where it was more apparent which beams were intersecting the polariser to any significant level. The number of feed horns shadowed by the side detector (shown in green) drops and the number of those affected by the polariser (shown in blue for shadowing and red for loss of capture) increases. There are now about 11 beams that the polariser is unable to completely capture.

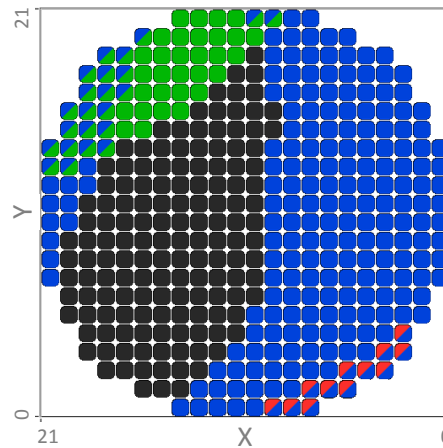


Figure 4.40: The result of GBM visual inspection in MODAL showing which feed horns correspond to beams intersecting components within $r = 1.5w$. Green shows side detector plane intersection for beams traversing from the secondary to the main detector plane. Blue shows if an intersection with the polariser occurred for beams propagating from the primary to the secondary. Red shows beams that cannot be fully captured by the polariser. Split colouring indicates both aberrations apply to that source. The detector plane separation was 110 mm.

Using PO, the percentage of power from each feed horn incident on the detector plane was calculated and is illustrated in Figure 4.41. The number of sources affected was 34 and all were located in one corner of the source array. The maximum power blocked is 8% for source x14y21.

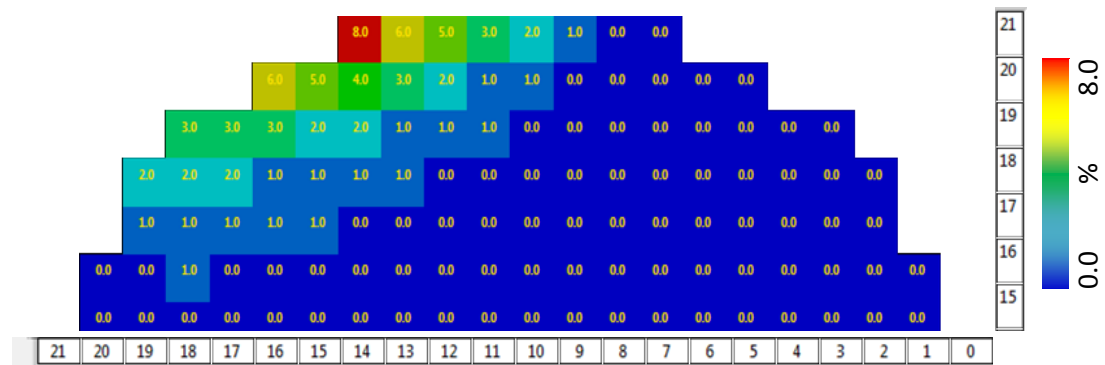
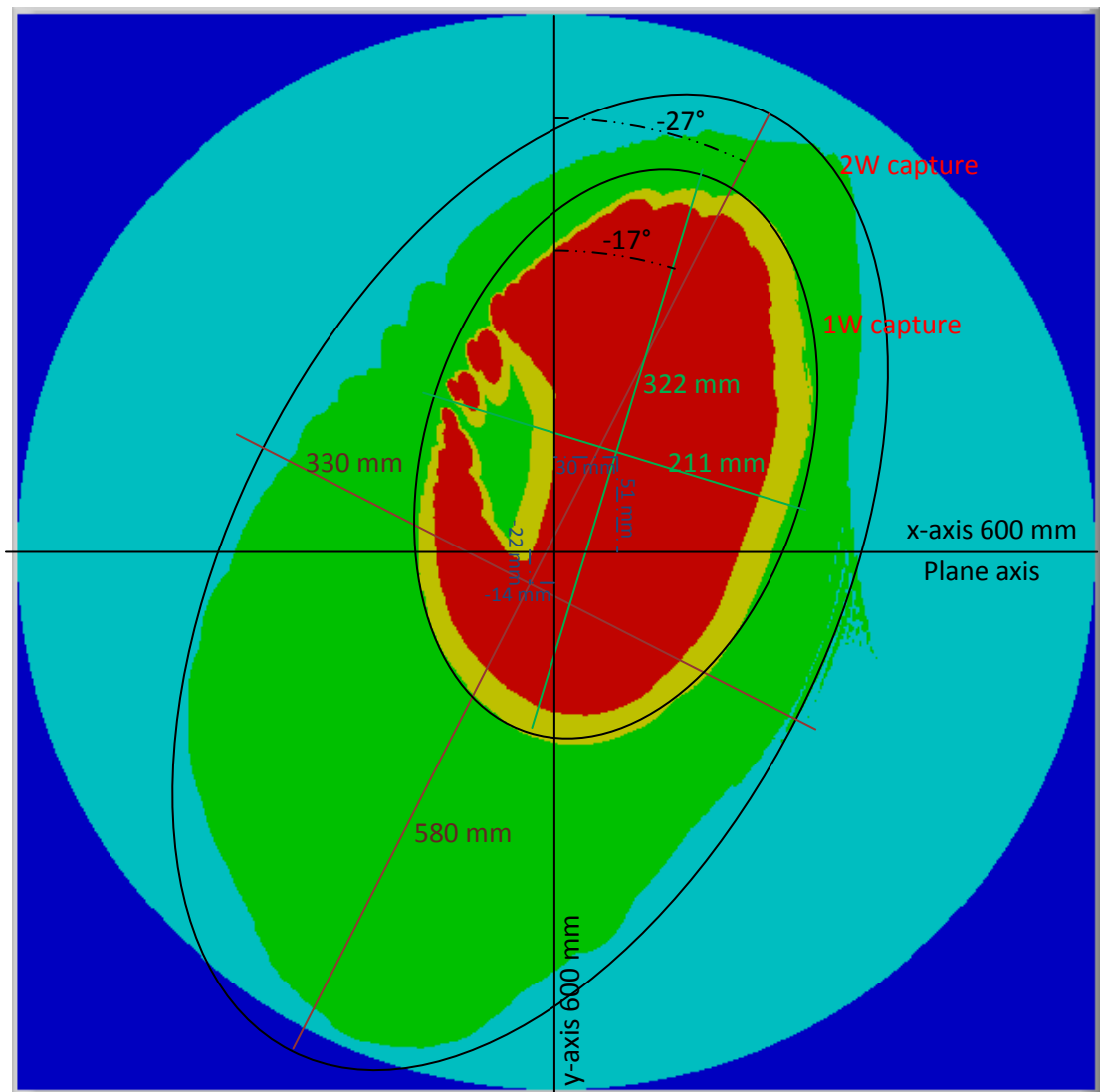


Figure 4.41: Blockage by the side detector plane for a 110 mm detector plane separation. The feed horn corresponding to each power value is indicated by its x and y value.

This work shows that detector blockage increases with decreasing detector plane separation. Increased separation distance however requires a larger polariser but the polariser is an obstruction for beams traversing between the primary and secondary mirrors. A design trade off is evident but optimising the shape of the polariser may mitigate this effect to some degree. A decision on the selection of the optimum detector plane separation distance will require determination of the shape and extent of the polariser. This is discussed next.

4.3.3 Determination of polariser dimensions

Starting with a detector plane separation distance of 88.4 mm the optimum size of the polariser was determined (balancing the detector and polariser blockages as described in §4.3.2). For this a large circular plane measuring 600 mm × 600 mm was centred at the intersection of the detector plane normals and tilted at 45° (as illustrated in *Figure 4.30*). The polariser's local coordinate system is defined as this centre point (as shown in *Figure 4.23*). The footprint of the edge feed horn beams was then calculated using PO and the shape, orientation and offsets of the polariser required for beam capture were calculated as shown in *Figure 4.42*.



*Figure 4.42: Polariser footprint for an 88.4 mm separation at 150 GHz for a 14° beam. The test plane is 600 mm in diameter with x- and y-axis along those of the local reference frame, as defined in *Figure 4.23*. The colour scheme is the same as in *Figure 4.5* image key.*

Analysis of *Figure 4.42* yielded the results tabulated in *Table 4.6*.

Table 4.6: 88.4 mm separation polariser parameters. See Figure 4.42 for an explanation of the parameters.

	1w capture	2w capture
Rotation about local z-axis (°)	-17	-27
Height (mm)	$600 \times (8.61/16.06) = 322$	$600 \times (15.52/16.06) = 580$
Width (mm)	$600 \times (5.63/16.06) = 211$	$600 \times (8.82/16.06) = 330$
Centre Offset X (mm)	$600 \times (0.81/16.06) = 30$	$600 \times (-0.37/16.06) = -14$
Centre Offset Y (mm)	$600 \times (1.36/16.06) = 51$	$600 \times (-0.60/16.06) = -22$

From this analysis an elliptical polariser of size 580 mm × 330 mm with centre offsets of -14 mm and -22 mm and a rotation of -27° about its normal will capture almost all power from all feed horns, ignoring for the moment blockages caused by the polariser itself.

For the 110 mm separation the design was modified to minimise the size of the polariser and hence the blockages within the combiner. After running several simulations the parameters and shape for the polariser were selected: rotation about $z = -25.2^\circ$, a centre point translation $x' = 10$ mm and $y' = 52$ mm and surface dimensions of width = 240 mm and height = 460 mm. The bounding volume is a union of an ellipse and a rectangle. The simulation implementation in MODAL is shown in *Figure 4.43* with the specifics of the polariser illustrated in *Figure 4.44*.

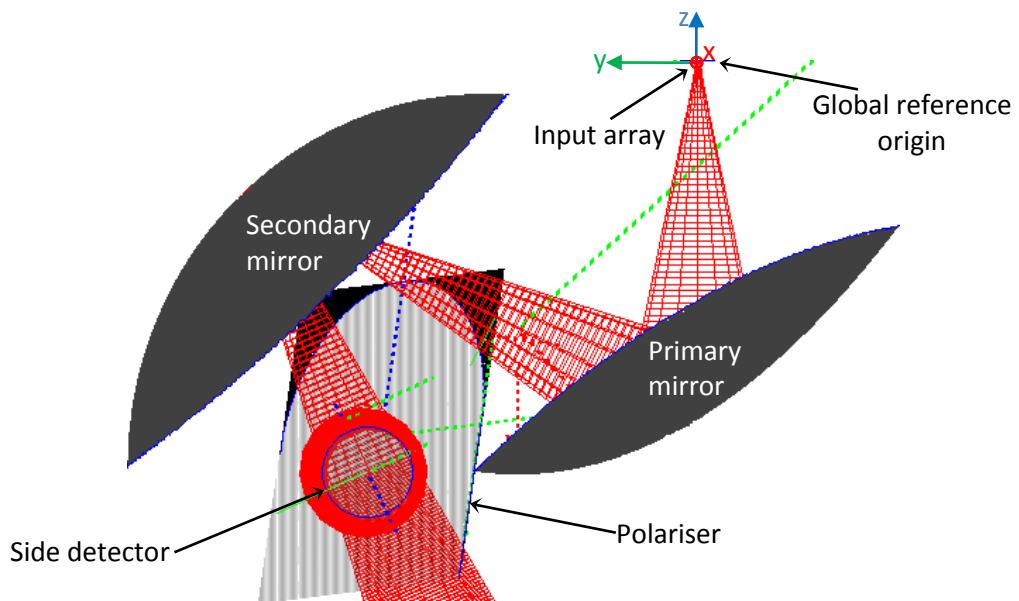


Figure 4.43: Optimised polariser in the QUBIC combiner (detector plane separation of 110 mm)

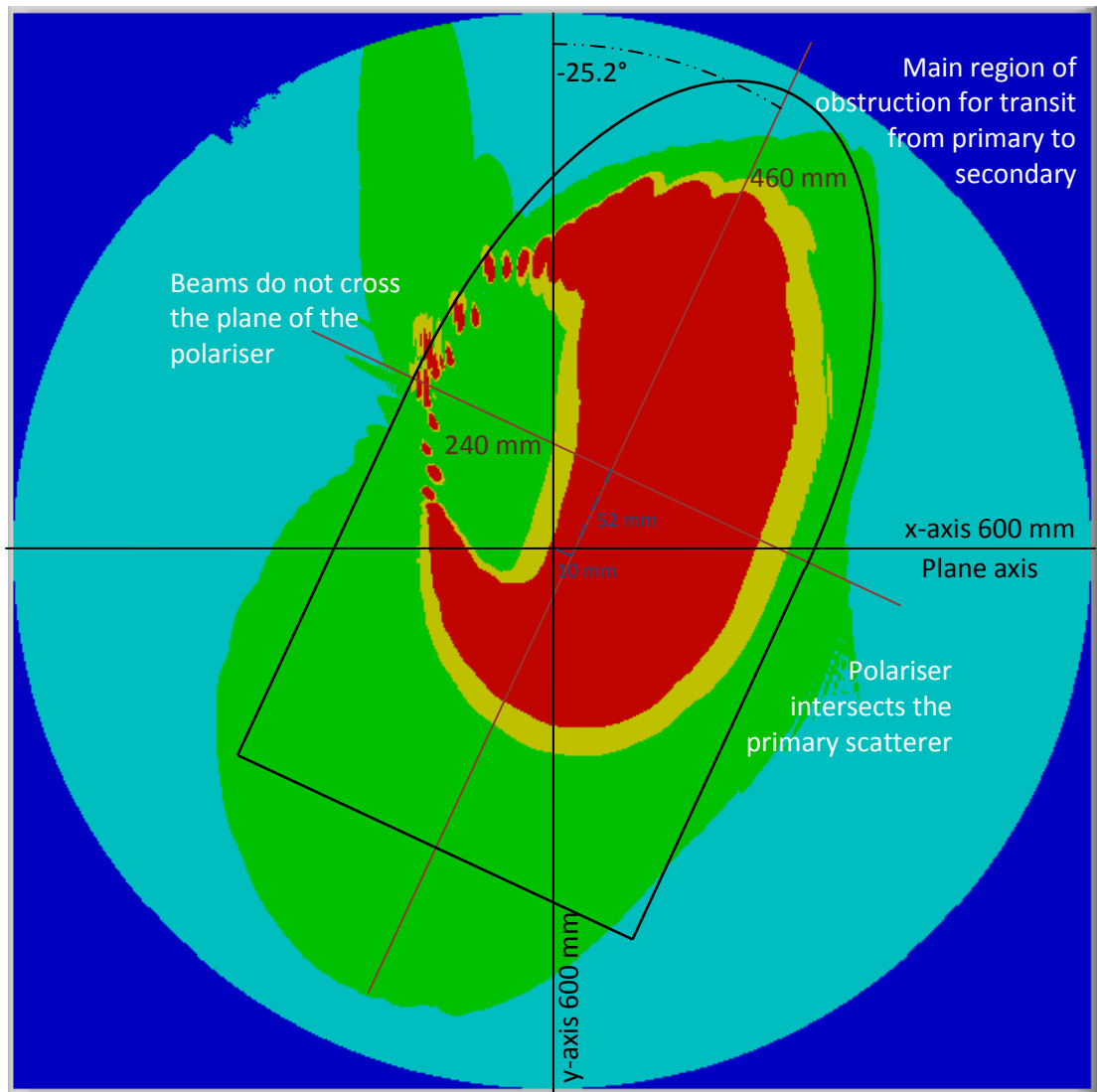
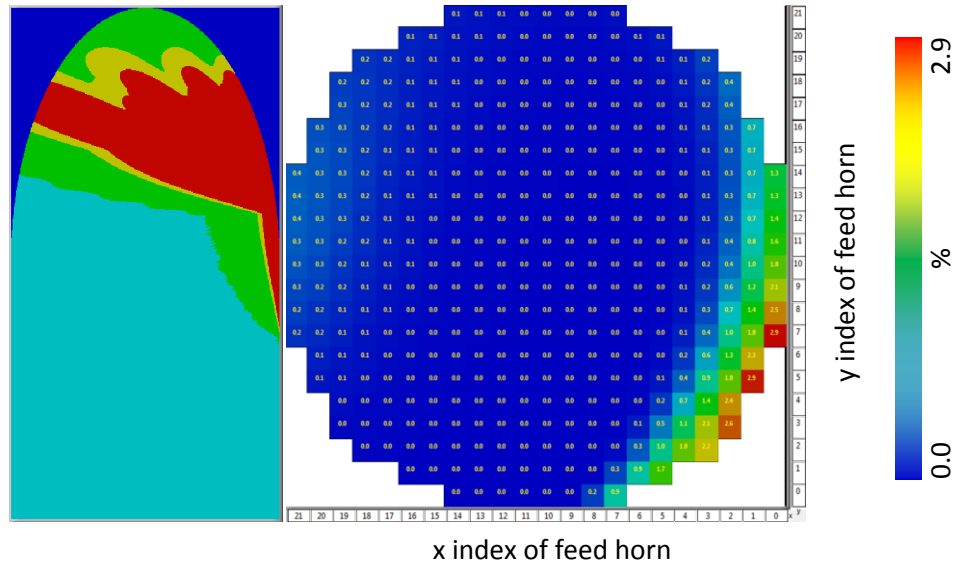


Figure 4.44: Polariser footprint for a 110 mm detector plane separation at 150 GHz for a 14° beam. The test plane is 600 mm in diameter with x- and y-axis with respect to local reference frame, as defined in Figure 4.23. Colour is the same as in Figure 4.5 image key.

Using the design in Figure 4.44 the power blocked by the polariser for beams in transit from the primary to the secondary mirror was calculated. This simulation was implemented in MODAL by replacing the polariser by an aperture, where the power through the aperture (of exactly the same position, orientation and size as the polariser) is the power blocked by the polariser. The effect this blockage had on the secondary mirror's incident beam profiles was not so easy to calculate. At this stage a new feature was added to MODAL which allows the subtraction of one field from another. The total field on the secondary in the absence of the polariser was first calculated. Next, the field on the polariser aperture (blocked field) was

calculated. The polariser aperture field was then propagated to the secondary mirror and subtracted from the total field leaving just the field that was not blocked. *Figure 4.45* shows the percentage power blocked by the polariser for beams traversing from the primary to the secondary mirrors. The worst affected sources are those in the bottom left corner, reaching up to 2.5% of the beam's power.



*Figure 4.45: 110 mm detector plane separation polariser operating at 150 GHz for 3.074 mm waist (14° Gaussian). Left is the footprint of the beams blocked by the polariser and right an overview of the power blocked by the polariser for beams propagating from the primary to the secondary. The feed horn corresponding to each power value is indicated by its x and y value. Colour is the same as in *Figure 4.5* image key.*

All sources were propagated onto the polariser taking into account all the blockages in the system up to this point. The design captured an average of 98.9% of the power emitted by the sources as shown in *Figure 4.46*. Some further reductions could be made by removing the remaining section in cyan, as shown in *Figure 4.46*, but as this part of the polariser does not contribute to the shadowing in the combiner this is not required. This analysis shows that in principle the combiner is capable of accommodating a polariser into the existing layout, although it does cause some blockages.

Figure 4.46 also shows the power at the polariser taking into account the impact from each element due to capture losses or blockages. The power missing can be classed into 4 categories, power lost at the primary mirror due to truncation, power

that does not get through the polariser, polariser blockage on route from the primary to the secondary mirror and off-axis detector plane blockage. A trade-off for the polariser position and shape was made to achieve a balance between the power blocked on the way from the primary to the secondary mirror and the power transmitted from the secondary mirror to the detector plane.

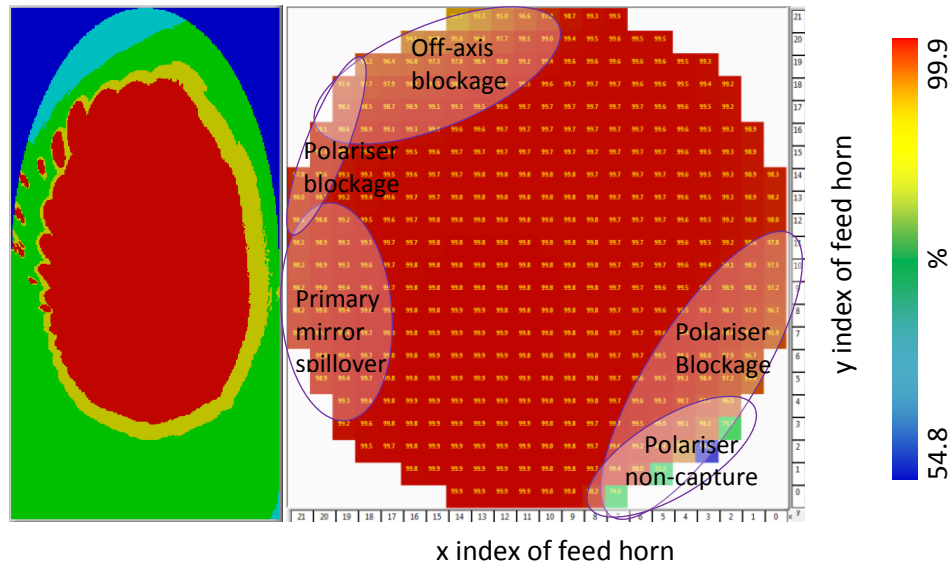


Figure 4.46: 110 mm detector plane separation polariser operating at 150 GHz for 3.074 mm waist (14° Gaussian). Left is the footprint of the beams incident on the polariser and right an overview of the power captured by the polariser for beams incident upon reflection off of the secondary. The feed horn corresponding to each power value is indicated by its x and y value. The colour scheme is the same as in Figure 4.5 image key.

The author issued a report to the QUBIC group (*private communication, QUBIC group, 2013*) detailing results found in this section. The conclusion was that some blockage within the combiner is unavoidable but given the low levels the design the combiner is capable of housing a polariser. It was also noted that, if required, the affected feed horns can be switched off. In mid 2013 a decision by the consortium to use the polariser position, orientation, shape and size as detailed in *Table 4.7* was made with the selection of the 110 mm separation (a final decision was pending a modification to the design of the combiner as will be discussed in Chapter 6). At this point in the project the collaboration favoured the larger (110 mm) separation as it would better accommodate the likely size of the detector plane electronics.

Table 4.7: QUBIC element optimised sizes. Translations and rotations are with respect to the elements local reference frame.

	Translation (mm)			Rotation (°)			Dimensions (mm)		
	X	Y	Z	X	Y	Z	X	Y	Z
Primary mirror	190						480	600	
Secondary mirror	-130						600	600	
Polariser	-10	52				25.2	240	460	

Until now it has been assumed that all power hitting the polariser will reach the detector plane and could be detected. However, there is a degree of cross-polarisation introduced by the combiner, as shown in work done by Gayer (Gayer, 2015) and, taking the cross-polarisation into account, power levels on each detector plane will vary. To determine the extent of this, the polariser's optical axis was aligned with the global reference frame x-axis and a Gaussian beam excitation source polarised along the same axis was used. The field incident on the polariser will result in the x-component being transmitted and the y-component being reflected off of the surface onto the side detector plane. The levels of transmission are shown in Figure 4.47, where the image on the left shows the x-polarised power transmitted through the polariser and for comparison on the right hand side the total power when the polariser is represented as a clear aperture.

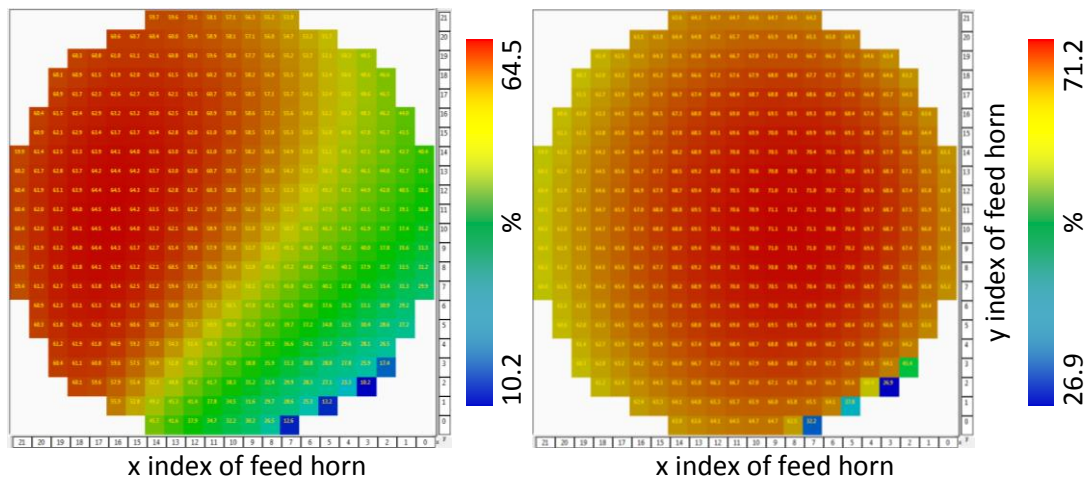


Figure 4.47: On the left is an overview of the power transmitted by the polariser and on the right is equivalent when the polariser is replaced by a clear aperture. The source corresponding to each power value is indicated by its x and y value. These results are for a polariser designed for a 110 mm detector plane separation and operating at 150 GHz for 3.074 mm waist (14° Gaussian) x-polarised (x-axis of the global reference frame).

The degree of instrumental polarisation in the design is large, at up to $\sim 40\%$ in the worst cases (e.g.: x03y03 with 64.1% of the power detected in total \rightarrow 25.9% x-polarised and 38.2% y-polarised), 0% in the best and a average of $\sim 14\%$.

4.3.4 Polariser optical surface imperfections

The polariser is one of the most important components of the QUBIC combiner and as such some measurements were carried out in the vector network analyser (VNA) laboratory to determine the degree to which modelling can determine the impact of polariser optical surface distortions and aberrations. Available equipment limited the possible testing to a 140 mm diameter circular polariser with 10- μm diameter tungsten wires spaced 25 μm apart (QMC Instruments, 2012) and a 100 GHz source. The source was a feed horn, as shown in *Figure 4.48*. A simulation was first set up to predict the effects of polariser orientation (*Figure 4.49*).

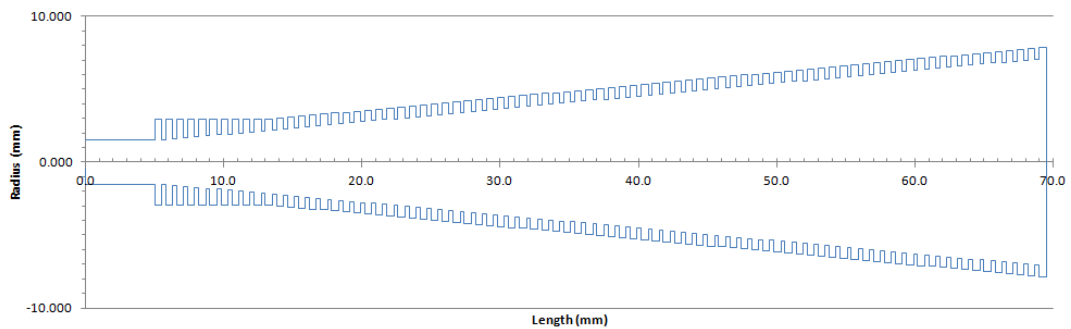


Figure 4.48: Profile of the TK feed horn designed for operation at 100 GHz.

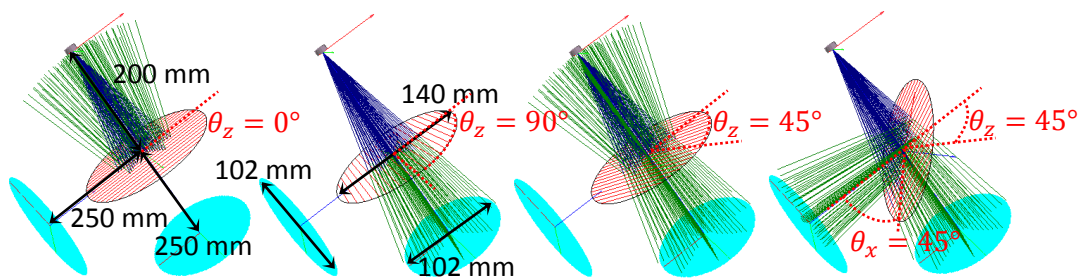


Figure 4.49: GRASP polariser simulation: Left is for the alignment of the polariser grid optical axis and excitation sources yielding 0% transmission. Second is the rotation of $\theta_z = 90^\circ$ about the polariser normal axis to yield 100% transmission. Third is the rotation back by $\theta_z = 45^\circ$ to yield a partial transmission and reflection. Right is the tilting of the polariser by $\theta_x = 45^\circ$ for the case of partial transmission/reflection.

Rotating the polariser by 45° about the polariser normal and tilting it by 45° off-axis (right-most picture in [Figure 4.49](#)) we have a setup that approximates the one used in QUBIC, where the beam is split into its constituent components and projected onto 2 detector planes for independent analysis. Each detector plane receives a component of the incident beam. Simulations were carried out in GRASP (using a tabulated field as the source) and MODAL (using the feed horn geometry with a 100 GHz plane-wave excitation source) with results tabulated in [Table 4.8](#). The relationship between polarisation direction angle and power transmitted (the difference between the 2 angles being θ) is given by Malus's law, $P_{Transmitted} = P_{Incident} \cos^2(\theta)$ (see for example Collett (Collett, 2005)). As can be seen in [Table 4.8](#) the polariser model in both GRASP and MODAL follows this distribution of transmitted power and the side image plane only receives power in cases where the polariser is correctly angled towards it.

Table 4.8: Results from simulations of transmission and reflection properties of polarisers in MODAL (equivalent to results from GRASP) for various angles (angle measured for polariser optical axis with respect to incident radiation polarisation angle)

Angle θ_z ($^\circ$)	Angle θ_x ($^\circ$)	Power Transmitted (%)	Power reflected (%)	Power at image main (%)	Power at image side (%)
0.0	0.0	0.00	97.92	0.00	0.00
22.5	0.0	14.34	83.58	5.83	0.00
45.0	0.0	48.96	48.96	19.92	0.00
67.5	0.0	83.58	14.34	34.01	0.00
90.0	0.0	97.92	0.00	39.84	0.00
0.0	45.0	1.37	92.21	0.11	39.61
22.5	45.0	23.75	69.45	10.19	29.54
45.0	45.0	61.57	31.36	26.47	13.26
67.5	45.0	85.63	7.57	36.57	3.15
90.0	45.0	93.20	0.00	39.73	0.00

For $\theta_x = 0$ the polariser captures $\sim 98\%$ of emitted power and at $\theta_x = 45^\circ$ the tilting of one side of the polariser away from the source results in a drop of $\sim 5\%$ in the power captured. At the image plane the power captured is $\sim 40\%$. In the QUBIC combiner beams are incident on the detector plane from various angles depending how far towards the edge of the secondary they originate. The angles extended by

the secondary are shown in *Figure 4.50* (GRF y-axis shown although incident angle varies along the x-axis also).

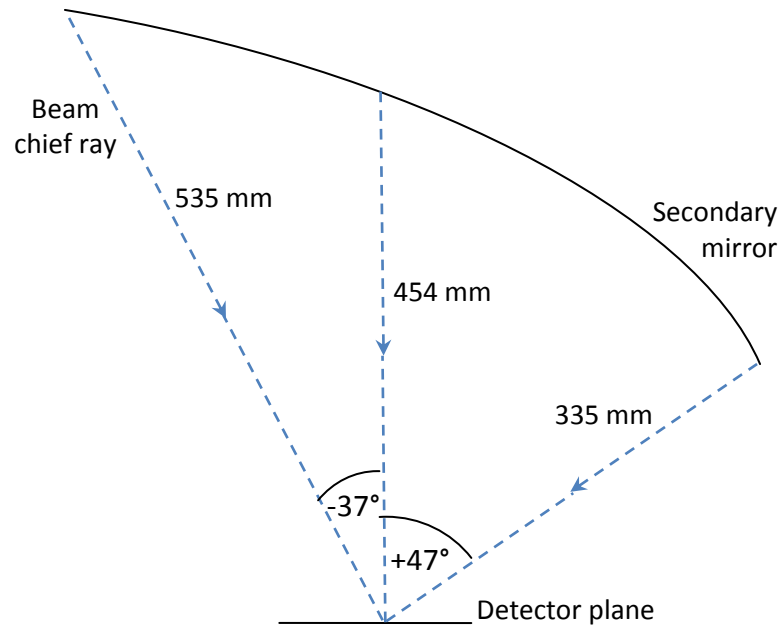


Figure 4.50 QUBIC system extremes of beam incident angle on the detector plane

Various incident angles and orientations of polariser wire grids were tested. For these tests the VNA was used to measure both amplitude and phase of the signals transmitted through the polariser. The VNA has a built-in signal generator capable of generating frequencies in the range of 75 GHz to 110 GHz (W-band). The first step was configured for 2-port measurement, giving us access to all S_{11} , S_{12} , S_{21} and S_{22} , parameters. In order to determine system parameters accurately the VNA had to be correctly aligned and calibrated before each use (apart from periodic manufacturer apparatus calibration) following the procedure as detailed by Tynan (Tynan, 2015) and described briefly here. The method used in Maynooth University's VNA laboratory is called TOSM (Through, Offset, Short, Match) (Hiebel, 2008). The order of the calibration components is irrelevant, as once all data are available, the VNA can compensate for systematics.

Firstly, the emitter and detector heads are screwed together creating the first test, 'Through', as shown in *Figure 4.51*. The VNA determines insertion loss and electrical insertion length (~ 0 mm in this test). Next the heads are separated and a short is

placed on each head (separately if required, if only one short is available). The short causes all power to be reflected back through the head to the VNA, with a reflection coefficient of 1 in the ideal case. The known length, l , allows the VNA to determine the electrical characteristics such as inductance for each head. The same test is then done with the addition of a $\frac{1}{4}\lambda$ offset between the short and the head allowing additional characteristics such as parasitic inductance to be calculated. Finally a match (nominally a 50Ω device) is attached to each head (again separately if required) which acts as an absorber allowing the VNA to determine reflection coefficients.

The tests are carried out over the frequency range of operation (75 GHz – 110 GHz) and the configuration data are stored on the VNA. The last three tests (single port tests) allow the determination of: source match, directivity, and reflection tracking, for each head. All four tests combined in dual directions allow the determination of faulty connections and cross-talk coefficients.

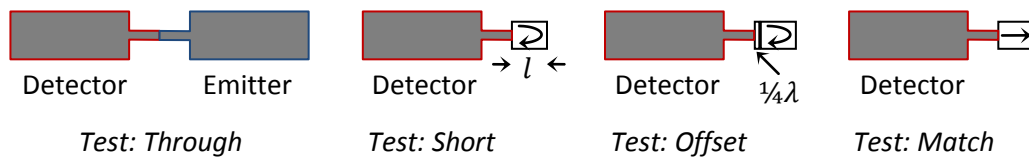


Figure 4.51: VNA setup, showing detector/emitter setup for test; through, offset, short and match.

With the system calibrated the next step was to align the various components. First the translation stage was aligned to the scan plane. Three scans are taken at known but different z -translation distances from the scan plane. The translation stage shifts the emitter head along the translation stage axis (shown in [Figure 4.52](#) in green). If there is a misalignment of the scan-plane to the translation stage propagation axis this will show in a shift in the position of the peak in each of the 3 scans allowing for correction of α_T . Secondly the alignment of the detector head to the emitter head: the same scans already taken are re-used but the image is analysed to check for symmetry in the phase, the asymmetry is used to correct for α_E . Finally with everything centred the alignment of the detector, α_D , is achieved by

moving the detector head until maximum amplitude is detected. This is a brief summary of the alignment procedure for the VNA for a 1D case. The same approach is used in 2D where the scans also give the offsets for, β_x (orthogonal angular offset where x refers to D, E and T as used in α calculations).

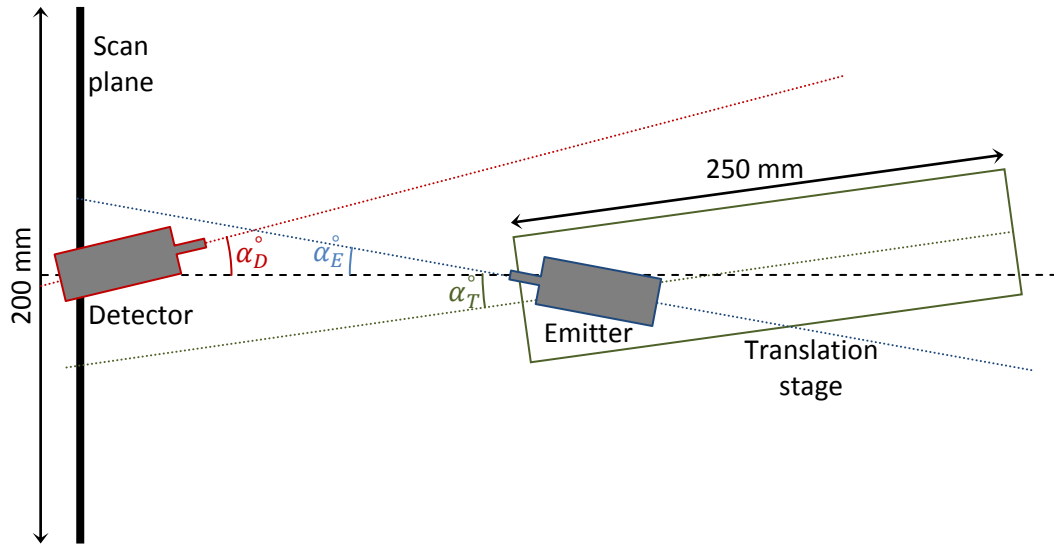


Figure 4.52 VNA setup, showing the translation stage, scan plane and emitter and detector heads.

Once the system is calibrated and aligned, the VNA can be used to determine the properties of the device under test (DUT), in our case the polariser. The QUBIC feed horns were not available for testing, therefore a feed horn available in the laboratory, called the TK feed horn, profile as previously shown in [Figure 4.48](#), was used.

MODAL was used to predict the 100 GHz beam radius at several propagation distances from the feed horn aperture. At 220 mm away it was found to be ~ 51 mm, ~ 76 mm at 330 mm and ~ 102 mm at 440 mm. These values were used to find the waist of the best fit equivalent Gaussian of 4.1 mm (giving an equivalent $\sim 15.5^\circ$ divergence angle), as shown in [Figure 4.53](#). The percentage power from such a beam captured by a 70-mm radius polariser, at a distance of 110 mm is 100% ($\sim 3.0w$), at 220 mm it is $\sim 98\%$ ($\sim 1.4w$), at 330 mm it is $\sim 82\%$ ($\sim 0.9w$) and at 440 mm it is $\sim 61\%$ ($\sim 0.7w$). There is nothing special about the distances chosen

except that they cover a range of beam capture levels similar to that expected at the QUBIC polariser.

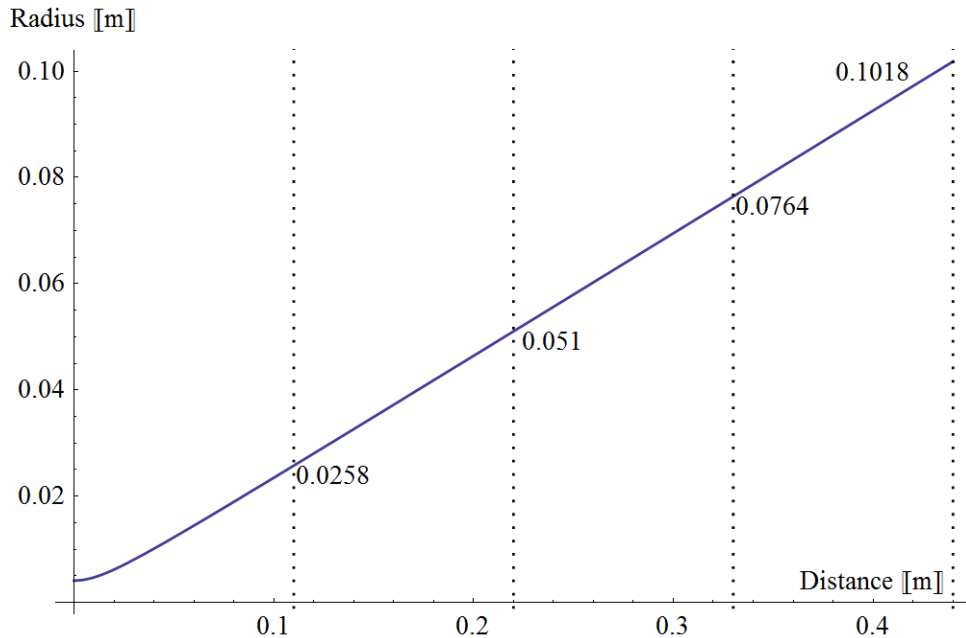


Figure 4.53: TK feed horn beam radius as a function of propagation distance, at 100 GHz.

The QUBIC combiner has beams incident on the detector plane at up to 47° off-axis. The setup for experimental testing is shown in Figure 4.54. The polariser was tested for beams incident at 0° and 45° to the normal and the results are shown in Figure 4.55 and Figure 4.56. The on-axis system produced a beam shaped as expected on the detector plane but the 45° off-axis incidence yielded a small distortion on the left side of the beam. This is unexpected for an ideal polariser.

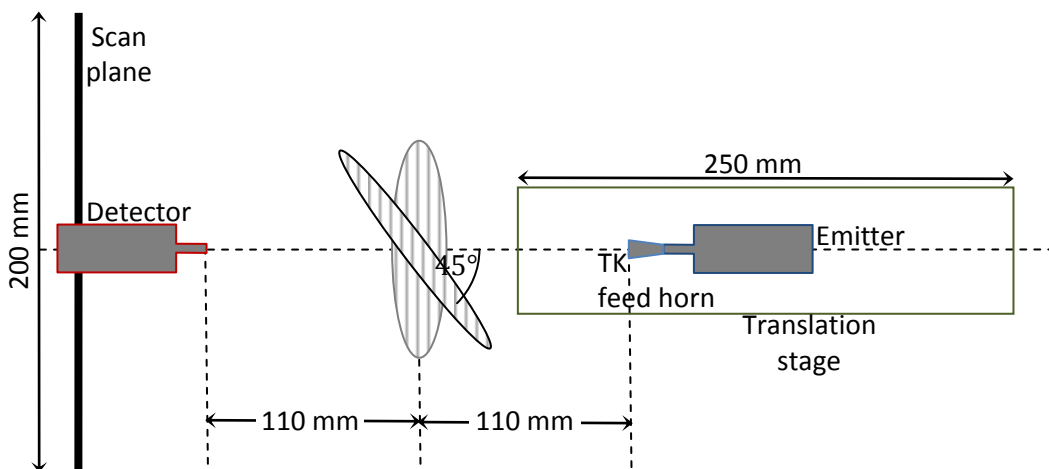


Figure 4.54: Setup for polariser tests shown in an on-axis and 45° rotated off-axis position.

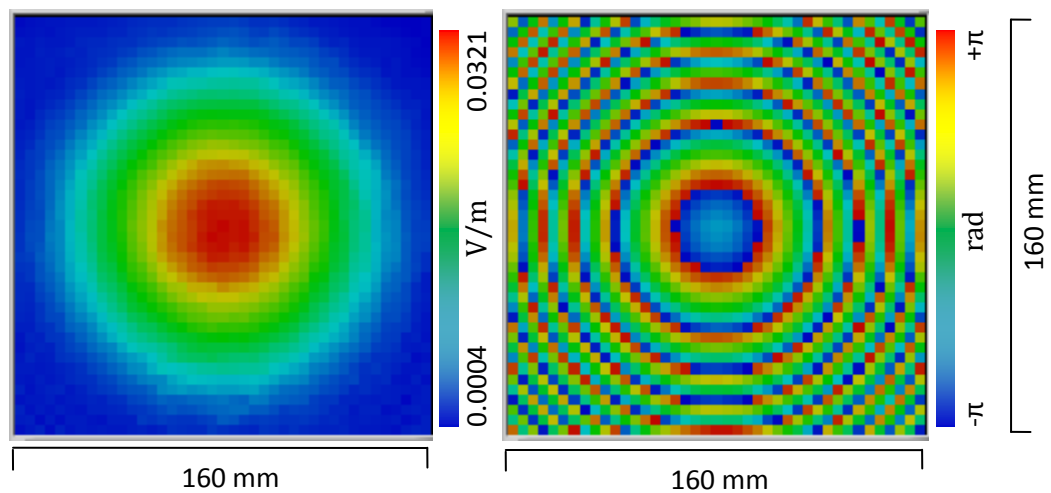


Figure 4.55: Beam amplitude (left) and phase (right) for the polariser tangential to the source beam propagation direction and the source and polariser optical axes aligned

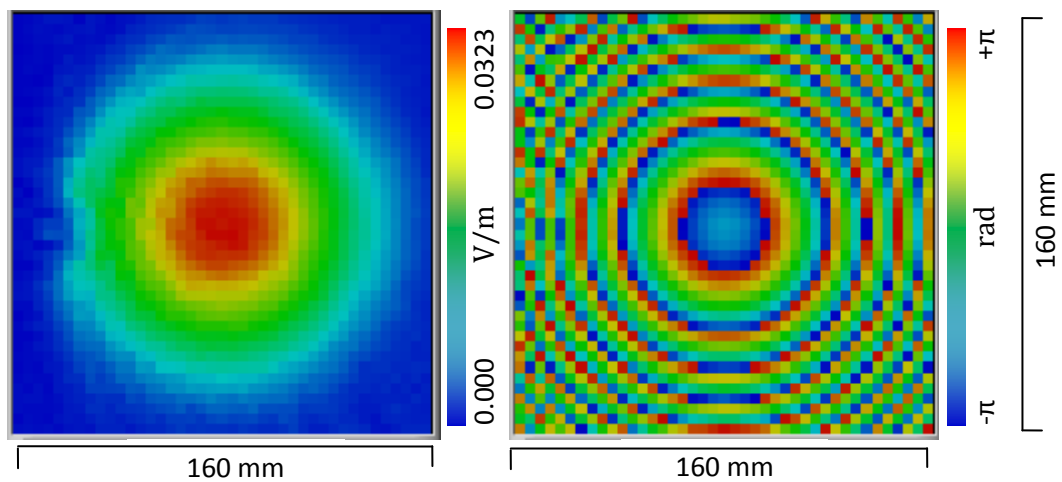


Figure 4.56: Beam amplitude (left) and phase (right) for the polariser 45° to the source beam propagation direction and the source and polariser optical axes aligned

The distortion noted on the left hand side of the image was attributed to a tear in some of the polariser wires as shown in Figure 4.57, the angled polariser leading to a wider beam at the point of intersection and hence more power at this part of the polariser surface leading to the distortion.

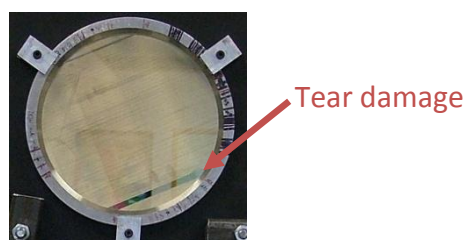


Figure 4.57: Wire-grid polariser used in testing in VNA lab.

To confirm the suspicion that the distortions were caused by the polariser tears the polariser to source distance was increased. This should cause more distortions at the detector plane as relatively more power will hit the torn surface due to the greater extent of the diverging beam. The polariser's optical axis was rotated by 60° about its normal out of alignment with that of the sources polarisation orientation. This leads to a relative increase in the power through the tear compared with that through the polariser grid. From *Figure 4.58* to *Figure 4.60* it was noted that as the source polariser distance was increased the beam became increasingly distorted.

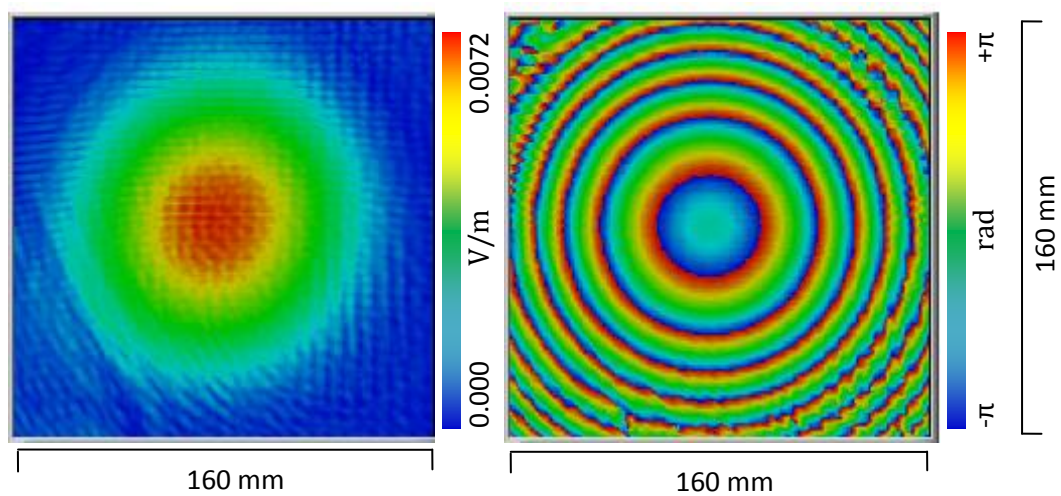


Figure 4.58: Measuring the distortion as a function of distance for a 100 GHz beam for the case of an on-axis emission and detection with a polariser 45° off-axis tilt and rotated 30° about its own normal at a distance of 110 mm (left amplitude and right phase)

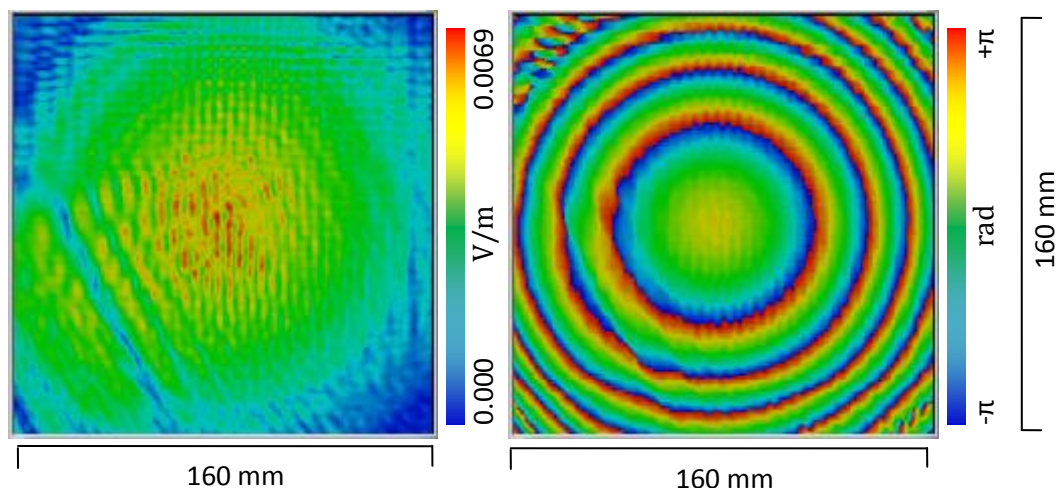


Figure 4.59: Measuring the distortion as a function of distance for a 100 GHz beam for the case of an on-axis emission and detection with a polariser 45° off-axis tilt and rotated 60° about its own normal at a distance of 220 mm (left amplitude and right phase)

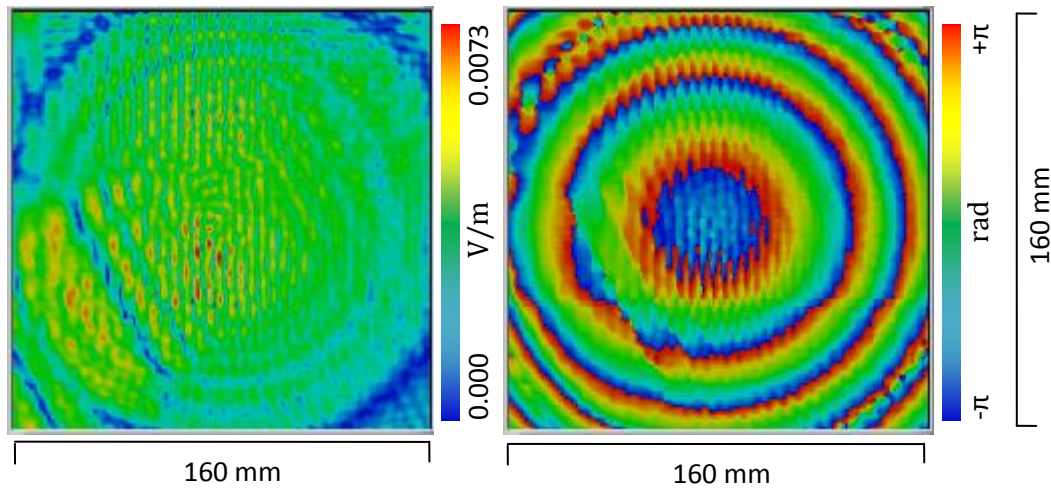


Figure 4.60: Measuring the distortion as a function of distance for a 100 GHz beam for the case of an on-axis emission and detection with a polariser 45° off-axis tilt and rotated 30° about its own normal at a distance of 330 mm (left amplitude and right phase)

MODAL was used to simulate the system in an effort to reproduce these effects and to show the feasibility of modelling real distortions in the future if they should arise. The tears in the polariser surface were included in the model. The polariser surface was defined as the region that was not torn and the tears were added as additional apertures. The power that got through the polariser was then added to that which got through the apertures. The 2 tears were measured and defined as having a centre offset from the centre of the polariser by -60 mm and a width of 9 mm and a centre offset of $+64$ mm and a width of 2 mm, respectively. In both cases they extended parallel to the wires of the polariser extending fully to the edge of the polariser. The separation between the centre of the polariser and both the emitter and detector is 110 mm as in the VNA measurement setup in [Figure 4.54](#).

The outputs from the simulations are shown in [Figure 4.61](#) to [Figure 4.63](#). As the polariser optical axis offset with respect to the polarisation direction of the emitter increases, the power through the undamaged polariser sections lowers resulting in an increased percentage contribution from the damaged (torn) sections.

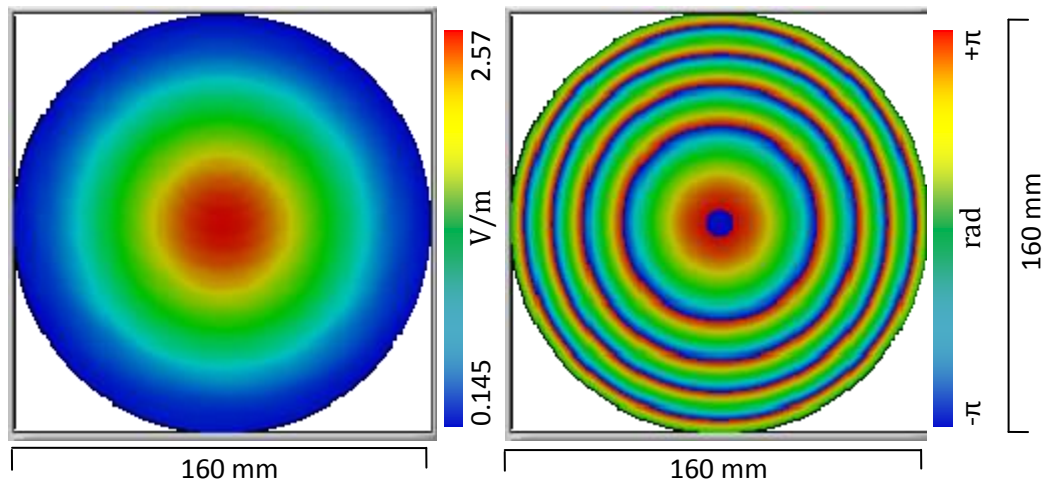


Figure 4.61: Simulation of an on-axis polariser with tears for a 110 mm separation from source to polariser and 110 mm from polariser to detection plane with an optical axis misalignment of 30° . (left amplitude and right phase)

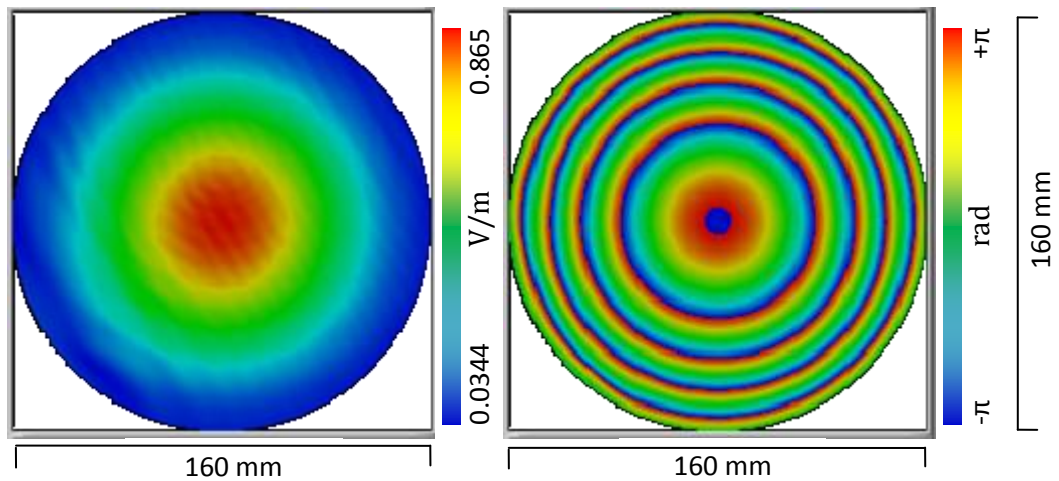


Figure 4.62: Simulation of an on-axis polariser with tears for a 110 mm separation from source to polariser and 110 mm from polariser to detection plane with an optical axis misalignment of 60° . (left amplitude and right phase)

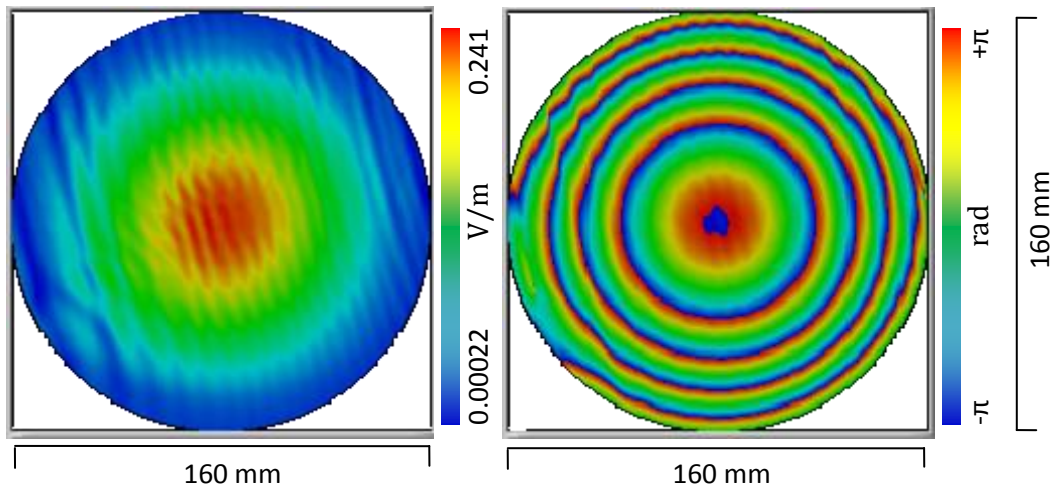


Figure 4.63: Simulation of an on-axis polariser with tears for a 110 mm separation from source to polariser and 110 mm from polariser to detection plane with an optical axis misalignment of 75° . (left amplitude and right phase)

Using the 30° polariser optical axis offset, as was the case for the VNA measurement data from Figure 4.58 to Figure 4.60, the distance from the emitter to the polariser was increased from 110 mm to 220 mm and 330 mm. The simulations were repeated and the results are shown in Figure 4.64 and Figure 4.65. The distortions increase with distinct lines on the images as the diverging beam encompasses the tear to a greater degree. The distortion is due to a combination of the finite size of the polariser and the tears.

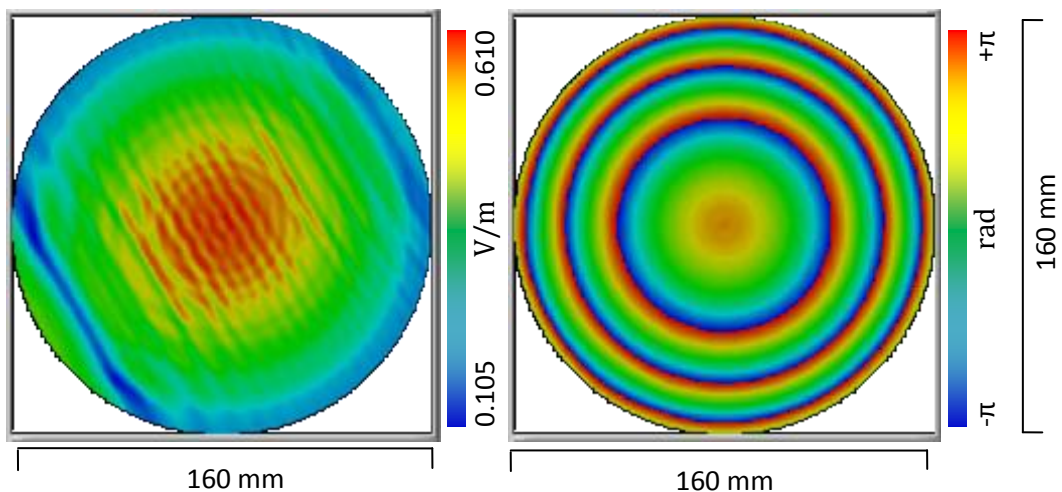


Figure 4.64: Simulation of an on-axis ideal polariser with tears for a 220 mm separation from source to polariser and 110 mm from polariser to detection plane with an optical axis misalignment of 30° . (left amplitude and right phase)

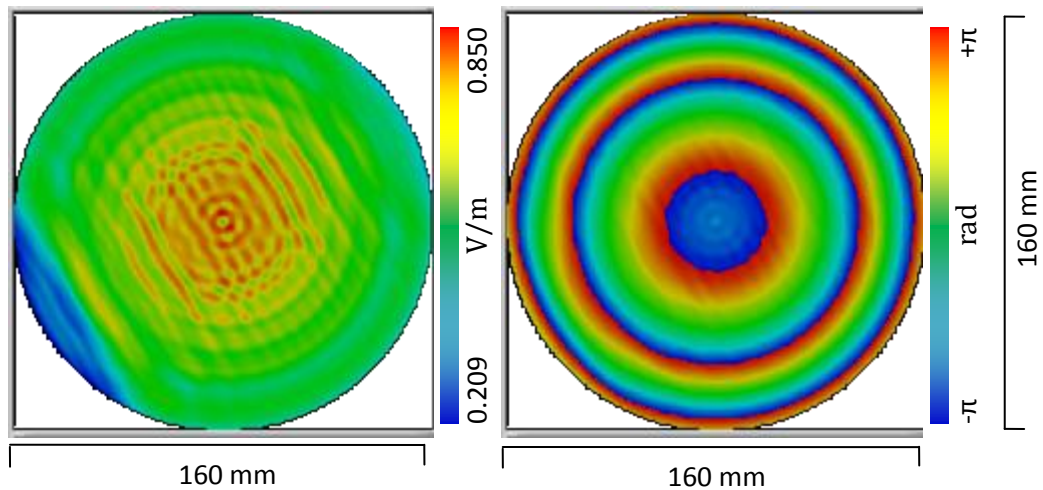


Figure 4.65: Simulation of an on-axis ideal polariser with tears for a 330 mm separation from source to polariser and 110 mm from polariser to detection plane with an optical axis misalignment of 30° . (left amplitude and right phase)

In order to determine the level to which the finite size of the polariser contributed to the distortions, the same simulations were repeated for an idealised polariser, without tears and the results are shown in *Figure 4.66* to *Figure 4.68*. It is evident that the output of the system is affected by the increased distance from the polariser as the diverging beam is increasingly truncated by the finite polariser. It should be noted that the distortion is azimuthally symmetric owing to the removal of the asymmetries of the tears on the surface. This shows that the majority of the distortions seen previously caused by the tears. With a sufficiently sized polariser (capture of $2w$ of the incident beams power as designed for QUBIC) there should be no significant adverse affects due to the polariser.

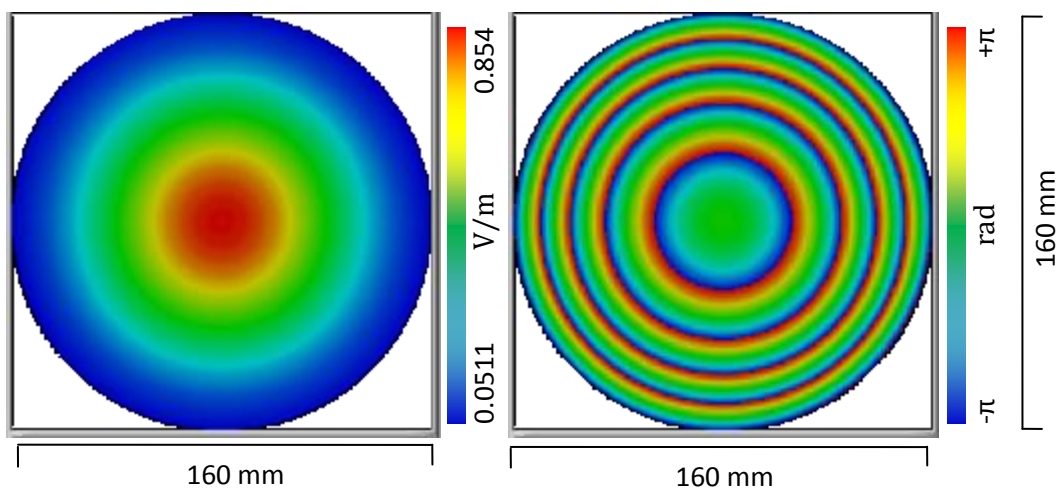


Figure 4.66: Simulation of beam transmitted by an on-axis ideal polariser for 110 mm separation from source to polariser and 110 mm from polariser to detection plane with polariser rotated about its own normal by 30° . (left amplitude and right phase)

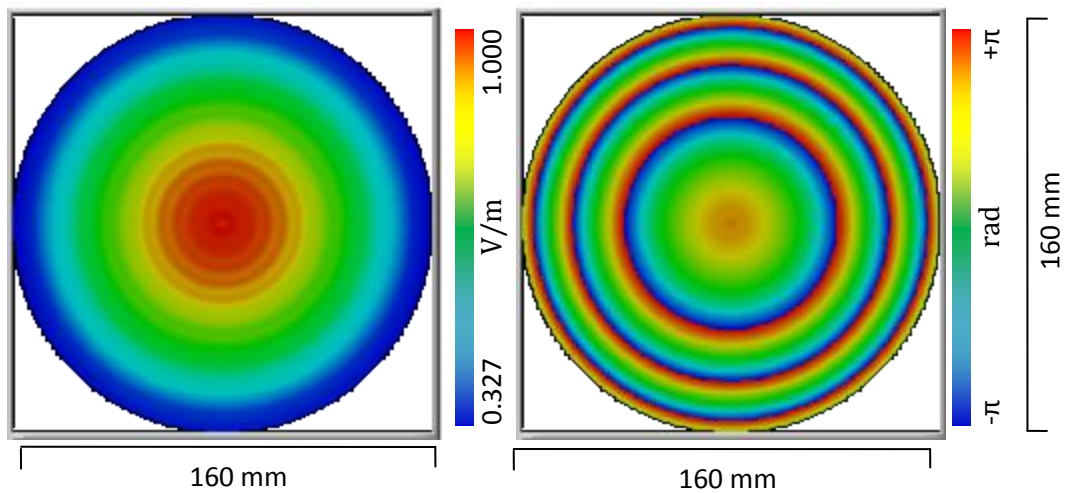


Figure 4.67: Simulation of beam transmitted by an on-axis ideal polariser for a 220 mm separation from source to polariser and 110 mm from polariser to detection plane with polariser rotated about its own normal by 30° . (left amplitude and right phase)

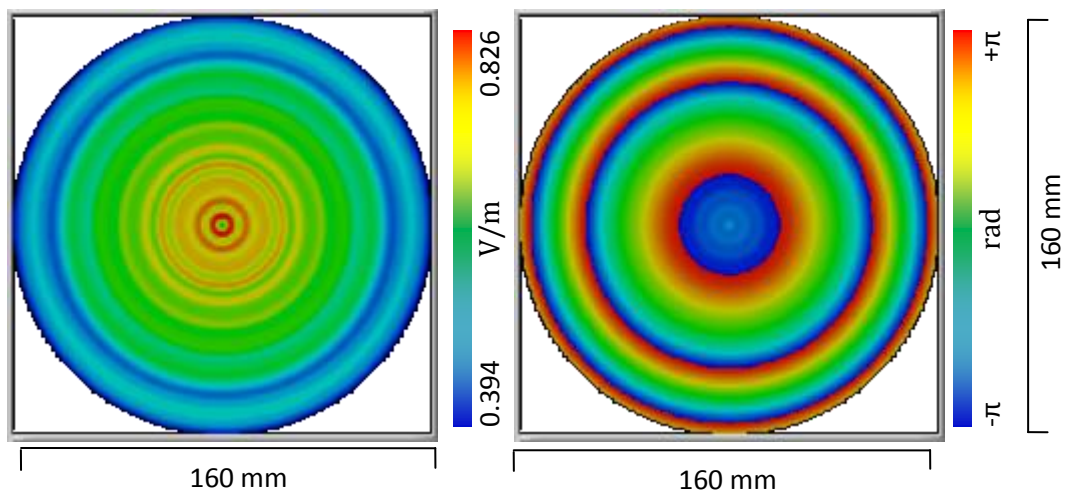


Figure 4.68: Simulation of beam transmitted by an on-axis ideal polariser for a 330 mm separation from source to polariser and 110 mm from polariser to detection plane with polariser rotated about its own normal by 30° . (left amplitude and right phase)

The QUBIC combiner sources are incident on the polariser from all directions and at angles up to 47° and are polarised in all possible orientations. Work by Whale (Whale, 2009) for ALMA Band 7 and 9 showed potential advantages for some orientations of the polariser optical axis with respect to the source but due to the large variation in incident angle at the polariser in QUBIC and the fact that sources are polarised in all orientations (OMT's were used in tests by Whale giving specific orientation of propagated radiation) this prevents optimisation of optical axis angle

(with respect to incident angle of source radiation) as previously investigated for the Herschel space telescope (Pilbratt, 2003).

4.4 Coldstop

To achieve the sensitivity required for the detection of the B-mode signal the detector array of bolometers must be cryogenically cooled. This will be achieved with a 2 stage cryostat using a thermal barrier with an aperture window, known as a coldstop, positioned between the primary and secondary mirrors. Another function of the coldstop relates to the bare bolometer array. The bare array, not coupled to feed horns, will detect radiation from all angles, including the 'hot' cryostat walls. Therefore the coldstop will encase the bare bolometers on the cold side restricting stray light. The position and size of the coldstop will be the focus of this section. The warm side is to include the primary mirror and the aperture plane with all 400 feed horns and the cold side the secondary mirror, polariser and detector planes. Due to the combiner's symmetric design the coldstop will be in a plane orthogonal to the optical axis, as shown in *Figure 4.69*. The exact extent, position and angle are dependent on the spread of the beams, as the path lengths vary for each beam at this plane.

The first task is to determine the plane of the coldstop wall, where beams propagating from the aperture array to the primary mirror and from the secondary mirror to the polariser and detector planes would not be obstructed. To determine the best position for the coldstop wall the beams footprints at various points were calculated on three planes using PO.

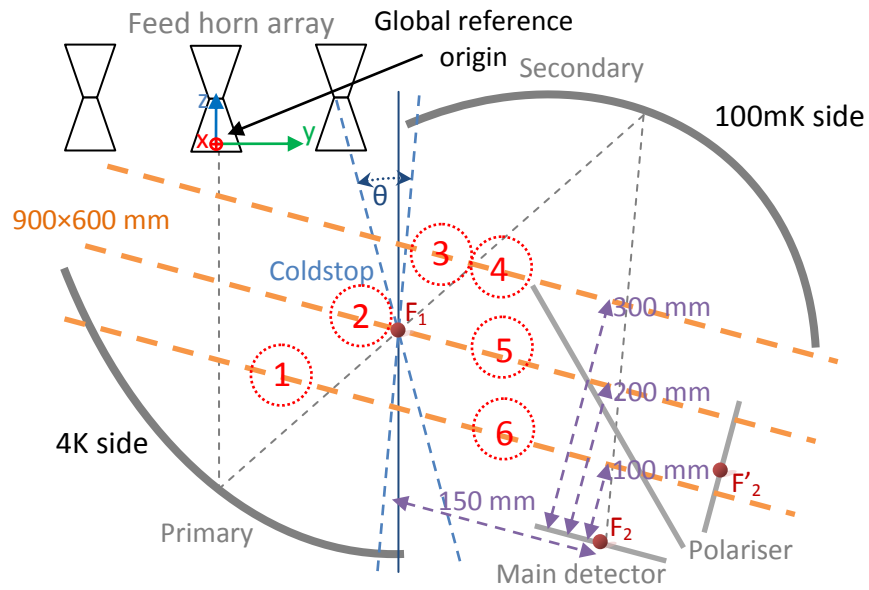


Figure 4.69: QUBIC (not to scale) schematic showing the position of the coldstop and the footprint calculation planes. The planes are parallel to the plane of the detector, with the centre of the plane 150 mm back from the centre of the detector. The 3 planes are vertically offset from the detector at 100 mm, 200 mm and 300 mm. The extent of the planes is 900 mm wide and 600 mm deep.

The footprints shown in Figure 4.70 are arranged according to the order of intersection of the beam with each plane, starting with reflection off of the primary mirror. The plane order is shown in red circled text in Figure 4.69. The edge feed horns were selected for these tests giving a footprint outline of the power distribution for the beams in the combiner.

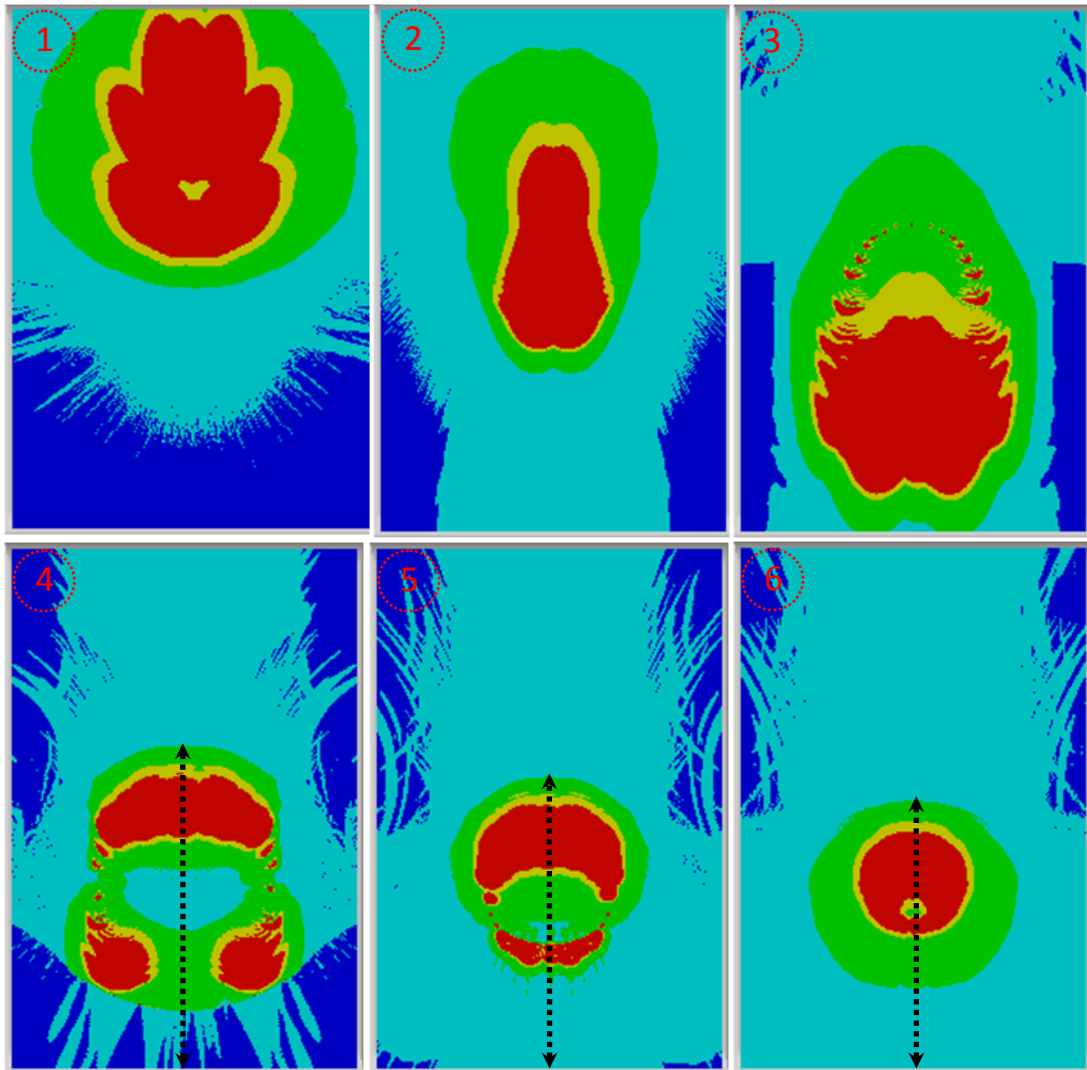


Figure 4.70 Display of the footprints for the beams through the combiner with the top of the image on the primary side and the bottom of the image on the secondary side.

Footprint #1 at $z = +100\text{mm}$ from the detector plane upon reflection off of the primary mirror.
 Footprint #2 at $z = +200\text{mm}$ from the detector plane upon reflection off of the primary mirror.
 Footprint #3 at $z = +300\text{mm}$ from the detector plane upon reflection off of the primary mirror.
 Footprint #4 at $z = +300\text{mm}$ from the detector plane upon reflection off of the secondary mirror.
 Footprint #5 at $z = +200\text{mm}$ from the detector plane upon reflection off of the secondary mirror.
 Footprint #6 at $z = +100\text{mm}$ from the detector plane upon reflection off of the secondary mirror.
 Colour is the same as in Figure 4.5 image key. The black dotted lines are an approximation of the extent of power on the footprint used in Figure 4.71 to aid in positioning of the coldstop.

Using the footprints in Figure 4.70 in conjunction with the GBM analysis in MODAL shown in Figure 4.71 the optimum angle of the coldstop was determined. The GBM analysis in MODAL was also used to give an approximate location of the centre of the window within the coldstop wall, with parameterisation as tabulated in Table 4.9.

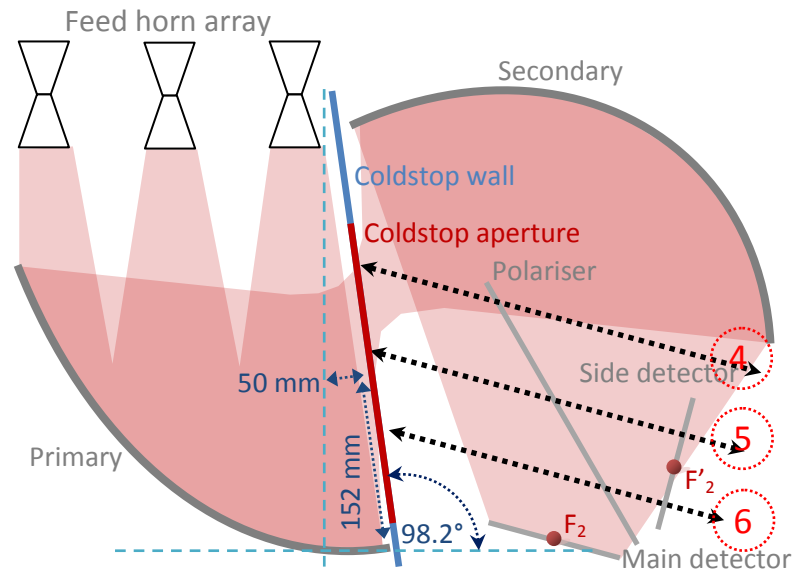


Figure 4.71 A schematic of the QUBIC combiner with coldstop. The black dotted lines are an approximation of the extent of power on the footprints from Figure 4.70. The pink region is the GBM approximation of the edge source's beams out to $1w$. The red line shows the aperture within the coldstop wall.

Table 4.9: Coldstop approximate parameters (values are with respect to global reference frame)

	X	Y	Z
Translation (mm)	-152	0	-50
Rotation (°)	0	98.2	0
Dimension (mm)	305	337	-

To determine the exact position of the coldstop window a similar approach to that used for the polariser was employed. Using the setup in Table 4.9, a large plane was used to determine the extent of power distribution yielding the required dimensions. The footprint for the edge sources was calculated on the plane as shown in Figure 4.72.

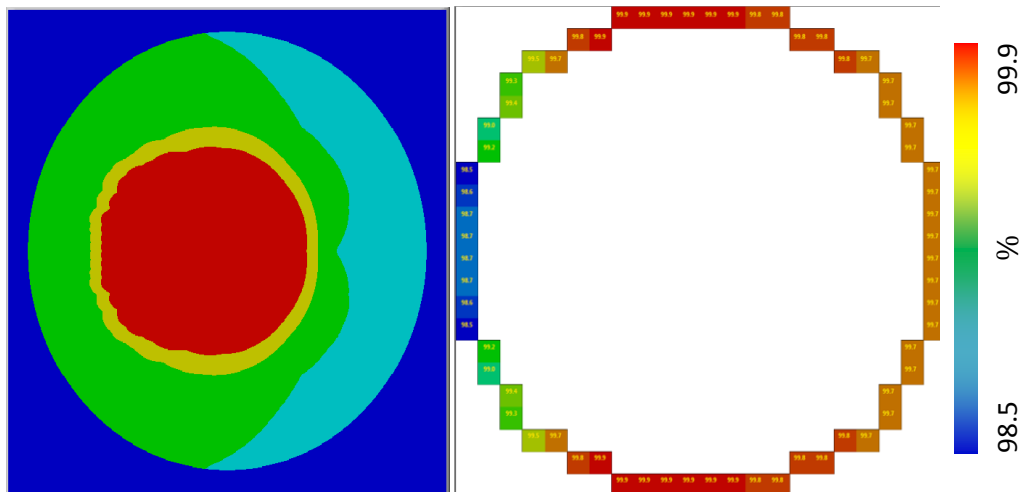


Figure 4.72: Combination of edge beams at coldstop aperture window (left) and individual beam capture power (right). Colour is the same as in Figure 4.5 image key.

From the footprint it is apparent that the initial visually placed coldstop window is not ideal and should be shifted by 30 mm in the x-direction. Table 4.10 shows the updated parameters and Figure 4.73 the output from the re-simulation.

Table 4.10: Coldstop parameters (values are with respect to global reference frame)

	X	Y	Z
Translation (mm)	-182	0	-50
Rotation (°)	0	98.2	0
Dimension (mm)	305	337	

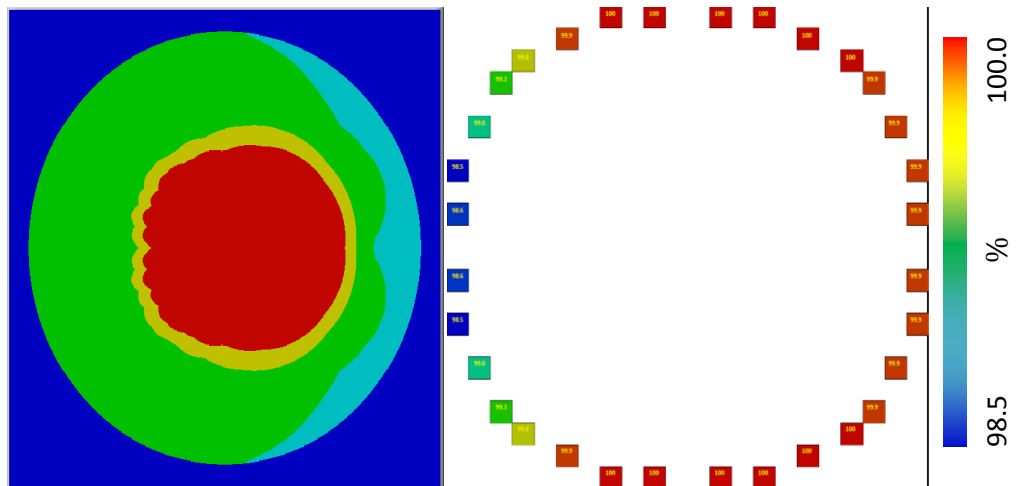


Figure 4.73: Left, coldstop shifted 30mm to the right. Right, edge sources power collected (transmitted) by coldstop. There is about 0.2% drop on all sources compared to the power levels captured by the primary mirror. This indicates that the coldstop position is more or less centred on the combined beam set. The overall size may need to be increased if closer to 100% of primary transmitted power is required to be collected. Minimum power level is 98.5%. Colour is the same as in Figure 4.5 image key.

The throughput from all feed horns is at least 98.5%. Extending the window to encompass more from the feed horns with the lowest throughput requires a large extension due to the incident angle of the corresponding beams. It was therefore decided not to extend the aperture as the combiner detector plane can capture only ~70% of power anyway.

4.5 Manufacturing limitations

The manufacturing of mirrors of 600 mm in diameter represents a challenge and the team charged with the manufacture of the mirrors asked for ways to reduce the extent of the mirrors required (if possible to ≤ 420 mm). Additionally, the 600 mm mirror sizes were a concern for the cryostat mass and limits from the size of the door on the plane being used for transport to Antarctica. The first idea was to move the aperture array closer to the primary, hence automatically reducing the beam footprint on the primary mirror. This is not ideal as it restricts the space within the combiner for the inclusion of components such as a half-wave plate. In this section the effect of moving the input feed horn array closer to the primary mirror and truncating the mirrors were investigated.

4.5.1 Source relocation

The distance from the aperture plane to the primary mirror vertex is 466.76 mm. By moving the aperture plane closer to the primary mirror by 100 mm (to 366.76 mm) it was hoped to reduce the beam footprint and hence the mirror diameter required. Here the degree to which the primary and subsequent surfaces can be reduced is investigated. The current setup is shown in *Table 4.11* and the proposed setup in *Table 4.12* and for each test the modified parameters will be shown in blue.

Table 4.11: Original system setup (parameters with respect to local coordinate frames)

Parameters	Translation (mm)			Rotation (mm)			Dimension (mm)		
	X	Y	Z	X	Y	Z	X	Y	Z
Source	0	0	466.76						
Primary	190	0					480	600	
Secondary	-130	0					600	600	

Table 4.12: Proposed System Setup

Parameters	Translation (mm)			Rotation (mm)			Dimension (mm)		
	X	Y	Z	X	Y	Z	X	Y	Z
Source	0	0	366.76						
Primary	190	0					480	600	
Secondary	-130	0					600	600	

Ideally mirrors capture out to $r = 2w$ of every beam (>99.9% of the power). For the original configuration the primary mirror captured, in the worst case (x21y07), 98.7% of power, as shown in Figure 4.74 (as the system is symmetric up to this point we will only test with the lower 200 sources). This will be the baseline to compare against.

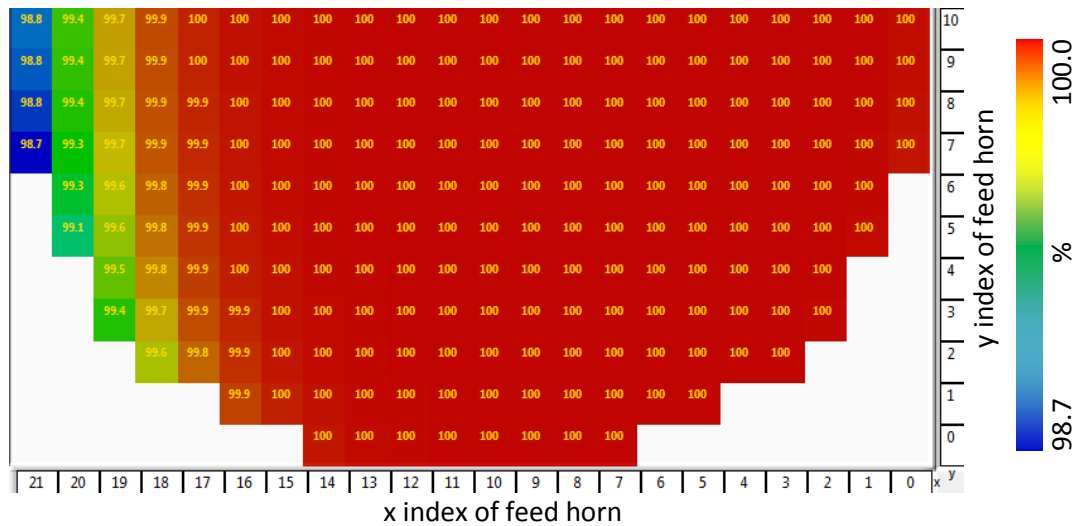


Figure 4.74: Primary mirror power capture for 480x600mm with a 190mm offset & sources at 466.76mm. The feed horn corresponding to each power value is indicated by its x and y value.

A selection of sources was used in tests for the GBM visual analysis, see Table 4.13, so that each part of the array was represented and in addition those with minimum and maximum angle of throw were considered.

Table 4.13: Selected sources

Source	Reason
x21y07 and x21y14	Closest to the secondary
x00y07 and x00y14	Greatest angle of throw
x11y11	Centre
x07y00 and x07y21	Edge source, mid way out
x14y00 and x14y21	Edge source, mid way out

Figure 4.75 shows the original and relocated aperture plane positions. There is no impasse here as the array looks to have sufficient clearance past the edge of the secondary mirror. To check for blockages for the beam, the visualisation was increased in extent to $1w$ and $2w$ as shown in Figure 4.76.

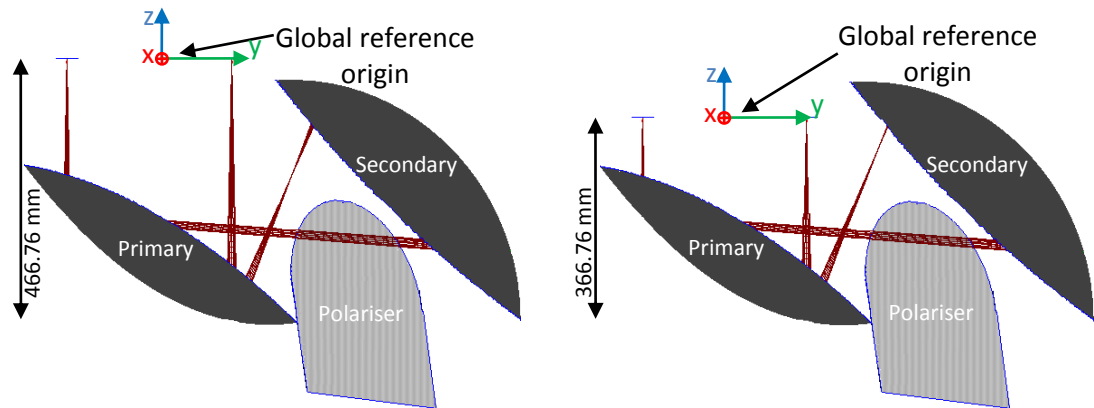


Figure 4.75: QUBIC simulation showing the original 466.76 mm aperture plane offset on the left and the relocated 366.76 mm offset on the right. The extent in both cases is for a $0.1 W$ beam.

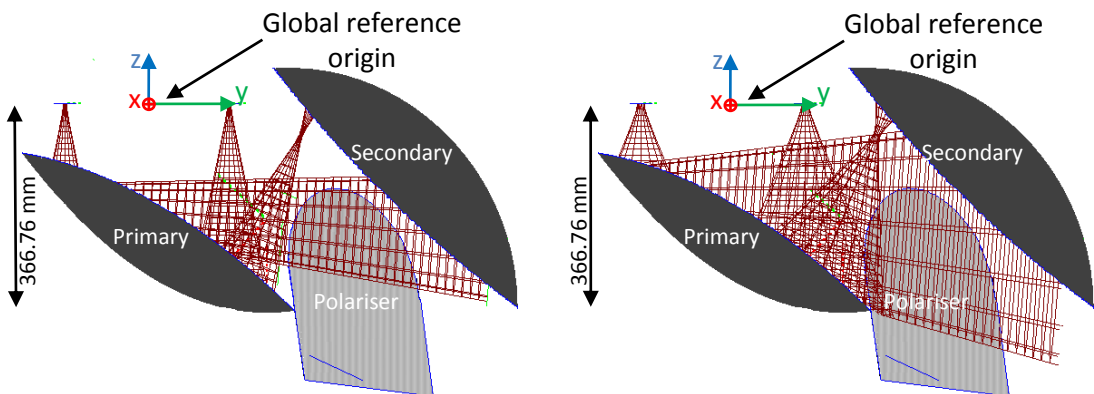


Figure 4.76: QUBIC simulation showing the beams out to $1 W$ on the left and the $2 W$ on the right. The position in both cases is for a 366.76 mm offset.

Again there are no obvious problems as both the path to and from the primary mirror look unimpeded by the relocated array. From this point forward in the combiner there is no impact from the aperture array that could impede the sources. I therefore, using PO, calculated the footprint on each of the surfaces in the combiner and determined if any corrections to the rim's position or extent needed to be made. For these calculations the full array was used for the original position and the edge sources only for the relocated position. The detector plane separation was 110 mm. Figure 4.77 to Figure 4.80 show the footprints on each element's surface.

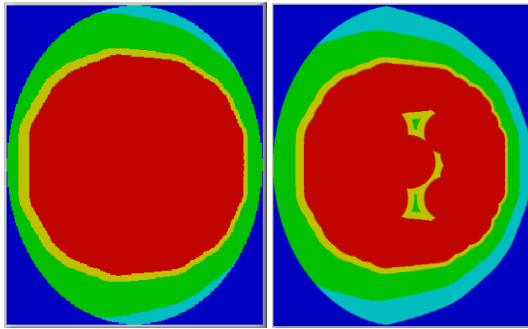


Figure 4.77: Footprint on the primary mirror for an aperture array at the 466.76 mm offset on the left and the relocated 366.76 mm offset on the right. Colour is the same as in Figure 4.5 image key.

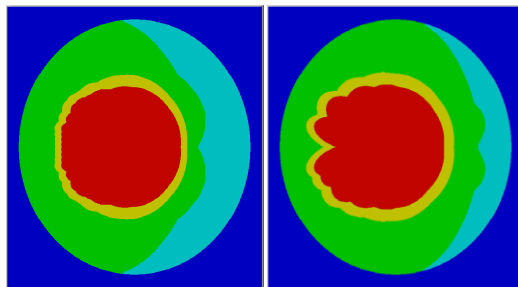


Figure 4.78: Footprint on the coldstop for an aperture array at the 466.76 mm offset on the left and the relocated 366.76 mm offset on the right. Colour is the same as in Figure 4.5 image key.

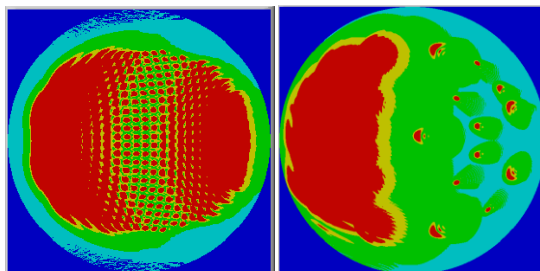


Figure 4.79: Footprint on the secondary mirror for an aperture array at the 466.76 mm offset on the left and the relocated 366.76 mm offset on the right. Colour is the same as in Figure 4.5 image key.

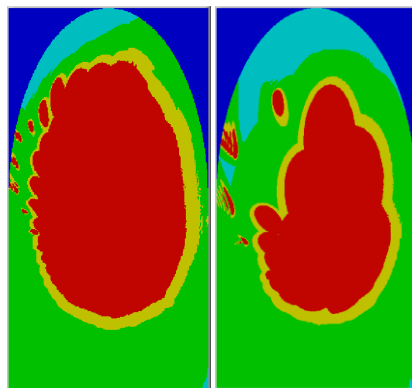


Figure 4.80: Footprint on the polariser for an aperture array at the 466.76 mm offset on the left and the relocated 366.76 mm offset on the right. Colour is the same as in Figure 4.5 image key.

The size of the beams' footprints on the primary mirror is reduced and from these footprints it is clear that the mirror can be reduced in extent from 480 mm × 600 mm to 450 mm × 510 mm. The power incident on the reduced primary mirror from each of the 400 sources was calculated and found to be, in the worst case, 99.2% (x21y07) of the incident power, see *Figure 4.81*, which outperforms the original setup by 0.5% for the worst case source in *Figure 4.74*.

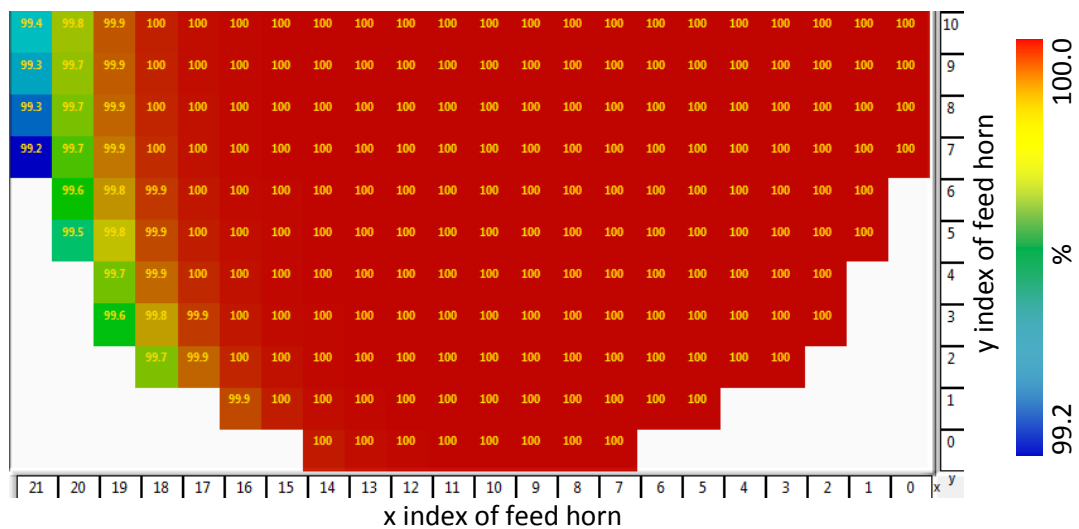


Figure 4.81: Power on the reduced size (450 mm × 510 mm with 190 mm rim offset primary mirror. The lowest level is 99.2% (x21y07). The feed horn corresponding to each power value is indicated by its x and y value.

Column x21 relates to the edge nearest the centre of the combiner and it is where most power loss is occurring. To recover more power we can laterally shift the mirror towards the secondary by 10 mm changing the offset from 190 mm to 180 mm placing this edge of the mirror back towards its original position. The mirror can then be further reduced from 450 mm × 510 mm to 450 mm × 480 mm, the results shown in *Figure 4.82*. There is a drop in power on the right hand side of less than 0.05% (indicated by the rounding to 100% but a change in colour in *Figure 4.82*). The left hand side improved but a further translation of about the width of a horn is needed as the 3rd column of horns from the left has a similar power level colouring to that of the right hand side. The top and bottom do not look adversely affected by the reduced size (510 mm → 480 mm).

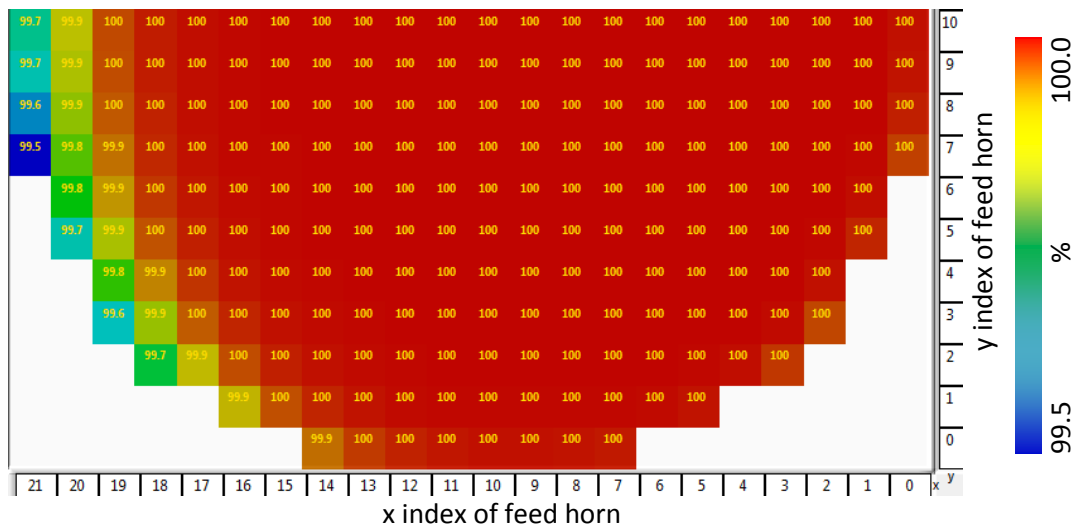


Figure 4.82: Power on the reduced size (450 mm × 480 mm with 180 mm rim offset primary mirror. The lowest level is 99.5% (x21y07). The feed horn corresponding to each power value is indicated by its x and y value.

The primary mirror was then shifted from an offset of 180 mm to 175 mm, the minimum offset without the edge of the primary mirror physically impeding the polariser or coldstop, the recalculated edge sources are shown in Figure 4.83. There is power drop on the left of 0.3% and on the right of 0.2%.

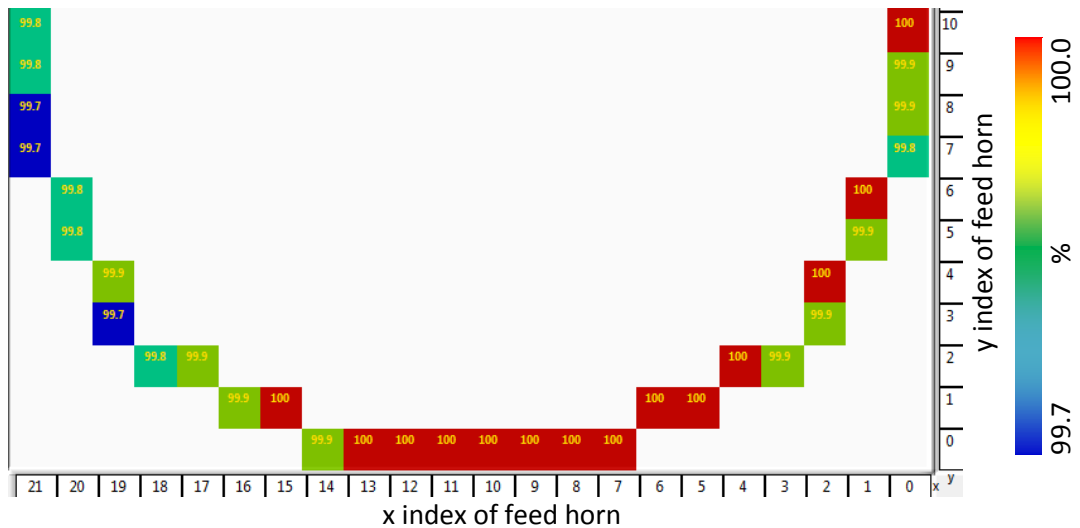


Figure 4.83: Power on the reduced size (450 mm × 480 mm with 175 mm rim offset primary mirror. The lowest level is 99.7% (x21y07). The feed horn corresponding to each power value is indicated by its x and y value.

The power drops at the bottom and right are directly related to the reduction in reflector surface area and it looks like the mirror is too small. The mirror dimensions were increased giving recommended minimum dimensions for the primary mirror

of 480 mm × 500 mm with a 190 mm offset with the possibility of using 450 mm × 480 mm with a 175 mm offset with losses as defined in *Figure 4.83*. Analysis of the secondary mirror showed its footprint remained roughly the same size but shifted to the left as shown in *Figure 4.79*. This can be compensated by repositioning the mirror rim, changing the offset from -130 mm to -150 mm. The revised footprints from the main elements in the system are shown in *Figure 4.84*.

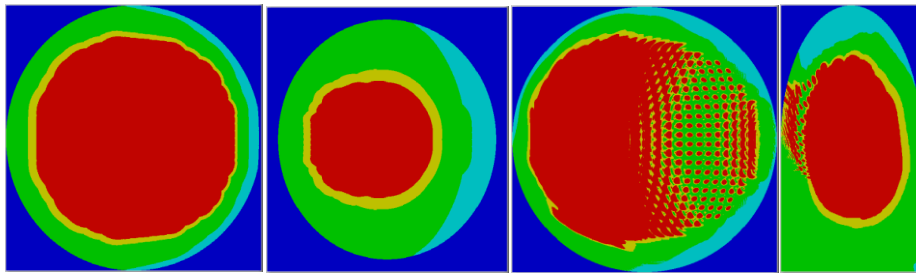


Figure 4.84: Revised footprints on each element for the relocated sources. From left to right, primary (480×500 mm), coldstop (305×337 mm), secondary (600×600 mm) and polariser (240×460 mm). Colour is the same as in Figure 4.5 image key.

The repositioned aperture plane, 366.76 mm from the primary mirror, caused a shift of the secondary footprint by 20 mm and allowed a reduction in the primary by 100 mm without adverse affects. These parameters are tabulated in *Table 4.14* but alone are insufficient to cater for manufacturing limitations as a milling machine that was readily available has an upper size limitation of 420 mm.

Table 4.14: Reduced system setup (primary)

Element	Translation (mm)			Rotation (mm)			Dimension (mm)		
	X	Y	Z	X	Y	Z	X	Y	Z
Source input array	0	0	366.76	0	0	0	0	0	
Primary mirror	190	0	0	0	0	0	480	500	
Secondary mirror	-150	0	0	0	0	0	600	600	

Next the mirrors were reduced in size to 420 mm in each dimension, this will cause a spillover but as the repositioned aperture array gives an increased capture power level, there is some room to manoeuvre.

4.5.2 Truncation (420 mm limit)

One of the manufacturing options being considered by the QUBIC group has a 420 mm limitation on the mirror diameter, it is therefore desirable to determine the impact that truncating mirrors to 420 mm will have on the output of the QUBIC combiner. It may be possible to orient the mirror in such a way as to need to apply this limitation in one dimension only (tilting the mirror within the milling machine). This may give a greater than 420 mm limit in the other direction but truncating the mirrors in both dimensions will be investigated for completeness. As a baseline to compare the impact of the truncation, *Figure 4.85* and *Table 4.15* show the reduced but untruncated setup. Here we show the results of several tests, for a more complete set see Appendix 3.

Table 4.15: System mirror and truncation setup

Element	Translation (mm)			Rotation (°)			Dimensions (mm)		
	X	Y	Z	X	Y	Z	X	Y	Z
Primary mirror	190	0	0	0	0	0	480	500	
Secondary mirror	-150	0	0	0	0	0	600	600	

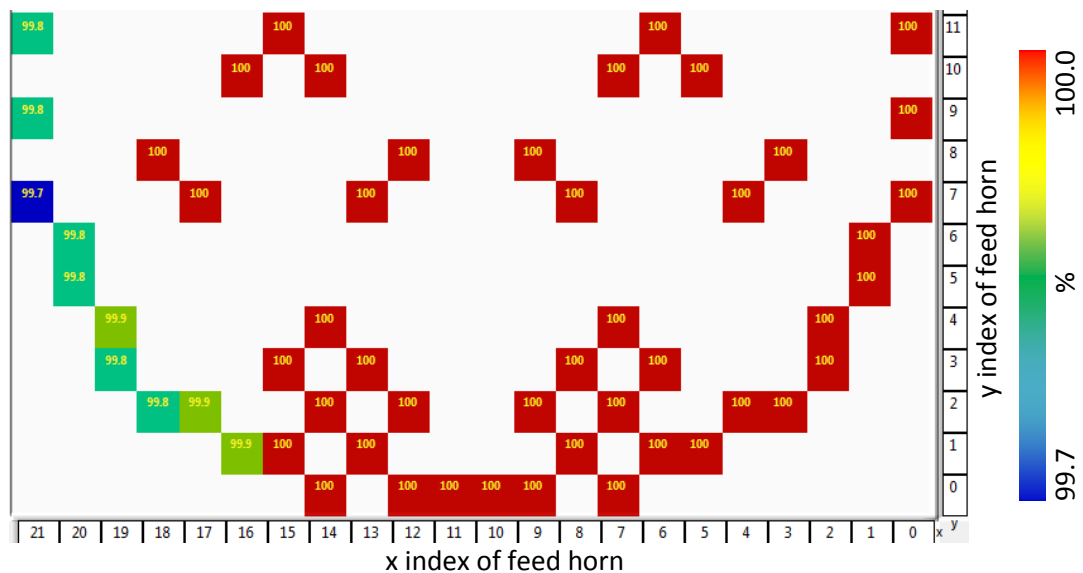


Figure 4.85: Power on the reduced size (480 mm × 500 mm with 190 mm rim offset primary mirror). The lowest level is 99.7% (x21y07). The feed horn corresponding to each power value is indicated by its x and y value.

For truncation in both directions the approach taken was to maximise the utilised surface area of the mirrors. From a visual inspection orienting the truncation with the edges of the aperture array maximises the power captured by the mirror. The mirrors were extended to the corners of the bounding region. The parameters for this setup are shown in *Table 4.16*. The capture levels for the primary, secondary and detector plane calculated using PO and the results are shown in *Figure 4.86* to *Figure 4.89*. This is the worst case scenario and from the results we can see that it is the secondary that has the biggest impact on power loss with the left hand row (x21) of source beams losing about 99% of their power. At the detector plane the impact can be seen in lower power levels with rows y0, y1, half of y2, half of y20 and y21 showing major distortions and similarly for columns x0, x1, x2, x3, x20 and x21. A total of 90 (22%) sources are adversely affected.

Table 4.16: System mirror and truncation setup

Element	Translation (mm)			Rotation (°)			Dimensions (mm)		
	X	Y	Z	X	Y	Z	X	Y	Z
Primary mirror	190	0	0	0	0	0	480	500	
Primary truncation	160	0	0	0	0	0	420	420	
Secondary mirror	-130	0	0	0	0	0	600	600	
Secondary truncation	-130	0	0	0	0	0	420	420	

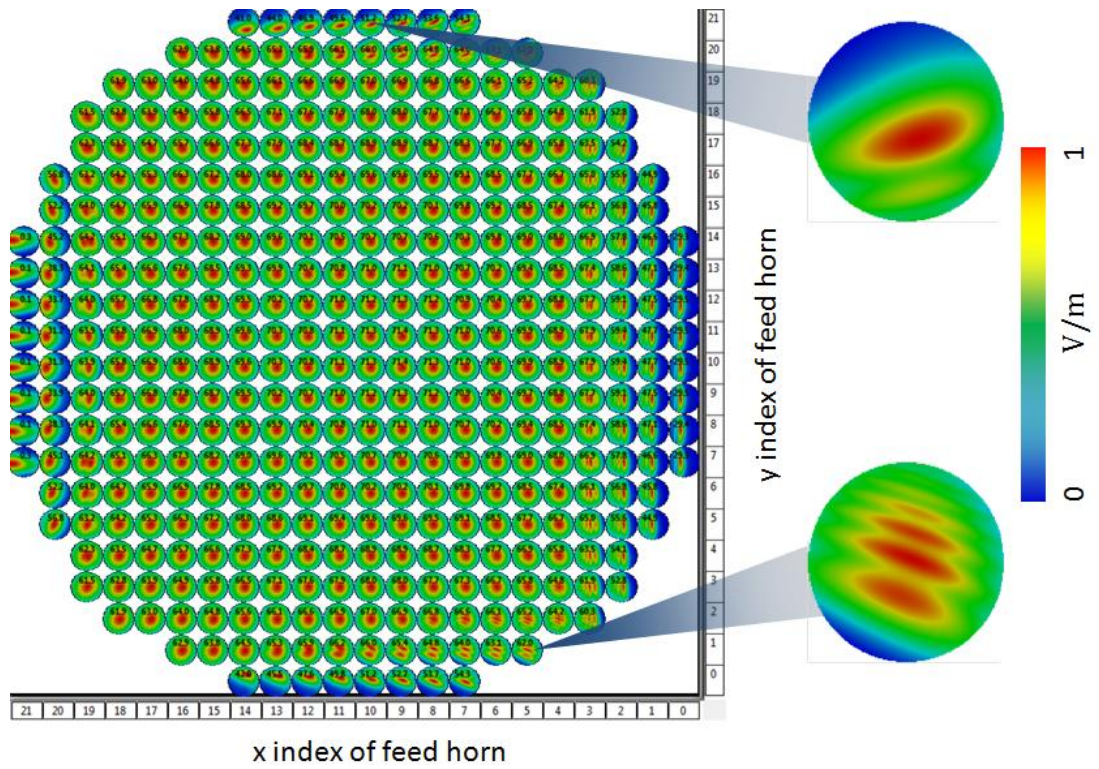


Figure 4.88: Detector plane (51 mm radius) output with levels shown as a percentage of source power (average capture at 68.2%). The feed horn corresponding to each power value is indicated by its x and y value.

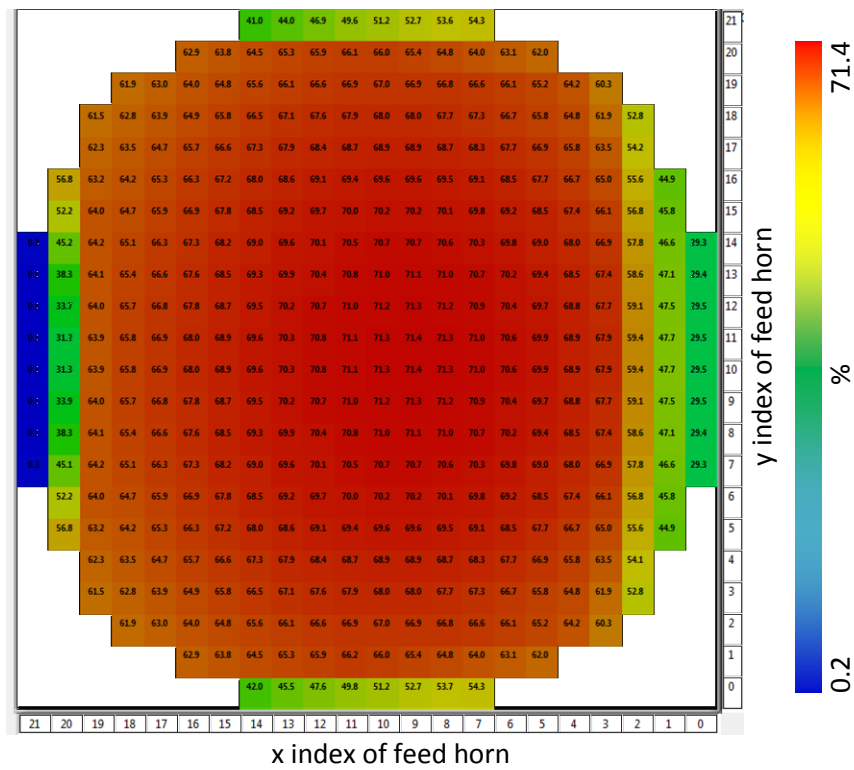


Figure 4.89: Detector plane power (51 mm radius) with levels shown as a percentage of source power (average capture at 68.2%). The feed horn corresponding to each power value is indicated by its x and y value.

For the case of truncation in one direction the primary mirror is analysed initially in isolation. Taking into account the inclusion of the polariser and a 110 mm detector plane separation there are several sources that are not fully captured or are partially shadowed. The primary mirror truncation was aligned with the already aberrated sources, which are shown in *Figure 4.90*.

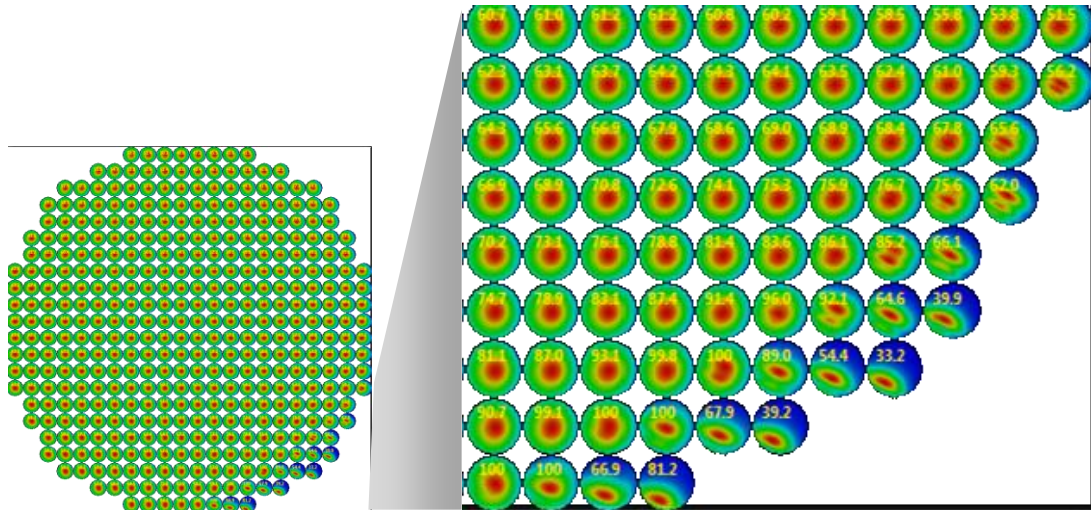


Figure 4.90: Detector plane image output for full untruncated system with aperture plane at 366.76 mm and primary dimensions of 480×500 mm. (Untruncated output shown for comparison)

The primary mirror was truncated to 420 mm at an angle of 45° and the truncation was centred 25 mm from the centre of the mirror as shown in *Figure 4.91* and tabulated in *Table 4.17*. *Figure 4.92* shows the outputs where the bottom right corner power levels are the most affected (the same sources affected by the polariser, minimising additional degradation).

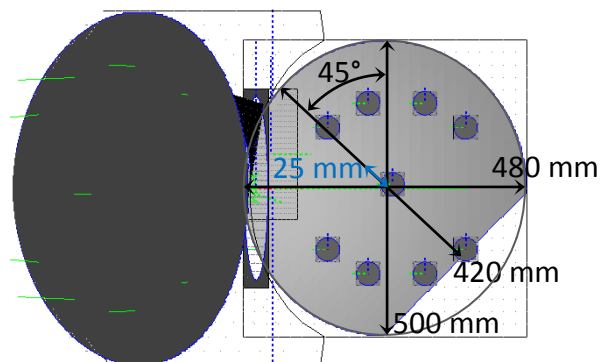


Figure 4.91: Primary mirror with elliptical rim dimensions of 480 mm × 500 mm. The ellipse is then truncated to 420mm, with the truncation being applied at an angle of 45° and off-centre by 25 mm.

good alignment. The parameters are tabulated in *Table 4.18*, the schematic diagram in *Figure 4.93* and *Figure 4.94* shows the power captured at the detector plane.

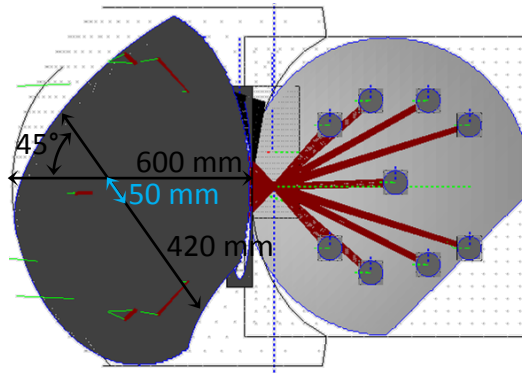


Figure 4.93: Truncated mirrors (primary 420 mm × 500 mm at 45° and secondary 420 mm × 600 mm at 45° offset 50 mm)

Table 4.18: System mirror and truncation setup

Element	Translation (mm)			Rotation (°)			Dimensions (mm)		
	X	Y	Z	X	Y	Z	X	Y	Z
Primary mirror	190	0	0	0	0	0	480	500	
Primary truncation	165	25	0	0	0	-45	420	500	
Secondary mirror	-150	0	0	0	0	0	600	600	
Secondary truncation	-100	50	0	0	0	45	420	600	

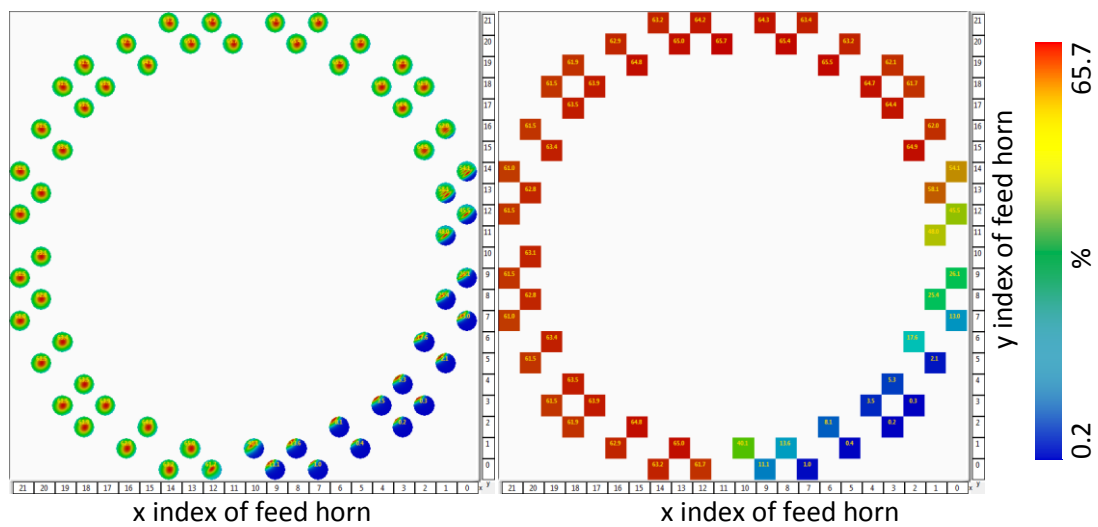


Figure 4.94: Detector plane capture at 51 mm radius after accounting for truncation from primary, secondary and polariser. The feed horn corresponding to each power value is indicated by its x and y value.

Several more iterations were tried and the best orientation and offsets were found and tabulated in *Table 4.19*. The primary was rotated back by 5° to 40° in order to align the truncation with the polariser. The secondary was rotated a further 15° to 60° and as the sources in the top left were unaffected by the truncation the centre offset was reduced from 50 mm to 15 mm. The sources for testing were concentrated in the top left and bottom right in the affected threshold regions and the other sources were removed. The parameters are tabulated in *Table 4.19* and the schematic in *Figure 4.95*. *Figure 4.96* shows the output from the primary mirror and *Figure 4.97* shows the output from the secondary mirror and detector plane where there is good overlap of the truncated sources.

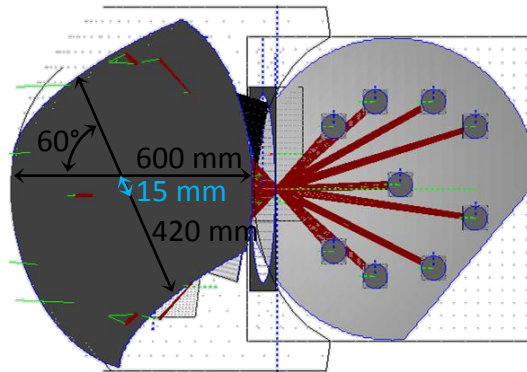


Figure 4.95: Truncated mirrors (primary 420 × 500 mm at 40° and secondary 420 mm × 600 mm at 60° with an offset of 15 mm)

Table 4.19: System mirror and truncation setup

Element	Translation (mm)			Rotation (°)			Dimensions (mm)		
	X	Y	Z	X	Y	Z	X	Y	Z
Primary mirror	190	0	0	0	0	0	480	500	
Primary truncation	165	25	0	0	0	-40	420	500	
Secondary mirror	-150	0	0	0	0	0	600	600	
Secondary truncation	-135	15	0	0	0	60	420	600	

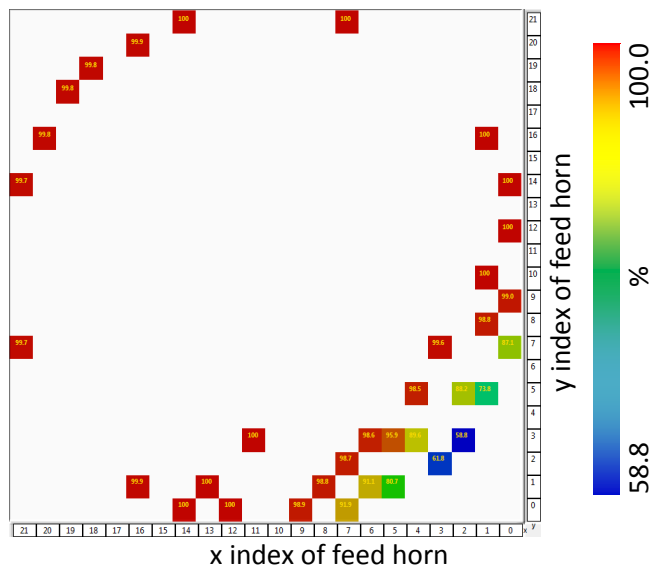


Figure 4.96: Primary mirror power captured by the primary mirror (480 mm × 500 mm clipped at 40° to 420 mm)

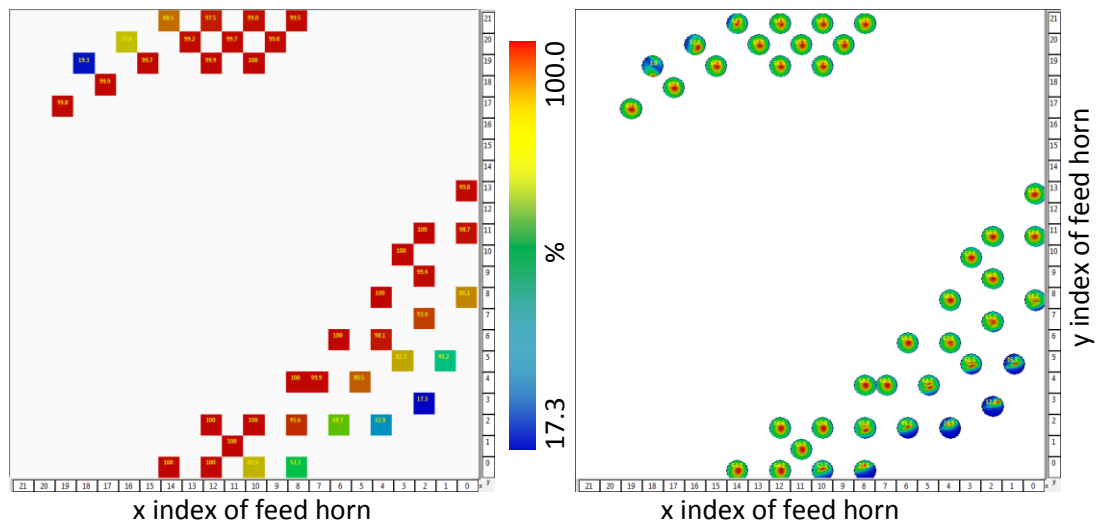


Figure 4.97: Left power captured by the secondary mirror (600 mm × 600 mm truncated at 60° to 420mm with xy offsets of 15 mm) and right, the power captured by the detector plane (51 mm radius) after accounting for truncation from primary and polariser. The feed horn corresponding to each power value is indicated by its x and y value.

The impact of the secondary truncation is of the same order as that of the 420 mm truncation of the primary mirror and polariser. The polariser accounts for about 40 to 50 obscured sources to varying degrees. The truncation of the mirrors to 420 mm affects in the region of 70 sources. Ignoring those already blocked by the polariser the truncation of the primary and secondary mirrors causes an additional 20 to 30 sources to be obscured to varying degrees. The configuration here seems to offer

the best solution for a truncation of the mirrors in one dimension and the output for the full 400 sources can be seen in *Figure 4.98* and *Figure 4.99*. The truncation of the mirrors to 420 mm in one direction blocks some sources yielding a total average power from all 400 sources of 65%, with levels ranging from 3% to 71%. The truncation of the mirrors to 420 mm in both directions results in a total average power from all 400 sources of 63%, with levels ranging from 0% to 71%. So an additional 2% power is lost from the truncation in the second direction. These compare to the original untruncated setup with a total average power of 67%, ranging from 60% to 71%. The above losses requiring a number of sources to be removed were too great. So an alternative to the manufacturing was found in the summer of 2014 where up to 600 mm in one axis was possible with extended limits in the orthogonal direction.

Table 4.20: Summary of system element setup including truncation for relocated sources (input array plane to primary mirror vertex separation of 366.76 mm). All dimensions are with respect to the respective elements local reference frame.

Element	Translation (mm)			Rotation (°)			Dimensions (mm)		
	X	Y	Z	X	Y	Z	X	Y	Z
Primary mirror	190	0	0	0	0	0	480	500	
Primary truncation	165	25	0	0	0	-40	420		
Coldstop	-152	0	-50	0	98.2	0	260	300	
Secondary mirror	-150	0	0	0	0	0	600	600	
Secondary truncation	-135	15	0	0	0	60	420		
Polariser	10	52	0	0	0	-25.2	240	460	
Detector plane	0	0	0	0	0	0	102	102	

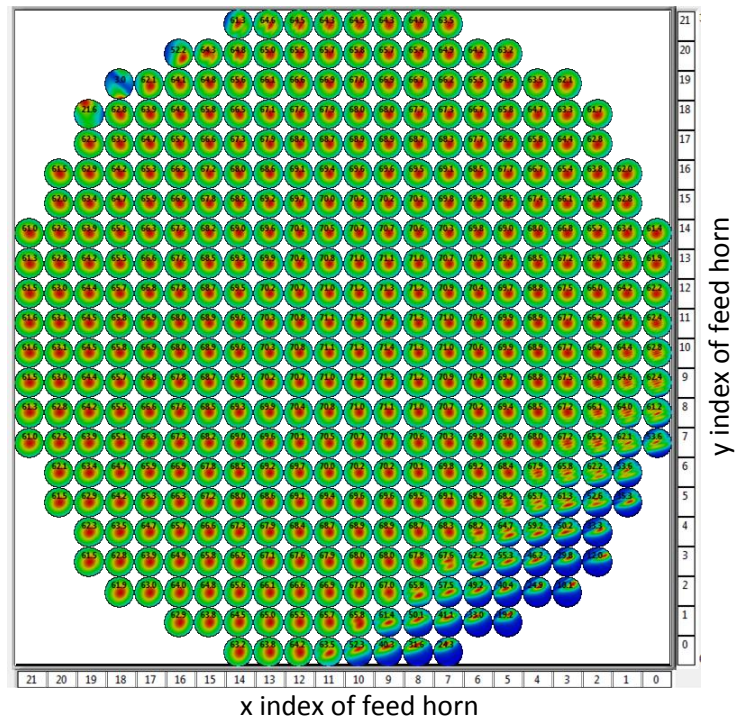


Figure 4.98: Output at detector plane for relocated sources and truncated mirrors showing the power levels at the detector plane as a percentage of the source power emitted for the setup in Table 4.19. The feed horn corresponding to each power value is indicated by its x and y value.

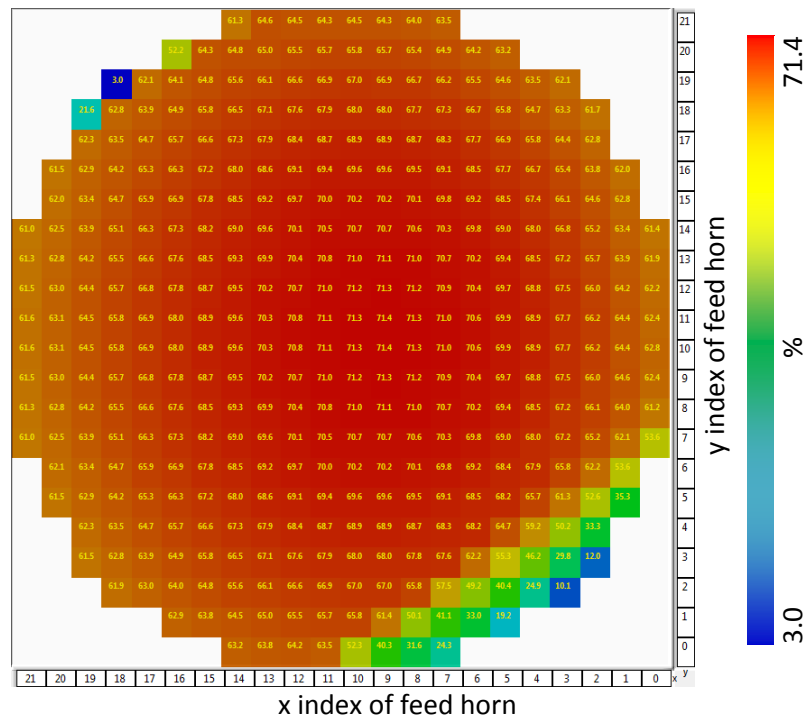


Figure 4.99: Power variation at detector plane for relocated sources and truncated mirrors showing the power levels at the detector plane as a percentage of the source power emitted for the setup in Table 4.19. The feed horn corresponding to each power value is indicated by its x and y value.

4.6 Conclusion

In this chapter I have presented a design for the updated QUBIC v2.0 instrument. I started with the input feed horn array layout and the footprint of the array on each of the elements in the system. At each stage the spillover and truncation was determined and where appropriate the element modified to cope as best as possible within the limitations of the overall instrument footprint.

I have shown that the combiner is capable of supporting a polariser and a second detector plane. In the author's opinion the most important conclusion of this chapter is that the combiner is capable of catering for simultaneous detection of both the x - and y -components of the CMB radiation. The design is spatially very restrictive and a drop in throughput is inevitable when the polariser is included. Narrower beams or reduction in the diameter of the input feed horn array will aid in reducing the truncation and the associated stray light.

I have shown that a coldstop, required as a baffle for the bare bolometer array, will fit within the design allowing for the use of 2-stage cooling (4 K and 100 mK) within the cryostat.

I have shown that a 420 mm manufacturing limitation, if needed, is possible although it will reduce the performance of the instrument through the necessitated reduction of the size of the main elements (primary and secondary mirrors). Relocating the re-emitting input aperture feed horn array from a 466.76 mm to a 366.76 mm separation from the primary mirror vertex will aid in reducing these losses, especially on the primary mirror, without causing additional truncation.

There are several issues in the optical combiner's design, primarily in relation to truncation and spillover, which will greatly benefit from a reduced footprint in the array's beams. In Chapter 5 I will investigate the performance of the combiner as designed here and assess the effects of the aberrations and truncation shown in this chapter.

5 QUBIC performance

In Chapters 3 and 4 I described how the QUBIC beam combiner design was developed with the aim of minimising aberrations and beam truncation. However, in such a fast optical system, both are expected to be present to some degree. In this chapter I investigate the effect that these will have on QUBIC's performance as a synthetic imager.

First I look at the fringe patterns produced by a selection of baselines - for an ideal imager these would be unaberrated and equivalent baselines would produce identical fringe patterns. Next, a quantitative measure of the real combiner's performance is found by comparing its window function to the ideal one shown in Chapter 3. Finally I use the PO model to generate a point-spread function for the instrument; again, this can be compared with the ideal case.

5.1 Baseline separation

The number of fringes measured at the detector plane depends on the focal length of the combiner (300 mm) and the baseline separation chosen (in multiples of the 13.7-mm feed horn separation). In QUBIC, the bolometer array at the detector plane extends to 32 bolometers at the widest point giving a diameter of 102 mm. For a focal length of 300 mm this corresponds to a field-of-view of $\pm \tan^{-1}(51/300) \approx \pm 9.7^\circ$. Equation (5.1) gives the approximate number of fringes that should be produced on the detector plane for a given baseline s_λ , and some values are tabulated in Table 5.1.

$$\#Fringes \lesssim \frac{\theta}{\sin^{-1}\left(\frac{1}{s_\lambda}\right)} \approx \theta s_\lambda \quad (5.1)$$

The range of the number of fringes expected at the detector plane.

where

- r* is the radius of the detector plane
- f* is the focal length of the optical combiner
- θ is the FOV of the combiner given by $\theta = 2 \tan^{-1}\left(\frac{r}{f}\right)$
- s_λ is the baseline separation in terms of wavelengths

Table 5.1: Relationship between baseline separation and fringes on the detector plane (at 150 GHz)

Baseline separation (feed horns)	Baseline separation (mm)	s_λ	Fringes	Bolometers	multipole $l = 2\pi s_\lambda$	Angular scale $\alpha^\circ = 180/l$
1	13.7	6.85	2.3	≥ 5	43	4.2
2	27.4	13.70	4.6	≥ 10	86	2.1
3	41.1	20.55	6.9	≥ 14	129	1.4
4	54.8	27.40	9.2	≥ 19	172	1.0
5	68.5	34.25	11.5	≥ 23	215	0.8
6	82.2	41.10	13.8	≥ 28	258	0.7
7	95.9	47.95	16.2	≥ 33	301	0.6
8	109.6	54.80	18.5	≥ 37	344	0.5
9	123.3	61.65	20.8	≥ 42	387	0.5
10	137.0	68.50	23.1	≥ 58	430	0.4
11	150.7	75.35	25.4	≥ 66	473	0.4
12	164.4	82.20	27.7	≥ 72	516	0.3

At least 2 bolometers per fringe are required for Nyquist sampling and so it is clear from *Table 5.1* that baselines larger than 7 feed horn spacings ($s_\lambda \approx 48$) will not be adequately sampled by QUBIC. This upper limit corresponds to an upper limit on multipole detection of $l = 258$.

The real QUBIC combiner was modelled using PO to determine the fringe patterns from a selection of baselines and a few examples are shown in *Figure 5.1* to *Figure 5.6*. These patterns were found by propagating Gaussian beams from two horns and adding them on the detector plane (for these simulations only the mirrors were included as they are the main source of aberrations, using the setup in *Table 4.11*).

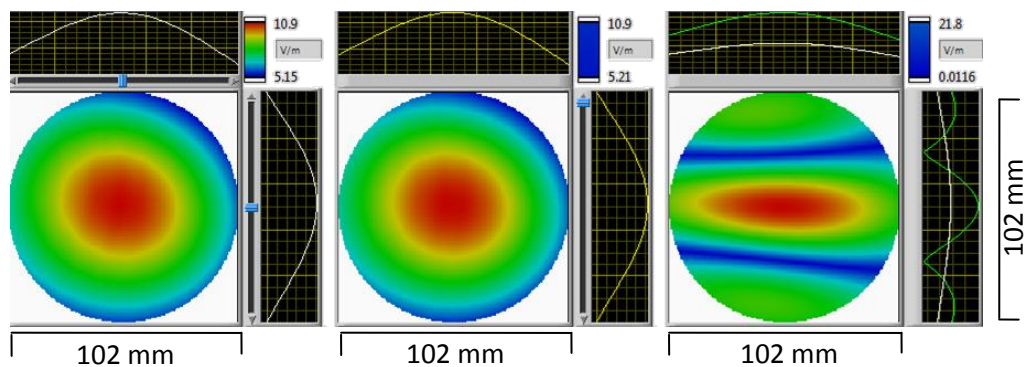


Figure 5.1: Left is the beam from source x00y07 at the detector plane; centre is the beam from source x00y08 at the detector plane and right is the addition of the beams from source 1 and source 2. To the top and right of each image a central cut through each beam is shown with all 3 cuts overlaid on the combined cut.

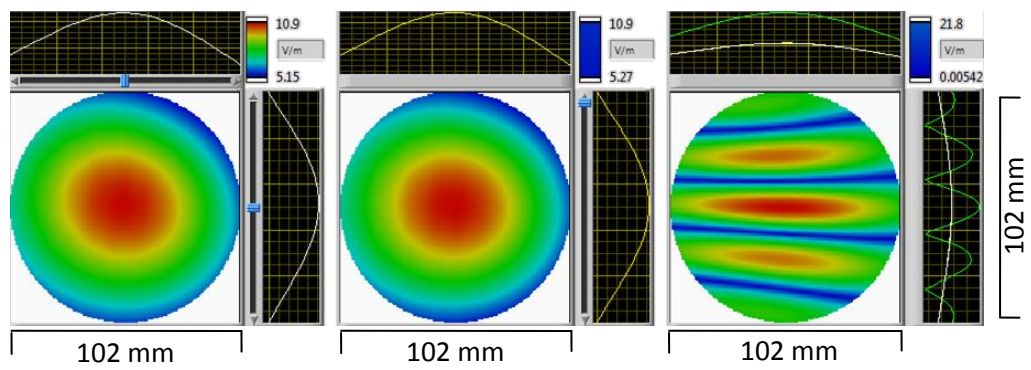


Figure 5.2: Left is the beam from source $x00y07$ at the detector plane; centre is the beam from source $x00y09$ at the detector plane and right is the addition of the beams from source 1 and source 2. To the top and right of each image a central cut through each beam is shown with all 3 cuts overlaid on the combined cut.

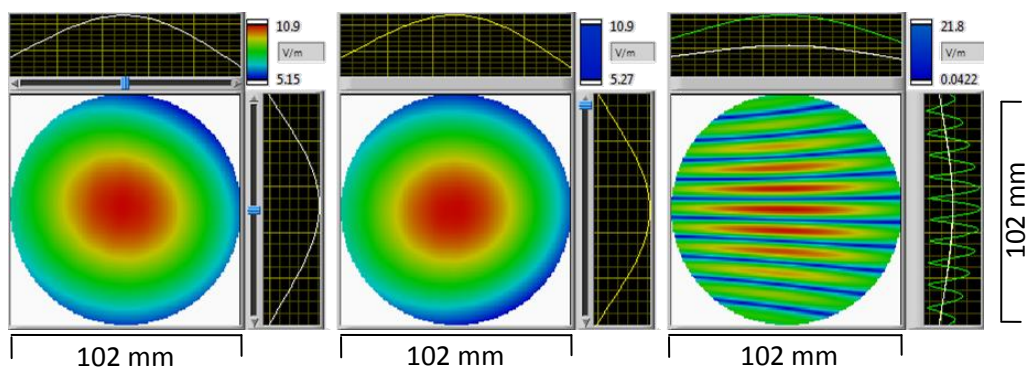


Figure 5.3: Left is the beam from source $x00y07$ at the detector plane; centre is the beam from source $x00y12$ at the detector plane and right is the addition of the beams from source 1 and source 2. To the top and right of each image a central cut through each beam is shown with all 3 cuts overlaid on the combined cut.

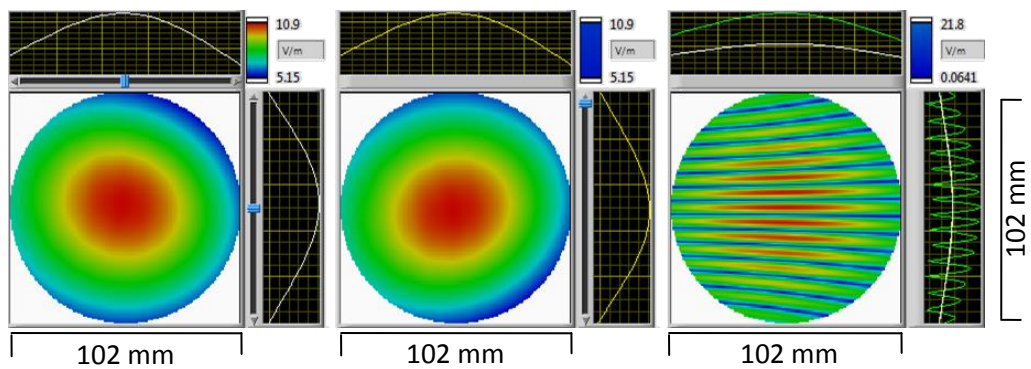


Figure 5.4: Left is the beam from source $x00y07$ at the detector plane; centre is the beam from source $x00y14$ at the detector plane and right is the addition of the beams from source 1 and source 2. To the top and right of each image a central cut through each beam is shown with all 3 cuts overlaid on the combined cut.

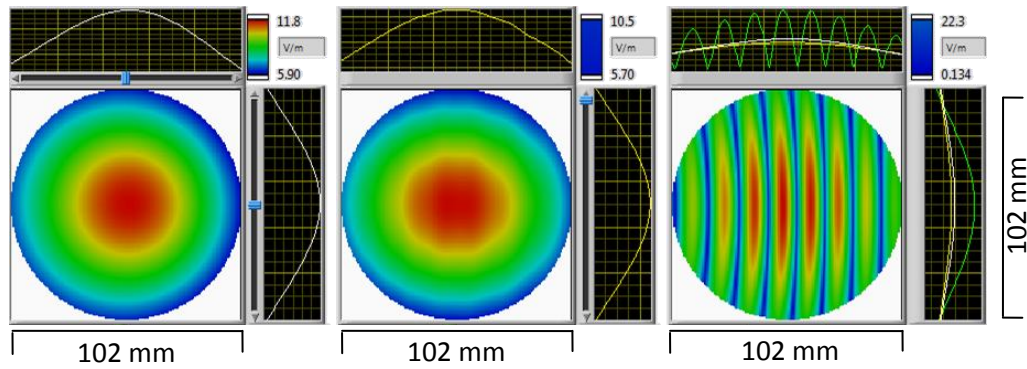


Figure 5.5: Left is the beam from source $x17y11$ at the detector plane; centre is the beam from source $x21y11$ at the detector plane and right is the addition of the beams from source 1 and source 2. To the top and right of each image a central cut through each beam is shown with all 3 cuts overlaid on the combined cut.

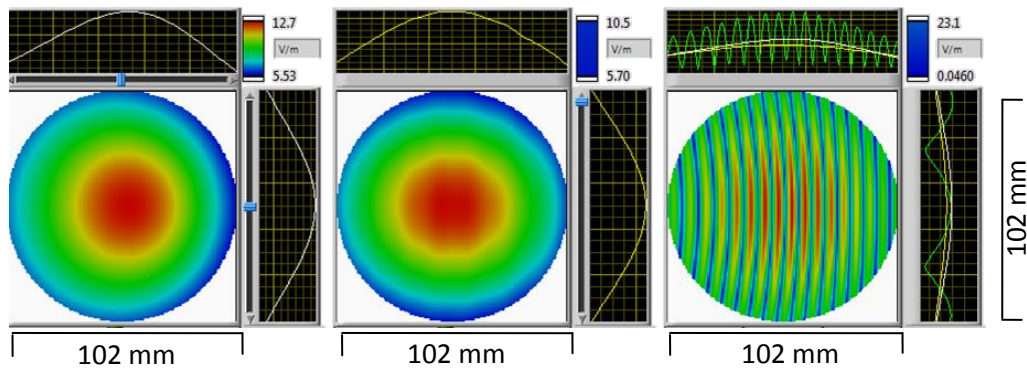


Figure 5.6: Left is the beam from source $x13y11$ at the detector plane; centre is the beam from source $x21y11$ at the detector plane and right is the addition of the beams from source 1 and source 2. To the top and right of each image a central cut through each beam is shown with all 3 cuts overlaid on the combined cut.

From the PO calculations the maximum baseline that can be used is just less than 8 feed horns as shown by Figure 5.6 where just over 16 fringes (to be sampled by 32 bolometers) are visible. The lower end of the band is limited by the horn centre-to-centre spacing of 13.7 mm. These PO simulations therefore show sensitivity in the multipole range $43 \leq l \leq 340$ which gives good coverage in the region where the primordial B-modes are most likely to be observed as discussed in §3.2.2.

The baselines chosen for the example fringe patterns were either along or perpendicular to the plane of symmetry of the QUBIC combiner. These correspond to the worst (Figure 5.1 to Figure 5.4) and best (Figure 5.5 to Figure 5.6) cases in terms of aberrations. The effect of the aberrations is clear from these figures, especially towards the edges of the detector plane.

In an ideal combiner, equivalent baselines would produce identical fringe patterns on the detector plane but in the case of a real instrument, aberrations mean that fringe patterns from equivalent baselines in different parts of the aperture plane produce slightly different fringe patterns. The fringe patterns from an example set of equivalent $s_\lambda = 50$ baselines (145 equivalent baselines in total in this case) were calculated as before and the standard deviation (shaded region) and average (solid line) pattern plotted. These are compared with the ideal pattern (dashed line) in *Figure 5.7* (O’Sullivan, et al., 2015).

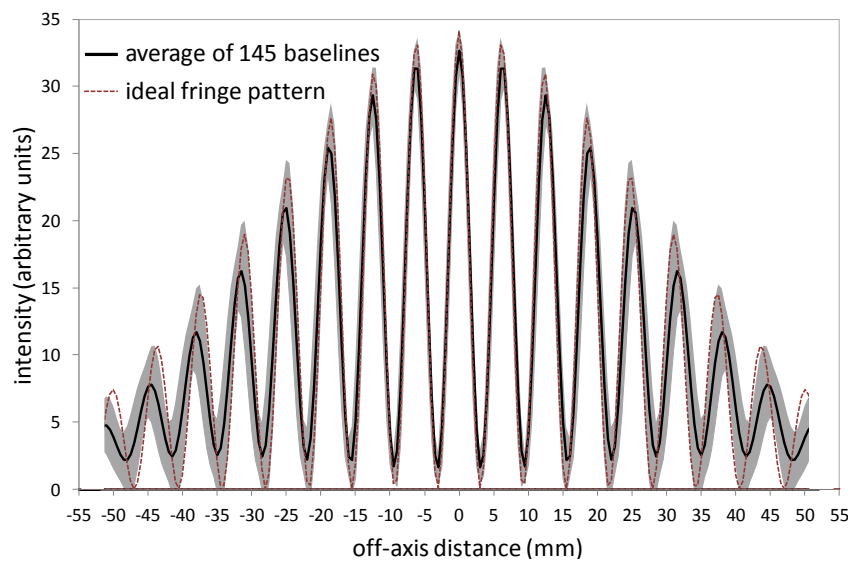


Figure 5.7: Average of the fringe patterns generated by 145 equivalent $s_\lambda = 50$ baselines. The standard deviation of the patterns is indicated by the grey shading and the dashed line shows the ideal fringe pattern.

The equivalent baselines do indeed produce slightly different patterns due to the wavefront aberrations introduced by the combiner. The effect of the variations between the fringe patterns is to reduce the fringe contrast and therefore the sensitivity to the particular multipole corresponding to that baseline spacing. This can be seen in *Figure 5.7* where there is no complete constructive or destructive interference in the average pattern. The variation between patterns increases towards the edges of the detector plane as expected.

5.2 The window function

We have quantified the reduction in sensitivity illustrated by *Figure 5.7* by calculating the window function of the real combiner. The diagonal elements of the window function, $W_l(\mathbf{b}, \mathbf{n}_0, \mathbf{b}', \mathbf{n}'_0)$, introduced in Chapter 3, were first calculated for an ideal combiner (Bigot-Sazy, 2013). *Figure 5.8*, reproduced here for convenience, shows this for an ideal combiner with point bolometers, with 3-mm bolometers and for 3-mm bolometers and 25% bandwidth. The same function was then calculated using 400 'real' focal-plane beam patterns provided by MU. (Again, for these simulations only the mirrors were included as they are the main source of aberrations.) Dividing the real window function by the ideal one gave the plot in *Figure 5.9*. This shows that the aberrations in the combiner reduce its sensitivity by just over 10%. The reduction in sensitivity was considered acceptable by the QUBIC collaboration.

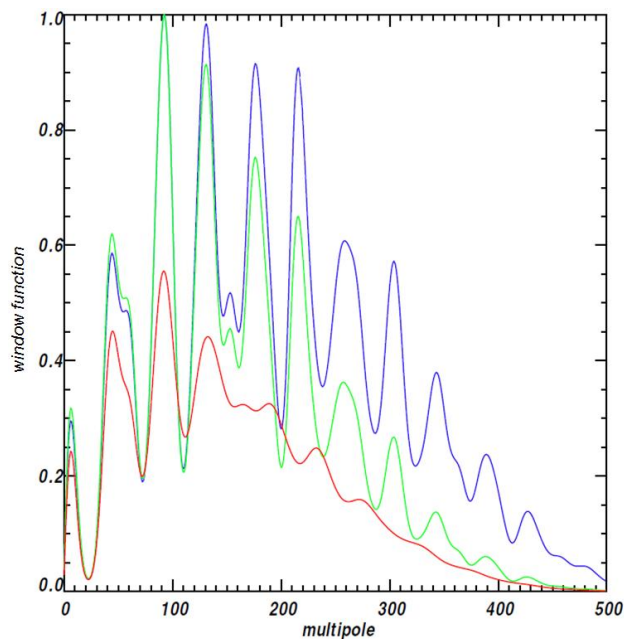


Figure 5.8: Window-function of an instrument with 400 primary feed horns. In blue the window function is shown for a monochromatic instrument with point detectors, green for a monochromatic instrument with 3 mm diameter detectors and red for an instrument with 25% bandwidth and 3 mm detectors. (Bigot-Sazy, 2013)

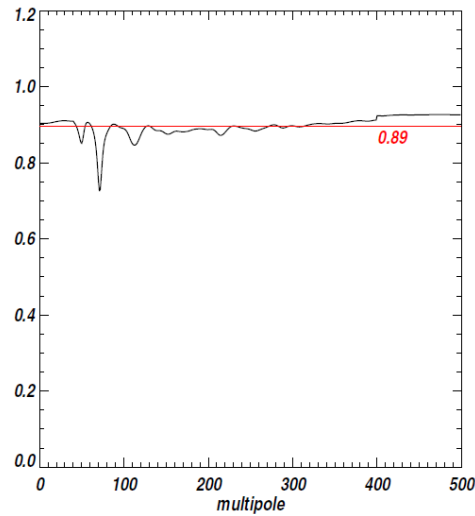


Figure 5.9: The window function of the real aberrated instrument divided by that of the ideal one as a function of multipole number (taken from (Bigot-Sazy, 2013)).

5.3 The point spread function (PSF)

5.3.1 Calculation of the real PSF

The point spread function (PSF) of the QUBIC combiner was calculated by exciting the 400-element input array of horns with an on-axis plane wave. The plane wave coupled to a set of guide TE/TM modes and from these the field at each horn aperture was calculated using the SCATTER mode-matching technique described in Chapter 2. These fields were then propagated through the combiner using PO (not including the polariser and coldstop to allow comparison with the system of *Figure 5.9*) and the 400 fields on the detector plane were added. The result is shown in *Figure 5.10*. The PSF consists of a central peak and three smaller secondary peaks.

We can estimate what we would expect for the PSF of an ideal combiner by considering it as an imager that produces the Fourier transform of the aperture field distribution. The Fourier transform of a finite array of Gaussian beams (we have shown that the aperture field of our feed horns are very close to Gaussian) is an array of Bessel functions (the width of which depends on the array size) with a Gaussian envelope (the envelope being the Fourier transform of the input Gaussians i.e. a single beam pattern on the detector plane). A 1-D simulation is shown in *Figure 5.11*. This shows that an ideal combiner would produce a central peak and two subsidiary peaks along orthogonal axes. In the case of the real

combiner, aberrations at the edge of the detector plane have caused the secondary peak locations to change slightly, pushing one off the edge of the detector plane.

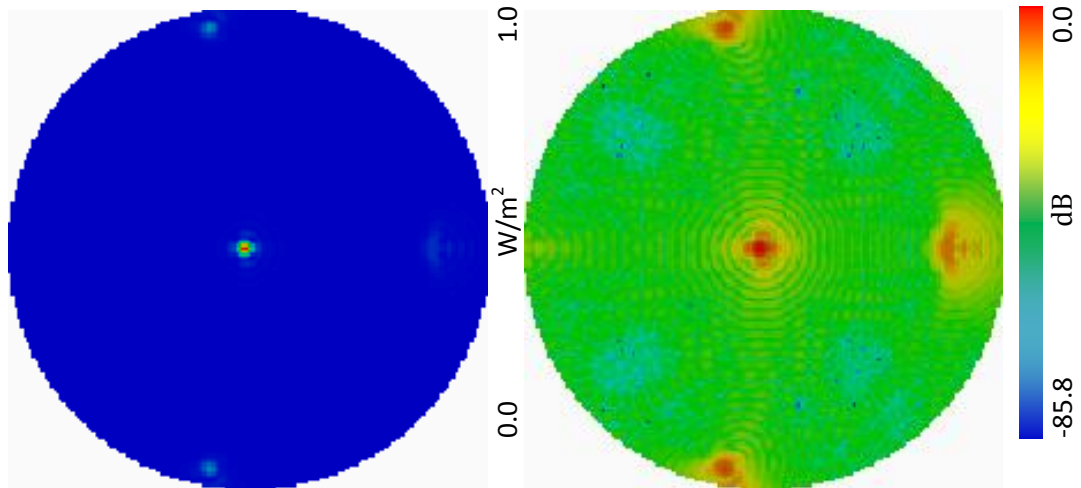


Figure 5.10: The combined output of all 400 14° feed horns on in a circular array of diameter 22 with a 14 mm spacing on the detector plane (point detectors) showing the convolution with the PSF of array an multiplied by the feed horn pattern. Excited at 150 GHz with an on-axis plane wave and propagated through the 300 mm equivalent focal length QUBIC combiner onto the 51 mm radius detector plane (left intensity and right dB scale).

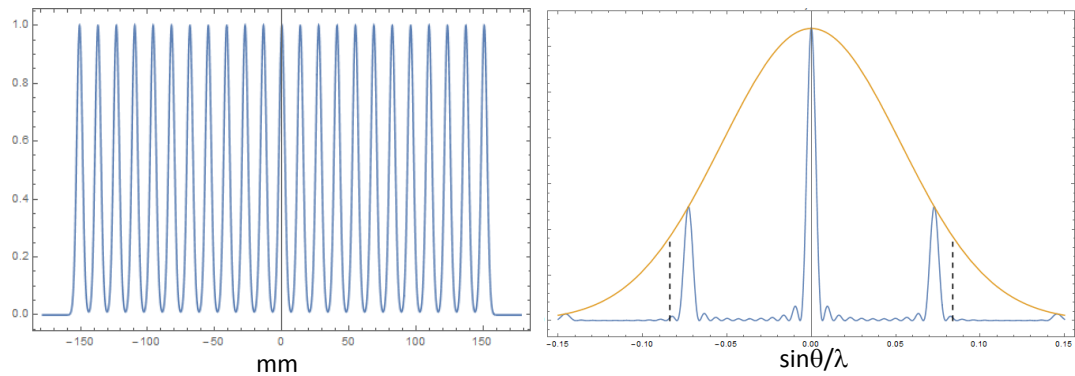


Figure 5.11: An array of Gaussian beams (left) and its Fourier transform (right). Intensity is in arbitrary units. The dashed lines indicate the edge of the 51-mm detector plane.

An ideal 2D PSF was calculated by Bigot-Sazy (Bigot-Sazy, 2013) and is reproduced in Figure 5.12. The left image shows an idealised system where the source is monochromatic and the bolometers are point detectors, in the right image a 25% bandwidth and 3 mm detectors are considered.

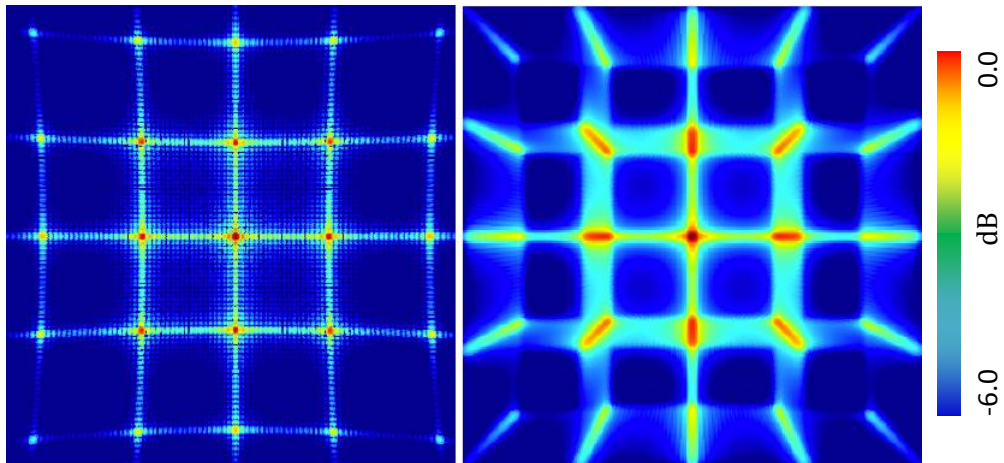


Figure 5.12: Left a monochromatic instrument and a point detector and on the right a 3 mm detector and 25% of bandwidth. The two images are for synthetic arrays of a matrix of 400 primary feed horns, with 14° beams at a frequency of 150 GHz (Bigot-Sazy, 2013).

A pure imager with a 100% fill factor (a single large aperture, essentially giving an infinite set of baselines) would have a PSF consisting of a single central Bessel function (Airy pattern). QUBIC's finite number of baselines reduces the combiner's sensitivity and resolution (Battistelli, et al., 2010) compared to such an imager but in return allows for a novel equivalent baselines calibration technique (maximising amplitude and phase consistency).

5.3.2 Input and detector array orientation

Generating the PSF for this analysis showed that its peaks fall on gaps in the bolometer array (*Figure 5.13*, left); this will result in a loss in detected power for an on-axis source (the darkened sections in the figure illustrate the main vertical and horizontal 2 mm gaps in the detector array). A partial solution implemented by the QUBIC group was to rotate the input aperture array by 45° as shown in *Figure 5.14*. This placed each subsidiary peak in the centre of the bolometer array quadrants (*Figure 5.13*, right). The central peak also falls into this gap but due to space constraints within the cryostat is difficult to remedy. As only large scale features are being sought, those $> 1^\circ$, which span beyond the 2 mm gap ($1^\circ \sim 5$ mm) they are therefore not completely obscured.

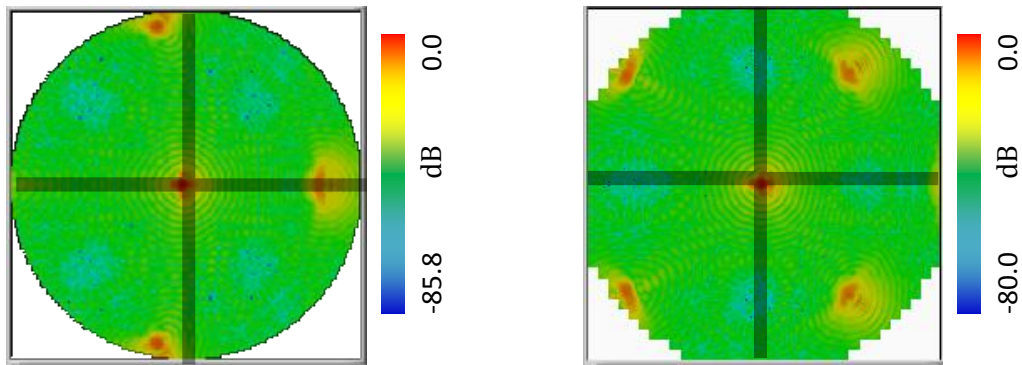


Figure 5.13: The combined output of all 400 12.9° feed horns, (45° rotated about the aperture array's normal) on a circular array of diameter 22 with a 14 mm spacing on the detector plane (point detectors) showing the convolution with the PSF of array and multiplied by the feed horn pattern. Excited at 150 GHz with an on-axis plane wave and propagated through the 300 mm equivalent focal length QUBIC combiner onto the bolometer array at the detector plane.

The position and orientation of the feed horn array is shown in Figure 5.14, the new axis is X_{GRF} , Y_{GRF} and the local feed horn input array axis is X_H , Y_H .

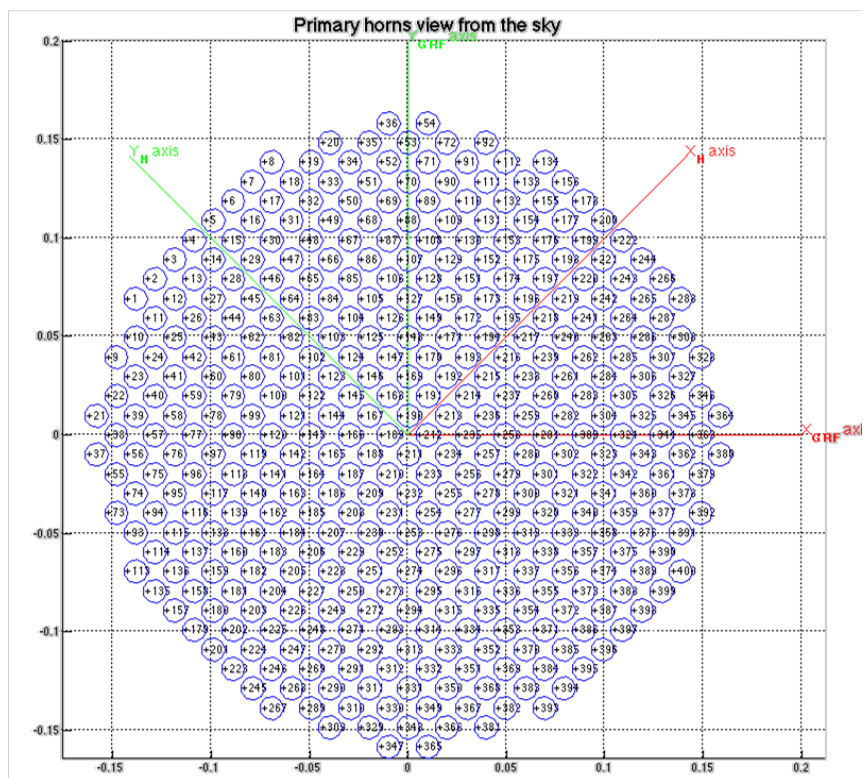


Figure 5.14 Aperture feed horn array shown in the new orientation with the X_H , Y_H axis showing the feed horn axis and the X_{GRF} , Y_{GRF} axis showing the direction of the new GRF axis. Note: The indexing of the feed horns is in the negative y-direction and positive x-direction, placing x01y01 in the top-left corner and x01y22 in the bottom-left of this image.

5.4 Summary and conclusions

In this chapter the performance of the optical combiner was examined. Fringe patterns were produced as expected with the effects of aberrations clearly seen. The effect that these aberrations have on QUBIC was found to be equivalent to a loss in sensitivity of approximately 10% and this was considered acceptable by the collaboration. The PSF of the instrument corresponding to this sensitivity was calculated and showed a central and multiple secondary peaks, as expected, but aberrations caused one peak to lie just outside the detector plane. The input feed horn array was rotated by 45° so that the PSF of an on-axis source would not fall on the gaps between bolometers.

6 Dual-band combiner optimisation

The QUBIC instrument underwent a set of design review meetings in early 2014 partly in response to the release of BICEP2 results (Ade, et al., 2014) announcing the measurement of a significant B-mode signal in the CMB. In order to separate the contribution from polarised foregrounds it was concluded that QUBIC would benefit greatly from dual band observations. The second frequency selected was 220 GHz with 25% bandwidth, the frequency that was originally chosen for module 2 (this will allow for the removal of foregrounds from measurements). The first QUBIC module was now to operate in 2 bands, $150 \text{ GHz} \pm 12.5\%$ and $220 \text{ GHz} \pm 12.5\%$. A new feed horn capable of stable operation over the extended range (130 – 250 GHz) was required. In 2014 it was suggested that the new feed horn, designed in Manchester (*B. Maffei, Manchester*), be modified to produce a narrower beam of 12.9° FWHM. In this chapter, modifications to the 14° design, of Chapter 4, to accommodate the 12.9° source array are now presented along with investigation into the feasibility of a dual band design.

6.1 12.9° element optimisation

6.1.1 Primary mirror

In the first instance the combiner was checked to see the effect of changing the 150 GHz beam size to 12.9° . The original primary mirror design was tested to see if the new narrower beams allowed it to be further reduced in size. The feed horn beams were approximated as a Gaussian beam (3.324 mm waist at 150 GHz to give a 12.9° FWHM far-field), propagated to the primary mirror where their footprint was calculated as before. The 12.9° tests were carried out with the 64 edge sources using the configuration defined in *Table 6.1*. The footprint for the outer sources, shown in *Figure 6.1* for 131.25 GHz, 150 GHz and 168.75 GHz were calculated, covering the bandwidth range of $150 \text{ GHz} \pm 12.5\%$. From the extent of the outer footprint it can be seen that even though the individual beams are narrower they utilise the entire surface area of the mirror. *Figure 6.2* shows the percentage power captured by the detector plane for the edge sources at 150 GHz where it can be seen that sources x19y03 and x20y04 have the worst power capture at 98.5%.

Sources x19y03 and x20y04 are located closest to the centre of the combiner, as indicated in *Figure 6.2*, and the primary mirror cannot be extended further towards the secondary mirror (as it will impede upon the propagation of beams from the secondary mirror). It follows that no further improvement in the percentage power captured can be achieved for this source. For all other edges sources the percentage power capture is better than 99%, as shown in *Figure 6.2*. By extension all sources closer to the array centre will have a capture approaching 100% and it is therefore concluded that the minimum size for the primary which captures out to $2w$ for the majority of sources without impeding upon the secondary is $0.480\text{ m} \times 0.600\text{ m}$ with a rim centre offset of 0.190 m regardless of which set of feed horns is used. *Figure 4.5* is the equivalent plot for the 14° design; the performance is similar in both cases.

Table 6.1: QUBIC element sizes

	Element centre offset wrt LRF (mm)			Rim extent (mm)	
	X	Y	Z	X	Y
Primary mirror	190	0	0	480	600

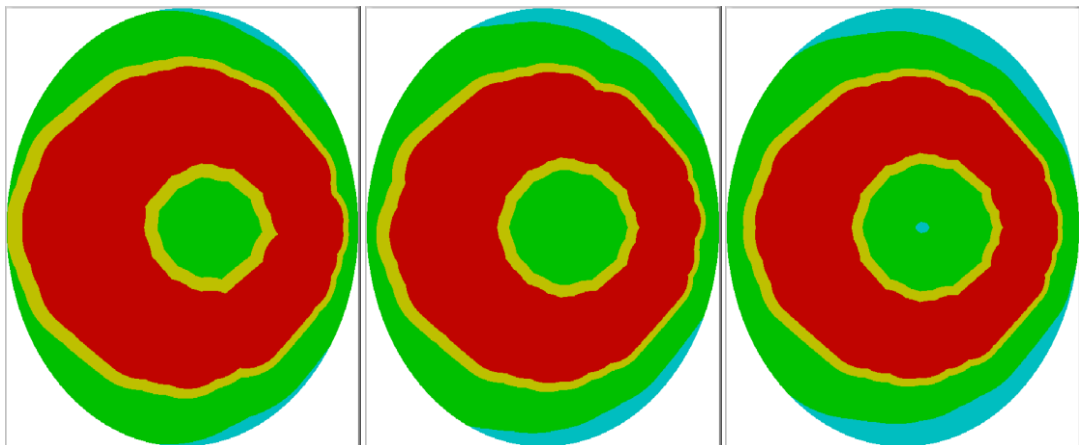


Figure 6.1: Primary mirror ($\Phi 0.48 \times 0.6\text{ m}$) footprint at 131.25 (left), 150.00 (centre) and 168.75 GHz (right). Colour is the same as in Figure 6.1 image key

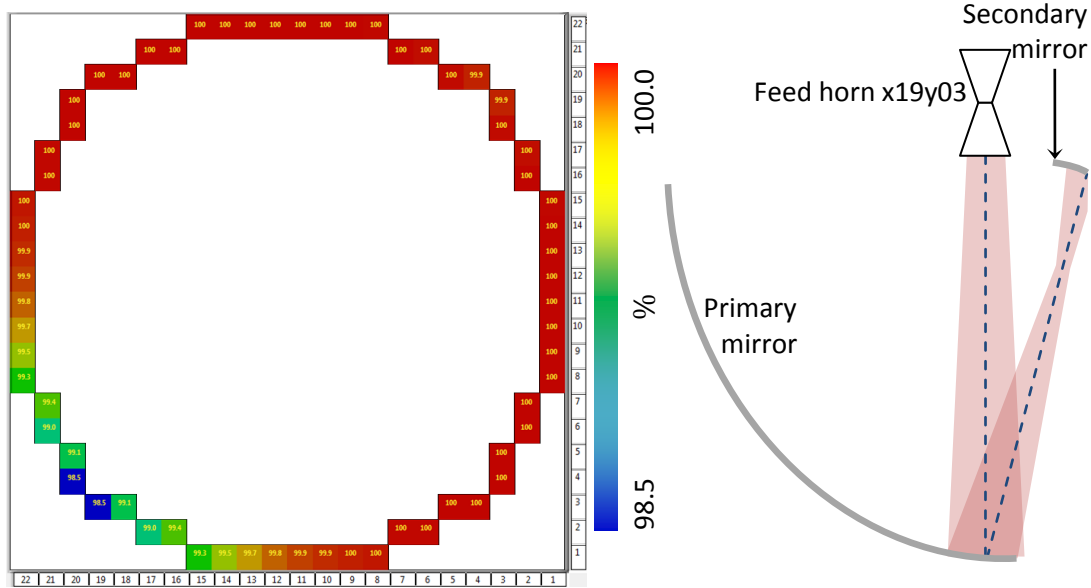


Figure 6.2: (left) Primary mirror (Φ 0.48x0.6 m) power capture for edge sources and (right) source x19y03 illustrated (which is one of the sources with 98.5% power captured in the left image) showing beam at edge of mirror for the selected source.

6.1.2 Secondary mirror

Figure 6.3 shows the outer beam footprint on the secondary mirror across the band for the 12.9° source. It is apparent that in this case the secondary mirror is oversized. Visually inspecting the footprint a width reduction of 100 mm looks possible reducing the secondary mirror to 0.6 m \times 0.5 m. On the left hand side of the centre image in Figure 6.3 it also appears that there is unused surface ~10 mm wide (the cyan region to the left of the image). Shifting the rim centre to the right, from -0.13 m to -0.12 m, will aid in capturing a higher percentage of incident power. The footprint of the edge horns was recalculated using these settings, see Figure 6.4, the major losses can still be attributed to the capture levels at the primary.

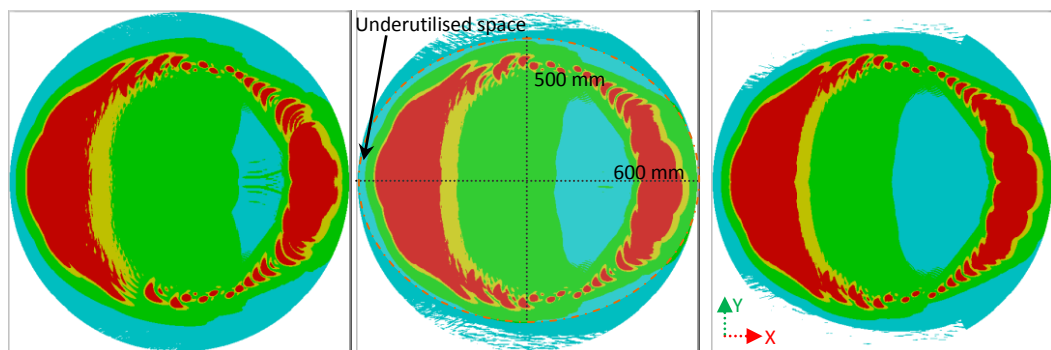


Figure 6.3: Secondary mirror (Φ 0.6 \times 0.6 m) footprint at 131.25 (left), 150.00 (centre) and 168.75 GHz (right). The colour scheme is the same as in Figure 6.1 image key.

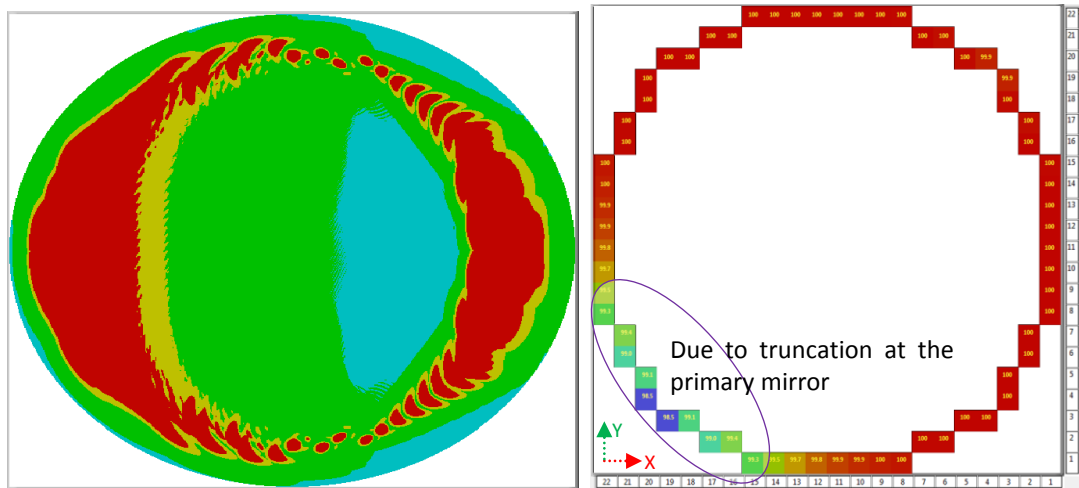


Figure 6.4: Left secondary mirror (Φ 0.6x0.5 m) footprint at 150 GHz with rim offset at -0.12 m and right power capture% for edge sources. The colour scheme is the same as in Figure 6.1 image key.

6.1.3 Polariser and side detector

At this time 110 mm detector plane separation was confirmed and the polariser position, orientation, shape and size were re-examined. The QUBIC instrument will particularly benefit from the optimisation of the polariser surface as it has the most impact on detector plane contamination and blockages within the combiner. The polariser plane was again extended to encompass a diameter 600 mm \times 600 mm, and the power incident upon this calculated. From Figure 6.5 the beam footprint on the polariser is elliptical, with a rotation of about 20° to 30° and a translational offset of about 10 mm in both x and y. As before, there was no setup that completely satisfied all criteria (capture all power and cause no obstructions) and an elliptical polariser with an additional squared-off section to the top right was selected. The ellipse was rotated by 23° and an offset from the centre of the detector plane of 8 mm x 14 mm offers the best capture/blockage trade off. The extended section introduces a non-standard shape which may be difficult to manufacture. Typically, a polariser is circular, for example a copper patterned photolithographic polariser (QMC Instruments, 2012) but, depending on the type selected for QUBIC, non-circular shapes can also be manufactured (for example a wire grid where the wire is wound and glued across a supporting metal frame).

Figure 6.7 shows the polariser with and without the extended squared section, the external dimensions of both are the same (253 mm × 482 mm). This additional section increases the capture potential of the polariser without significant additional obstruction in the combiner. The extended section of the polariser captures power from a small group of sources extending from the top left corner of the array (from x15y22). The difference in power capture between the two versions is shown *Figure 6.8*. Up to 30% more power is captured but the extended section only captures significant power from 5 feed horns. The design in the left hand image in *Figure 6.7* is used in the calculations in this document but if manufacturing requires a simpler structure the impact in terms of power losses and additional spillover can be obtained from *Figure 6.8*, most likely simply leading to the removal of these 5 sources.

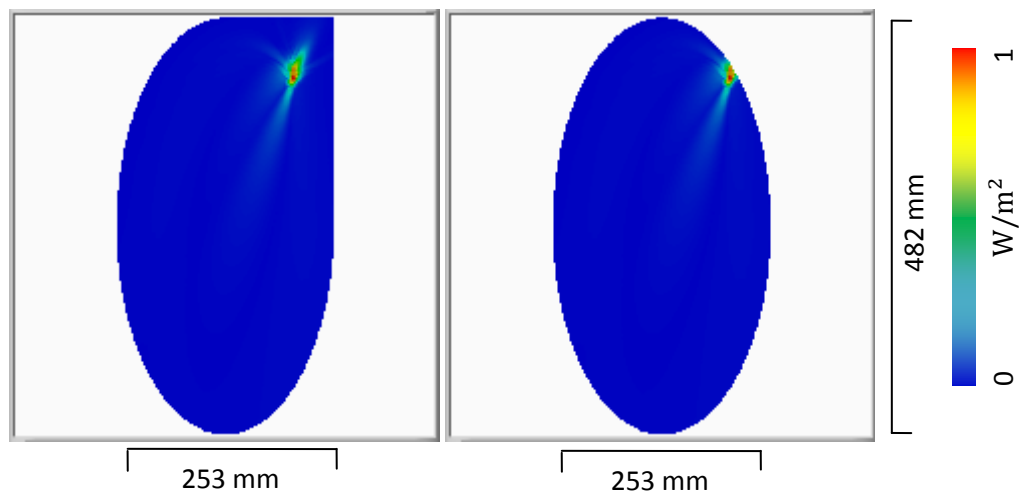


Figure 6.7: Polariser footprint for source x19y20 at 150 GHz showing the impact region for the source on the surface.

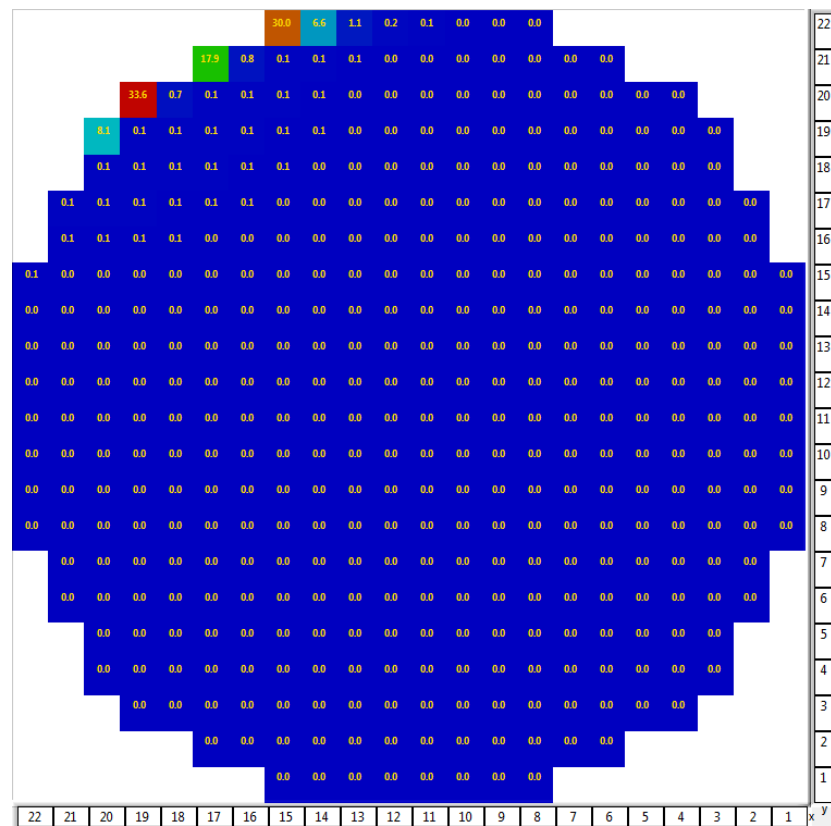


Figure 6.8: Power captured in the extended rectangular corner section of the polariser. Here we see a select group of sources in both cases, with and without the extension, indicating the variation in power capture from one to the other. Power difference between the two cases in Figure 6.7 for capture from each source.

6.1.4 Polariser thickness

Although the polariser itself can be very thin (\ll mm) the frame has a significant thickness and due to the small window within which we can place a polariser the thickness is potentially a significant blockage and must also be modelled. From the QUBIC CAD model the thickness of the polariser is ~ 4 mm (*private communication, QUBIC group, 2015*). The simulation was enhanced to include a thickness for the polariser in order to determine the extent to which a polariser of finite thickness would impact the combiner. An additional surface following the profile of the polariser, extending ± 2.5 mm from the plane of the polariser was added, as shown in *Figure 6.9*. It was implemented for the leading edge of the polariser, that is, the half-edge facing the primary mirror.

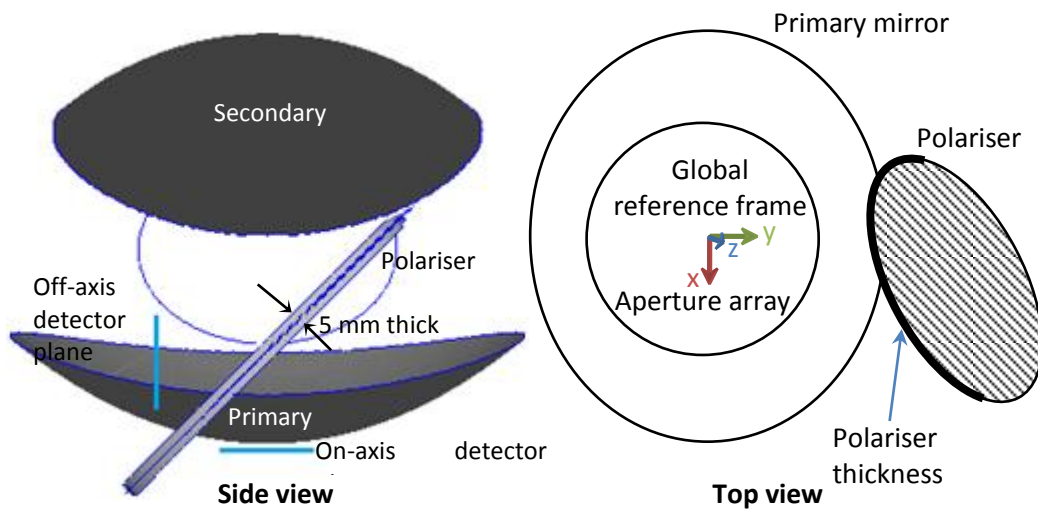


Figure 6.9: QUBIC system showing edge of polariser, 5 mm thick.

The simulations showed that the impact of such polariser thicknesses in the combiner is minimal; the power blockage reached a maximum of $\sim 1\%$ for source x08y22, as shown in Figure 6.10, with the vast majority of sources unaffected.

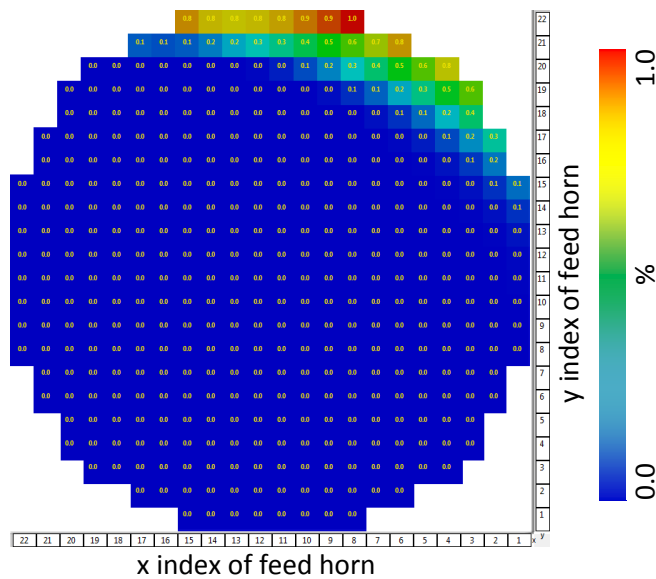


Figure 6.10 QUBIC array power incident on the polariser edge, interpreted as blocked power within the combiner.

Figure 6.11 shows the power blocked by the side detector plane. The worst cases for the 12.9° sources, 7.4% for source x04y03 and 7.3% for source x06y02, are a slight improvement over the 14° worst case, 8.0% for source x14y21, shown in §4.3.2. The side detector blockage is reduced for the 12.9° beams but for a combiner which

includes a polariser and is within the constraints of the current cryostat dimensions they are still unavoidable (as previously found in §4.3.3).

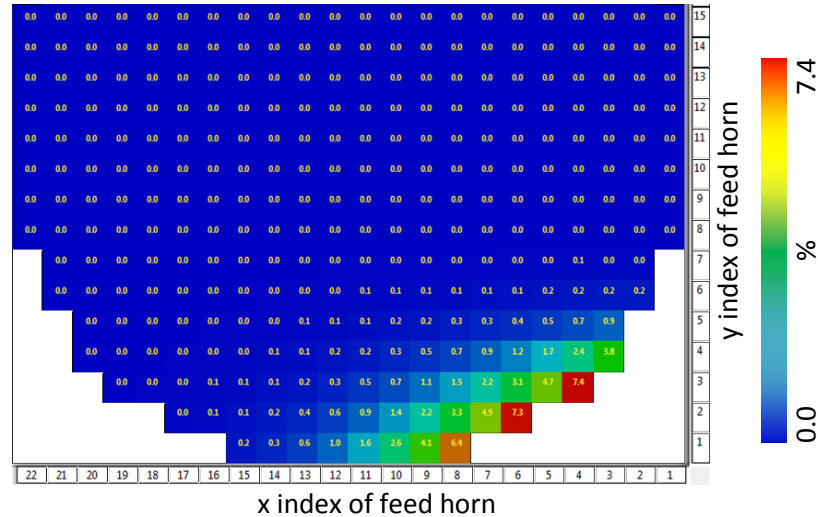


Figure 6.11: Detector plane off-axis blockage for 110 mm detector plane separation at 150 GHz for emission from a Gaussian source with waist 3.324 mm (12.9° beam).

Figure 6.12 shows the power at the polariser taking into account the impact from each element due to capture losses or blockages. The power missing can be classified into 4 categories, power lost at the primary mirror due to truncation, power that does not get through the polariser, polariser blockage on route from the primary to the secondary mirror and off-axis detector plane blockage. As before, a trade-off for the polariser position and shape was made to achieve a balance between the power blocked on the way from the primary to the secondary mirror and the power transmitted from the secondary mirror to the detector plane. A summary of the modified element's size and local orientation is shown in [Table 6.2](#) and size, frame origin and orientation in [Table 6.3](#).

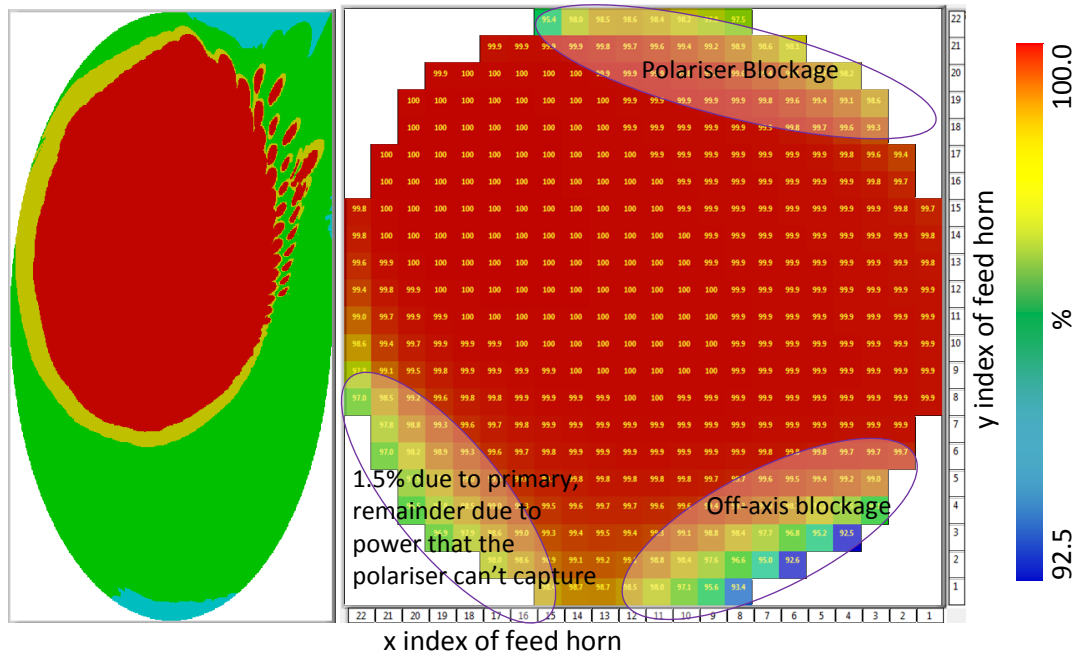


Figure 6.12: Power intercepted by the polariser. Left shows the footprint of the normalised power on the polariser and right the total power for each source. The colour scheme on the left is the same as in Figure 6.1 image key.

Table 6.2: QUBIC element optimised sizes. Translations and rotations are with respect to the elements local reference frame as previously defined in Table 6.3

	Translation (mm)			Rotation (°)			Dimensions (mm)		
	X	Y	Z	X	Y	Z	X	Y	Z
Primary mirror	190						480	600	
Secondary mirror	-120						600	500	
Polariser	8	-14				23	253	482	

Table 6.3: QUBIC system local reference frames defined with respect to the global reference frame.

Frame	Local reference frame origin [m]			Rotation [rad]			Rim origin [m]		Rim dimension [m]	
	X	Y	Z	Z	Y'	Z''	X	Y	W	H
Primary mirror	0	0.209576	-0.466757+Δz	0	π	$-\pi/2$	0.19	0	0.48	0.6
Secondary mirror	0	0.209576	-0.302273+Δz	$\pi/2$	-2.40253	0	-0.12	0	0.6	0.5
Polariser	0	0.378438	-0.463773+Δz	0.40555	0.87800	1.38033	0	0	0.253	0.482
On-axis detector	0	0.331210	-0.563118+Δz	$-\pi/2$	-0.44377	0	0	0	0.1036	0.1036
Off-axis detector	0.11	0.378428	-0.463773+Δz	0	$-\pi/2$	-1.12702	0	0	0.1036	0.1036

6.1.5 Large side detector blockage

In mid 2015 the updated CAD model (see Figure 6.14) showed that the side detector plane had a larger footprint than was previously modelled (when all electronics,

housing and mounts were considered). As previously discussed in *Figure 4.34* the dimensions were selected to determine power to the back of the side detector and do not indicate any real device dimensions. The rectangular plane dimensions are $0.186\text{ m} \times 0.186\text{ m}$ at 90° to and offset by 0.093 m from the side detector centre.

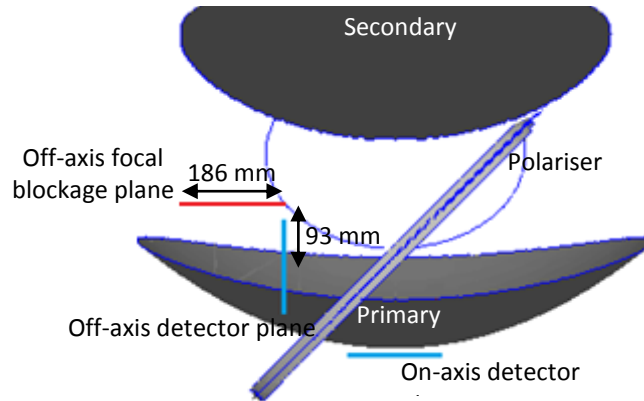


Figure 6.13: Side detector plane blockage shown in red as a plane that captures all power to the back of the side detector plane.

The model was subsequently updated and *Figure 6.15* shows the power from each source that is incident on the side image plane box (that region which the housing, mounts and electronics block). The impact on the output image will be discussed in §6.5 but it is evident from the increased blockages that there are ~ 10 sources that will possibly need to be disabled in order to control the re-scattered radiation within the cryostat.

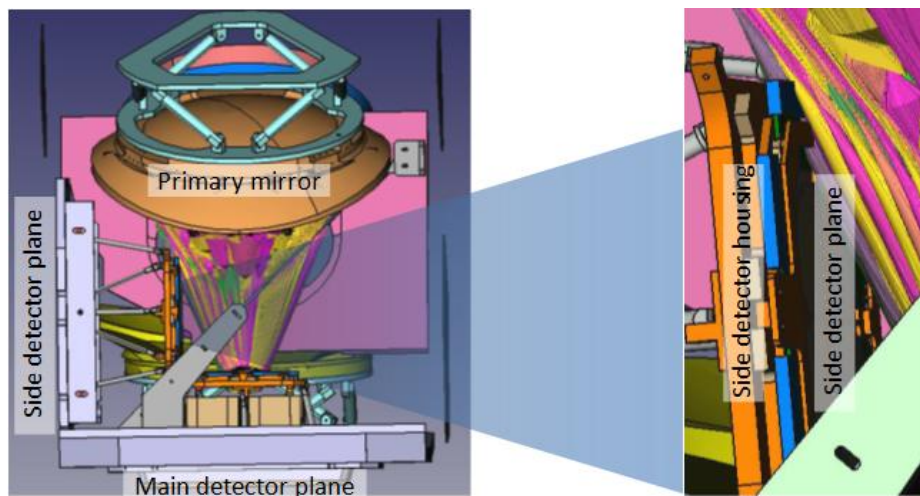


Figure 6.14: Updated CAD model showing (left) the QUBIC system and (right) a zoomed in version on the side detector plane, housing and beams that propagate in that region. All beams are shown out to their 3dB level.

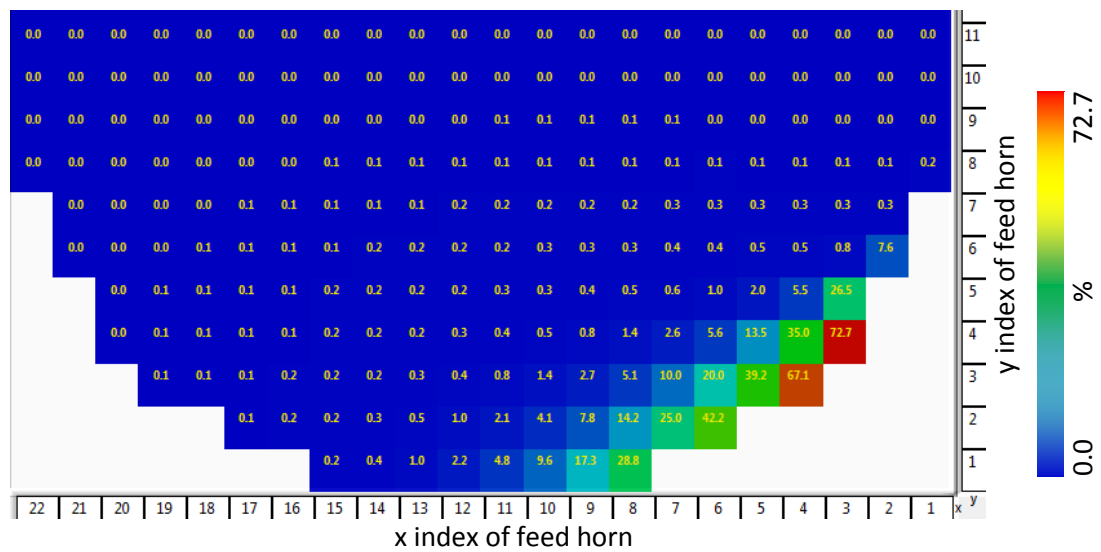


Figure 6.15: Power blocked by side detector plane for 12.9° beams at 150 GHz. The primary was mirror $480 \text{ mm} \times 600 \text{ mm}$ with a 190 mm rim offset. The secondary mirror was $600 \text{ mm} \times 500 \text{ mm}$ with a 120 mm rim offset, polariser, coldstop, enlarged side blockage and detector plane without any gaps. The side detector power blockage ranges from 0.0% to 72.7% (for feed horn x03y04).

6.1.6 Coldstop

The analysis of the coldstop was rechecked for any optimisation (reduction in window size) that might be possible. The consortium was looking to reduce this aperture as much as possible to minimise stray light from the primary mirror side onto the bolometers and to minimise heat transfer between the sections. From [Figure 6.16](#) it can be seen that an aperture of $0.26 \text{ m} \times 0.3 \text{ m}$ will encapsulate almost all power at 150 GHz and above with a small loss of power towards the lower end of the band. The increased size required to capture all power over the entire band was deemed too large (*private communication, QUBIC group*) and a small loss of $<1.5\%$ was preferable for each of 2 sources in the overall array. Using these dimensions the footprint of the edge horns was reconfirmed at higher resolution, the results shown in [Figure 6.17](#) at 150 GHz and [Figure 6.18](#) at 131.25 GHz. The lowest power capture at 150 GHz is 98.1% and at 131.25 GHz this drops to 96.4%. The overall power capture for almost all sources approaches 100% and so this size was selected for the coldstop aperture.

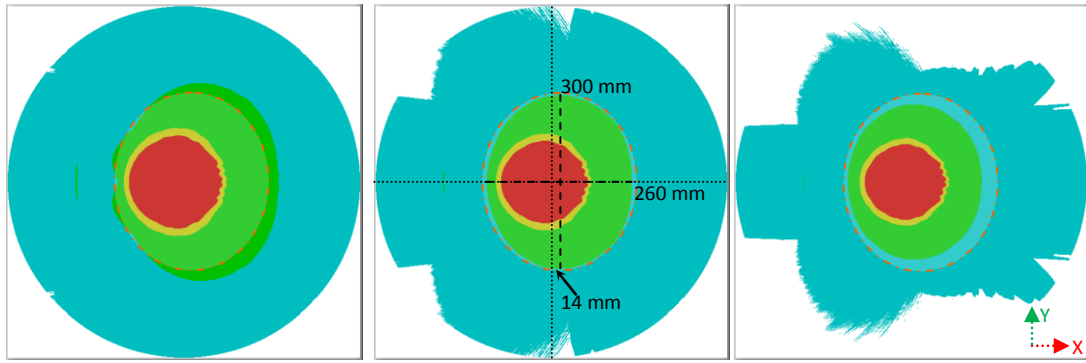


Figure 6.16: Beam footprints at the coldstop aperture (Φ 0.6x0.6 m) footprint at 131.25 (left), 150.00 (centre) and 168.75 GHz (right). Colour is the same as in Figure 6.1 image key.

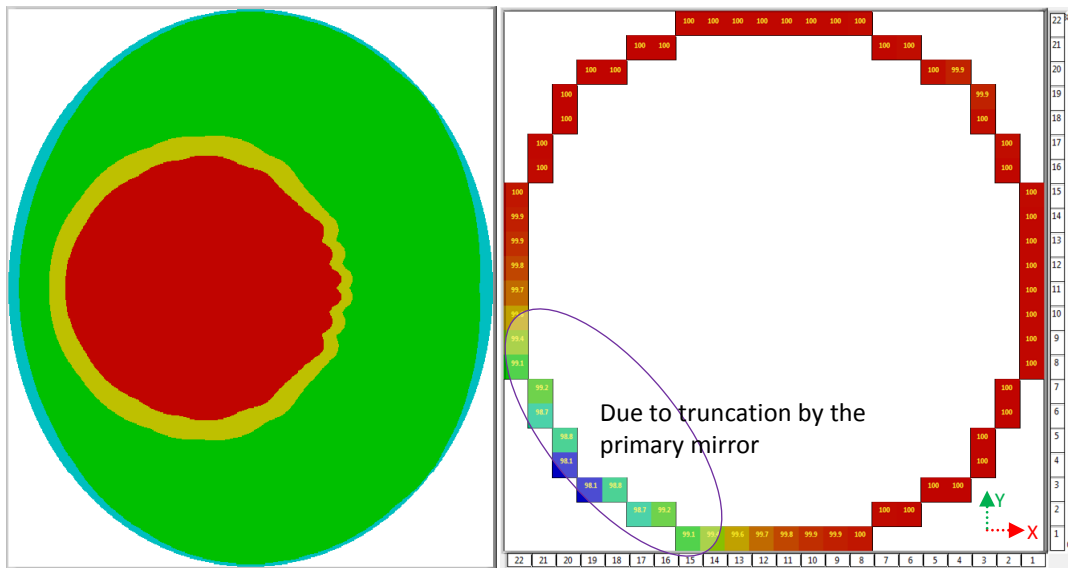


Figure 6.17: Left coldstop surface (Φ 0.26 m x 0.3 m) footprint at 150 GHz and right power capture % for edge sources. Colour is the same as in Figure 6.1 image key.

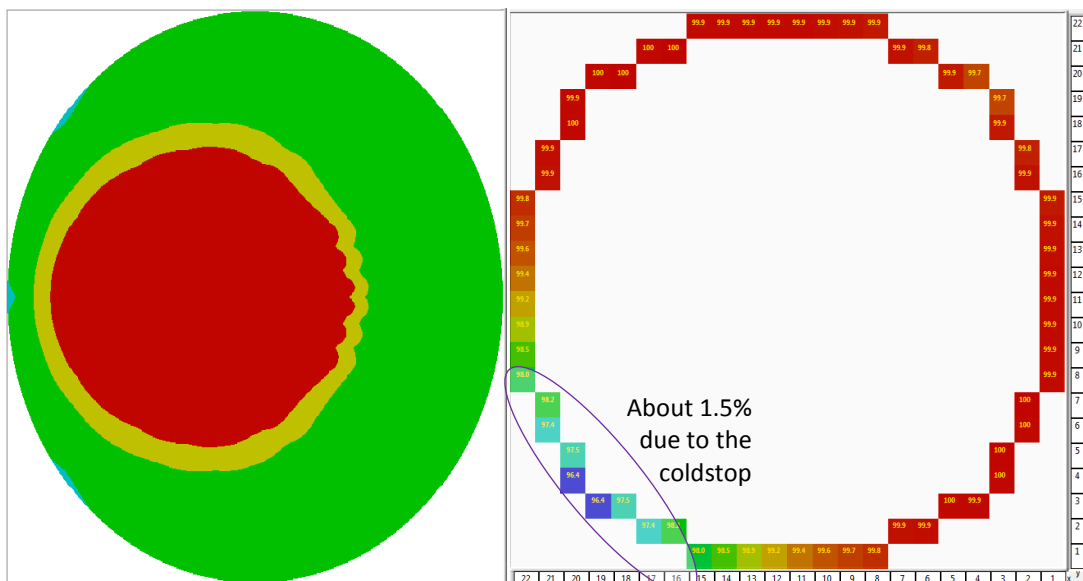


Figure 6.18: Left coldstop surface (Φ 0.26 m x 0.3 m) footprint at 131.25 GHz and right power capture % for edge sources. Colour is the same as in Figure 6.1 image key.

6.1.7 Bolometer array

The total power falling on the different bolometer layouts (the bolometer array tests from §4.1.5 using the test planes defined in *Figure 4.16*) was calculated for the new 12.9° beams. The tests gave power capture levels of 76.2%, 80.0% and 74.4%, as tabulated in *Table 6.4* (the 14° beam results are included for comparison). There was ~5% power drop due to power incident on the main 2 mm gaps in the bolometer array which is almost cancelled by the slightly larger array size compared to the original 51 mm circular test plane used previously.

Figure 6.19 shows an example source (x10y10) on the detector plane with the main 2 mm and inter-bolometer 0.2 mm gaps. The power was found to drop to 62.4%, a loss of 12.0% (in line with 11.3% from the 14° tests). Including losses for the gaps between bolometers ~10% drop in power was noted although again this is not expected to be the case in the actual system as the small 0.2 mm gaps are $\ll \lambda$. The result is a net power loss of ~2% for the 3.324 mm (12.9°) sources compared to the ~1% for the 3.074 mm (14°) sources. Taking account of the narrower (12.9°) beam and the resultant increased power collection at the detector plane we get a gain of ~4%. It is therefore expected that an overall increase in total collected power will be achieved, when everything is considered, for the new feed horns.

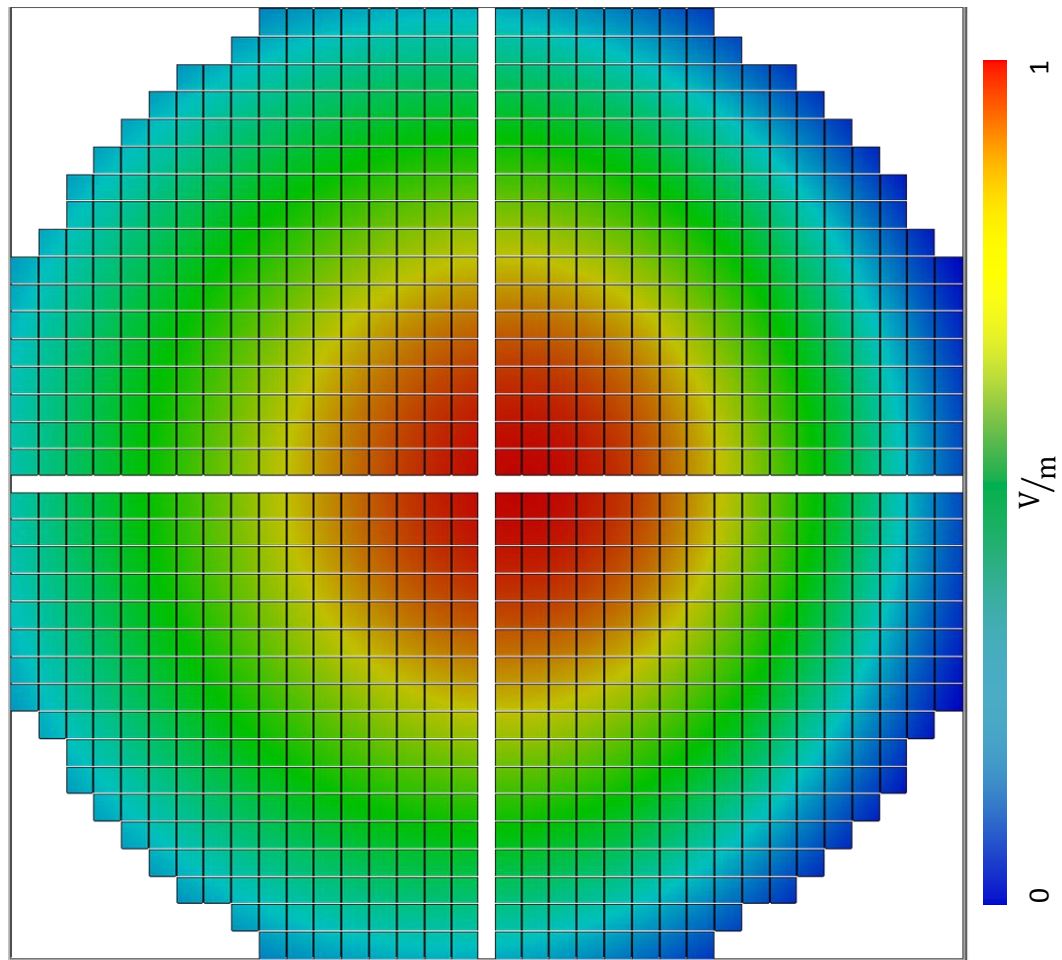


Figure 6.19: Detector plane on-axis power levels, ignoring polariser & coldstop, for source x10y10 (as defined in §3.3.4) with a 3.324 mm waist at 150 GHz (12.9°). Bolometer array and the main central gap are as outlined with all small 0.2 mm gaps between the 2.8 mm bolometers

Table 6.4: Bolometer array detector power capture tests

Test source	Test type	3.074 mm waist (14° beam)	3.324 mm waist (12.9° beam)
x10y10	Circular (r= 51 mm)	71.0%	76.2%
	Bolometer Footprint	75.0%	80.0%
	Bolometers + Main Gaps	70.0%	74.4%
	Bolometers + All Gaps	58.7%	62.4%
x05y05	Bolometers + All Gaps	57.1%	61.0%
x17y17	Bolometers + All Gaps	53.7%	57.8%

6.1.8 Stray light

Stray light directly from the feed horns can get imaged on the detector plane due to the large field of view of the bare bolometer array, as shown in *Figure 6.20*. This is curtailed by the addition of a coldstop. *Figure 6.21* left shows the stray light from the source if the coldstop was not in place and right shows the reduced levels at the image plane when the coldstop is included. In both cases the contribution is minimal and it would not be expected to significantly impact the synthetic image.

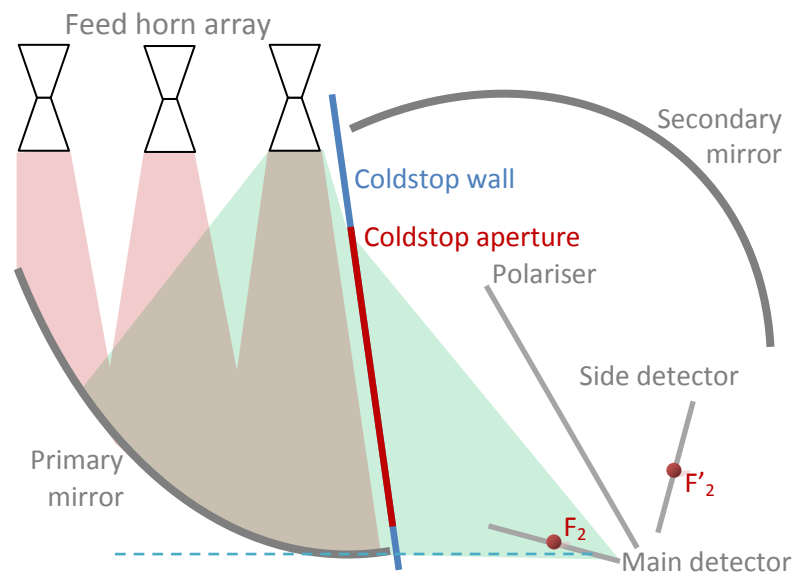


Figure 6.20 QUBIC stray light. The pink regions are the nominal, 12.9° FWHM beam spread. The cyan region for the right-most feed horn shows the non-zero power spread beyond the 12.9° beam width. Some of this power can reach the detector plane (stray-light)

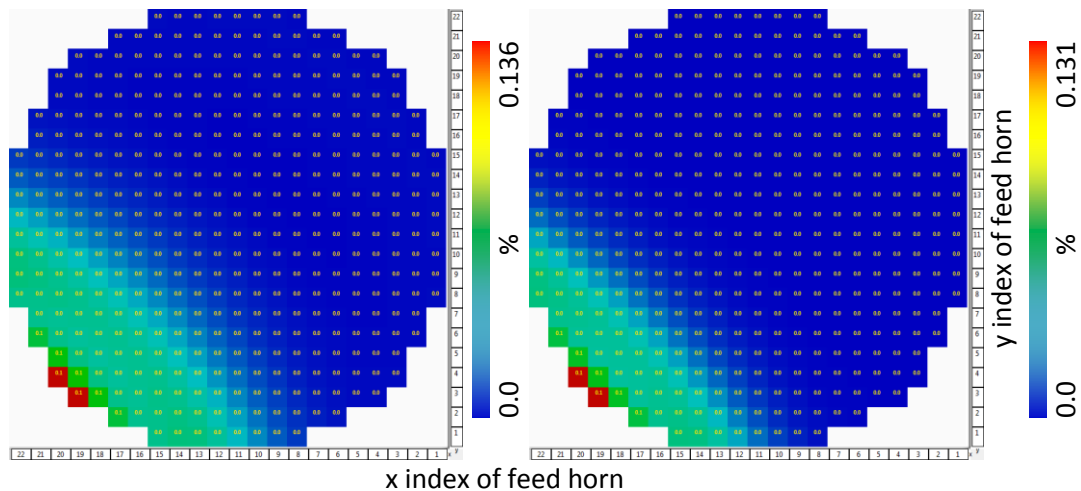


Figure 6.21: Stray light tests for 12.9° beams at 150 GHz propagated directly to the detector plane (left) and after inclusion of the coldstop (right).

At 220 GHz the levels are even lower due to more tightly confined beams. *Figure 6.22* left shows stray light from the source without the coldstop and right shows the levels when the coldstop is included. Both cases show similar contribution and are lower than the 150 GHz case and it would again not be expected to significantly impact the synthetic image.

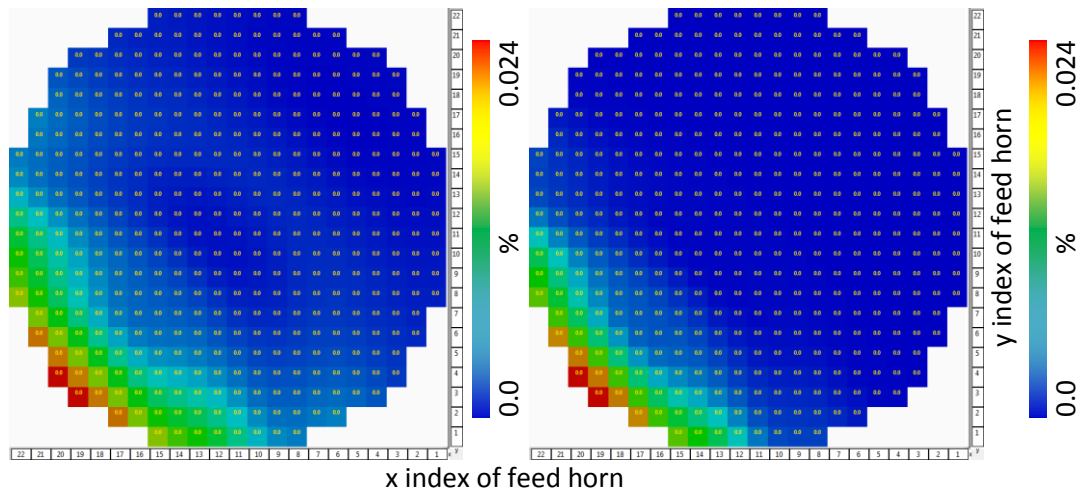


Figure 6.22: Stray light tests for 12.9° beams at 220 GHz direct to detector plane (left) and after inclusion of the coldstop (right) to the detector plane.

6.2 Aperture feed horn array position optimisation

This work has shown that there are several sources that suffer from significant power loss at various points in the combiner (up to ~8% by the polariser). There is a possibility that, keeping within the confines of a 300 mm width, placing feed horns in the corner of a square array might be a better choice for some of the 400 sources. Such an extended array was defined to include all possible positions in a square array whose sides did not exceed the 300-mm limit imposed by the aperture window. As a first step the feasibility of placing sources in these regions was determined. In order to perform these tests the size of the primary and secondary mirrors were increased to cater for the extended array positions. This was approximated visually using GBM in MODAL and the sizes chosen are shown in *Table 6.5* and illustrated in *Figure 6.23*.

Table 6.5: QUBIC system definitions of primary and secondary mirror positions with respect to the GRF for the extended source array tests. Rotations are taken about the vertex for the primary mirror and the focal point F_1 for the secondary mirror, as defined in Figure 3.28. Rim centres are defined with respect to the local reference frame of the mirror.

Element		X	Y	Z	Unit
Primary mirror	Vertex location	0	0.20957580	-0.46675728	m
	Local axis rotation	0	0	-90	°
	Rim diameter	0.520	0.600	0	m
	Rim centre	0.210	0	0	m
Secondary mirror	Focal point 1 location	0	0.20957580	-0.30227328	m
	Semi-major axis rotation	90	-137.655375	0	°
	Rim diameter	0.650	0.600	0	m
	Rim centre	-0.160	0	0	m

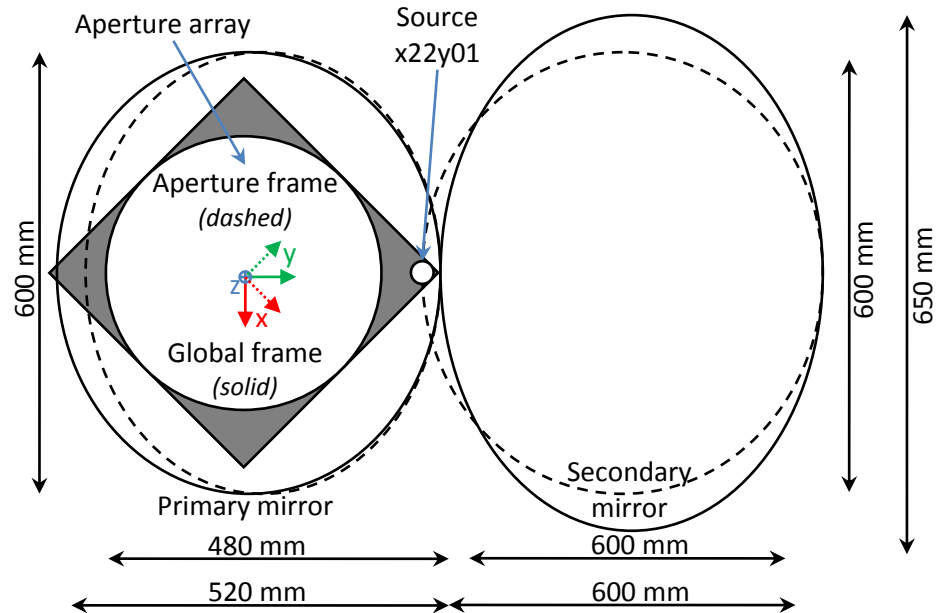


Figure 6.23 QUBIC extended array calculation setup showing the mirrors extended in order to capture the beams from array elements in the corners of the aperture array. The original rim (shown by the dotted line) indicates the original extent of the mirrors (primary mirror of size 480×600 mm with a rim offset of 190 mm as defined in §3.3 and secondary mirror of size 600×500 mm with a rim offset of -120 mm as defined in §3.3) and the new extents with larger rims (primary mirror 520×600 mm with rim offset 210 mm and secondary 600×650 mm with rim offset -160 mm) where the impact of the most extreme sources was observed using GBM in MODAL. It should be noted that the right hand position of the primary mirror is unchanged and the left hand position of the secondary mirror extends up to the position of the corner source x22y01.

The first element is the primary mirror. The footprint of beams from the extended array is shown on the left hand side in Figure 6.24 and the power captured from each source on the right hand side. It can be seen that apart from the feed horns on the combiner's inside (left side of footprint) the mirror captures almost 100% power and very little spillover is evident. The worst case spillover <14% is for source

x22y01 (position shown in *Figure 6.23* and power capture in *Figure 6.24*). In order to cater for these sources the primary mirror would have to be extended further to the inside of the combiner which immediately rules this out due to space restrictions impeding the path from the secondary mirror towards the detector plane.

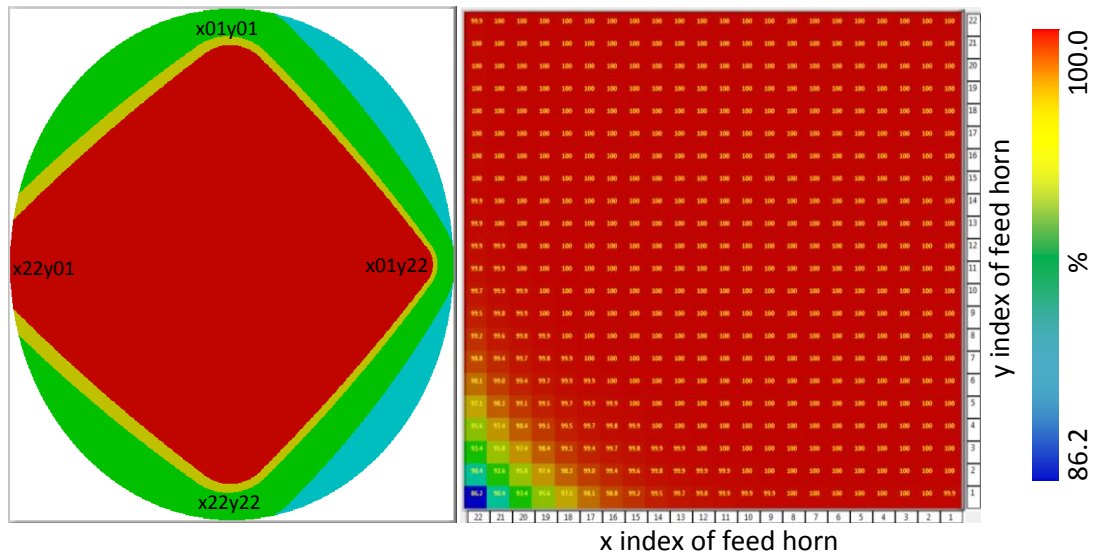


Figure 6.24 QUBIC extended array power capture at the primary mirror. The colour scheme is the same as in *Figure 6.1* image key. The size of the primary mirror is given in *Table 6.5*

Propagating beams on towards the coldstop as shown in *Figure 6.25* the sources that suffered from truncation at the primary mirror are the same ones that are affected at the coldstop. They are truncated further bringing the power levels down by about another 40% to 44.6% in the worst case (for source x22y22) and there is also a drop of ~2% in the region around x01y22. To cater for these sources the coldstop aperture would need to be extended. The potential here is in the x01y22 corner where extending the coldstop will correct for losses at this stage in the combiner.

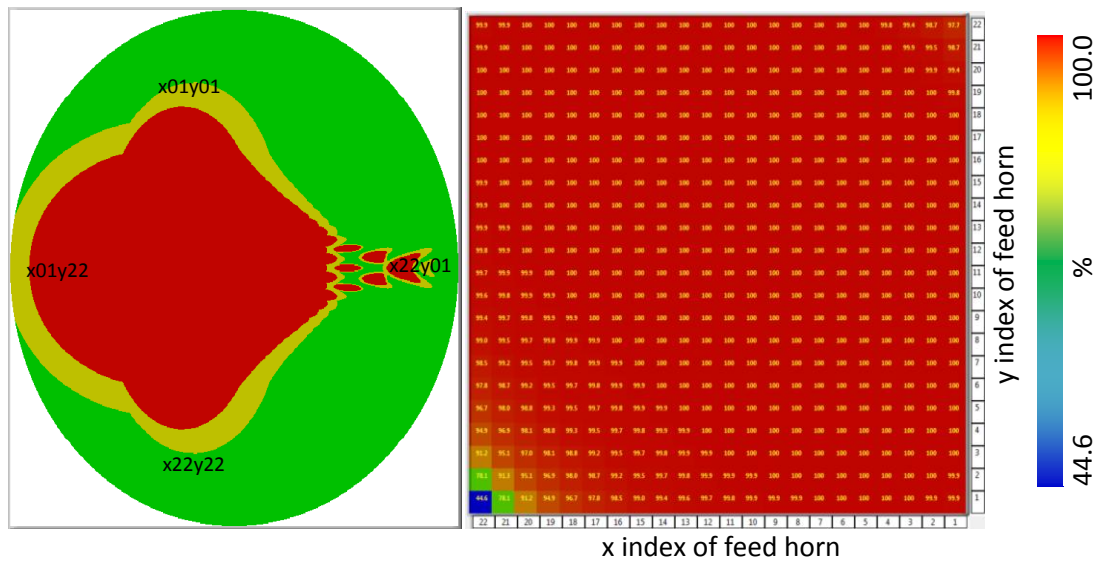


Figure 6.25 QUBIC extended array power capture for the coldstop aperture. The colour scheme on the left is the same as in Figure 6.1 image key. The size of the coldstop is given in Table 6.2 and Table 6.3

In the region around x01y22 there is a loss of power for beams propagating between the primary and secondary mirrors due to the polariser obstructing the path. These losses add to those due to the coldstop, as shown in Figure 6.26. Sources in this region would require a smaller polariser reducing the power captured by it. It would be advisable to avoid this section of the array.

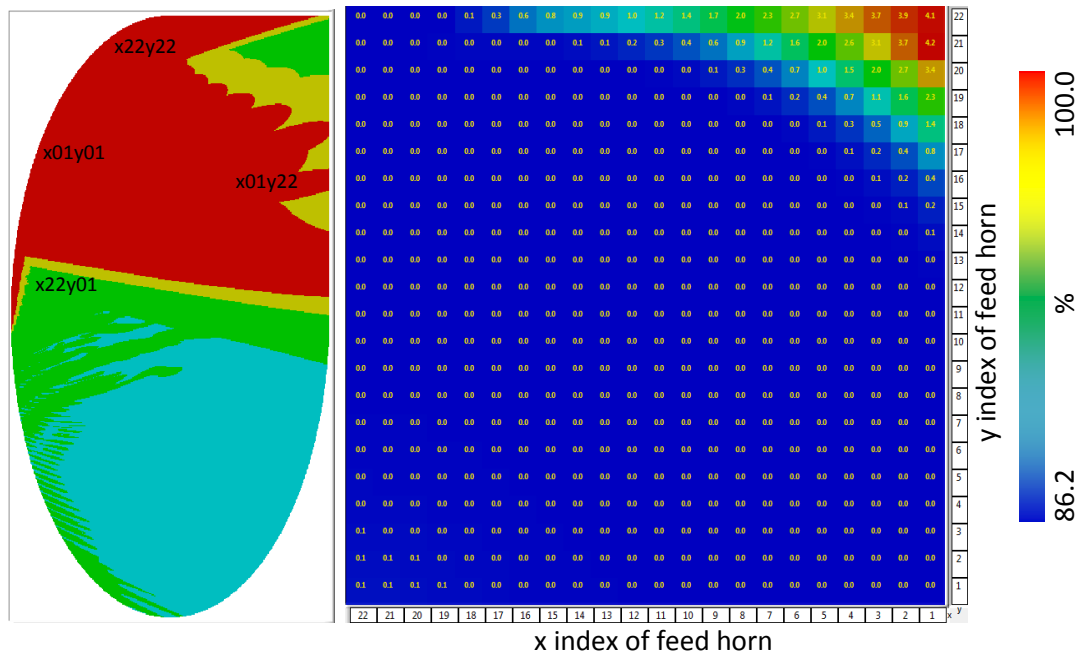


Figure 6.26 QUBIC extended array power incident on the polariser (i.e. the blockage caused by the polariser as beams traverse from the primary mirror towards the secondary mirror). The colour scheme on the left is the same as in Figure 6.1 image key. The size of the polariser is given in Table 6.2 and Table 6.3

For beams at the secondary mirror there is a loss of power for the region around x22y01, as shown in *Figure 6.27*. This is the same region that causes an issue at the primary mirror and to extend the secondary mirror would be problematic as the extension would encroach upon the extended aperture position causing the problem in the first place. This is essentially a beam that passes back along its own propagation path after reflection off of the primary mirror. In the opposite corner where there are also some losses the main concern would be that beams in this part of the secondary would not cross the plane of the polariser. This will be looked at when considering the polariser surface as shown in *Figure 6.30*.

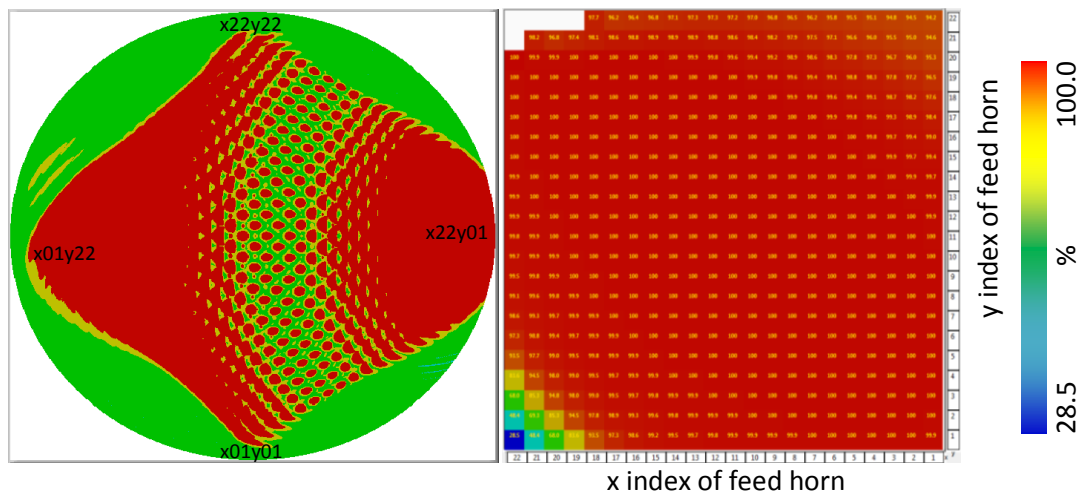


Figure 6.27 QUBIC extended array power incident on M2. Colour is the same as in *Figure 6.1* image key. Note: Missing sources in top-left are due to PO failure in the case of extreme incident angles of beams crossing the surface. The size of the secondary mirror is given in *Table 6.5*

Upon reflection off of the secondary mirror the side detector plane blocks beams emitted in the region around x01y01. The extended positions near x01y01 suffer massive blockages up to 91.3% as shown in *Figure 6.28*. It would be advisable to avoid this section of the array.

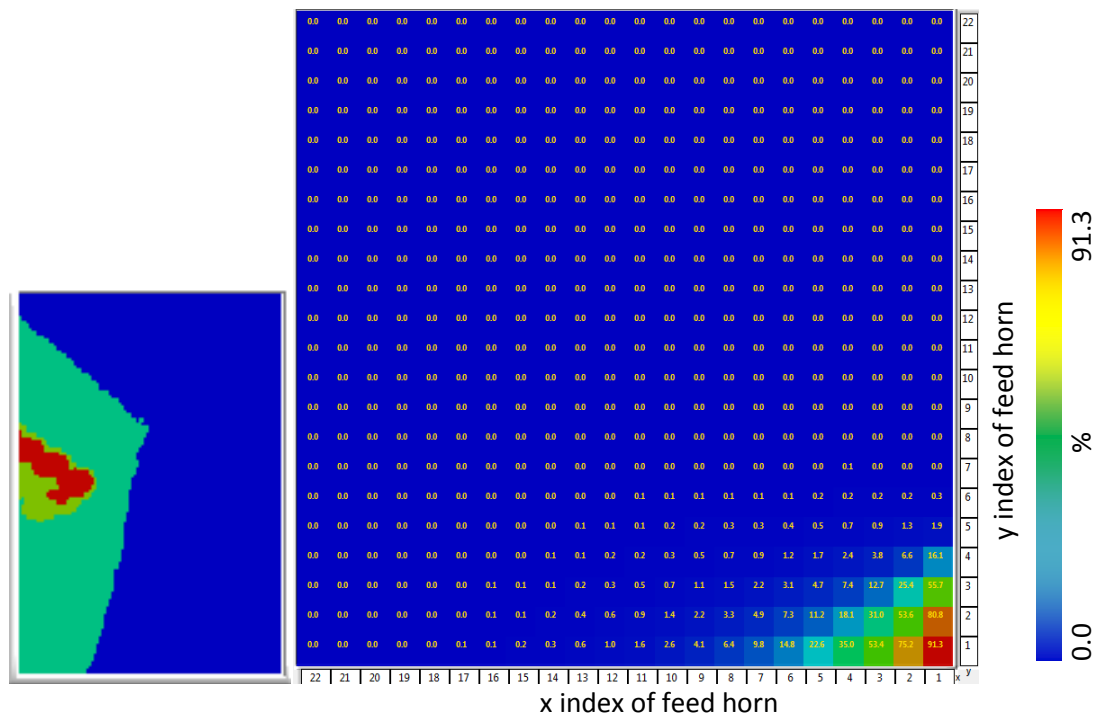


Figure 6.28 QUBIC extended array power incident on the side detector plane when it is considered as a blockage in the system. The colour scheme on the left is the same as in Figure 6.1 image key. The footprint in this case is presented without pre-combination normalisation as this presents a red rectangle due to the spread of power over the surface from each possible source. The size of the side detector is given in Table 6.2 and Table 6.3

The polariser captures power from almost all the extended array. The only region to suffer from a significant loss of power is that around x22y22, as shown in Figure 6.29. On closer inspection of the path of the beams through the instrument it was noted that the beams in this section reflect off of the secondary mirror and fail to intersect the plane of the polariser (passing under the polariser), as shown in Figure 6.30. The plane of the polariser was then projected out to the secondary mirror, as shown in Figure 6.30. The region of the secondary mirror above this intersection is that which is reflected onto the polariser and is labelled as the nominal section. The part below, reflection from which misses the polariser, is labelled as the contaminated section. By source position x22y22 almost the entire beam traverses directly onto the on-axis detector plane. The beams that fail to intersect the polariser result in the contamination of the detector plane.

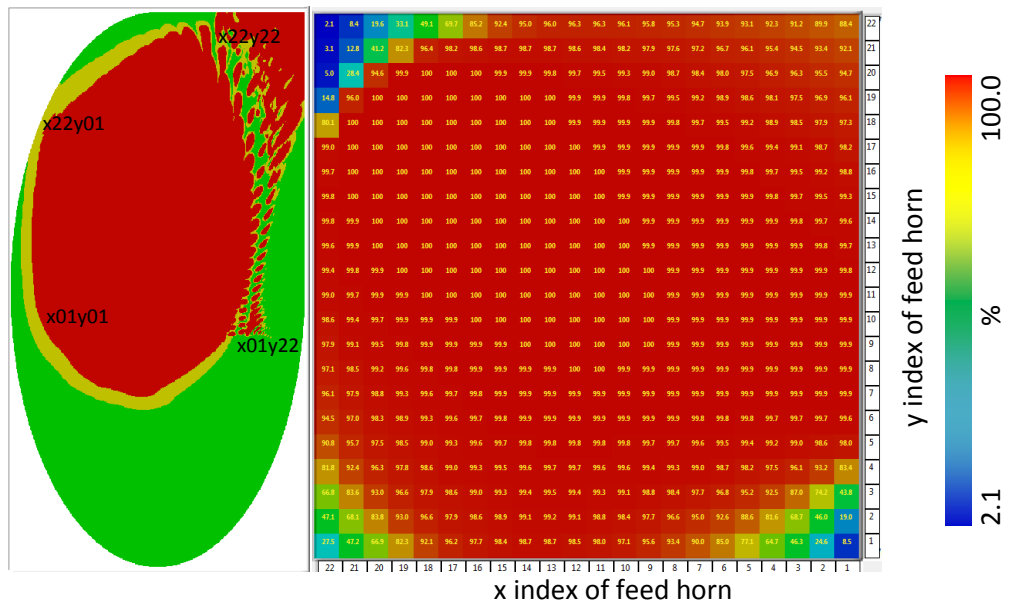


Figure 6.29 QUBIC extended array power incident on the polariser. The colour scheme on the left is the same as in Figure 6.1 image key. The size of the polariser is given in Table 6.2 and Table 6.3

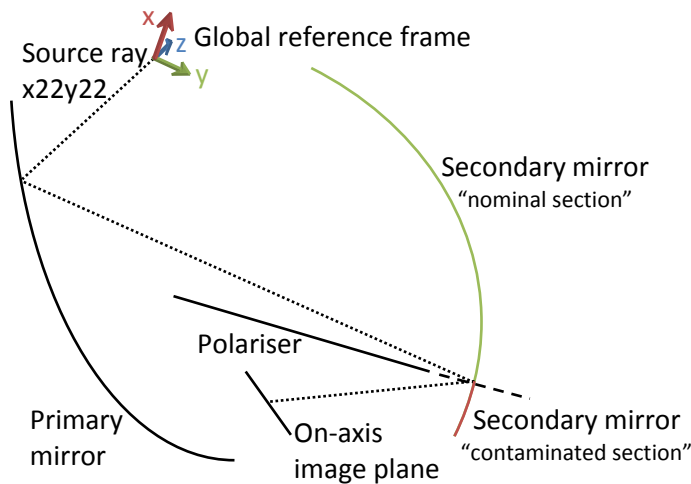


Figure 6.30 QUBIC showing beam for source x22y22 with reflection from the primary mirror and the secondary mirror passing across and under the polariser. This test was carried out considering a 12.9° FWHM beam out to 1W at 150 GHz. The secondary mirror is shown divided into 2 sections, above (nominal region) and below (contaminated region) the plane of the polariser.

Figure 6.31 and Figure 6.32 show the power falling on each of the two sections. The power calculations show that the beams that miss the polariser belong to only a few horns in the corner (x22y22) and top row (y22). More sources were selected to help determine the extent of the overall power losses expected for each source. Figure 6.32 shows the contaminating power levels that miss the polariser for each source upon reflection from the secondary mirror. Sources x20y20, x21y19, x21y18, x22y18, x22y17 and x22y16 have losses <0.1%, so they offer the best choice as

replacements for existing sources. Choosing sources x20y04, x19y03, x17y02 and x15y22 (the 4 lowest power levels at the detector plane) and replacing them with the best extended position sources above will yield a net power increase of $\sim 0.02\%$. Considering the minimal power increase in the overall system from this change (a bespoke array shape which may yield its own manufacturing issues) it is recommended that this region of the array is not used and absorber is used in the 2 first rows to curtail the contamination, which is $\sim 0.2\%$ in the worst cases as shown in *Figure 6.32*.

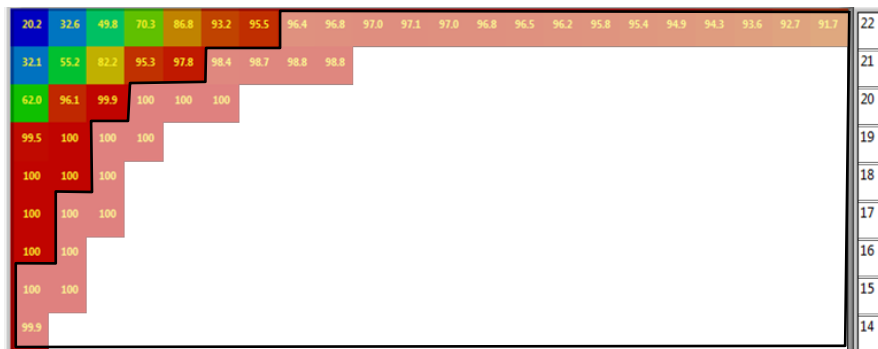


Figure 6.31: Power captured at the secondary mirror, in the nominal section.

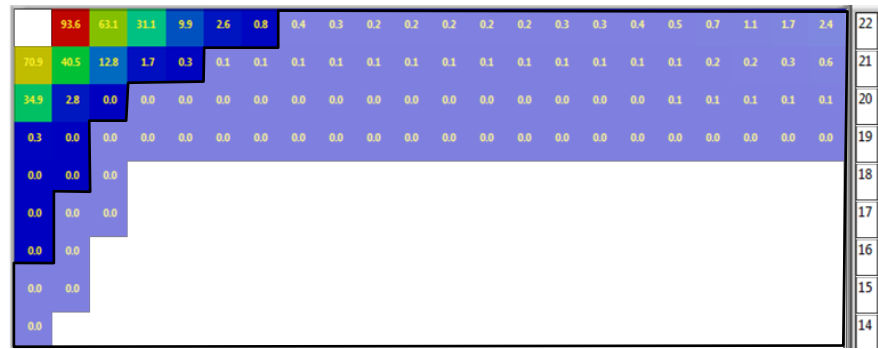


Figure 6.32: Power captured at the secondary mirror, in the contaminated section.

The simulation was next setup to include blockages from a finite thickness polariser, as previously discussed in §6.1.4 and shown in *Figure 6.33*. There were 2 cases tested, that of 5 mm and 20 mm thicknesses. 5 mm is the expected thickness but for a worst case scenario 20 mm was also simulated. The blockage reached a maximum of $\sim 2.6\%$ (5 mm case) and $\sim 10.5\%$ (20 mm case) for source x22y01 (in both cases), as shown in *Figure 6.34* and *Figure 6.35*. The top 2 rows, y22 and y21,

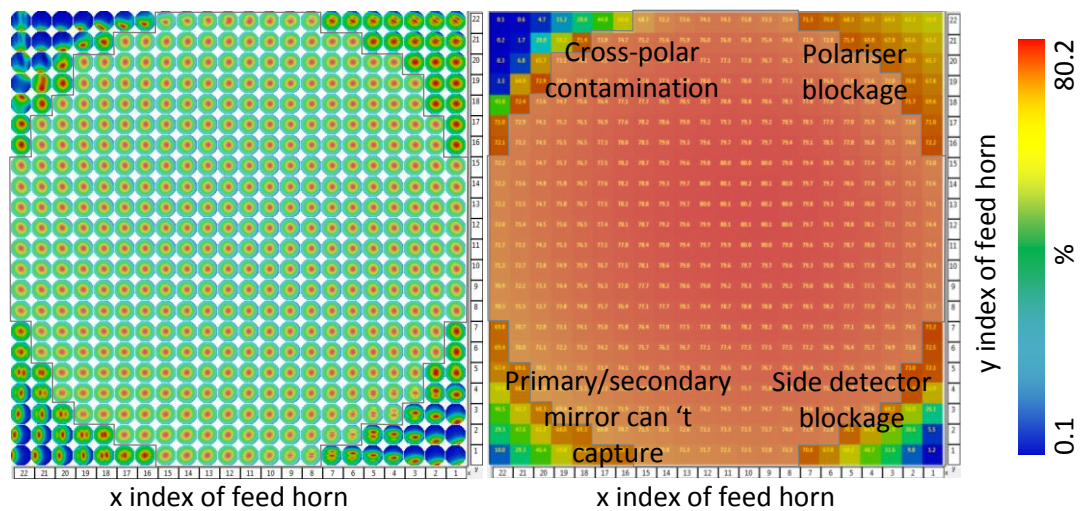


Figure 6.36 QUBIC extended array power incident on the main detector plane at 150 GHz for a 3.324 mm waist source Gaussian beam.

6.3 New feed horn design

In order to separate the contribution from polarised foregrounds it was concluded that QUBIC would benefit greatly from a dual band observation. This extended range is split into the 2 sub-bands centred at frequencies of 150 GHz and 220 GHz both with a 25% bandwidth (*private communication, QUBIC group, 2014*). It was first decided to test the behaviour of the original scaled (14°) CLOVER feed horns in the higher frequency band. The power transmitted and reflected for plane wave excitation of the feed horn was calculated as a function of frequency over a range of input angles from 0° (on-axis) to 40° off-axis in 10° steps, as shown in *Figure 6.37*. This is an extension of the analysis carried out in *Figure 2.5*. The response of the 14° feed horn becomes unstable beyond 180 GHz and so while a good fit for the single band design (130 – 170 GHz), it could not be used for the dual band instrument (130 – 250 GHz).

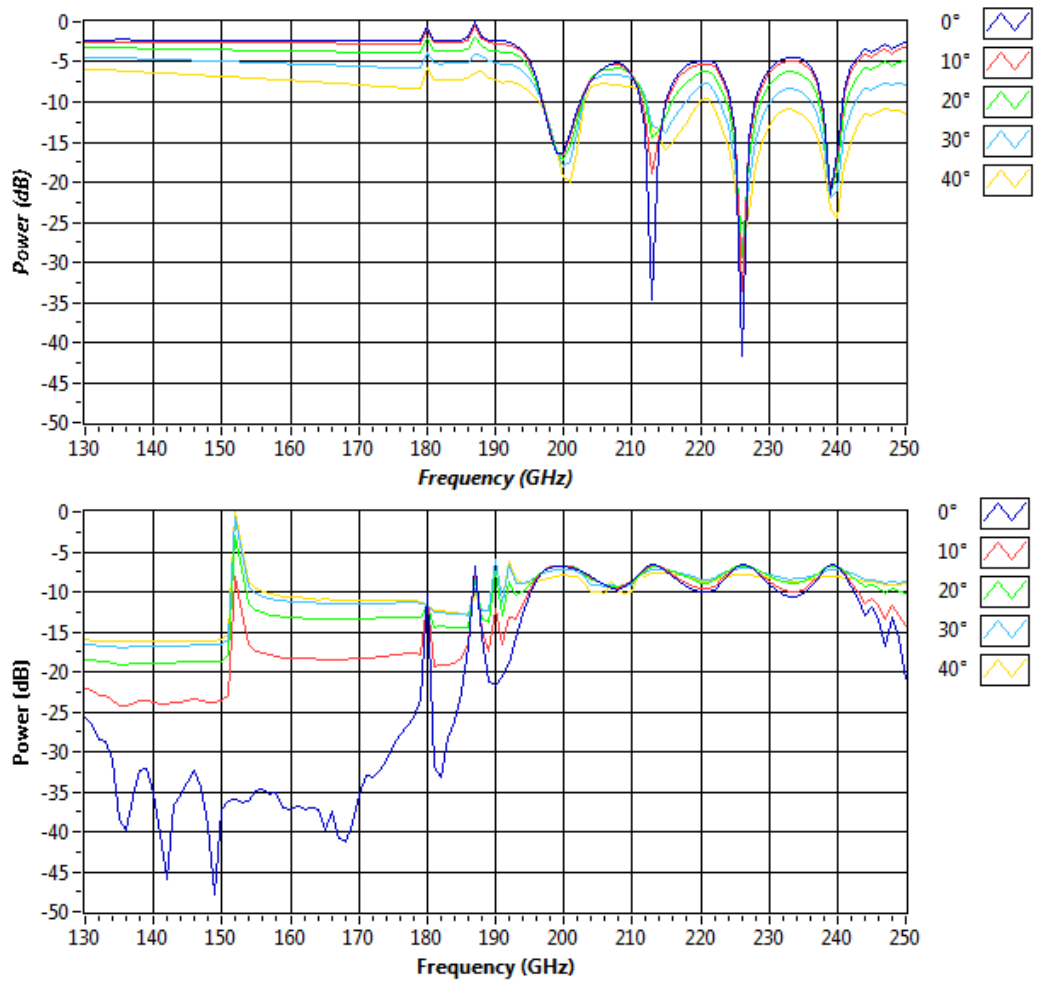


Figure 6.37: Frequency response of the 14° feed horn for a plane wave excitation at angles from 0° (on-axis) to 40° in 10° steps. (Top) the normalised (to a common peak) power in transmission and (bottom) normalised (to a common peak) power in reflection.

Modifications to the design of the scaled CLOVER feed horn were made (B. Maffei, Manchester) to allow the first module to operate as dual a band detector over the extended range. The re-design gave a uniform power output as a function of frequency for the extended range and also provided an opportunity to narrow the beam to 12.9° . Shown in Figure 6.38 is the updated geometry of the QUBIC feed horn (in green) in comparison with the scaled 14° CLOVER feed horn (in red). The position of the beam-waist within the feed horn was determined by the Manchester group (private communication, B. Maffei, Manchester) to be $\Delta z = 2.5$ mm behind the aperture.

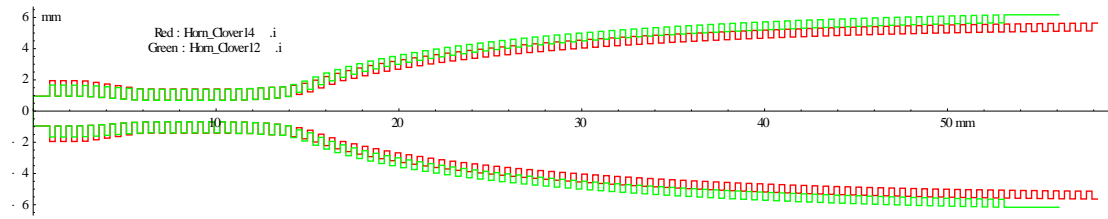


Figure 6.38: Original 14° beam feed horn is shown in red. The new version (green) emits a 12.9° Gaussian beam and has a much better response over the dual band range

The power in transmission and reflection as a function of frequency for the new 12.9° feed horn is shown in Figure 6.39 for a plane wave excitation over a range of input angles from 0° (on-axis) to 40° off-axis in 10° steps. It can be clearly seen that the response of the 12.9° feed horn remains stable until ~ 245 GHz.

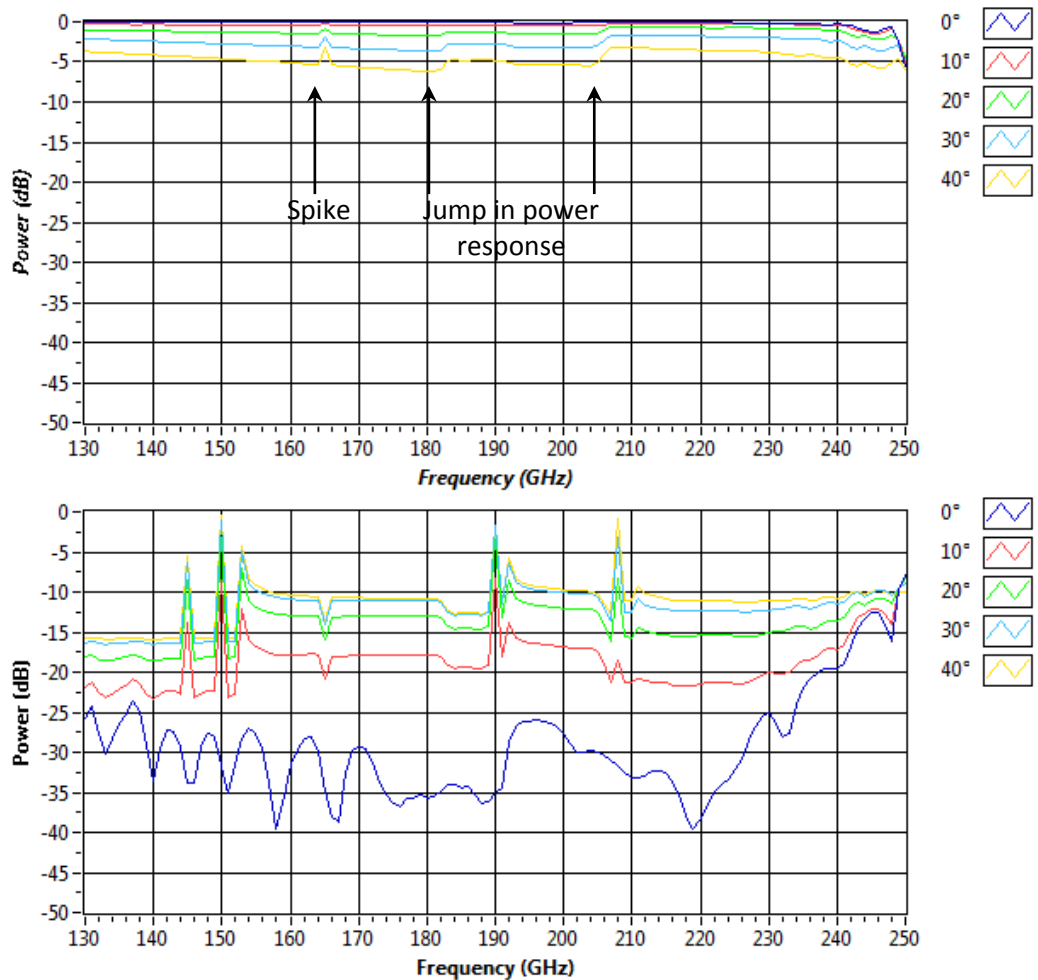


Figure 6.39: Frequency response of the 12.9° feed horn for a plane wave excitation at angles in 10° steps from 0° (on-axis) to 40° . Top is the normalised (to a common peak) power in transmission and bottom normalised (to a common peak) power in reflection (scales chosen for comparison with Figure 6.37).

There are 2 noteworthy points in the response; the first is a spike in the power at ~ 170 GHz, the second at ~ 185 and ~ 205 GHz where there are noticeable jumps in the power response of the feed horn. The former was suspected to be due to numerical instabilities in SCATTER's matrix inversion (see §2.1.2), and the latter a sign of mode cut-on leading to an increase in the overall transmitted power.

The spikes in transmitted power at ~ 170 GHz seen in *Figure 6.39* were briefly investigated to determine if their bandwidth had significant power contribution over the operating range. Using SCATTER and taking a range of 163 to 167 GHz in 0.1 GHz steps, for azimuthal orders 0 to 3 and 80 TE/TM modes, the effect was noted to be contained in very specific narrow bands at 164.0, 165.1 and 166.3 GHz as shown in *Figure 6.40* on the left. Looking closer at the first of these the S_{21} matrix was calculated for frequencies from 163.5 to 164.5 GHz in 0.01 GHz steps. From the SVD of the S_{21} matrix, at each junction, several occurrences where an SVD $[W]$ entry >1 were present. An example subset of the output data from SCATTER is shown in *Table 6.6*. The large values in the S_{21} matrix are indicative of a numerical instability resulting from matrix inversion within SCATTER, as suspected. It is worth noting that the instability cannot be simply dismissed as it is indicating that something maybe occurring at these frequencies (possibly resonance) which may impact the output from the feed horn. This is further evidenced from the output of the dispersion curves shown in *Figure 6.41* where a reverse cut-on/off mode exists in this region. From the investigations conducted the FWHM of the spikes was found to be ~ 30 MHz and so will contribute little to the overall power ($\ll 1\%$) at the detector when the broadband nature of the feed horn is considered. It is concluded for this reason that the impact to the measurements will be minimal and hence these numerical instabilities can be ignored.

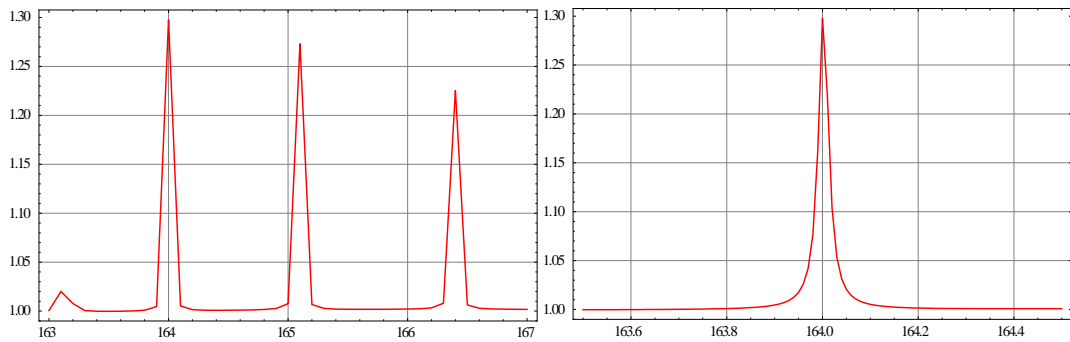


Figure 6.40: Frequency response of the 12.9° feed horn for an on-axis plane wave excitation taken in the range 163-167 GHz in 0,1 GHz steps (left) and 163.5-164.5 GHz in 0.01 GHz steps (right).

Table 6.6: Scatter matrix singular values from the SVD of the 12.9° feed horn S_{21} matrix at 164.0 GHz for azimuthal orders 0 to 3 and 50 radial modes. The scatter matrix was generated using the SCATTER code with equal excitation of all input modes. The azimuthal and radial mode order is as previously discussed in §2.1.

Azimuth 0 Section 3 {1.00207, ...}	
Azimuth 0 Section 6 {1.00097, ...}	
Azimuth 0 Section 11 {1.25479, ...}	
Azimuth 1 Section 1 {1.00433, ...}	
Azimuth 1 Section 2 {1.0012, ...}	
Azimuth 1 Section 3 {1.00151, ...}	
Azimuth 1 Section 4 {1.0033, ...}	
Azimuth 1 Section 5 {1.00319, ...}	
Azimuth 1 Section 6 {1.0009, ...}	
Azimuth 1 Section 7 {1.00149, ...}	
Azimuth 1 Section 8 {1.00265, ...}	
Azimuth 1 Section 9 {1.00315, ...}	
Azimuth 1 Section 10 {1.00002, ...}	
...	
...	
Azimuth 1 Section 77 {1.00007}	
Azimuth 2 Section 3 {1.02133, ...}	
Azimuth 2 Section 5 {1.00981, ...}	
Azimuth 2 Section 10 {1.0771, ...}	
Azimuth 2 Section 15 {1.28791, ...}	
Azimuth 2 Section 36 {1.03821}	
Azimuth 2 Section 38 {2.63234}	
Azimuth 2 Section 40 {1.34037}	

The approximate surface impedance (hybrid mode) model (see §2.1.4 and §2.1.5) treats the corrugated walls of a feed horn as a surface with different average impedance in the longitudinal and azimuthal directions. It works well so long as there are several corrugations per wavelength although it cannot model detailed

profiles. Taking the narrowest part of the feed horn, which acts as a filter section determining what modes get through to the remainder of the feed horn, and applying the surface impedance model results in a set of dispersion curves from which you can infer the mode content of the feed horn (*Figure 6.41*). Here we can see that a mode of azimuthal order 1 (HE_{11} , green line) will exist over the extended band, a second mode of order 0 (red line) will cut on just below 190 GHz, a mode of order 2 and 3 around 210 GHz and order 1 around 240 GHz.

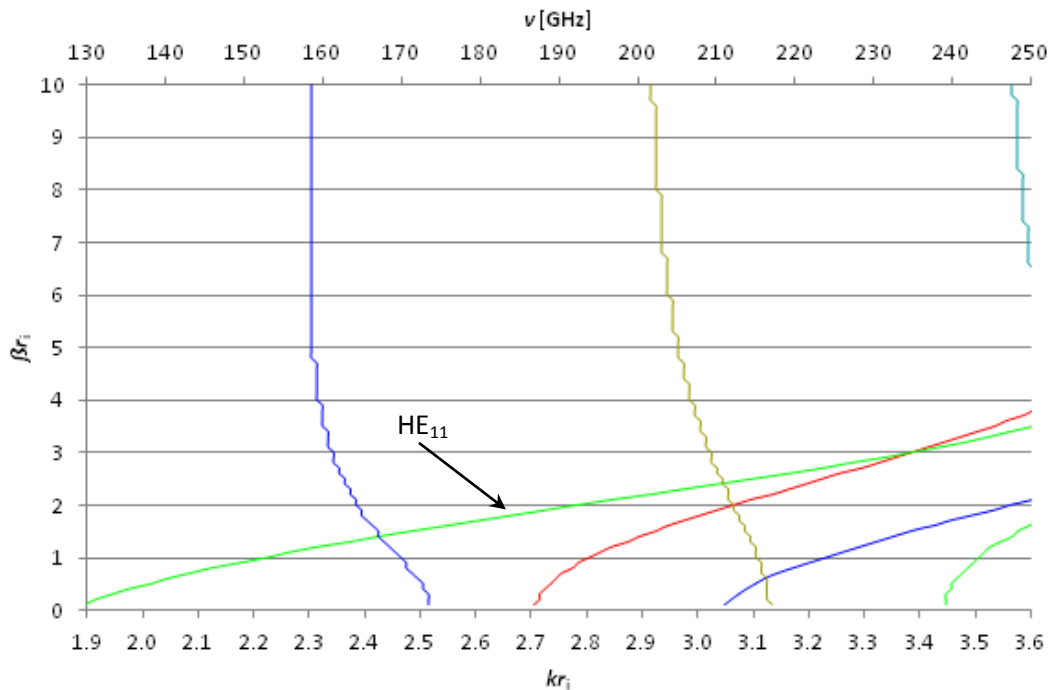


Image Key

RED	: Azimuthal order 0
GREEN	: Azimuthal order 1
BLUE	: Azimuthal order 2
TAN	: Azimuthal order 3
CYAN	: Azimuthal order 4

Figure 6.41: Dispersion curves for 12.9° feed horn showing the modes that can propagate (β , is the waveguide wave number for a given mode and frequency) at various frequencies in the narrowest point of the feed horn. In this case for QUBIC's 12.9° feed horn the narrowest inner (r_i) and outer (r_o) radii are 0.684 mm and 1.394 mm respectively. Refer to discussion in §2.1.4, §2.1.5 and for a good overview see (Clarricoats & Olver, 1984).

Comparing this to the output from *Figure 6.39* there are corresponding spikes in the reflected power around 210 GHz where the second backwards mode cuts on. From *Figure 6.39* there are also jumps in power evident at frequencies that correspond quite well to the cutting-on of modes as predicted by the dispersion curves

generated from the surface impedance model shown in *Figure 6.41*. From further analysis carried out in MODAL, at 150 GHz the feed horn is single moded but at 220 GHz there were 5 hybrid modes that successfully propagated, the relative power in each mode dependant on the excitation. These modes will be discussed in §6.4.

Finally to determine the beam profile over the new extended frequency range (130 - 250 GHz) the beams were plotted out to $\pm 45^\circ$ in frequency steps of 10 GHz, as shown in *Figure 6.42* and *Figure 6.43*. The main beam narrows as the frequency increases but as modes cut-on the side lobes become more prominent increasing the overall power through-put at that frequency. This is difficult to see in the overlaid cuts so 2D graphs, shown in *Figure 6.44*, were generated. The gradual narrowing of the beams is evident with increasing frequency and the cutting on of modes, for example at ~ 205 GHz, is visible. *Figure 6.44* (left) shows excellent agreement with the power drops evident in *Figure 6.37* (top), where noticeably reduced levels are evident at ~ 198 , ~ 212 , ~ 225 and ~ 240 GHz.

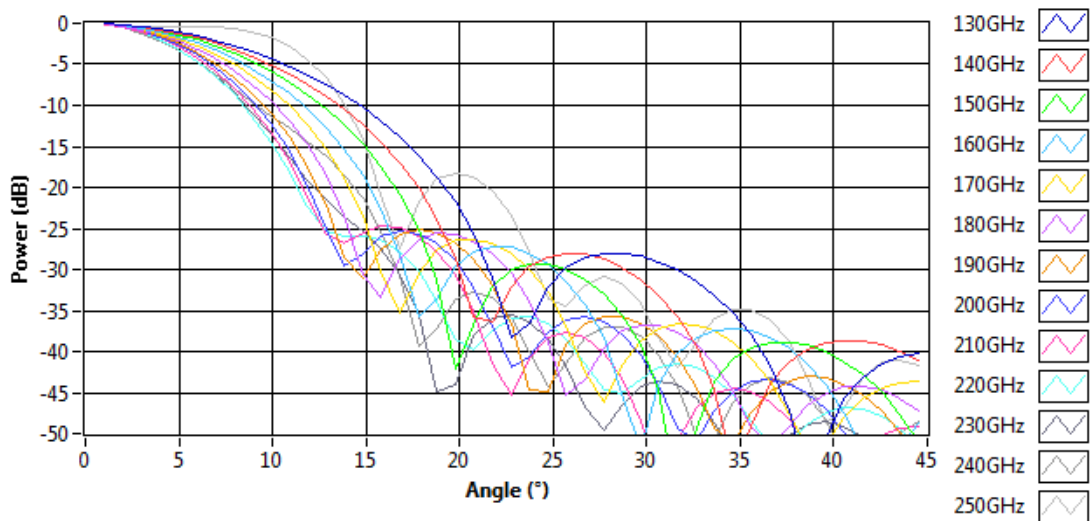


Figure 6.42 Beam profiles for the 14.0° feed horn, for non-polarised on-axis plane wave excitation

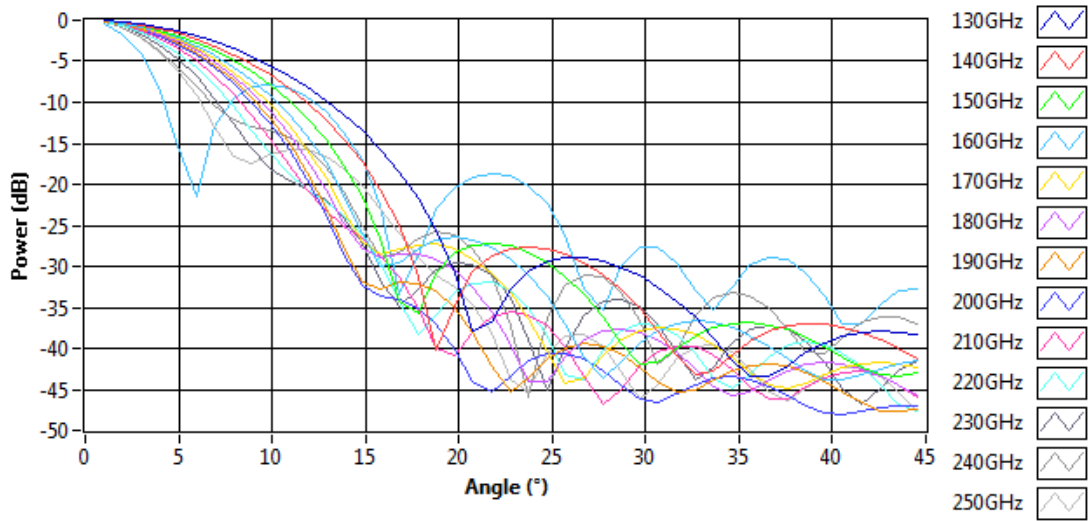


Figure 6.43 Beam profiles for the 12.9° feed horn, for non-polarised on-axis plane wave excitation

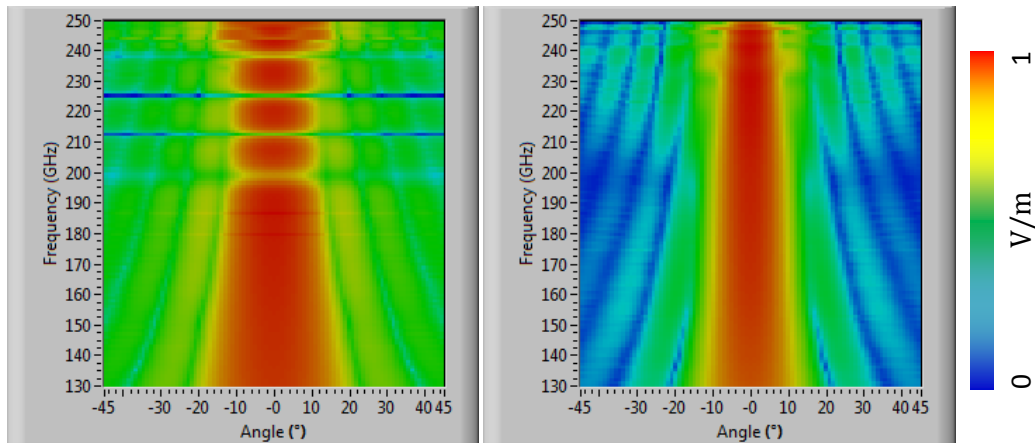


Figure 6.44: The evolution of the beam profile with frequency of the feed horns excited using an on-axis plane wave. Left is the beam profile for the 14.0° feed horn and on the right the beam profile for the 12.9° feed horn.

6.4 Dual band operation (220 GHz analysis)

Late 2014 saw the finalisation of the design of the dual band combiner. The polariser was replaced with a dichroic, which splits the beam by frequency rather than field components. The current extent, shape, orientation and position of the polariser can be re-used for the dichroic at 150 GHz but a check will need to be performed to confirm the current design is adequate at 220 GHz. For the 220 GHz band each element within the combiner also required spillover testing prior to the design being validated. The polariser, still required to discriminate between the components of the incoming radiation, was repositioned to a plane parallel to the aperture plane, in front of the detecting feed horns. To allow for the selection of

the various polarisation components a rotating half-wave plate (RHWP) is positioned above the polariser and parallel to it. As previously shown in *Figure 4.47* and from work done by Gayer (Gayer, 2015) the optical combiner introduces a degree of cross-polarisation contamination, of the order of 2% when all 400 sources are considered, a secondary benefit of the relocated polariser is the complete removal of any cross-polar combiner artefacts, as they are introduced after the RHWP. The incident sky field will contain a modulation at 4 times the rotation frequency of the half wave plate (Charlassier, et al., 2010b) and any measured data at the detector planes not exhibiting this modulation is by definition an undesired artefact contributed by some part of the combiner. The schematic for this new design is shown in *Figure 6.45*.

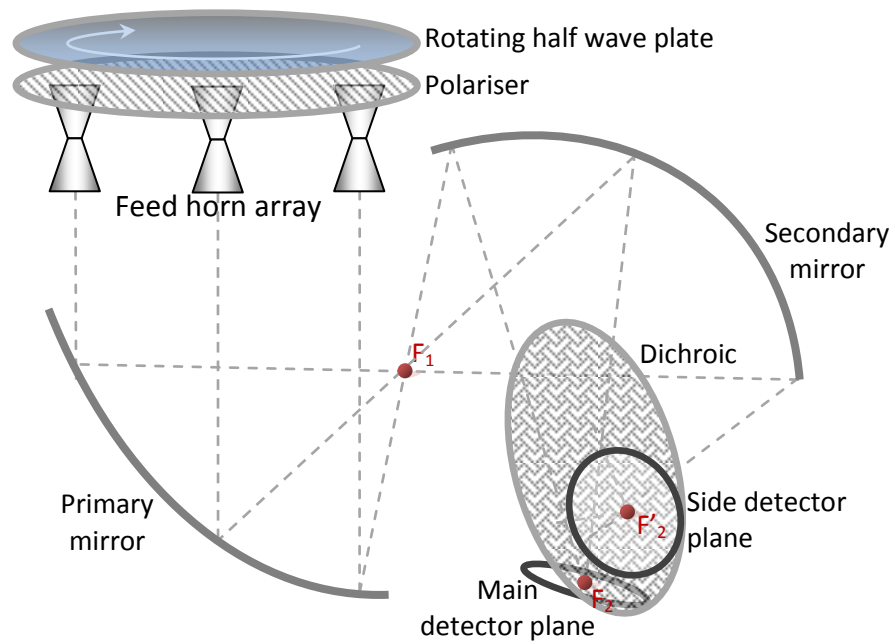


Figure 6.45: Schematic of QUBIC dual band design, showing the dichroic, relocated polariser and rotating half wave plate.

Using an ABCD Gaussian beam mode analysis, as described in §2.2.3, the 220 GHz beams widths at the detector plane were calculated and compared with the 150 GHz beams. The goal was to quickly assess with GBMA if the beams would yield similar footprints to that of their 150 GHz counterparts and hence that the current design of the optics would be suitable for this new band. To determine the feed horn beam evolution and footprint through the combiner, the Gaussian content of

the hybrid modes from the feed horn was calculated using overlap integrals. The Laguerre-Gaussian mode definition used is given in *Equation (6.1)* (Goldsmith, 1998) and the overlap integral used to calculate mode coefficients given in *Equation (6.2a)* with the approximation for a sampled field given in *Equation (6.2b)*. The form of *Equation (2.92)* was modified in order to allow for more efficient programming: for N azimuthal orders, i.e. $n = 0 \rightarrow N$, taking the modulus of n for all but the term $e^{jn\psi}$ gives *Equation (6.1)*. For *Equation (6.1)* taking $n = -N \rightarrow N$, generates the orthogonal modes for negative n and naturally only executes a single iteration at $n = 0$.

$$G_{nl}(r, \phi) = \sqrt{\frac{2(l!)}{\pi(|n| + l)!}} \frac{1}{w(z)} (\sqrt{2}r_w)^{|n|} L_l^{|n|} \left[(\sqrt{2}r_w)^2 \right] \cdot e^{-r_w^2 - jkz - j\frac{\pi}{\lambda R(z)} r^2 - j(|n| + 2l + 1)\phi_0(z) + jn\psi} \quad (6.1)$$

Laguerre Gaussian of azimuthal order n and radial order l

where

z is the propagation distance from the waist

r is the transverse distance from the centre of the beam, calculated from

$$r = \sqrt{x^2 + y^2} \text{ where } x \text{ and } y \text{ are the Cartesian distances}$$

$w(z)$ is the width of the beam as a function of z

$r_w = \frac{r}{w(z)}$, the transverse distance in terms of beam width

$R(z)$ is the radius of curvature of the beam as a function of z

L_l^n is the associated Laguerre Gaussian mode of order l and associate order n

ψ is the angle calculated from $\tan^{-1} \left(\frac{y}{x} \right)$

ϕ_0 is the Gouy phase, an on-axis longitudinal phase delay seen in Gaussian beams calculated from $\tan^{-1} \left(\frac{z\lambda}{\pi w^2} \right)$

The coefficients, η_{nl} , were calculated for azimuthal orders, $n = -5 \rightarrow 5$, and radial orders, $l = 0 \rightarrow 12$. w and R for the Laguerre-Gaussian mode set were chosen as $w = 3.324$ mm and $R = \infty$. The coefficients are complex values. Using the ABCD matrices from *Equation (2.103)* generated from the parameterisation defined in *Table 2-3*, for each of the upper, lower and central frequency of each band and a waist of 3.324 mm (12.9° farfield divergence at 150 GHz) the beam parameters $[w(z), \phi(z), R(z)]$ were calculated for the primary and secondary mirrors and the detector plane. Each significantly contributing Gaussian mode multiplied by its respective complex coupling coefficient was combined coherently to re-create the beam profile for each hybrid mode. The results were tabulated in *Table 6.7* and beam widths shown graphically over the propagation range in *Figure 6.46*.

$$\eta_{nl} = \frac{\int_0^\infty \int_0^\infty F(r, \phi) G(r, \phi)^* r dr d\phi}{\sqrt{\int_0^\infty \int_0^\infty F(r, \phi) F(r, \phi)^* r dr d\phi \int_0^\infty \int_0^\infty G(r, \phi) G(r, \phi)^* r dr d\phi}} \quad (6.2a)$$

and approximated for a field, sampled over a Cartesian grid

$$\eta_{nl} = \frac{\sum_x \sum_y F(x, y) G(x, y)^* \Delta x \Delta y}{\sqrt{\sum_x \sum_y F(x, y) F(x, y)^* \Delta x \Delta y \sum_x \sum_y G(x, y) G(x, y)^* \Delta x \Delta y}} \quad (6.2b)$$

Overlap integral

where for a given λ (wavelength), w_0 (beam waist radius) and z (propagation distance) η_{nl} is the coefficient for a given azimuthal order, n , and radial order, l . F is the sampled beam field and G a Laguerre-Gaussian beam mode r and ϕ denote the radial offset and direction from the centre of the beam $r = \sqrt{x^2 + y^2}$ and $\phi = \tan^{-1}\left(\frac{y}{x}\right)$ where x and y are the transverse offsets $*$ denotes the complex conjugate

Table 6.7: Width of the equivalent Gaussian beams, starting with waist of 3.324 mm (equivalent to a 12.9° beam at 150 GHz) and propagated through the QUBIC system. The beams were propagated at frequencies of 130, 150 and 170 GHz (primary bands lower, central and upper values) and 190, 220 and 250 GHz (secondary bands lower, central and upper values)

Frequency	Primary mirror		Secondary mirror		Detector plane	
	ν [GHz]	w [m]	ϕ_0 [rad]	w [m]	ϕ_0 [rad]	w [m]
130	0.088457	-0.037586	0.007230	2.37646	0.066131	-3.14121
150	0.076681	-0.043362	0.006745	2.30500	0.057313	-3.14115
170	0.067678	-0.049134	0.006401	2.24330	0.050571	-3.14109
190	0.060572	-0.054904	0.006149	2.18987	0.045247	-3.14103
220	0.052339	-0.063551	0.005880	2.12243	0.039077	-3.14095
250	0.046085	-0.072189	0.005695	2.06710	0.034388	-3.14086

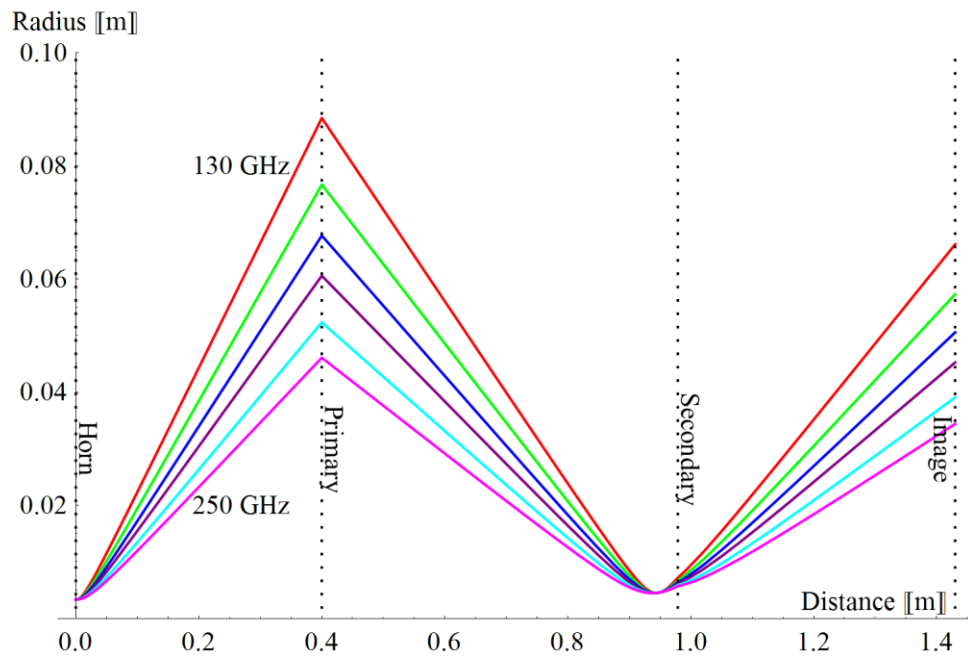


Figure 6.46: Width of Gaussian beams, starting with waist of 3.324 mm (equivalent to a 12.9° beam at 150 GHz used as the w value for each mode in the set) and propagated through the QUBIC system. The beams were propagated at frequencies of 130, 150 and 170 GHz (primary bands lower, central and upper values) and 190, 220 and 250 GHz (secondary bands lower, central and upper values)

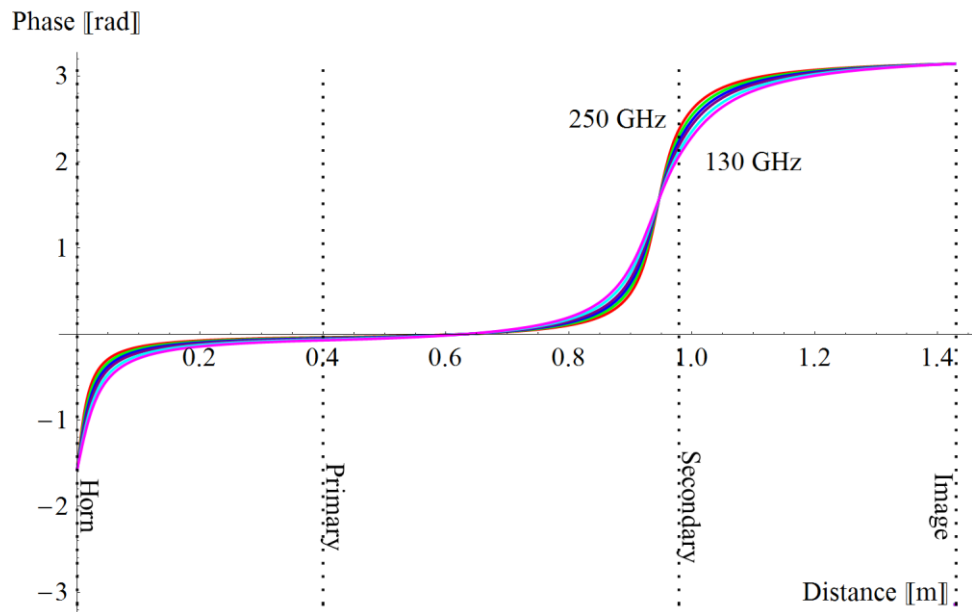


Figure 6.47: Phase slippage of the Gaussian beams, starting with waist of 3.324 mm (equivalent to a 12.9° beam at 150 GHz) and propagated through the QUBIC system. The beams were propagated at frequencies of 130, 150 and 170 GHz (primary bands lower, central and upper values) and 190, 220 and 250 GHz (secondary bands lower, central and upper values)

From the calculations above the Gaussian beam radius at the detector plane is expected to be 0.0573 m at 150 GHz with a detector plane radius of 0.0518 m, the expected power capture for a Gaussian can be calculated from *Equation (2.104)* to be ~83%. This compares favourably with the previous figure of ~74% as shown in *Table 3-9* for the 14° beam at 150 GHz.

Starting with a 3.324 mm waist, the beam radius and Gouy phase values in *Table 6.7* were used for the reconstruction of each hybrid mode from the Gaussian set at 150 and 220 GHz on the primary and secondary mirrors and the detector plane. The total field was then calculated from the incoherent addition of each of the 5 possible hybrid modes, see §6.3, normalised to a total power of 1 (since the relative weighting of modes will depend on the source exciting the input feed horns, the aim here is to determine the possible extent rather than the exact profile of the beam patterns), giving a resultant field for an equal contribution from each mode. The complete set of results is shown in *Figure 6.48*.

The GBM analysis shows that the higher-order mode beam sizes are not significantly narrower to those of the 150 GHz case and therefore a more in-depth PO analysis is warranted. The edge sources for the combiner setup given in *Table 6.3* were excited by 5 220 GHz plane waves: an on-axis plane wave and 4 plane waves with an angle of incidence of $\pm 45^\circ$ in orthogonal planes (MODAL does not allow waveguide modes to be excited 'by-hand' so an excitation source must be chosen). There is no special significance to these input waves, any configuration can be used so long as each of the 5 possible hybrid modes are excited by at least 1 of them. The power distribution between the propagating modes was overwhelmingly in favour of the second mode, as shown in *Table 6.8*, but the independent propagation of each mode allows renormalisation so they can be recombined with any weighting.

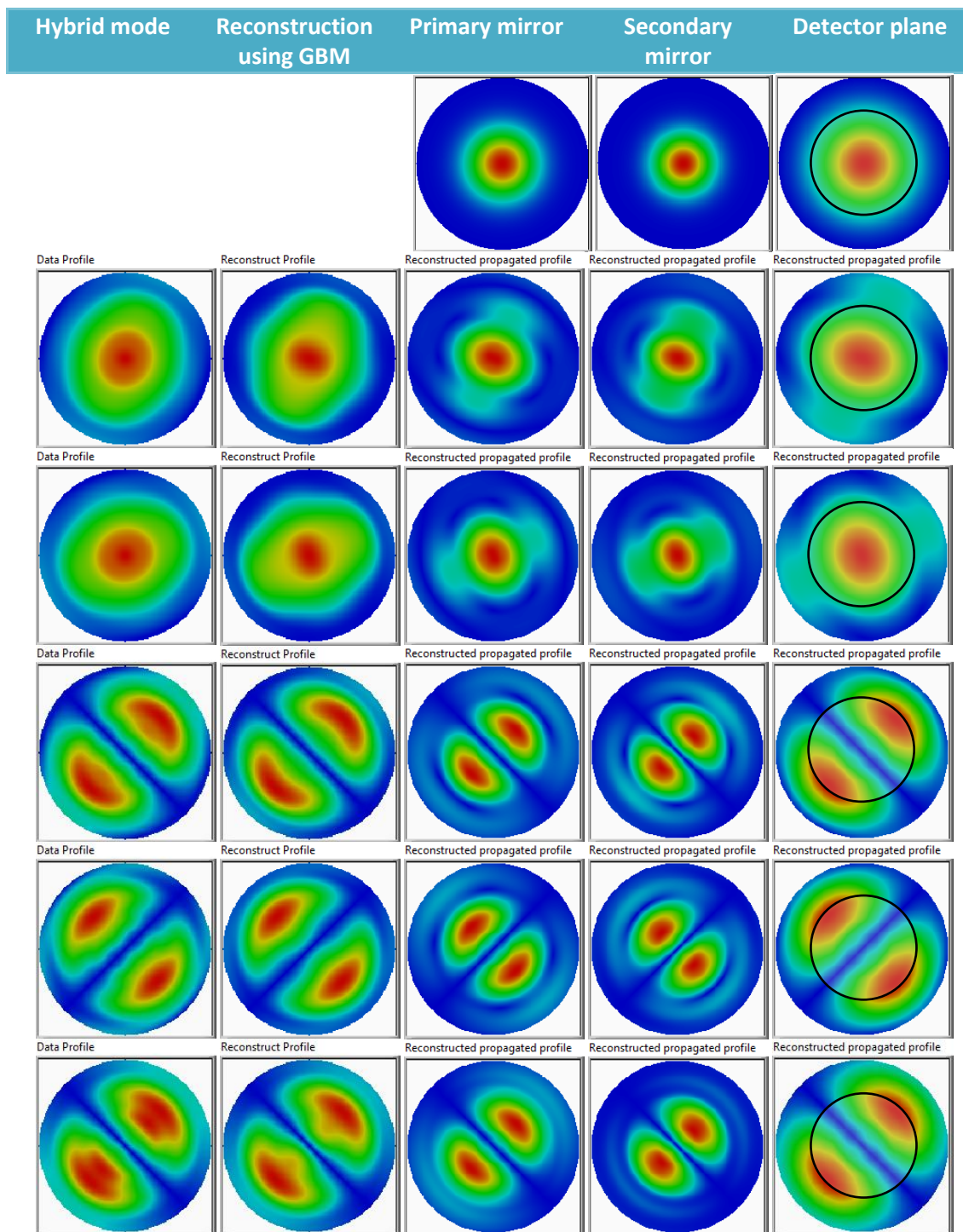


Figure 6.48: Normalised amplitude profile for each coherent hybrid mode at the aperture. Top row is a 150 GHz Gaussian with 3.324 mm waist, and rows 2 to 6 are each of the five hybrid modes at 220 GHz. Column 1 is the data output from modal analysis, column 2 is the reconstructed beam from the Gaussian decomposition, columns 3 to 5 are the beams on the primary mirror (plot is 400 mm wide), secondary mirror (plot is 40 mm wide) and detector plane (plot is 200 mm wide) using the ABCD widths and GBM calculations for each propagation distance. The black ring on the detector plane graphics represents the approximate size of QUBICs detector plane for comparison.

Table 6.8: Power distribution for propagating modes in 12.9° QUBIC feed horn operating at 220 GHz for excitation by 4 plane waves at 45° to the aperture plane each rotated 90° about the feed horn z-axis from one another.

Mode	1 st	2 nd	3 rd	4 th	5 th
Power (%)	12.7	52.6	5.3	8.8	20.6

The footprint (top left image in each set) and power capture for each of the 5 modes (subsequent images in each set) as a percentage of source emission is shown in Figure 6.49 to Figure 6.54, for each element in the combiner. In this case the second mode is that of the single-moded 150 GHz case, a HE₁₁ mode.

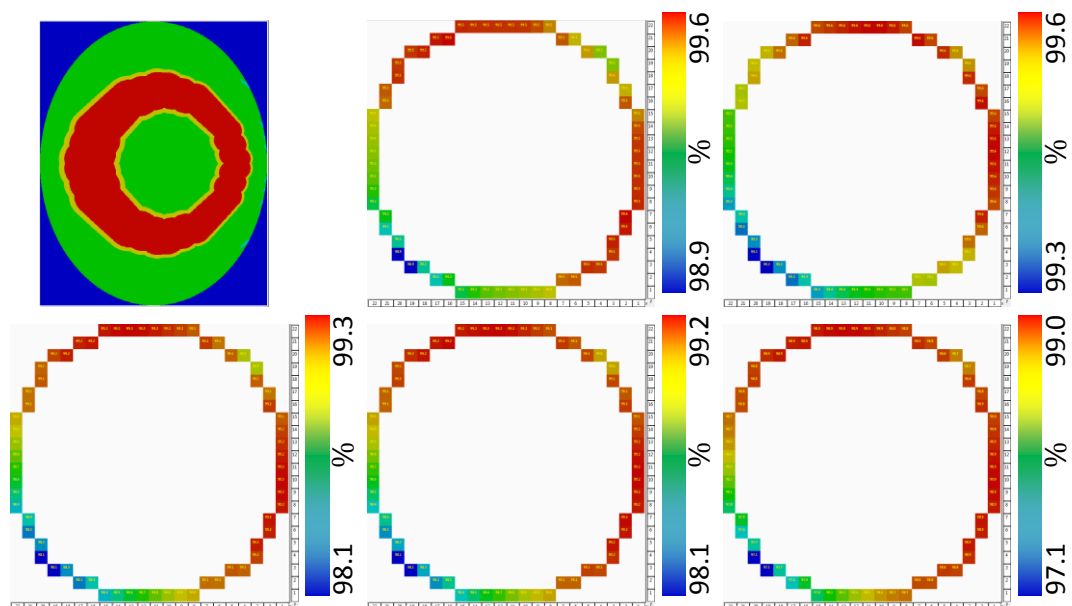


Figure 6.49: Shown in the top left is the footprint of the outer beams on the primary mirror using the combination of all 5 modes for an excitation as defined in Table 6.8. The power captured for each edge source is shown for each of the 5 possible modes in the following images with the lowest power levels found to be 98.9%, 99.3%, 98.1%, 98.1% and 97.1% for source x19y03 in each case. Colour is the same as in Figure 6.1 image key.

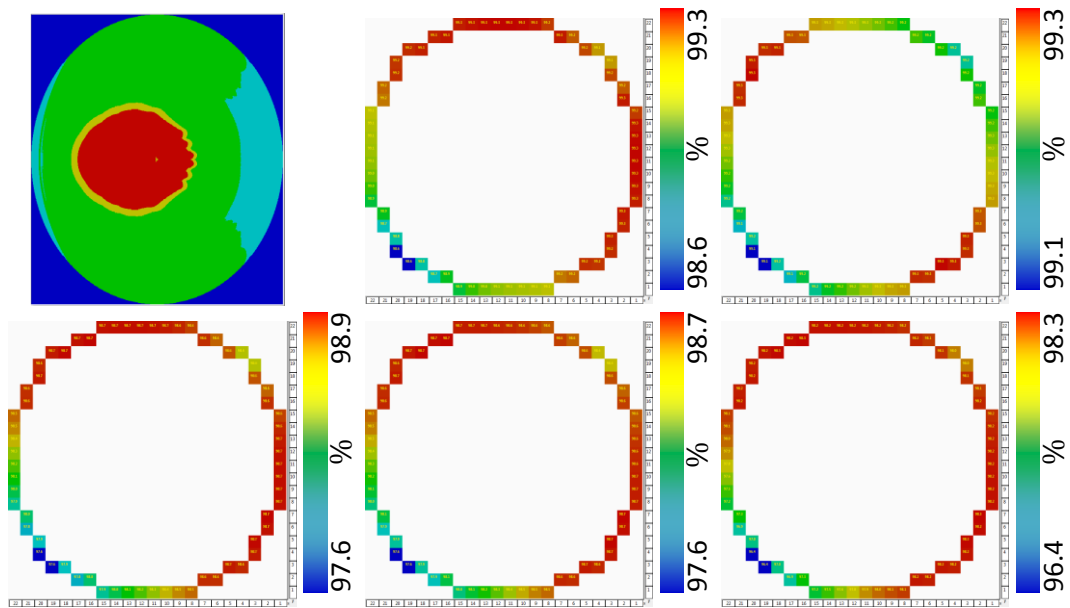


Figure 6.50: Shown in the top left is the footprint of the outer beams on the primary mirror using the combination of all 5 modes for an excitation as defined in Table 6.8. The power captured for each edge source is shown for each of the 5 possible modes in the following images with the lowest power levels found to be 98.6%, 99.1%, 97.6%, 97.6% and 96.4% for source x19y03 in each case. Colour is the same as in Figure 6.1 image key.

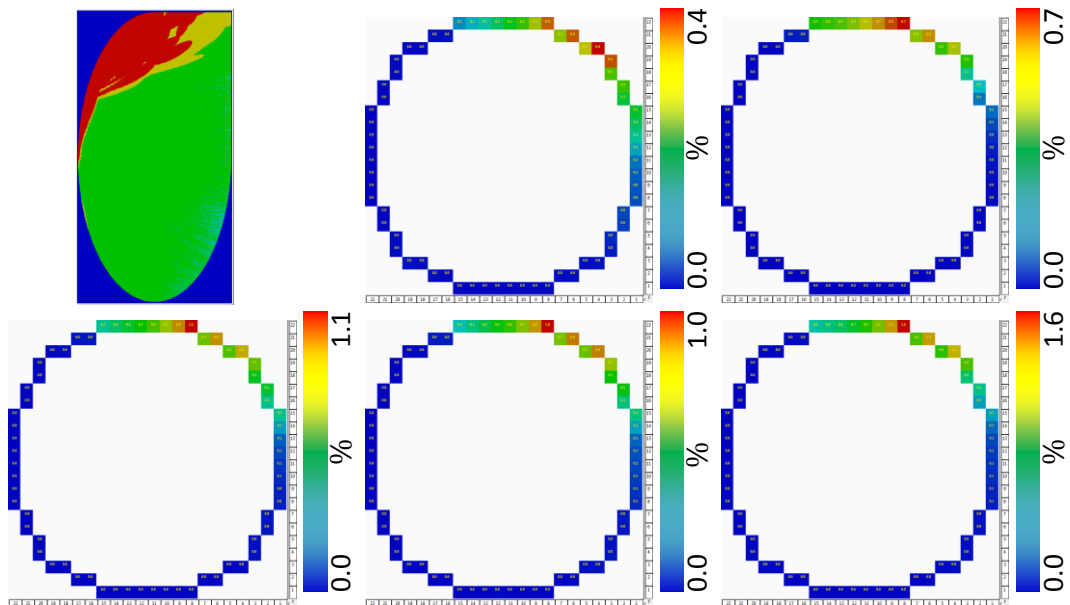


Figure 6.51: Shown in the top left is the footprint of the outer beams on the dichroic (as a blockage for beams traversing from the primary to the secondary mirror) using the combination of all 5 modes for an excitation as defined in Table 6.8. The power blocked for each edge source is shown for each of the 5 possible modes in the following images with the lowest power levels found to be 0.4% for source x04y20, 0.7%, 1.1%, 1.0% and 1.6% for source x08y2 in the latter 4 cases. Colour is the same as in Figure 6.1 image key.

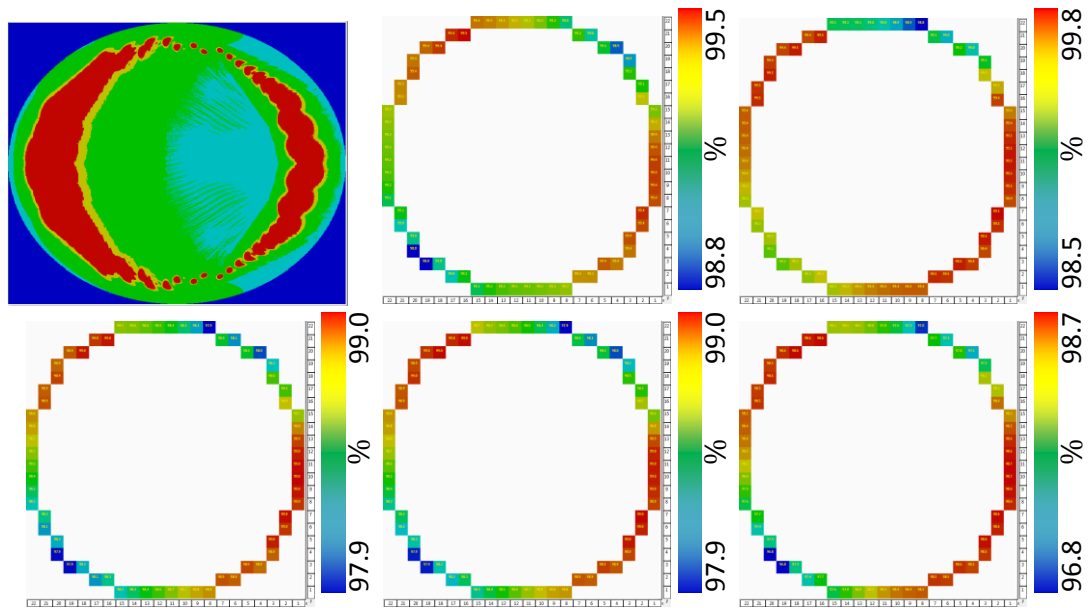


Figure 6.52: Shown in the top left is the footprint of the outer beams on the secondary mirror using the combination of all 5 modes for an excitation as defined in Table 6.8. The power captured for each edge source is shown for each of the 5 possible modes in the following images with the lowest power levels found to be 98.8% for source x19y03, 98.5% for source x08y22, 97.9%, 97.9% and 96.8% for source x19y03 in latter 3 cases. Colour is the same as in Figure 6.1 image key.

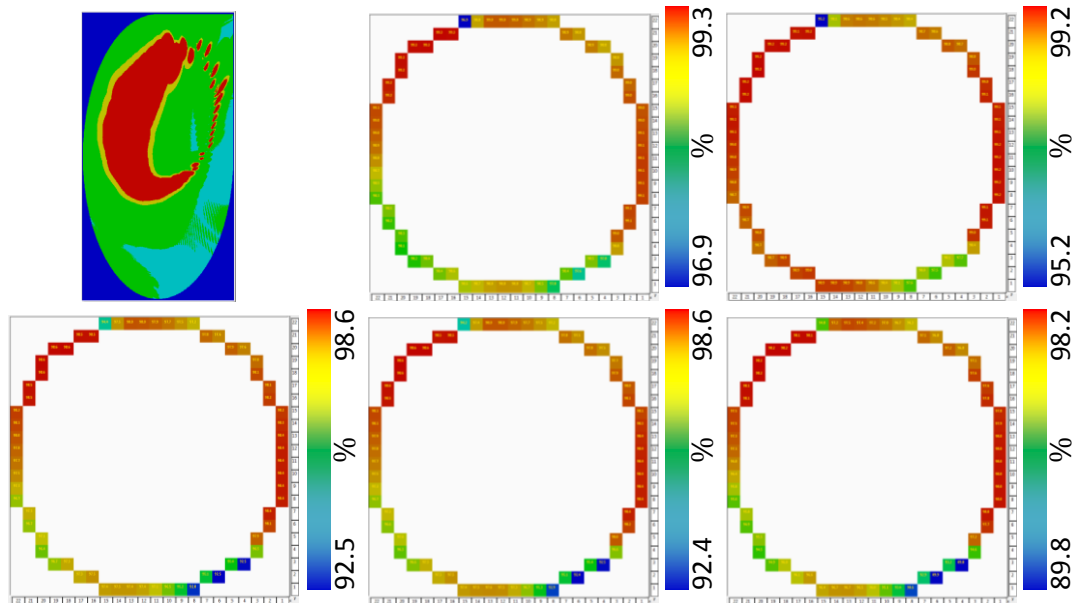


Figure 6.53: Shown in the top left is the footprint of the outer beams on the dichroic aperture using the combination of all 5 modes for an excitation as defined in Table 6.8. The power captured for each edge source is shown for each of the 5 possible modes in the following images with the lowest power levels found to be 96.9% for source x15y22, 95.2% for source x15y22, 92.5% for source x06y02, 92.4% for source x06y02 and 89.8% for source x04y03. Colour is the same as in Figure 6.1 image key.

The dichroic is the last element prior to the detector plane and so there are no blockages beyond this point. Therefore we look at the power levels at the dichroic

for each hybrid mode individually propagated and find the lowest captured power levels for any source for each mode to be 96.9%, 95.2%, 92.5%, 92.4% and 89.8%. This compares quite favourably to the 150 GHz cases for the original 14.0° beam of *Figure 4.46* with the lowest power capture of 54.8% and the 12.9° beam of *Figure 6.12* with the lowest power capture of 92.5%. As the majority of power is expected to be contained in mode no. 2 with smaller contributions from the other modes it is concluded that the system is capable of capturing beams at 220 GHz. For completeness the beams were also propagated to the detector plane.

The power captured at the detector plane was calculated for each mode, the results are shown in *Figure 6.54*. At 150 GHz for a 14° beam on the 51 mm circular detector $\sim 72\%$ power capture was the best obtainable, see *Figure 4.47*, which increased to $\sim 80\%$ for 12.9° beam, see *Figure 6.36*. The power captured, as detailed in *Figure 6.54*, shows that for beams with the largest component coming from mode no. 2 the power capture should exceed that of the 150 GHz case.

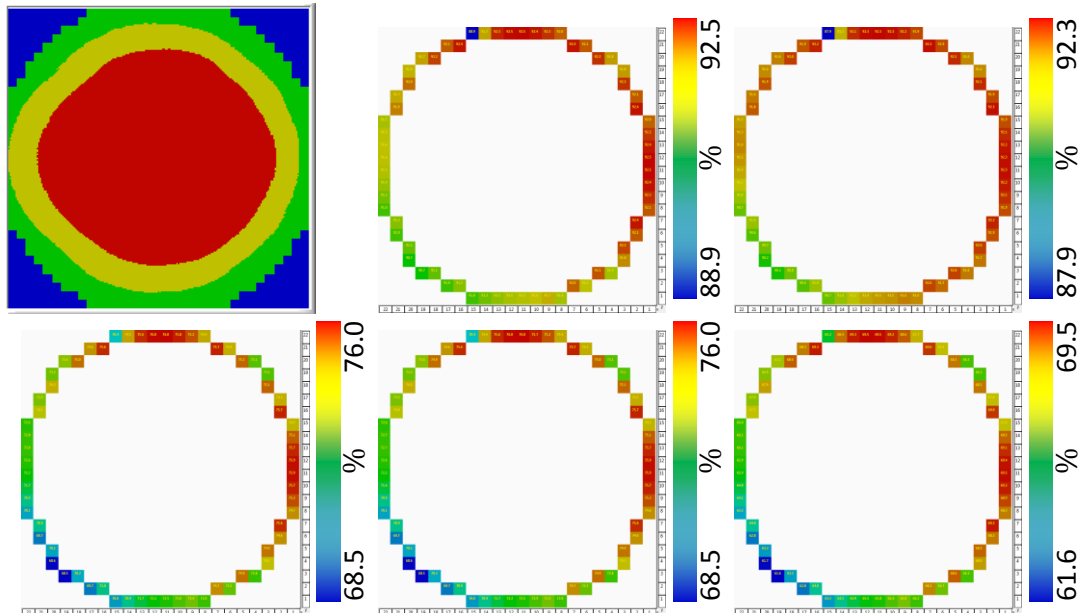


Figure 6.54: Shown in the top left is the footprint on the detector plane using the combination of all 5 modes for an excitation as defined in Table 6.8. The power captured for each edge source is shown for each of the 5 possible modes in the following images with the lowest power levels found to be 88.9% and 87.9% for source x15y22, 68.5%, 68.5% and 61.6% for source x19y03. Colour is the same as in Figure 6.1 image key.

In this case (multi-moded 220 GHz) we conclude that the truncation level is lower than that of the single-moded (150 GHz) and the system is capable of capturing sufficient power for all sources at each stage.

Finally the detailed PO analysis was compared to that of the GBM analysis from *Figure 6.48* for the central source x11y11 which has propagation distances corresponding to those shown in *Figure 6.46*. This source has a large angle of throw from the primary to the secondary mirror which will cause some deviation from the ABCD/GBM model but overall the predictions should yield similar sized beam profiles. The beam sizes show good agreement with that of the ABCD/GBM model. The beam radius at the primary mirror, secondary mirror and detector plane were calculated to be 53 mm × 47 mm, 8 mm × 6 mm and 39 mm × 36 mm respectively where the 2 numbers represent the widths of each beam in orthogonal directions. These are in very good agreement with the corresponding ABCD/GBM predictions of 52, 6 and 39 mm as tabulated in *Table 6.7*. The range in the PO value calculations is primarily due to the angles of incidence/throw of the beams which result in deviations from idealised radially symmetric beams.

The beam sizes and power captured give good indication as to the level of truncation within the combiner but not to the quality of the final image or sensitivity of the instrument. In order to compare the performance of the combiner to an ideal one the PSF is used as before. This will be the topic of the next section.

6.4.1 The PSF of the dual-band combiner

The PSF of the QUBIC combiner at 150 GHz was calculated as before by exciting the 400-element input array of horns with an on-axis plane wave. As a further test a 5° off-axis plane wave was also used. The plane waves were coupled to a set of guide TE/TM modes and using the SCATTER mode-matching technique the fields were generated (see Chapter 2). These fields were again propagated through the combiner using PO and the 400 fields on the detector plane were added (again not including the polariser and cold stop as in the first instance). The result is shown in *Figure 6.55* (150 GHz left and 220 GHz right).

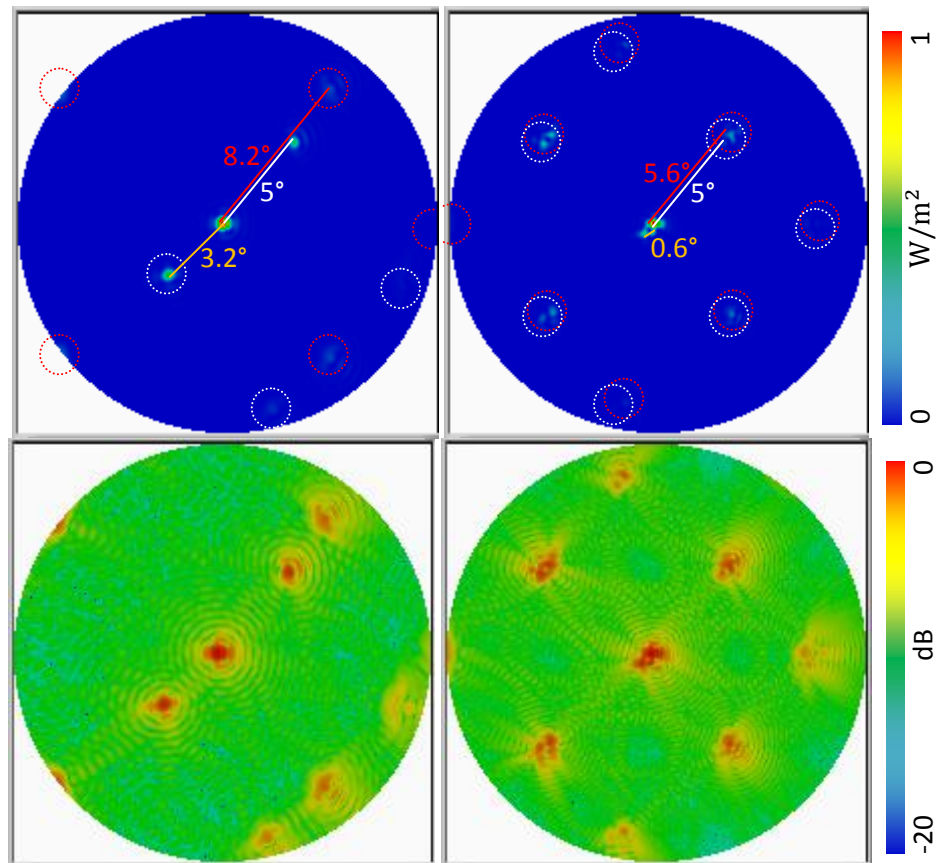


Figure 6.55: Detector plane intensity distribution resulting from excitation of the QUBIC combiner with (left) 0° and 5° off-axis plane waves at 150 GHz and (right) 0° and 5° off-axis plane waves at 220 GHz. Rows show the intensity scale (top) and dB scale (bottom) Red lines highlight the subsidiary peaks and white lines the position of the 5° off-axis central peak.

The PSF consists of a central peak for each of the 0° and 5° off-axis sources and smaller secondary peaks, those associated with the 0° source are highlighted with red dotted circles and those associated with the 5° off-axis source are highlighted with white dotted circles. Aberrations at the edge of the detector plane again cause the secondary peaks' locations to shift towards the left edge of the detector plane.

As can be clearly seen in *Figure 6.55* the repetition scale for the subsidiary peaks in the <100% fill factor aperture array PSF varies with frequency but the position of the off-axis source is frequency invariant with respect to the subsidiary peak (at 150 GHz $s_{\lambda_{min}} = 7.0$ giving $\theta_{repetition} = 8.2^\circ$ and at 220 GHz $s_{\lambda_{min}} = 10.3$ giving $\theta_{repetition} = 5.6^\circ$, as shown, in red). The subsidiary peaks from the 5° off-axis source are located at 3.2° (150 GHz case) and 0.6° (220 GHz case) from the centre.

In order to understand the PSF we can estimate what we would expect for the PSF of an ideal combiner by considering its constituent parts. Taking a simple 1D case, we consider only an on-axis point source incident on an ideal combiner consisting of a single row of 22 feed horns. The contributions from any single baseline pair was calculated from *Equation (1.3)* where the phase difference gives the varying amplitude profile of the form, *Equation (6.3)*.

$$\cos(2\pi s_{\lambda} \sin(\theta)) \quad (6.3)$$

Fringe pattern from a single baseline, assuming a point source

where

θ is the off-axis angle

s_{λ} is the baseline separation in terms of wavelengths

We add the contribution from each possible baseline pair (in this case for a 1D array of 22 equally spaced (separation of $s_{1\lambda}$) feed horns). There are 21 baselines at separation $s_{1\lambda}$, 20 at $2s_{1\lambda}$ and so on giving *Equation (6.4)*. The result is the array pattern, as shown in *Figure 6.56*.

$$\sum_{n=1}^{21} (22 - n) \cos(2\pi n s_{1\lambda} \sin(\theta)) \quad (6.4)$$

Fringe pattern for all baselines

where

θ is the off-axis angle

$s_{1\lambda}$ is the baseline separation of the nearest feed horns in terms of wavelengths

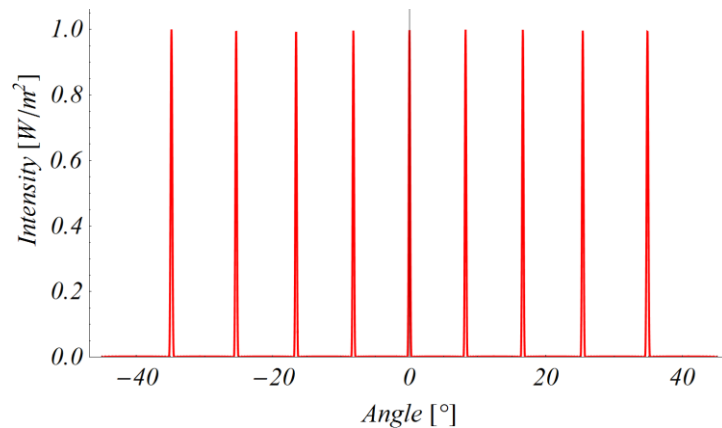


Figure 6.56: Model of the QUBIC feed horn array pattern, 22 feed horns across the diameter at 150 GHz with baseline separation of 14 mm (giving $s_\lambda = 7$). Excitation is a single on-axis source.

Equation (6.4) gives a series of peaks resulting from the finite number of baselines, with a repetition rate related to the shortest baseline, in this case 7λ (150 GHz with 14 mm between feed horn centres). The repetition angle can be calculated from $\theta = \sin^{-1}\left(\frac{1}{s_\lambda}\right)$, where s_λ is the baseline separation in terms of wavelengths, giving 8.2° in this case. The QUBIC image plane is only 9.6° ($\tan^{-1}\left(\frac{51}{300}\right)$ where the focal length is 300 mm and the radial extent of the image plane is 51 mm) in radius therefore the graphs from this point forth concentrate on the region of interest of $\pm 10^\circ$. In Figure 6.57 in addition to the on-axis source (red) the peaks resulting from a source at 5° (green) off-axis was added.

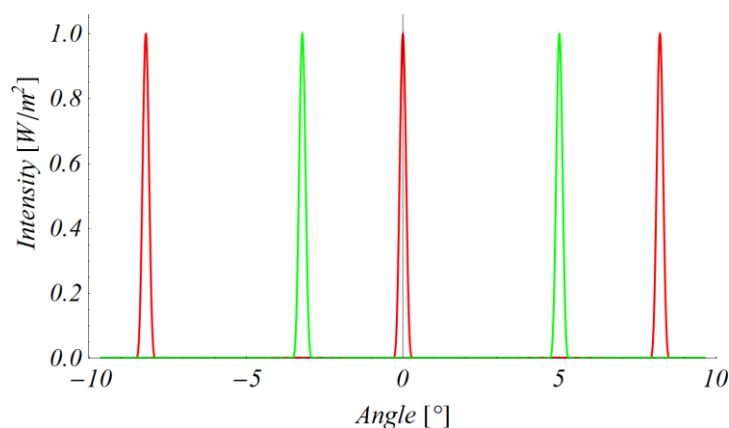


Figure 6.57: Model of QUBIC array pattern on the detector plane, (22 feed horns across the diameter at 150 GHz with baseline separation of 14 mm and 12.9° FWHM beams). The beams were excited by an on-axis source and a 5° off-axis source. Peaks corresponding to 2 sources are shown (red) an on-axis source and (green) a 5° off-axis source.

The central peak associated with the 5° source is at 5° , the spike at -3.2° is the subsidiary peak occurring at -8.2° from 5° . Next we take account of the attenuation of these sources by the feed horns (beam pattern on the sky). *Figure 6.58* shows the attenuation from the sky facing feed horns where the contribution from each source is attenuated by a factor from $e^{-\frac{\theta^2}{w_\theta^2}}$ (where θ is of the offset angle of the source and $w_\theta = \frac{12.9^\circ}{\sqrt{2 \ln(2)}}$).

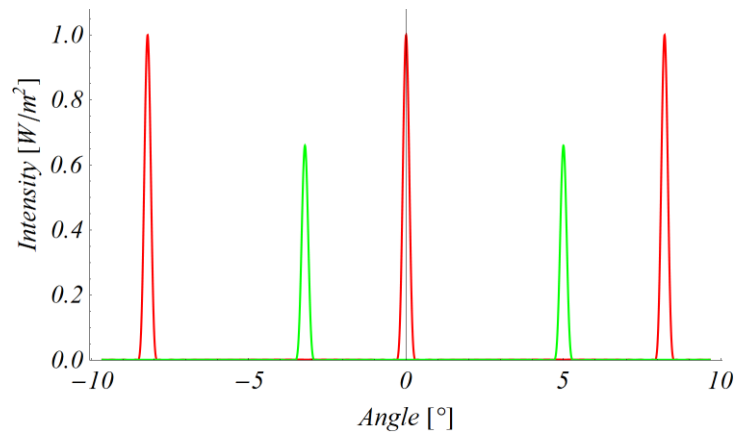


Figure 6.58: Mathematica model of QUBIC array pattern on the detector plane, (22 feed horns across the diameter at 150 GHz with baseline separation of 14 mm and 12.9° FWHM beams). Excitation is an on-axis source and a 5° off-axis source. The pattern takes into account the response of the skyward facing feed horns only.

In addition to this attenuation the pattern must also be multiplied by a Gaussian envelope ($e^{-\frac{r^2}{w^2}}$) where r is the off-axis distance on the detector plane and w is the beam radius at the detector plane to take account of the re-emitting feed horn beam pattern. The effect of both feed horn patterns are combined to give *Figure 6.59*. We now have a good approximation of what to expect at the detector plane, albeit for a 1D simplification for an idealised combiner. Taking now the complete PO simulation in 2D (see *Figure 6.55*) across the image plane we can see the on-axis and 5° off-axis PSF. Note that in this case, with the 45° angle between the input feed horn array and the image plane, the repetition is 8.2° along the diagonals. In this example, as shown in *Figure 6.59*, the main peak height is $\sim 40\%$ of the intensity of the on-axis (red) source and the subsidiary peak is $\sim 50\%$ of the intensity of the on-axis source.

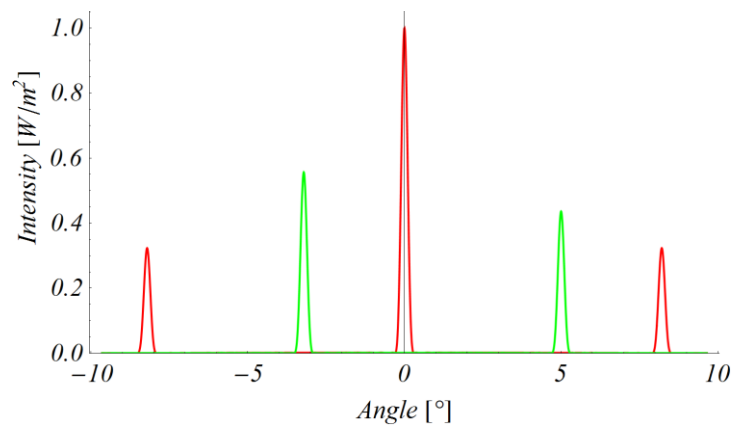


Figure 6.59: Model of QUBIC array pattern on the detector plane, (22 feed horns across the diameter at 150 GHz with baseline separation of 14 mm and 12.9° FWHM beams). Excitation is an on-axis source and a 5° off-axis source. The pattern takes into account the response of the skyward facing and combiner facing feed horns. Peaks corresponding to 2 sources shown (red) an on-axis source and (green) a 5° off-axis source (intensity is normalised to on-axis peak).

Due to the combiner induced aberrations, evident in the PSF in *Figure 6.55*, the peaks are not along a straight line making extraction of a cut for comparison with the PSF model, in *Figure 6.59*, difficult. This can be attributed to aberrations introduced by the combiner. The cut was generated in several sections from the centre to the maximum of each peak in the image. *Figure 6.60* shows the cut through *Figure 6.55* (black dashed line) compared with the PSF model (cuts were normalised to a common peak). The simple model can explain the number and relative heights of the peaks. Aberrations in the combiner shift the peaks slightly as expected (the shift of the central peak moves it away from the centre gap in the detector plane).

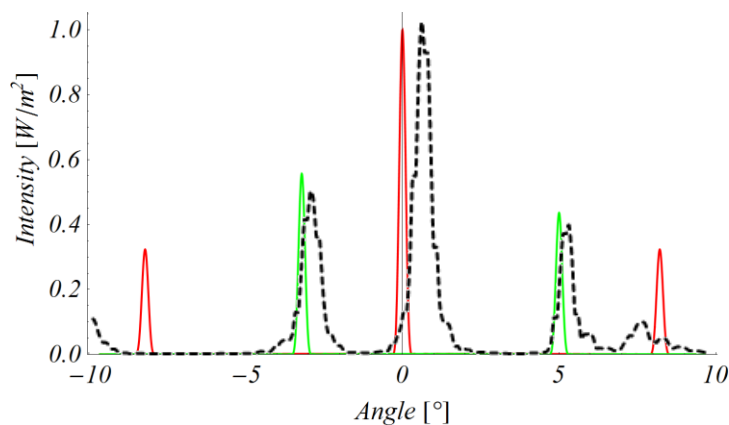


Figure 6.60: Overlaid cuts for comparison of *Figure 6.55* and *Figure 6.59*. Plots have been rescaled to match angular extent and normalised to a common central peak. There are 2 sources shown (red) an on-axis source and (green) a 5° off-axis source from the Mathematic and the same result from PO analysis (dashed line) in MODAL.

6.5 Effect of combiner elements on sensitivity

The effect of individual components was assessed by calculating the instrument PSF as each is added to the model. A basic system consisting only of the 12.9° input feed horn array, primary and secondary mirrors and detector plane, was used as a baseline for comparison. This setup should be at least as good as the original one (i.e. $\sim 11\%$ loss compared to the ideal) as the main difference is a narrower beam and larger image plane. *Figure 6.61* shows the PSF for the basic beam combiner with a primary mirror of $480\text{ mm} \times 600\text{ mm}$ and rim offset of 190 mm and a secondary mirror of $600\text{ mm} \times 600\text{ mm}$ with a rim offset of 130 mm . The dichroic, coldstop and various blockages within the system are ignored and the image is generated on the detector plane with the exact size of the bolometer array (all gaps between the bolometers and quadrants are ignored).

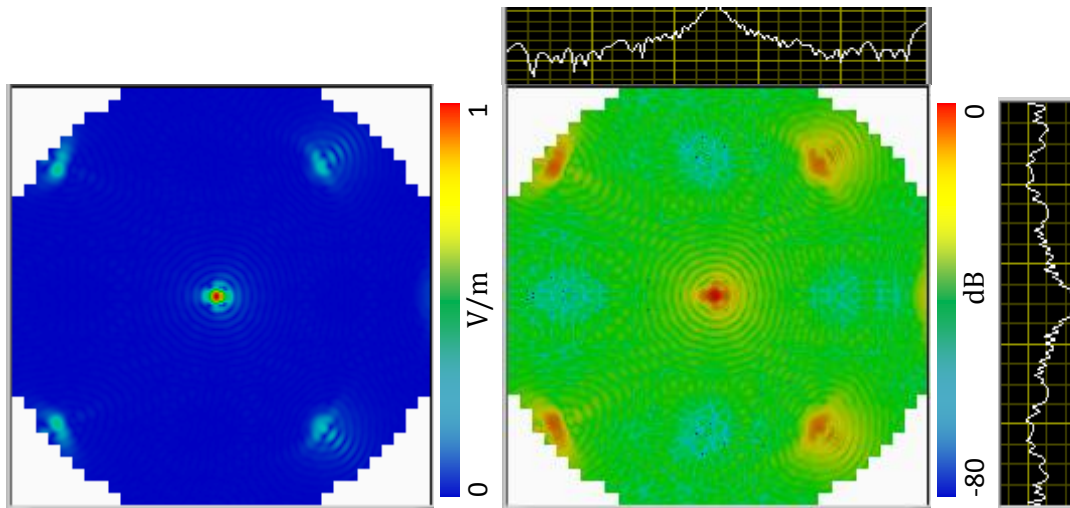


Figure 6.61: The PSF (amplitude) for 12.9° beams at 150 GHz with a primary mirror of $480\text{ mm} \times 600\text{ mm}$ and a 190 mm rim offset, a secondary mirror of $600\text{ mm} \times 600\text{ mm}$ and a 130 mm rim offset (the dichroic and coldstop were not considered). Detector plane power capture ranges from 74.7% to 84.9% with an average of 81.3% .

Figure 6.62 to *Figure 6.65* show PSFs calculated after the inclusion of additional combiner elements. *Figure 6.62* shows the PSF when the latest secondary mirror design is used ($600\text{ mm} \times 500\text{ mm}$) and *Figure 6.63* to *Figure 6.65* show it after the addition of the coldstop, then the dichroic and lastly the side detector plane blockage. *Figure 6.15* showed that the last element caused the largest drop in collected power. The cuts in each figure are an overlay of PSF from *Figure 6.61* (white) and the current PSF *Figure 6.62* (yellow). The PSFs were also compared by

calculating an overlap integral with the *Figure 6.61* PSF, coefficients dropped from ~ 1 for *Figure 6.62* to 0.996 for *Figure 6.65*. The changes at each stage (use of the minimised mirrors, inclusion of the coldstop, dichroic and side detector plane blockage) show that almost no degradation is expected in the PSF. Even though work in §4.3 showed that some truncation and aberrations are introduced, regardless of where the dichroic is put distortions were only due to a few feed horns and result in only small changes to the overall PSF (*Figure 6.65*).

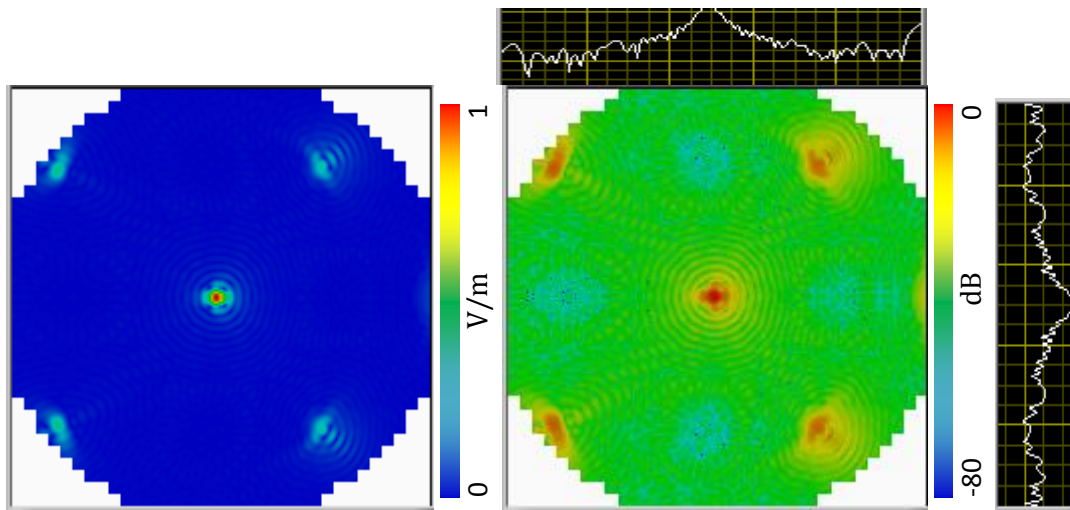
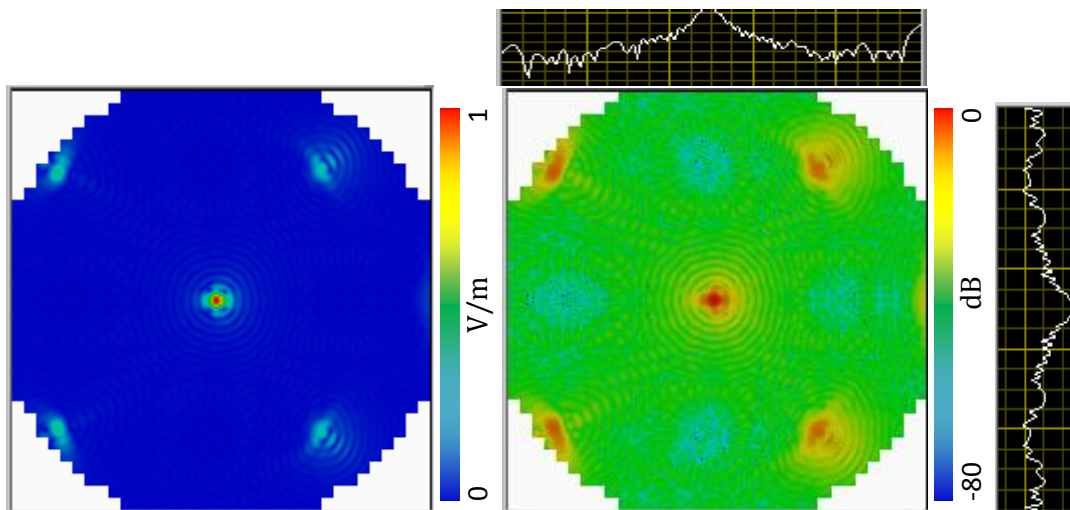


Figure 6.62: The PSF (amplitude) for 12.9° beams at 150 GHz with a primary mirror of $480\text{ mm} \times 600\text{ mm}$ and a 190 mm rim offset, a secondary mirror of $600\text{ mm} \times 500\text{ mm}$ and a 120 mm rim offset (the dichroic and coldstop were not considered). Detector plane power capture ranges from 74.5% to 84.9% with an average of 81.3%.



*Figure 6.63: The PSF (amplitude) for 12.9° beams at 150 GHz with a primary mirror of $480\text{ mm} \times 600\text{ mm}$ and a 190 mm rim offset, a secondary mirror of $600\text{ mm} \times 600\text{ mm}$ and a 130 mm rim offset, and the **coldstop** (the dichroic was not considered). Detector plane power capture ranges from 74.5% to 84.9% with an average of 81.3%. Most notable change is feed horn x15y22.*

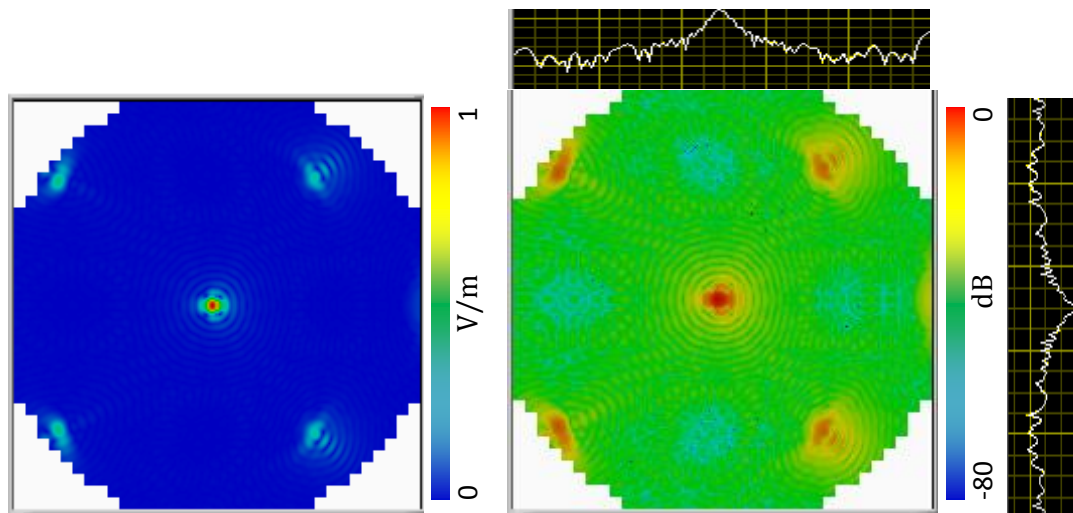


Figure 6.64: The PSF (amplitude) for 12.9° beams at 150 GHz with a primary mirror of $480\text{ mm} \times 600\text{ mm}$ and a 190 mm rim offset, a secondary mirror of $600\text{ mm} \times 600\text{ mm}$ and a 130 mm rim offset, and the coldstop and **dichroic** were considered. Detector plane power capture ranges from 74.6% to 84.9% with an average of 81.3%. Most notable change is feed horn x15y22.

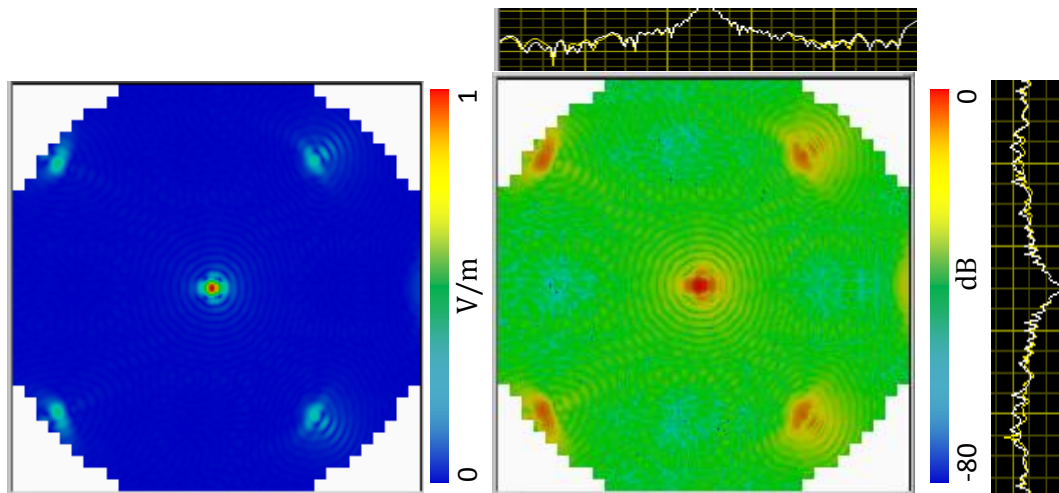


Figure 6.65: The PSF (amplitude) for 12.9° beams at 150 GHz with a primary mirror of $480\text{ mm} \times 600\text{ mm}$ and a 190 mm rim offset, a secondary mirror of $600\text{ mm} \times 600\text{ mm}$ and a 130 mm rim offset, and the coldstop, **dichroic** and **side detector plane blockages** were considered. Detector plane power capture ranges from 15.2% to 84.9% with an average of 80.4%. Most notable change is feed horn x03y04.

6.6 Conclusion

This chapter started with a check that original design could be updated to accommodate the new dual-band instrument. Using the new 12.9° feed horn beam the footprint of the outer array elements on each of the components in the combiner was calculated. At each stage the spillover and truncation was determined and where appropriate the element modified to cope as best as possible within the limitations of the overall instrument size.

There were several feed horns in the array that were not ideal for one or more of several reasons discussed in this chapter and Chapter 4 (blockages from the polariser/dichroic, blockages from the side image plane, etc.). The feed horn array was investigated to determine if some other feed horn locations to one side of the array could be exploited to obtain a better power level at the detector plane. The conclusion was simply that the existing circular array offered the best choice within the confines of the rest of the design.

The operation of the new 12.9° feed horn over the entire frequency range (130 GHz \rightarrow 250 GHz) was investigated. The feed horn was found to remain single moded up to 180 GHz and beyond this to contain up to 5 hybrid modes with the relative contribution dependent on the excitation source. The narrower beam meant that more power was detected at the detector plane (lower truncation throughout the combiner). The performance of the combiner at the highest frequency band was also analysed. The expected narrowing of the beam at the higher frequency was partially offset by the increased power in wider higher order modes. Even so it was shown that overall power capture at 220 GHz was higher in all cases (for each propagating hybrid mode) than the 150 GHz case.

Finally I looked at how the combiner performance deviated from an idealised optical system. This was assessed by comparing the simulated 'real' combiners PSF to that of an ideal optical system where all equivalent baselines give identical fringe patterns. The PSF of the instrument was simulated (for an on-axis and 5° off-axis source at 150 GHz and 220 GHz) and the location and intensity of its features were explained. The effect of aberrations were visible but the PSF was found to be closer to the ideal than the 14° QUBIC v2.0 design which was determined to have $\sim 89\%$ the sensitivity of an ideal unaberrated combiner.

7 Conclusions

This thesis described the design and modelling of the quasi-optical combiner for the QUBIC telescope. QUBIC aims to measure the elusive B-mode polarisation signature in the CMB or at least constrain the tensor-to-scalar ratio, r , to ≤ 0.01 . It will use the novel technique of bolometric synthetic-imaging interferometry.

In Chapter 1 the CMB was discussed. The Big Bang theory explains the origins of structure in the universe and predicts its fate, however, there are some phenomena which cannot be explained and this leads to the development of the theory of Inflation. A key prediction of Inflation is large-scale B-modes in the CMB. These large-scale polarisation structures are a ‘smoking-gun’ for Inflation and their detection is the main goal of the QUBIC combiner, the design of which is the topic of this thesis.

Chapter 2 described the analytical methods and tools used throughout this thesis for the modelling of the QUBIC instrument. A mode matching technique was discussed with a focus on one implementation used in the MU code SCATTER. This was then extended to include SVD which allowed a hybrid mode analysis of the feed horn outputs. The GRASP and MODAL software packages were discussed along with the various modelling methods employed by each. These are (1) geometric optics and the geometric theory of diffraction, (2) physical optics and the physical theory of diffraction and (3) Gaussian beam mode analysis and the application of ABCD matrices.

GO/GTD was useful in the initial design stages for approximating component positions and orientations but its inability to account for diffraction effects, which are prominent at these wavelengths, required that other methods were employed. PO is the most accurate of the methods used but also is the most time consuming due to the computations involved. This is especially concerning for a project like QUBIC with 400 individual sources to be considered. The time-intensive PO is required for the details, especially at the intermediary surfaces. Finally an intermediate method was investigated, GBM analysis, which accounts for

diffraction effects and is more efficient than PO. It represents the beam as a complex scalar field and as such cannot account for cross-polarisation effects. The field is constructed from the summation of independently propagating Gaussian modes. Examples from the QUBIC beam combiner were used throughout this chapter.

Chapter 3 gave a brief history of the QUBIC v1.0 instrument based on the novel concept of bolometric interferometry starting with its predecessors, MBI and BRAIN. From the results of MBI and BRAIN a collaboration was put together in 2008 to form the current mission, QUBIC. The operation of the instrument was detailed along with its scientific goals. It was shown how Stokes visibilities could be recovered from the Fizeau combiner image. Unfortunately the technical criteria of this design were too restrictive and the project was given a design overhaul in 2009. The outcome was QUBIC v2.0 which recovers the CMB polarisation properties from a synthetic image. The synthetic image is a convolution of the sky image and feed horn/combiner array PSF's. The new design used a feed horn array, 22 in diameter, operating at 150 GHz covering multipoles in the range $43 \leq l \leq 200$. An overall geometry and a detailed design of the combiner primary and secondary mirrors, and detector plane were presented. The combiner was forced to be a very fast optical system and so aberrations were inevitable.

In Chapter 4 a design for the updated QUBIC v2.0 instrument was presented. Starting with the input feed horn array layout, the footprint of the beam array on each of the elements in the system was calculated. At each stage the spillover and truncation was determined and where appropriate the element modified (in terms of size and location) to cope as best as possible within the limitations of the overall instrument design. The combiner was shown to be capable of supporting a polariser and a second detector plane. In the author's opinion the most important conclusion of this chapter is that this showed that the combiner was capable of catering for a simultaneous detection of both the x - and y -components of the CMB radiation. The design is spatially very restrictive and a drop in throughput was inevitable when the polariser was included. The coldstop, required as a baffle for the bare bolometer

array, fit within the design allowing for the use of a 2-stage cooling (4 K and 100 mK) within the cryostat. 420 mm manufacturing limitations and relocation of the input aperture source array from a 466.76 mm to a 366.76 mm separation from the primary mirror vertex were explored but were found to be too restrictive and lead to too much spillover. An alternative manufacturer was found in late 2013.

Whereas Chapter 4 analysed the design in terms of physically fitting in beams and components Chapter 5 investigated the performance of the combiner as a synthetic imager. For this I looked at fringe patterns, the window function and finally the instrument PSF. The location of the peaks in the PSF could be explained using a simple analysis and the effects of aberrations. The input feed horn array was rotated by 45° so that the subsidiary peaks of the PSF would not fall into gaps of the bolometer array. An important conclusion is that the aberrations are equivalent to only 10% drop in sensitivity when compared with an ideal instrument.

As the project developed it became clear that even the first QUBIC module should be able to observe at more than one frequency and so it was decided to adapt the QUBIC v2.0 design so that it could operate at both 150 GHz and 220 GHz. The dual-frequency instrument is described in Chapter 6. The feed horns were redesigned so that they would support operation over this extended frequency range and at the same time the beam FWHM was reduced from 14° to 12.9° . The new design was analysed and it was shown to provide a stable output across both of the bands required (150 GHz $\pm 12.5\%$ and 220 GHz $\pm 12.5\%$). The analysis showed that up to 5 hybrid modes could propagate at higher frequencies. The original QUBIC v2.0 (14°) design was checked to make sure the performance with the new beams (including the 220 GHz multi-moded beams) was at least as good as the previous single-frequency design. This was shown to be the case. Footprint diagrams were again used to optimise the size of the components. In the new dual-frequency design the polariser is replaced with a dichroic. Instrument PSFs were generated for both bands and for an on- and off-axis source. The location and intensity of the peaks were as expected.

This dual-frequency design has been accepted by the collaboration for the first module and is now under construction. Simulations by colleagues in APC (*Hamilton, J.C., private communication*) have shown that the QUBIC instrument should be capable of observing $r = 0.05$ in 2 years when foregrounds and an observing efficiency of 30% are considered. This is reduced to $r = 0.04$ if PLANCK 353-GHz data are included.

Future work

The work described in this thesis was carried out as part of an international collaboration. My specific role was the design and detailed analysis of the quasi-optical combiner. Design constraints and requirements changed regularly on the basis of input from other working groups in the collaboration but I have concentrated on the main design steps QUBIC v1.0 (measuring visibilities), QUBIC v2.0 (synthetic imager, 14° beams, coldstop, polariser and 2 detector planes) and dual-frequency QUBIC (12.9° beams, extended frequency range). The design of the first module is frozen but work will continue on the design of future modules taking account of improvements in technology and measurements by the first module.

A key tool in the analysis of the optical combiner was MODAL (which was run on the 106-core cluster at MU). Developments were made to the program as the need arose for the QUBIC modelling. In particular I contributed to the design of a module to model deformed surfaces. Other modules that could be incorporated in the future include mode-matching for rectangular geometries and the facility to model 3-dimensional shapes (e.g. the finite thickness polariser and the focal plane housing in the QUBIC combiner).

Publications

The work described in this thesis has contributed to the following papers:

Techniques for the modelling of QUBIC: a next-generation quasi-optical bolometric interferometer for cosmology

Authors: **Sully, S**; Gayer, D; Bennet, D; O'Sullivan, C; Gradziel, M.

Published: 07 Mar 2014

Terahertz, RF, Millimeter, and Submillimeter-wave Technologies and Applications VII, Proceedings of the SPIE, Volume 8985, article id. pp 898516-1 (2014).

The optical design of the QUBIC beam combiner

Authors: Donnacha Gayer; David Bennett; Cr  idhe O'Sullivan; **Stephen Scully**; Gareth Curran; Jean-Christophe Hamilton; Marie-Anne Bigot-Sazy; Michel Piat; Jean Kaplan; Andrea Tartari; Massimo Gervasi; Mario Zannoni

Published: 24 Sep 2012

Millimeter, Submillimeter, and Far-Infrared Detectors and Instrumentation for Astronomy VI. Proceedings of the SPIE, Volume 8452, article id. 845229, 8 pp. (2012).

Latest Progress on the QUBIC Instrument

Authors: A. Ghribi , J. Aumont, E. S. Battistelli, A. Bau, B. B  lier, L. Berg  , J.-Ph. Bernard, M. Bersanelli, M.-A. Bigot-Sazy, G. Bordier, E. T. Bunn, F. Cavaliere, P. Chaniel, A. Coppolecchia, T. Decourcelle, P. De Bernardis, M. De Petris, A.-A. Drilien, L. Dumoulin, M. C. Falvella, A. Gault, M. Gervasi, M. Giard, M. Gradziel, L. Grandsire, D. Gayer, J.-Ch. Hamilton, V. Haynes, Y. Giraud-H  raud, N. Holtzer, J. Kaplan, A. Korotkov, J. Lande, A. Lowitz, B. Maffei, S. Marnieros, J. Martino, S. Masi, A. Mennella, L. Montier, A. Murphy, M. W. Ng, E. Olivieri, F. Pajot, A. Passerini, F. Piacentini, M. Piat, L. Piccirillo, G. Pisano, D. Pr  le, D. Rambaud, O. Rigaut, C. Rosset, M. Salatino, A. Schillaci, **S. Scully**, C. O'Sullivan, A. Tartari, P. Timbie, G. Tucker, L. Vibert, F. Voisin, B. Watson, M. Zannoni

Journal of Low Temperature Physics

Submitted: 2014-09

DOI: 10.1007/s10909-013-1024-1

QUBIC: a Fizeau interferometer targeting primordial B-modes

Authors: A. Tartari J. Aumont S. Banfi E.S. Battistelli A. Ba  u P. Battaglia B. B  lier L. Berge J.Ph. Bernard M. Bersanelli M.A. Bigot-Sazy N. Bleurvacq G. Bordier J. Brossard E.F. Bunn D. Buzi D. Cammilleri F. Cavaliere P. Chaniel C. Chapron A. Coppolecchia T. Decourcelle P. De Bernardis F. Del Torto M. DePetris A.A. Drilien L. Dumoulin M.C. Falvella C. Franceschet A. Gault M. Gervasi A. Ghribi M.Giard M. Gradziel L. Grandsire D.Gayer J.Ch. Hamilton V. Haynes Y.Giraud-H  raud N. Holtzer J. Kaplan A. Korotkov J. Lande A. Lowitz B.Maffei S. Marnieros J. Martino S. Masi S. Melhuish A. Mennella5 M. McCulloch13 L. Montier8 A. Murphy12 M.W. Ng E. Olivieri C. O'Sullivan F.Pajot A. Passerini C. Perbost F.Piacentini M. Piat L. Piccirillo G.Pisano D. Pr  le D. Rambaud O.Rigaut C. Rosset M. Salatino A.Schillaci **S. Scully** M.M. Stolpovskiy P. Timbie G. Tucker L. Vibert D.Vigano F. Voisin B. Watson M.Zannoni

To be submitted 2015

Journal of Low Temperature Physics

(ESA Antennas, Noordwijk)

Optical simulations of the QUBIC beam combiner.

Authors: O'Sullivan, C., **Scully, S.** & Gayer, D.,

Submitted 2015. (O'Sullivan, et al., 2015)

8 Bibliography

- Abbon, P. et al., 2007. The COMPASS Experiment at CERN. *Nucl.Instrum.Meth*, A577(March), pp. 455-518.
- Ade, P. A. R. et al., 2014. Detection of B-mode polarisation at degree angular scales by BICEP 2. *Physical Review Letters*, 01 11, p. 112.
- Ade, P. et al., 2008. First season QUaD CMB temperature and polarisation power spectra. *ApJ*, Issue 674, pp. 22-28.
- Alpher, R. A. & Herman, R. C., 1948. *On the Relative Abundance of the Elements*. 12 ed. Maryland: s.n.
- Arnold, K. et al., 2010. The POLARBEAR CMB polarization experiment. *Society of Photo-Optical Instrumentation Engineers (SPIE) Conference Series*, 7741(July).
- Austermann, J. E. et al., 2012. SPTpol: an instrument for CMB polarization measurements with the South Pole Telescope. *SPIE*, 8452(September), p. 84520E.
- Balanis, C. A., 1989. Circular cross-section waveguides and cavities. In: *Advanced engineering electromagnetics*. Tempe, Arizona: John Wiley & Sons, Inc., pp. 470-491.
- Barkats, D. et al., 2005. First Measurements of the Polarization of the Cosmic Microwave Background Radiation at Small Angular Scales from CAPMAP. *Astrophysical Journal*, 619(February), pp. L127-130.
- Barr, A. H., 1984. Global and local deformations of solid primitives. *Computer graphics*, 18(3), pp. 21-30.
- Barr, A. H., 1986. Ray Tracing Deformed Surfaces. *California Institute of Technology*, August, 20(4), pp. 287-296.
- Battistelli, E. et al., 2010. QUBIC: The QU Bolometric Interferometer for Cosmology. *Astronomy & Astrophysics*, p. 12.

Bennett, D., 2014. *Design and analysis of a quasi-optic beam combiner for the QUBIC CMB interferometer*. Thesis ed. Maynooth: Maynooth University.

Benoit, A. et al., 2004. First detection of polarization of the submillimetre diffuse galactic dust emission by Archeops. *Astronomy and Astrophysics*, 424(September), pp. 571-582.

Bigot-Sazy, M.-A., 2013. *Thèse: Mesure des anisotropies de polarisation du fond diffus cosmologique avec l'interféromètre bolométrique QUBIC*, Paris: Laboratoire Astroparticule et Cosmologie (APC).

Bischoff, C. et al., 2011. First season QUIET observations: Measurements of CMB polarisation power spectra at 43 GHz in the multipole range $25 \leq l \leq 475$. *Astrophysical Journal*, 741(111).

Brown, M. L. et al., 2009. Improved measurements of the temperature and polarization of the Cosmic Microwave Background from QUaD. *Astrophysical Journal*, Volume 705, pp. 978-999.

Bunn, E. & White, M., 2007. Mosaicking with Cosmic Microwave Background Interferometers. *ApJ*, Volume 655, pp. 21-29.

Carlstrom, J. E., Kovac, J., Leitch, E. M. & Pryke, C., 2003. Status of CMB Polarization Measurements from DASI and other Experiments. *New Astronomy Review*, Volume 47, p. 953–966.

Charlassier, R., 2008. *The BRAIN experiment - A bolometric interferometer dedicated to the CMB B-mode measurement*, Paris: Laboratoire APC - Université Paris.

Charlassier, R. et al., 2010a. Bandwidth in bolometric interferometry. *Astronomy and astrophysics*, Volume 514, p. A37+.

Charlassier, R. et al., 2009. An efficient phase-shifting scheme for bolometric additive. *Astronomy & Astrophysics*, 497(3), pp. 963 - 971.

Charlassier, R. et al., 2010b. *QUBIC 2.0: A new design for bolometric interferometry*, Paris: APC: QUBIC Internal note.

Cittert, P. v., 1934. Die Wahrscheinliche Schwingungsverteilung in Einer von Einer Lichtquelle Direkt Oder Mittels Einer Linse Beleuchteten Ebene. *Physica*, 1(1-6), pp. 201-210.

Clarricoats, P. & Olver, A., 1984. *Corrugated Horns for Microwave Antennas*. s.l.:Institute of engineering and technology.

Colgan, R., 2001. *Electromagnetic and quasi-optical modelling of horn antennas for far-IR space applications*. 1st ed. Maynooth: Maynooth University.

Collett, E., 2005. *Field Guide to Polarization*. Bellingham, WA, SPIE Press.

Collin, R. E. & Zucker, F. J., 1969. *Antenna Theory, Part 1*. New York: McGraw-Hill Book Company.

Crill, B. P. et al., 2008. SPIDER: A Balloon-borne Large-scale CMB Polarimeter. *SPIE*, 7010(Space Telescopes and Instrumentation).

Curran, G., 2010. Quasi-Optical Design and Analysis of Bolometric Interferometers for Cosmic Microwave Background Experiments. In: *Thesis*. Maynooth: NUI, p. 62.

Delabrouille, J., Kaplan, J., Piat, M. & Rosset, C., 2003. Polarisation Experiments. *C. R. Physique*, Volume 4, p. 925–934.

Dicke, R. H., Peebles, P. J. E., Roll, P. G. & Wilkinson, D. T., 1965. Cosmic Black-Body Radiation. *Astrophysical Journal*, Volume 142, pp. 414-419.

Dragone, C., 1978. Offset multireflector antennas with perfect pattern symmetry and polarization discrimination. *Bell Syst. Tech. J.*, 57(7), pp. 2663-2684.

Efstathiou, G., 1988. Large Scale Motions in the Universe. In: V. C. Rubin & G. V. Coyne, eds. *A Vatican Study Week*. s.l.:Princeton University Press.

ESA, 2014. *PLANCK*. [Online]
Available at:
http://www.esa.int/Our_Activities/Space_Science/Planck/Planck_reveals_an_almost_perfect_Universe
[Accessed 25 July 2014].

ESA, 2015. *PLANCK's new cosmic recipe*. [Online]
Available at: <http://sci.esa.int/planck/51557-planck-new-cosmic-recipe/>
[Accessed 23 07 2015].

Figueiredo, N. et al., 2005. The optical design of the Background Emission Anisotropy Scanning Telescope (BEAST). *The Astrophysical Journal Supplement Series*, 158(May), p. 118–123.

Gamow, G., Alpher, R. A. & Bethe, H., 1948. The Origin of Chemical Elements. *Physical review*, 73(7), p. 803.

Gayer, D., 2015. *PhD Thesis in preparation*, Maynooth: National University of Ireland.

Génova-Santos, R. et al., 2014. The QUIJOTE experiment: project overview and first results. *Cosmology and Nongalactic Astrophysics*, Issue April.

Ghribi, A. et al., 2010. Experimental Study of an Adding Interferometer at Millimeter Waves. *J Infrared Milli Terahz Waves*, 31(DOI 10.1007/s10762-009-9562-y), p. 88–99.

Gleeson, E., 2004. *Single and multimoded corrugated horn design for cosmic microwave background experiments*. 1st ed. Maynooth: Maynooth University.

Goldsmith, P. F., 1998. Quasi-optical systems: Gaussian Beam Quasi-optical Propagation and Applications. *IEEE Press*.

Gradziel, M. L. et al., 2008. *Modeling of the Optical Performance of Millimeter-Wave Instruments using MODAL*. Maynooth, Ireland, SPIE.

Gundersen, J. O., 2003. The Ku-band Polarization Identifier. *New Astronomy Reviews*, 47(11-12), p. 1097–1106.

Guth, A. H., 1981. Inflationary Universe: A possible solution to horizon and flatness problems. *Physical Review D*, 23(2), pp. 347-356.

Guth, A. H. & Pi, S. Y., 1982. Fluctuations in the new inflationary universe. *Physical Review Letters*, Volume 49, pp. 1110-1113.

Hamilton, J. C., Charlassier, R. & Kaplan, J., 2009. *QUBIC white paper - QUBIC design optimisation*, Paris: APC.

Hamilton, J. et al., 2008. *Sensitivity of a bolometric interferometer to the CMB power spectrum*, s.l.: Astronomy & Astrophysics.

Hanany, S. et al., 2000. MAXIMA-1: A Measurement of the Cosmic Microwave Background Anisotropy on Angular Scales of 10° - 5° . *The Astrophysical Journal*, 545(1), pp. L5-9.

Hanson, D., Hoover, S., Crites, A. & Ade, P. A., 2013. Detection of B-mode Polarization in the Cosmic Microwave Background with Data from the South Pole Telescope. *Phys. Rev. Lett.*, 141301(September 30th), p. 111.

Hiebel, M., 2008. *Vector network analyzer (VNA) calibration: the basics*, USA: Rohde & Schwarz.

Hinderks, J. R. et al., 2009. QUaD: A high-resolution cosmic microwave background polarimeter. *The Astrophysical Journal*, 20 February, Volume 692, p. 1221–1246.

Hinshaw, G. et al., 2013. Nine-year Wilkinson Microwave Anisotropy Probe (WMAP) observations: Cosmological parameter results. *ApJS*, 208(19).

Hinshaw, G., Nolta, M. R., Bennett, C. L. & Bean, R., 2007. Three-Year Wilkinson Microwave Anisotropy Probe (WMAP) Observations: Temperature Analysis. *Astrophysical Journal*, Volume 170, pp. 288-334.

Holmes, W. A. et al., 2008. Initial test results on bolometers for the Planck high frequency instrument. *Applied Optics*, 47 (32)(ISSN 0003-6935), pp. 5996-6008.

Hoyle, F., 1948. A New Model for the Expanding Universe. *Royal Astronomical Society*, Volume 108, p. 372.

Hu, W. & White, M., 1997. A CMB polarization primer. *New Astronomy*, Issue 2, pp. 323-344.

Hu, W. & White, M., 2004. The Cosmic Symphony. *Scientific American*, pp. 44-53.

Jansky, K. G., 1933. Radio waves from outside the solar system. *Nature*, 07, 132(3323), p. 66.

J Jeans, J. H., 1928. *Astronomy and Cosmogony*, Cambridge: s.n.

Johansen, P. M., 1996. Uniform physical theory of diffraction equivalent edge currents for implementation in general computer codes. *Antennas and Propagation Society International Symposium*, Volume 2, pp. 784-787.

Kajiya, J. T., 1982. Ray Tracing Parametric Patches. *Computer graphics*, July, 16(3), pp. 245-254.

Kaplan, J. & collaboration, t. Q., 2009. *QUBIC, a bolometric interferometer to measure the B modes of the CMB*. Blois, Windows on the Universe.

Kaplan, J., Delabrouille, J., Fosalba, P. & Rosset, C., 2003. CMB polarisation as complementary information to anisotropies. *C.R. Academy of sciences, Paris*, Volume 4, pp. 1-9.

Kay, T. L. & Kajiya, J. T., 1986. Ray Tracing Complex Scenes. *California Institute of Technology*, August, 20(4), pp. 269-278.

Keating, B. G. et al., 2003. BICEP: A large angular scale CMB polarimeter. *SPIE Int. Soc. Opt. Eng.*, Volume 4843, p. 284.

Keating, B. G. et al., 2003. BICEP: a large angular scale CMB polarimeter. *Society of Photo-Optical Instrumentation Engineers (SPIE) Conference Series*, 4843(February), pp. 284-295.

Keating, B. G. et al., 2001. An instrument for investigating the large angular scale polarisation of the CMB. *Ap.J*, 144(December), pp. 1-20.

Kogut, A. et al., 2006. ARCADE: Absolute Radiometer for Cosmology, Astrophysics, and Diffuse Emission. *New Astron.Rev*, 50(11-12), pp. 925-931.

Kouyoumjian, R. G. & Pathak, P. H., 1974. A uniform GTD for an edge in a perfectly conducting surface. *Proceedings of the IEEE*, 62(11), pp. 1448-61.

Kovac, J. et al., 2002. Detection of polarisation in the CMB using DASI. *astro-ph*, Issue 0209478.

Lau, K., Tang, J. & Chu, M. C., 2014. Cosmic microwave background constraints on the tensor-to-scalar ratio. *Res. Astron. Astrophys.*, 6(3), p. 13.

Leitch, E. M., Kovac, C. & Pryke, C., 2002. Measuring polarisation with DASI. *Nature*, 23 9, Volume 420, pp. 763-771.

Lemaître, G., 1927. Un univers homogène de masse constante et de rayon croissant rendant compte de la vitesse radiale des nébuleuses extragalactiques. *Annales de la Societe Scientifique de Bruxelles*, 47A(41), pp. 49-59.

Lesurf, J., 1990. Millimetre-wave optics, Devices & Systems. *IOP publishing Ltd*.

Liddle, A. R. & Lyth, D. H., 2000. *Cosmological inflation and large scale structure*. June ed. Cambridge, New York: Cambridge University Press.

MacTavish, C. J. et al., 2006. Cosmological Parameters from the 2003 Flight of BOOMERANG. *Astrophysical Journal*, 647(August), pp. 799-812.

Martinache, F., MOOC 2015. *France Universite Numerique: L'Observatoire de la Côte d'Azur* - 27001: *Eagle-Eye Astronomy*. [Online]

Available at: www.france-universite-numerique.fr
[Accessed 18 08 2015].

Masi, S. et al., 2005. Precision CMB polarisation from dome-c: The BRAIN experiment. *EAS Publications Series*, Volume 14, pp. 87-92.

Mather, J. C. et al., 1990. A preliminary measurement of the Cosmic Microwave Background Spectrum by the Cosmic Background Explorer(COBE) Satellite. *Astrophysical Journal*, Volume 354, pp. L34-L40.

McKay, N., McKay, D. & Wieringa, M., 2006. *VRI - Virtual Radio Interferometer*.
[Online]

Available at: <http://www.narrabri.atnf.csiro.au/astronomy/vri.html>
[Accessed 04 07 2013].

Melchiorri, A., Ade, P. A. & de Bernardis, P., 2000. A Measurement of Ω from the North American Test Flight of Boomerang. *Astrophysical Journal*, 536(2), pp. L63-66.

Mizuguchi, Y., Akagawa, M. & Yokoi, H., 1978. *Electronics & Comm. in Japan*, 61-B(3), p. 58.

Murphy, J. A., 1987. *Distortion of a simple Gaussian beam on reflection from off-axis ellipsoidal mirrors*, Cambridge: Mullard Radio Astronomy Observatory.

Murphy, J. A. & Egan, A., 1993. Examples of Fresnel diffraction using Gaussian modes. *Eur. J. Phys*, Volume 14, pp. 121-127.

Murphy, J. A. & Withington, S., 1996. Perturbation analysis of Gaussian beam mode scattering at off-axis ellipsoidal mirrors. *Infrared Physics & Technology*, 37(2), pp. 205-219.

NASA / WMAP Science Team, 2010. *CMB65*. [Online]
Available at: <http://wmap.gsfc.nasa.gov/media/030635/index.html>
[Accessed 25 July 2014].

NASA/WMAP Science Team, 2010. *National Aeronautics and Space Administration*. [Online]

Available at: http://map.gsfc.nasa.gov/universe/bb_concepts_exp.html

[Accessed 28 01 2016].

NASA, 2012. *LAMBDA - CMB Experiments*. [Online]

Available at: <http://lambda.gsfc.nasa.gov/product/expt/index.cfm?sort=15>

[Accessed 10 Auust 2015].

Netterfield, C. B. et al., 1996. A Measurement of the Angular Power Spectrum of the Anisotropy in the Cosmic Microwave Background. *ApJ*, 474(arXiv:astro-ph/9601197v1), p. 47.

Niemack, M. D. et al., 2010. ACTPol: A polarization-sensitive receiver for the Atacama Cosmology Telescope. *SPIE*, Volume 7741, p. 77411S.

O'Sullivan, C., Scully, S. & Gayer, D., 2015. *Optical simulations of the QUBIC beam combiner*. Noordwijk, ESA (Antennas).

Olver, A. D., Clarricoats, P. J., Kishk, A. A. & Shafai, L., 1994. *Microwave horns and feeds*. 1st ed. New York: The Institution of Engineering and Technology.

Ostlie, D. A. & Carroll, B. W., 2007. *An introduction to modern astrophysics*. 2nd ed. s.l.:Pearson Addison-Wesley.

Padin, S. et al., 2001. First Intrinsic Anisotropy Observations with the Cosmic Background Imager. *Astrophysical Journal*, 549(March), pp. L1-5.

Park, C.-G. & Park, C., 2002. Simulation of Cosmic Microwave Background Polarization Fields for AMiBA Experiment. *J.Korean Astron.Soc.*, 67(March), p. 35.

Peebles, P. J., 1968. Recombination of the Primeval Plasma. *Astrophysical Journal*, 153(July), p. 1.

Penzias, A. A. & Wilson, R. W., 1965. A Measurement of Excess Antenna Temperature at 4080 Mc/s. Volume 142, pp. 419-422.

Pilbratt, G., 2003. *Herschel space observatory mission overview*. s.l., International Society for Optics and Photonics, pp. 586-597.

PLANCK-Collaboration, 2013a. Planck 2013 results. I. Overview of products and scientific results. *Astronomy & Astrophysics*, Issue March, pp. 1-44.

PLANCK-Collaboration, 2013b. Planck 2013 results. XXII. Constraints on inflation. *Astronomy & Astrophysics*.

PLANCK-Collaboration, 2013c. Planck 2013 results. XVI. Cosmological parameters. *Astronomy & Astrophysics*.

Polenta, G. et al., 2007. The BRAIN CMB polarization experiment. *New Astronomy Reviews*, Volume 51, p. 256–259.

Prêle, D. et al., 2009. Superconducting niobium/silicon bolometer developments in the dcmb french collaboration. *EAS Publications Series*, Volume 37, pp. 107-117.

QMC Instruments, 2012. *QMC Instruments: Excellence in toolmaking, THz systems and components*. [Online]

Available at:

http://www.terahertz.co.uk/index.php?option=com_content&view=article&id=211&Itemid=538

[Accessed 20 08 2015].

Ramo, S., Whinnery, J. R. & van Duzer, T., 1994. *Fields and waves in communication electronics*. 3rd ed. New York, Chichester, Brisbane, Toronto, Singapore: John Wiley & Sons, Inc..

Reese, M., 2006. *Superconducting Hot Electron Bolometers for Terahertz Sensing*. Thesis ed. New Haven: Yale.

Rees, M. J., 1968. Polarization and spectrum of the primeval radiation in anisotropic universe. *ApJ*, Volume 153, pp. L1-5.

Rusch, W., Prata, J., Rahmat-Samii, Y. & Shore, R., 1990. Derivation and application of the equivalent classical offset cassegrain and gregorian antennas. *IEEE*, 38(Transactions on Antennas and Propagation), pp. 1141-9.

Sederberg, T. W. & Anderson, D. C., 1984. Ray tracing of steiner patches. *Computer Graphics*, July, 18(3), pp. 159-164.

Sheehy, C. D. et al., 2010. The keck array: a pulse tube cooled cmb polarimeter. *SPIE*, Volume 7741, p. 77411R.

Siegman, A. E., 1986. *Lasers*. United States: University Science Books.

Simon, S. M. et al., 2014. Characterization of the Atacama B-Mode Search. *Proc. of SPIE*, 9153(mm, sub-mm, far-IR Detectors and Instrumentation for Astronomy), p. 91530Y.

Smoot, G. F. et al., 1992. Structure in the COBE Differential Microwave First-Year Maps. *Astrophysical Journal Letters*, Volume 396, p. 1.

Spencer, R., 2013. *Global warming*. [Online] Available at: <http://www.drroyspencer.com/2013/12/> [Accessed 19 08 2015].

Spergel, D. N. et al., 2007. Wilkinson Microwave Anisotropy Probe (WMAP) Three Year Results: Implications for Cosmology. *Astrophysical Journal Supplement Series*, Volume 170, p. 377.

Spergel, D. N. et al., 2008. Wilkinson Microwave Anisotropy Probe (WMAP) Three Year Results: Implications for Cosmology. *Astrophysical Journal Supplement Series*, Volume 170, p. 377.

Stokes, G. G., 1852. *Mathematical and Physical Papers*. 3(9), p. 399.

Taylor, A. C. et al., 2004. *CLOVER - A new instrument for the measurement of the B-Mode polarisation of the CMB*, s.l.: Astrophysics e-prints July.

Tegmark, M., 1996. The angular power spectrum of the 4 year COBE data. *Astrophysical Journal*, June(Lett 464), pp. L35-38.

TICRA, 2005. *GRASP Technical Description*. 9 ed. Copenhagen: Ticra Engineering Consultants.

TICRA, 2011. *GRASP Reference Manual*. v9.8.02 ed. Copenhagen: TICRA.

Timbie, P. T. et al., 2006. The einstein polarization interferometer for cosmology (EPIC) and the millimeterwave bolometric interferometer (MBI). *New Astr. Rev.*, Volume 50, pp. 999-1008.

Toth, D. L., 1985. On Ray Tracing Parametric Surfaces. July, 19(3), pp. 171-179.

Tran, H. et al., 2008. Comparison of the crossed and the Gregorian Mizuguchi–Dragone for wide-field millimeter-wave astronomy. *Applied optics*, 47(2).

Tucker, G. S. et al., 2003. Bolometric interferometry: the millimeter-wave bolometric interferometer. *New Astronomy Reviews*, 47(11-12), pp. 1173-1176.

Tucker, G. S. et al., 2008. The Millimeter-Wave Bolometric Interferometer (MBI). *SPIE*.

Tynan, N., 2015. *Masters Thesis in progress*. Thesis ed. Maynooth: Maynooth University.

Wexler, A., 1967. Solution of waveguide discontinuities by modal analysis. *IEEE TRANSACTIONS ON MICROWAVE THEORY AND TECHNIQUES*, MTT-15(9), pp. 508-517.

Whale, M., 2009. *PhD. Thesis*, Maynooth: Maynooth University.

White, D. R., 2006. *The Development of Efficient CAD Software for Terahertz Optical Design and Analysis*, Maynooth: PhD. Thesis, NUI Maynooth.

White, M., Carlstrom, J. E., Dragovan, M. & Holzappel, W. L., 1999a. Interferometric observation of CMB anisotropies. *ApJ*, Volume 514, pp. 12-24.

White, M. & Cohn, J. D., 2002. *Cosmic Microwave Background: The Theory of Anisotropies*, California: Astro-ph.

White, M. & Wu, H., 1999b. Anisotropies in the CMB. *Proceedings of the Los Angeles Meeting, DPF 99, UCLA*.

Wollack, E. J. et al., 1994. The Saskatoon Experiment: A Measurement of the Anisotropy in the Cosmic Microwave Background. *American Astronomical Society*, 26(184th AAS Meeting), p. 888.

Wootten, A., 2003. Atacama large millimeter array (ALMA). *Astronomical Telescopes and Instrumentation*, pp. 110-118.

Yun, M. et al., 2004. Fabrication of antenna coupled transition edge polarization-sensitive bolometer arrays. *Nuclear Instruments and Methods in Physics Research Section A: Accelerators, Spectrometers, Detectors and Associated Equipment*, 520(1-3), pp. 487-9.

Zaldarriaga, M., 2001. Nature of the E-B decomposition of CMB polarization. *Physical Review D*, 64(103001), p. 8.

Zhan, H. et al., 2014. Large-Scale Structure and Baryon Oscillations.. In: http://www.lsst.org/files/docs/sciencebook/SB_13.pdf, ed. *Large Synoptic Survey Telescope: Science Book*. Tucson, Az, USA: LSST, p. Ch. 13.

Appendix 1. Scripting

a. Bash script

```
mkdir -p "Data(150.00)/Image Main"

xarray=( '13' '12' '11' '10' ... )
yarray=( '21' '15' '02' '12' ... )

echo $(date) "Started bash operation" | tee modal.log
SleepTime=3600
echo $(date) Forced timeout $$SleepTime seconds | tee -a modal.log

for ((r=0;r<=2;++r)); do
if [ $r -gt 0 ]
then
echo "*****" | tee -a modal.log
echo "* RETRYING MISSED/SKIPPED/ERROR OUTPUTS - ATTEMPT $r *" | tee -a modal.log
echo "*****" | tee -a modal.log
fi

for ((i=0;i<${#xarray[@]};++i)); do
if [ -e "Data(150.00)/Image Main/x${xarray[i]}y${yarray[i]}.dat" ]
then
echo $(date) "Found x${xarray[i]}y${yarray[i]} @ 150.00 GHz Skipping" | tee -a modal.log
else
echo $(date) "Processing x${xarray[i]}y${yarray[i]} @ 150.00 GHz" | tee -a modal.log

echo $(date) Starting | tee -a modal.log
( modal -b -L QUBIC.mdl -S 'Parameters.Frequency.frequency=150 GHz' -S "Source.OffsetU=${xarray[i]}" -S
"Source.OffsetV=${yarray[i]}" \
-S "Source.Export.Image Main.filename=Data(150.00)/Image Main/x${xarray[i]}y${yarray[i]}.dat" -E
"Source.Export.Image Main" -S "Source.Report.Image Main.target.filename=Data(150.00)/Image
Main/x${xarray[i]}y${yarray[i]}.pwr" -R "Source.Report.Image Main" \
) &

for ((t=0;t<=$SleepTime;++t)); do
if [ -z "$(pgrep -u $USER modal)" ]
then
break
fi
sleep 1
done

if [ $t -eq $SleepTime ]
then
echo $(date) MODAL Hung | tee -a modal.log
kill $(pgrep -u $USER modal)
sleep 1
else
echo $(date) MODAL Completed | tee -a modal.log
fi
fi
done
done
echo $(date) Everything Completed
```

b. vb script

```

Sub Generate_Batch()
  Dim doClip As DataObject, xarray As String, yarray As String
  Const ISleepTime As Long = 3600

  sCmnd = ""
  xarray = "xarray=( "
  yarray = "yarray=( "
  For x = 0 To 21
    For y = 0 To 21
      xVal = ActiveSheet.Cells(y + 1, (x * 2) + 1).Value
      yVal = ActiveSheet.Cells(y + 1, (x * 2) + 2).Value
      If Not IsEmpty(xVal) And Not IsEmpty(yVal) Then
        xarray = xarray & "" & Format(xVal, "00") & " "
        yarray = yarray & "" & Format(yVal, "00") & " "
      End If
    Next y
  Next x
  xarray = xarray & ")"
  yarray = yarray & ")"
  sItem = cPolarisation & "x${xarray[i]}y${yarray[i]}"

  'aElements = Array("Primary", "Coldstop", "Polariser Block", "Polariser Rim", "Secondary", "Image Side Block",
  "Polariser", "Image Main", "Image Side")
  'aElements = Array("Primary", "Coldstop", "Polariser Block", "Secondary", "Image Side Block", "Polariser",
  "Image Main")
  aElements = Array("Image Main")
  'aElements = Array("Primary", "Secondary", "Image Main")
  dFrequency = 150 '131.25 150 168.75 (12.5% Bandwidth)

  For Each aElement In aElements
    sCmnd = sCmnd & "mkdir -p " & Chr(34) & "Data(" & Format(dFrequency, "#0.00") & ")/" & aElement &
    Chr(34) & vbCrLf
  Next
  sCmnd = sCmnd & vbCrLf
  sCmnd = sCmnd & "# " & ActiveSheet.Name & vbCrLf

  sCmnd = sCmnd & xarray & vbCrLf
  sCmnd = sCmnd & yarray & vbCrLf & vbCrLf

  sCmnd = sCmnd & "echo $(date) " & Chr(34) & "Started bash operation" & Chr(34) & " | tee modal.log" & vbCrLf
  sCmnd = sCmnd & "SleepTime=" & ISleepTime & vbCrLf
  sCmnd = sCmnd & "echo $(date) Forced timeout $ISleepTime seconds | tee -a modal.log" & vbCrLf & vbCrLf

  sCmnd = sCmnd & "for ((r=0;r<=2;+r)); do" & vbCrLf
  sCmnd = sCmnd & " if [ $r -gt 0 ]" & vbCrLf
  sCmnd = sCmnd & " then" & vbCrLf
  sCmnd = sCmnd & "   echo " & Chr(34) & "*****"
  & Chr(34) & " | tee -a modal.log" & vbCrLf
  sCmnd = sCmnd & "   echo " & Chr(34) & "** RETRYING MISSED/SKIPPED/ERROR OUTPUTS - ATTEMPT $r **" &
  Chr(34) & " | tee -a modal.log" & vbCrLf
  sCmnd = sCmnd & "   echo " & Chr(34) & "*****"
  & Chr(34) & " | tee -a modal.log" & vbCrLf
  sCmnd = sCmnd & " fi" & vbCrLf & vbCrLf

  sCmnd = sCmnd & " for ((i=0;i<${#xarray[@]};+i)); do" & vbCrLf
  sCmnd = sCmnd & "   if [ -e " & Chr(34) & "Data(" & Format(dFrequency, "#0.00") & ")/" &
  aElements(UBound(aElements)) & "/" & sItem & ".dat" & Chr(34) & "]" & vbCrLf
  sCmnd = sCmnd & " then" & vbCrLf
  sCmnd = sCmnd & "     echo $(date) " & Chr(34) & "Found x${xarray[i]}y${yarray[i]} @ " &
  Format(dFrequency, "#0.00") & " GHz Skipping" & Chr(34) & " | tee -a modal.log" & vbCrLf

```

```

sCmnd = sCmnd & " else" & vbCrLf
sCmnd = sCmnd & "      echo $(date) " & Chr(34) & "Processing x${xarray[i]}y${yarray[i]} @ " &
Format(dFrequency, "#0.00") & " GHz" & Chr(34) & " | tee -a modal.log" & vbCrLf & vbCrLf

'sCmnd = sCmnd & " if [ -z " & Chr(34) & "$(pgrep -u $USER modal)" & Chr(34) & " ]" & vbCrLf
'sCmnd = sCmnd & " then" & vbCrLf
'sCmnd = sCmnd & "      echo $(date) PVM Active | tee -a modal.log" & vbCrLf
'sCmnd = sCmnd & "      ( echo halt | pvm ) & sleep 1" & vbCrLf
'sCmnd = sCmnd & " fi" & vbCrLf & vbCrLf

'sCmnd = sCmnd & " if [ -e " & Chr(34) & "$HOME/tmp/pvmd.$UID" & Chr(34) & " ]" & vbCrLf
'sCmnd = sCmnd & " then" & vbCrLf
'sCmnd = sCmnd & "      echo $(date) PVM Dirty | tee -a modal.log" & vbCrLf
'sCmnd = sCmnd & "      ( rm $HOME/tmp/pvmd.$UID ) & sleep 1" & vbCrLf
'sCmnd = sCmnd & " fi" & vbCrLf & vbCrLf

sCmnd = sCmnd & "      echo $(date) Starting | tee -a modal.log" & vbCrLf

sCmnd = sCmnd & "      ( modal -b -L QUBIC.mdl -S 'Parameters.Frequency.frequency=" & dFrequency & "
GHz"
sCmnd = sCmnd & " -S " & Chr(34) & "Source.OffsetU=${xarray[i]}" & Chr(34)
sCmnd = sCmnd & " -S " & Chr(34) & "Source.OffsetV=${yarray[i]}" & Chr(34)
sCmnd = sCmnd & " \" & vbCrLf

For Each aElement In aElements
    sCmnd = sCmnd & "          -S " & Chr(34) & "Source.Export." & aElement & ".filename=Data(" &
Format(dFrequency, "#0.00") & ")/" & aElement & "/" & sltem & ".dat" & Chr(34)
    sCmnd = sCmnd & " -E " & Chr(34) & "Source.Export." & aElement & Chr(34)
    sCmnd = sCmnd & " -S " & Chr(34) & "Source.Report." & aElement & ".target.filename=Data(" &
Format(dFrequency, "#0.00") & ")/" & aElement & "/" & sltem & ".pwr" & Chr(34)
    sCmnd = sCmnd & " -R " & Chr(34) & "Source.Report." & aElement & Chr(34)
    sCmnd = sCmnd & " \" & vbCrLf
Next
sCmnd = sCmnd & "      )" & vbCrLf & vbCrLf

sCmnd = sCmnd & "      for ((t=0;t<$SleepTime;++t)); do" & vbCrLf
sCmnd = sCmnd & "          if [ -z " & Chr(34) & "$(pgrep -u $USER modal)" & Chr(34) & " ]" & vbCrLf
sCmnd = sCmnd & "          then" & vbCrLf
sCmnd = sCmnd & "              break" & vbCrLf
sCmnd = sCmnd & "          fi" & vbCrLf
sCmnd = sCmnd & "          sleep 1" & vbCrLf
sCmnd = sCmnd & "      done" & vbCrLf & vbCrLf

sCmnd = sCmnd & "      if [ $t -eq $SleepTime ]" & vbCrLf
sCmnd = sCmnd & "      then" & vbCrLf
sCmnd = sCmnd & "          echo $(date) MODAL Hung | tee -a modal.log" & vbCrLf
sCmnd = sCmnd & "          kill $(pgrep -u $USER modal)" & vbCrLf
sCmnd = sCmnd & "          sleep 1" & vbCrLf
sCmnd = sCmnd & "      else" & vbCrLf
sCmnd = sCmnd & "          echo $(date) MODAL Completed | tee -a modal.log" & vbCrLf
sCmnd = sCmnd & "      fi" & vbCrLf
sCmnd = sCmnd & "      fi" & vbCrLf
sCmnd = sCmnd & "      done" & vbCrLf
sCmnd = sCmnd & "      "done" & vbCrLf
sCmnd = sCmnd & "      echo $(date) Everything Completed" & vbCrLf

Set doClip = New DataObject
doClip.SetText sCmnd
doClip.PutInClipboard
Set doClip = Nothing
End Sub

```

Appendix 2. Tolerance test data

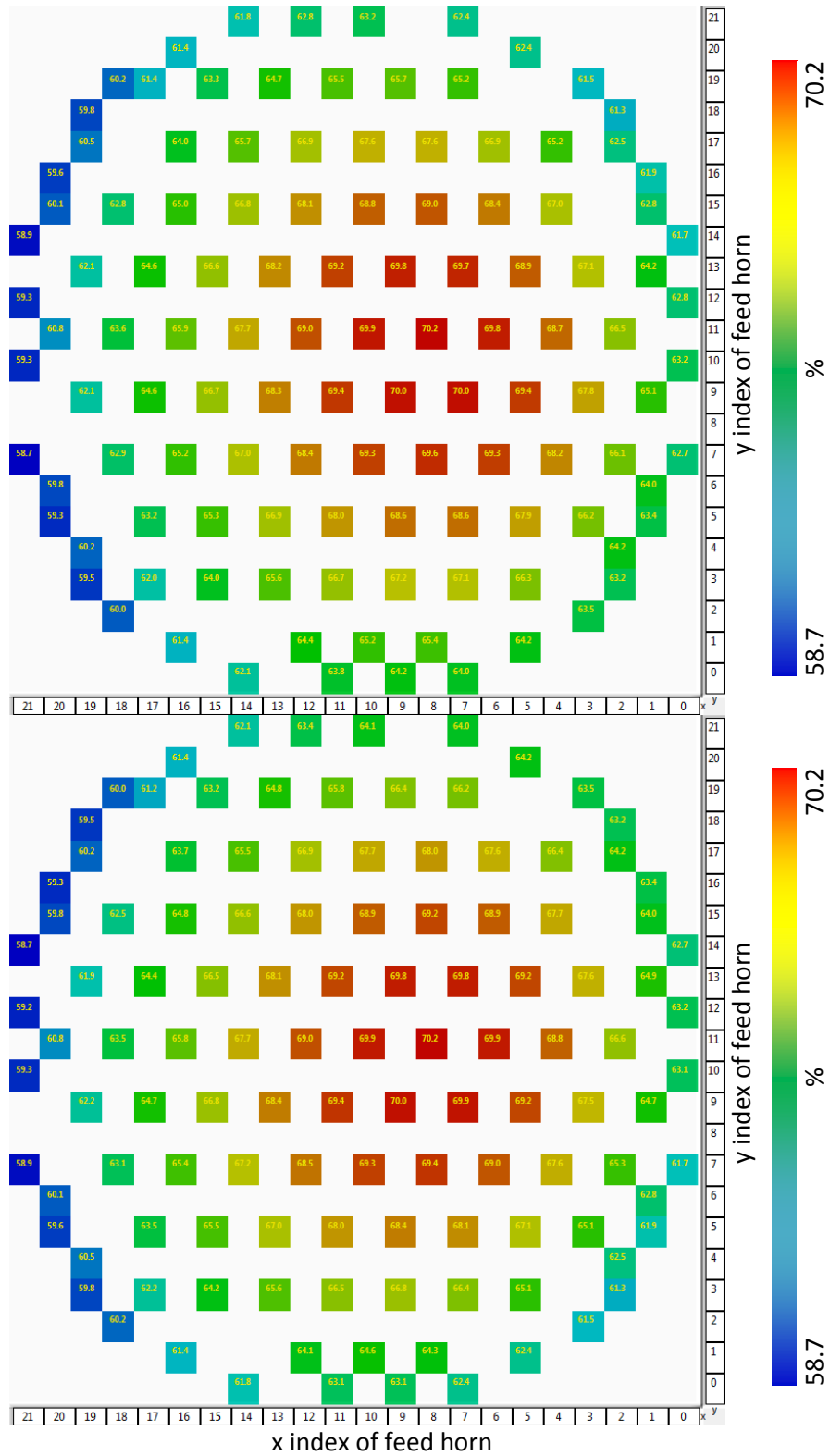


Figure A2.1: Detector plane power captured as a percentage of emitted power for primary mirror tolerance test for an x-axis rotational offset of -1° (top image) and $+1^\circ$ (bottom image). The pivot points and axis orientation are defined as shown in Figure 4.18.

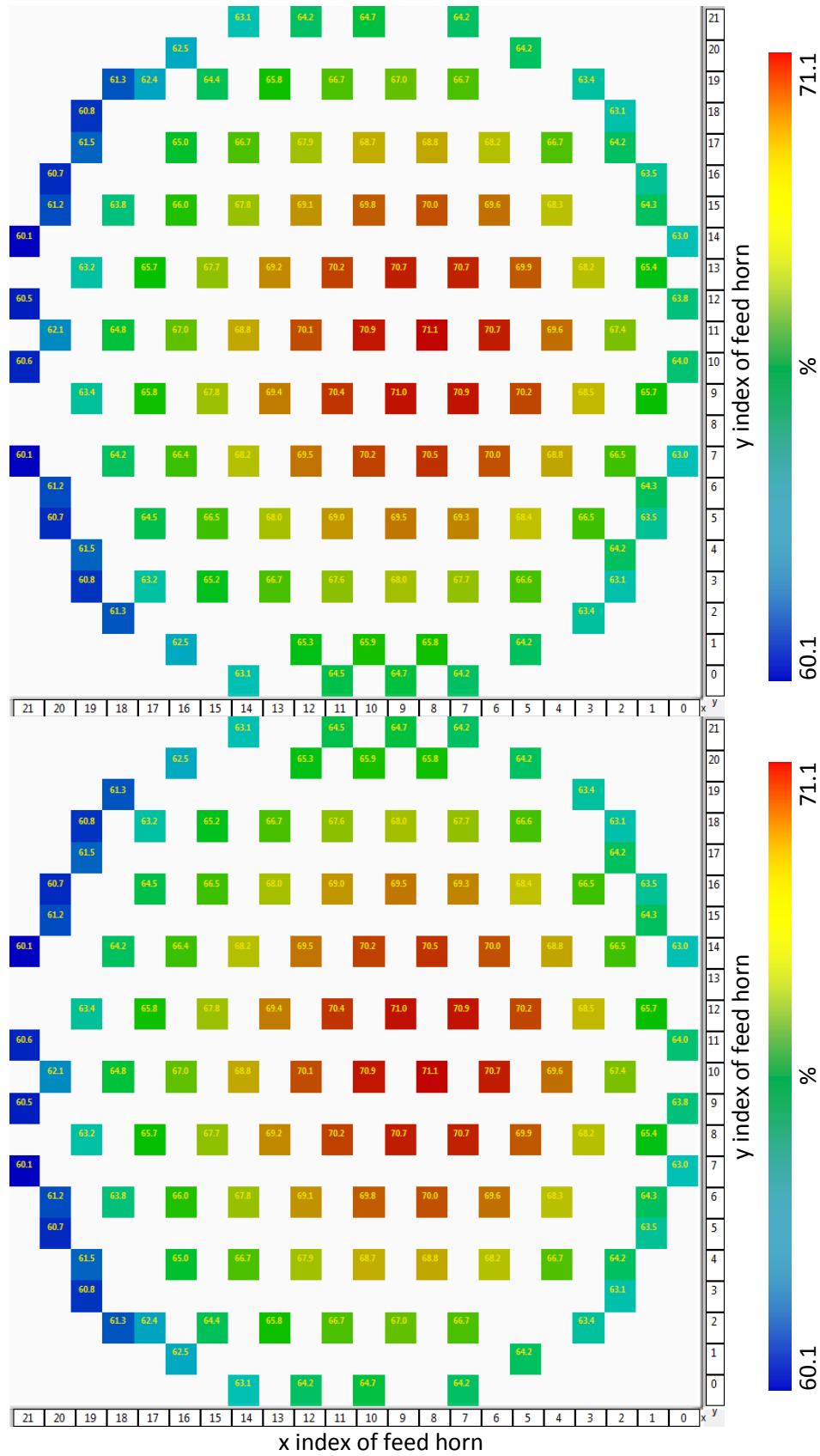


Figure A2.2: Detector plane power captured as a percentage of emitted power for primary mirror tolerance test for an x-axis translational offset of -1 mm (top image) and +1 mm (bottom image). The pivot points and axis orientation are defined as shown in Figure 4.18.

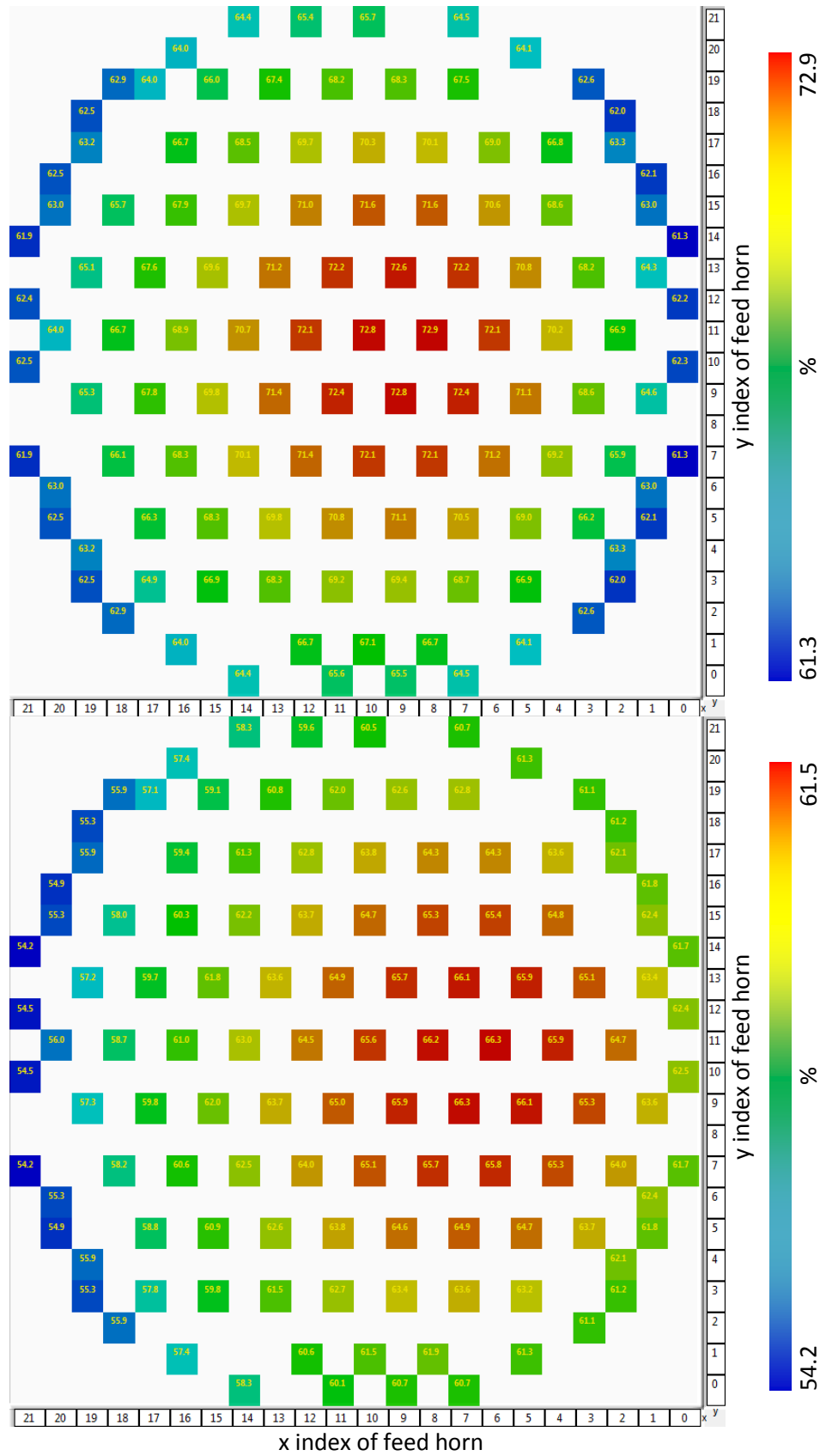


Figure A2.3: Detector plane power captured as a percentage of emitted power for primary mirror tolerance test for an y-axis rotational offset of -1° (top image) and $+1^\circ$ (bottom image). The pivot points and axis orientation are defined as shown in Figure 4.18.

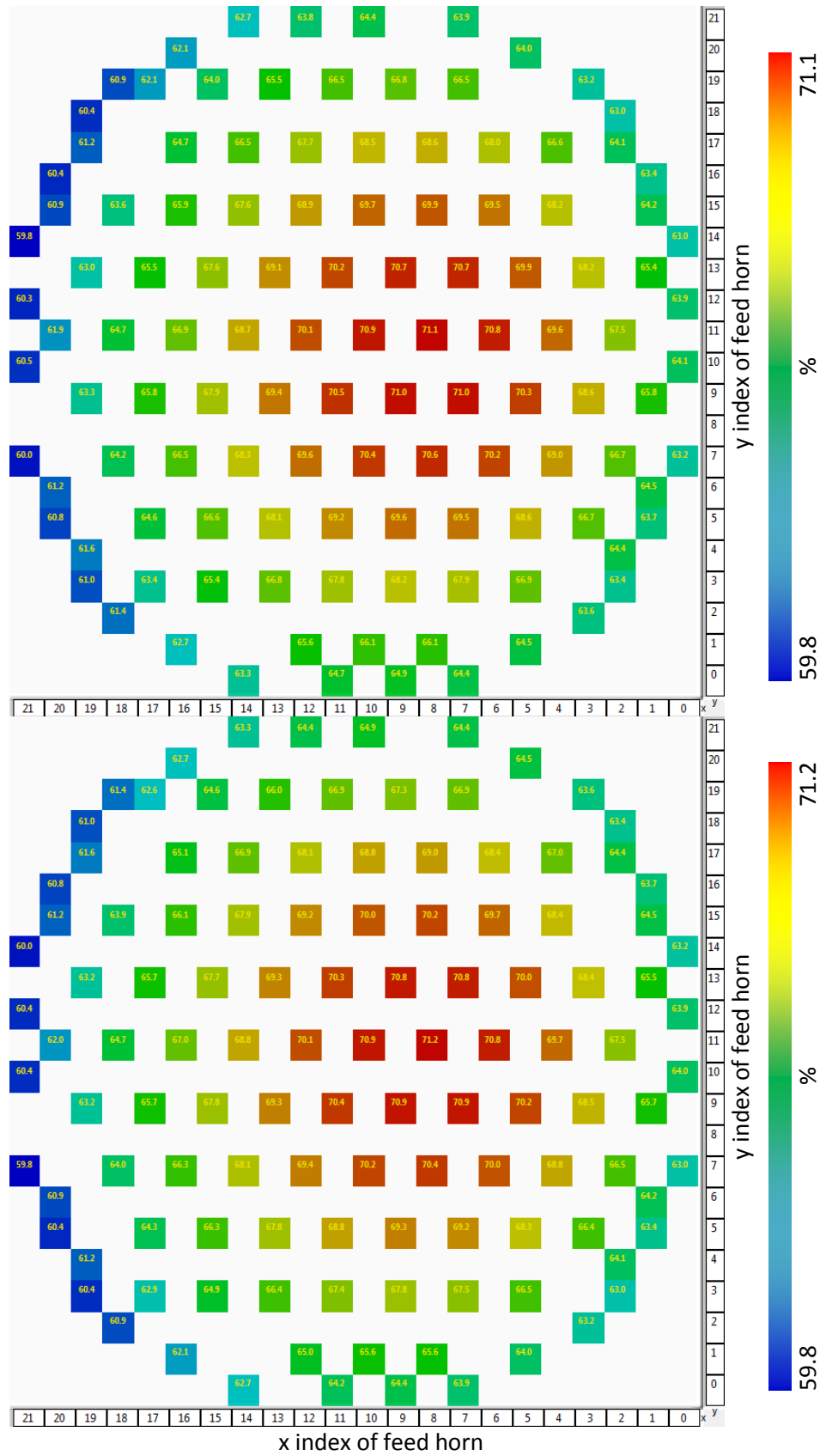


Figure A2.4: Detector plane power captured as a percentage of emitted power for primary mirror tolerance test for an y-axis translational offset of -1 mm (top image) and +1 mm (bottom image). The pivot points and axis orientation are defined as shown in Figure 4.18.

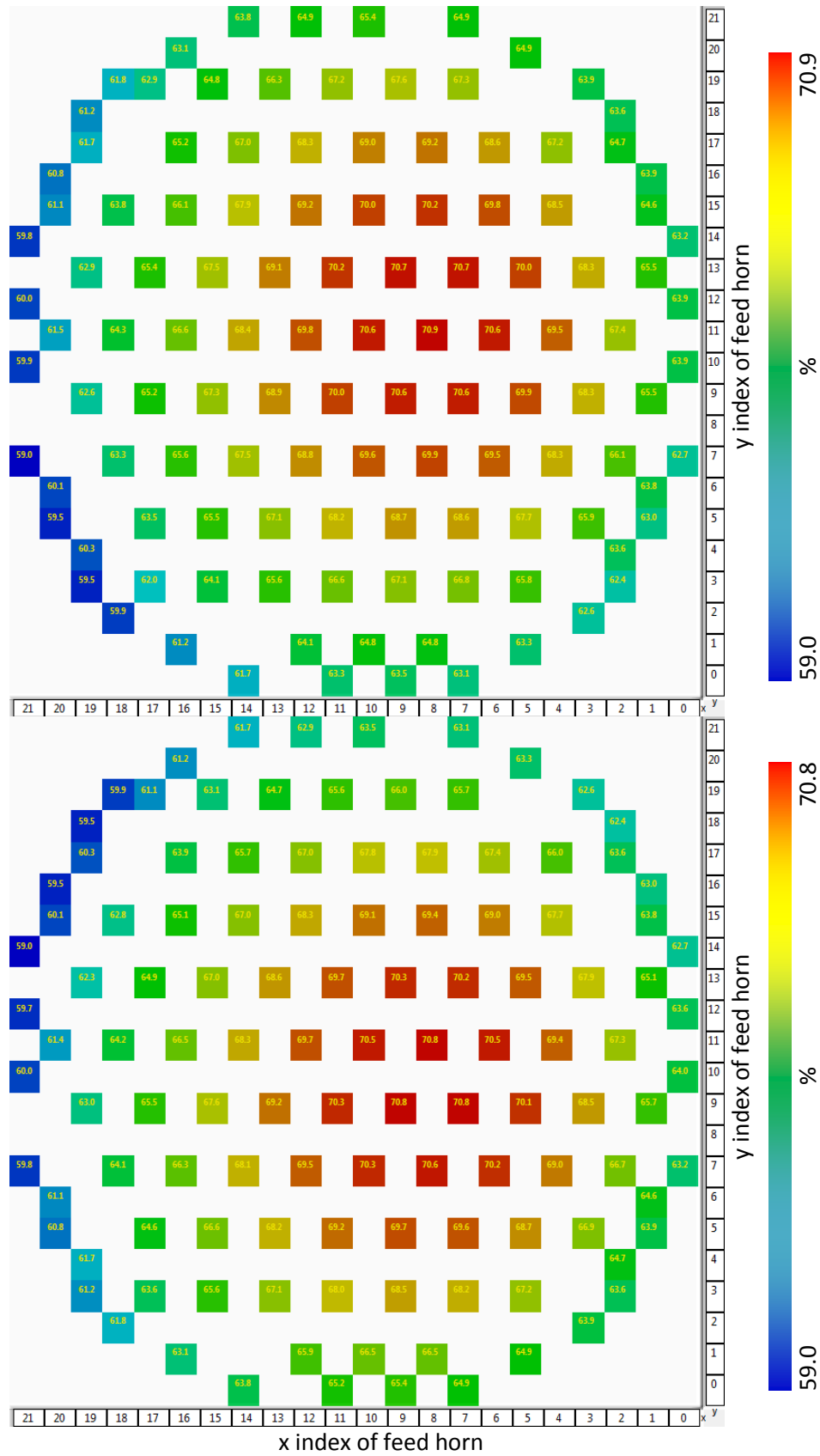


Figure A2.5: Detector plane power captured as a percentage of emitted power for primary mirror tolerance test for an z-axis rotational offset of -1° (top image) and $+1^\circ$ (bottom image). The pivot points and axis orientation are defined as shown in Figure 4.18.

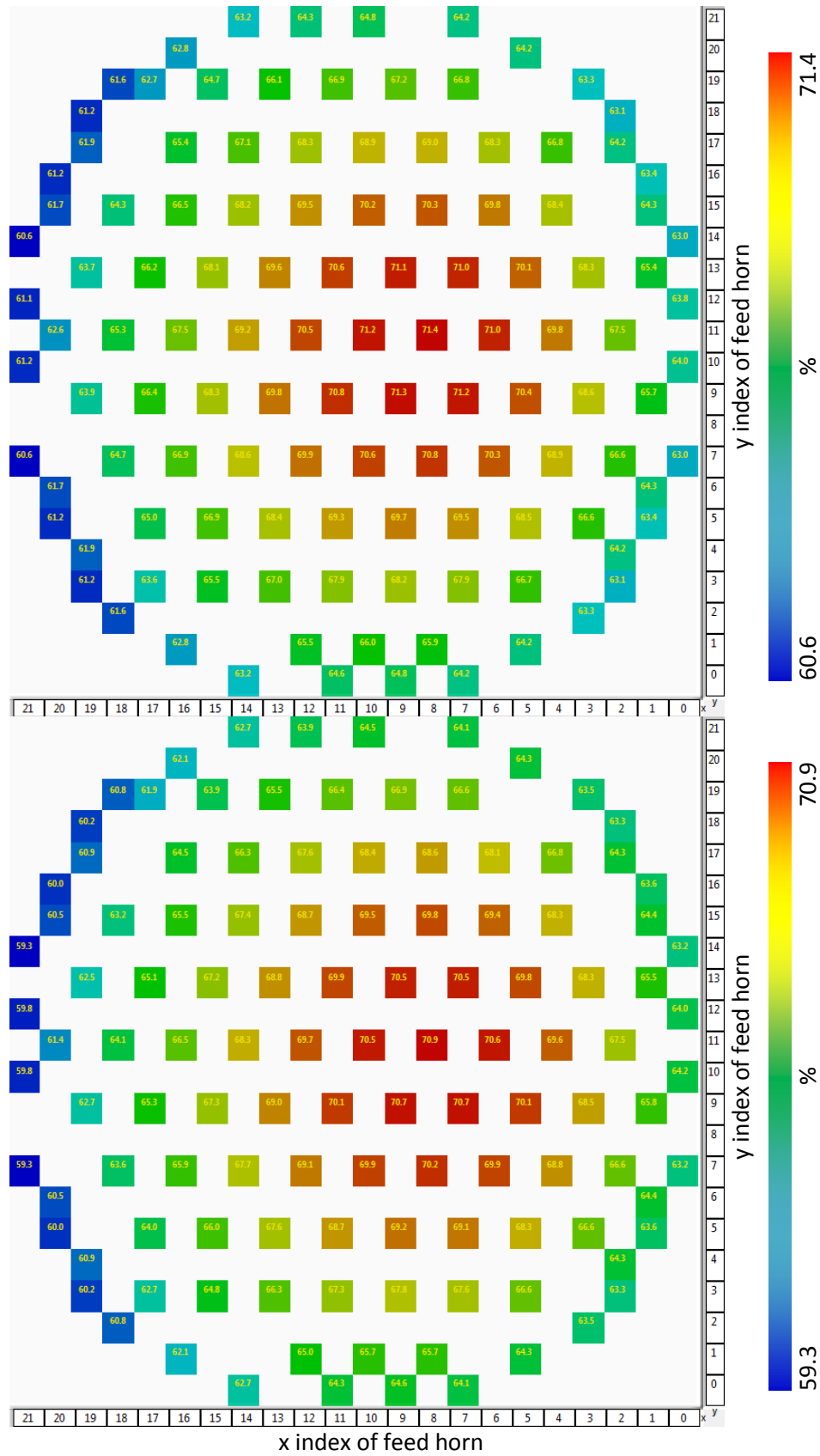


Figure A2.6: Detector plane power captured as a percentage of emitted power for primary mirror tolerance test for an z-axis translational offset of -1 mm (top image) and +1 mm (bottom image). The pivot points and axis orientation are defined as shown in Figure 4.18.

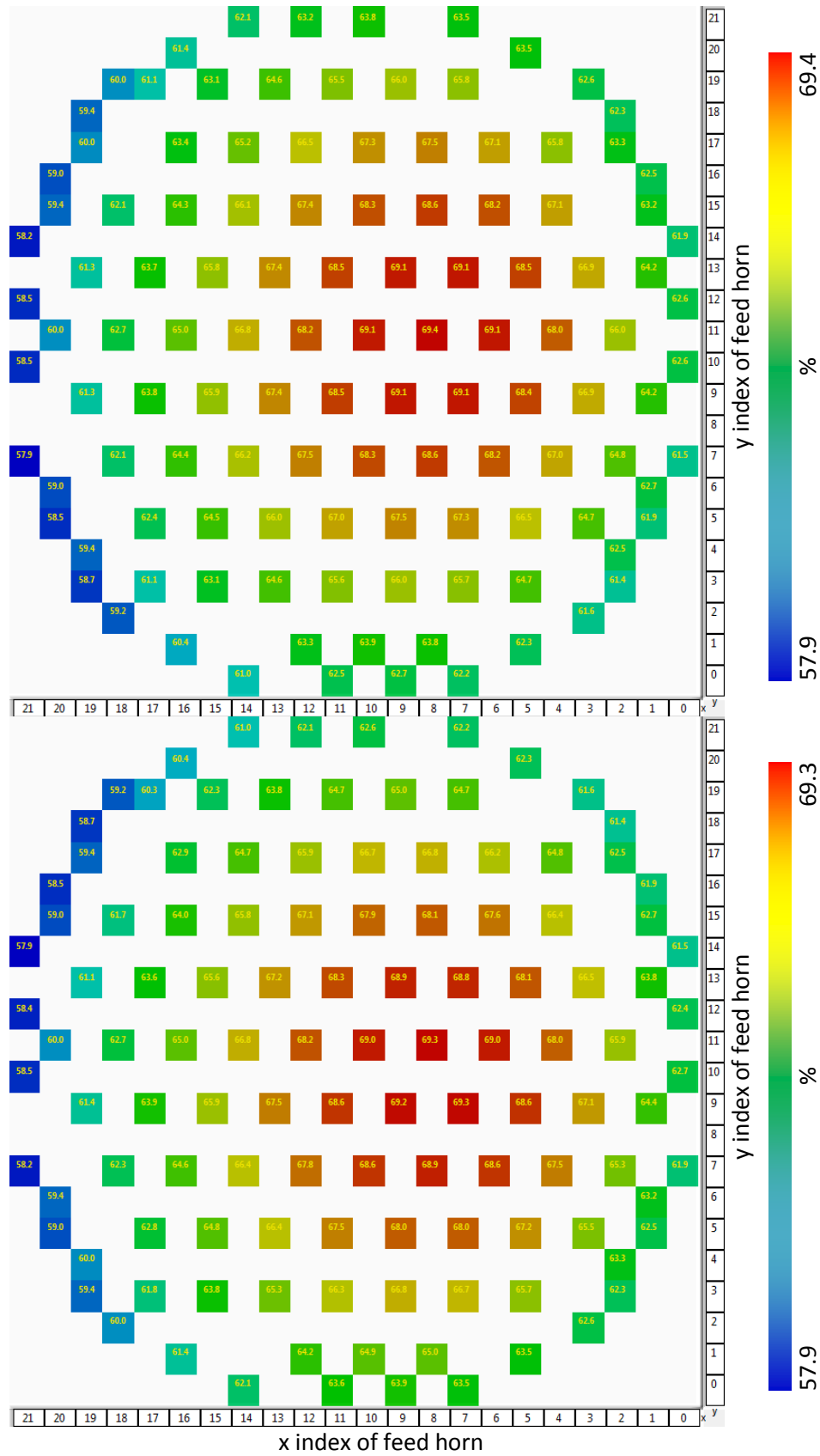


Figure A2.7: Detector plane power captured as a percentage of emitted power for secondary mirror tolerance test for an x-axis rotational offset of -1° (top image) and $+1^\circ$ (bottom image). The pivot points and axis orientation are defined as shown in Figure 4.18.

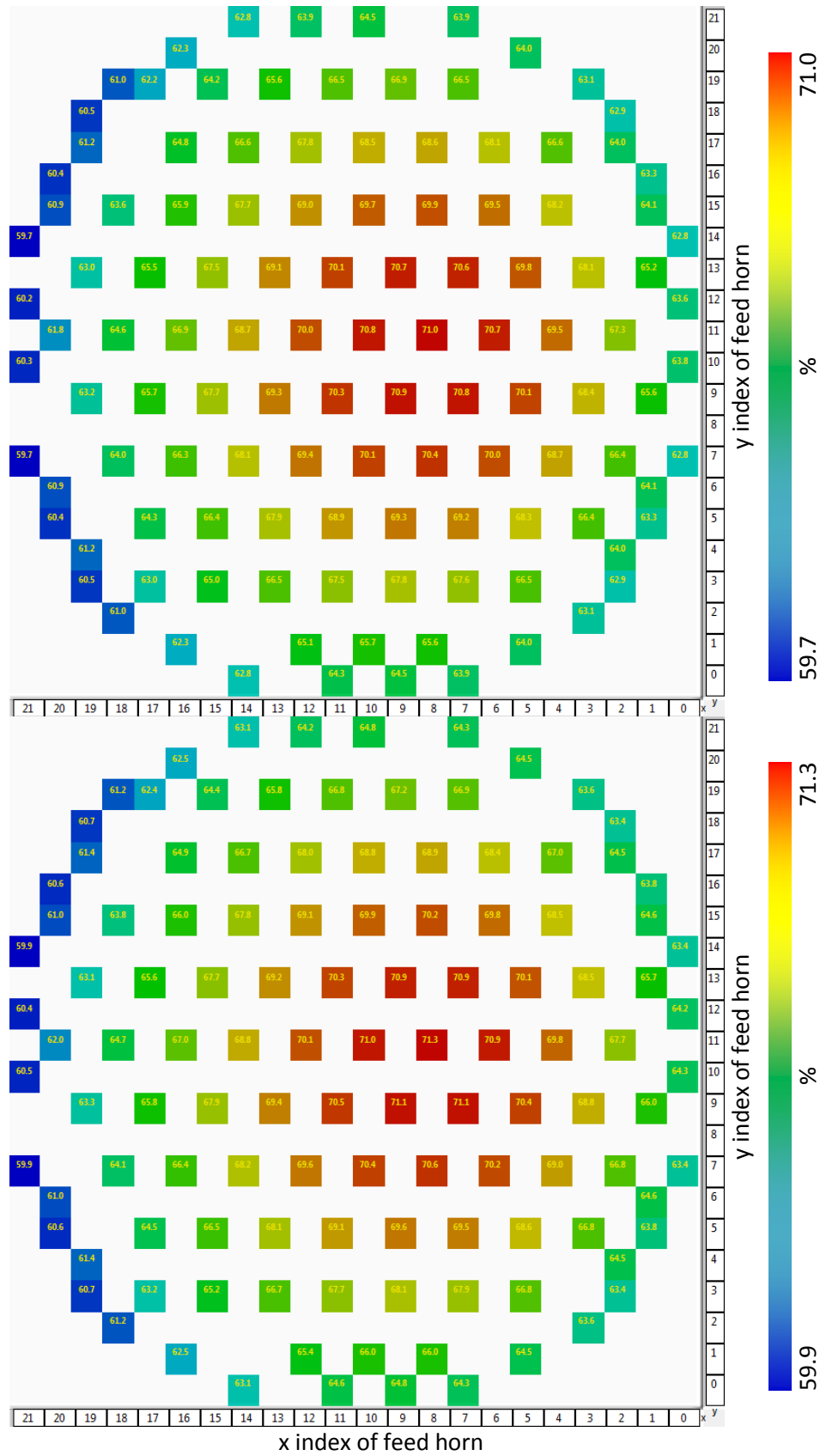


Figure A2.8: Detector plane power captured as a percentage of emitted power for secondary mirror tolerance test for an x-axis translational offset of -1 mm (top image) and +1 mm (bottom image). The pivot points and axis orientation are defined as shown in Figure 4.18.

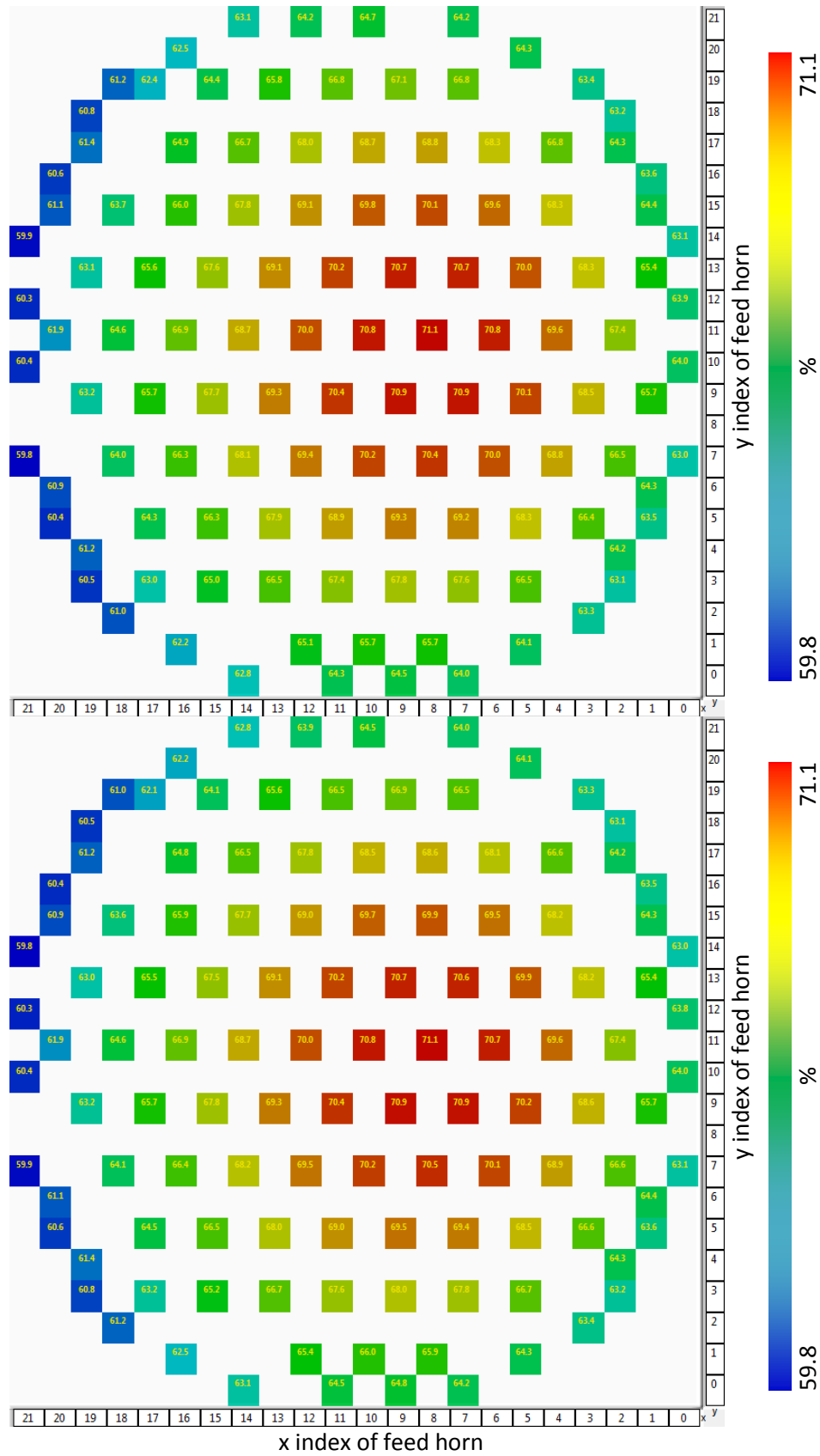


Figure A2.10: Detector plane power captured as a percentage of emitted power for secondary mirror tolerance test for an y-axis translational offset of -1 mm (top image) and +1 mm (bottom image). The pivot points and axis orientation are defined as shown in Figure 4.18.

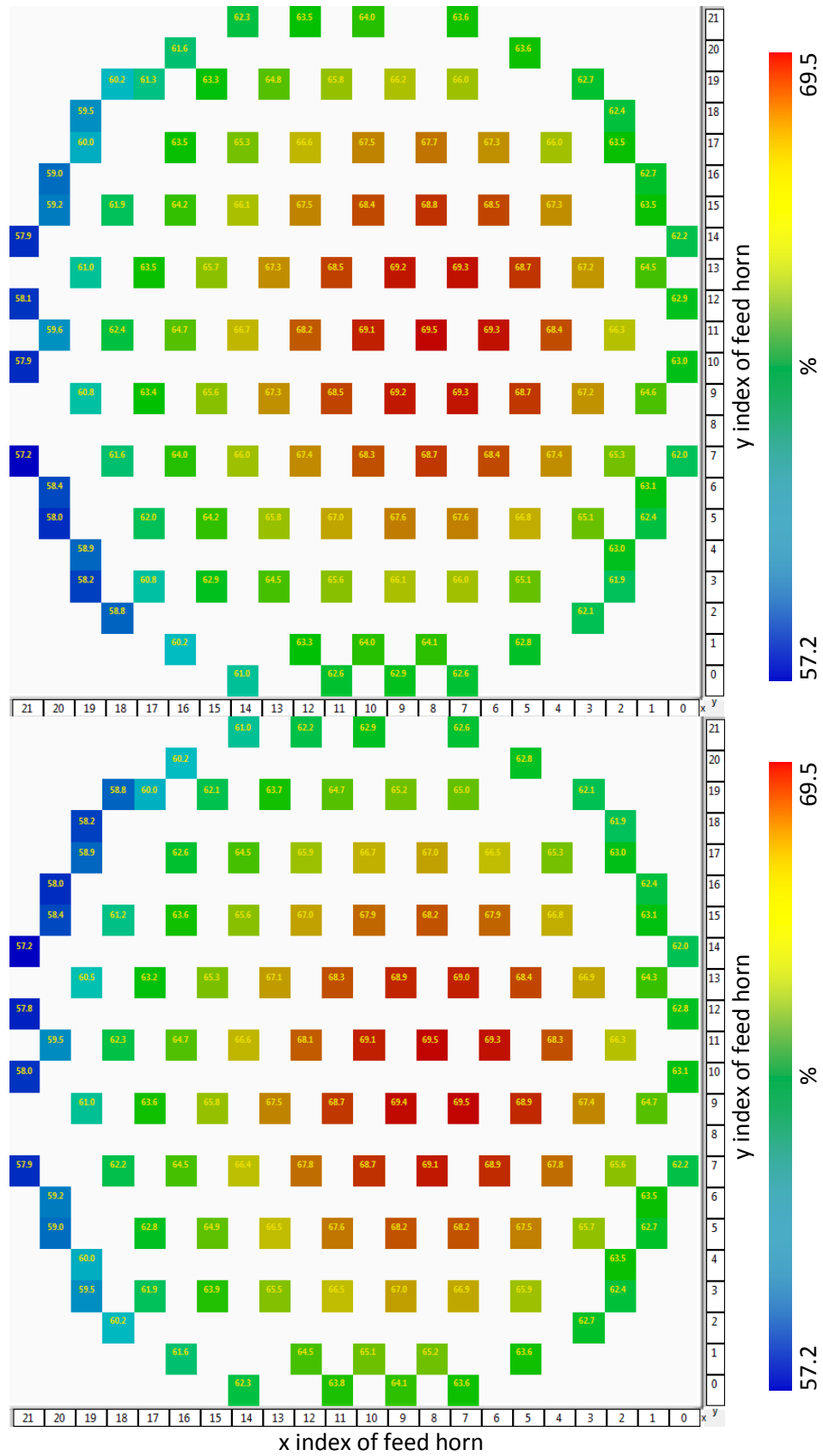


Figure A2.11: Detector plane power captured as a percentage of emitted power for secondary mirror tolerance test for an z-axis rotational offset of -1° (top image) and $+1^\circ$ (bottom image). The pivot points and axis orientation are defined as shown in Figure 4.18.

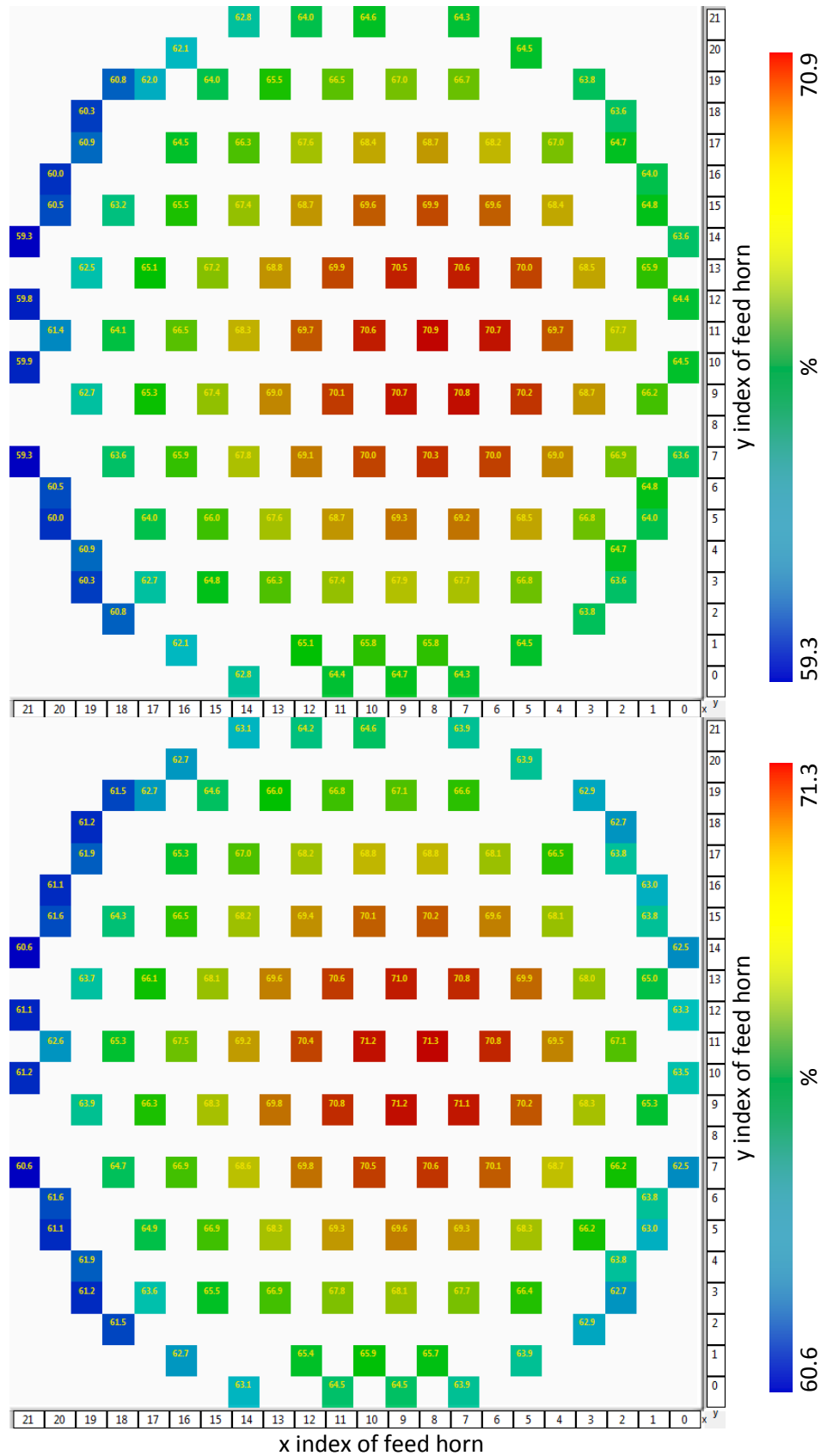


Figure A2.12: Detector plane power captured as a percentage of emitted power for secondary mirror tolerance test for an z-axis translational offset of -1 mm (top image) and +1 mm (bottom image). The pivot points and axis orientation are defined as shown in Figure 4.18

Appendix 3. Truncation: 420 mm limit

Where system symmetry holds, only half of the array will be tested.

a. Primary mirror one dimension horizontal centred truncation

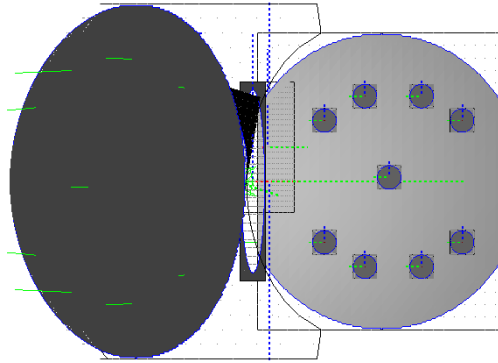


Figure A3.1: Truncated Mirrors (Primary 420x500mm and Secondary 600x600mm)

Table A3.1: System Mirror and Truncation Setup

	Translation (mm)			Rotation (°)			Dimensions (mm)		
	X	Y	Z	X	Y	Z	X	Y	Z
Primary Mirror	190						480	500	
Primary Truncation	190	0				0	420	500	

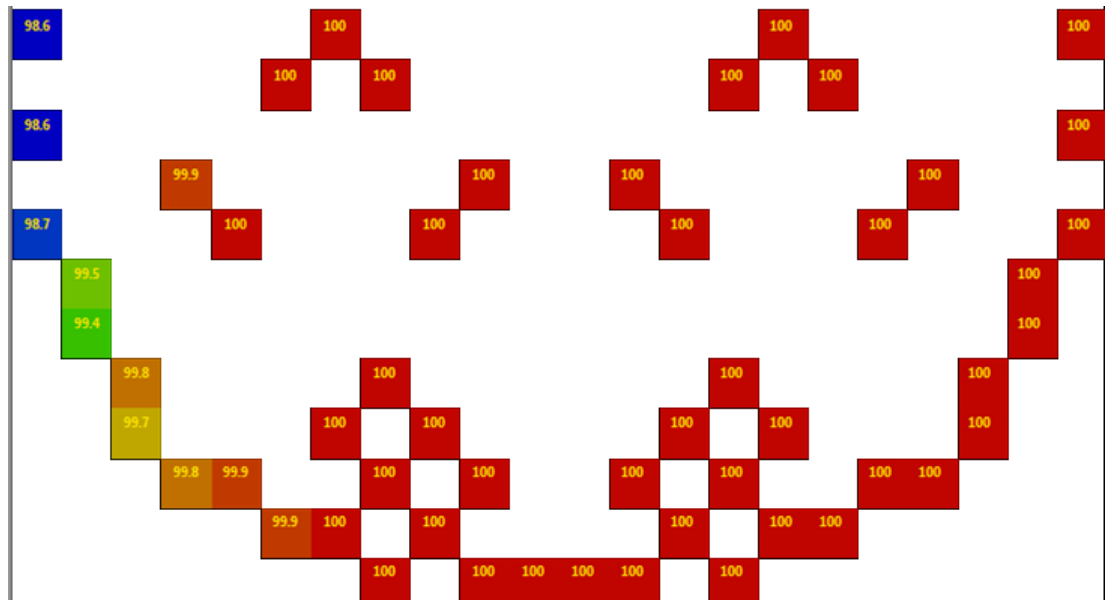


Figure A3.2: Primary Mirror Output (Primary 480x500mm, centrally truncated to 420mm laterally)

b. Primary mirror one dimension vertical centred truncation

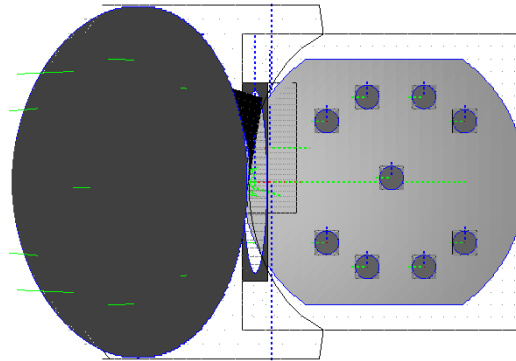


Figure A3.3: Truncated Mirrors (Primary 420x500mm and Secondary 600x600mm)

Table A3.2: System Mirror and Truncation Setup

	Translation (mm)			Rotation (°)			Dimensions (mm)		
	X	Y	Z	X	Y	Z	X	Y	Z
Primary Mirror	190						480	500	
Primary Truncation	190	0				90	420	500	

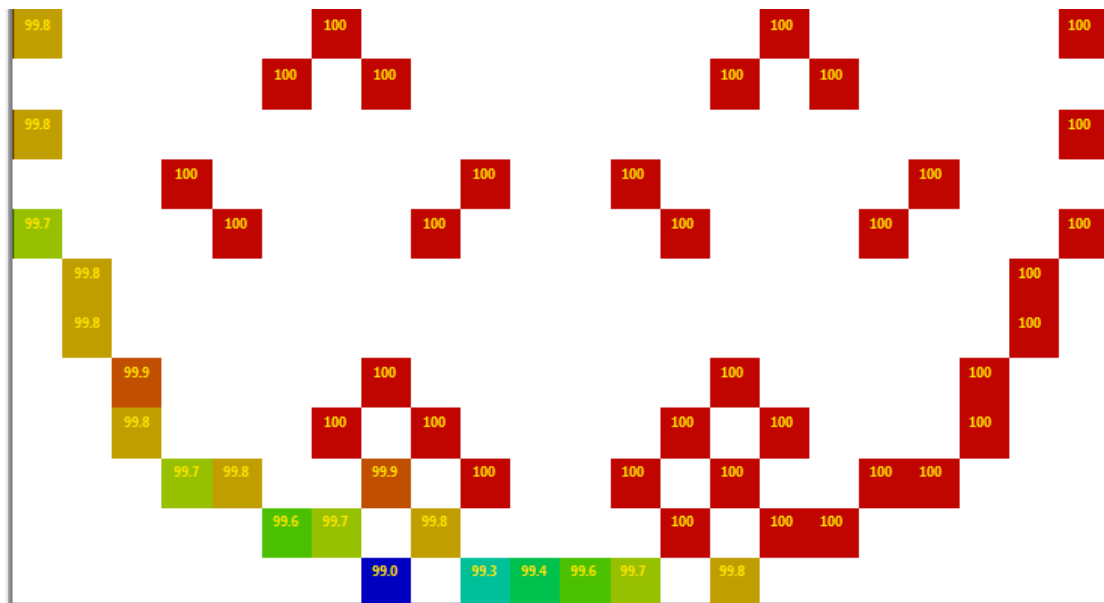


Figure A3.4: Primary Mirror Output (Primary 480x500mm, centrally truncated to 420mm vertically)

c. Primary mirror one dimension 45° centred truncation

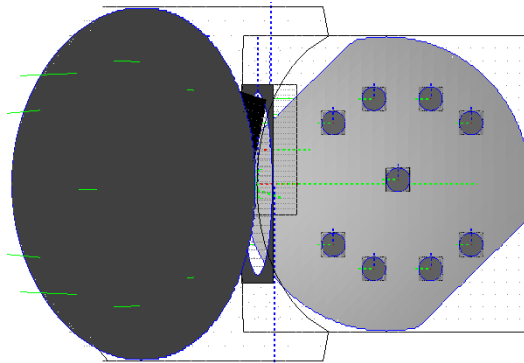


Figure A3.5: Primary Mirror Output (No Offset; Primary 480x500mm truncated at -45° to 420mm)

Table A3.3: System Mirror and Truncation Setup

	Translation (mm)			Rotation (°)			Dimensions (mm)		
	X	Y	Z	X	Y	Z	X	Y	Z
Primary Mirror	190						480	500	
Primary Truncation	190					-45	420	500	

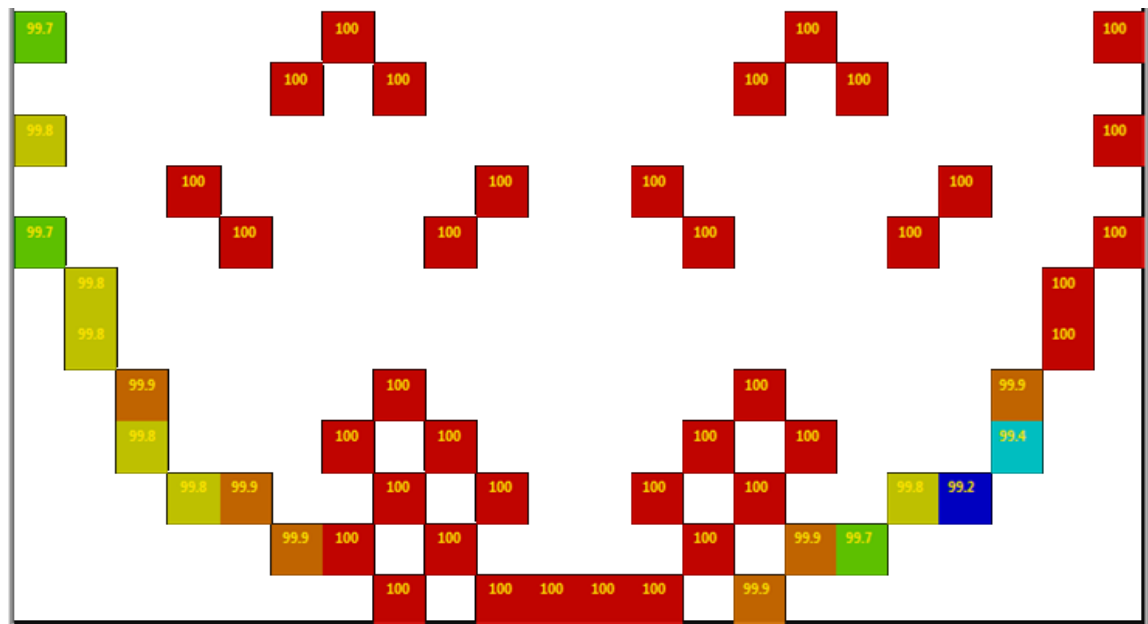


Figure A3.6: Primary Mirror Output (Primary 480x500mm truncated at 45° to 420mm)

d. Primary mirror one dimension 45° 12.5 mm offset truncation

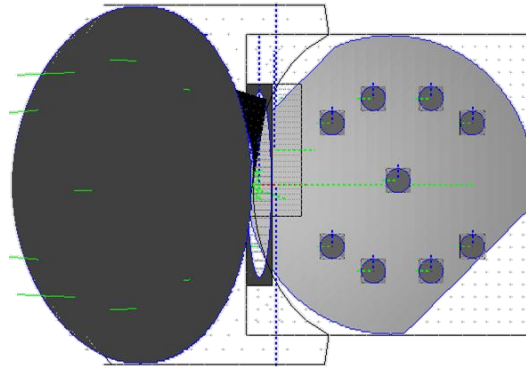


Figure A3.7: Primary mirror with dimensions 480x500 mm truncated with a centre offset of 12.5 mm in x and y at 45° to 420mm

Table A3.4: System Mirror and Truncation Setup

	Translation (mm)			Rotation (°)			Dimensions (mm)		
	X	Y	Z	X	Y	Z	X	Y	Z
Primary Mirror	190						480	500	
Primary Truncation	177.5	12.5				-45	420	500	

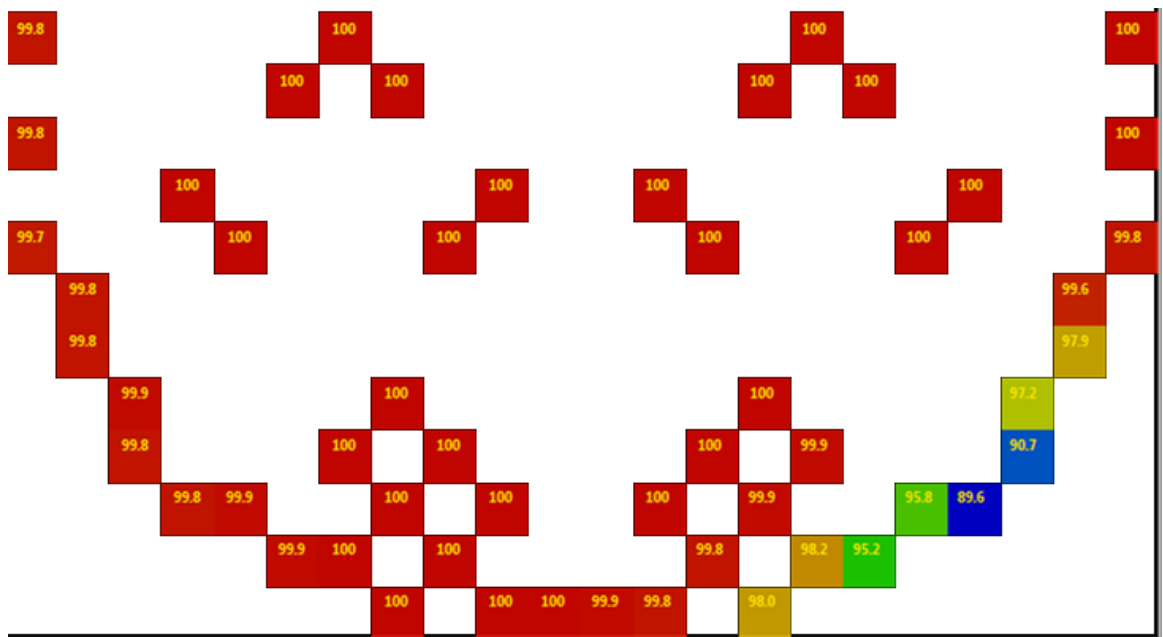


Figure A3.8: Primary Mirror Output (Primary 480x500mm truncated at 45° to 420mm with 12.5mm offset)

e. Primary mirror one dimension 40° 25 mm offset truncation

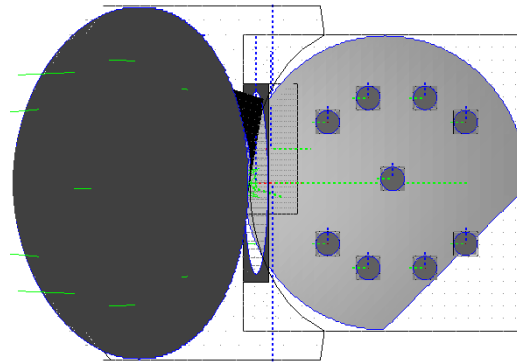


Figure A3.9: Primary mirror at 480×500mm and truncated at 40° to 420 mm on the x00y00 corner using a truncation centre offset of 25 mm in X and Y

Table A3.5: Primary mirror and truncation setup

	Translation (mm)			Rotation (°)			Dimensions (mm)		
	X	Y	Z	X	Y	Z	X	Y	Z
Primary Mirror	190						480	500	
Primary Truncation	165	25				-40	420	500	

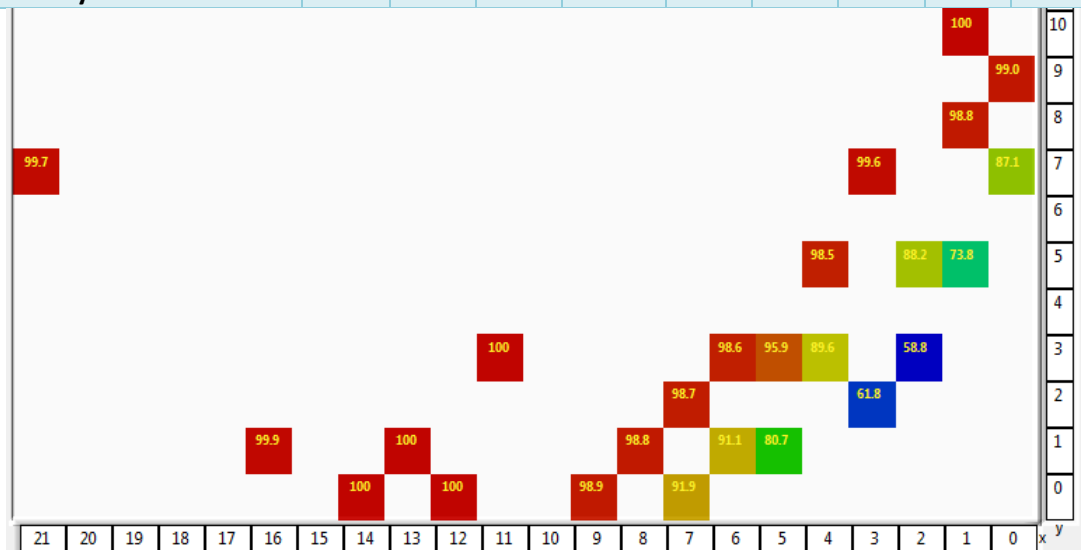


Figure A3.10: Primary mirror at 480×500mm and truncated at 40° to 420 mm on the x00y00 corner using a truncation centre offset of 25 mm in X and Y

- f. Primary mirror one dimension 45° 25 mm offset and secondary mirror one dimension 50° 40 mm offset truncation

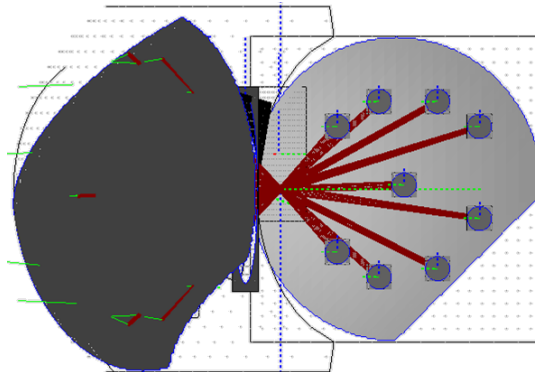


Figure A3.11: Truncated Mirrors (Primary 420x500 mm @ 45° and Secondary 420x600 mm @ 50° Offset 40 mm)

Table A3.6: System Mirror and Truncation Setup

	Translation (mm)			Rotation ($^\circ$)			Dimensions (mm)		
	X	Y	Z	X	Y	Z	X	Y	Z
Primary Mirror	190						480	500	
Primary Truncation	165	25				-45	420	500	
Secondary Mirror	-150						600	600	
Secondary Truncation	-110	40				50	420	600	

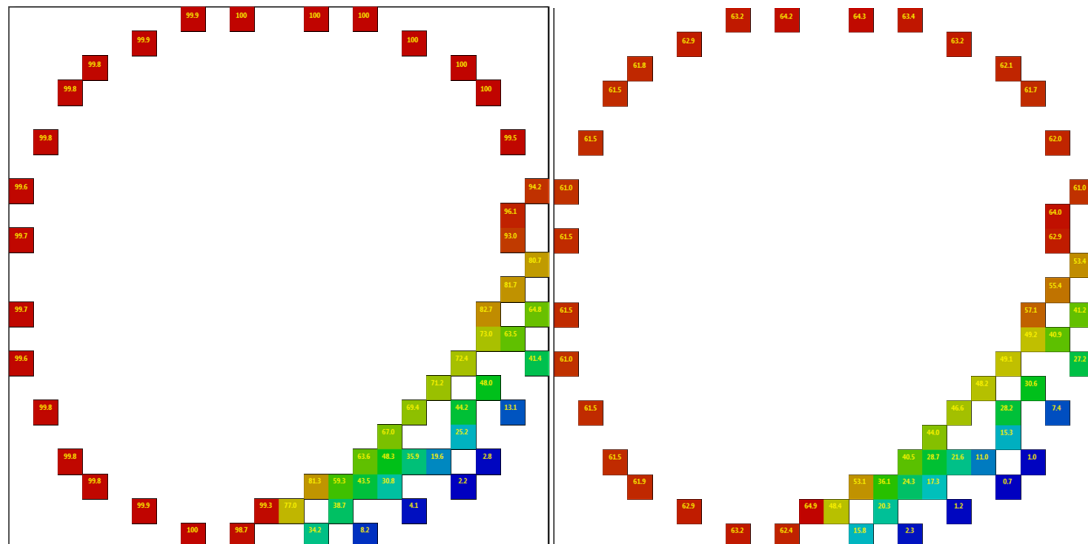


Figure A3.12: Left is the secondary mirror capture (600x600 mm truncated at 50° to 420mm with xy offsets of 40 mm) and right the detector plane capture at 51 mm radius after accounting for truncation from primary, secondary and polariser.